SCHOLARLY PUBLICATIONS

A CURRENT AWARENESS BULLETIN
OF RESEARCH OUTPUT

@DTU

(53rd Edition)

MAY 2017

BY: CENTRAL LIBRARY

DELHI TECHNOLOGICAL UNIVERSITY
(FORMERLY *DELHI COLLEGE OF ENGINEERING)*
GOVT. OF N.C.T. OF DELHI
SHAHBAD DAULATPUR, MAIN BAWANA ROAD
DELHI 110042

PREFACE

This is the **Fifty third** Issue of Current Awareness Bulletin started by Delhi Technological University, Central Library. The aim of the bulletin is to compile, preserve and disseminate information published by the faculty, students and alumni for mutual benefits. The bulletin also aims to propagate the intellectual contribution of Delhi Technological University (DTU) as a whole to the academia.

The bulletin contains information resources available in the internet in the form of articles, reports, presentations published in international journals, websites, etc. by the faculty and students of DTU. The publications of faculty and student which are not covered in this bulletin may be because of the reason that the full text either was not accessible or could not be searched by the search engine used by the library for this purpose.

The learned faculty and students are requested to provide their uncovered publications to the library either through email or in CD, etc to make the bulletin more comprehensive.

This issue contains the information published during **May 2017**. The arrangement of the contents is alphabetical. The full text of the article which is either subscribed by the university or available in the web is provided in this bulletin.

Central Library

CONTENTS

1. A facile amidation of chloroacetyl chloride using DBU, ***6.Deepak Mishra***, ***3.Ram Singh*** and Chittaranjan Rout, Applied Chemistry, DTU

2. A Novel Facial Image Resolution Enhancement Algorithm using Pixels Homogeneity, Vikram Mutneja and ***7.1.Dr. Satvir Singh***, ECE, DTU

3. An eco-friendly and inexpensive solvent for solution processable CuSCN as a hole transporting layer in organic solar cells, ***6.Neeraj Chaudhary***, ***3.Rajiv Chaudhary***, ***3.J.P. Kesari*** and Asit Patra, Mechanical, DTU

4. Application of Big Data in Supply Chain Management, ***8.Ankit Singh***, Deepak Jain, Ishant Mehta, Jishnu Mitra and Saurabh Agrawal, Mechanical and Automotive, DTU

5. CFD Analysis of Wavy Microchannel Heat Sink with Hemispherical Obstructions and Comparing it with Experimental Results of Rectangular Microchannel Heat Sink, ***7.Rajnish Kumar*** and ***3.M. Zunaid***, Mechanical, DTU

6. Characterization of magnetic abrasive particles based Magnetorheological polishing fluid, ***3.M. S. Niranjan***, ***6.Krishna Pratap Singh*** and ***3.Qasim Murtaza***, Mechanical, DTU

7. Comments on Modulus Ratio and Joint Factor Concepts to Predict Rock Mass Response, ***3.Ashutosh Trivedi***, Civil, DTU

8. Comparative Analysis of Biodiesel as A Additive with Pure Diesel in Single Cylinder Four Stroke Diesel Engine Processes, Ashutosh Kumar, Hukam Singh, Avnish Kumar Shukla, Pawan Mishra and ***7.1.Ashutosh Kumar Rai***, Mechanical, DTU

9. Design and Control of DC Microgrid based on Solar PV and Storage, ***6.Priyanka Chaudhary*** and ***3.M. Rizwan***, Electrical, DTU

10. Design and Solidification Simulation of Exhaust Manifold Made of SiMo Ductile Cast Iron, ***3.Vijay Gautam***, ***8.1.Sahil Ahuja*** and ***6.Nanak Ram***, Mechanical, DTU

11. Direction of Arrival estimation of underwater acoustic signal via Virtual Steering, ***6.Vikas Kumar Singh*** and ***6.Rashmi***, Electrical and Computer, DTU

12. Dynamic Motion Planning for Aerial Surveillance on a Fixed-Wing UAV, ***6.Vaibhav Darbari***, ***6.Saksham Gupta*** and ***3.Om Prakash Verma,*** CSE, DTU

13. Effect of trench depth and gate length shrinking assessment on the analog and linearity performance of TGRC-MOSFET, ***6.Ajay Kumar***, Electrical, DTU

14. Electronic Properties and Migration Pathways of Cl Functionalized Zigzag Graphene Nanoribbons, Neeraj K. Jaiswal, Amit Kumar, ***6.Neha Tyagi*** and Pankaj Srivastava, Applied Physics, DTU

15. Energy and performance analysis of multi droplets shower cooling tower at different inlet water temperature for air cooling application, ***3.Mohammad Zunaid***, Qasim Murtaza and ***3.Samsher Gautam***, Mechanical, DTU

16. Estimation of stochastic environment force for master–slave robotic system, ***6.1.NEELU NAGPAL***, ***3.BHARAT BHUSHAN*** and VIJYANT AGARWAL, Electrical, DTU

17. Evaluation of Energy Ratios Using Life Cycle Analysis for Mahua, Jatropha and Neem Biodiesels, Mukesh Kumar, Onkar Singh and ***3.Naveen Kumar,*** Mechanical, DTU

18. Experimental Analysis of Performance and Emissions of a Diesel Engine Fuelled With Biodiesels (Mahua and Neem), Mukesh Kumar, Onkar Singh and ***3.Naveen Kumar***, Mechanical, DTU

19. Experimental Analysis of Surface Roughness in CNC Taper Turning of Aluminum 6061 Using Taguchi Technique, ***7.Sanchay Gupta, 8.Vimanyu Chadha, 8.Vishal Sardana, 8.Viplav Setia*** and ***3.Ranganath M Singari***, Mechanical, Production and Industrial, DTU

20. Experimental investigation of performance and emission characteristics of Palm oil, P. K. Chaudhary1, ***3.A. Pal***, Kunal Chauhan and Shailendra Nath Tiwari, Mechanical, DTU

21. Fatigue failure prediction in spur gear pair using AGMA approach, ***3.Paras Kumara***, Harish Hiranib and ***3.Atul Agrawala***, Mechanical, DTU

22. Hydrochemical characterization and suitability assessment of groundwater in Baga–Calangute stretch of Goa, India, ***3.A. K. Haritash***, ***6.Karamveer Mathur***, ***6.Priyanka Singh*** and ***3.S. K. Singh***, Environmental Engineering, DTU

23. Improvement in dielectric, ferroelectric and ferromagnetic characteristics of Ba0.9Sr0.1Zr0.1Ti0.9O3-NiFe2O4 composites, ***7.Aditya Jain***, ***3.Amrish K. Panwar***, A.K. Jhab and Yogesh Sharma, Applied Physics, DTU

24. Major ions chemistry of surface water in Bhindawas wetland, ***6.Vandana Shan, 3.SK Singh*** and ***3.AK Haritash*****,** Environmental, DTU

25. Multicolor and white light emitting Tb3+/Sm3+ doped zinc phosphate barium titanate glasses via energy transfer for optoelectronic device applications, ***3.Kaushal Jha***, ***3.Amit K. Vishwakarma***, ***3.M. Jayasimhadri*** and D. Haranath, Applied Physics, DTU

26. Numerical simulations of novel SiGe-based IBC-HJ solar cell for standalone and mechanically stacked tandem applications, ***7.Rahul Pandey*** and ***3.Rishu Chaujar***, Physics, DTU

27. Object picking using robotic arm mounted with a camera for detection using image processing, ***6.Vikas Kumar Singh*** and Sugandha Singh, Electrical, DTU

28. Ontology Driven Sentiment Analysis on Social Web for Government Intelligence, ***3.Akshi Kumar*** and ***6.Arunima Joshi***, Computer Science, DTU

29. Opportunistic Self Organizing Migrating Algorithm for Real-Time Dynamic Traveling Salesman Problem, [1]***8.Shubham Dokania***, [2]***8.Sunyam Baggay*** and [2]***8.Rohit Sharma***, [2]Computer Science and [1]Applied Mathematics, DTU

30. Optical effective mass of photon in single and bilayer graphene in 10 MHz to 26.5 GHz frequency range, ***7.Kamlesh Patel*** and ***3.Pawan K. Tyagi***, Applied Physics, DTU

31. Optimization of Machining Parameters in CNC Turning of Hybrid Metal Matrix Composites Using Different Techniques: A Review, ***6.Vaibhav Sharma*** and ***3.Ravi Butola***, Mechanical, DTU

32. Potential application of multilayer n-type tungsten diselenide (WSe2) sheet as transparent conducting electrode in silicon heterojunction solar cell, ***7.Pranjala Tiwari***, ***6.Kamlesh Patel***, ***6.Lucky Krishnia***, ***6.Reetu Kumari*** and ***3.Pawan K. Tyagi***, Applied Physics, DTU

33. Quantum Key Distribution Simulation, Suhail Akhtar, ***7.1.Pradeep Kumar***, Abdul Wahid, Computer, DTU

34. Realization of all optical logic gates using universal NAND gates on photonic crystal platform, ***6.Preeti Rani***, ***7.Shiba Fatima***, ***3.Yogita Kalra*** and ***3.R.K. Sinha***, Applied Physics, DTU

35. Review based emotion profiles for cross domain recommendation, ***8.1.Shampa Chakraverty*** & Mala Saraswat, Electronics and Communication, DTU

36. Structural Design &Optimization Of An Unmanned Aerial Vehicle Wing For SAE Aero Design Challenge, ***8.Harsh Raj Chauhan***, ***8.Harsh Panwar*** and ***3.Vikas Rastogi***, Mechanical, DTU

37. Structural Insights of Induced pluripotent stem cell regulatory factors Oct4 and its Interaction with Sox2 and Fgf4 Gene, ***6.Vimal Kishor Singh***, Neeraj Kumar and Ramesh Chandra, Biotechnology, DTU

38. Study of Concentrated Solar Power and Their Application in Metro Stations, Hukam Singh, Shailesh Kumar Singh, ***7.1.Ashutosh Kumar Rai*** and ***3.Rangnath MS***, Mechanical, DTU

39. STUDY OF SHEAR BEHAVIOUR OF YAMUNA SAND BLENDED WITH SOFT SOIL, ***7.Deepak Rana***, ***7.Ankit Soni*** and Farukh Ali, Civil, DTU

40. Two start and Three Start Helical Abrasive Flow Machining for Brittle Materials, ***3.Ravi Butola***, Qasim Murtaza, ***3.R.S.Walia*** and ***3.Pradeep Kumar***, Mechanical, Production & Industrial and Automobile, DTU

41. Volterra Model of Silicon Controlled Rectifier, ***6.Amit Kumar Gautam*** and ***3.Sudipta Majumdar***, Electronics & Communication, DTU

42. X-ray diffraction patterns and diffracted intensity of Kα spectral lines of Helike ions, Arun Goyal, Indu Khatri, A. K. Singh, ***3.Rinku Sharma*** and Man Mohan, Applied Physics, DTU

1. *Chancellor*

2. *Pro Vice Chancellor*	***2.1.*** *Ex Pro Vice Chancellor*
3. *Faculty*	***3.1.*** *Ex Faculty*
4. *Teaching-cum-Research Fellow*	***4.1.****Asst. Librarian*
5. *Alumni*	
6. *Research Scholar*	***6.1.*** *Ex Research Scholar*
7. *PG Scholar*	***7.1.*** *Ex PG Scholar*
8. *Undergraduate Student*	***8.1.*** *Ex Undergraduate Student*

International Journal of ChemTech Research
CODEN (USA): IJCRGG, ISSN: 0974-4290, ISSN(Online):2455-9555
Vol.10 No.3, pp 365-372, 2017

A facile amidation of chloroacetyl chloride using DBU

Deepak Mishra[1,2], Ram Singh[1]* and Chittaranjan Rout[2]

[1]Department of Applied Chemistry, Delhi Technological University, Delhi – 110 042, India
[2]Department of Biotechnology and Bioinformatics, Jaypee University of Information Technology, Himachal Pradesh, India

Abstract : A facile one-pot process for the synthesis of amides from aromatic amines and chloroacetyl chloride has been developed using DBU. The method gave 75 to 95% yields in 3-6 h using tetrahydrofuran (THF) as a solvent at room temperature. The products have been characterized by mp, IR, ^{1}H NMR and elemental analysis.
Keywords: Amide bond formation, Aryl amines, chloroacetyl chloride, DBU, DABCO, THF.

Introduction

Amide functional group plays a vital role in organic synthesis.[1] A large number of natural and synthetic molecules possess this functional group. The synthetic chemists are always looking for better methods for the formation of amide bond.[2-6] The condensation of an amine or aniline with carboxylic acid or its derivatives is commonly employed method for amide bond formation.[2-6] The reported methods are not suitable for all the universally applicable substrate classes. We needed an efficient process to synthesize different N-aryl amides for a drug discovery program. The synthesized N-phenylacetamides, N-benzothiazol-2-ylacetamides and N-(4-phenylthiazol-2-yl)acetamides have great interest in recent years due to their wide role in the synthesis of biologically active compounds that exhibit pharmaceutical properties like analgesic activities,[7] $S1P_1$ receptor agonist,[8] A_2B adenosine receptor,[9] HIV-1 reverse transcriptase inhibitor,[10] anticancer activity,[11] antimicrobial and antituberculosis,[12-14] COX-2 inhibitors[15]. Several synthetic methodologies has been adopted for the synthesis of 2- chloroacetamide in solution phase using a various solvent with different bases such as TEA in DMF,[16] TEA in DCM,[8] toluene,[17] K_2CO_3 in benzene,[13] TEA in THF[18], TEA in dioxane.[15] However, in spite of their potential utility, many of these reported methods suffer from drawbacks such as harsh reaction conditions, long reaction times, unsatisfactory yields, tedious product isolation procedures and needs purification by column chromatography.[15-18] So the development of an improved protocol is of considerable interest. As a part of our ongoing effort towards the synthesis of biologically active compounds, we herein developed an efficient high yielding synthetic protocol for the synthesis of amides like N-phenylacetamides, N-benzothiazol-2-ylacetamide and N-(4-phenylthiazol-2-yl)acetamides.

Experimental

The chemicals used in the synthesis were purchased from reputed companies and used as received. The purities of the compounds and progress of the reactions were determined on silica-coated Al plates (Merck). Melting points were determined on a melting point apparatus and are uncorrected. IR (KBr) spectra were recorded using Perkin-Elmer FTIR spectrophotometer and the values are expressed as cm^{-1}. The ^{1}H NMR spectra were recorded on Joel Delta 400 MHz and Bruker Spectrospin spectrometer at 400 MHz using TMS as

an internal standard. The chemical shift values are recorded on δ scale and the coupling constants (J) are in Hz. Elemental analysis was performed on a Carlo Erba Model EA-1108 elemental analyzer.

General procedure for synthesis:

In a 50 mL round bottom flask, substituted aniline/amino thiazole (6 mmol) was dissolved in THF (5 ml). To this solution, DBU (1.2 mmol) was added. The reaction mixture was placed on freezing mixture of ice and salt & mechanically stirred for 15 min. To this reaction mixture, chloroacetyl chloride (6.1 mmol) was added from dropping funnel at such rate that the temperature does not rise beyond 5^{o}C. After all chloroacetyl chloride was added to the reaction mixture, it was stirred for 3-6 h at rt. The progress of reaction was monitored by TLC (Hexane: EtOAc; 7:3). After completion, the reaction mixture was poured into cold water. The compound was precipitated out. This was filtered and washed with water. The precipitate was dried and recrystallized by using ethanol as solvent. The product was obtained as solid powder.

N-benzothiazole-2-yl-2-chloroacetamide (10) - IR (cm^{-1}): 772, 1268, 1438, 1550, 1581, 1651, 1689, 2972, 3228; ^{1}H NMR (400 MHz, DMSO): δ 4.47 (2H, s, CH_2), 7.43-8.01 (4H, ArH), 12.72 (1H, NH, bs); Anal. calc. for $C_9H_7N_2OSCl$: C, 47.69; H, 3.11; N, 12.36; S, 14.15; found C, 47.59; H, 3.08; N, 12.21; S, 14.09.

2-chloro-N-(6-chlorobenzothiazole-2-yl)-acetamide (11) - IR (cm^{-1}): 781, 1275, 1378, 1554, 1595, 1645, 1692, 2945, 3248; ^{1}H NMR (400 MHz, DMSO): 4.46 (2H, s, CH_2), 7.35-8.05 (3H, m, ArH), δ 12.78 (1H bs, NH); Anal. calc. for $C_9H_6N_2OSCl_2$: C, 41.40; H, 2.32; N, 10.73; S, 12.28; found C, 41.23; H, 2.26; N, 10.68; S, 12.23.

2-chloro-N-(4-phenylthiazol-2-yl)acetamide (12) – IR (cm^{-1}): 575, 686, 722, 849, 1025, 1140, 1264, 1327, 1442, 1572, 1657, 3354; ^{1}H NMR (400 MHz, $CDCl_3$): δ 4.23 (2H s, CH_2), 6.75(1H s, CH Thiazole) 7.28-7.81(5H m, ArH), 10.20 (1H, bs NH); Anal. calc. for $C_{11}H_9N_2OSCl$: C, 52.28; H, 3.59; N, 11.08; S, 12.69; found C, 51.82; H, 3.23; N, 11.02; S, 12.36.

2-chloro-N-[4-(4-chlorophenyl)-thiazol-2-yl]-acetamide (13) – IR (cm^{-1}) : 593, 670, 761, 841, 1012, 1084, 1177, 1291, 1312, 1403, 1478, 1543, 1692, 3373; ^{1}H NMR (400 MHz, $CDCl_3$): δ 4.27 (2H, s, CH_2), 6.73 (1H, s, CH Thiazole), 7.35-7.37 (2H, d, J= 8.4 Hz, ArH), 7.72-7.74 (2H, d, J= 8.4 Hz, ArH), 9.75 (1H, bs, NH); Anal. calc. for $C_{11}H_8N_2OSCl_2$: C, 46.01; H, 2.81; N, 9.76; S, 11.17. found C, 44.23; H, 2.62; N, 9.56; S, 11.02;

2-chloro-N-[4-(4-fluorophenyl)-thiazol-2-yl]-acetamide (14) -IR (cm^{-1}): 519, 707, 831, 1067, 1161, 1266, 1488, 1576, 1662, 3362; ^{1}H NMR (400 MHz, $CDCl_3$): δ 4.25 (2H ,s, CH_2), 6.67 (1H, s, CH Thiazole), 7.06-7.10 (2H, d, J= 8.8 Hz, ArH), 7.74-7.78 (2H, d, J= 8.8 Hz, ArH), 9.34 (1H, bs, NH); Anal. calc. for $C_{11}H_8N_2OSFCl$: C, 48.80; H, 2.98; N, 10.35; S, 11.84; found C, 48.51; H, 2.70; N, 10.21; S, 11.34.

2-chloro-N-[4-(4-bromophenyl)-thiazol-2-yl]-acetamide (15) -IR (cm^{-1}): 521, 712, 843, 1072, 1268, 1515, 1586, 1675, 3472; ^{1}H NMR (400 MHz,$CDCl_3$): δ 4.12 (2H, s, CH_2), 6.69 (1H, s, CH Thiazole), 7.19-7.21 (2H, d, J= 7.6Hz ArH), 7.67-7.69 (2H, d, J= 7.6Hz, ArH), 9.04 (1H, bs, NH); Anal. calc. for $C_{11}H_8N_2OSBrCl$: C, 39.84; H, 2.43; N, 8.45; S, 9.67; found C, 39.78; H, 2.38; N, 8.41; S, 9.62.

2-chloro-N-(4-p-tolyl-thiazol-2-yl)-acetamide (16) -IR (cm^{-1}): 508, 700, 820, 974, 1070, 1140, 1268, 1328, 1426, 1567, 1699, 3320; ^{1}H NMR (400 MHz, $CDCl_3$): δ 2.40 (3H, s, CH_3), 4.20 (2H, s, CH_2), 7.15 (1H, s, CH Thiazole), 7.24-7.26 (2H, d, J= 6.8 Hz, ArH), 7.72-7.73 (2H, d, J= 6.8 Hz, ArH), 10.23 (1H, bs, NH); Anal. calc. for $C_{12}H_{11}N_2OSCl$: C, 54.03; H, 4.16; N, 10.50; S, 12.02; found C, 53.98; H, 4.10; N, 10.41; S, 11.96.

2-chloro-N-[4-(4-methoxyphenyl)-thiazol-2-yl]-acetamide (17) -IR (cm^{-1}): 534, 735, 843, 972, 1029, 1171, 1255, 1330, 1429, 1538, 1694, 3328; ^{1}H NMR (400 MHz, $CDCl_3$): δ 3.87 (3H s, OCH_3), 4.27 (2H, s, CH_2), 6.96-6.98 (2H, d, J= 8.4 Hz, ArH), 7.08 (1H, s, CH Thiazole), 7.76-7.78 (2H, d, J= 8.4 Hz, ArH), 9.93 (1H, bs, NH); Anal. calc. for $C_{12}H_{11}N_2O_2SCl$: C, 50.97; H, 3.92; N, 9.91; S, 11.34; found C, 50.51; H, 3.70; N, 9.41; S, 11.16.

2-chloro-N-[4-(4-nitrophenyl)-thiazol-2-yl]-acetamide (18) -IR (cm^{-1}): 532, 738, 854, 1038, 1180, 1265, 1345, 1436, 1542, 1560, 1678, 3315; ^{1}H NMR (400 MHz, DMSO): δ 4.27 (2H, s, CH_2), 7.41 (1H, s, CH Thiazole), 8.03-8.06 (2H, d, J= 8.8 Hz, ArH), 8.22- 8.24 (2H, J= 8.8 Hz, ArH.), 9.87 (1H, bs, NH); Anal. calc. for $C_{11}H_8N_3O_3SCl$: C, 44.38; H, 2.71; N, 14.11; S, 10.17; found C, 44.21; H, 2.60; N, 13.96; S, 10.06.

2-chloro-N-[4-(4-cyanophenyl)-thiazol-2-yl]-acetamide (19) -IR (cm^{-1}): 532, 738, 854, 1038, 1180, 1265, 1345, 1435, 1542, 1560, 1678, 3315; ^{1}H NMR (400 MHz, DMSO): δ 4.24 (2H, s, CH_2), 6.98 (1H, s, CH Thiazole), 7.44-7.46 (2H, d, J= 8.4 Hz, ArH), 7.92-7.93 (2H, d, J= 8.4 Hz, ArH), 9.84 (1H, bs, NH); Anal. calc. for $C_{12}H_8N_3OSCl$: C, 61.34; H, 4.58; N, 15.90; S, 18.19; found C, 63.51; H, 3.70; N, 19.41; S, 8.96.

2-chloro-N-[4-(3,4-dichlorophenyl)-thiazol-2-yl]-acetamide (20)-IR(cm^{-1}): 538, 746, 832, 1060, 1132, 1246, 1355, 1415, 1528, 1652, 3349; ^{1}H NMR (400 MHz, DMSO): δ 4.23 (2H, s, CH_2), 7.23 (1H, s, CH Thiazole) 7.61-8.02 (3H m, ArH), 9.76 (1H, bs, NH); Anal. calc. for $C_9H_8N_2S$: C, 41.08; H, 2.19; N, 8.71; S, 9.97; found C, 40.96; H, 2.06; N, 8.41; S, 9.86.

Results and Discussion

Figure 1 shows the reaction between aryl amine and chloroacetyl chloride to give N-substituted acetamides. The optimization of reaction conditions is given in table 1 and figure 2. To check the versatility of the reactions, wide range of substrate have been used and results are summarized in table 2. The result shows that the combination of DBU and THF gave the best result.

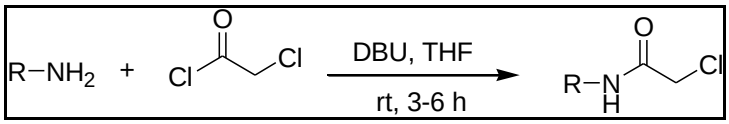

Figure 1.Reaction of aryl amine with chloroacetyl chloride in the presence of DBU

DBU (1,8-Diazabicyclo-[5.4.0]undec-7-ene) is commercially available, cheap homogenous catalyst. It is a sterically hindered bicyclic amidine base and especially useful where side reactions due to nucleophilicity of basic nitrogen are a problem.[19-21] DBU is one of the strongest organic neutral base (pKa = 12), in which the +M effect of the adjacent nitrogen stabilizes the protonated species, and it has been used in many organic reactions including amide bond formations in recent years.[22]

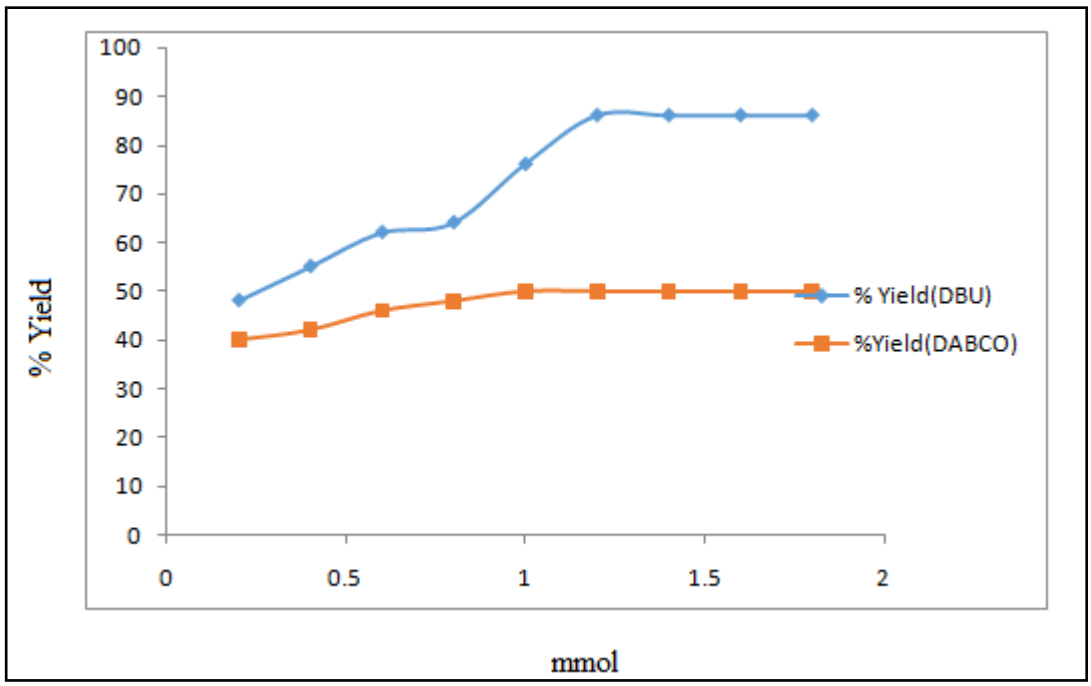

Figure 2. Comparative % yield optimization with DBU & DABCO for aniline (6 mmol)

The reaction of aniline and chloroacetyl chloride was carried out in the presence of catalytic amount of DBU (Figure 1). We were pleased to observe that use of 1.2 mmol of DBU for 6 mmol of aryl amine significantly increases the rate of reaction and yield of the product at room temperatures (Figure 2). A wide

range of aryl amines such as aniline, 2-aminobenzothiazole, and 2-amino-4-phenylthiazole underwent one-pot reaction to produce the corresponding amides in 75-95% isolated yield. All the utilized functionalities were found to be compatible under the given reaction conditions. In a typical reaction, aniline (6 mmol) was dissolved in THF (5 ml) and then DBU (1.2 mmol) was added. The reaction mixture was placed on the freezing mixture of ice and salt & mechanically stirred for 15 min. Further, the chloroacetyl chloride (6.1 mmol) was added from dropping funnel at such rate that the temperature does not rise beyond 5^{o}C. The reaction mixture was further stirred at room temperature for 3 h. The progress of the reaction was monitored by TLC. After completion of the reaction, the reaction mixture was poured into cold water. The compound was precipitated out which was filtered and washed with water. The precipitate was dried and recrystallized using ethanol. The product, N-phenylacetamide (**1**) was obtained as a solid powder in 86% yield (Table 1 & 2). The same procedure was also followed for the substrates 2-aminobenzothiazole (entries 2, 5, 8, 11 & 14) and 2-amino-4-phenylthiazole (entries 3, 6, 9, 12 & 15) to check the versatility of the process. The optimization of catalysts DBU and DABCO (1,4-diazobicyclo(2,2,2)-octane) has been done for aniline in the different solvent system, and the same ratio applied to all other substrates under optimized reaction conditions (Figure 2). Out of many reactions, the ratio of 1:5 (DBU: aniline) in THF gave the best result (Table 1).

Table 1.Optimization of catalysts and solvents for compounds 1, 10&12.

Entry	Compd. No.	Solvent	% yield by using catalyst		
			DBU	DABCO	Et_3N
1	**1**	THF	86	68	70
2	**10**	THF	83	60	62
3	**12**	THF	86	63	64
4	**1**	1,4 dioxane	75	70	68
5	**10**	1,4 dioxane	71	64	69
6	**12**	1,4 dioxane	74	66	68
7	**1**	Benzene	58	50	56
8	**10**	Benzene	52	No reaction	50
9	**12**	Benzene	51	No reaction	51
10	**1**	DCM	72	62	65
11	**10**	DCM	70	58	61
12	**12**	DCM	70	59	64
13	**1**	DMF	74	74	69
14	**10**	DMF	71	69	64
15	**12**	DMF	73	68	65

Table 2.Amidation of chloroacetyl chloride with different aryl amines

Comp. No.	R	Time(h)	% Yield DBU	Mp (^{o}C)	Lit mp[ref]
1	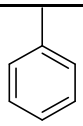	3	86	136	134[24]
2	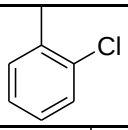	3	82	69-70	73[24]
3	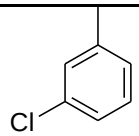	3	80	100	98-100[12]
4	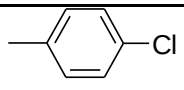	3	85	176	178[24]

5	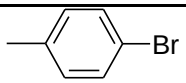	3	85	182	180-184[12]
6	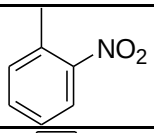	5	76	98	96-98[11]
7	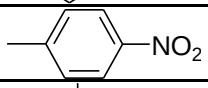	5	79	180	178-180[11]
8	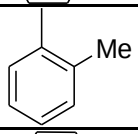	4	86	98-100	105-107[24]
9	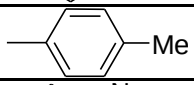	4	88	164	164-166[24]
10	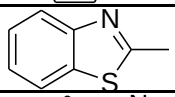	6	83	145	-
11	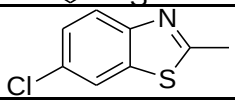	6	76	213	-
12	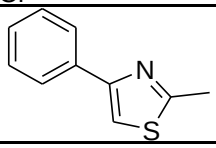	4	86	181	-
13	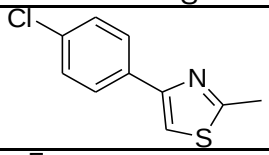	5	85	188-189	-
14	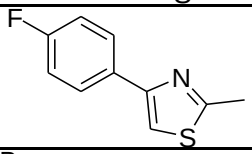	5	85	134-136	-
15	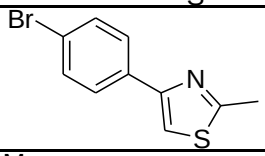	5	86	206	-
16	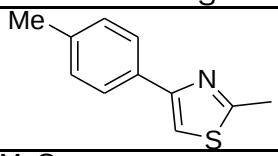	4	90	149	-
17	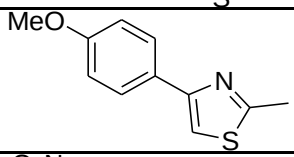	4	95	234	-
18	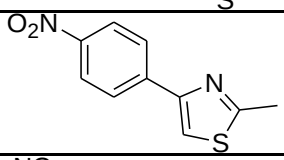	6	75	295-297	-
19	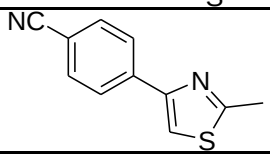	6	76	276-278	-

20	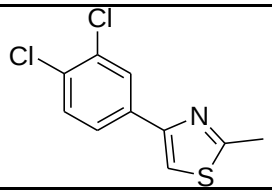	6	79	230	-

The reactions in the bases like TEA (triethylamine) and DABCO remained non-completed even after performing the reaction for the longer time. The reactant, aryl amines in both the cases was not consumed completely even after stirring for 10 hours at room temperature as observed in TLC. Hence, the products were separated by using column chromatography leading to low yield in comparison to DBU. The summary of comparative studies for different bases in the different solvent is given in table 1. The comparison of % isolated yield in case of DABCO and DBU for 6 mmol of aniline is in figure 1.

According to the proposed mechanisms, DBU provides significant acceleration compared to other amine bases. This suggests that DBU is not only acting as a base rather playing another role also. There are different pathways postulated to explain the role of DBU in these types of reactions.[23] According to our observation, the most suitable catalytic mechanism is the displacement of chloride ion by DBU and hence activates the carbonyl for attack by the lone pair of nitrogen present on aryl amines (Figure 3). However, further work to understand the pathways of the reaction is ongoing.

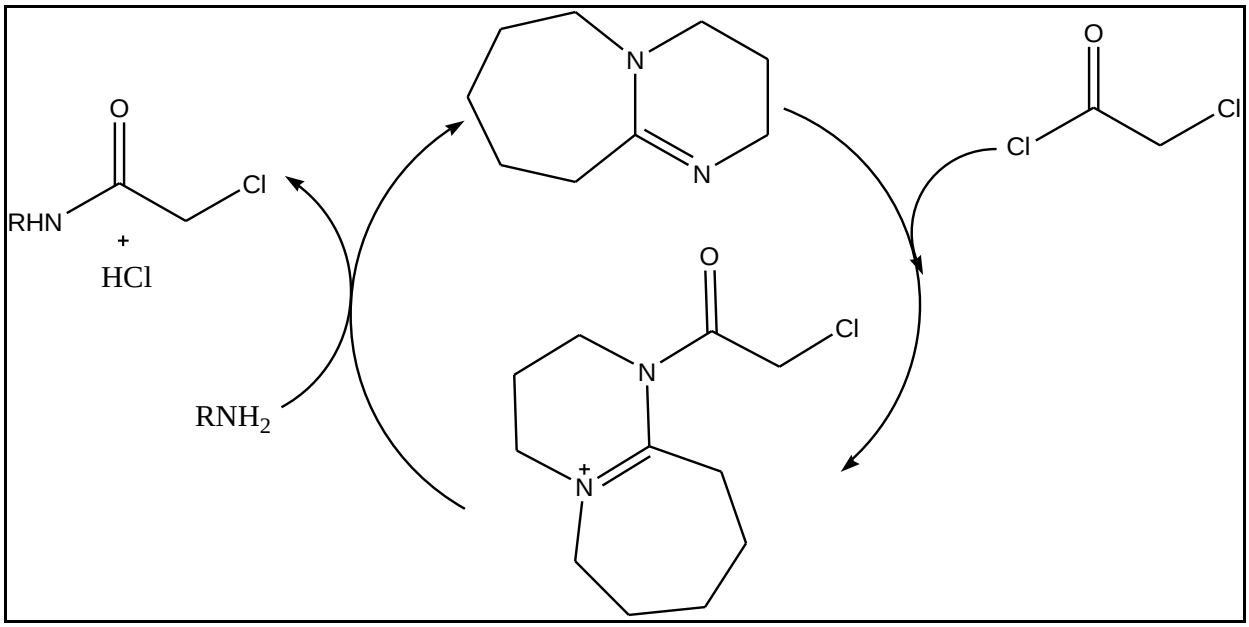

Figure 3.Proposed catalytic cycle

Conclusion

In present work, we have developed a facile method for the one-pot synthesis of amides from aryl amines and chloroacetyl chloride using DBU as non-nucleophilic base in THF solvent. The method gave 75 to 95% yields in 3-6 h at room temperature (rt). The reactions have also been performed in TEA and DABCO using different solvent system. The combination of DBU and THF gave best result. This method ensures the wide substrate scope with excellent yields and the products were isolated and purified by recrystallization.

Acknowledgements:

DM is thankful to University Grant Commission, Delhi for fellowship through CSIR-NET JRF examination. RS is thankful to Council of Scientific and Industrial Research (CSIR)-India for the financial support under Extramural Research Grant -No. 02(0048)/12/EMR-II.

References

1. Montalbetti CAGN, Falque V. Amide bond formation and peptide coupling. Tetrahedron, 2005,61: 10827-10852.
2. (a) OrmerodD, WillemsensB, MermansR,LangensJ, Winderickx G, Kalindjian SB, BuckIM, McDonaldIM. Development of a scalable synthesis of gastrazole (jb95008): a potent CCK_2 receptor antagonist.Org. Process Res. Dev., 2005, 9: 499-507. (b)LenstraDC, NguyenDT, MecinovicJ. Zirconium-catalyzed direct amide bond formation between carboxylic esters and amines. Tetrahedron, 2015, 71: 5547-5553.
3. TangP.Boric acid catalyzed amide formation from carboxylic acids and amines: N-benzyl-4-phenylbutyramide. Org. Synth., 2005,81: 262-272.
4. AgerDJ, BablerS, EricksonRA, Froen DE,KittlesonJ, PantaleoneDP, PrakashI, ZhiB.The synthesis of the high-potency sweetener, NC-00637. Part 3: The glutamyl moiety and coupling reactions.Org. Process Res. Dev.,2004, 8: 72-85.
5. VaidyanathanR,KalthodVG, NgoDP, Manley JM, LapekasSP. Amidations using N,N'-Carbonyl diimidazole: remarkable rate enhancement by carbon dioxide. J. Org. Chem.,2004, 69: 2565-2568.
6. ChenJ, CorbinSP,HolmanNJ.An improved large scale synthesis of the scho¨llkopf chiral auxiliaries: (2R)- and (2S)-2,5-dihydro-3,6-dimethoxy-2-isopropylpyrazine.Org. Process Res. Dev., 2005, 9: 185-187.
7. Özkay ÜD, Özkay Y, Can ÖD. Synthesis and analgesic effects of 2-(2-carboxyphenylsulfanyl)- N-(4-substitutedphenyl)acetamide derivatives. Med.Chem. Res., 2011, 20: 152-157.
8. Bolli MH, AbeleS, BinkertC, BravoR, BuchmannS, BurD, GatfieldJ, HessP, KohlC, MangoldC.2-imino-thiazolidin-4-one derivatives as potent, orally active $S1P_1$receptor agonists. J. Med. Chem., 2010, 53: 4198-4211.
9. Baraldi PG, Preti D, Tabrizi MA, Fruttarolo F, Saponaro G, BaraldiS, Romagnoli R, Moorman AR, GessiS, VaraniK, BoreaPA.N6 -[(Hetero)aryl/(cyclo)alkyl-carbamoyl-methoxy-phenyl]-(2- chloro)-50 -N-ethylcarboxamido-adenosines: The first example of adenosine-related structures with potent agonist activity at the human A2B adenosine receptor. Bioorg. Med. Chem., 2007, 15: 2514-2527.
10. ChanderS, AshokP, SinghA, MurugesanS. De-novo design, synthesis and evaluation of novel 6,7-dimethoxy-1,2,3,4-tetrahydroisoquinoline derivatives as HIV-1 reverse transcriptase inhibitors. Chem. Cent. J., 2015, 9:33: 1-13.
11. KumarR, KaurM, BahiaMS, SilakariO.Synthesis, cytotoxic study and docking based multidrug resistance modulator potential analysis of 2-(9-oxoacridin-10(9H)-yl)-N-phenyl acetamides. Eur. J. Med. Chem., 2014, 80: 83-91.
12. PatelRV, KumariP, RajaniDP, ChikhaliaKH.Synthesis of coumarin-based 1, 3, 4-oxadiazol-2ylthio-*N*-phenyl/benzothiazolylacetamides as antimicrobial and antituberculosis agents. Med. Chem. Res.,2103, 22: 195-210.
13. PatelRV, PatelPK, KumariP,RajaniDP, ChikhaliaKH.Synthesis of benzimidazolyl-1,3,4-oxadiazol-2ylthio-*N*-phenyl (benzothiazolyl) acetamides as antibacterial, antifungal and antituberculosis agents.Eur. J. Med. Chem., 2012, 53: 41-51.
14. Shukla, MB, Mahyavanshi JB, Parmar KA. Synthesis and antimicrobial activities of various N-phenyl-2-{[5-(3, 4, 5-trimethoxyphenyl)-1, 3, 4-oxadiazol-2-yl] sulfanyl} acetamides. Ind. J. Chem., 2016, 55B: 374-380.
15. RaghavendraNM, JyothsnaA, RaoAV, SubrahmanyamCVS.Synthesis, pharmacological evaluation and docking studies of *N*-(benzo[*d*]thiazol-2-yl)-2-(piperazin-1-yl)acetamide analogs as COX-2 inhibitors.Bioorg. Med. Chem. Lett., 2012, 22: 820-823.
16. PedgaonkarGS, SrideviJP, JeankumarVU, SaxenaS, DeviPB, RenukaJ, YogeeswariP, SriramD. Development of benzo[*d*]oxazol-2(3*H*)-ones derivatives as novel inhibitors of *Mycobacterium tuberculosis* InhA.Bioorg. Med. Chem., 2014,22: 6134-6145.
17. Ozawa T,Kitagawa H,Yamamoto Y,Takahata S,Iida M,Osakib Y,Yamadab K.Phenylimidazole derivatives as specific inhibitors of bacterial enoyl-acyl carrier protein reductase FabK.Bioorg. Med. Chem.,2007, 15: 7325-7336.
18. 18.Duran M,Canbaz MC.pK_a determination of newly synthesized N-(benzothiazole-2-yl)-2-(4,5-dimethyl-1-(phenylamino)-1H-imidazol-2-ylthio)acetamide derivatives.Ind. Eng. Chem. Res.,2013, 52: 8355-8360.

19. Yeom C-E,Kim MJ,Kim BM. 1,8-Diazabicyclo[5.4.0]undec-7-ene (DBU)-promoted efficient and versatile aza-Michael addition.Tetrahedron,2007, 63: 904-909.
20. Shieh W-C,Dell S,Repic O.Nucleophilic catalysis with 1,8-diazabicyclo[5.4.0]undec-7-ene (DBU) for the esterification of carboxylic acids with dimethyl carbonate.J. Org. Chem.,2002, 67: 2188-2191.
21. Ghosh N. DBU (1,8-diazabicyclo[5.4.0]undec-7-ene) - A nucleophillic base.Synlett, 2004, 574-575.
22. (a) Chauhan SMS, Singh R, Geetanjali.An improved synthesis of *N*-substituted-2-nitroanilines.Synth. Commun.2003, 33:2899-2906; (b) Geetanjali, Singh R, Chauhan SMS. A new and improved *N* -3 alkylation of 10-substituted isoalloxazines using 1,8-diazabicyclo[5.4.0]undec-7-ene in benzene. Synth. Commun.2003, 33: 613-620; (c) Mamgain R, Singh R, Rawat DS. DBU-catalyzed three-component one-pot synthesis of highly functionalized pyridines in aqueous ethanol.J. Heterocycl. Chem.2009, 46: 69-73; (d) Lima EC, Souza CC, Soares RO, Vaz BG, Eberlin MN, Dias AG, Costa PRR. DBU as a catalyst for the synthesis of amides via aminolysis of methyl esters.J. Braz. Chem. Soc.2011, 22: 2186-2190; (e) Kumar KN, Sreeramamurthy K,Palle S, Mukkanti K, DasP. Dithiocarbamate and DBU-promoted amide bond formation under microwave condition.Tet. Lett.2010, 51: 899-902.
23. Price KE,Larrive´e-Aboussafy C,Lillie BM.McLaughlin RW,Mustakis J,Hettenbach KW,Hawkins JM,Vaidyanathan R.Mild and efficient DBU-catalyzed amidation of cyanoacetates.Org. Lett.,2009, 11: 2003-2006.
24. Gowda BT, Usha KM, Jayalakshmi KL. ^{1}H and ^{13}C NMR Spectral Studies on N-(Aryl)-Substituted Acetamides, $C_6H_5NHCOCH_{3-i}X_i$ and 2/4-$XC_6H_4NHCOCH_{3-i}X_i$ (where X = Cl or CH_3 and i = 0, 1, 2 or 3).Naturforsch.,2003, 58a: 801-806.

*****

Volume 8, No. 3, March – April 2017
ISSN No. 0976-5697
International Journal of Advanced Research in Computer Science
RESEARCH PAPER
Available Online at www.ijarcs.info

A Novel Facial Image Resolution Enhancement Algorithm using Pixels Homogeneity

Vikram Mutneja
Ph.D. Research Scholar
I.K. Gujral Punjab Technical University
Kapurthala, Punjab (India)

Dr. Satvir Singh
Associate Professor
I.K. Gujral Punjab Technical University
Kapurthala, Punjab (India)

Abstract: Facial image processing is an important step in the surveillance cameras based biometric identification systems. The resolution of the facial images from surveillance videos is usually very less owing to the factors such as hardware constraints, distance between the subjects and CCTVs etc. In this work, a novel spatial domain based face resolution enhancement technique using single LR image has been proposed. It is based on the homogeneity levels of the pixels in respective neighboring four quadrants in 3×3 scanning window, used as LR patch which is replaced by interpolated 5×5 HR patch. The kernel matrix is generated for all the pixels in the source image which encodes the homogeneity of all pixels in image. The performance analysis of proposed technique has been done for different values of resolution enhancement factors, in terms of quality metrics Structural Similarity Index Measure (SSIM), Peak Signal to Noise Ratio (PSNR), Signal to Noise Ratio (SNR) and Mean Square Error (MSE). From the results, we contend that the proposed algorithm is very effective in generating good quality HR facial image from single LR facial image.

Keywords: Face Resolution Enhancement, Low Resolution Surveillance Videos, Spatial Domain Processing, Neighbourhood Processing, Image Quality Enhancement

I. INTRODUCTION

Most of the times images of people received from the surveillance videos are of low resolution because of different factors such as distance between the camera and place of footage, environment factors, wide coverage area, installation problems, out of focus and bandwidth issue etc. There are hardware constraints such as storage space limitations because of which the frames need to be compressed or converted to lower resolution for storage. Therefore it is always required to preprocess the frames from surveillance videos before passing them to the biometric identification system. The performance of the biometric systems largely depends upon the quality of the input facial images in terms of image as well as face quality metrics. Out of the various properties to judge the quality of the input facial images, resolution of faces is very important factor.

The face biometric systems can be broadly categorized into two types, local and global. Local methods are based upon using position and/or size of facial landmarks such as eyes, nose tip, lip center, chin center etc. [19, 13], and while global are independent of measurement of facial landmarks. Supposedly the facial images, in which the facial landmarks are localizable are of better quality. Secondly the accuracy of the system also depends upon the accuracy in locating the facial landmarks. The chances of accurately locating the facial landmarks is directly related the face resolution. It is easier to locate the facial landmarks in high resolution images, which in turn increases the hit rate of the system. Face resolution enhancement aims at enhancing the overall signal strength of the facial image by applying the resolution enhancement technique which are classified in two broad categories. Firstly reconstruction based method such as works done by [1, 9, 19]. Secondly learning based techniques such as [21, 18]. Some of the works have done hybridization of both techniques such as by [20]. Reconstruction based models are based on the generalized smoothness priors while the learning based techniques select recognition based priors. Most of the spatial domain based techniques are based on neighbor embedding [2, 5, 11].

Face resolution enhancement techniques are also classified based on number of input facial images. In super-resolution, the final enhanced HR image is computed from multiple images which may be captured from consecutive frames of video or other source. Other are the techniques which use single LR facial input image using relative intensity level of the pixels in surrounding quadrants within N×N LR patch, N>=2. Normally learning based techniques, also known as face hallucination, are based on single facial image as input and use the trained system or dictionary to estimate the missing HR details.

This work is based on neighborhood embedding using single LR facial input image. This paper is structured as follows: Section II provides Literature Survey, Section III describes experimental setup. The proposed technique based on pixels homogeneity has been explained in Section IV, Section V discusses experimental results, and finally Section VI gives conclusions and future scope.

II. LITERATURE SURVEY

[3] Authors proposed a novel super resolution technique of noisy facial images by using the contour features to suppress noise and used the standard deviation prior to enhance the low quality contour feature. Authors demonstrated the superiority of their method as compared to existing techniques using simulations as well as real-world scenario based experiments.

[14] Proposed a new method of face resolution enhancement using a recursive error back projection of example based learning. Authors exploited the use of shape and texture information from low resolution facial image in spatial domain to estimate optimal coefficients for a linear

© 2015-19, IJARCS All Rights Reserved

combination of prototypes of shape and those of texture by solving least square minimization to reconstruct its high resolution version.

[10] Proposed facial image super-resolution method using missing image interpolation based on smooth regression with a novel local structure prior (SRLSP). However the proposed technique is based on assumption of uniformity in local structures of face image patches at same position so as to enable smooth regression function to learn the relationship between LR pixels and missing HR pixels of respective patches. The proposed method was tested on

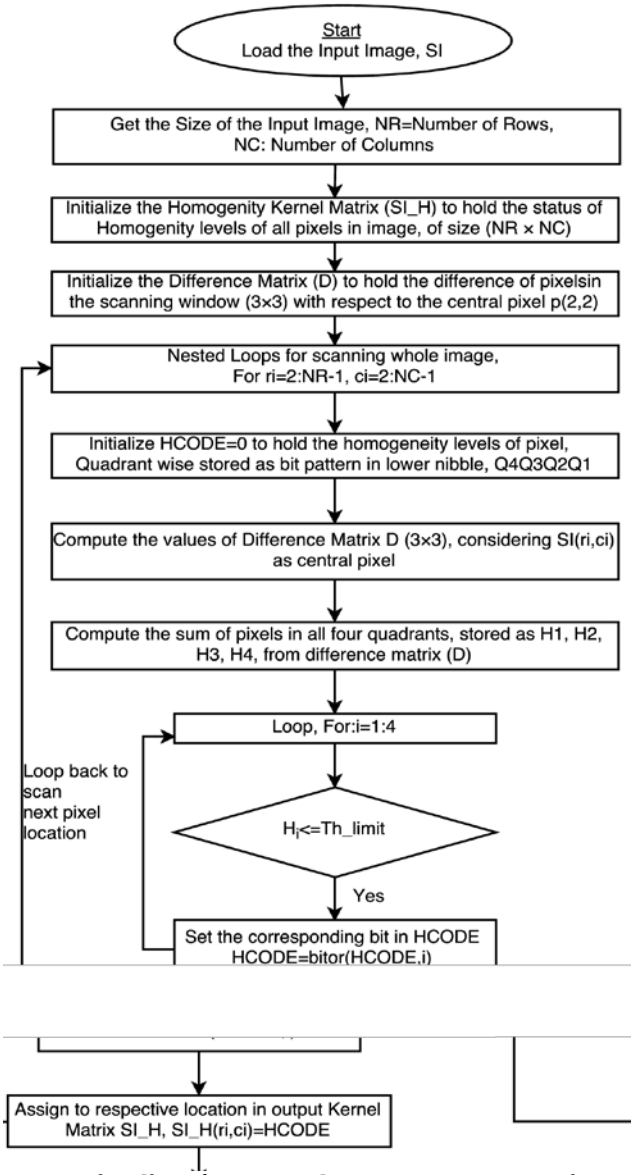

Figure 2: Flow Chart of Function to Generate Homogeneity Kernel Matrix

Yale-B database and reported the results superior to state-of-the-art face super-resolution methods in face recognition.

[6] Proposed a novel sparse coding based face hallucination method by incorporating intrinsic geometric structure of training samples for dictionary learning to minimize artificial effects in reconstructed HR face image. The method is based on graph construction in HR manifold and K-selection mean constraints for finding optimal weight HR face reconstruction. [17] Proposed single image super-resolution using sparse representation and neighbor embedding in learning based approaches using partitioned feature space and statistical prediction model. [18] Emphasized on reducing the dependence of proposed face hallucination technique on size and number of training samples using direct combined approach. [8] Used single LR input and used the concepts such appearance and geometrical features, optical flow model to estimate the local structure in resultant HR image. [4] is also based on

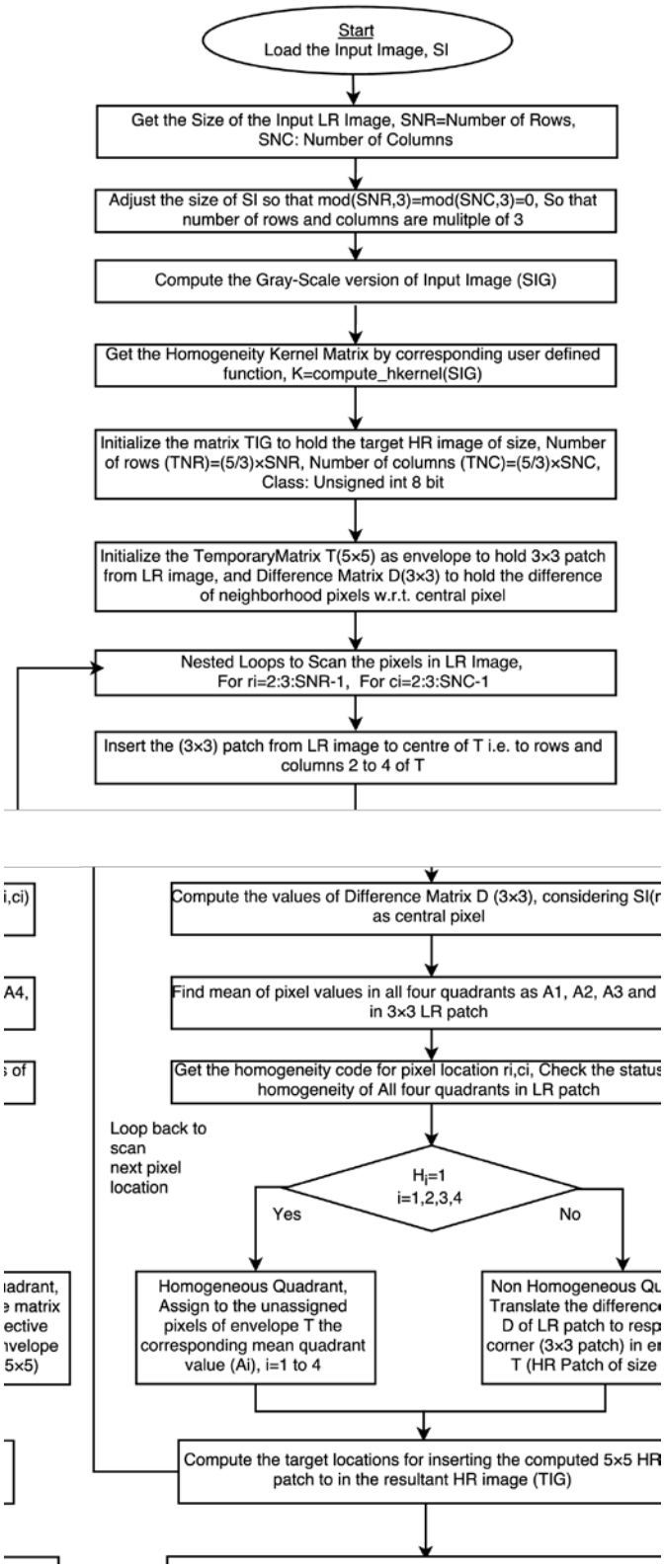

Figure 3: Flow Chart Proposed Technique

© 2015-19, IJARCS All Rights Reserved

single image face hallucination which uses similarity measurements between each input LR patch and all local LR and HR neighborhood patches of training images.

III. EXPERIMENTAL SETUP

The machine running windows 7 (64 Bit) on Intel core i3 1.9 GHz and having NVIDIA graphics processing unit GeForce GT 740M has been used to develop and test the proposed method. The work has been done in MATLAB version 8.5.0.197613 (R2015a).

IV. PROPOSED TECHNIQUE

The proposed technique works on the basis of creating homogeneity kernel matrix for all the pixels of input LR image. The scanning is done in 3×3 local window size, which is slid over whole input LR image pixel by pixel. The homogeneity level corresponding to four quadrants (refer Figure 1) is encoded based on criteria as per Equation 1.

$$\sum_{i=1}^{4} [p_{ij}] < th_limit \quad (1)$$

Where j denotes the particular quadrant (j=1,2,3,4) and i iterates for all the pixels in respective quadrant. The parameter *th_limit* has been set empirically to value 15. Figure 2 shows the working of function compute_hkernel(SI) for generating the kernel matrix and figure 3 the flow chart of proposed technique to generate the HR image by applying the homogeneity kernel matrix to input LR image in gray-scale version. To apply the proposed technique on the color image, the algorithm depicted in figure 3 is applied recursively to channels R, G and B to generate the resultant color image.

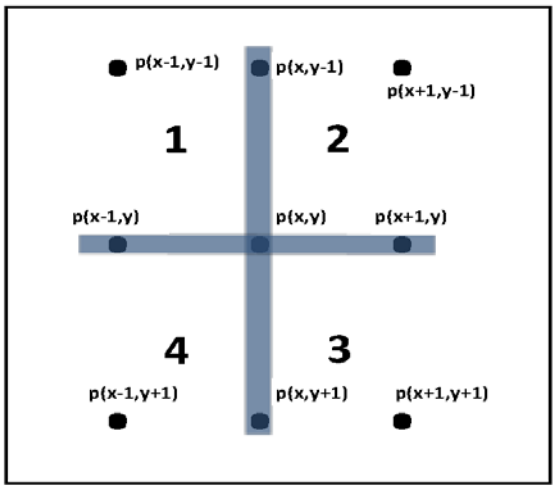

Figure 1: 3×3 Pixels Scanning Window Showing Quadrants (1-4)

Table 1 shows the comparison of homogeneity levels of pixels in the facial images at various stages of application of proposed resolution enhancement technique. It includes input low resolution images for the tests corresponding to single iteration and double iterations, original HR Image and generated HR images. In the types of the homogeneity column, Q refers to quadrant, numeric value as number of quadrants, H as horizontal, V as vertical, L as lower, U as upper, LE as left, R as right and C as cross. e.g. 3QRU can be read as 3 quadrants, right upper. The numeric values attached with H in first column specifies the position number of quadrant e.g. H23 means, homogeneity has been found in quadrants 2 and 3. (refer Figure 1). Figure 4 shows the diagrammatic representation of impact of resolution enhancement on variations of homogeneity levels in image.

From Table 1 and Figure 4 it is inferred that there is rise in percentage of pixels of different homogeneity levels (except for H12, H34 and H1234) with increase in image resolution, being maximum in original HR image.

Table 1: Comparison Number of Pixels Having Different Homogeneity Levels in Input LR, Intermediate and Output HR Facial Images

Homogenity Levels	***Type of Homogeneity*** ***Image Size*** ***Type of Homogeneity***	***Input LR Image (1 Iteration Test)*** ***241×269***	***Input LR Image (2 Iterations Test)*** ***145×161***	***Intermediate Image (2 Iterations Test)*** ***245×270***	***Generated HR Image (1 Iteration Test)*** ***405×450***	***Generated HR Image (2 Iterations Test)*** ***410×455***	***Original HR Image*** ***401×449***
H0	0Q	155	80	80	143	183	708
H1	1Q	183	118	155	248	264	475
H2	1Q	316	178	284	428	431	604
H12	2QHU	701	458	1044	1518	1939	1661
H3	1Q	89	49	100	120	147	258
H13	2QCN	24	8	5	13	1	89
H23	2QVR	1033	505	1172	2306	2403	2691
H123	3QRU	1040	625	1049	2094	1834	2562
H4	1Q	99	63	111	130	128	298
H14	1QVLE	907	492	1020	1973	2215	2166
H24	2QCP	6	1	4	4	1	67
H124	3QLEU	1044	616	1073	1741	1742	2393
H34	2QHL	826	581	1143	1503	1874	1678
H134	3QLEL	740	377	796	1602	1444	2146
H234	3QRL	664	287	702	1325	1391	1812
H1234	4Q	55986	18299	56386	165396	168827	158745

© 2015-19, IJARCS All Rights Reserved

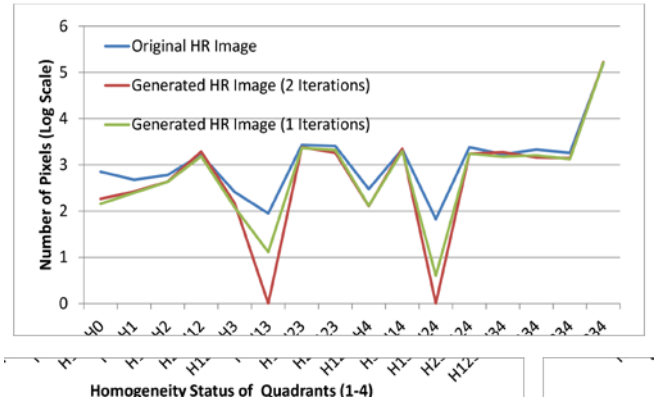

Figure 4: Comparison Homogeneity Levels of Pixels

V. RESULTS AND DISCUSSION

The proposed technique was tested on the test images from the database Color FERET [15,16]. Portions of the research in this paper use the FERET database of facial images collected under the FERET program, sponsored by the DOD Counterdrug Technology Development Program Office FERET [16, 15]. The quality metrics used to evaluate the performance of the proposed technique are Structural Similarity Index Measure (*SSIM*), Peak Signal to Noise Ratio (*PSNR*), Signal to Noise Ratio (*SNR*) and Mean Square Error (*MSE*), which have been measured of generated HR image with respect to the original HR image. *PSNR* gives the measure of peak signal to noise power ratio, while *SNR* uses average signal power.

The proposed method has been tested on color as well as gray-scale images. Figures 5 and 6 show the results of application of proposed technique for scaling factor 2.7779 on gray-scale images corresponding to iteration 1 and 2 respectively while figure 7 shows the results for scaling factor 1.6667. Table 2 shows the corresponding measured values of quality metrics. Figures 8, 9 10 show the corresponding results of application of proposed technique on original color images and Table 3 the measured values of quality metrics. By comparison of results in Table 2 and Table 3, it is inferred that application of proposed technique with color based processing (i.e. of channels R,G and B) gives better results as compared to gray-scale only based processing.

Table 2: Quality Metrics for Resolution Enhancement (Gray-Scale)

Quality Metric	***Output HR Image (Single Iteration) Size(450×405), SF=1.667***	***Intermediate Image (Double Iteration) Size(245×270), SF=1.667***	***Output HR Image (Double Iteration) Size(450×405), SF=2.7789***
SSIM	0.919	0.924	0.856
PSNR	34.959	32.854	29.434
SNR	28.096	25.995	22.571
MSE	20.759	33.702	74.074

To study the efficiency of the proposed technique for different resolution enhancement factors and different resolutions of input facial image (for same HR output), the test images from FERET are down-scaled to the factors 0.6000, 0.3600, 0.2160, 0.1296 and 0.0778. The corresponding results are shown in table 4. We have been able to achieve good results in terms of various quality metrics.

To compare the performance of the proposed algorithm with the previous work, a test dataset of hundred images taken from color FERET was created. The resolution enhancement factor was set as 2.7889. Table 5 shows the comparison of the proposed algorithm with some of the previous works in terms of SSIM and PSNR (db), computed as mean value by application of proposed algorithm on this test dataset.

Figure 5: Result Homogeneity Technique on Gray Scale Image for resolution enhancement factor 1.667×1.667, First Stage

© 2015-19, IJARCS All Rights Reserved

Figure 6: Result Homogeneity Technique on Gray Scale Image for resolution enhancement factor 1.667×1.667, Second Stage

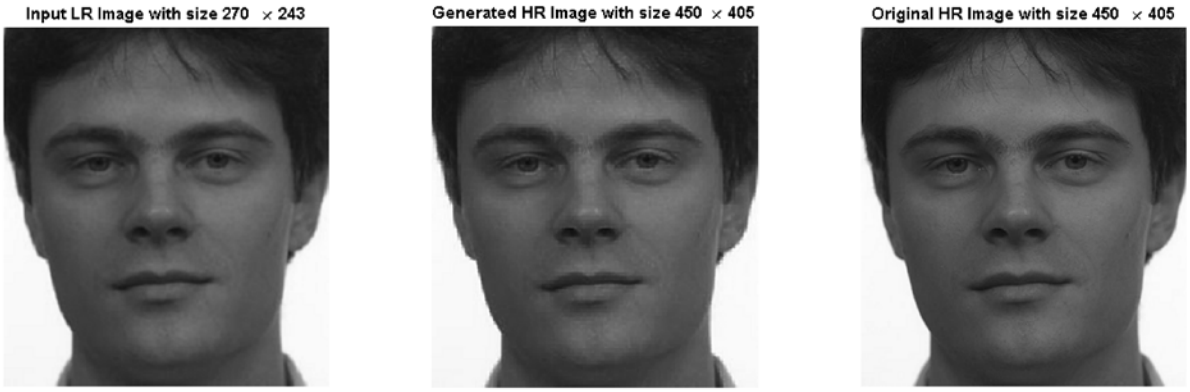

Figure 7: Result Homogeneity Technique on Gray Scale Image for resolution enhancement factor 1.667

Figure 8: Result Homogeneity Technique on Color Image for resolution enhancement factor 1.667×1.667, First Stage

Figure 9: Result Homogeneity Technique on Color Image for resolution enhancement factor 1.667×1.667, Second Stage

© 2015-19, IJARCS All Rights Reserved

Figure 10: Result Homogeneity Technique on Color Image for resolution enhancement factor 1.667

Table 3: Quality Metrics for Resolution Enhancement (Color Image)

Quality Metric	***Output HR Image (Single Iteration) Size(450×405), SF=1.667***	***Intermediate Image (Double Iteration) Size(245×270), SF=1.667***	***Output HR Image (Double Iteration) Size(450×405), SF=2.7789***
SSIM	0.963	0.959	0.926
PSNR	34.343	32.263	28.955
SNR	27.389	25.312	22.000
MSE	23.921	38.613	82.709

Table 4: Results For Various Image Resolution Enhancement Factors

Resolution Enhancement Factor	***1.67 by 1.67***	***3.10 by 2.53***	***5.22 by 4.34***	***8.89 by 7.25***	***15.45 by 12.64***
Initial Resolution	270×243	147×162	90×99	54×60	33×36
Final Resolution	450×405	455×410	470×430	480×435	510×455
SSIM	0.963	0.926	0.894	0.848	0.781
PSNR	34.343	28.955	26.958	24.099	20.866
SNR	27.389	22	20.003	17.144	13.911
MSE	23.921	42.709	91.017	151.016	205.706

Table 5: Comparison of Mean SSIM and Mean PSNR with Previous work

Method	***Mean SSIM***	***Mean PSNR(db)***
[7]	0.8692	28.5
[12]	0.8444	28.5072
[3]	0.7067	22.3266
Proposed	0.925	30.89

VI. CONCLUSIONS AND FUTURE SCOPE

In this work, we have developed improved face resolution enhancement technique based on homogeneity of pixels in 3×3 LR patches, scanned over whole input facial image. The homogeneity kernel matrix is computed which is used to generate resultant HR image. 3×3 LR patches are slid to the nucleus of 5×5 HR patches and remaining pixels in HR patch are computed by application of homogeneity kernel matrix. We have tested the proposed technique for different resolution enhancement factors at minimum (1.67 by 1.67) to maximum (15.45 by 12.64) and low resolution facial images with minimum size 33×36. The accuracy of the proposed technique has been measured in terms of quality metrics *SSIM*, *PSNR*, *SNR* and *MSE*. *SSIM* being most representative measure to reflect the quality of resultant HR image with respect to original HR image, we have been able to achieve *SSIM* value 0.963 corresponding to lowest resolution enhancement factor 1.67*by*1.67 which falls down to 0.781 for highest resolution enhancement factor (15.45 by 12.64) and lowest size of LR facial image (33×36). From the results, we conclude that the proposed system is very effective in generating good quality HR facial image from single input LR facial image.

In near future, we intend to do improvements in the proposed technique by introducing adaptability in selection of LR patch size and number of iterations so as to achieve desired resolution enhancement factor. The proposed technique can be integrated with the video based search space reduction techniques such as frame difference, motion segmentation in processing surveillance videos. Further we intend to make the improvements in time efficiency of the proposed technique by using GPU acceleration.

VII. REFERENCES

[1] S. Baker and T. Kanade. Limits on super-resolution and how to break them. *IEEE Transactions on Pattern Analysis and Machine Intelligence*, 24(9):1167–1183, 2002.

[2] H. Chang, D.-Y. Yeung, and Y. Xiong. Super-resolution through neighbor embedding. In *Computer Vision and Pattern Recognition, 2004. CVPR 2004. Proceedings of the 2004 IEEE Computer Society Conference on*, volume 1, pages I–I. IEEE, 2004.

[3] L. Chen, R. Hu, C. Liang, Q. Li, and Z. Han. A novel face super resolution approach for noisy images using contour feature and standard deviation prior. *Multimedia Tools and Applications*, 76(2):2467–2493, 2017.

[4] M. Gong and K. Wang. Single face hallucination via local neighbor patches. *AEU-International Journal of Electronics and Communications*, 74:88–93, 2017.

[5] K. Huang, R. Hu, J. Jiang, Z. Han, and F. Wang. Face image super-resolution through improved neighbor embedding. In *International Conference on Multimedia Modeling*, pages 409–420. Springer, 2016.

[6] K. Huang, R. Hu, J. Jiang, Z. Han, and F. Wang. Hrm graph constrained dictionary learning for face image super-resolution. *Multimedia Tools and Applications*, 76(2):3139–3162, 2017.

[7] Z. Hui and K.-M. Lam. Eigentransformation-based face super-resolution in the wavelet domain. *Pattern Recognition Letters*, 33(6):718–727, 2012.

[8] Z. Hui, W. Liu, and K.-M. Lam. A novel correspondence-based face-hallucination method. *Image and Vision Computing*, 2017.

[9] J. Jiang, C. Chen, K. Huang, Z. Cai, and R. Hu. Noise robust position-patch based face super-resolution via tikhonov regularized neighbor representation. *Information Sciences*, 367:354–372, 2016.

© 2015-19, IJARCS All Rights Reserved

[10] J. Jiang, C. Chen, J. Ma, Z. Wang, Z. Wang, and R. Hu. Srlsp: A face image super-resolution algorithm using smooth regression with local structure prior. *IEEE Transactions on Multimedia*, 19(1):27–40, 2017.

[11] J. Jiang, R. Hu, Z. Wang, Z. Han, and J. Ma. Facial image hallucination through coupled-layer neighbor embedding. *IEEE Transactions on Circuits and Systems for Video Technology*, 26(9):1674–1684, 2016.

[12] H. Li, L. Xu, and G. Liu. Face hallucination via similarity constraints. *IEEE signal processing letters*, 20(1):19–22, 2013.

[13] S. Liu and M.-H. Yang. Compressed face hallucination. In *Image Processing (ICIP), 2014 IEEE International Conference on*, pages 4032–4036. IEEE, 2014.

[14] J.-S. Park and S.-W. Lee. Resolution enhancement of facial image using an error back-projection of example-based learning. In *Automatic Face and Gesture Recognition, 2004. Proceedings. Sixth IEEE International Conference on*, pages 831–836. IEEE, 2004.

[15] P. J. Phillips, H. Moon, S. A. Rizvi, and P. J. Rauss. The feret evaluation methodology for face-recognition algorithms. *IEEE Transactions on pattern analysis and machine intelligence*, 22(10):1090–1104, 2000.

[16] P. J. Phillips, H. Wechsler, J. Huang, and P. J. Rauss. The feret database and evaluation procedure for face-recognition algorithms. *Image and vision computing*, 16(5):295–306, 1998.

[17] V. A. Rahiman and S. N. George. Single image super resolution using neighbor embedding and statistical prediction model. *Computers & Electrical Engineering*, 2017.

[18] C.-T. Tu, M.-C. Ho, and M.-Y. Lin. A new approach for face hallucination based on a two-dimensional direct combined model. *Pattern Recognition*, 62:1–20, 2017.

[19] J. Yang, J. Wright, T. S. Huang, and Y. Ma. Image super-resolution via sparse representation. *IEEE transactions on image processing*, 19(11):2861–2873, 2010.

[20] F. Yeganli, M. Nazzal, M. Unal, and H. Ozkaramanli. Image super-resolution via sparse representation over multiple learned dictionaries based on edge sharpness. *Signal, Image and Video Processing*, 10(3):535–542, 2016.

[21] Q. Yin, Z. Cao, and E. Zhou. Face hallucination using convolutional neural networks, Aug. 2 2016. US Patent 9,405,960.

Biographies

Mr. Vikram Mutneja is Ph.D. research scholar in I.K. Gujral Punjab Technical University, Kapurthala (Punajb, India) in the discipline Electronics Engineering. He received his Bachelor's degree (B.Tech.) from Guru Nanak Dev University, Amritsar, Punjab (India) with specialization in Electronics & Communication Engineering in year 1998, Master's degree (M.Tech.) from Giani Zail Singh College of Engineering & Technology, Bathinda (Punjab) (India) under Punjab Technical University (PTU, Jalandhar) with first division in Electronics & Communication Engineering in year 2008. He is a Life Member of ISTE. He has industrial experience of around 5 years (1998-2003) in which he worked in diverse fields such as Hardware and Networking Technical Support, Software Development for Web and Embedded Systems. During his teaching experience of around 13 years (2003-2016) he worked mainly in the areas of embedded systems, VLSI and Digital Signal Processing. He is working presently as Assistant Professor in department of Electronics & Communication Engineering in Shaheed Bhagat Singh State Technical Campus, Ferozepur, Punjab (India). His current field of research includes areas of image processing for detection and extraction of facial features from low resolution surveillance videos, and acceleration using GPU computing.

Dr. Satvir Singh is Associate Professor in I.K. Gujral Punjab Technical University, Kapurthala (Punajb, India). He received his Bachelor's degree (B.Tech.) from Dr. B. R. Ambedkar National Institute of Technology, Jalandhar, Punjab (India) with specialization in Electronics & Communication Engineering in year 1998, Master's degree (M.E.) from Delhi Technological University (Formerly, Delhi College of Engineering), Delhi (India) with distinction in Electronics & Communication Engineering in year 2000 and Doctoral degree (Ph.D.) from Maharshi Dayanand University, Rohtak, Haryana (India) in year 2011. He is a Life Member of ISTE and Corporate Member of IETE. During his 15 years of teaching experience he served as Assistant Professor and Head, Department of Electronics & Communication Engineering at BRCM College of Engineering & Technology, Bahal, (Bhiwani) Haryana, India and as Professor & Head, Department of Electronics & Communication Engineering at Shaheed Bhagat Singh State Technical Campus (Formerly, SBS College of Engineering & Technology), Ferozepur Punjab, India. His fields of special interest include Evolutionary Algorithms, High Performance Computing, Type-1 & Type-2 Fuzzy Logic Systems, Wireless Sensor Networks and Artificial Neural Networks for solving engineering problems.

© 2015-19, IJARCS All Rights Reserved

Optical Materials 69 (2017) 367–371

Contents lists available at ScienceDirect

Optical Materials

journal homepage: www.elsevier.com/locate/optmat

An eco-friendly and inexpensive solvent for solution processable CuSCN as a hole transporting layer in organic solar cells

Neeraj Chaudhary [a, b], Rajiv Chaudhary [b], J.P. Kesari [b], Asit Patra [a, *]

[a] Flexible Organic Energy Devices Group, Advanced Materials Devices and Division, CSIR-National Physical Laboratory, Dr. K. S. Krishnan Marg, New Delhi, 110012, India

[b] Department of Mechanical Engineering, Delhi Technological University, New Delhi, India

ARTICLE INFO

Article history:
Received 12 January 2017
Received in revised form
21 April 2017
Accepted 27 April 2017

Keywords:
Photovoltaics
CuSCN
Hole transport material
Optical property
DMSO
Eco-friendly

ABSTRACT

During past few years, significant research on solution-processable deposition of copper(I)thiocyanate (CuSCN) as an efficient hole transporting layer (HTL) for excitonic solar cells have been successfully reported. Surprisingly, till now only two solvents diisopropyl sulfide and diethyl sulfide are known which have been used for CuSCN film deposition as a HTL for device fabrication. Here, we have used eco-friendly and inexpensive solvent dimethyl sulfoxide (DMSO) for solution processed thin film deposition of CuSCN for organic solar cells. The photovoltaic devices were fabricated using two different donor polymers PCDTBT and PTB7 blended with $PC_{71}BM$ as an acceptor material with device structure of ITO/CuSCN/active layer/Al. The power conversion efficiency (PCE) based on CuSCN using DMSO as a deposition solvent have been achieved up to 4.20% and 3.64% respectively, with relative higher fill factor (FF) as compared to previously reported values in literature. The resultant HTLs were characterized by UV–vis–NIR spectroscopy, X-ray diffraction (XRD), scanning electron microscope (SEM) and atomic force microscope (AFM) for better understanding.

© 2017 Elsevier B.V. All rights reserved.

1. Introduction

Power conversion efficiency (PCE) with adequate stability in excitonic solar cells is the most difficult challenge for their possible commercial applications [1,2]. Particularly, solution processable organic solar cells are most often referred due to their easy fabrication process, cost effectiveness and large area devices [3]. Commonly, conventional bulk heterojunction (BHJ) solar cells have been fabricated based on five different components as active layer (donor/acceptor materials), hole transport layer (HTL), electron transport layer (ETL), indium tin oxide (ITO) as a positive electrode and metal as a negative electrode. Among them, active layer is widely studied to achieve the highest possible performance [4–6]. With respect to effort on active layer, very scanty is known about solution processed HTL, while HTL in photovoltaic device plays an important role for device stability and PCE [7,8]. It is observed that water soluble poly(3,4-ethylenedioxythiophene):poly(styrenesulfonate) (PEDOT:PSS) is frequently used HTL in organic solar cells, although it influences the device stability and degradation [9–11]. Transition metal compounds [12–17] are also well reported for efficient HTL in organic solar cells including copper(I)iodide (CuI) [18] and copper(I)thiocyanate (CuSCN) [19–21]. Nowadays CuSCN has been successfully used as an efficient HTL in excitonic solar cells such as organic solar cells (PCE; 8.22%) [22], dye sensitized solar cells (DSSCs) [20] and perovskite [23,24] solar cells (PCE; 15.6%) [21,25].

In past few years, significant research on solution-processable deposition of CuSCN as an hole transporting layer for fabrication of efficient electronic devices namely field effect transistors [26,27], organic light emitting diodes [28] and solar cells have been successfully reported. Recently, our group reported CuSCN as an efficient and solution-processable HTL in low band gap polymeric solar cells using diisopropyl sulfide solvent for thin film deposition [29]. Anthopoulos and co-workers reported CuSCN as a solution-processable transparent anodic interface material as a replacement of PEDOT:PSS for highly efficient solution processable BHJ device using different combination of donor and acceptor materials [30]. In 2015, another report on advantages of solution-processable CuSCN used as a hole collection/transport layer for polymer/fullerene based organic solar cells have been reported [31]. Very recently, Mishra et al. reported solution-processable CuSCN as an interfacial hole transporting layer in organic solar cells using

* Corresponding author.
E-mail address: apatra@nplindia.org (A. Patra).

http://dx.doi.org/10.1016/j.optmat.2017.04.063
0925-3467/© 2017 Elsevier B.V. All rights reserved.

acceptor-donor-acceptor type oligomers and achieved PCE to 8.22% [22]. However, it is shocking that all the cases, diisopropyl sulfide and diethyl sulfide were used as a solvent for thin film deposition of CuSCN as a HTL. It is also noticeable that diisopropyl sulfide is an irritant solvent having very foul smell. The use of these solvents for CuSCN thin film deposition is limited its application as a solution-processable HTL for cost effective, large area and flexible substrate applications. This is due to harmful, irritant, foul smell and expensive nature of these two solvents. Indeed, Ivlentina and co-workers reported electrodeposited CuSCN nanowires as hole transporting layer in conventional polymeric solar cells [32].

Here we use CuSCN as solution-processable HTL for low band gap organic solar cells. Dimethyl sulfoxide (DMSO) was used for solution processed thin film deposition of CuSCN to examine the effectiveness of the solvents in solar cells. The photovoltaic devices were fabricated using two different low band gap polymers PCDTBT [33] and PTB7 [34] as donor materials blended with phenyl-C_{71}-butyric acid methyl ester ($PC_{71}BM$) as an acceptor material with device structure of ITO/CuSCN/active layer/Al (120 nm). The PCE based on CuSCN using DMSO as a HTL deposited solvent have been achieved up to 4.20% and 3.64% respectively. In this present work, the resulted HTLs were characterized by UV–vis–NIR spectroscopy, scanning electron microscope (SEM) and atomic force microscope (AFM) for better understanding to achieve the highest possible efficiency.

2. Results and discussion

CuSCN is well known *p*-type transparent conductor material. Due to wide band gap and excellent optical transparency, CuSCN is used as a semiconductor for optoelectronic devices [35]. Previously reported, CuSCN has relatively good solubility in diisopropyl sulfide and diethyl sulfide for solution-processable optoelectronic devices fabrication. Here in, we dissolved CuSCN in DMSO (10 mg in 1 mL) using sonicator for 2 h and this solution was kept for 30 min. In contrast to previous report, in which CuSCN dissolve partially in diisopropyl sulfide solvent, while in this study CuSCN dissolved in DMSO for thin film deposition.

Considering significant and even better performance of solution-processable CuSCN as a HTL over PEDOT:PSS and other traditional transition metal oxides, we decided to explore eco-friendly and inexpensive DMSO solvent for CuSCN thin film deposition as an HTL in organic solar cells as a replacement of diethyl sulfide solvent and diisopropyl sulfide. To examine the effectiveness of the DMSO solvent for CuSCN films deposition as HTL in photovoltaic devices, BHJ solar cells were fabricated using device geometry of ITO/CuSCN/active layer/Al as presented in Fig. 1. It is worthy to mention here that PCDTBT and PTB7 are the most studied low band gap donor polymers in combination with $PC_{71}BM$ acceptor for PEDOT:PSS and other traditional HTL in efficient solar cells fabrication. The band diagram and chemical structures of the materials are shown in Figs. 2 and 3 respectively.

Fig. 4 shows the optical spectra of CuSCN thin films to investigate the absorption and transmission across the range of the solar spectrum. CuSCN film shows very little absorption in the range vis-NIR. The transmission spectrum reveals that the CuSCN thin film is highly transparent in the vis-NIR region. Thus, CuSCN thin film exhibits good optical transparency compared to other efficient HTL [22,29,30]. To examine the crystalline nature of the CuSCN thin film, we performed X-ray diffraction (XRD) studies on thin films (on glass deposited from DMSO and diisopropyl sulfide) and powder (Fig. 5). Even though both the thin films are significantly disordered, compared to powder samples (strong and sharp peaks observed at $2\theta = 16, 20, 22, 24, 25, 27, 29, 30, 33, 35, 37, 38, 43, 47, 49, 50, 51, 52, 53, 55, 58$). A broad peak was observed for both thin films of CuSCN. While the thin film was deposited from DMSO ($2\theta = 16, 23, 27, 32, 34, 36, 47, 50$) is more ordered compared to the thin film deposited from diisopropyl sulfide ($2\theta = 16, 27, 32$). CuSCN has a wide band gap semiconductor material and is therefore expected for have very few deep native defect levels in the gap. It has been earlier predicted that the lowest band transition in β-CuSCN is indirect which has very low optical absorption as phonons are required to conserve crystal momentum [35,36]. Hence, the effects of intrinsic defects are not significant.

To study the performance of DMSO as a deposited solvent for CuSCN thin film as HTL in solar cells, we have fabricated the device using PCDTBT as a donor polymer with $PC_{71}BM$ as an acceptor material with geometry of ITO/CuSCN/PCDTBT:$PC_{71}BM$/Al. The CuSCN film was deposited from a solution of DMSO (10 mg/mL) followed by the active material PCDTBT:$PC_{71}BM$ (1.0:4.0 wt%) deposition on the annealed HTL and finally 120 nm aluminum layer was deposited by thermal evaporation. We have observed that the resulting devices show average PCE of 4.20% with open circuit voltage (V_{oc}), short-circuit current (J_{sc}) and fill factor (FF) are 0.72 V, 10.55 mA/cm^2 and 54.98% respectively (Fig. 6a). In this work the device show excellent average photovoltaic parameters which are presented in Table 1. We observed small deviations of the results, which show that our devices are reliable and reproducible. Since the PCE of the device shows slightly lower performance than that of previously reported CuSCN thin film deposited from diisopropyl sulfide as HTL under identical conditions. The lower performance of

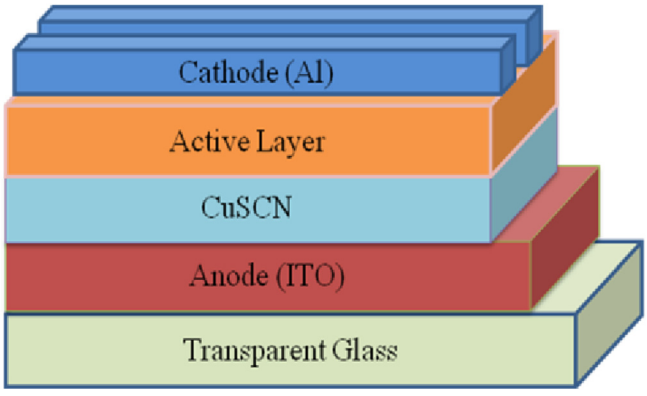

Fig. 1. Device geometry of organic solar cells in which CuSCN (HTL) thin film was deposited from DMSO solvent.

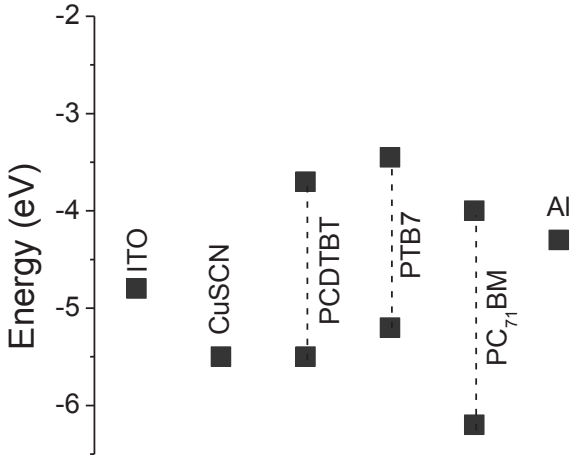

Fig. 2. Energy level diagram of materials.

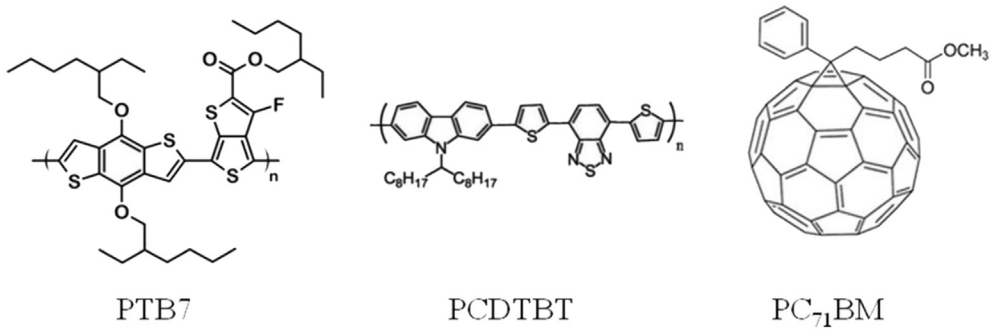

Fig. 3. Chemical structures of PTB7, PCDTBT and $PC_{71}BM$.

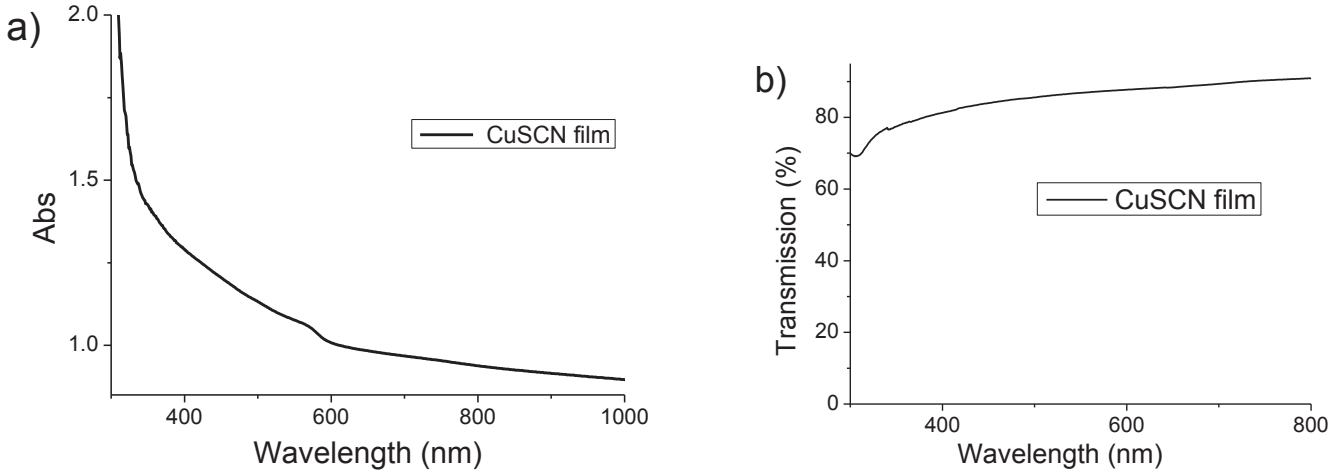

Fig. 4. Optical spectra of CuSCN thin films were deposited using DMSO solution on glass substrates, a) absorption and b) transmission.

the device is mainly due to the slightly lower J_{sc} of the device as compared to previously reported which may be related to the ohmic contact between the CuSCN and active layer [29].

In order to further examine the DMSO as an efficient solvent for CuSCN thin film deposition as HTL, we have chosen PTB7 as a donor material blended with $PC_{71}BM$ as an acceptor. The HTL layer of CuSCN film using DMSO solution (10 mg/mL) on ITO coated glass and annealed for device fabrication. Finally device structure ITO/CuSCN/PTB7:$PC_{71}BM$/Al was completed by deposition of active layer and metal cathode as previously mentioned. The resulting device shows PCE of 3.64% with V_{oc}, J_{sc} and FF are 0.60 V, 16.7 mA/cm^2 and 36.41% respectively (Fig. 6b and Table 1). In contrast to PCDTBT, device based on the PTB7 show lower FF. While both the results with low band gap polymeric solar cells based on PCDTBT and PTB7 clearly demonstrate that DMSO as an alternative, efficient and inexpensive solvent for solution processable CuSCN as HTL for organic solar cells.

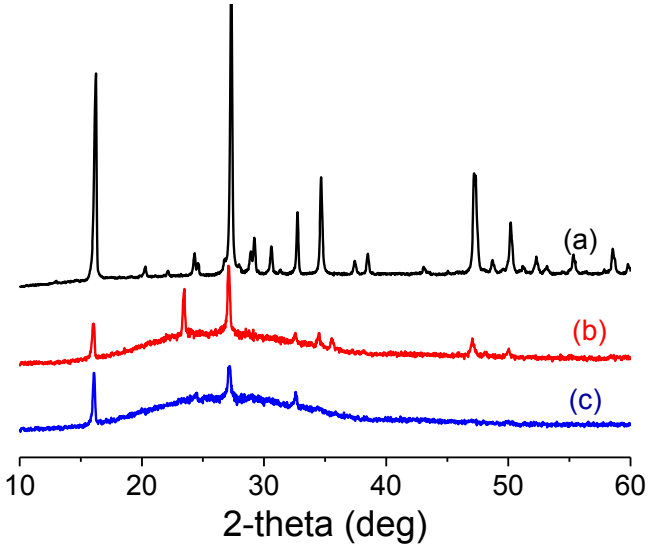

Fig. 5. XRD spectra of CuSCN (a) solid power, film on glass deposited from (b) DMSO and (c) diisopropyl sulfide.

To understand the surface morphology of the CuSCN thin film deposited from DMSO solvent, the films were characterized by scanning electron microscopy (SEM) and atomic force microscope (AFM) (Fig. 7). The film was prepared by spin coating on glass substrates. The SEM image of CuSCN exhibits discontinuous path like structure in contrast to previously reported smooth surface. The AFM image of CuSCN film is rough which supports the SEM image.

3. Experimental section

3.1. Materials

Active materials including low band gap polymer (PTB7 and PCDTBT) along with $PC_{71}BM$ were purchased from 1-material, Canada whereas different solvents were purchased from sigma-aldrich, and alfa-aesar and used as received without further purification.

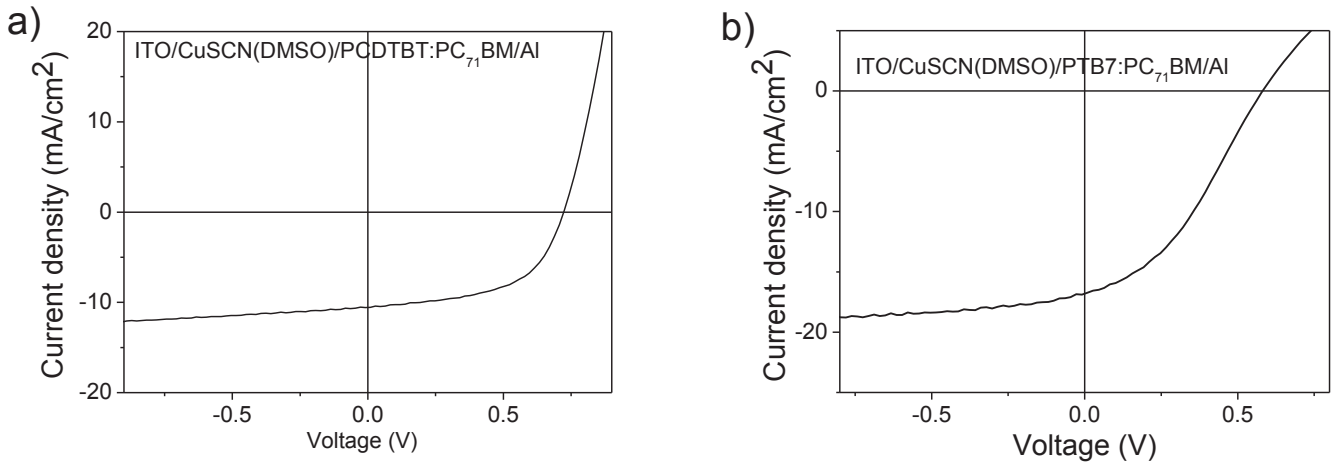

Fig. 6. Current density *versus* voltage (J–V) curves of photovoltaic device based a) PCDTBT:$PC_{71}BM$ and b) PTB7:$PC_{71}BM$ active layers.

Table 1
Solar cells parameters of the devices from the solution-processable CuSCN as an HTL and donor materials with $PC_{71}BM$ of active area 6.0 mm^2 (average of 4 devices).

Entry	Active materials	J_{sc} (mA/cm^2)	V_{oc} (V)	FF%	PCE (%)
1	PCDTBT:$PC_{71}BM$	10.55 (±0.32)	0.72 (±0.02)	54.98 (±2.03)	4.20 (±0.25)
2	PTB7:$PC_{71}BM$	16.7 (±0.63)	0.60 (±0.03)	36.41 (±1.63)	3.64 (±0.20)

3.2. Preparation of CuSCN solutions

10 mg of copper(I)thiocyanate (CuSCN) was dissolved in 1.0 mL dimethyl sulfoxide (DMSO), and the resulting suspension mixture was sonicated for 2 h at room temperature. After sonication the mixture was kept for 30 min and the resulting clear solution was used for solution-processable HTL in organic solar cells.

3.3. Preparation of active materials

The standard weight ratio of PTB7:$PC_{71}BM$ is 1:1.5 to dissolve in a combination of chlorobenzene and 1,8-diiodoctane (97:3 vol%) in a concentration of 25 mg/ml. While in case of PCDTBT:$PC_{71}BM$, the weight ratio of PCDTBT:$PC_{71}BM$ is 1:4 to dissolved in a blend of chlorobenzene and dichlorobenzene (1:3 ratio) in a concentration of 35 mg/mL. Both solutions were stirred overnight inside the glove box.

3.4. Device fabrication

All OPV devices were manufactured on ITO coated glass slide (80 nm thickness, 15Ω/sq sheet resistance) which act as anode while low work function metal aluminum was used as cathode for the fabrication of organic solar cells with the device geometry ITO/CuSCN/active layer/Al. ITO was etched with 2.5 mm width by using laser scribing system. The etched ITO slides were cleaned with distilled water through ultrasonication to remove oil particles. These slides were further cleaned in hot acetone followed by trichloroethylene and isopropanol for 10 min each, further, these were dried in a vacuum oven at 100 °C and then exposed to UV ozone cleaner for 10min to modify its surface into hydrophilic state for better adhesion. Thin film of prepared solution of CuSCN (act as HTL) was deposited by spin-coating process over it at 3500 rpm for 60 s, drying in oven at 100 °C for 15 min followed by drying at room temperature for 1 h. Afterward, the mixed solutions consisting of

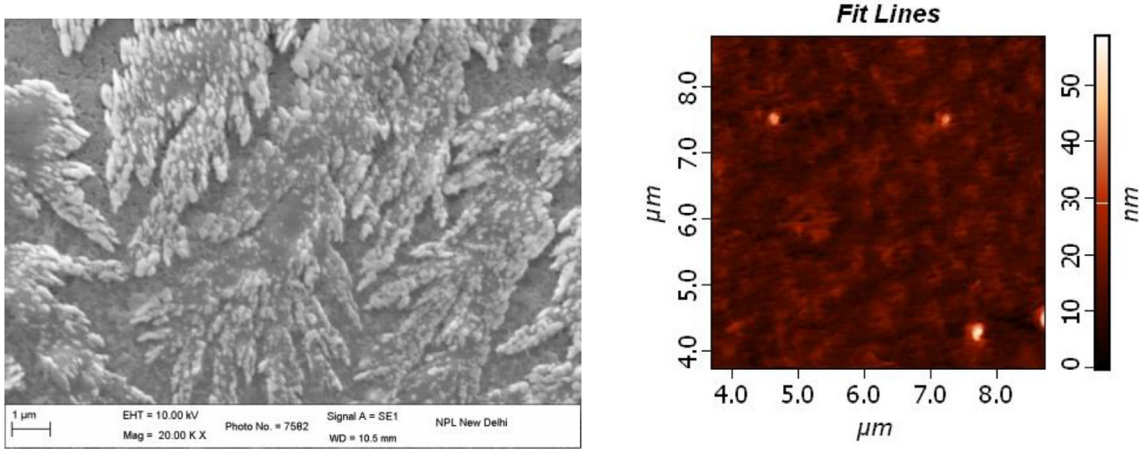

Fig. 7. (left) SEM and (right) AFM images of CuSCN thin films deposited from DMSO solution on glass substrate.

PCDTBT:$PC_{71}BM$ and PTB7:$PC_{71}BM$ were spin coated at 1000 rpm for 90 s in a nitrogen-filled glove-box to form the active layer. Then the slides were directly dried for 10 min on a hot plate at 70 °C. Finally, aluminum metal (cathode) of 120 nm thickness was deposited by thermal evaporation under high vacuum of 5×10^{-6} mbar with a rate of 0.3 nm/s.

3.5. Device characterization

All the device measurements were performed under ambient atmosphere without encapsulation at room temperature. The current-voltage (J-V) characteristics and PCEs were measured with a computer programmed keithley 2400 source/meter. To measure the current density under illumination, the devices were illuminated from the transparent ITO electrode side using solar simulator with an air mass 1.5G (AM 1.5G) (100 mW/cm^2). UV/Vis spectra were obtained on UV-1800, shimadzu spectrophotometer in chlorobenzene, fluorescence spectra were recorded on a fluorolog fluorimeter in a 1 cm quartz cuvette, atomic force microscope (AFM) images were obtained on model number NT-MDT Solver Pro and SEM images were obtained on model number NT-MDT Solver Pro and Zeiss EVO MA-10, variable pressure.

4. Conclusion

In summary, first time we have demonstrated an eco-friendly solution-processable deposition of CuSCN using DMSO solvent as HTL in efficient organic solar cells. The CuSCN thin films were obtained by spin casting from DMSO solvent and found highly transparent. The photovoltaic devices were fabricated with the device structure of ITO/CuSCN/active layer/Al and PCE up to 4.20% has been achieved. We have observed that the solvent DMSO provides compatible interface layers suitable for organic solar cells fabrication which are comparable to diisopropyl sulfide and diethyl sulfide which exhibit displeasing properties like unpleasant smell, detrimental and irritant nature. We have provided further examples of inexpensive and solution-processable CuSCN as an efficient HTL in organic solar cells, which is crucial for possible large area organic solar cells.

Acknowledgments

The work is financially supported by DST, Indo-UK energy initiative project entitled “Advancing the efficiency and production potential of excitonic solar cells (APEX Phase-II)”.

References

[1] J.U. Lee, J.W. Jung, J.W. Job, W.H. Jo, J. Mater. Chem. 22 (2012) 24265–24283.
[2] M.Y. Ameen, S. Pradhan, M.R. Suresh, V.S. Reddy, Opt. Mater. 39 (2015) 134–139.
[3] L. Lu, T. Zheng, Q. Wu, A.M. Schneider, D. Zhao, L. Yu, Chem. Rev. 115 (2015) 12666–12731.
[4] P.M. Beaujuge, J.M.J. Fréchet, J. Amer. Chem. Soc. 133 (2011) 20009–20029.
[5] H. Dong, H. Zhu, Q. Meng, X. Gongb, W. Hu, Chem. Soc. Rev. 41 (2012) 1754–1808.
[6] L. Ye, S. Zhang, L. Huo, M. Zhang, J. Hou, Acc. Chem. Res. 47 (2014) 1595–1603.
[7] W. Yan, S. Ye, Y. Li, W. Sun, H. Rao, Z. Liu, Z. Bian, C. Huang, Adv. Energy Mater. 6 (2016) 1600474.
[8] L. Cali, S. Kazim, M. Gra'tzel, S. Ahmad, Angew. Chem. Int. Ed. 55 (2016) 2–26.
[9] B. Roth, G. A. d. R. Benatto, M. Corazza, R.R. Søndergaard, S.A. Gevorgyan, M. Jørgensen, F.C. Krebs, Adv. Energy Mater. 5 (2015) 201401912.
[10] B. Ecker, J. Posdorfer, E. von Hauff, B. Ecker, Sol. Energ. Mat. Sol. Cells 116 (2013) 176–181.
[11] M. Jørgensen, K. Norrman, S.A. Gevorgyan, T.S. Tromholt, B. Andreasen, F.C. Krebs, Adv. Mater. 24 (2012) 580–612.
[12] F. Ongul, Opt. Mater 50 (2015) 244–249.
[13] S. Shao, J. Liu, J. Bergqvist, S. Shi, C. Veit, U. Würfel, Z. Xie, F. Zhang, Adv. Energy Mater. 3 (2013) 349–355.
[14] E.L. Ratcliff, J. Meyer, K.X. Steirer, N.R. Armstrong, D. Olson, A. Kahn, Org. Electron 13 (2012) 744–749.
[15] P. Qin, G. Fang, F. Cheng, W. Ke, H. Lei, H. Wang, X. Zhao, ACS Appl. Mater. Interfaces 6 (2014) 2963–2973.
[16] Z. Tan, L. Li, F. Wang, Q. Xu, S. Li, G. Sun, X. Tu, X. Hou, J. Hou, Y. Li, Adv. Energy Mater. 4 (2014) 1300884–1300890.
[17] H. Pan, L. Zuo, W. Fu, C. Fan, B. Andreasen, X. Jiang, K. Norrman, F.C. Krebs, H. Chen, Org. Electron. 14 (2013) 797–803.
[18] N. Chaudhary, J.P. Kesari, R. Chaudhary, A. Patra, Opt. Mater. 58 (2016) 116–120.
[19] (a) K. Tennakone, W.M. Ariyasingha, Electrochimica Acta 25 (1980) 731–733; (b) B. O'Regan, D.T. Schwartz, Chem. Mater. 7 (1995) 1349–1354; (c) B. O'Regan, D.T. Schwartz, S.M. Zakeeruddin, M. Grätzel, Adv. Mater. 12 (2000) 1263–1267.
[20] G. Kumara, A. Konno, G.K.R. Senadeera, P.V.V. Jayaweera, D.D. Silva, K. Tennakone, Sol. Energ. Mat. Sol. Cells 69 (2001) 195–199.
[21] P. Qin, S. Tanaka, S. Ito, N. Tetreault, K. Manabe, H. Nishino, M.K. Nazeeruddin, M. Gratzel, Nat. Commun. 5 (2014) 3834.
[22] A. Mishra, T. Rana, A. Looser, M. Stolte, F. Wurthner, P. Bauerlea, G.D. Sharma, J. Mater. Chem. A 4 (2016) 17344–17353.
[23] S. Ye, W. Sun, Y. Li, W. Yan, H. Peng, Z. Bian, Z. Liu, C. Huang, Nano Lett. 15 (2015) 3723–3728.
[24] G. Murugadoss, R. Thangamuthu, S.M.S. Kumar, Sol. Energ. Mat. Sol. Cells 164 (2017) 56–62.
[25] G. Morán, S. Arrechea, P. d l Cruz, V. Cuesta, S. Biswas, E. Palomares, G.D. Sharma, F. Langa, J. Mater. Chem. A 4 (2016) 11009–11022.
[26] P. Pattanasattayavong, N. Yaacobi-Gross, K. Zhao, G.O.N. Ndjawa, J. Li, F. Yan, B.C. O'Regan, A. Amassian, T.D. Anthopoulos, Adv. Mater. 25 (2013) 1504–1509.
[27] P. Pattanasattayavong, G.O.N. Ndjawa, K. Zhao, K.W. Chou, N. Yaacobi-Gross, B.C. O'Regan, A. Amassianb, T.D. Anthopoulos, Chem. Commun. 49 (2013) 4154–4156.
[28] A. Perumal, H. Faber, N. Yaacobi-Gross, P. Pattanasattayavong, C. Burgess, S. Jha, M.A. McLachlan, P.N. Stavrinou, T.D. Anthopoulos, D.D.C. Bradley, Adv. Mater. 27 (2015) 93–100.
[29] N. Chaudhary, R. Chaudhary, J.P. Kesari, A. Patra, S. Chand, J. Mater. Chem. C 3 (2015) 11886.
[30] N. Yaacobi-Gross, N.D. Treat, P. Pattanasattayavong, H. Faber, A.K. Perumal, N. Stingelin, D.D.C. Bradley, P.N. Stavrinou, M. Heeney, T.D. Anthopoulos, Adv. Energy Mater. 5 (2014) 1401529.
[31] N.D. Treat, N. Yaacobi-Gross, H. Faber, A.K. Perumal, D.D.C. Bradley, N. Stingelin, T.D. Anthopoulos, Appl. Phys. Lett. 107 (2015) 013301.
[32] C. Chappaz-Gillot, S. Bersona, R. Salazar, B. Lechêne, D. Aldakov, V. Delaye, S. Guillerez, V. Ivanova, Sol. Energ. Mat. Sol. Cells 120 (2014) 163–167 and reference therein.
[33] Poly[N-9'-heptadecanyl-2,7-carbazole-alt-5,5-(4',7'-di-2-thienyl-2',1',3'-benzothiadiazole)] (PCDTBT). (b) S. Beaupré, M. Leclerc, J. Mater. Chem. A 1 (2013) 11097–11105.
[34] (a) Poly[[4,8-bis[(2-ethylhexyl)oxy]benzo[1,2-b:4,5-b']dithiophene-2,6-diyl][3-fluoro-2-[(2-ethylhexyl)carbonyl]thieno[3,4-b]thiophenediyl]] (PTB7). (b) F. He, L. Yu, J. Phys. Chem. Lett. 2 (2011) 3102–3113; (c) L. Ye, S. Zhang, W. Zhao, H. Yao, J. Hou, Chem. Mater. 26 (2014) 3603–3605.
[35] J.E. Jaffe, T.C. Kaspar, T.C. Droubay, T. Varga, M.E. Bowden, G.J. Exarhos, J. Phys. Chem. C 114 (2010) 9111–9117.
[36] P. Pattanasattayavong, V. Promarak, T.D. Anthopoulos, Adv. Electron Mater. 3 (2017) 1600378.

Available online at www.sciencedirect.com

ScienceDirect

Materials Today: Proceedings 4 (2017) 1106–1115

materialstoday: PROCEEDINGS

www.materialstoday.com/proceedings

5th International Conference of Materials Processing and Characterization (ICMPC 2016)

Application of Big Data in Supply Chain Management

Ankit Singh*, Deepak Jain, Ishant Mehta, Jishnu Mitra, Saurabh Agrawal

Mechanical and Automotive Engineering Department, Delhi Technological University, Delhi-110042, India

Abstract

Big data is a term used to describe the massive volume of both structured and unstructured data that is too large that it is difficult to process using conventional database and software techniques. Even though Big Data is in its early stages, it has remarkably transformed nearly each and every sector in the industry. It has also revamped the Supply Chain Management giving it a new dimension by increasing efficiency of production and optimization of operations. This paper identifies the issues regarding Supply Chain Management by employing Delphi technique and aims to resolve them by incorporating Big Data Analytics.Finally, an example of big data analytics application is also presented as a way of unveiling some of the relatively unexplored territories in big data analytics research.
©2017 Elsevier Ltd. All rights reserved.
Selection and peer-review under responsibility of Conference Committee Members of 5th International Conference of Materials Processing and Characterization (ICMPC 2016).

*Keywords:*Supply Chain Management; Delphi Technique; Big Data; Issues; Case Study

1. Introduction

1.1. Supply Chain Management

Supply chain management is the management of the flow of goods and services. It includes the movement and storage of raw materials, work-in-process inventory, and finished goods from point of origin to point of consumption.[1] Even though the definition might sound facile, it is quite a complicated process with multifarious bottlenecks at different stages. Businesses from manufacturers, wholesalers and retailers, to warehouses, healthcare providers and government agencies use supply chain management principles to plan, assemble, store, ship, and track products from the beginning to the end of the supply chain.

*Corresponding author. Tel.: +91 9953159447
*Email address:*ankit10sevs@gmail.com

2214-7853©2017 Elsevier Ltd. All rights reserved.
Selection and peer-review under responsibility of Conference Committee Members of 5th International Conference of Materials Processing and Characterization (ICMPC 2016).

Fig. 1. Supply Chain Model[2]

Figure 1 represents the model of supply chain management .The main role of a supply chain in an industry is discussed in as shown in below table 1:

Table1 . Role of Supply Chain Management in an industry

SUPPLY CHAIN MANAGEMENT			
PLANNING		**OPERATIONS**	
1	Deamnd Forecasting	1	Day to Day management
2	Inventory Control	2	Storage
3	Customer Service	3	Distribution
4	Purchasing	4	Fulfillment

1.2. Big Data

Big data is a term used to describe the exponential growth and availability of data, both structured and unstructured and big data may be as important to business – and society – as the Internet has become**.**

1.2.1. The Three V's of Big Data

Table 2: Causes of Big Data[3]

Type of Data	Volume	Velocity	Variety
Sales	More detail around the sale, including price, quantity, items sold, time of day, date, and customer data.	From monthly and weekly to daily and hourly.	Direct sales, sales of distributors, Internet sales, international sales, and competitor sales
Consumer	More detail regarding decision andpurchasing behavior, includingitemsbrowsed and bought, frequency,dollar value, and timing.	From click through to card usage.	Face profiling data for shopper identification and emotion detection; eye-tracking data; customer sentiment about products purchased based on "Likes," and product reviews.
Inventory	Perpetual inventory at more locations, at a more disaggregate level (e.g., style/color/size).	From monthly updates to hourly updates.	Inventory in warehouses, stores, Internet stores, and a wide variety of vendors online.
Location and Time	Sensor data to detect location in store, including misplaced inventory, in distribution center (picking, racks, staging, etc.), in transportation unit.	Frequent updates for new location and movement.	Not only where it is, but hat is close to it, who moved it, its path to get there, and its predicted path forward; location positions that are time stamped from mobile devices.

Currently the world has around 2.8 zeta bytes of data and by 2016 the cumulative size of the entire world's data is expected to exceed 16,000 acres and by 2020 this data is going to become 50 times larger and the same is depicted

within the figure 2 a and 2 b. It is estimated that only 33% of this information can be appropriately targeted and analyzed but currently only 0.5% of this information is only analyzed as shown in above table 2. [4]

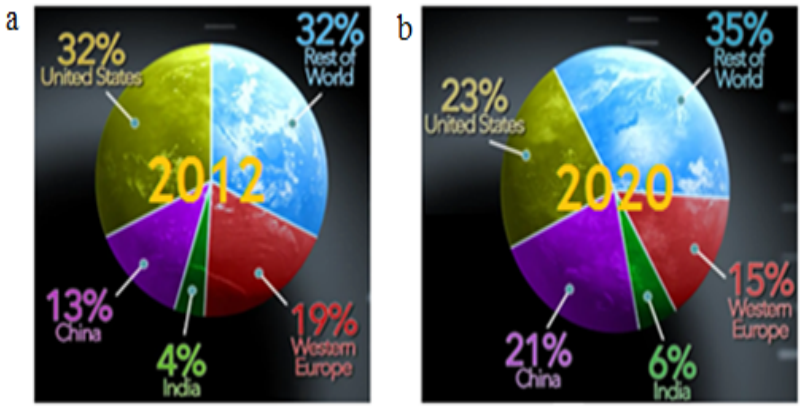

Fig. 2. (a) Data Distribution in 2012; (b) Expected Data Distribution in 2020[4]

2. Literature Review and Research Gap

Supply Chain Management is a way of managing the business and its relationships.[5]The conventional meaning of supply chain management needs to be transformed with the upcoming trends in SCM. With the dramatic changes taking place within a span of few years in this industry, the SCM needs to be adequately updated and adapt accordingly to the needs of the industry.

With the introduction of Reverse supply chain which is defined as the process of planning, implementing and controlling the backward flows of raw materials, in process inventory, packaging and finished goods, from a manufacturing, distribution or use point to a point of recovery or point of disposal [6], which has made the supply chain complex and a dynamic value web hence making the optimization of operations intractable.Hence, the older techniques need to be updated and new technological changes are the need of the hour.

We concur with Waller and Fawcett who more or less argue that previous research have not yet properly closed the gap between supply chain functional knowledge. The research papers provide clarification on key aspects of SCM that will aid practitioners and researchers in their desire to understand and implement SCM,[5] but sometimes find it more difficult to see the direct connection of big data to SCM.[3] Even though these research papers have found solutions to the existing problems in SCM, they find it difficult to concentrate on each aspect and optimize every function.

Chaeexamined the role of social media platforms in generating big data useful within supply chains. [8]Ivanov and Sokolov provided an inter-disciplinary modeling framework for model-based decision support within collaborative supply chains.[9] Sensors and transaction logs within organizations, as well as Internet linkages both from fellow supply chain participants as well as from other Internet sources have led to an explosive growth in big data, which can be valuable to track materiel by location, and can be useful for supply chain planning.[10]Taguchi method used by Shouvik and Prasantais a powerful tool for designing high quality systems with an optimum setting of process control parametersintroduces an integrated approach that is simple and efficient to find the best range of designs for quality, performance and computational cost in SCM. [18]

The emergence of new terms, such as SCA, reflects a broad interest in leveraging the business value of supply chain data and harnessing the power of various analytical technologies and methods. Top performing companies are better at utilizing their data for business planning and execution and this has led to the increase in supply chain integration and visibility. In general, academic research expects the benefits of analytics in supporting supply chain operations.[11]

Thus after reviewing studies and research papers on supply chain management, we have identified the research gap in supply chain management which requires technological changes along with better implementation to tackle the upcoming and the current issues subsequently. Thus we need to come up with the software that provides better

data analytics along with easy implementation to help sought the issues pertaining to SCM. Big Data Analytics can be one of the best solutions to the SCM issues, which can not only store and utilize the data successfully, but even provide the best solutions.

Only 20% of the companies have taken up Big Data Analytics. This implies that there is much to be understood and worked upon in Big Data analytics' implementation in SCM. This gives us further prospects of working and successfully incorporating the big data techniques into SCM.

3. Research Objective

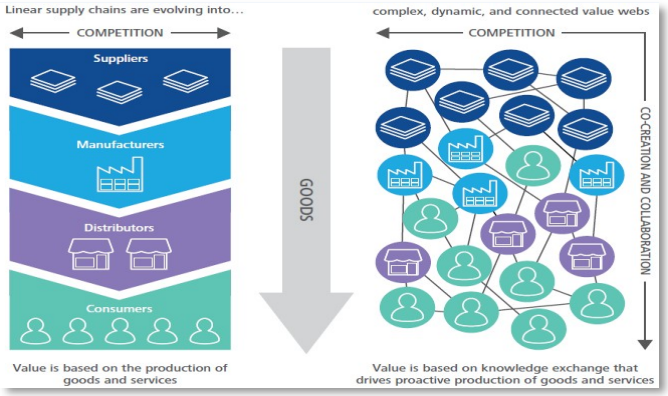

Fig.3. Supply Chain Evolve into value web[5]

As can be seen from the above figure 3earlier the supply chain had a linear relationship between the suppliers, manufacturers, distributors and the consumers but now with the advent of e-commerce and rising customer demands the supply chain has become complex and hence the managers are finding it difficult to optimize the operations.

So the main objective of the research is to find a way to reduce the complexity of the supply chain by using Big Data Analytics and to identify the data sources that may be considered for decision-making purposes in each of the SCM levers: procurement, marketing, transportation, and warehouse operations.

Also the research is aimed to identify the issues of supply chain management that can be resolved using Big Data Analytics and to find solutions to them by applying Delphi Technique.

4. Research Methodology

The research methodology delineates the processes and methods equipped to conduct the research on any subject. It includes basically three steps: collecting material, descriptive analysis and final evaluation.

One of the most effective research methods that have been used recently is the Delphi Technique. The Delphi Technique is an effective tool for thorough research and analysis of any issue. The Delphi Technique allows individuals to get in depth knowledge of any topic by asking the experts. The experts are able to guide the individuals on the issues providing them with personal experiences and proper guidance.

Online websites like OpenIDEO, Techcast and Horizon serve as medium to these techniques. It allows people to interact with individuals personally online. There is usually a panel of 3-4 individuals, each expert in their own domain. We have utilized the Delphi Technique to get acclimatized to the issues of supply chain management and the tree diagram for the application of Delphi technique is shown in figure 4. The experts have delineated the issues in recent times and the various techniques that were being used to solve the upcoming issues. Figure 5 shown below representation of aquestionnaire which was presented to the experts to get insights on the issues and their solutions,

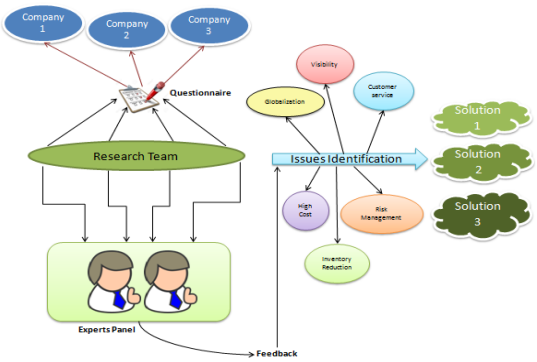

Fig. 4 . Application of Delphi Technique

APPLICATION OF BIG DATA IN SUPPLY CHAIN MANAGEMENT
QUESTIONNAIRE

NAME		AGE		DATE	
COMPANY			EXPERIENCE		
Email id			CONTACT		

Q1. What is your cardinal area of concern regarding the firm's supply chain?

Ans.

Q2. As we understand, inventory costs are a major bottleneck when it comes to reducing overall operational costs of the supply chain. Is it true? How do you plan to combat these costs?

Ans.

Q3. How does the firm prepare itself to handle situations where the suppliers or vendors are not able to supply the requisite amount of raw materials or parts?

Ans.

Q4. What type of services do you provide to the customer to keep them pacified?

Ans.

Q5. What are the most important of these services without which the customer would not be happy?

Ans.

Q.6 How has technology like sensors in inventory control system played a major role in the past few years ?

Ans.

Are you aware of the Big data Analytics?	YES ☐	NO ☐
Has your company used big data analytics yet?	YES ☐	NO ☐
Are you facing challenges due to disruptions caused by external factors?	YES ☐	NO ☐

FORM NUMBER - A1001

Fig. 5 . Questionnaire

The questions were answered by experts that have helped us in finding the solutions to these issues that can be successfully resolved using Big Data.

The other method that has been utilized is the study of different case studies. The inclusion of the case study is done to maintain practicality at the core. Case Studies investigated simultaneous big data analytics examples, typically in emerging practices, thus being a successful way of including the latest trends detected in the industry. [8].We have traced the case study of United Parcel Service (UPS)to gain practical experience of what can be achieved through incorporation of Big Data Analytics in SCM.

5. Research Findings

One of the most significant paradigm shifts of modern business management is that individual businesses no longer compete as solely autonomous entities, but rather as supply chains. Business management has entered the era of internetwork competition. Instead of brand versus brand or store versus store, it is now suppliers - brand - store versus suppliers – brand - store, or supply chain versus supply chain. [5]

Any company that has undertaken the mission of implementing a supply chain management strategy knows that one of the greatest challenges it faces is the significant change in internal culture that is required to make the supply chain redesign successful. However difficult it may be to accomplish, change can be implemented successfully when directed by a strong and knowledgeable leader, who understands the tools available for achieving positive change, as well as their role in initiating and sustaining these changes.

5.1 Issues in Supply Chain management

5.1.1. Primary Issues

- Reducing Operating Cost: One of the most common goals for any industry includes cost reduction and is so applicable for Supply Chain Management as well.
- Overall Inventory Cost (Shorter Lead Time and Better Throughput): With shorter product life cycles andchanging market demands, companies are forced to embark on a lean journey. Realistic forecasting of future sales is the need of the hour for optimizing the inventory and reducing its cost. [13]

5.1.2. Secondary Issues

- Improve Customer Service: A number of industries have established themselves in the Supply chain industry and providing customers with more and more services making it compulsory for other industries to provide the same or even furthermore to stay in the market and compete with their rivals.

- Speed of Product Delivery to Markets: In recent times, with quick and timely deliveries from various industries has made it mandatory for other companies to match up their delivery time. It has become essentially a requirement for the companies and natural for the customers to have their goods delivered within a limited period of time.

- Visibility: With the ever growing competition in the supply chain management and new companies foraying their way in the supply chain industry, the products are differentiated and must match the customer requirements.

- Risk Management: Companies that are too reliant on one supplier are vulnerable if that supplier can't meet demands. This means that supply chain managers must mitigate risks, for example an earthquake in Asia should not halt the supply in North America. Both mitigation and contingency strategies must be taken care of by an industry to ensure minimum disruptions in supply due to external and natural factors.[14]

- Increasing Customer Demands (Growing Expectations): With in numerous ways of advertising products to each household, makes it further more competitive for each firm to not only better display these products but provide the best product offered in the market. Also each company needs to keep itself updated with the market, and develop subsequent strategies to tackle other companies in ever growing cut throat competitive market. [15]

- Globalization: With globalization, each and every product that is being sold must match the quality of products made in other countries for customer satisfaction. Today people are well aware of the products being offered in the outside world, and hence are intelligent enough to distinguish between good and just satisfactory products. The companies are hence required to provide the best they have to their customers. In

these cases a company is required to have global procurement network which can support and react to their supply chain needs. Also a company needs to select suppliers that provide manufacturing locations with consistent global quality and a reliable local service to compete effectively in the market.[16]

- Making Supply Chain Less Complex: With so many suppliers, manufacturing location, different products and varied costumer needs make the supply chain complex. Thus making supply chain less complex is also required for increased efficiency and optimized operations.

Fig. 6 . Issues in Supply Chain[12]

6. Solutions to issues using Big Data

- **In Reducing Delivery Time**

  The organizations which adopt big data analysis will have the capacity to connect their systems with systems of millions of their customers. This would allow them to move the data ahead of packages. For example, for a delivery company, packages arriving from a different city could be directly send to a warehouse near the intended delivery address and shipped out to their destination the next day without any delay. This would save valuable time and effort which is wasted in storing all the packages arriving at a particular city at the same warehouse, and then sorting them according to localities.

  Big data analytics would also enables companies to develop algorithms that can predict the maintenance requirements of their systems. With the multitude of products produced and delivered daily, an unplanned breakdown of a system can have serious consequences resulting in late packages and angry customers. Analyzing the data from the various machines involved in production, or analyzing the data from the delivery vehicles, would give a signal as to when should the machine or vehicle be serviced. This would give the organization time to arrange for a back-up mechanism. This would help in keeping the delivery time unaffected. Predictive maintenance would save millions in preventing unnecessary and unplanned maintenance and would also keep the customers pacified.

- **In Improving Customer Service**

  To keep a customer loyal to the organization, the customer needs to be pampered with newer services and offers frequently. To know which offer or service is apt for a particular customer, the organization need to know the likings of the customer. This is where big data comes in. Collecting data about the buying habits, delivery choices, payment methods, shopping seasons etc of the customer would give the organization proper knowledge about the consumer. Using this knowledge, the apt offers and services could be pitched to the customer. This would make the customer feel like he or she is receiving personal care. And pitching the right offers and services, would also lead to increase in sales.An example of using big data to provide improved customer care services could be found in the delivery business. Data could be collected regarding when a customer is available to collect the package, based on previous experiences. This would allow the company to decide the windows of time, when the packages should be delivered to

respective customers. Receiving packages at their preferred time slots would give a positive view of the company to the customers, and encourage them to choose the company in the future as well.

- **In Reducing Inventory Costs**

  The purpose of inventory is to act as a buffer in cases pertaining to sudden increase in demand, sudden shortage of supply of essential raw materials and parts from the supplier or break down of machinery. Using big data can drastically reduce the level of inventory needed to be maintained. Data related to past demand can be used to accurately predict future demands. Similarly, the history of the supply patterns of a particular supplier can be used to predict the situations in which a shortage of supply can be expected. And analyzing performance data of the machines can help in formulating preventive algorithms to service the machines before they break down. Using these techniques can significantly reduce the inventory levels, leading to savings of wealth and space.

- **In Reducing Operational Cost**

  Reducing operational costs is a primary area of concern for most industry leaders. Reduced operational costs lead to increased profits and greater productivity. But operational cost is a function of costs associated with multiple variables like raw materials, maintenance of machineries, outsourcing, inventory, electricity, transportation and many more. All these variables are interlinked. An alteration in any one of them might have an adverse effect on the others. For example, a reduction in inventory of raw materials will lead to reduction in inventory costs. But if the reduction is too much, then the extra costs incurred due to the increased frequency of raw material transportation will outweigh the reduction in inventory costs. Hence the reduction of overall operational costs is a complex problem. The primordial task is the selection of variables, which can be altered or modified to the right extent, to get substantial reductions in their costs, without increasing other costs. If a firm tries to tackle the majority of the variables simultaneously, without creating a priority order, then in invariably leads to wastage of resources, without getting any appreciable results.

  Big Data Analysis can play a decisive role in this process of prioritization. It can also play a role in balancing the reductions in each variable cost so that they do not increase other costs. Considerable volume of data relating to each of the variables can be collected. Analysis of these data, would give the firm insights into the independent cost functions as well as the relationship between different variables. This would enable the firms to prioritize variables for alterations. Using these analyses, precisely calculated changes (based on the analyses) can be made to prioritized individual variables, which though affecting other variables, would lead to overall reduction in operational cost. Different models can be created using different alterations based on the analyses.

7. Case Study

7.1 United Parcel Service

United Parcel Service (UPS) is the biggest package shipping company in the world. It was founded in 1907 and on a daily basis they make more than 16 million shipments to over 8.8 million customers globally. In addition, they receive on average 39.5 million tracking requests from customers per day. They gather data at every possible moment and already store over 16 petabytes of data.

They use Big Data to analyze such huge data. UPS uses proprietary package flow technology to determine what packages are loaded on each vehicle, then gathers data from several aspects of fleet operations using a telematics technology system.

UPS uses telepathic trucks which have sensors that capture over 200 data points for more than 80,000 vehicles every day. The data analyzed includes:

- Engine Monitoring
- Speed
- Mileage

- Number of Stops
- Miles per gallon
- Safety aspects

Analyses on these parameters have resulted in exponential results:

- 2.6 million X 10 million minutes of idling time reduced in 2012, saving more than 1.5million gallons of fuel.
- 13000 metric tons of carbon emissions avoided due to reduced miles per stop- 12.1 million miles of driving eliminated in 2012.
- 39 million x 1 million gallons of fuel saved since 2001 due to route optimization.

UPS takes a holistic approach to integrating data into technology. Arguably the world's largest operations research project, ORION uses fleet telematics and advanced algorithms to take route optimization to a new level. In 2013, UPS began the first major deployment of ORION, with plans to deploy the technology to all 55,000 North American routes by 2017. [17]

8. Conclusion

From our study on Supply chain management, we can infer that the structure of supply chain has transformed rapidly in the past few years. Thus to overcome this complexity in supply chain and handle the humongous data that has compiled over the years, we need a powerful tool. Big Data provides us with the perfect solution, by not only abating the complexity, but also successfully optimizing the operations.

The above stated results along with the successful story of the above company, provides enough evidence and supports the big data implementation in the supply chain industry.

Thus we can see that big data analytics can be successfully implemented in Supply chain management producing fruitful results for the organization. This integration has allowed companies to come up with highly innovative solutions and accelerate the widespread adoption of these core supply chain principles.

Also we intend to work further on big data analytics using hypothetical data to further resolve the remaining issues of supply chain.

References

[1]OBE, Graham Hoyle, Association of Employment and Learning Providers, January 3, 2013.

[2] Akcali E., Etinkaya S. and Uster H. , *Networks*, 2009: 231-248.

[3]Fawcett, Matthew A. Waller and Stanley E. , Journal of Business Logistics, 2013: 77-84.

[4]Davenport, Thomas H. , International Institute of Analytics, SAS, 2013.

[5]Douglas M. Lambert, Martha C. Cooper. , Industrial Marketing Management. New York: Elsevier Science Inc, 2000. 65-83.

[6]Navendu Sharma, Amish, ManishaMeena,Saurabh Agrawal. , 4th International Conference on Materials Processing and Characterization. Hyderabad: Elsevier, 2015. 3100-3016.

[7] Marchese, Eamonn Kelly and Kelly. , Business ecosystems come of age report. Texas: Deloitte University Press, 2015.

[8] Chae, International Journal of Production Economics, 2015: 247-259.

[9] Ivanov, D., and Sokolov, B. , Journal of Manufacturing Technology Management, 2012: 976-997.

[10]Olson, David L. , Lincoln: College of Business Administration, 2015.

[11]Bongsug (Kevin) Chae, David Olson &ChwenSheu. , International Journal of Production Research, 2013.

[12]Braunstein, Cal. , Wilton: Robert Frances Group, 2013.

[13] Dean, David. , Zug: Bossard Group, 2012.

[14]Montroy, Jeannette. , Canada: Procurement Sense, 2015.

[15] O'Marah, Kevin. , Supply management, October 1, 2013.

[16] Berrios, David, Madison: Wisconsin School Of Business, 2014.

[17]Jack Levis, Dale Spencer., California: Mother Nature Network, 2013.

[18] Shouvik Ghosh, PrasantaSahoo, GoutamSutradhar., International Journal of Advanced Materials Manufacturing and Characterization. Hyderabad: Advanced Materials Manufacturing & Characterization, 2014. 93-99.

CFD Analysis of Wavy Microchannel Heat Sink with Hemispherical Obstructions and Comparing it with Experimental Results of Rectangular Microchannel Heat Sink

Rajnish Kumar[1], M. Zunaid[2]

[1]*M. Tech Scholar, Department of Mechanical Engineering, Delhi Technological University, New Delhi-110042, India*

[2]*Assistant Professor, Department of Mechanical Engineering, Delhi Technological University, New Delhi-110042, India*

Abstract: **In the present analysis of fluid flow, there are two cases. In first case, CFD Analysis of wavy microchannel heat sink with hemispherical obstructions is done in Ansys CFX package and the simulation results are obtained for pressure drop and heat transfer characteristics for single phase laminar flow. For this analysis the geometry of the channel has been made wavy edge with rectangular entry and exit. Then the obstructions with hemispherical shape have been put at the particular wavelength. Water is taken as coolant and cooper is used as a sink material. The main aim of changing the geometry of the straight channel to wavy channel with the inclusion of hemispherical obstructions is to increase the surface area and contact time of coolant with the heated surface to increase the temperature rise by decreasing thermal resistance. In the second case, comparison of simulation results of the first case with experimental results of rectangular microchannel obtained by Weilin Qu and Issam Mudawar. Both the micro-channels have a width of 0.23mm and height of 0.71 mm. The aspect ratio (ɣ) and the length of both the channels is kept same as 0.32 and 44.7mm respectively. The diameter of hemispherical obstruction is taken as 0.22 mm. The analysis for both the micro-channels is done for five sets of Reynolds number which are 400, 600, 800, 1000 and 1200 respectively. The two values of heat flux used are 100W/cm^{2}and 200W/cm^2.After constructing the geometry in solid works and partially in the Design Modular, the simulation is done on ANSYS CFX.**

I. INTRODUCTION

Micro-channel heat sink-

Micro-channels have become very popular in applications where very high heat transfer rates are necessary. Its development trend as electronics equipment becomes more advanced and smaller in size with continuing innovations. It faces thermal engineering challenges from the high level of heat generation and the reduction of available surface area for heat removal. In the absence of sufficient heat removal, the working temperature of this component may exceed a desired temperature level which then increases the critical failure rate of equipment. Therefore, advanced electronic equipment with high heat generation requires an efficient and compact device to provide proper cooling operation. In order to meet the cooling requirement, needs to increase the product of heat transfer coefficient (h) and heat transfer surface area (A) for a device. Since heat transfer coefficient is related to the channel hydraulic diameter. The heat transfer surface area can be increased by incorporating micro channels on the device surface. One promising solution to the problem is liquid cooling incorporating on micro-channels. Micro-channel heat transfer has the potential of cooling high power density microchips. One can expect that as the size of the channel decrease, the value of convective heat transfer coefficient(h) becomes increasing in order to maintain a constant value of the Nusselt number (hD_h/kf). These chips have machined micro-channels through which cooling fluid like water is circulated. The cooling liquid removes heat by single phase forced convection. Flow within the micro-channel is considered as fully developed laminar flow with constant heat flux. Therefore, heat sinks with larger extended surfaces, highly conductive materials and more coolant flow are key parameters to reduce the base temperature.

Straight Microchannel

In Today's world the basic requirement in the field of heat transfer is compact heat exchanger, for cooling of electronic chips, micro level biological instruments etc. As we are having fixed surface area so, the solution is to vary the surface properties by having surface obstacles (delta-wings), surface indentation (dimples), surface channels (wavy, zigzag channel).

The major advantages of straight channels includes, increased surface area for heat flow, better flow mixing at curved portion results in better distribution of heat, and effective cooling . In normal heat flow as in straight channel same molecule remains in contact with the surface throughout the flow causes poor heat transfer, but in wavy or zig-zag channel, due to the phenomenon known as boundary layer regeneration fluid particle from free layer gets chance to come in contact with the surface which enhances the heat transfer characteristics. But its disadvantage is that it causes pressure

drop. But the value of effectiveness of channel is greater than one which shows that heat transfer enhancement is more as compared to pressure drop.

Wavy Microchannel

In Today's world the basic requirement in the field of heat transfer is compact heat exchanger, for cooling of electronic chips, micro level biological instruments etc. As we are having fixed surface area so, the solution is to vary the surface properties by having surface obstacles (delta-wings), surface indentation (dimples), surface channels (wavy, zigzag channel).

The major advantages of wavy channels includes, increased surface area for heat flow, better flow mixing at curved portion results in better distribution of heat, and effective cooling . In normal heat flow as in straight channel same molecule remains in contact with the surface throughout the flow causes poor heat transfer, but in wavy or wavy channel, due to the phenomenon known as boundary layer regeneration fluid particle from free layer gets chance to come in contact with the surface which enhances the heat transfer characteristics. But its disadvantage is that it causes pressure drop. But the value of effectiveness of channel is greater than one which shows that heat transfer enhancement is more as compared to pressure drop.

NOMENCLATURE

A_c Cross-sectional area of channel (m^2)
C_p Specific heat at constant pressure (J/kg-K)
D_h Hydraulic diameter of channel perimeter (m)
H Height of micro-channel heat sink (m)
H_{ch} Height of micro-channel (m)
H_{w1} Substrate thickness on insulated side of microchannel heat (m)
H_{w2} Substrate thickness on heated side of microchannel heat sink(m)
K Thermal conductivity (W/m-K)
L Length of microchannel heat sink (m)
P Pressure (Pa)
q Heat flux (W/m^2)
Re Reynolds number based on channel hydraulic diameter
R_{th} Thermal resistance (m-K/W)
T Temperature (K)
T_{in} Fluid inlet temperature (K)
T_{bm} Fluid bulk temperature (K)
W Width of micro-channel heat sink unit cell (m)
W_{ch} Width of micro-channel (m)
W_{w1}, W_{w2} Half-thickness of wall separating micro-channels (m)
ɣ aspect ratio

Greek symbols

μ dynamic viscosity ($N\text{-}s/m^2$)
ρ density (kg/m^3)

II. MATHEMATICAL FORMULATION

In the present study the single phase model of computational fluid dynamics is used for the purpose of computing and solving the problem of particular category. This single phase model will solve and calculate one transport equation for continuity and one for momentum for each phase, and after this the energy equations are solved for studying the fluid and thermal performance of the system. The simulation for this single phase model is done using ANSYS CFX.

The equations used in this model include the equation of momentum, equation of continuity and energy equation (ANSYS CFX). The use of energy equation is done for finding out temperature distribution on the wall. The equation for conservation of mass, continuity equation, can be written as follows:

Mass conservation equation

The equation for conservation of mass, or continuity equation, can be written as follows:

$$\frac{\partial \rho}{\partial t} + \nabla.(\rho \vec{v}) = S_m$$

The equation written above is a general equation for conservation of mass. Here S_m is the mass added from any user defined sources.

Momentum conservation equation

Momentum conservation in a reference frame which is non accelerating can be written as

$$\frac{\partial}{\partial t}(\rho \vec{v}) + \nabla.(\rho \vec{v}\vec{v}) = -\nabla p + \nabla.(\bar{\bar{\tau}}) + \rho g + \vec{F}$$

Where,

p is the static pressure ,τ is the stress tensor
F and ρg are the external forces on body and gravitational force on body.

Energy equation-

ANSYS CFX solves the energy equation in the following form:

$$\frac{\partial}{\partial t}(\rho E) + \nabla.(\vec{v}\,(\rho E + p)\,) = \nabla.\left(k_{eff}\nabla T + \sum_J h_j \overrightarrow{J_J} + \overline{\overline{\tau_{eff}}}.\vec{v}\right) + S_h$$

Where,
k_{eff} is the effective conductivity ($k+k_t$), where k_t is the turbulent thermal conductivity, defined on the basis of turbulence model being used, and J_j is the diffusion flux of species J . On the right-hand side of the equation the first

three terms represents energy transfer due to species diffusion, conduction, and viscous dissipation, respectively, S_h denotes the chemical reaction heat, and some other sources of heat.

Standard relations and associated equations

The bulk mean temperature, T_{bm} and the wall temperature, T_{wx} with distance x from the micro-channel entrance can be obtained by doing the thermal energy balance around the micro-channel which is given by the following equations.

$$T_{bm} = T_{in} + \frac{q\pi Dhx}{mCp}$$

Where,

T_{bm} is the bulk mean temperature.
T_{in} is inlet temperature.
q is the heat flux.
D_h is hydraulic diameter of channel.
m is mass flow rate across channel.

The relation between the hydraulic diameter and Reynolds number in a channel is given by

$$Re=\rho v D_h/ \mu$$

Where,
ρ is density
v is average velocity.
μ is dynamic viscocity.
D_h is hydraulic diameter of channel

III. METHODOLOGY

Straight rectangular micro-channel heat sink

In this chapter a three dimensional CFD simulation is done for the heat transfer and pressure drop characteristics of rectangular micro-channel. Material used for heat sink construction is copper. The experimental set up shown in figure was developed by Mudawar and Qu (2002).

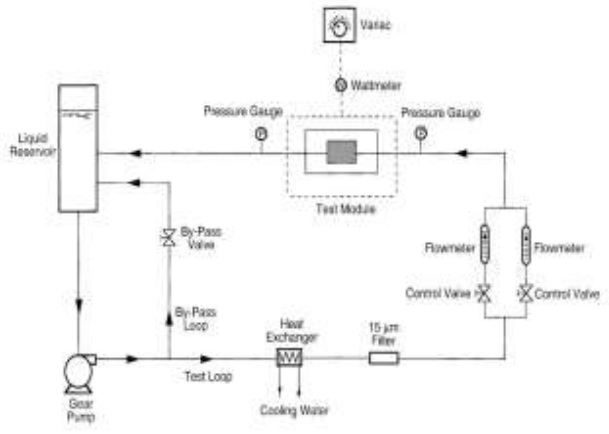

Figure 4.1: Schematic diagrams of flow loop [1]

Description of problem

The experimental work done by Qu and Mudawar, (2001) on the test apparatus is modelled and simulated in this present study. Water is moving through a straight rectangular smaller scale channel implanted in a test module. 21 rectangular smaller scale openings were machined into micro- channel surface by an accuracy machining procedure. The miniaturized scale openings were equidistantly divided inside of the 1-cm heat sink width and had the cross-sectional measurements of 231 μ m wide and 712 μm profound. There are 21 parallel rectangular small scale directs in the module. Figure shows the flow loop that was constructed to supply deionized water to the heat sink at the desired pressure, temperature, and flow rate. The water was pumped from a liquid reservoir and circulated through the flow loop by a gear pump. Upon exiting the pump, a portion of the flow, controlled by a by-pass valve, entered the test loop containing the heat sink, while the remaining portion returned to the reservoir though a by-pass loop. The test loop water first passed through a heat exchanger where the water was cooled to the desired inlet temperature. The water then passed through a 15 lm filter to prevent any solid particles from blocking the heat sink micro-channels. After exiting the filter, the water was routed to one of two rotameters for volume flow rate measurement. The water then entered the micro-channel heat sink test module where the electric power supplied to the heat sink was removed by the water. Leaving the test module, the water returned to the reservoir where it mixed with the bypassed flow.

Geometry of the rectangular microchannel heat sink

In the present analysis, only one micro channel of the remaining 21 micro-channels is considered as a computational domain. Figure shows the micro-channel heat sink with single unit cell used for simulation.

Table 4.1: Dimensions of the rectangular channel unit cell used for simulation

W_w (μm)	$W_{channel}$(μm)	H_{w1} (μm)	H_{ch} (μm)	H_{w2} (μm)	L (mm)
118	231	12700	713	5637	44.7

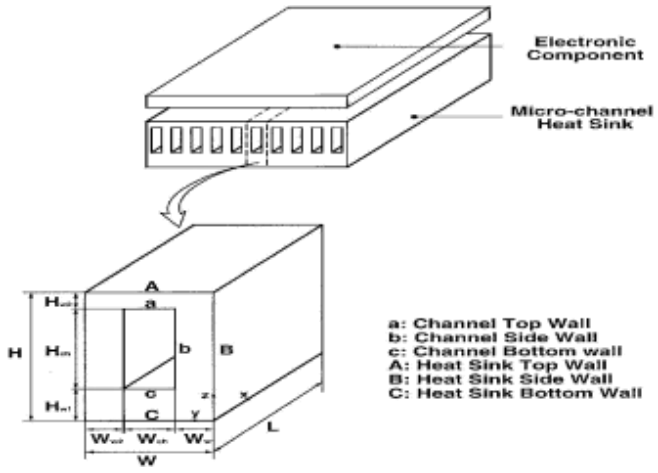

Figure 4.2: Schematic diagram of rectangular microchannel unit cell [1]

Experimental Results

Pressure drop for heat flux value=100W/cm^2

Reynolds number	Experimental pressure drop (bar)
400	0.10
600	0.17
800	0.23
1000	0.32
1200	0.41

Pressure drop for heat flux value=200W/cm^2

Reynolds number	Experimental pressure drop(bar)
400	0.08
600	0.15
800	0.21
1000	0.30
1200	0.40

Temp rise for heat flux value=100W/cm^2

Reynolds number	Experimental temp rise (°C)
400	22
600	16
800	10
1000	8
1200	6

Temp rise for heat flux=200 W/cm^2

Reynolds number	Experimental temp rise (°C)
400	44
600	31
800	22
1000	18
1200	15

CASE-1

Simulation of Wavy edge type rectangular micro-channel heat sink with hemispherical obstructions by taking water as a coolant and cooper as a sink material

In this chapter a three dimensional CFD simulation is done for the heat transfer and pressure drop characteristics of wavy edge rectangular micro-channel heat sink. Material used for heat sink construction is copper.

Problem description-

Water is moving through a wavy edge rectangular smaller scale channel heat sink assembly. In this analysis a design for wavy edge type of micro-channel heat sink is constructed. The dimensions of the micro-channel assembly are same as that of the rectangular micro-channels used in the experiments, the only difference being the length is made wavy along with hemispherical obstruction.

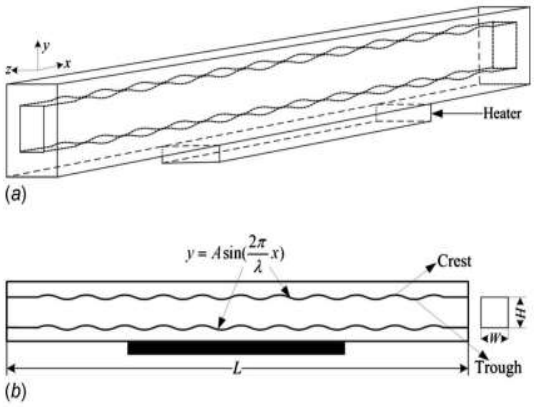

Figure: Schematic diagram of wavy microchannel heat sink.

Table: Dimensions of the wavy channel unit cell used for simulation

W_{wall} (µm)	W (µm)	H_{wall2} (µm)	H (µm)	H_{wall1} (µm)	L (mm)
118	231	12700	713	5637	44.7

In this analysis the only the length of the micro-channel heat sink is made wavy and the pressure drop and heat transfer characteristics are simulated.

Wave equation used- In this analysis, for the construction of geometry a sine wave is used which has the following equation.

$$y = Asin(2\pi x/\lambda)$$

Here, A is wave amplitude and λ is the wavelength.

Geometry construction-

For the analysis of computational fluid dynamics problem, the geometry of the heat sink was constructed using solid works, and was imported to ANSYS workbench CFX for further meshing and CFD simulations.

For creating geometry, first the heat sink was made in solid works as per the dimensions given in table. The wave dimensions were given according to the length of the channel which is 44.7 mm. A sinusoidal wave was assumed and constructed in the solid heat sink. The amplitude of the wave was taken as 0.15 mm while the wavelength was taken as 2 mm, and at a particular wavelength a hemispherical obstruction is made on the wavy edge and repeated to get fully along the channel. However, fluid channel was created in the design modular of Ansys CFX and not in the solid work as it was easy to make in the design modular and also it is made of the same dimensions as of the wavy rectangular slot along the

length of heat sink with hemispherical depression for proper mating and was given the name of fluid part.

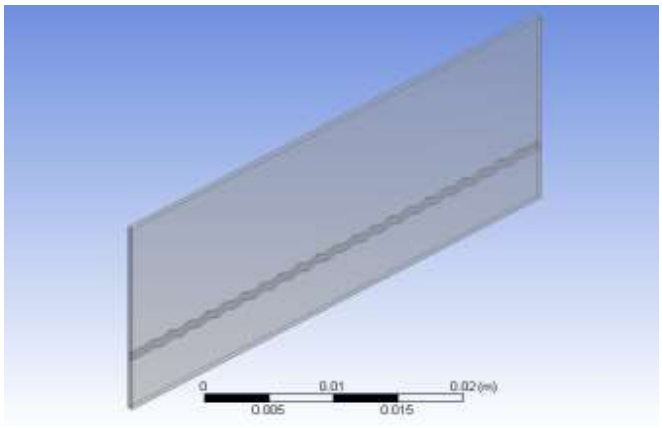

Figure: Geometry of wavy micro-cannel heat sink used in simulation

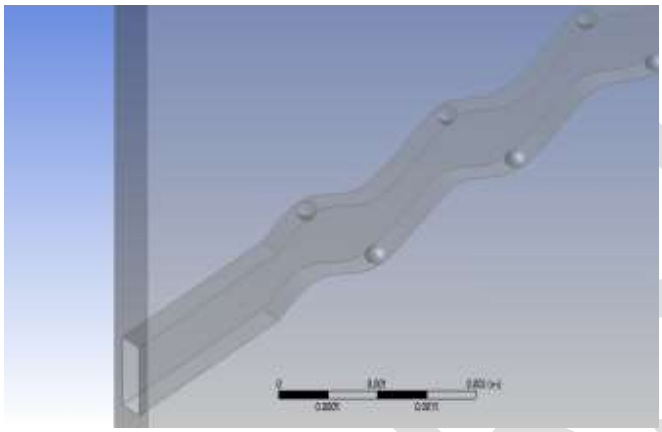

Figure: Detailed view of wavy micro-cannel heat sink with hemispherical obstructions

Meshing-

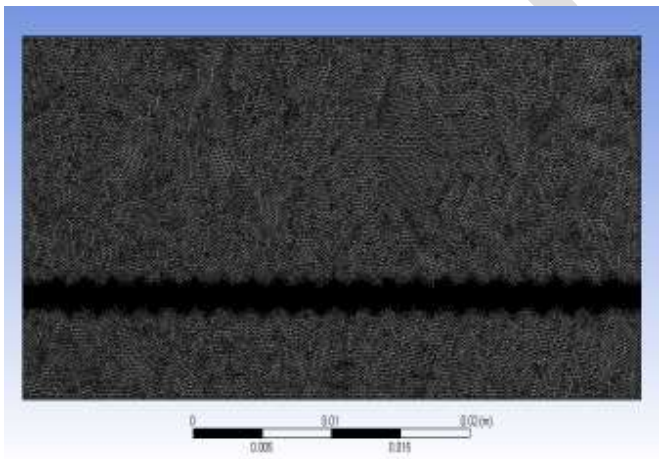

Figure: Meshing of geometry in ANSYS CFX

Table: Mesh details-

Physics preference	CFD
Solver preference	CFX
Smoothing	Medium
Transition	Slow
Transition ratio	0.77
Minimum size	1.2e-5
Maximum face size	1.21e-3
Maximum size	2.42e-3
Nodes	631403
Elements	3125145

Boundary conditions-

1. No slip on the surface.
2. Uniform inlet temperature and static pressure were given at the entry of the channel.
3. Outlet of the channel is based on mass flow rate.
4. A uniform heat flux of 100W/cm^2 and 200 W/cm^2 at the bottom wall of the heat sink for two separate cases was applied.

Table: Zone specification

Front wall of solid heat sink	Wall
Top wall of solid heat sink	Wall
Back wall of solid heat sink	Wall
Bottom wall of solid heat sink	Heat flux
Heat sink right wall	Wall
Heat sink left wall	Wall
Channel entry	Static pressure
Channel exit	Mass flow rate
Default Interface	Wall

Table: Solver settings

Following are the solver settings which are to be used in simulation.

Min. Iterations	1
Max. Iterations	250
Residual type	RMS
Residual target	1E-4
Time scale control	Auto time scale

IV. SIMULATION RESULTS

In the following computational fluid dynamics analysis the results are plotted for temperature rise and heat transfer in wavy edge type rectangular microchannel for two different values of heat fluxes applied at the bottom of the heat sink for varying set of values of Reynolds number. The value of heat flux used in the analysis are 100W/$cm^2$and 200W/cm^2. Five values of Reynolds number are taken for the analysis which are 400, 600, 800, 1000 and 1200 respectively

Results for heat flux= 100W/cm^2 for different sets of Reynolds number

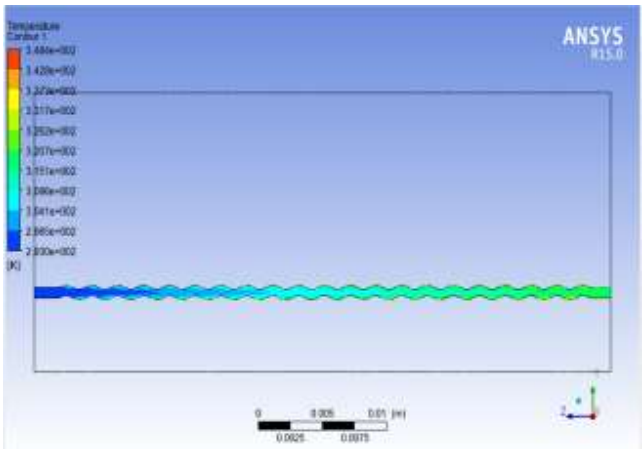

Figure: Temperature contour of water along wavy channel at Re=400

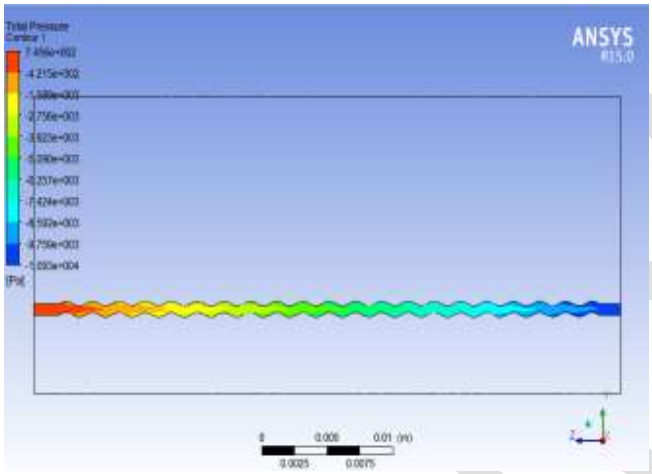

Figure: Pressure contour of water along wavy channel at Re=400

Results for heat flux of 200 W/cm^2 and different sets of Reynolds number

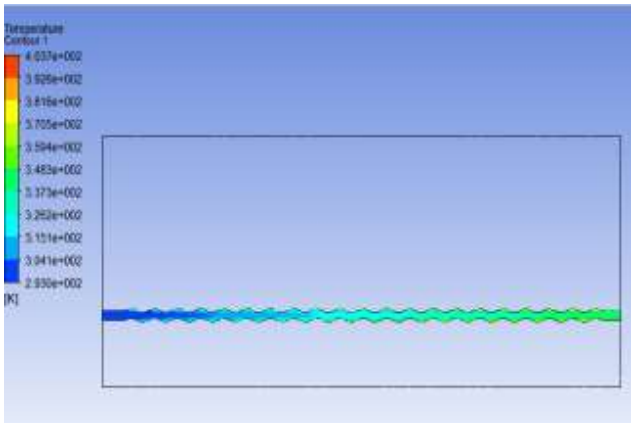

Figure: Temperature contour along wavy channel at Re=400

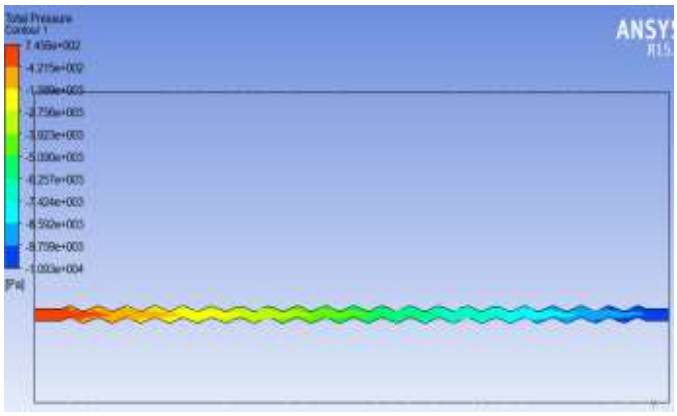

Figure: Pressure contour along wavy channel at Re=400

In the above figures, contours for temperature rise and pressure drop along the channel has been shown at Reynolds number 400 for bottom wall heat flux at 100 W/cm^2 and 200 W/cm^2 respectively. Similarly all the contours for Reynolds number 600, 800, 1000 and 1200 at heat flux 100 W/cm^2 and 200 W/cm^2 are obtained and put in the table in the form of numerical values.

Table: Computational Temperature Rise for heat flux=100W/cm^2

Reynolds number	**Computational temperature rise(°C)**
400	27
600	23
800	21
1000	19
1200	18

Table: Computational Temperature Rise for heat flux =200W/cm^2

Reynolds number	Computational temperature rise (°C)
400	55
600	47
800	43
1000	40
1200	38

Table:Computational pressure drop for heat flux =100W/cm^2

Reynolds number	**Computational Pressure Drop(bar)**
400	0.116
600	0.183
800	0.255
1000	0.344
1200	0.418

Table: Computational pressure drop for heat flux =200W/cm^2

Reynolds number	Computational Pressure Drop(bar)
400	0.115
600	0.181
800	0.254
1000	0.341
1200	0.416

CASE-1

Comparison of simulation results of the Wavy microchannel with hemispherical obstructions with experimental results of rectangular microchannel obtained by Weilin Qu and Issam Mudawar

Table: Temperature Rise for different Reynolds number for heat flux=100W/cm^2

Reynolds number	Experimental Temperature Rise(°C) (rectangular)	Computational Temperature Rise(°C) (wavy)
400	22	27
600	16	23
800	10	21
1000	8	19
1200	6	18

Table: Temperature Rise for different Reynolds number for heat flux=200 W/cm^2

Reynolds number	Experimental Temperature Rise(°C) (rectangular)	Computational Temperature Rise(°C) (wavy)
400	44	55
600	31	47
800	22	43
1000	18	41
1200	15	38

Table: Pressure Drop for different Reynolds number for heat flux=100 W/cm^2

Reynolds Number	Experimental Pressure Drop(bar) (rectangular)	Computational Pressure Drop(bar) (wavy)
400	0.10	0.116
600	0.17	0.183
800	0.23	0.255
1000	0.32	0.344
1200	0.41	0.418

Table: Pressure Drop for different Reynolds number for heat flux=200 W/cm^2

Reynolds Number	Experimental Pressure Drop(bar) (rectangular)	Computational Pressure Drop(bar) (wavy)
400	0.08	0.115
600	0.15	0.181
800	0.21	0.254
1000	0.30	0.341
1200	0.40	0.416

GRAPH-

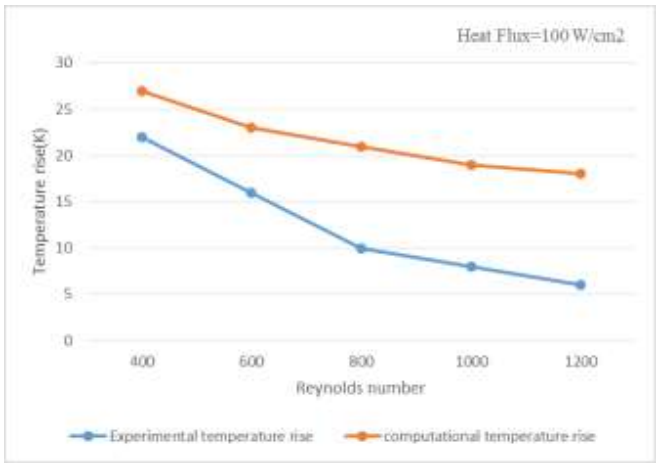

Figure: Temperature rise vs Reynolds number (Heat flux=100 W/cm^2)

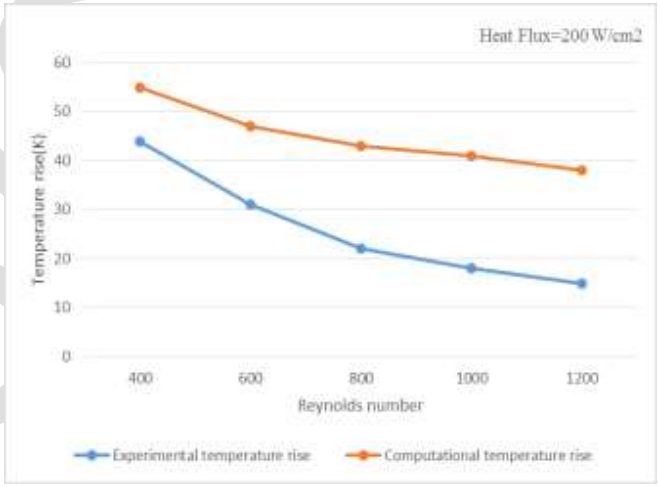

Figure: Temperature rise vs Reynolds number (Heat Flux=200 W/cm^2)

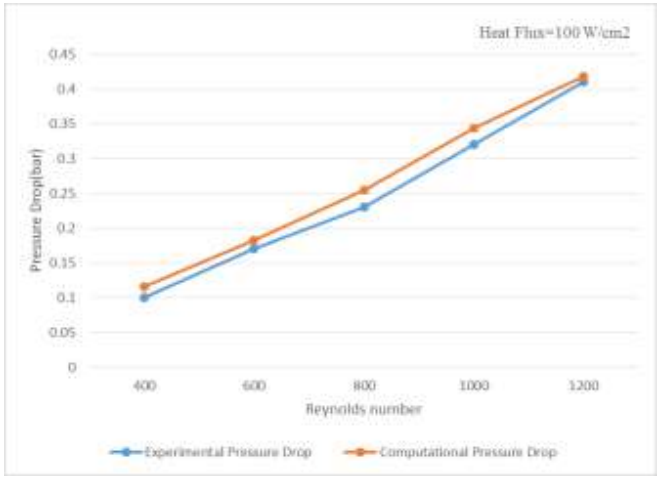

Figure: Pressure Drop vs Reynolds number (Heat Flux=100 W/cm^2)

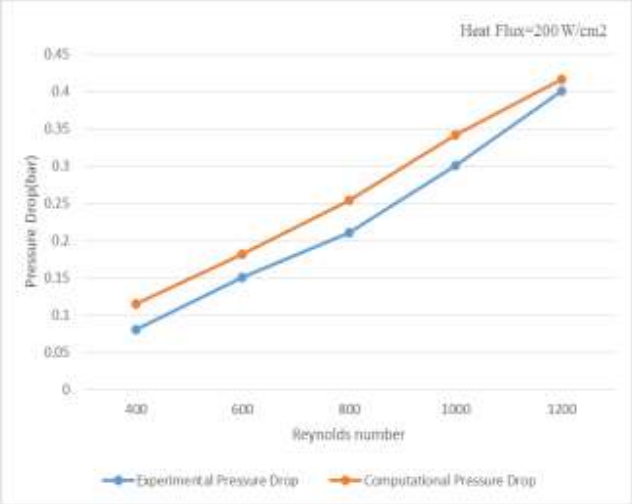

Figure: Pressure Drop vs Reynolds number (Heat Flux=200 W/cm^2)

V. CONCLUSION

Based on the numerical study on both straight and wavy edge type micro-channel with hemispherical obstructions the following conclusions can be made-

- Water temperature rise is more at the outlet of wavy edge type of micro-channels with hemispherical obstructions in comparison to straight micro-channels for same values of Reynolds number and heat flux.
- From the above results both for straight rectangular micro-channel and wavy edge type micro-channel the thermal performance of wavy edge micro-channel is found to be better in comparison to that of straight micro-channel of same hydraulic diameter.
- With the inclusion of hemispherical obstructions in wavy channel, surface area as well as contact time of fluid with heated surface increases due to which thermal resistance decreases which ultimately increases the heat transfer as a result, we get the higher temperature rise of the fluid.
- Pressure drop is found to be more in wavy edge micro-channels in comparison to that of straight micro-channels, however the loss in pressure is compensated by the better heat transfer characteristics of the wavy micro-channel.
- Velocity of water decreases along the flow direction in wavy micro-channels due to loss in energy of fluid while travelling along wavy channel with hemispherical obstructions.
- As the value of heat flux in wavy type of channel is increased from 100W/cm^2 to 200W/cm^2 there is an increase in the outlet temperature of water, however the pressure drop along the channel decreases. But the difference in pressure drop is very less.

REFERENCES

[1] I. Mudawar, W. Qu, Experimental and numerical study of pressure drop and heat transfer in a single-phase micro-channel heat sink, Int. J. Heat and Mass Transfer 45(2002) 2549-2565.

[2] G.M. Mala, D. Li, J.D. Dale, Heat transfer and fluid flow in micro-channels, International Journal of Heat and Mass Transfer 40 (1997) 3079-3088.

[3] L.T. Yeh, Review of heat transfer technologies in electronic equipment, ASME J. Electron. Packag. 117 (1995) 333–339.

[4] D.B. Tuckerman, R.F.W. Pease, High-performance heat sinking for VLSI, IEEE Electron. Dev. Lett. EDL-2 (1981) 126–129.

[5] I. Mudawar, M.B. Bowers, Ultra-high critical heat flux (CHF) for subcooled water flow boiling —I: CHF data and parametric effects for small diameter tubes, Int. J. Heat Mass Transfer 42 (1999) 1405–1428.

[6] I. Mudawar, W. Qu, Analysis of three dimensional heat transfer in micro-channels, Int. J Heat and Mass Transfer 45 (2002) 3973-3985.

[7] K. Kawano, K. Minakami, H. Iwasaki, M. Ishizuka, Micro channel heat exchanger for cooling electrical equipment, Application of Heat Transfer in Equipment, Systems and Education, ASME HTD-361-3/PID-3, 1998, pp. 173–180.

[8] A. Bejan, A.M. Morega, Optimal arrays of pin fins and plate fins in laminar forced convection, ASME J. Heat Transfer 115 (1993) 75–81.

[9] A.G. Fedorov, R. Viskanta, Three-dimensional conjugate heat transfer in the microchannel heat sink for electronic packaging, Int. J. Heat Mass Transfer 43 (2000) 399–415.

[10] X.F. Peng, G.P. Peterson, Convective heat transfer and flow friction for water flow in microchannel structures, Int. J. Heat Mass Transfer 39 (1996) 2599–2608.

[11] K.K. Ambatipudi, M.M. Rahman, Analysis of conjugate heat transfer in microchannel heat sinks Numer. Heat Transfer A, 37 (2000), pp. 711–731.

[12] Y. Sui, C.J. Teo, P.S. Lee, Y.T. Chew, C. Shu, Fluid flow and heat transfer in wavy micro-channels Int. J. Heat Mass Transfer, 53 (2010), pp. 2760–2772.

[13] P. Gunnasegaran, H.A. Mohammed, N.H. Shuaib, R. Saidur, The effect of geometrical parameters on heat transfer characteristics of micro-channels heat sink with different shapes Int. Commun. Heat Mass Transfer, 37 (8) (2010), pp. 1078–1086

[14] E. Utriainen, B. Sunden, Numerical analysis of primary surface trapezoidal cross wavy duct Int. J. Numer. Method Heat Fluid Flow, 10 (6) (2000), pp. 634–648.

[15] S. Kandlikar, S. Garimella, D. Li, S. Colin, M.R. King, Heat Transfer and Fluid Flow in Minichannels and Microchannels, Elsevier, USA, 2005.

[16] E. Utriainen, B. Sunden, Numerical analysis of primary surface trapezoidal cross wavy duct, Int. J. Numer. Method Heat Fluid Flow 10 (6) (2000) 634–648.

[17] W. Yang, J. Zhang, H. Cheng, The study of flow characteristics of curved microchannel, Appl. Therm. Eng. 25 (2010) 1894–1907.

[18] R.K. Shah, A.L. London, Laminar Flow Forced Convection in Ducts, Academic Press, New York, 1978.

[19] S.G. Kandlikar, W.J. Grande, Evaluation of single phase flow in microchannels
for high heat flux chip cooling – thermohydraulic performance enhancement and fabrication technology, Heat Transfer Eng. 25 (8) (2004) 5–16.

[20] S.V. Garimella, C.B. Sobhan, Transport in microchannels – a critical review, Annu. Rev. Heat Transfer 13 (2003) 1–50.

Available online at www.sciencedirect.com

ScienceDirect

Materials Today: Proceedings 4 (2017) 752–757

materialstoday: PROCEEDINGS

www.materialstoday.com/proceedings

5th International Conference of Materials Processing and Characterization (ICMPC 2016)

Characterization of magnetic abrasive particles based Magnetorheological polishing fluid

M. S. Niranjan[1], Krishna Pratap Singh[2], Qasim Murtaza[3]

[123] Department of Mechanical Engineering, Delhi Technological University, New Delhi 110042, India,

Abstract

Magnetic abrasive particles (MAPs) were developed by solid phase sintering method at 1000^0C in argon atmosphere. The Magnetorheological (MR) polishing fluid has been synthesized with 45 volume% MAPs and 55 volume% base fluid. The MR polishing fluid was characterized at different current on MCR-301 magnetorheometer and steady state rheograms have been drawn. The flow behavior of MAPs based MR polishing fluid has been compared with flow behavior of unbonded magnetic abrasives based MR polishing fluid at same conditions. The result shows better yield behavior and viscosity of MAPs based MR polishing fluid as compared to unbonded magnetic abrasives based MR polishing fluid.

©2017 Elsevier Ltd. All rights reserved.
Selection and peer-review under responsibility of Conference Committee Members of 5th International Conference of Materials Processing and Characterization (ICMPC 2016).

*Keywords:*MAPs; Sintering; MR; Rheology; Yield Behavior, Viscosity.

E-mail address: mahendraiitr2002@gmail.com

2214-7853©2017 Elsevier Ltd. All rights reserved.
Selection and peer-review under responsibility of Conference Committee Members of 5th International Conference of Materials Processing and Characterization (ICMPC 2016).

1. Introduction

Magnetorheological (MR) fluids are thesmart materialswhich are reversibly transformed from the fluid like state to a solid like state within few milliseconds under the effect of an externally applied magnetic field and shows dramatic change in the rheological properties. Magnetorheological fluids (MRFs) are the suspensions of micron sized ferro or ferri magnetic particles in the base fluid. The rheological as well as magnetorheological behaviours of extremely bidisperse (nano-micro) magnetic fluid have been studied and analyzed for the fixed quantity of magnetic solid contents.

Nomenclature

MR	magnetorheogical
CIP	carbonyl iron powder
SiC	silicon carbide abrasives
τ	shear stress (Pa)
η	viscosity (Pa-s)
γ	Shear rate (sec^{-1})

It has been observed that the relative viscosity of an extremely bidisperse magnetic fluidwhich contains magnetic nanoparticles has been found significantly increasedwith respect to commercially available MR fluid of same magnetic solid content having micron sized particles [1]. The nanometer sized carbonyl iron powder (CIP) was used as an additive for the conventional MR fluid and characterization of MR fluid has been done on magnetorheometer. The flow behaviour of MR fluid with and without nano-sized magnetic additive has been studied and analyzed at a steady shear mode in the presence of applied magnetic field. It has been observed that the MR fluidhaving nano-sized magnetic carbonyl iron particles showed higher yield behaviours with strengthened structure [2].

From the microscopic study, it has been observed that the micostructural cavities were formed due to the association of large magnetic particles. These structural microcavities were observed filled in the presence of the magnetic field by nano-sized magnetic particles and found some nano-sized magnetic particles attached at the end of chains formed by the large particles [3]. It was studied that the aggregation of large particles was found restricted on the use of magnetic nano particles along with the large magnetic particles and causes field induced phase separation in MR fluid.There is a common problem of sedimentation of iron particles in the base fluid. Before using the MR fluid, it is very important to study the stability against sedimentation of particles in the base fluid and the redispersibility of MR fluid for its potential application. It was observed that the volume fraction of nano-sized magnetic particles not more than 3% has been found enough to provide a long lastingstabilization to the MR fluid which contain above 30% iron microparticles. The performance of MR fluid was evaluated by steady state rheograms with the different combination of magnetite under applied magnetic field strengths. The yield stress was found high with improved stability and redispersibility [4]. The magnetorheological characterization of synthesized MR polishing fluid has been done with zero and non zero magnetic field to obtain the steady state rheograms to study the yield behavior of MR polishing fluid and viscosity [5]. The response surface methodology was applied to study the effect of each factor on yield shear stress and viscosity.

2. Sample preparation

Magneticabrasive particles have been developed by mixing 20 volume% carbonyl iron powder (CIP)of CS grade and25 volume% silicon carbide abrasives of 3000 mesh size in ball mill. The pellets were prepared at 8 ton pressure in a die of 7 mm diameter and 50 mm length and held for 25 minutes duration for getting uniform compaction. These pellets were sintered in argon atmosphere in the tubular furnace at 1000^0C and held at this temperature for three hours for getting complete phase transformation.The sintered pellets were crushed in ball mill and MAPs were delveloped. The MR polishing fluid sample (S1) has been synthesized with 45 volume% MAPs and 55 volume% base fluid. Another unbonded magnetic abrasives based MR polishing fluid sample (S2) has been synthesized with 20 volume% carbonyl iron powder, 25 volume% silicon carbide abrasives of 3000 mesh size, and 55 volume% base fluid for comparison purpose as shown in table 1.

Table 1. Composition of MRP fluid

S.No.	Sample No.	Composition
1.	Unbonded magnetic abrasives based (S_1)	20 volume% CIP of CS grade , 25 volume% SiC of 3000 mesh size, 55volume% of base fluid
2.	Bonded magnetic abrasive particles based (S_2)	45 volume% magnetic abrasive particles (MAPs), 55volume% base fluid

3. Characterization

A magnetorheometer (Physica MCR-301with MRD 180 attachment, Anton Paar), with 1 mm gap with parallel plate geometry and 20 mm diameter has been used to get the flow curves at envirnment temperature of 25^0C and 60% relative humidity. The MR fluid was filled in a constant gap between parallel plates during the experiment.The top disc rotates while the bottom disk remains stationary. A coil is placed below the bottom disk while flux returns are mounted above and around the upper disk, to close the magnetic circuit. After putting the sample between the upper rotating plate and the stationary bottom plate, the magnetic circuit is closed using the flux returns. Homogeneous magnetic field was set perpendicular to the shear flow direction of MR fluid.The performance of synthesized MR polishing fluid samples was evaluated with steady state rheograms at different current.

4. Result and discussion

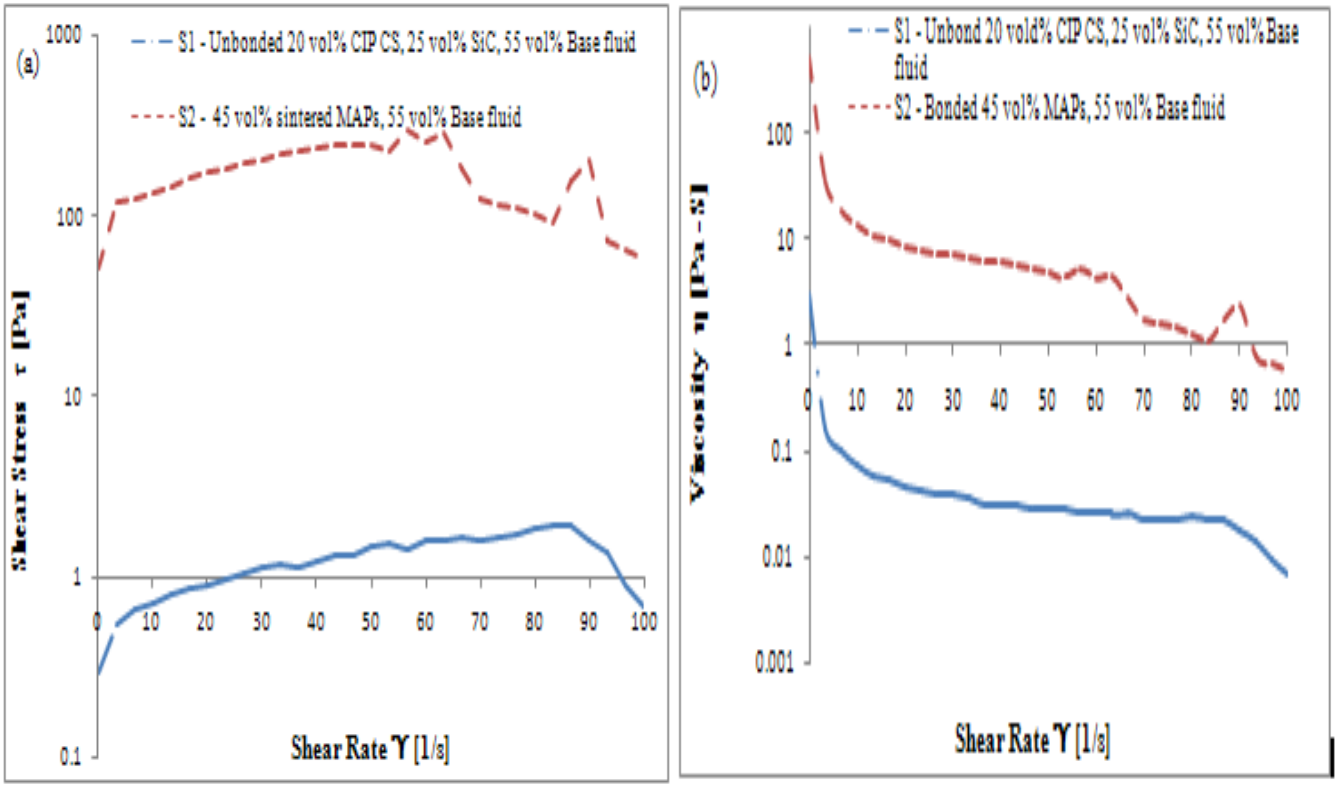

Fig.1. (a) Shows Shear Stress; (b) Viscosity at 0 A

Fig.1 shows shear stress as well as viscosity vs shear rate in shear rate range 0 to 1000 sec^{-1} for synthesized MR polishing fluid samples at current of 0A. The flow behaviour of preparedMRP fluid is strongly field dependent and found better for MAPs based MR polishing fluid (S_2). The yield shear stress of MAPs based MR polshing fluid was observed as52.8 Pa and viscosity as 529 Pa-s while the yield shear stress of unbonded magnetic abrasives based MR polishing fluid (S_1) was observed as 0.302Pa and viscosity as3.02Pa-s at current of 0A.

Fig. 2 shows shear stress as well as viscosity vs shear rate in shear rate range 0 to 1000 sec^{-1} for synthesized MR polishing fluid samples at current of 0.7A. The flow behaviour of preparedMR polishing fluid is strongly field dependent and found better for MAPs based MR polishing fluid (S_2) as compared to unbonded magnetic abrasives based MR polishing fluid (S_1). The yield shear stress of MAPs based MR polshing fluid was observed as 1,580 Pa and viscosity as 15,800 Pa-s while the yield shear stress of unbonded magnetic abrasives based MR polishing fluid (S_1) was observed as 902Pa and viscosity as9,020 Pa-s at current of 0.7A.

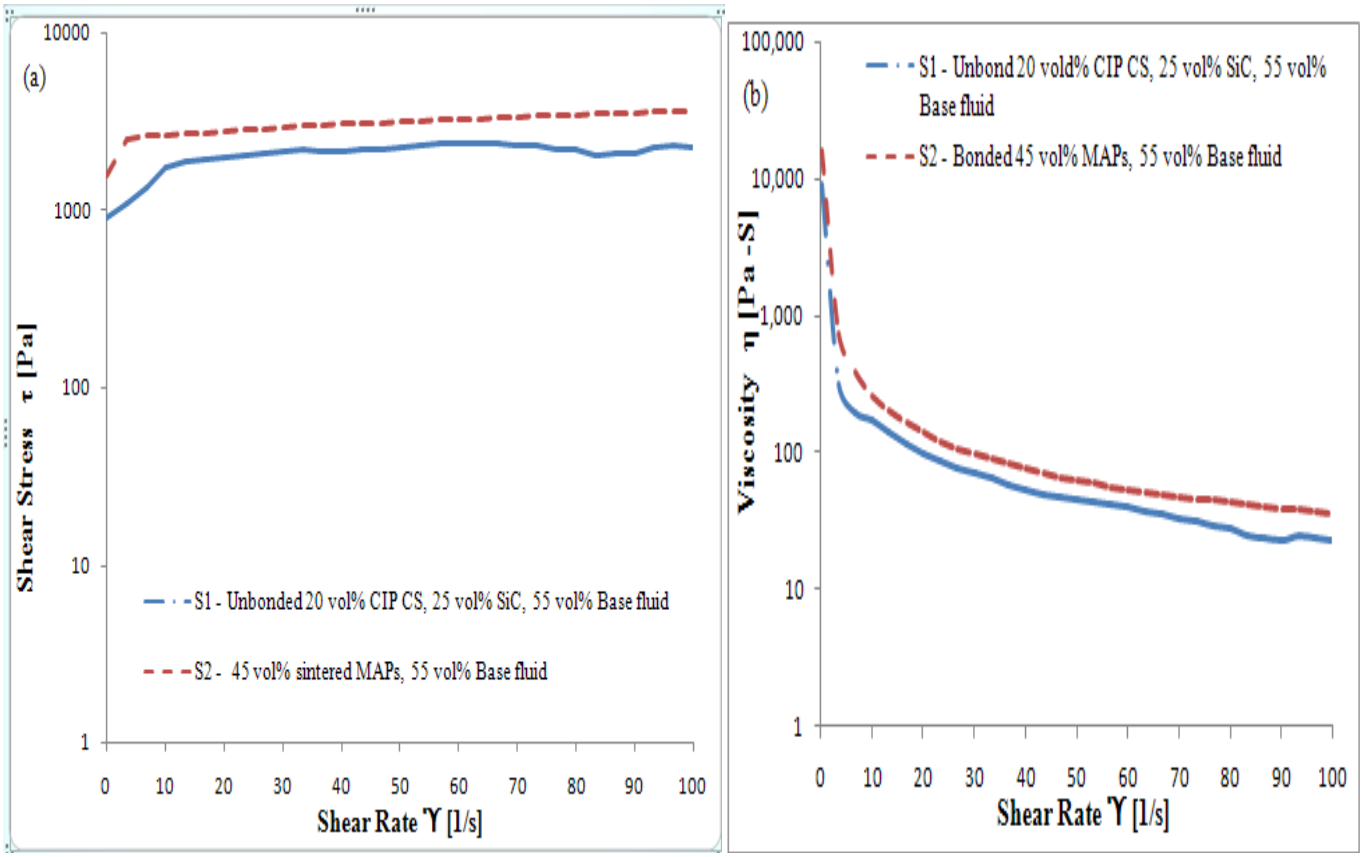

Fig.2. (a) Shows Shear Stress; (b) Viscosity at 0.7 A

Fig. 3 shows the shear stress as well as viscosity vs shear rate in shear rate range 0 to 1000 sec^{-1} for synthesized MR polishing fluid samples at current of 1.0A. The flow behaviour of preparedMR polishing fluidhas been foundmagnetic field dependent and it was found better for MAPs based MR polishing fluid (S_2) as compared to unbonded magnetic abrasives based MR polishing fluid (S_1). The yield shear stress of MAPs based MR polshing fluid was observed as 2,690 Pa and viscosity as 24,500 Pa-s while the yield shear stress of unbonded magnetic abrasives based MR polishing fluid (S_1) was observed as 1,750Pa and viscosity as17,900 Pa-s at current of 1.0A.

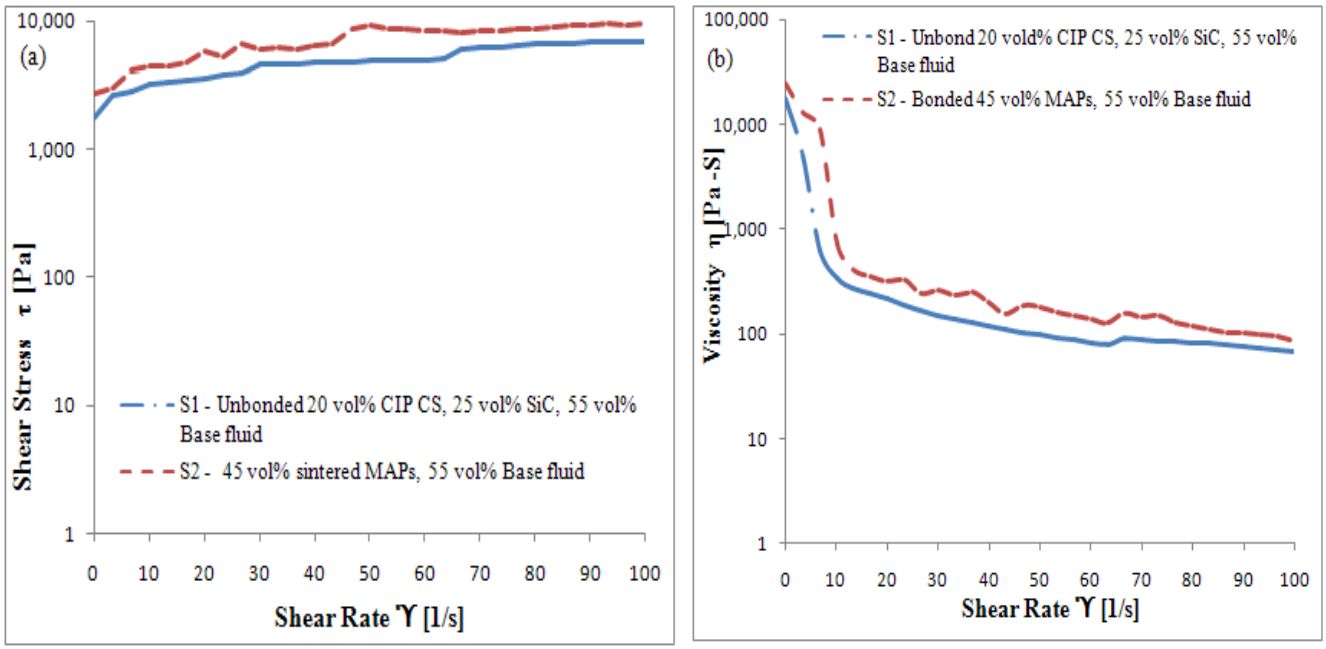

Fig.3. (a) Shows Shear Stress; (b) Viscosity at 1A

Fig. 4 shows the shear stress as well as viscosity vs shear rate in shear rate range 0 to 1000 sec^{-1} for synthesized MR polishing fluid samples at current of 2.0A. The flow behaviour of preparedMR polishing fluidhas been foundmagnetic field dependent and it was found better for MAPs based MR polishing fluid (S_2) as compared to unbonded magnetic abrasives based MR polishing fluid (S_1). The yield shear stress of MAPs based MR polshing fluid was observed as 5,650 Pa and viscosity as 46,700 Pa-s while the yield shear stress of unbonded magnetic abrasives based MR polishing fluid (S_1) was observed as 4,060Pa and viscosity as40,600 Pa-s at current of 2.0A.

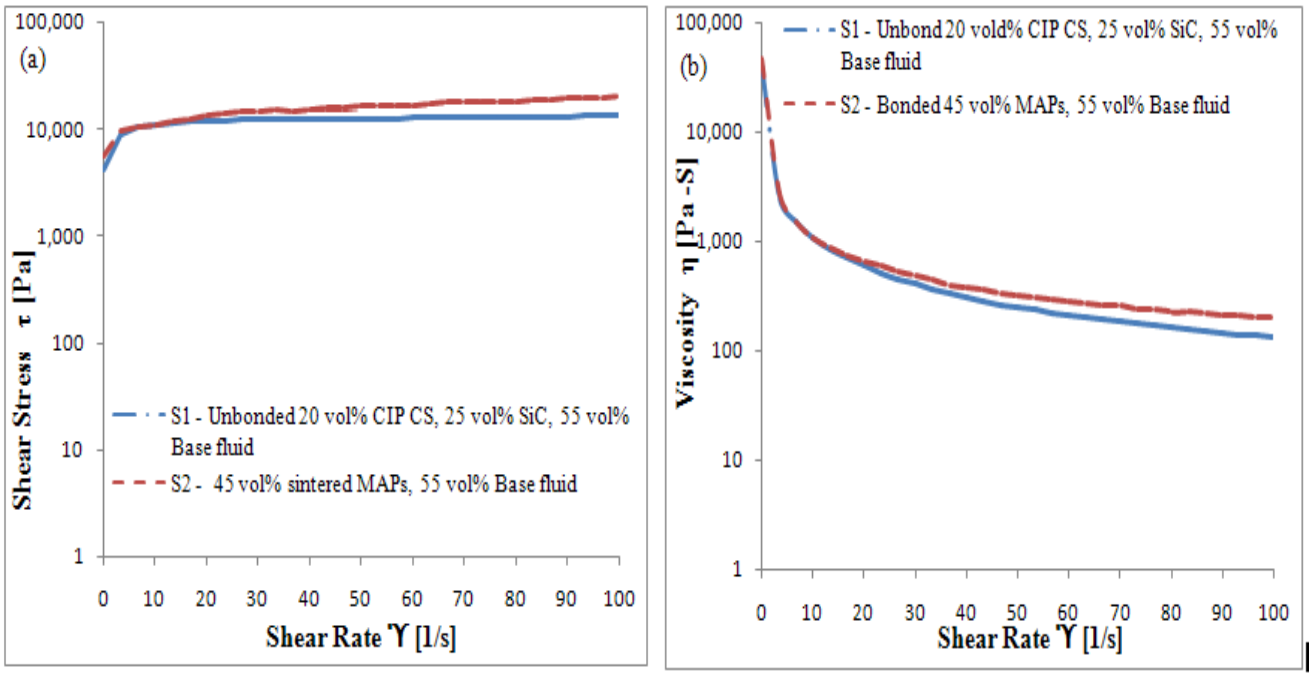

Fig.4. (a) Shows Shear Stress; (b) Viscosity at 2A

From these rheograms, it has been observed that the yield shear stress and viscosity of MAPs based MR polishing fluid have been found better as compared to unbonded magnetic abrasives based MR polishing fluid. It is due to the fact that the abrasive particles are diffused on the surface of carbonyl iron particles and make MAPs which behave as one body while in case of unbonded magnetic abrasives, the particles behave as two body.

5. Conclusions

(i) The magnetic abrasive particles were developed in inert atmosphere of argon in the tubular furnace.
(ii) MR polishing fluid samples were synthesized.
(iii) Magnetorheological characterization has been carried out at different current values and steady state rheograms were drawn. It has been observed from steady state rheograms that the yield shear stress and viscosity of magnetic abrasive particles (MAPs) based MR polishing fluid have been found better as compared to unbounded magnetic abrasive particles based MR polishing fluid.

References

[1]S.R. Daniela, B. Doina, L. Vekas, Flow behaviour of extremely bidisperse magnetisable fluids. J. Magnetism and MagneticMaterials. 322 (2010) 3166-3172.

[2] J.P. Bong, H.S. Kang, J.C. Hyoung, Magnetic carbonyl iron nano particle based magnetorheological suspension and its characteristics. J. Materials Letters. 63 (2009) 1350-1352.

[3] R. Patel, Mechanism of chain formation in nano fluid based MR fluids. J. Magnetism and Magnetic Materials. 323(2011) 1360-1363.

[4] G.R.M. Iglesias, L.T. Lopez, J.D. Duran, C.G.F. Gonzalez, A.V. Delgado, Dynamic characterization of exteremly bidisperse magnetorheological fluids. J. Colloid and Interface Science. 377 (2012) 153-159.

[5] A. Sidpara, M. Das, V.K. Jain, Rheological characterization of magnetorheological finishing fluid. J. Materials and Manufacturing Processes. 24/12 (2009) 1467 – 1478.

Rock Mech Rock Eng
DOI 10.1007/s00603-017-1229-8

DISCUSSION

Comments on Modulus Ratio and Joint Factor Concepts to Predict Rock Mass Response

Ashutosh Trivedi[1]

© Springer-Verlag Wien 2017

1 Introduction

The use of modulus ratio and joint factor (Ramamurthy et al. 2017) to predict rock mass response is an interesting concept. The formulation of joint factor invoked a keen interest among the field engineers ever since originally proposed by Arora (1987), Ramamurthy and Arora (1994), Arora and Trivedi (1992), Trivedi and Arora (2007) and modified by Ramamurthy (2004) to correlate this concept with GSI. The example of several slope failures indicates that the failure surface is often well oriented. It exhibits the importance of preexisting joint-induced sliding in jointed rock mass despite very significant intact rock strength. The evaluation of rock mass strength has been historically based on empirical observations of cumulative visible strain history appearing in the form of fractures, discontinuities and joints. The authors have presented an interesting account on the empirical correlation of joint factor with GSI, RMR and Q systems for the rock masses. Accordingly, the authors have used these observations to access compressive strength (σ_{cj}), modulus (E_j), cohesion (c_j) and friction angle and to predict stress–strain response of rock mass.

This discussion aims to focus on the interesting observation of strength and modulus obtained by the authors, several other investigators and the discusser with innate similarities but using varied connotation in relation to the original and generalized HB criterion, respectively. The discusser uses a generic expression for strength and modulus which returns authors' expression as a special case.

The joint factor is defined by the authors as, $J_f = J_n/n.\ r$, where J_n is the number of joints for unit run of scan line on rock mass, n is orientation parameter and r is friction parameter obtained by Ramamurthy and his co-workers. For the joints containing infills, Trivedi (2010) proposed an infill parameter c_g depending upon gouge properties to evaluate a modified joint factor as $J_{fg} = c_g\ (J_f)$ which returns joint factor for $c_g = 1$ for the clean joints. This infill often called gouge material undergoes varied degrees of consolidation and hardening eventually to become a part of rock mass (Trivedi et al. 2014; Trivedi and Trivedi 2015). Palchik and Hatzor (2004) observed detrimental effect on the strength of rock masses due to the porosity of chalk similar to the effect of presence of gouge at varied degree of consolidation.

The strength and modulus can be evaluated based upon the knowledge of joint factor, infill parameters, RQD, GSI, RMR, or Q. Such a supposition brings the admissibility of a mutual relationship among joint factor, GSI, RMR, RQD or Q with or without considerations of dilatancy and damage. The maximum plastic dilatancy experienced by various geomaterials is listed in Table 1.

2 Evaluation of Strength and Modulus by the Authors in Relation to the Original HB Criteria

The authors (Ramamurthy et al. 2017) have proposed the strength ratio considering a constant empirical multiplier to joint factor as to evaluate strength and modulus (Eqs. 1, 2), respectively, as,

✉ Ashutosh Trivedi
atrivedi@dce.ac.in

[1] Department of Civil Engineering, Delhi Technological University, Delhi, India

Published online: 08 May 2017

Table 1 Observed plastic dilatancy for soil and rock mass compositions (Trivedi 2015)

Material		Maximum observed plastic dilatancy
Clay	Marl clay	~0.50
	Leda clay	~0.64
Sand	Different sands	1.00–1.25
Rocks	Natural calcarenite	~0.50
	Cemented soft rock	1.50
	Soft rocks	~3.00
	Jointed rocks	0.60 at high confinement
		3.00 at low confinement
	Vosges sandstone	~0.60 at confinement of 30 MPa
		~8 at confinement of 0.5 MPa
	Gebdykes dolomite	~0.06 at confinement of 90 MPa
		~8 at confinement of 5 MPa
	Rock masses	~1 to 5 for dilation of joints
	Rock masses	~1 to 10 inclusive of associated damages

$$\sigma_{cj}/\sigma_r = \left(s_j\right)^{0.5} = \exp(-0.008\, J_f) \tag{1}$$

$$E_{cj}/E_r = \exp(-0.0115\, J_f) \tag{2}$$

σ_{cj} is the unconfined compressive strength of rock mass and σ_{r} is unconfined compressive strength of intact rock. The ratio of rock mass modulus (E_{cj}) to the intact rock modulus (E_r) is estimated by Eq. 2. s_j relates the rock mass strength with the intact rock strength in the original Hoek–Brown criteria (1980) and is expressed in terms of GSI (for GSI >25) as,

$$s_j = \exp(\mathrm{GSI} - 100)/9. \tag{3}$$

3 Evaluation of Strength and Modulus by the Discusser in Relation to the Generalized HB Criteria

The discusser considered a variance in this empirical multiplication factor (α_p and C_h) to propose a general solution (Trivedi 2010, 2013) for strength (σ_{cj}/σ_r) and modulus which is presented as,

$$\sigma_{cj}/\sigma_r = \left(s_{jd}\right)^{a} = \exp(\alpha_p J_f); \Rightarrow \alpha_p = \left[\ln\left(\sigma_{cj}/\sigma_r\right)\right]/J_f \tag{4}$$

$$E_{cj}/E_r = \exp(C_h J_f); \Rightarrow C_h = \left[\ln\left(E_{cj}/E_r\right)\right]/J_f \tag{5}$$

α_p and C_h are plasticity- and damage-dependent parameter defined by Trivedi (2010, 2013, 2015). The variation in the values of α_p and C_h observed in the data of various investigators has been compiled by Trivedi (2015) as listed in Tables 2 and 3, respectively. Kachanov (1992) reported similar trends for the deformation of cracked elastic solids depending upon crack measurement. Back-calculated values of α_p and C_h from joint factor, strength ratio and modulus ratio for various rock masses are presented in Figs. 1 and 2, respectively. Figure 3 shows plot of modulus ratio and joint factor from the in situ data of GSI. s_{jd} and a relate the rock mass strength with the intact rock strength in the generalized Hoek and Brown criteria (1997) and are expressed in terms of GSI and a damage factor D (Hoek et al. 2002) as,

$$\begin{aligned} s_j &= \exp(\mathrm{GSI} - 100)/(9 - 3D);\ a \\ &= 0.5 + (1/6)\left[e^{-\mathrm{GSI}/15} - e^{-20/3}\right] \end{aligned} \tag{6}$$

It may be noted that the switching formula for GSI > *25* is not necessary for Eq. 6. The factor D depends upon the degree of disturbance to which rock mass has been subjected by stress relaxation. The factor D takes a value of one for most disturbed state and zero for undisturbed state.

4 Complementarities of the Observations

Equations 4, 5 return the authors correlation as a particular solution where C_h and α_p take a value of -0.008 and -0.0115 as given in Eqs. 1, 2, respectively.

Subsequently as a consequence of generalized Hoek–Brown (1997) criteria, using from Eq. 4, it is implied that,

$$s_{jd} = \exp\left(\alpha_p J_f / a\right) \tag{7}$$

Equations 1, 3 imply that $\alpha_p/a = -0.016$ and $s_{jd} = s_j$, accordingly,

Table 2 Estimates of maximum, average, minimum values of α_p and a range of values of α_p/a

Mass material	Values of α_p			Values of α_p/a	
	Maximum	Average	Minimum	Maximum	Minimum
Gypsum	−0.0053	−0.00815	−0.011	−0.0106	−0.0183
Gypsum	−0.0032	−0.0091	−0.015	−0.0064	−0.0250
Concrete blocks	−0.001	−0.006	−0.011	−0.0020	−0.0183
Plaster of Paris, Kota sandstone, Granite	−0.0017	−0.043	−0.085	−0.0034	−0.1417
Jamrani sandstone, Agra sandstone[a]	−0.0001	−0.00955	−0.019	−0.0002	−0.0317
All rock masses[b]	–	−0.008	–	−0.0160	−0.0133
Kota sandstone[c]	−0.0054	−0.018	−0.031	−0.0108	−0.0517
Plaster of Paris	−0.0016	−0.0076	−0.012	−0.0032	−0.0200
Cement blocks	−0.002	−0.0085	−0.015	−0.0040	−0.0250
All rock masses[d]	−0.0001	–	−0.010	−0.0002	−0.0167

[a] Arora (1987)

[b] Authors

[c] Trivedi (1990)

[d] Discusser

Table 3 Average hardening parameter C_h for rocks and rock masses (Trivedi 2013, 2015)

Rock mass classification	Rock type	C_h
Intact rock	Westerly Granite	−0.00240
Intact rock	KTB Amphibolite	−0.00200
Intact rock	Dunham Dolomite	−0.00200
Intact rock	Solenhofem Limestone	−0.00016
Intact rock	Muzeho Trachyte	−0.00380
Intact rock	Shrihama Sandstone	−0.01000
Intact rock	Dense Marble	−0.00040
Intact rock	Yuubari Shale	−0.00180
Jointed rock	All types[a]	−0.01150
Rock masses	All types (based upon in situ J_{fg})	−0.02400
Rock masses	All types (based upon RMR)	−0.03500
Rock masses	All types[b]	−0.0001 to −1

[a] Authors, Arora (1987)

[b] Discusser, Trivedi (2013)

$$s_j = \exp\left(-0.016\, J_f\right) \tag{8}$$

Equation 7 returns the correlation of Eq. 8, where α_p/a takes a value of −0.016, which is a particular case as given in Table 2. Additionally, there are wide-ranging variations observed in α_p/a over and above the value considered by the authors.

In Eq. 5, C_h is a pressure-dependent hardening parameter as per Trivedi (2013), as,

$$C_h = \kappa(p_i/\alpha_r)^{\eta} \tag{9}$$

The parameter C_h is sensitive to plastic yielding, hardening and crushing characteristics of the joint material. The confining pressure ratio (p_i/σ_r) transforms empirical parameter C_h due to yielding, hardening and crushing characteristics and end conditions of the joint. $C_h = -0.0115$ as considered by the authors appears as a special case in Fig. 4.

It is evident from the relationship proposed by the authors that Eqs. 1, 2 predict strength and modulus appropriately for the rock masses having higher values of GSI, while the

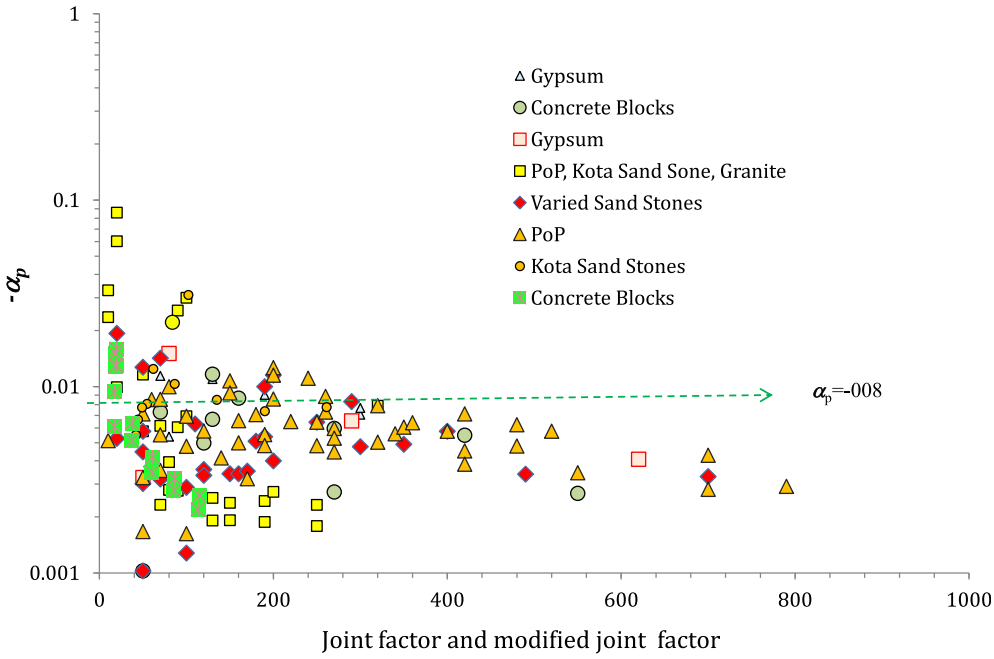

Fig. 1 Variation of α_p with joint factor and modified joint factor (Trivedi 2013)

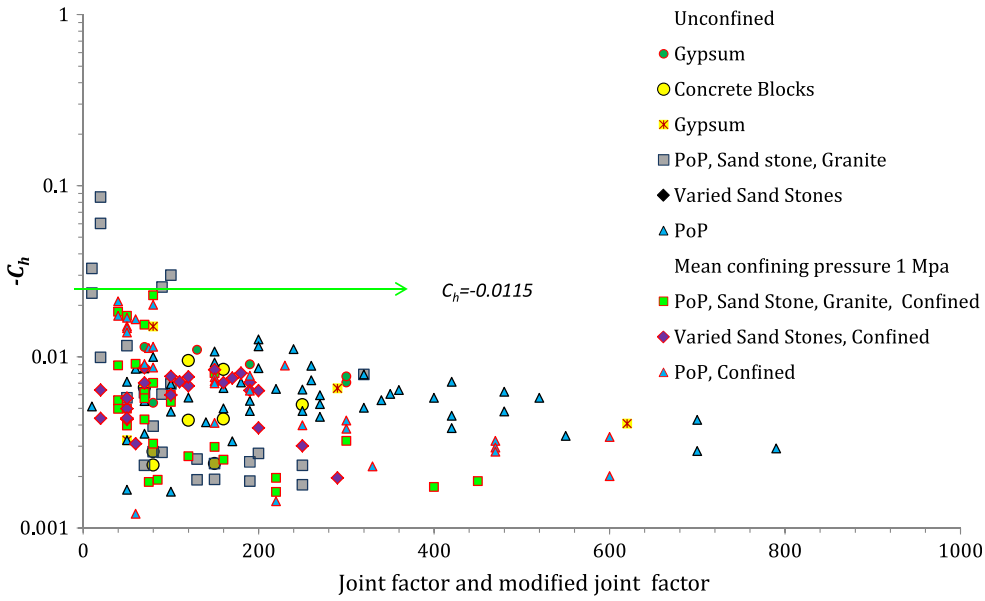

Fig. 2 Variation of hardening parameter C_h with joint factor and modified joint factor (Trivedi 2013)

relationship proposed by discussers applies (Hoek et al. 2002) well for the entire range of GSI and damage.

The rock mechanics has passed through several important mile stones, namely evolution of HB criterion (Hoek and Brown 1980, 1997). The concept of joint factor as proposed by the authors and assimilation of the concepts of plasticity and damage sensitive parameters by the discusser has brought significant advancement to the knowledge of the mechanics of rock masses.

Thus, the evaluation of strength and modulus as proposed by the discusser compliments the original proposal by Arora (1987), Ramamurthy and Arora (1994), Ramamurthy (2004) and subsequently improved by the authors (Ramamurthy et al. 2017).

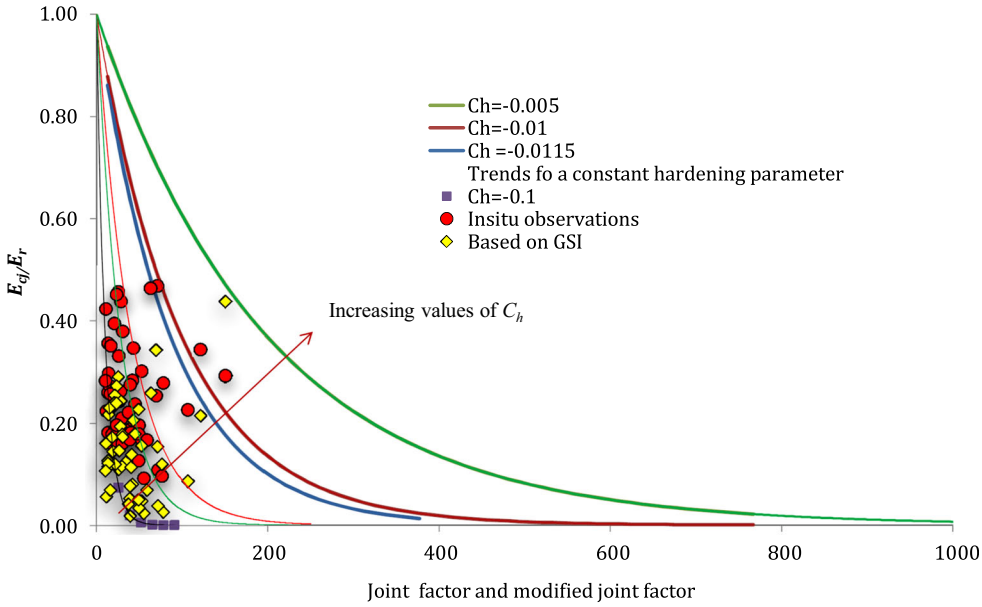

Fig. 3 Variation of modulus with joint factor and modified joint factor (Trivedi 2013)

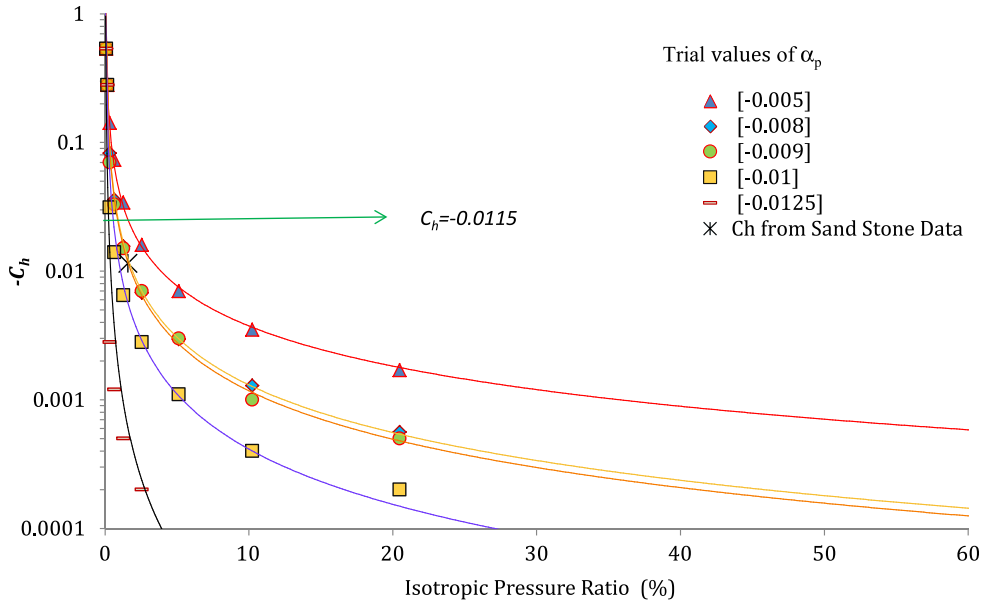

Fig. 4 Variation of hardening parameter C_h with isotropic pressure ratio (Trivedi 2013)

Compliance with Ethical standards

Conflict of interest The author hereby declares that there is no conflict of interest in this work.

References

Arora VK (1987) Strength and deformation behaviour of jointed rocks. Ph.D. Thesis, IIT Delhi, India

Arora VK, Trivedi A (1992) Effect of Kaolin gouge on strength of jointed rocks. In: Asian regional symposium on rock slope, New Delhi, pp 21–25

Hoek E, Brown ET (1980) Empirical strength criterion for rock masses. J Geotech Geoenviron Eng ASCE 106(9): 1013–1035

Hoek E, Brown ET (1997) Practical estimates of rock mass strength. Int J Rock Mech Min Sci Geomech Abstr 34(8):1165–1186

Hoek E, Carranza-Torres C, Corkum B (2002) Hoek-Brown criterion–2002 edition. Proceedings of NARMSTAC Conference, vol 1, Toronto, pp 267–273

Kachanov M (1992) Effective elastic properties of cracked solid: critical review of some basic concepts. App Mech Rev ASME 45(8):304–335

Palchik V, Hatzor YH (2004) The influence of porosity on tensile and compressive strength of porous chalks. Rock Mech Rock Eng 37:331–341

Ramamurthy T (2004) A geo-engineering classification for rocks and rock masses. Int J Rock Mech Min Sci Geomech Abstr 41:89–101

Ramamurthy T, Arora VK (1994) Strength prediction for jointed rocks in confined and unconfined states. Int J Rock Mech Min Sci Geomech Abstr 31(1):9–22

Ramamurthy T, Madhavi Latha G, Sitharam TG (2017) Modulus ratio and joint factor concepts to predict rock mass response. Rock Mech Rock Eng 50:1–14

Trivedi A (1990) Effect of gouge on the strength of jointed rocks. Dissertation, REC Kurukshetra, India

Trivedi A (2010) Strength and dilatancy of jointed rocks with granular fill. Acta Geotech 5(1):15–31

Trivedi A (2013) Estimating in situ deformation of rock masses using a hardening parameter and RQD. Int J Geomech ASCE 13(4):348–364

Trivedi A et al (2014) Consolidation of clayey gouge amid permeating rock masses. EnvironmentalGeotechnics. http://www.icevirtuallibrary.com/content/article/10.1680/envgeo.13.00043

Trivedi A (2015) Computing in situ strength of rock masses based upon RQD and modified joint factor: using pressure and damage sensitive constitutive relationship. J Rock Mech Geotech Eng 7(5):540–565

Trivedi A, Arora VK (2007) Discussion of bearing capacity of shallow foundations in anisotropic non-Hoek–Brown rock masses. J Geotech Geoenviron Eng ASCE 133(2):238–240

Trivedi A, Trivedi A (2015) Discussion on principle of super position of rate of settlement in 2D and 3D consolidations. Geotech Geol Eng 33(6):1581–1586

Volume 5, Issue 1 (2017) 137-140 ISSN 2347 - 3258
International Journal of Advance Research and Innovation

Comparative Analysis of Biodiesel as A Additive with Pure Diesel in Single Cylinder Four Stroke Diesel Engine Processes

Ashutosh Kumar*[,1], Hukam Singh[1], Avnish Kumar Shukla[1], Pawan Mishra[1], Ashutosh Kumar Rai[2]
[1]Department of Mechanical Engineering, Krishna Engineering College, Ghaziabad (UP) India
[2]Department of Mechanical Engineering Delhi Technological University, Delhi India

Article Info
Article History:
Received 25 January 2017
Received in revised form
20 February 2017
Accepted 28 February 2017
Available online 15 March 2017

Keywords:
Biodiesel, Performance, emissions, diesel engine

Abstract
At present, the demand of energy resources is increasing while their stocks are decreasing with high rate. Bio-diesel is an energy source which is renewable and would help in controlling the demand and supply of fuel but also in the reduction of pollution. Bio-diesel is simple to use and easy to transport. Different ratios of bio-diesel and diesel were mixed to prepare blends which showed viscosity, heat content, density, efficiency closer to diesel. The performance of various blends was tested on four stroke single cylinder compression ignition engine. Testing showed that partial substitution of diesel by bio-diesel can result in increase performance of engine. The results conclude that bio-diesel would be a better alternative to diesel in coming days.In this investigation we were planed to investigate fuel consumption, power in different loading condition, break specific fuel consumption, break mean effective pressure from bio-diesel (Blend of 5% Growdiesel + HSD, 2% Growdiesel + HSD,1% Growdiesel +HSD, .5% Growdiesel +HSD) with HSD. Planed to take 10 hr trials in cache combination and comparison of data and valuable findings related cost. The results that the performance of high percentage blends and pure bio-diesel doesn't fit the engine due to their viscosity and low thermal efficiency.

1.Introduction

Biodiesel is the name of a clean burning alternative fuel produced from domestic, renewable resources. Biodiesel contains no petroleum, but it can be blended at any level with petroleum diesel to create a biodiesel blend. It can be used in compression-ignition (diesel) engines with no major modifications. Biodiesel is simple to use, biodegradable, nontoxic, and essentially free of sulfur and aromatics[1]

Biodiesel derives from vegetable oil by a process of transesterification. Alcohol, usually methanol, is added to the vegetable oil, and using sodium or potassium hydroxide a is a catalyst, the glycerin and methyl esters are separated. The glycerin is then removed to be sold and biodiesel remains. This process is economical and straightforward because it occurs at low temperature (150° F) and low pressure (20 psi). Once the oil, methanol and catalyst are mixed, the entire transesterification process takes 3-6 minutes. In this chemical reaction, methanol substitutes for the glycerin in a chemical reaction, generally using lye as a catalyst. The final part of the process is separation of the less dense esters floating above the denser glycerol. The floating esters are usually drawn out of the primary vessel and the process is repeated, with less methanol and catalyst used in the secondary transesterification. This ensures the greatest yield of esters.[2]

Vegetable oils with low free fatty acid levels are best suited for biodiesel. Catalysts are used to free the esters from the fatty acids, and when free fatty acids are present in the vegetable oil, they consume catalyst without providing and energy in the form of esters. Oils can be neutralized, reducing the free fatty acids to less than 0.5% of the oil, at which catalyst consumption is acceptable. High phosphorous content in biodiesel is also problematic because it leads to emulsification of natural rubbers, which can cause gasket failure. Phosphorous in safe in levels below 3 to 4 ppm is hazardous to use because the risk of emulsification is too high. Insolubles in the fuel will not filter out in the transesterification process, ending up in the final fuel, so no more than 0.8% of the oil may be insoluble.

***Corresponding Author,**
E-mail address: ashume2007@gmail.com
All rights reserved: http://www.ijari.org

The methanol used in the transesterification process is flammable and toxic, and great caution must be used in its handling. Biodiesel is more viscous than regular diesel fuel because as vegetable oils cool, wax crystals form and the oil clouds and begins to solidify. Soy oil solidifies at –16° C. Biodiesel made with ethanol usually has a lower clouding point than biodiesel made with methanol, but ethanol is prohibitively more expensive[3].

Table 1 Biodiesel versus Dino diesel: Emissions

Pollutant	Percent Change in Emissions compared to Petroleum Diesel
Particulate	48 % decrease
Hydrocarbons	67 % decrease
CO	48 % decrease
NO_X	10 % increase
CO_2	0.2 % increase

So burning biodiesel releases a lot less smoke, hydrocarbons and carbon monoxide, but significantly more nitrogen oxides, and slightly *more* carbon dioxide.

The overall ozone (smog) forming potential of biodiesel is almost 50% less than diesel fuel. Sulfur emissions are eliminated. Substantial reductions of unburned hydrocarbons (-93%), carbon monoxide (-50%), and particulate matter (-30%). Biodiesel NOx emissions can be efficiently eliminated as a concern. Substantial reductions of cancer-causing PAH (-80%) and nitrited PAH compounds (-90%).

1.1 The Advantages of Using Biodiesel Fuel

You might have heard a lot about biodiesel. Biodiesel is diesel than can power up your car that is made from vegetable oils and other natural sources. It does not come from the regular crude oil that usually has to be imported from oil-producing countries.

Biodiesel can be considered a new technology, taking into account all the years consumers have had to settle for traditional diesel. Using biodiesel for your car has many advantages:

1. Biodiesel is not harmful to the environment. Unlike its counterpart, a car using biodiesel produces fewer emissions. If a vehicle uses traditional diesel, the vehicle

emits black, stinky smoke. With biodiesel, the smoke becomes very clean indeed.

2. Biodiesel may not require an engine modification. Some cars can take advantage of biodiesel without the need to undergo engine alterations. Some mix 20% biodiesel with regular diesel. Doing so enables the car to benefit from the good points of biodiesel without the hassle.

3. Biodiesel is cheap. You can even make biodiesel in your backyard. If your engine can work with biodiesel fuel alone, then you really need not go to the gas station to buy fuel. You can just manufacture some for your own personal use.

4. Biodiesel can make the vehicle perform better. It is noted that biodiesel has a cetane number of over 100. Cetane number is used to measure the quality of the fuel's ignition. If your fuel has a high cetane number, you can be sure that what you get is a very easy cold starting coupled with a low idle noise.

5. Biodiesel can make your car last longer. Because of the clarity and the purity of biodiesel, you can be sure it will not have too many impurities to harm your car. It is actually more lubrication. A car's power output is unaffected by this type of diesel.

6. Biodiesel reduces the environmental effect of a waste product. Because biodiesel is made out of waste products itself, it does not contribute to nature's garbage at all. Biodiesel can be made out of used cooking oils and lards. So instead of throwing these substances away, the ability to turn them into biodiesel becomes more than welcome.[4]

7. Biodiesel is energy efficient. If the production of biodiesel is compared with the production of the regular type, producing the latter consumes more energy. Biodiesel does not need to be drilled, transported, or refined like petroleum diesel. Producing biodiesel is easier and is less time consuming.

8. Biodiesel is produced locally. A locally produced fuel will be more cost efficient. There is no need to pay tariffs or similar taxes to the countries from which oil and petroleum diesel are sourced. Every country has the ability to produce biodiesel.

Biodiesel is surely a viable fuel alternative. Moreover, it is also a sustainable fuel. Using biodiesel not only helps maintain our environment, it also helps in keeping the people around us healthy.

2. Analysis of Biodiesel with Diesel

2.1. Specifications of Engine Used

Engine Make and type- Kirloskar (AVI-5.0)
Single cylinder, four stroke, water cooled
Vertical Engine
Bore (mm) - 80mm
Stroke (mm) - 110mm
Displacement Volume (cc) - 553cc
Compression Ratio- 16.5:1
Rated Output - 3.7KW (5.0 H.P.)

2.2 Formulae Used For Calculation Of Various Engine Performance Parameters

Calculations

3.1.1 Break Power

In the present case cradle type electrical dynamometer has been used.

Let S□ = Spring balance reading (kg)
Let S2 = Spring balance reading (kg)
L = Length of the force arm
N = Revolution per minute

Break Torque = 9.81(S□ - S2) Reff Nm

$$\text{Break power} = \frac{2\pi (N/60)\{9.81\times(S\square - S2)\}\text{Reff}}{1000} \quad KW$$

$$= 1.027\times10^{-3} N \frac{(S\square - S2)\, L}{} \quad KW$$

The load on the engine is applied by switching on the electric bulbs in turn.

3.1.2 Break Mean Effective Pressure

$$\text{Bmep} = \frac{60{,}000\times\text{break power}}{L\, AN\times n} \quad N/m^2$$

Where
L = Length of stroke (m)
A = Area of piston (m^2)
N = Revolution per minute (rpm)
n = no. of power stroke per cycle
= ½ for four stroke engines
= 1 for two stroke engines.
Where break power in kW.

3.1.3 Break specific fuel consumption

Break specific fuel consumption is defined as rate of fuel consumption per unit break power produced

$$\text{Bsfd} = \frac{\text{Fuel consumption per unit time}}{\text{Break power}}$$

3.1.4 Break thermal efficiency

It is defined as the ratio of break power to the energy supplied to the engine.

$$\eta\text{bth} = \frac{\text{break power}}{\text{Mass of fuel/s} \times \text{calorific value of fuel}}$$

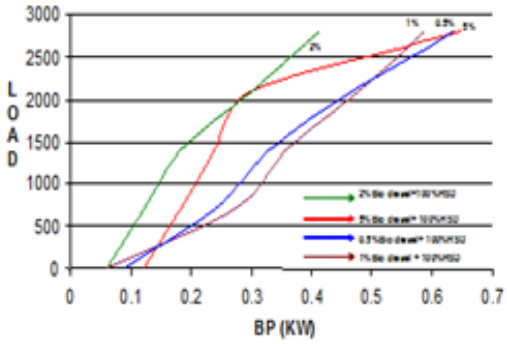

Fig.-1: Load Vs Break Power

In figure 1, shows the break power at different load condition. At no load condition, the blend of 1% biodiesel (miracle) +100% pure diesel gives minimum break power (.061 kw), the blend of 2% biodiesel (miracle) + 100% pure diesel gives break power of .062 kw, the blend of .5% biodiesel (miracle) + 100% pure diesel gives break power of .091 kw, the blend of 5% biodiesel (miracle) + 100% pure diesel gives maximum break power (.122 kw).

At max load condition, the blend of 2% biodiesel (miracle) + 100% pure diesel gives minimum break power (.415 kw), the blend of 1% biodiesel (miracle) +100% pure diesel gives break power of .588 kw, the blend of .5% biodiesel (miracle) + 100% pure diesel gives break power of .638 kw, the blend of 5% biodiesel (miracle) + 100% pure diesel gives maximum break power (.650 kw).

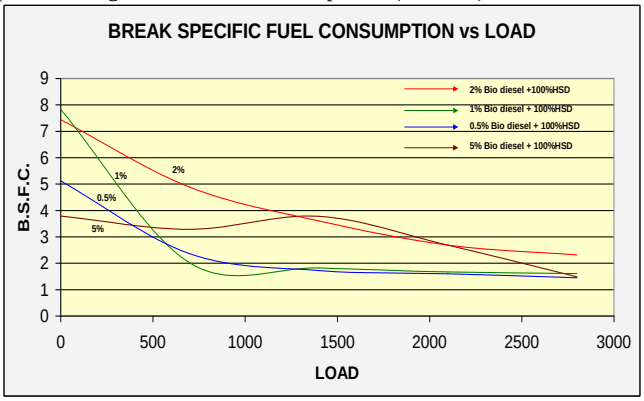

Fig.2: Load Vs Fuel Consumption

In figure 2, shows the fuel consumption at different load condition. At no load condition, the blend of 0.5% bio diesel (miracle) + 100% pure diesel gives minimum fuel consumption (461ml/hr), the blend of 5% bio diesel + 100% pure diesel and 2% bio diesel + 100% pure diesel gives equally fuel consumption (461.5ml/hr) and the blend of 1% bio diesel + 100% pure diesel gives maximum fuel consumption (477.70ml/hr).

At maximum load condition (2800 watt), the blend of 0.5% bio diesel + 100% pure diesel gives minimum fuel consumption (923ml/hr), the blend of 1% bio diesel +100% pure diesel gives fuel consumption of 946.37ml/hr, the blend of 2% bio diesel +100% pure diesel gives fuel consumption of 960ml/hr and the blend of 5% bio diesel + 100% pure diesel gives maximum fuel consumption.

In figure 3 the break specific fuel consumption at different load condition. At no load condition, the blend of 5% bio diesel + 100% pure diesel gives minimum break specific fuel consumption (3.782 lr/kw hr), the blend of 0.5% bio diesel + 100% pure diesel gives break specific fuel consumption (5.12 lr/kw hr), the blend of 2% bio diesel + 100% pure diesel gives break specific fuel consumption (7.44 lr/kw hr), the blend of 1% bio diesel + 100% pure diesel gives maximum break specific fuel consumption (7.83 lr/kw hr).At maximum load condition (2800w), , the blend of 0.5% bio diesel + 100% pure diesel gives minimum break specific fuel consumption (1.45 lr/kw hr), the blend of 5% bio diesel + 100% pure diesel gives break specific fuel consumption (1.48 lr/kw hr), the blend of 1% bio diesel + 100% pure diesel gives break specific fuel consumption (1.61 lr/kw hr), the blend of 2% bio diesel + 100% pure diesel gives max break specific fuel consumption (2.31 lr/kw hr).

In figure 4 the break mean effective pressure at different load condition. At no load condition, the blend of 1% bio diesel + 100% pure diesel gives minimum break mean effective pressure (2089. 2 N/ m²), the blend of 2% bio diesel + 100% pure diesel gives break mean effective pressure(2103.5N/ m²), the blend of 2% bio diesel + 100% pure diesel gives break mean effective pressure(3146.4N/ m²)and the blend of 5% bio diesel + 100% pure diesel gives max break mean effective pressure (4191.62 N/ m²) At maximum load condition (2800w), the blend of 2% bio diesel + 100% pure diesel gives minimum break mean effective pressure(14628.7N/ m²), the blend of 1% bio diesel + 100% pure diesel gives break mean effective pressure (20889.7 N/ m²), the blend of 5% bio diesel + 100% pure diesel gives break mean effective pressure (22987.3 N/ m²), and the blend of 0.5% bio diesel + 100% pure diesel gives max break mean effective pressure (23012.5 N/ m²)

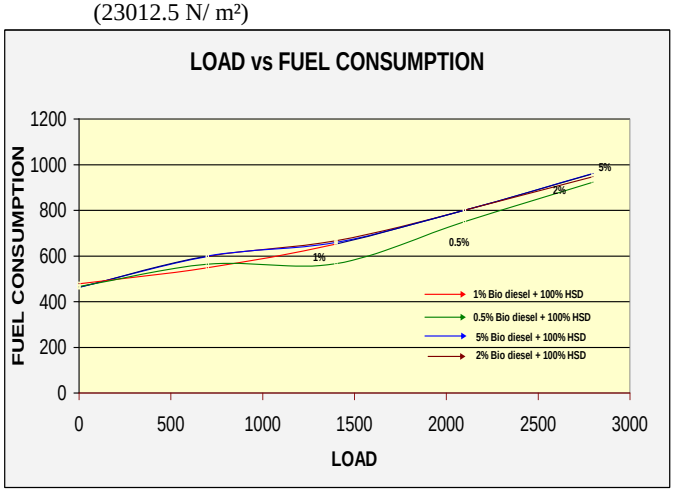

Fig.-3: Break Specific Fuel Consumption Vs Load

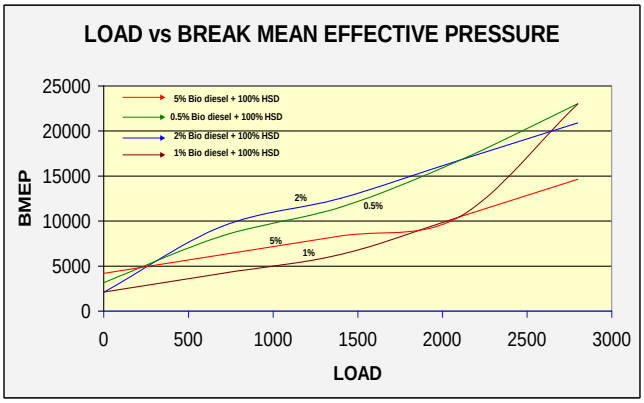

Fig-4: Load Vs Break Mean Effective Pressure

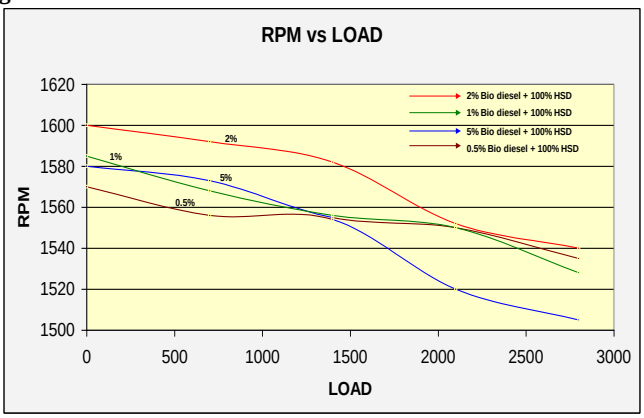

Fig.-5: RPM Vs Load

In figure 5 the RPM at different load condition. At no load condition, the blend of 0.5% bio diesel + 100% pure diesel gives minimum RPM (1570), the blend of 5% bio diesel + 100% pure diesel gives RPM (1580), the blend of 1% bio diesel + 100% pure diesel gives RPM (1585), And the blend of 2% bio diesel + 100% pure diesel gives max RPM (1600).

At maximum load condition (2800w), the blend of 0.5% bio diesel + 100% pure diesel gives minimum RPM (923), the blend of 1% bio diesel + 100% pure diesel gives RPM (946.7), the blend of 2% bio diesel + 100% pure diesel gives RPM (960) and the blend of 5% bio diesel + 100% pure diesel gives max RPM (961).

4. Conclusions

The ozone forming potential of the speciated hydrocarbon emissions is 50 percent less than that measured for diesel fuel. The exhaust emissions of sulfur oxides and sulfates (major components of acid rain) from biodiesel are essentially eliminated compared to diesel. .

Tests show the use of biodiesel in diesel engines results in substantial reductions of unburned hydrocarbons, carbon monoxide, and particulate matter. Emissions of nitrogen oxides stay the same or are slightly increased. The exhaust emissions of carbon monoxide (a poisonous gas) from biodiesel are on average 48 percent lower than carbon monoxide emissions from diesel. Breathing particulate has been shown to be a human health hazard. The exhaust emissions of particulate matter from biodiesel are about 47 percent lower than overall particulate matter emissions from diesel.

The exhaust emissions of total hydrocarbons (a contributing factor in the localized formation of smog and ozone) are on average 67 percent lower for biodiesel than diesel fuel. Nitrogen Oxides(NOx)emissions from biodiesel increase or decrease depending on the engine

family and testing procedures. NOx emissions (a contributing factor in the localized formation of smog and ozone) from pure (100%) biodiesel increase on average by 10 percent.

Refrences

[1.] X.Shia, X Panga, Y Mu, H He, SJ Shuai, JX Wang, H Chen, RL Li. Emission reduction potential of using ethanol–biodiesel–diesel fuel blend on a heavy-duty diesel engine Atmospheric Environment 40, 2006, 2567-2574.

[2.] PK Sahoo, LM Das, MKG Babu, SN Naik. Biodiesel development from high acid value polanga seed oil and performance evaluation in a CI engine. Fuel 86, 2007, 448-454.

[3.] MJ Haas, KM Scott, WN Marmer, TA Foglia. In situ alkaline transesterification: An effective method for the production of fatty acid esters from vegetable oils. J Am Oil Chem Soc 81, 2004, 83–89

[4.] S Sinha, AK Agarwal, S Garg. Biodiesel development from rice bran oil: Transesterification process optimization and fuel characterization. Energy Conversion and Management 49, 2008, 1248-1257.

[5.] CC Enweremadu, MM Mbarawa. Technical aspects of production and analysis of biodiesel from used cooking oil—A review. Renewable and Sustainable Energy Reviews 13, 2009, 2205-2224.

[6.] VB Veljkovic´, SH Lakic´evic´, OS Stamenkovic, Z B Todorovic, ML LazicL. Biodiesel production from tobacco (Nicotiana tabacum L.) seed oil with a high content of free fatty acids. Fuel 85, 2006, 2671-2675.

[7.] SV Ghadge, H Raheman. Biodiesel production from mahua (Madhuca indica) oil having high free fatty acids. Biomass and Bioenergy, 28, 2005, 601-605.

[8.] AK Tiwari, A Kumar, H Raheman. Biodiesel production from jatropha (Jatropha curcas) with high free fatty acids: An optimized process. Biomass and Bioenergy, 31, 2007, 569-575.

[9.] A Demirbas, FM Demirbas. Importance of algae oil as a source of biodiesel. Energy Conversion and Management 2010, doi:10.1016/j.enconman.2010.06.

Asian Journal of Convergence in Technology *Volume III, Issue II*
ISSN No.:2350-1146, I.F-2.71

Design and Control of DC Microgrid based on Solar PV and Storage

Priyanka Chaudhary
Department of Electrical Engineering
Delhi Technological University
Delhi, India
priyankach.iilm@gmail.com

M. Rizwan
Department of Electrical Engineering
Delhi Technological University
Delhi, India
rizwan@dce.ac.in

***Abstract*— Microgrids are the solution to accommodate high penetration of renewable energy sources (RES) by achieving good coordination. However, in India, many households do not have access to electricity and some has interrupted and poor quality of electric power supply. The reason for this is large number of houses in remote areas are remaining off grid and which are connected with the grid have long hours of load shedding because shortage of power. Solar PV based DC microgrids with energy storage technologies in low- and medium-income households provides solution to above mentioned challanges. This paper presents a solar PV and BESS based DC microgrid with MPPT and BESS controller and energy management system. The solar PV and the battery energy storage system (BESS) are integrated with the help of dc-dc converters. The load requirements of small society of low demand households can be easily and cost effectively full filled by the proposed PV system and energy storage systems with energy management system.**

Keywords*— *DC microgrid; solar PV system; battery energy stogage system (BESS); DC/DC converter; MPPT control

I. INTRODUCTION

The idea of microgrid gaining more attention due to increasing penetration of renewable energy sources (RES) and electricity transmission capacity constraints, losses at transmission and distribution level for long distance transmission of electric power [1]. Microgrids allow generation close to the load end increases the power quality and reliability (PQR) of supplied electricity. RES can significantly reduce requirement to expand the existing traditional transmission systems. Coordination and control of large numbers of RES in the system creates numerous difficulties from security and operation point of view.

Microgrid offers attractive solution with effective coordination of RES and reduce RES control burden on the utility grid with acquiring full benefits of RES. RES includes various alternative sources for power generation such as wind, solar, hydro and fuel cell etc. Increasing demand of electricity and environmental concern are the main drivers behind the adoption of RES for electricity production. Energy from sun is being utilized now a days and becoming one of the most prominent and promising form of RES. Since the output power of solar PV is always intermittent in nature an Energy storages system (ESS) is required in order to mitigate the intermittency of the solar PV power generation system.

Multiple power conversion stages are required for integration of dc-inherent system in the traditional AC utility grid. Mostly ESS used with Solar PV systems like batteries, ultra capacitors etc. are dc inherent in nature. There are numerous dc-compatible loads like communication systems, computation devices, LEDs, etc. are gaining more attention now a days. Due to above mentioned reasons DC micro grids are providing attractive solution with high penetration of DC compatible energy sources, storages and loads and need less number of power conversion stages. There are numerous applications of DC microgrids are available such as data center, residential applications, electric vehicle etc. DC microgrid system offers around 10-20% high efficiency as compared to AC systems. In addition, dc systems are more reliable due to minimized power conversion stages. In case of DC systems power transmission cables are utilized more effectively due to absence of reactive power flow.

However, in India, many households do not have access to electricity and some has interrupted and poor quality of electric power supply. A study conducted by the Council for Energy, Environment, and Water (CEEW) with six states (Bihar, Jharkhand, Madhya Pradesh, Uttar Pradesh, West Bengal, and Odisha) and concluded that about 50% of the houses do not have electricity despite having a grid connection [2]. Thousands of villages of different states are being electrified over the past decade under the Government's rural electrification scheme and over 85% of the households in five of the six states are considered as having no electricity or have electricity for less than 8 h with maximum load of 50 W. Other states have better situation than this but people with less income also have poor access to power [3-4].

These challenges need new technology and advance approaches. One approach can be adoption of novel solar and energy storage technologies integrated with DC microgrid in low- and medium-income households. Electricity authorities of many states such as Uttar Pradesh authorities are using 24 V solar powered DC microgrid for lighting loads [4]. Many problems can be mitigate with a DC microgrid having solar PV

and battery storage for a household which have access to grid supply but suffers long hours of power cuts. Another advantage is this is highly cost effective for off-grid homes.

One important task in DC microgrids is power management. As the Solar PV is not available in night, ESS is required to operate and proper design of energy management system is necessary. From the stability point of view, the DC bus voltage regulation plays a key role. Researchers carried out various studies on design, operation and control of DC microgrids [5-8]. In this paper, design and control of DC microgrid based on solar PV and energy storage for remote areas is presented with an energy management system. The proposed system consists solar PV array, a battery energy storage system (BESS) with various loads and all are connected to a common DC bus.

This work is organized in following manner: Section 2 presents the system configuration. Section 3 describes the control techniques. Results and discussions are presented in Section 4 followed by the conclusion in section 5.

II. System Design

The DC microgrid considered in the present work consists of PV array, DC/DC converter, battery energy storage system (BESS), bi directional DC/DC controller for BESSand various loads. The dc microgrid proposed in this work is shown in Fig.l. The battery energy storage system is composed of lead acid battery with high energy density.

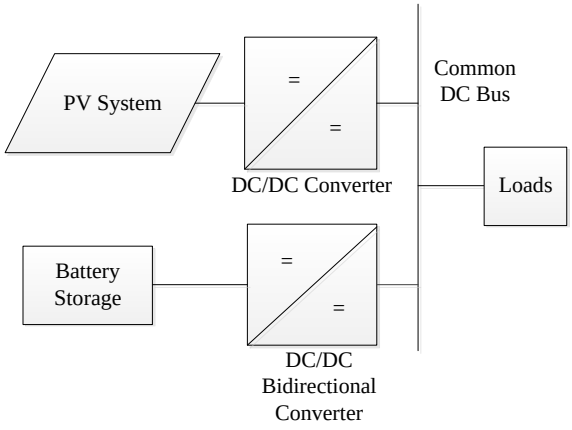

Fig. 1. DC microgrid system

A. Solar PV array

A photovoltaic (PV) array consists of several PV modules which are series or parallel interconnection of several PV cells. Power produced by single PV cell is not sufficient to drive any application hence PV cells are connected to obtain PV module. PV modules are further interconnected in array form to achieve more power to fulfill load requirement. To form PV array, modules are first connected in series configuration to produce the high voltages and further, to produce more current, the individual single modules are then connected in parallel configuration. Most widely used single diode model of basic solar PV cell is presented in fig.2 followed by mathematical equations to model a module [9-10].

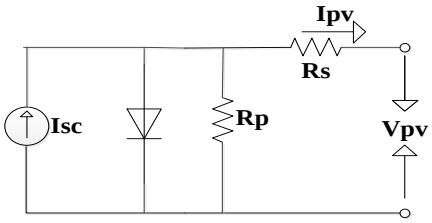

Fig. 2. Single diode model of PV cell

Equations for the output current using fig.2 can be obtained as follows:

$$I_{sc} - I_D - \frac{V_D}{R_v} - I_{PV} = 0 \quad (1)$$

Where

$$I_D = I_{scref}[\exp\left(\frac{qVoc}{kAT}\right) - 1] \quad (2)$$

The incident current measured with respect to some standard conditions depends on irradiance and temperature.

Thus,

$$I_{sc} = [I_{scref} + K_i(T_k - T_{ref})] * S/1000 \quad (3)$$

In above expression I_{sc} denotes the photocurrent in amperes which is generated from solar incident current at the standard condition (25°C and 1000W/m^2), Ki represents the short-circuit current/temperature coefficient at I_{scref} (0.00065A/K), T_k and T_{ref} are the actual and reference temperature in Kelvin, S shows the actual solar irradiance coming at the surface of device and 1000W/m^2 is the irradiation at standard reference conditions.

Reverse saturation current I_{rs} of diode can be written as:

$$I_{rs} = I_{scref} + [\exp\left(\frac{qVoc}{NskAT}\right) - 1] \quad (4)$$

The saturation current of module varies with the cell temperature which is given by;

$$I_o = I_{rs}\left[\frac{\left(\frac{T}{T_{ref}}\right)^3 e^{qcg}}{Ak} * \left(\frac{1}{T_{ref}} - \frac{1}{T}\right)\right] \quad (5)$$

The output current equation can be written as:

$$I_{PV} = I_{sc}N_p - N_s I_o\left[\exp\left\{\frac{q(V_{PV} + I_{PV}Rs)}{N_s AkT}\right\} - 1\right] V_{PV} + \frac{I_{PV}Rs}{Rp} \quad (6)$$

In equation (6) k is the Boltzmann constant (1.38 x 10^{-23} J K^{-1}), q is the electronic charge (1.602 x 10^{-19} C), T is the cell temperature (K); A is the diode ideality factor, R_s the series resistance (Ω) and R_p is the shunt resistance (Ω). N_S is the

number of cells connected in series and N_p is the number of cells connected in parallel.

B. DC/DC Converter

Numerous meteorological parameters such solar irradiance, temperature, wind speed, wind direction, humidity, incident angle etc. significantly makes impact on solar PV output, that is the reason of intermittency of the PV output power. A DC/DC converter is needed in order to implement the algorithm which keeps on tracking the maximum power point of the PV array and to match the load with the source. In the present system a DC/DC boost converter is used to step up the voltage level. Basic DC/DC boost converter configuration is presented in fig. 3.The design of input inductor of DC/DC boost converter is depend on the input ripple current (ΔI_1) and switching frequency (f_{sw}). ΔI_1 is considered as 6% of input current to the DC/DC boost converter and switching frequency (f_{sw}) is chosen as 10 kHz. The value of input inductor (L_b) can be calculated as:

$$L_b = \frac{V_{PV}\,D}{\Delta i f_{sw}} \quad (7)$$

Where, $D = 1 - \frac{V_{PV}}{V_{DC}}$

DC link Capacitors (C)

$$C = \frac{I_{in} D}{\Delta v f_{sw}} \quad (8)$$

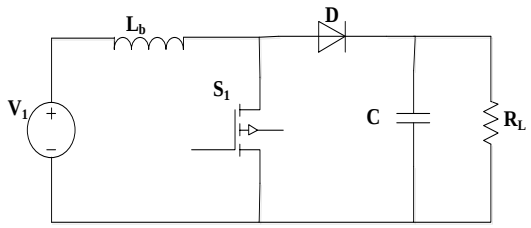

Fig. 3. DC/DC boost converter

C. Battery Energy Storage System (BESS)

The BESS can be modeled as a controlled voltage source in series with constant resistance. Output voltage of which depends on the current and state of charge (SOC) of battery which is nonlinear function of the current and time. State of a battery can be modeled as a function of two parameters; terminal voltage and state of charge [11-12].

$$V_b = V_o + R_b i_b - K\frac{Q}{Q - \int i_b dt} + A * \exp(B \int i_b dt) \quad (9)$$

$$SOC = 100\ (1 + \frac{\int i_b dt}{Q}) \quad (10)$$

In above mentioned expressions V_b denotes battery voltage, V_o is no load voltage, R_b represent constant series resistance, i_b is battery current, K is polarization constant, is capacity of battery, A and B are exponential voltage and capacity respectively. A lead acid battery is being considered in present work using a DC source and internal resistance.

D. DC/DC Bidirectional Buck-Boost Converter

In case of excessive generation from solar PV system during day time battery storage gets charged and this power may be used during night time or when the generation from solar PV is not sufficient to feed the load. A DC/DC bi-directional converter performs the regulation of dc link voltage at a constant level.

During charging mode of BESS converter works in buck mode by using duty cycle provided by the BESS controller. Boost mode comes in picture during discharge operation required. Two IGBT switches operates complementary with single Pulse Width Modulation (PWM) signal. Input and output voltage relationship during buck and boost mode are presented in equation (11) and (12) respectively. D denotes the duty cycle in below given expressions.

$$\frac{V_{bat}}{V_{dc}} = D \quad (11)$$

$$\frac{V_{bat}}{V_{dc}} = \frac{1}{1-D} \quad (12)$$

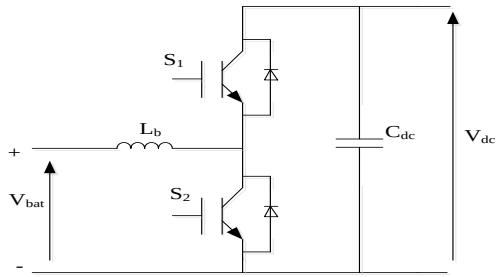

Fig. 4. DC/DC bidirectional buck boost converter

III. Control Design

A. DC/DC Converter control

A MPPT algorithm is used to extract the maximum power from PV array. PV array output voltage/current is varied by MPPT controller according to the P-V or I-V characteristic curves of PV array. A large number of MPPT techniques are reported in the literature to track the maximum power point [13]. MPPT techniques like perturb and observe, incremental conductance, constant voltage, open circuit voltage, short circuit current, extremum seeking control and hybrid etc are widely being used in systems. MPPT techniques based on artificial intelligence like artificial neural networks, fuzzy logic, genetic algorithms are also provided in the literature.

An Incremental conductance (INC) based method is being considered in the present work. This method is based on the concept that the slope of the solar PV array curve is zero at maximum power point. The slope of PV curve will be positive for values of output power smaller then maximum power point (MPP) and negative for output power greater then maximum power point.

Maximum output power is obtained by using the derivative of PV output power with respect to voltage and equating this to zero.

$$\frac{dP}{dV} = I + V\frac{dI}{dV} = 0 \quad (13)$$

Equation (13) can be further used to obtain below given expression:

$$\frac{dI}{dV} \cong \frac{\Delta I}{\Delta V} = -\frac{I_{MPP}}{V_{MPP}} \quad (14)$$

$$\frac{dP}{dV} = 0 \qquad \frac{\Delta I}{\Delta V} = -\frac{I}{V} \qquad \text{at MPP}$$

$$\frac{dP}{dV} > 0 \qquad \frac{\Delta I}{\Delta V} > -\frac{I}{V} \qquad \text{left side of MPP}$$

$$\frac{dP}{dV} < 0 \qquad \frac{\Delta I}{\Delta V} < -\frac{I}{V} \qquad \text{right side of MPP}$$

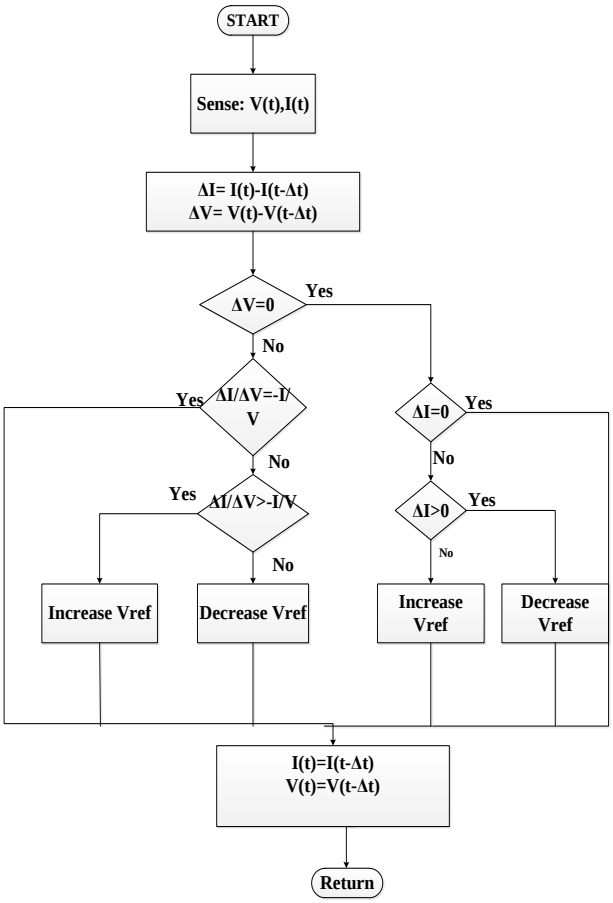

Fig. 5. Flowchart of MPPT algorithm

In INC algorithm compares instantaneous conductance with the incremental conductance to achieve the maximum power point operation of solar PV array. After reaching at MPP, the operation of PV array system is forced to remain at this point unless a change in current occurs due to varying meteorological parameters which further leads to the variation in MPP. The flowchart for this technique is presented in Fig. 5.

B. BESS control

Battery energy storage systems (BESS) are most widely adopted ESS especially for low power residential applications. BESS are the storage devices that cannot be overcharged or depleted entirely. For a long life, charging and discharging has to be properly controlled. State of the charge (SOC) of the BESS is a key parameter to develop control methodology [14-15]. The BESS is integrated with the Solar PV system is used to supply or consume real power to support the SPV generator in form of charging and discharging.

In case of surplus power production by solar PV, the battery bank will be get charged. If there is no sufficient power from SPV available then the battery will supply the remaining power in order to fulfill load requirements in night time or unavailability of solar power. Controller for bidirectional DC/DC converter of BESS is presented in fig. 6. The proposed controller consists of a PI controller, which receives the error signal of actual battery power (P_b) and battery reference power (P_{bref}). The output of PI controller further compared with a triangular carrier waveform of unity magnitude to generate the PWM signal G. K_p and K_I are the proportional and integral gains of PI controller, respectively. The controller action equation is given in equation 15.

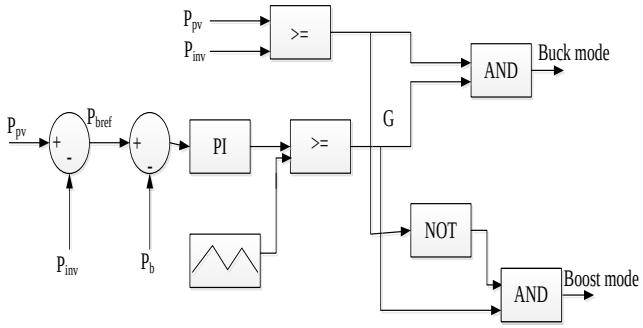

Fig. 6. Bi-directional DC/DC converter controller

$$G = K_p(P_{bref} - P_b) + K_I\int(P_{bref} - P_b)dt \quad (15)$$

Energy management system (EMS) control algorithm for the proposed system is presented in Fig. 7. SOC indication is used to maintain the charging and discharging of BESS within prescribed limits which are considered as 25% and 85% respectively here. The actions taken by the controller according to state of charge condition of BESS are presented in table I.

TABLE I. OPERATION OF ENERGY MANAGEMENT SYSTEM

Condition	Battery SOC	P_{pv} and P_{load}	Action
I	SOC<85%	$P_{pv}>P_{load}$	Charge battery
II	SOC<25%	$P_{pv}>P_{load}$	Charge battery
III	SOC>85%	$P_{pv}<P_{load}$	Discharge battery
IV	SOC>25%	$P_{pv}<P_{load}$	Discharge battery
V	SOC<25%	$P_{pv}<P_{load}$	Load Shedding
VI	SOC>85%	$P_{pv}>P_{load}$	Idle (If no additional available)

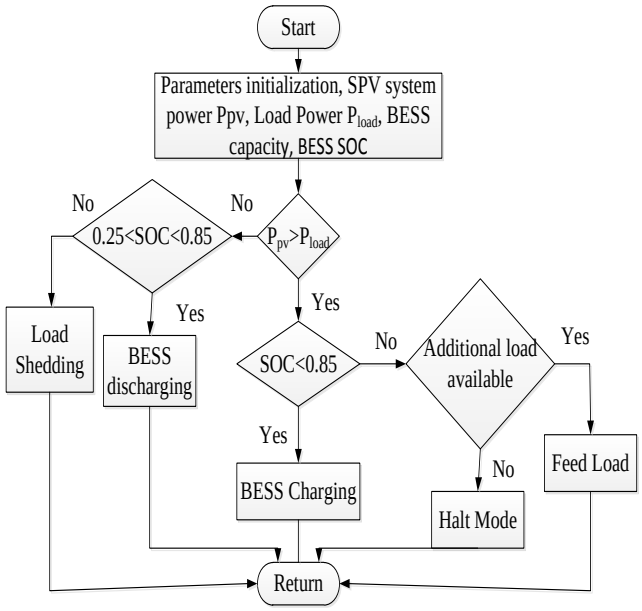

Fig. 7. Flowchart for BESS control

IV. RESULTS

The simulations studies of the proposed system is presented in this section with controllers and energy management system of DC microgrid based on solar PV and battery. Typical loads for a household application powered by DC microgrid are presented in table II. For a practical application, a 2 kW PV array has been considered here to power a small locality of such type of houses. A typical solar irradiance profile for a day is presented in fig. 8.

TABLE II. TYPICAL LOADS FOR RESIDENTIAL APPLICTIONS

DC Load Type	Power Rating (W)	Numbers	No. of operational hours
Fan	24	3	8
Tubelight	18	2	10
Bulb	5	3	10
TV	30	1	4
Phone	5	2	10

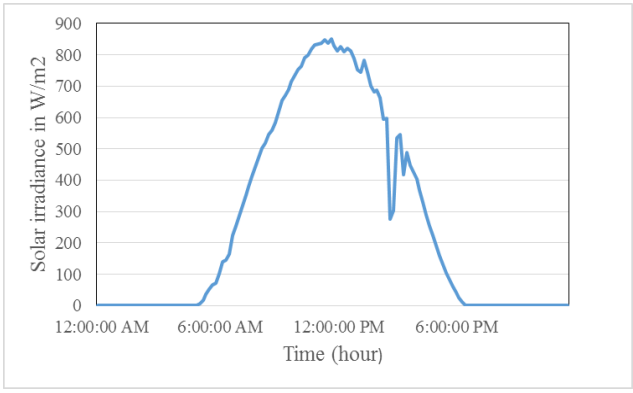

Fig. 8. Typical solar irradiance profile for a day

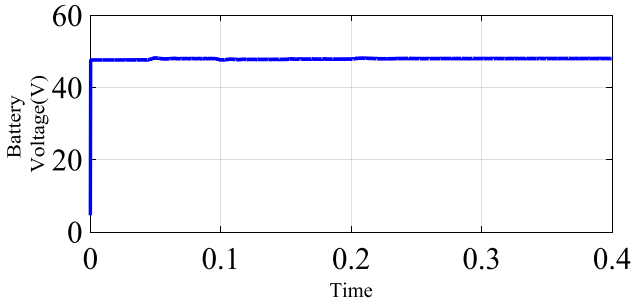

Fig. 9. Battery voltage in volts

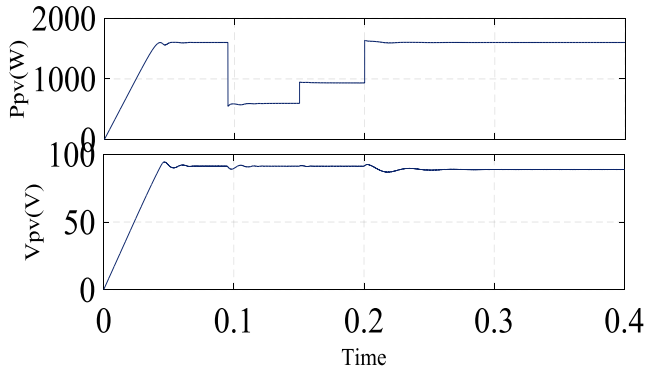

Fig. 10. Solar PV power (W) and voltage (V)

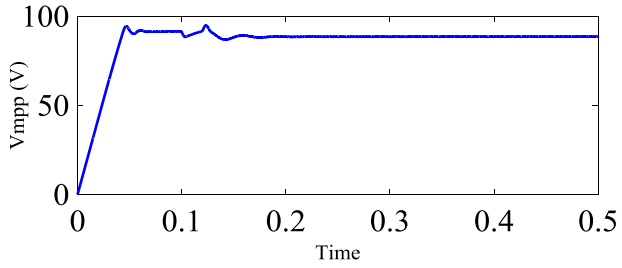

Fig. 11. Solar PV voltage at maximum power point maintained by INC MPPT Technique

By using BESS controller a constant voltage of 48 V maintained across the BESS and shown in fig. 9. Fig. 10 shows the output PV power at varying solar irradiance level and depicting practical case. INC MPPT technique regulates the PV voltage at constant MPP level and shown in fig. 11. When excess PV power is generated battery is getting charged otherwise feeding to the load. Power of PV, load and battery is given in fig. 12. If solar irradiance comes down battery follows a rapid discharging rate. While during large amount of solar irradiance BESS get charged until the maximum SOC level.

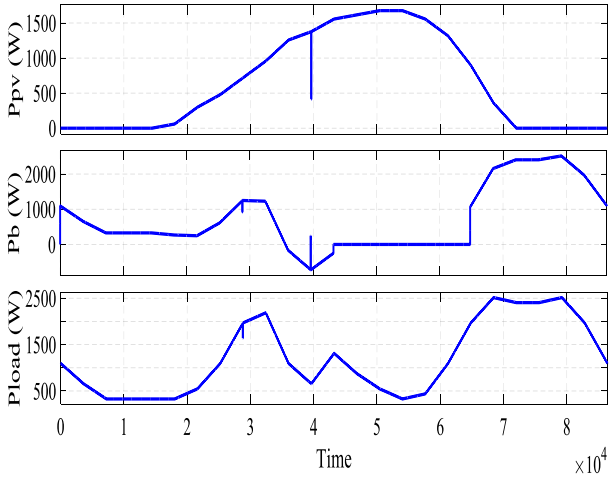

Fig. 12. Solar PV power, BESS power and load power

V. Conclusion

A solar PV system and battery energy storage based DC microgrid has been developed in this paper with MPPT and BESS controllers. The performance of proposed system in terms of PV output power, PV voltage, BESS voltage, BESS power and SOC is presented. Disruptive technology is the demand of the present time in order to get uninterruptable power supply. A DC microgrid based on solar PV and BESS for households seems attractive solution. As a result of which the overall cost of power can be reduced and become affordable in the presence of a utility grid also by reducing load shedding significantly.

References

[1] R. H. Lasseter and P. Paigi, “Microgrid: A conceptual solution,” in Proc. IEEE 35th PESC, Jun. 2004, vol. 6, pp. 4285–4290.

[2] International Energy Agency, “World Energy Outlook 2015,” Int. Energy Agency, Paris, France, annual report, 2015.

[3] A. Jain, S. Ray, K. Ganesan, M. Aklin, C.- Y. Cheng, and J. Urpelainen, “Access to clean cooking energy and electricity: Survey of states,” Council on Energy, Environment, and Water, New Delhi, India, 2015.

[4] M. H. F. Ahamed, U. D. S. D. Dissanayake, H. M. P. De Silva, H. R. C. G. P. Pradeep and N. W. A. Lidula, "Modelling and simulation of a solar PV and battery based DC microgrid system," 2016 International Conference on Electrical, Electronics, and Optimization Techniques (I J. Lee, H. Kim, B. Han, Y. Jeong, H. Yang and H. Cha, ‘‘DC Microgrid.

[5] P. Kaur, S. Jain, and A. Jhunjhunwala, “Solar-DC deployment experience in off-grid and near off-grid homes: Economics, technology and policy analysis,” in Proc. IEEE First Int. Conf. DC Microgrids (ICDCM), Atlanta, GA, 2015, pp. 26–31.

[6] L. A. de Souza Ribeiro, O. R. Saavedra, and J. G. de Lima, S. L. abd de Matos, "Isolated micro-grids with renewable hybrid generation: The case of Lencois Island," IEEE Trans. on Sustain. Energy, vol. 2, no. 1, pp. 1-11, January 2011.

[7] N. Mendis, M. A. Mahmud, T. K. Roy, M. E. Haque and K. M. Muttaqi, "Power management and control strategies for efficient operation of a solar power dominated hybrid DC microgrid for remote power applications," 2016 IEEE Industry Applications Society Annual Meeting, Portland, OR, 2016, pp. 1-8.

[8] Operational Analysis with Detailed Simulation Model for Distributed Generation’’ Journal of Power Electronics, vol. 11, no. 3, pp. 350-359, 2011.CEEOT), Chennai, 2016, pp. 1706-1711.

[9] N. Pandiarajan, R. Ramaprabha and M. Ranganath, “Application of circuit model for photovoltaic energy conversion system,” International Journal of Advanced Engineering Technology. Vol. 2, No. 4, 2011, pp. 118-127.

[10] J. A. Gow and C. D. Manning, “Development of a photovoltaic array model for use in power-electronics simulation studies,” IEE Proceedings on Electric Power Applications. Vol. 146, No. 2, 1999, pp. 193–200.

[11] K. Rahbar, J. Xu, and R. Zhang, “Real-time energy storage management for renewable integration in microgrid: An off-line optimization approach,” IEEE Trans. on Smart Grid, vol. 6, no. 1, pp. 124–134, Jan 2015.

[12] Marwan M. Mahmoud, “On the storage batteries used in solar electric power systems and development of an algorithm for determining their ampere-hour capacity,” Electric Power System Research, vol. 71, issue 1, pp. 85-89, Sept. 2004.

[13] Y. C. Kuo, T. J. Liang and J. F. Chen, “Novel maximum-power point tracking controller for photovoltaic energy conversion system,” IEEE Transaction on Industrial Electronics. Vol. 48, No. 3, 2001, pp. 594–601.

[14] Zhen Jin, Meiyi Hou, Fangfang Dong and Ying Li, "A new control strategy of dc microgrid with photovoltaic generation and hybrid energy storage," 2016 IEEE PES Asia-Pacific Power and Energy Engineering Conference (APPEEC), Xi'an, China, 2016, pp. 434-438.

[15] Corneliu Marinescu, Luminita Barote and Daniel Munteanu, “PV-Battery system with enhanced control for microgrid integration,” in proc. ICATE 2016.

ELK
Asia Pacific Journals

ELK Asia Pacific Journals – 978-93-85537-06-6
ARIMPIE -2017

Design and Solidification Simulation of Exhaust Manifold Made of SiMo Ductile Cast Iron

Vijay Gautam
Department of Mechanical Engineering,
Delhi Technological University,
Delhi, India.
vijaygautam@dce.ac.in

Sahil Ahuja
Department of Mechanical Engineering,
Delhi Technological University,
Delhi, India.
sahila796@gmail.com

Nanak Ram
Department of Mechanical Engineering,
Delhi Technological University,
Delhi, India.
nanak_saini@yahoo.com

Abstract: The demand for more environment-friendly vehicles with increased fuel efficiency has expanded the need for specialized materials like SiMo Ductile cast iron (high silicon and molybdenum) in various automotive castings. SiMo Ductile cast iron is a special material designed for high-temperature applications like exhaust manifolds, turbo charger housings used in automotives. These castings can perform and maintain dimensions for many thousands of cycles that can range from below freezing temperatures to those greater than 750°C. The present study deals with the solidification simulation of exhaust manifolds, four in numbers in sand moulds, made of SiMo Ductile cast iron using MAGMASOFT. A proper top gating system was designed with the help of the software to remove the hot spots responsible for shrinkage in the castings and consequently a sound casting was designed. A trial casting was successfully produced and the material was tested for microstructure and mechanical properties. Microstructural analysis revealed that trial casting consists of 79% Nodularity with 10% Pearlite and a maximum of 5% carbide. A series of uniaxial tensile tests were conducted on the specimens taken from the actual casting, and it was observed that the average tensile strength of the designed material is approximately 527MPa with 14% of uniform elongation. The hardness of the material varies from 200-230 BHN for different specimens.

Keywords*:* SiMo Ductile cast iron, exhaust manifold, gating system, microstructure, nodularity, tensile test, casting simulation, MAGMASOFT.

I. INTRODUCTION

The concerns related to the environment have been increasing which focuses the industry to use more environment-friendly vehicles with higher fuel efficiency, and this has increased the use of SiMo Ductile cast iron material which has high percentages of silicon and molybdenum. SiMo ductile cast iron is a versatile material and is widely used in automotive components manufactured by the sand casting method. This special material exhibits various advantageous characteristics including high tensile strength, fatigue strength and wear resistance [1]. Moreover, the castings of SiMo ductile iron can perform and maintain their dimensional accuracy for thousands of fatigue cycles that can range from below freezing temperatures to those greater than 750°C [2-3]. These properties also make these materials suitable for large turbine castings and many types of furnace applications. Ductile Iron containing higher silicon and molybdenum has been developed to meet the desired characteristics of oxidation prevention, growth resistance, and wear resistance at high temperatures. Increasing silicon content promotes the stability of the microstructure and properties at high temperature by forming a highly ferritic matrix structure, and by raising the austenite transformation temperature. SiMo Ductile Iron resistance to growth and oxidation is much improved, when compared to gray iron, because gray iron grows by graphitization and oxidation both, and also the nodular shape of graphite plays an important role. It is also more resistant to creep, which increases at higher stress levels and higher temperatures. In general, SiMo Ductile Iron has a silicon content of 2.0–3.0%. Increasing the silicon concentration above these levels improves resistance to scaling and increases yield strength, but lowers toughness and elongation [4]. Therefore, the material can be very brittle at room temperature with high silicon percentages. Mechanical properties are influenced by microstructure and solidification defects of the alloy. In ductile iron castings , major defects that negatively influence the material properties are correlated to graphite particles shape and dimensions in the thermal center of castings [2]. It usually has a ferritic structure which has higher ductility and toughness but may also contain pearlite and carbides (cause brittleness). Heat treatment is necessary to transform pearlite and carbides,

if present, to reduce the brittleness. The addition of molybdenum and other alloying elements may be needed to improve the serviceability and properties of the material at high temperature [5-6]. This material possesses excellent castability but at high pouring temperatures it necessitates the proper design of the gating system for sand mould with top pouring for production [7]. The design of gating and risering system is very important for obtaining a sound casting. It has been reported that 90-95% of the defects in the castings results only because of improper design of gating and feeding system [8-9]. Casting simulation necessarily reduces shop-floor trials to achieve the desired internal quality at the highest possible casting yield and hence saves time, labor, energy and money. Various casting simulation softwares are accessible today, such as CastCAE, MAGMA, Novacast, ProCAST, and SolidCAST. Most of these use Finite Element Method to discretise the domain and solve the heat transfer and/or fluid flow equations. The main inputs include the 3D CAD model of the mould cavity (which includes the part cavity, feeders, and gating system), thermo-physical properties (density, specific heat, and thermal conductivity of the cast metal as well as the mould material, as a function of temperature), boundary conditions (such as the metal-mould heat transfer coefficient, for normal mould as well as feed-aids including chills, insulation and exothermic materials), and process parameters (such as pouring rate, time and temperature). The results of solidification simulation include colour-coded freezing contours at different instants of time starting from beginning to end of solidification. This provides a much better insight of the casting phenomenon compared to shop-floor trials (real moulds being opaque).With the results obtained after the simulation, the user can verify if the location and size of feeders are adequate, and carry out iterations of design modification and simulation until satisfactory results are obtained [10]. Hassan et al. (2012)[11] studied the effects of gating system parameters such as filling pattern, pressure, and speed, cooling rate, solidification on casting related defects with the help of MAGMASOFT and optimized the design to achieve a sound casting of an impeller. The similar studies were done by Sun and Su (2008)[12] in magnesium alloy base castings.

The present paper is focused on the design and optimization of the gating system for production of exhaust manifold by casting four number of castings simultaneously in one pouring. To achieve this MAGMASOFT is used and various designs of gating and risering are tried as iterations before reaching to the best one for a sound casting free from defects. SiMo Ductile iron is prepared by charge calculations, and a trial casting is prepared. The produced material is tested for various microstructural and mechanical properties to ascertain the correct chemical compositions, grain size, nodularity, nodule count, tensile properties, microstructure contents, and Brinell hardness number.

II. RESEARCH METHODOLOGY

The research methodology adopted is discussed in detail as below. The entire research is carried out in different stages: design of feeder and gating system, numerical simulation by using MAGMASOFT based on Finite Difference Method (FDM) which relies on discretizing the domain of interest (mould, cast part, feeders, gating channels, feed aids, etc.) into small elements, applying the boundary conditions corresponding to each material and interfaces between them, and solving the differential equations for heat transfer followed by determination of material properties in as-cast component by conducting microstructural analysis uniaxial tension test as per the standard ASTM E8M, and hardness test.

A. Preparation of the SiMo ductile iron

The SiMo cast iron is prepared by melting steel scrap of cold rolled closed Annealed (CRCA) sheets with high purity pig iron containing high percentage of carbon in an induction furnace. Ferro silicon and molybdenum are added separately on charge calculation basis depending on the recovery of silicon and molybdenum. Inoculation is carried out as per the set procedures using Traditional inoculants which are based on ferrosilicon or calcium silicide. The purpose of inoculation is to aid in providing enough nucleation sites for the carbon to precipitate as graphite rather than iron carbide (cementite, Fe_3C). This is done by preventing under-cooling to temperatures below the meta-stable eutectic temperatures where carbide (white) structures are formed. The iron solidification mechanism is prone to form chilled iron structures when the inoculation is inadequate, and there are several reasons why chilled structures are undesirable. Chilled structures interfere with machining, necessitate additional heat treating operations, result in non-conformance with specifications and, in general, increase the total cost of production. The tundish cover ladle method is suitable for better magnesium recovery and was used in the present work for the production of SiMo cast iron. The use of a refractory dividing wall to form an alloy pocket in the bottom of the ladle gives an improved Mg recovery. It is essential that the Fe-Si-Mg alloy is not exposed to the liquid iron until quite late in the filling procedure, so the filling hole is positioned to introduce liquid iron away from the alloy pocket in the ladle bottom. The final chemical composition determined by spectroscopy test is given in Table 1.

TABLE 1. Chemical composition of the SiMo cast iron in wt%

C	3.32
Si	3.37
Mn	0.553
Cr	0.02
Ni	0.003
Mo	0.65
Cu	0.014
P	0.043
S	0.0171
Nb	<0.004
Ti	<0.051

B. Microstructure and hardness analysis

The primary purpose of mounting sectioned specimens of SiMo cast iron was to have convenience in handling specimens of small size and thickness. A compression type semi-automatic mounting press was used to mount the specimens with the thermosetting resin (Bakelite) in a mold of 25mm in diameter. The mounting press was set at a temperature of 150°C and pressure of 290bar. A heating and cooling cycle of 5min was adopted to set the thermosetting resin completely.

Generally, for polishing, grinding should start with a grit size of silicon carbide (SiC) enough to establish an initially flat surface. Therefore, an abrasive grit size of 220 was course enough to be used on the specimen surfaces sectioned by a diamond abrasive wheel. The grade (grit size) of emery papers used in the fine grinding sequence were in the ascending order of fineness i.e. grit sizes of 220, 320, 420, 600, 800, 1000 and 1200. The mounted specimens were finely polished with alumina of different grades which is the final step in producing the mirror like finish. The microscopic examination of mirror polished unetched specimen will only reveal a few microstructural features such as nodularity of graphite structures, nodule count, inclusions, porosity or cracks or some physical imperfections. Therefore, etching is used to reveal the grain boundaries clearly in the specimen. So, the specimens were etched with 3% Nital solution (3% Nitric acid + 97% Ethyl alcohol). The microstructure, shown in Fig. 1, clearly reveals the graphite spheroids in the matrix of pearlite (10%) and ferrite (85%). The average grain size was measured as per standard ASTM E112 and the grain size number is 6.

The Brinell hardness test is conducted as per the ASTM E10 standard, and the method consists of indenting the test material with a 5 mm diameter ball subjected to a load of 750 kgf. The full load is applied for a dwell period of 15 seconds on the specimen. The diameter of the indentation left in the test material is measured using powered microscope with a least count of 0.01 mm and Brinell hardness number (BHN) is determined to be in range of 210-228.

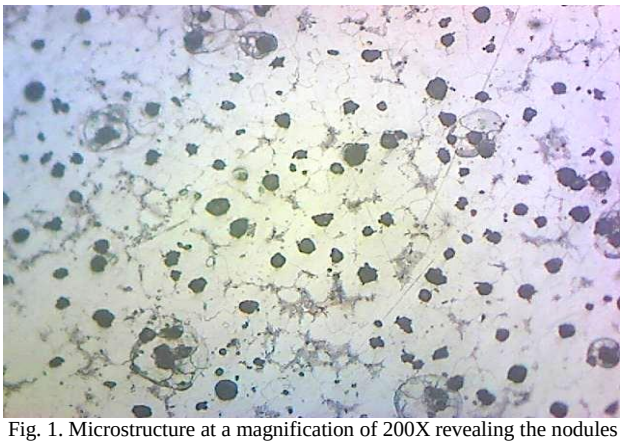

Fig. 1. Microstructure at a magnification of 200X revealing the nodules and grains

C.Tensile testing of samples

Tensile specimens were prepared as per ASTM A370 standard by machining and were tested on a 50kN UTM table top at a cross head speed of 2.5mm/min. One end of the specimen was held in the bottom grip which is stationery, and the other end was held in upper grip attached to the cross head mounted with a load cell of very high accuracy as shown in Fig. 2. A dedicated HORIZON software was used to acquire the load vs. elongation data. This data was further used to draw stress-strain plot, and the salient points were determined. The tensile tests were carried out thrice to capture the scatter in results.

Fig. 2. Tensile test in progress on a 50kN UTM

D. Numerical simulation using MAGMASOFT

A lot of information which is generated during casting simulation as discussed below is very useful for taking approximate corrective measures in the casting design, a lot of which would not be available when using conventional processes. To what extent this information can lead to a measurable improvement of casting design or process is depending on the level of integration of the simulation into development and manufacturing processes.

E. Modeling of gating and feeding system

First of all, a CAD model of exhaust manifold was created using SOLIDWORKS and then the model in STL format was imported to MAGMASOFT casting simulation software for designing of gating and feeding system. Once the part was imported, then mould cavity was made with parting line. The optimization of the feeding system was done in two iterations of simulations: 1. Designing with eight central risers and three side risers, 2. Designing with central runners and side risers. Design 1, resulted in an inadequate flow of molten metal into the cavity and thereby increasing the turbulence and hot spots in castings in the right side of the runner. Design 2 is a modification of the first one in which the flow is uniform in all the castings, and hence the hot spots are pushed to the risers to produce a sound casting.Thermo-physical properties i.e. density (varying from 7100 to 6850 kg/m^3 depending on temperature 100 to 1480°C), specific heat (in the range of 469 to 850J/kg-K), and thermal conductivity (32 to 14 W/m-K) of the SiMo cast metal as well as the mould material as a function of temperature were put in the software. Material model was designed based on the required composition of the melt. Boundary conditions, such as the metal-mould heat transfer coefficient, for normal mould were fixed based on the guidelines of the material model. The process parameters such as an initial temperature of the melt (1420°C), feeding effectiveness of 70%, pouring rate, time and sand mould temperature (40°C) were set to complete the simulations. The results of solidification simulation include colour-coded freezing contours at different instants of time starting from beginning to end of solidification. This provides a much better insight into the phenomenon compared to shop-floor trials.

III. Results and discussions

A. Microstructure and hardness

In SiMo cast iron, during magnesium treatment, the nodules of graphite nucleate on small inclusions of magnesium oxides and decides the nodule count. The growth of these nodules will take place by diffusion of C from the molten metal. Incidentally, after some time, these nodules ceases to grow further and gets surrounded by an austenite shell and further growth will occur by diffusion of carbon through the austenite shell. Since the diffusion of carbon is lower in austenite than in the liquid, the growth rate of the nodule decreases gradually. It is also observed that the growth rate for graphite nodules is lower now, therefore there will be a small number of nodules at the end of solidification. The nodularity is observed to be 79%, and the size of the nodule varies from 3µm to 5µm. Nodule count is found to be 287/mm^2. The micrograph shown in Fig. 1, clearly reveals the matrix of pearlite (10%) and ferrite (85%). The percentage of carbide is observed to be 5% max. Only. The average ASTM grain size number is 6. The hardness of the cast material varies from 210 to 228BHN.

B. Solidification Simulation

Simulation provides a magnitude of the result obtained for filling and solidification that allow designers, casting engineers and all people engaged in the casting process to make important decisions for improvements that need to be taken. Fig. 3 depicts the filling pattern of the moulds with design-1 of gating system. It is clearly observed that with this design the flow of material is intermittent and non-uniform leading to higher turbulence at various junctions. Turbulences in the melt should be reduced to avoid gas defects formed by entrapped air in the casting and flow velocities need to be consistent through ingates. Temperature distribution during solidification is shown Fig. 4. It is seen that some parts of the castings are with a low temperature of 1245°C which may lead to non-directional solidification in those parts leading to casting defects.

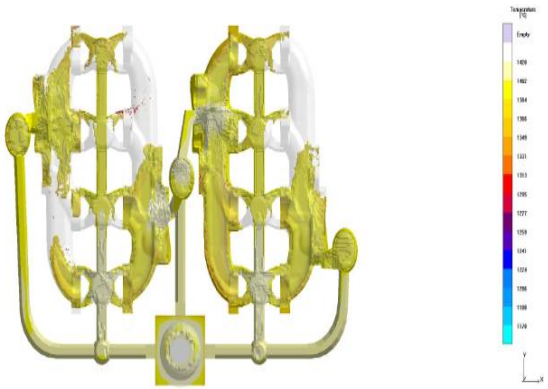

Fig. 3. Design-1 shows material flow in the sand moulds

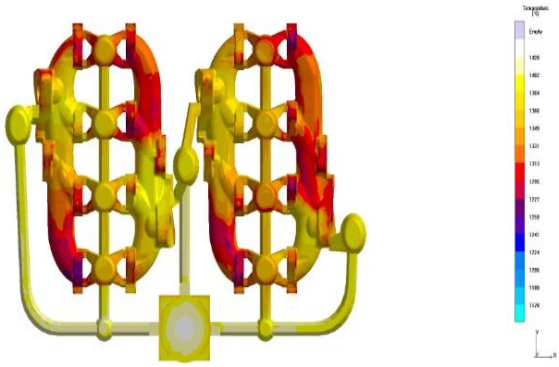

Fig. 4. Temperature distribution with design-1

The desired direction of the molten metal flow into the cavity is meeting in design-2 as shown in Fig. 5. There is less turbulence in the molten material, and the filling of the cavity is almost uniform. In this design, the temperature distribution also shows that the highest temperature remains in the feeding system leading to directional solidification as shown in Fig. 6. Solidification simulation as shown in Fig. 7 depicts that all the hot spots are restricted to the risers which is a clear indication of directional solidification to produce defect free sound castings. This design of gating system employs thirteen risers in total. The volume contraction of metal during the solidification leads to shrinkage cavities and dispersed porosity depending on the alloy and the wall thickness of the casting. Heavy sections of the casting usually form a stable metal skin, whereas thin walls and especially the in-gate start to freeze quickly. For this reason, feeding can only be used as a compensation of the shortfall in volume if the in-gates are thicker than the wall of the casting, where further feeding is necessary.

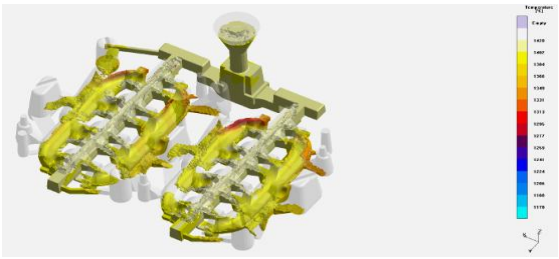

Fig. 5. Mould filling in design-2

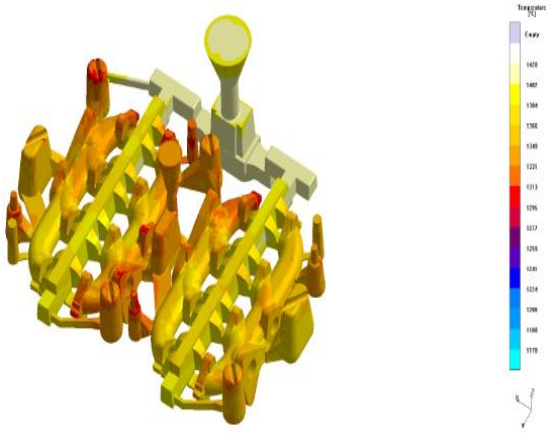

Fig. 6. Temperature distribution during solidification with design-2

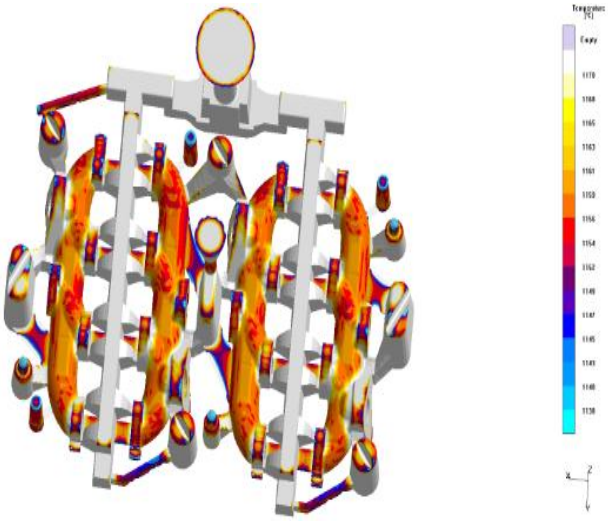

Fig. 7. Solidification Simulation with optimum design-2

To validate the simulation results, a trial casting is prepared in the sand mould with the guidelines following the gating system of design-2 as discussed above. Although the accuracy of these simulation results is limited to only 75%, the details of the simulation are very beneficial to produce a sound casting as shown in Fig. 8.

Fig. 8. A trial casting of exhaust manifold with runners and ingates

IV. Conclusions

The present paper discusses the design and optimization of the gating and rise ring system for an exhaust manifold by casting four number of castings simultaneously in one pouring using simulation software MAGMASOFT. The following conclusions are drawn on the basis of results:

1. The nodularity in the casting is observed to be 79% with nodule count of 287/mm^2 and the size of the nodule varies from 3µm to 5µm.
2. The percentage of carbide is observed to be 5% maximum. The average ASTM grain size number is 6, and the hardness of the cast material varies from 190 to 230BHN.
3. The microstructural analysis depicts 85% ferrite, 10% pearlite and less than 5% carbides in the matrix.
4. In the simulations, it is observed that with gating design-1, the flow of the metal is intermittent and non-uniform leading to higher turbulence at various junctions which may lead to non-directional solidification in those parts leading to casting defects. Hence, gating design-2 is better to produce sound castings.
5. A trial casting is prepared in the sand mould with the guidelines following the gating system of design-2. Although, the accuracy of these simulation results are limited to only 75%, the details of the simulation are very beneficial to produce a sound casting.

References

[1] Chaengkham, P. and P. Srichandr, Continuously cast ductile iron: Processing, structures, and properties. Journal of Materials Processing Technology, 2011. **211**(8): p. 1372-1378.
[2] Borsato, T., et al., Effect of in-mould inoculant composition on microstructure and fatigue behaviour of heavy section ductile iron castings. Procedia Structural Integrity, 2016. **2**: p. 3150-3157.
[3] Atzori, B., G. Meneghetti, and L. Susmel, Material fatigue properties for assessing mechanical components weakened by notches and defects. Fatigue & Fracture of Engineering Materials & Structures, 2005. **28**(1-2): p. 83-97.
[4] Beeley, P., 3 - Solidification 2 The feeding of castings, in Foundry Technology (Second Edition). 2001, Butterworth-Heinemann: Oxford. p. 100-VIII.
[5] Boettinger, W.J. and D.K. Banerjee, 7 - Solidification A2 - Laughlin, David E, in Physical Metallurgy (Fifth Edition), K. Hono, Editor. 2014, Elsevier: Oxford. p. 639-850.
[6] IRON, D., Ductile Iron Society. 2012.
[7] Labrecque, C. and M. Gagne, Ductile iron: fifty years of continuous development. Canadian Metallurgical Quarterly, 1998. **37**(5): p. 343-378.
[8] Nimbulkar, S.L. and R.S. Dalu, Design optimization of gating and feeding system through simulation technique for sand casting of wear plate. Perspectives in Science, 2016. **8**: p. 39-42.
[9] Dabade, U.A. and R.C. Bhedasgaonkar, Casting Defect Analysis using Design of Experiments (DoE) and Computer Aided Casting Simulation Technique. Procedia CIRP, 2013. **7**: p. 616-621.
[10] Ravi, B. and D. Joshi, Feedability analysis and optimisation driven by casting simulation. Indian Foundry Journal, 2007. **53**(6): p. 71-78.
[11] Iqbal, H., et al., Mold design optimization for sand casting of complex geometries using advance simulation tools. Materials and Manufacturing Processes, 2012. **27**(7): p. 775-785.
[12] Sun, Z., H. Hu, and X. Chen, Numerical optimization of gating system parameters for a magnesium alloy casting with multiple performance characteristics. Journal of Materials Processing Technology, 2008. **199**(1): p. 256-264.

Asian Journal of Convergence in Technology *Volume III, Issue III*
ISSN No.:2350-1146, I.F-2.71

Direction of Arrival estimation of underwater acoustic signal via Virtual Steering

Vikas Kumar Singh
Department of Electrical Engineering
Delhi Technological University
Delhi, India
kumarvikas15995@gmail.com

Rashmi
Department of Computer Engineering
Krishna Engineering College
Ghaziabad (UP), India
rashmicp2009@gmail.com

***Abstract*—For a long time direction of arrival estimation to localize the direction of a radiating or reflecting source has been carried out using SONAR technique or using scuba divers which does not give precise location in short time . So development of hydrophone was carried out and there various combinations were used to find the direction of arrival of radiating signal. In the same respect this paper discusses the method of direction of arrival estimation for underwater acoustic signal for various combinations of hydrophones i.e., triplet, linear array, triplet array via virtual steering of directivity pattern of mentioned combinations and GUI.**

Keywords —cardioid; direction of arrival; hydrophones; triplet array.

I. INTRODUCTION

In earlier times in underwater system for detection of enemy submarines and torpedo scuba divers were used who reported by different kind of signal such as flares. This system was not very reliable and thus resulting in loss of human resources as well as cost of ships and submarines. As a result for a very long time now study of underwater acoustic phenomena and their application for surveillance and detection and many more have been carried out. A hydrophone is a microphone designed to be used underwater for recording or listening to underwater sound. Most hydrophones are based on a piezoelectric transducer that generates electricity when subjected to a pressure change. Such piezoelectric materials, or transducers, can convert a sound signal into an electrical signal since sound is a pressure wave.

Hydrophones are the principle measurement device to probe acoustic signature underwater. Simplest type of hydrophones is omnidirectional hydrophone which is used to detect presence of acoustic signals but its directivity pattern is '0' so it can not differentiate between signals coming from any direction. Transducers operating in the receive mode - hydrophones - are assembled arrays to improve the response of the array in a desired direction, thereby increasing the signal-to-noise ratio and indicating the direction of a signal source [1].

Hence a combination of omnidirectional hydrophones is used for detection of position of acoustic source i.e. Direction of Arrival this paper discusses about method of virtual steering for various combinations of hydrophones such as triplet, linear array, triplet array. Due to the uniform distribution of sensors, relatively simple signal processing algorithms have been developed for tasks such as direction of arrival (DOA) estimation and beamforming.[2] The virtual steering discussed has been developed using these beamforming equations which gives an edge as it approximates the direction in relatively less time and no human resource is put in danger.

II. HYDROPHONE COMBINATIONS

A. Triplet Hydrophone

Triplet hydrophones are formed by placing three omnidirectional hydrophones on the edge of an equilateral triangle. Fig.1 [3] represents position of elements in triplet hydrophone. Here inter elemental spacing is given by 'a' such that it satisfies following condition $ka \leq \pi/2$ where k represents the wave number of minimum frequency at which the triplet is to be operated[4]. Directivity pattern of triplet hydrophones is cardioids shaped which gives it a view of 120°.But for better detection of source we need more precision which can be bought by using more no of hydrophones.

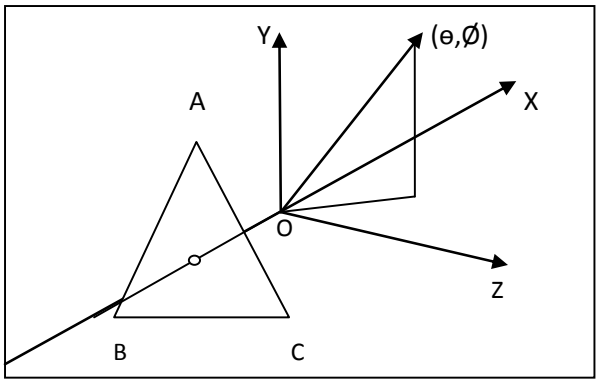

Fig.1 Position of element in triplet hydrophone

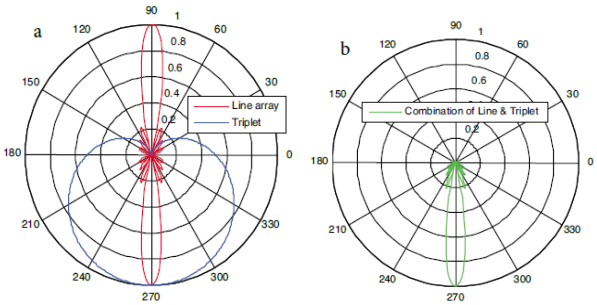

Fig.2 (a) line array and triplet directivity pattern overlap
(b) Triplet array directivity pattern

B. *Linear Array*

This is one of the most important types of combination as it helps in developing more combinations for better estimation. Linear arrays are formed by placing hydrophones in a straight line at a separation of λ/2 where λ represents the wavelength of min frequency at which the array is to be operated [1]. The directivity pattern of linear array combination is clover leaf shape. The angular resolution of leaf represents with increasing no of elements in the array. The maximum length of array is given by $d = 51\ \lambda/\theta$ (meters) where θ represents desired angular resolution [5]. But linear array suffers from port-starboard ambiguity which needs to be resolved for best estimation results.

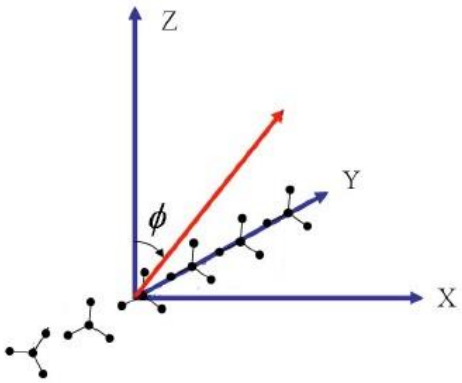

Fig.3 Positon of elements in a triplet array

C. *Triplet Array*

An alternative is to replace each omnidirectional hydrophone in the array with a set of three omnidirectional hydrophones (i.e., triplets) to form a cardioid response pattern for each triplet element [3]. Fig.2 [5] shows the difference of directivity pattern of all three combinations. In triplet array multiple triplets are aligned together on a common axis see Fig.3 [6] in such way that each element of triplet is spaced by λ/4 and inter triplet spacing is λ/2. As a result the directivity pattern obtained from triplet array consists of single lobe whose precision can be increased by adding more triplets to the array. The ambiguity of port starboard of linear array is solved in this array as there is only one lobe present in this also its angular resolution is better than that of triplet array.

III. Directivity Pattern for Hydrophones

Directivity pattern is obtained by beamforming of the given combination which are discussed in equations (i)-(iii) where Ø is the steering angle, *f* is operating frequency, *c* is speed of sound in water, α is assigned weight to all elements, *r* is inter elemental spacing.

$$R_c(\emptyset, f) = \sum_{k=1}^{3} a_c^{kj} \exp\left(\frac{\iota\pi}{c} fi(y_{kj} sin\emptyset - cr_c^{kj})\right) \quad \ldots (i)$$

Eq.(i) represents the beam forming relation for triplet hydrophone which is a function of minimum operating frequency and steering angle (ϕ). [3] The cardioid pattern (Fig.4(a)) is obtained by plotting Real(R) with respect to ϕ.

$$r(\emptyset, f) = R_c(f, \emptyset) \sum_{j=1}^{N} \exp\left(\frac{-\iota\pi i f}{c}(x_j cos\emptyset - cr \quad \ldots (ii)$$

Eq.(ii) represents the beam forming of equation of linear array which is also a function of minimum operating frequency and steering angle (ϕ).[3] Clover leaf pattern (Fig.4(b)) is obtained by plotting Real(r) with respect to ϕ.

$$r(\emptyset, f) = \sum_{j=1}^{n} \exp\left(\frac{-2\pi i f}{c}(x_j cos\emptyset - cr^j)\right) \sum_{k=1}^{3} a_c^{kj} \exp\left(\frac{2\pi}{c} fi(y_{kj} sin\emptyset - cr_c^{kj})\right)$$

… (iii)

The plot of single lobe(Fig.4(c)) is obtained by plotting Real(r) from eq.(iii) with respect to ϕ. This represents the directivity pattern of triplet array.

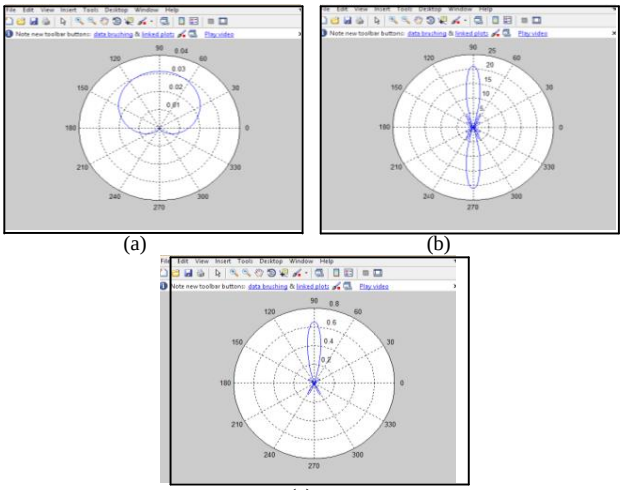

(a) (b) (c)

Fig.4 Directivity pattern plots using eq.(1-3) for (a) Triplet (b) Line array (c) Triplet array

IV. VIRTUAL STEERING

The directivity patterns obtained in Fig.4 are used for the purpose of virtual steering. The area around the hydrophone is divided into no. of hydrophones in such a way that only one of the hydrophone will receive signal first if the source is placed in that region. Now the time difference is calculated with respect to each of the hydrophones for all the other elements. Each region around hydrophone is represented by a directivity pattern formed using centrals algorithm on MATLAB [7].

Directivity pattern obtained for Line array is steered (Fig.5) via a GUI and each position represents real areas around the hydrophone. As it can seen that for 0° and 180° there is only a single lobe present (Fig.5(a),Fig.5(g)) as compared to other angle as at these positions ambiguity is not present as time difference increases from first hydrophone to last and only one position is possible for that case. But in rest of the cases port starboard ambiguity resides.

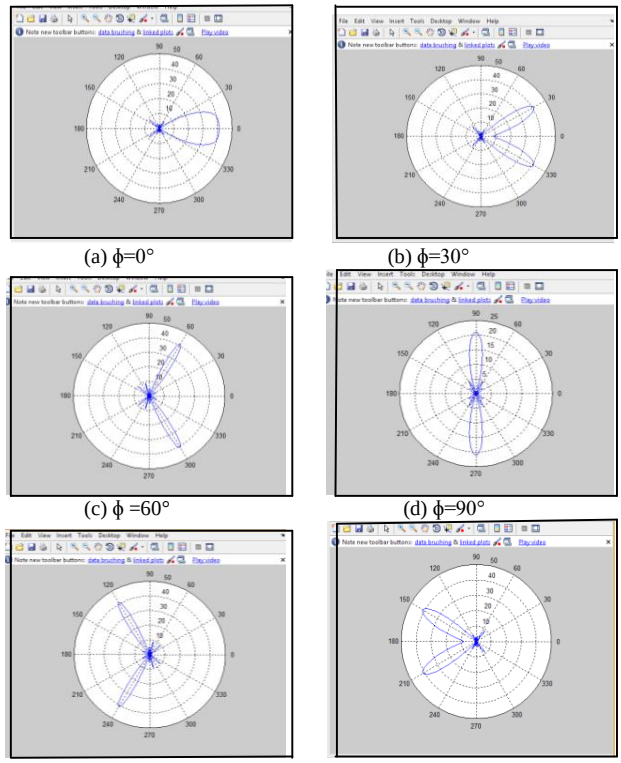

(a) ϕ=0° (b) ϕ=30° (c) ϕ =60° (d) ϕ=90°

(e) ϕ=120° (f) ϕ=150°

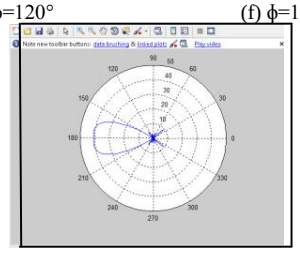

(g) ϕ=180°

Fig.5 Virtual steering of line array from 0°to180°

To remove the port starboard ambiguity triplet hydrophnoes are used whose directivity plot steering is represented in Fig.6. It is clearly visible that at steering position 0° and 180° the plot of line array and triplet array are similar. And at other positions one of the lobes of clover leaf has been removed in case of triplet array thus removing the ambiguity.

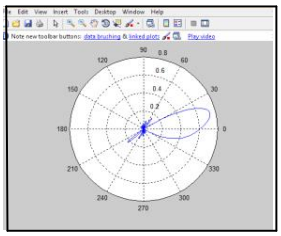

(a) ϕ=0°

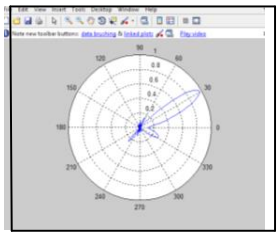

(b) ϕ=30°

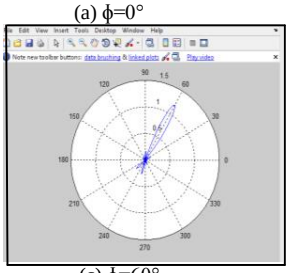

(c) ϕ=60°

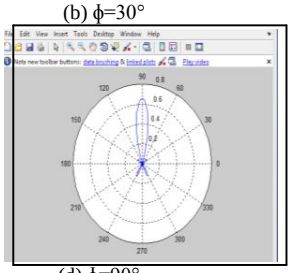

(d) ϕ=90°

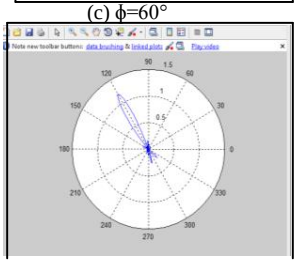

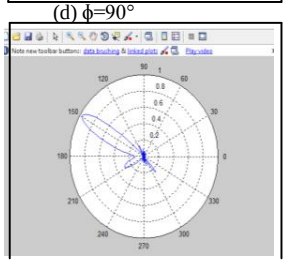

(e) ϕ=120° (f) ϕ=150°

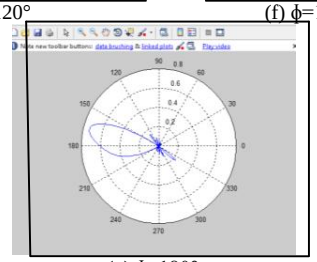

(g) ϕ=180°

Fig.6 Virtual steering of triplet array from 0°to 180°

V. CONCLUSION

This paper has made a simulation result for estimation of direction of arrival using virtual steering. The plot of directivity pattern is steered with respect to angle where each angle represents specified area in 3D world around hydrophone combination. The observation of pattern is closely observed for every angle and result is deduced. Also the comparative result of linear array and triplet array can also be seen from the observation. The results show that linear array suffers from port starboard ambiguity which has been solved using triplet array. Also the precision can be increased by adding no of elements in the array. This method of direction of estimation an be useful for enemy submarine detection and torpedo detection underwater and can help take important counter measures and thus saving valuable human resources.

ACKNOWLEDGEMENT

A part of this research has been carried out in SSPL (DRDO). I would like to thank administration of SSPL lab for allowing me to work in there Lab, Dr. D.K. Bhattacharya and Mr. Devendra Verma for helping me in carry out this work.

REFERENCES

[1] A. D. Waite, SONAR for Practising Engineers. Wiley, UK, 2002
[2] H. Krim and M. Viberg,"Two decades of array signal processing research", IEEE Sign. Proc. Mag., 67-94 July (1996).
[3] D. T. Hughes. Aspects of Cardioid Processing, SACLANTCEN Report SR-329, May (2000).
[4] M. van Velzen, G. Haralabus, A. Baldacci, "Calibration of Cardioid Beamforming Algorithms", NURC SR-435, 2005.
[5] Alessandro Barbagelata, Piero Guerrini, Luigi Troiano, "Thirty years of Towed Array at NURC" Oceanography Vol.21, No.2

[6] M. van Velzen, G. Haralabus, A. Baldacci, "Unambiguous triplet array beamforming and calibration algorithms to facilitate an environmentally adaptive active sonar concept", NURC SR-435, 2005.
[7] https://in.mathworks.com/help/phased/beamforming

Dynamic Motion Planning for Aerial Surveillance on a Fixed-Wing UAV

Vaibhav Darbari Saksham Gupta Om Prakash Verma

Department of Computer Science and Engineering
Delhi Technological University
Rohini, Delhi 110042, India
vaibhavdarbari@gmail.com, sakshamgupta_2k14@dtu.ac.in, opverma@dce.ac.in

arXiv:1705.08010v1 [cs.RO] 22 May 2017

***Abstract*— We present an efficient path planning algorithm for an Unmanned Aerial Vehicle surveying a cluttered urban landscape. A special emphasis is on maximizing area surveyed while adhering to constraints of the UAV and partially known and updating environment. A Voronoi bias is introduced in the probabilistic roadmap building phase to identify certain critical milestones for maximal surveillance of the search space. A kinematically feasible but coarse tour connecting these milestones is generated by the global path planner. A local path planner then generates smooth motion primitives between consecutive nodes of the global path based on UAV as a Dubins vehicle and taking into account any impending obstacles. A Markov Decision Process (MDP) models the control policy for the UAV and determines the optimal action to be undertaken for evading the obstacles in the vicinity with minimal deviation from current path. The efficacy of the proposed algorithm is evaluated in an updating simulation environment with dynamic and static obstacles.**

I. INTRODUCTION

In the last decade, Unmanned Aerial Vehicles (UAVs) have gained importance in a myriad of military and civilian applications. They are especially useful in missions pertaining to surveillance, rescue and exploration. In these tasks UAVs are often required to operate in unfavourable conditions where a complete description of operating environment may not be available.A fully autonomous UAV eliminate the need to plan the mission beforehand in an unknown , unpredictable environment, it is capable of handling any new situation which is thrown upon it spontaneously. Consider the following scenario:An urban setting where a UAV is released in an unknown airspace for the purpose of surveillance. The aim of the UAV is to maximize mapped area with constraints such as minimum turning radius and avoiding collision with other planes/UAVs operating in vicinity, buildings , other dynamic and unknown obstacles.In such a challenging scenario fully autonomous path planning plays a vital role in ensuring success of the mission specially for fixed-wing UAVs which lack hovering capability and hence need to maintain a minimum airspeed to maintain lift.

Several techniques have been proposed for 3D path planning like Rapidly-exploring Random Graph[1],Visibility Graphs[2],PRM[3],RRT*[4],Artificial Potential Field. All these techniques though effective,are computationally expensive and need to be recomputed as soon as the environment is changed.The above mentioned techniques suffer the curse of dimensionality and a combinatorial explosion takes place with increase in search space.

This paper proposes a 3D Dynamic path planning approach which overcome the aforementioned limitations and facilitates conduction of fully autonomous missions. The rest of the paper is organized as follows In Section II:Scenario describing the environment,obstacles and coordinate space is presented.Section III comprises of proposed approach giving details of global and local path generation along with the decision process for optimal control policy generation.The simulation results and analysis for the proposed approach are presented in Section IV.We conclude with final remarks and discuss future works in Section V.

II. SCENARIO

A fixed-wing autonomous UAV is to conduct surveillance of a pre-specified area(Search Space) within a given Geofence.Considering the given scenario, the aim of our approach is to:

- Maximize the area surveyed in minimum flight time.
- Avoid collision with any obstacle, be it stationary or dynamic.

The UAV has a constraint on its turning radius , climb-rate and minimum airspeed.The path planning problem is finding the optimal path in the search space given the constraints on UAV and environment.

A. Environment

We assume that the UAV is GPS enabled and carries some specialized sensors capable of accurately detecting the location of the obstacles. The search space is assumed to be partially known for the PRM and the approach is designed keeping in mind that any kind of obstacle can turn up at any coordinates on any given time.

1) Static Obstacles: Static or Stationary obstacles are assumed to be a solid cylinder. The coordinates of the centre of the cylinders along with its radius and height is updated whenever there is a change in the environment.

2) Dynamic Obstacles: Dynamic or Moving obstacles are assumed to be solid spheres. Similar to static obstacles the coordinates of sphere's centre, radius and velocity are synced with the changes in the environment.The trajectory of the dynamic obstacles are randomly selected from a pool of

precomputed paths so as to mimic real life aerial vehicles that may operate in the vicinity of the UAV.

B. Coordinates Transformation

1) WGS 84 to ECEF coordinates: Most navigation systems are based on World Geodetic System including GPS. WGS is modelled after the standard coordinate system for Earth, a standard ellipsoid reference surface for raw altitude data, and a gravitational equipotential surface that defines the nominal sea level. We need to convert to a Local Tangent Plane Coordinate System for the ease of mathematical computation so as to make the problem retractable. The order of approximation involved in the conversion is of the magnitude of 10^{-9} for the small distances involved for the scenario of our paper. Geodetic coordinates(latitude λ, longitude φ, height h) can be converted to ECEF coordinates using the equations:

$$X = (N(\lambda) + h)cos\lambda cos\varphi \tag{1}$$

$$Y = (N(\lambda) + h)cos\lambda sin\varphi \tag{2}$$

$$Z = (N(\lambda)(1 - e^2) + h)sin\lambda \tag{3}$$

where

$$N(\lambda) = \frac{a}{\sqrt{1 - e^2 sin^2\lambda}} \tag{4}$$

here a and e are semi-major axis and the first numerical eccentricity of the ellipsoid respectively. The values of which can be found in the definition of WGS 84[5].

2) ECEF to WGS 84: We need to transform the ECEF coordinates back to geodetic coordinate system so as to facilitate the waypoint planning on the on-board autopilot system.

$$\lambda = \arctan\frac{Y}{X} \tag{5}$$

$$\varphi = \arctan\frac{Z + e'^2 b sin^3\omega}{p - e^2 a cos^3\omega} \tag{6}$$

$$h = \frac{p}{cos\varphi} - N \tag{7}$$

where auxiliary values are:

$$p = \sqrt{X^2 + Y^2} \tag{8}$$

$$\omega = \arctan\frac{Za}{pb} \tag{9}$$

III. Proposed Approach

A. Overview

Two phase motion[6] planning is a widely adopted strategy for reducing the planning complexities of high-order dynamic systems[7][8]. At the first stage, a coarse but feasible path is generated taking into consideration the kinematics of the system and the known static elements of the environment. System design constraints and dynamic elements in the environment may be ignored in this phase. The primary objective of this phase is to confine the search space to the vicinity of the generated path and thus reduce the complexity of the planning task. At the second stage, a smoother more finely attuned path is generated in response to changes in the environment and dynamics of the system. The two stages compensate each other in terms of planning complexity, risk associated with the path and type of obstacles handled. Two phase planning combines the merits of both the methods and facilitates real-time operation in a cluttered environment.

The major components of our system along with the flow of control are represented in system architecture shown in the Fig.1. Global planner works in a 3D occupancy grid with boundaries demarcated by the geofence. The global planner takes starting location, geofence and known static elements of environment as input and generates a tour of search space with objective of maximizing area coverage while minimizing collision risk. The output of the global planner is a sequence of waypoints representing the tour. Certain waypoints in the search space are marked as milestones to avoid being trapped in local minima by virtue of heuristic search algorithm and to ensure maximum area coverage (details in later sections).Local planner works alongside the global planner and caters to moving obstacles and unforeseen stationary obstacles. Local planner checks for potential collision on the current path and assesses the risk associated with it. In case current path is deemed risky, the path is modified with a sequence of dynamic waypoints to avert the danger. The trajectory of the modified path is based on smooth Dubin curves to ensure a dynamically feasible and steerable path. A decision process determines the type of path adjustment to be undertaken by the global or local planner and accordingly waypoints maybe modified. If both original and modified paths are deemed risky, the current milestone is marked unsafe and local planner computes a route to the nearest unvisited safe milestone. In absence of such a milestone UAV is guided to last known safe milestone. When each milestone has been visited the UAV returns to the starting location and lands. A detailed explanation for each of the phases follows in the subsequent sections.

B. Global Planner

As mentioned earlier, the objective of global planner is to compute a kinematically feasible tour of the search space which maximizes area covered and minimizes collision risk. Initially, a discretised 3D occupancy grid is computed from the search space with each cell value indicating the risk associated with it. The grid is then sampled randomly for safe cells. A probabilistic road map (PRM) is built using the computed samples. The samples are clustered into safe regions and the centroid of every safe region is considered a milestone. Starting from the initial location, a greedy approach is used to form a tour going through all the milestones. The optimal path between individual milestones is determined by A* algorithm. The path so formed is bound to be kinematically viable as for each node in the path, only successors following the constraints are considered for path expansion.

1) Building Occupancy Grid: The search space within the confines of the geofence is represented as a discretised

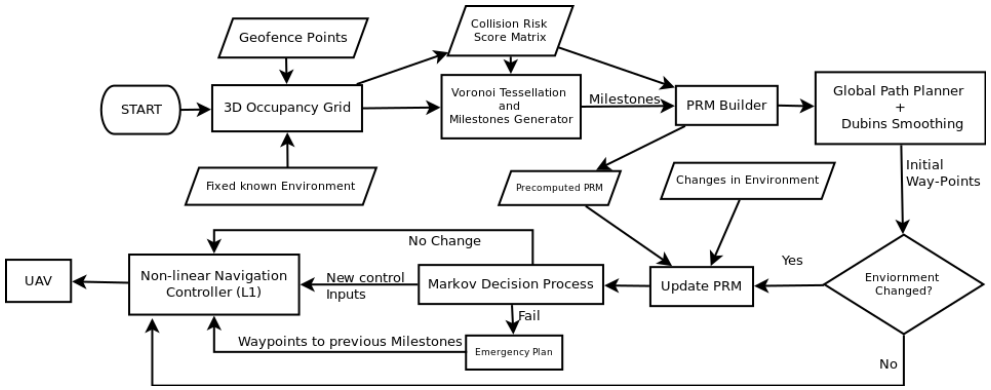

Fig. 1: Overview of the proposed architecture

3D grid. Each cell of the grid is associated with a collision risk involved with the cell. A global occupancy score for a cell is determined from the obstacle field distribution in the search space. Both static and dynamic obstacles contribute to this obstacle field. The global occupancy score for a cell is expressed as

$$S_{Global}^{(x,y,z)} = \begin{cases} 1, \textit{if the cell space overlaps with any obstacle} \\ \frac{\sum_{i=1}^{k} \frac{1}{D_i^{(x,y,z)} - R_i}}{k}, \textit{if cell lies outside obstacle} \end{cases} \tag{10}$$

where k is the count of known obstacles, $D_i^{(x,y,z)}$is the Euclidian distance of the cell centred at (x,y,z) from the i_{th} obstacle and R_i is the radius of the i_{th} obstacle. This score provides an accurate estimation to the proximity of the obstacle but leads to a coarse distribution of values in the occupancy grid around the obstacles. Thus a local score is also considered alongside the global score to facilitate a evener distribution of values in the grid.

$$S_{Local}^{(x,y,z)} = \sum_{i=x-1}^{x+1} \sum_{j=y-1}^{y+1} \sum_{k=z-1}^{z+1} S_{Global}^{(i,j,k)} \tag{11}$$

The local score, denoted as $S_{Local}^{(x,y,z)}$ for a cell centred at (x,y,z), is given as the mean of values of all the adjacent cells in the grid.The collision risk for the cell is taken as the maximum of its local and global occupancy score.

$$C_{Risk} = Max(S_{Global}^{(x,y,z)}, S_{Local}^{(x,y,z)}) \tag{12}$$

2) Voronoi Tessellation of search space: To ensure maximum coverage of search space for surveillance, it is necessary to ensure that the path planning algorithm does not remain confined to any one region as a result of being trapped in local minima which have been a problem with many planners including potential field-based methods. Thus there exists a need for division of target space (free space) into disjoint sub regions which must each be covered to facilitate maximum coverage.Voronoi tessellation of search space can provide the required partitions given the seed points. For a typical UAV mission, the number of seed points

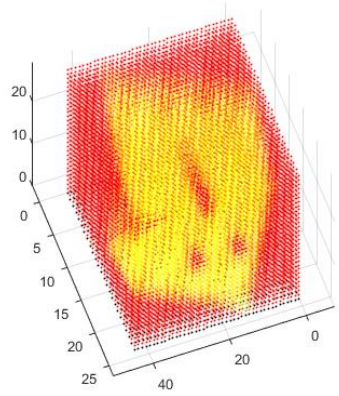

Fig. 2: Occupancy Grid for three obstacles inside geofence.The area inside,around the obstacle and in the vicinity of geofence receive a high C_{Risk} according to scoring policy and is thus shown in red in the figure.Safer area are marked with shades of yellow.

can be estimated to be roughly equal to the number of identified critical tasks. For a discretized configuration space as considered, voronoi tessellation can be achieved by means of K-Medoids Clustering[8] with K being set to the number of milestones.The objective function minimized during the iterations is given in Eq.13.

$$J = \sum_{j=1}^{K} \sum_{i \epsilon C^j} d(x^{(i)}, z^{(j)}) \tag{13}$$

where K is the number of milestones,$z^{(j)}$ is medoid of the j^{th} cluster, x is a sample data point and C^j is the j^{th} cluster.

Only a randomly chosen subset of safe points in target space are considered for clustering due to the high runtime complexity associated with the procedure.A sample cell is considered safe if the associated collision risk score is less than the collision risk threshold $'\delta'$.An adequate number of sample points are chosen to be a good indication of the overall distribution of large target spaces within the search space.

For a given scenario a good heuristic for estimating the number of milestones can be taken as

$$K = \frac{\Delta_{geofence}}{\pi h_{UAV}^2 \tan^2 \frac{\theta_{fov}}{2}} \tag{14}$$

where $\Delta_{geofence}$ is the area of geofence, h_{UAV} is the anticipated cruise altitude for the UAV for in the mission and θ_{fov} is the field of view of the onboard camera.

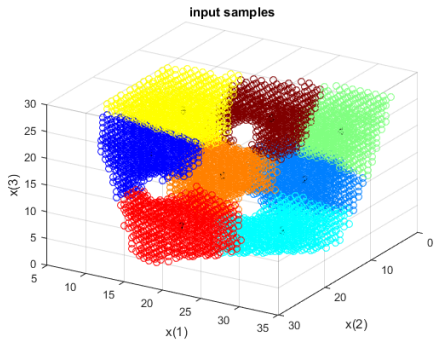

Fig. 3: Voronoi Tessellation for randomly chosen safe samples for the three obstacle scenario.The centroids of each region i.e. centers of the clusters are taken as milestones.In this illustration $K = 8$.

3) Building Probabilistic Road Map: The subset of points chosen from target space are taken as vertices for the Probabilistic Road Map construction. K-Nearest Neighbours (KNN)[10] algorithm is used for determining the vertices adjacent to a given vertex and Euclidian distance is chosen as the comparison metric. The value of K has to be high enough to maximise the probability of having at least one kinematically feasible path when the graph is traversed in real-time but at the same time it is required to keep the value of K as moderate as possible to curtail the runtime complexity. We found that in a typical urban city scenario the value of K varies between 40 and 120 for optimal results.

The initial order in which milestone way points are visited is determined from the nearest neighbour algorithm (greedy algorithm) which lets the UAV choose the nearest unvisited milestone as its next milestone.This technique has been chosen for approximating the shortest tour as it gives a path 25% longer than the optimal path on average. Also, Tassiulas[11] has shown that a tight upper bound of $\frac{d\sqrt{d}}{d-1} * N^{\frac{d-1}{d}} + o(N^{\frac{d-1}{d}})$ exists for the nearest neighbour tour. Here N is the number of cities and d is the optimal path distance for the Euclidian travelling salesman problem wherein the triangle inequality holds.

4) Kinematically feasible Path : Kinematic constraints of minimum turning radius $R_{h,min}$ and maximum climb rate p_{max} for the UAV in current state $(x, y, z, \omega, \varphi, \theta)$ are enforced during generation of motion primitives when the PRM is traversed using A* algorithm. At any given node, only those adjacent nodes are considered for shortest path which satisfies the kinematic constraints with respect to the current state of the UAV. This modification not only reduces the complexity of the graph but also leads to a smoother path for traversing.

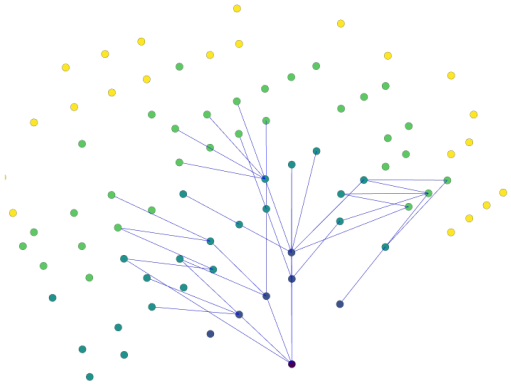

(a) Node Expansion from source node up to depth 3

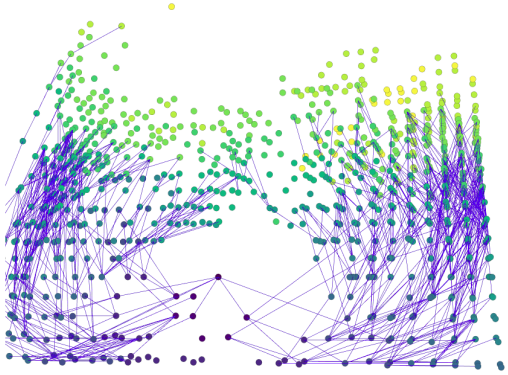

(b) Node Expansion from source node up to depth 10

Fig. 4: PRM Node Expansion

Thus the node expansion from the current node depends not only on its distance from the current node and occupancy grid value but also on its spatial orientation from it.The heuristic chosen for selection of next best node from the list of adjacent nodes is given by

$$h^{(x,y,z)} = C_{Risk}^{(x,y,z)} + p_{revisitation}^{(x,y,z)} \tag{15}$$

$$p^{(x,y,z)} = Ke^{(V_{count}-1)} \tag{16}$$

$$d^{(x,y,z)} = \left((x_{curr} - x)^2 + (y_{curr} - y)^2 + (z_{curr} - z)^2\right)^{1/2} \tag{17}$$

$$f^{(x,y,z)} = h^{(x,y,z)} + d^{(x,y,z)} \tag{18}$$

where d is the Euclidian path cost,V_{count} is the number of times the node has already been explored, f is evaluation function for node expansion and $K = 1000$ for imposing a high penality on revisitation. Revisitation penalty is imposed on an already visited node to ensure that preference is given to new unsearched areas rather than remaining confined to local minima and lose gatherable intelligence.

5) Pseudocode: Algorithm 1 gives the pseudo code of the approach described in previous sections:

In lines 1-2 we discretize the search space based on resolution distance along all the three axes.In lines 4-12

Algorithm 1: Global Path Generation

Input : Geofence, Initial location and nature of Obstacles, UAV parameters,Source Point
Output: Gloabal Path waypoints

1 $resolution_distance \leftarrow 2 * turning_radius$;
2 $space_matrix \leftarrow$*get_range*$(resolution_distance)$;
3 ***Convert*** *Geodatic coordinates to ECEF*;
4 **foreach** *point in space_matrix* **do**
5 **if** *point is outside geofence or point is inside obstacle* **then**
6 $point.score \leftarrow 1$;
7 **else**
8 $global_score(obstacle_list, point)$;
9 $local_score(space_matrix, point)$;
10 $point.score \leftarrow max(global_score, local_score)$;
11 **end**
12 **end**
13 sample_list$\leftarrow$ Randomly Sample minimum required points $\forall$ points whose score $< \delta$;
14 $milestones \leftarrow K - Medoids(sample_list, iterations)$;
15 $SetOrder(milestones, source_point)$;
16 initialize PRM;
17 **foreach** *point in sample_list* **do**
18 inititalize node;
19 Add node to PRM;
20 **end**
21 **foreach** *node in PRM* **do**
22 $neighbour_list \leftarrow Nearest_Neighbour(node, K)$;
23 **foreach** *node in neighbour_list* **do**
24 **if** *Collision_Free(Extend(node,neighbour_list))* **then**
25 $node.neighbour_list \leftarrow node$;
26 **end**
27 **end**
28 **end**
29 initialize Global Path;
30 **foreach** *node in milestone* **do**
31 $path \leftarrow A^*(node, node \rightarrow next)$;
32 $global_path.append(path)$;
33 **end**

collision risk score is computed for all the cells in the discretized grid.In line 13 random samples are acquired for which the collision risk score is less then the collision risk threshold(δ).In line 14 acquired samples are clustered and centroids of each cluster are set as milestones.In line 15, starting from the source point we rearrange the milestones according to the euclidean distance in a greedy manner such that nearest milestone to source point is taken first then the milestone nearest to the previous milestone which has not already been visited comes next till all milestones have been connected.In lines 16-28 PRM is built as described in Section III-B.3.In lines 29-33 the path segments between the consecutive milestones are computed using A^* with heuristic given in Eq. 15.Individual path segments are appended in order to obtain the final global path.

The computational complexities involved with each of the phases in the global planner are given as follows:

- Initial occupancy grid initialisation and collision risk score assignment collectively have a time complexity of order of $O(KN^3)$.
- Voronoi tessellation of discretized search space on the randomly sampled safe points has an associated time complexity of order of $O(mnt)$.
- Probabilistic Roadmap building phase by means of K-Medoid Clustering with max heap optimisation runs in $O(n^2 logk)$. This phase along with A^* run on chosen heuristic are the dominating factors during the execution of the algorithm.

Here, K = number of obstacles, N=discrete division along one dimmension of search space, m= number of milestones/clusters, n= count of sampled safe points, t= number of iterations, k = count of nearest neighbours.

C. Local Planner

The path generated in the grid planning phase though feasible has its limitations. Continuously updating the global path by querying the grid planner in response to changes in the environment is a computationally expensive process and also the path generated by the global planner is jagged. To remedy these limitations and provide a higher resolution of control in motion planning a local planner is built atop the global planner. The motion primitives generated between two configurations represented by successive nodes of the global path ensure that vehicle dynamics strictly adhere.
The local planner proposed generates motion primitives based on shortest Dubins path between the two configurations. The trajectory between these configurations is decomposed onto two orthogonal planes and for each of these 2D Dubins curves are calculated taking into account any obstacles that maybe present in between these configurations.

1) Dubins Motion Primitives: A node in the global path is defined as follows

$$node = \{x, y, z, \psi, v, C_{risk}\} \tag{19}$$

where the first four components (x, y, z, ψ) describe the location and desired heading vector, v represents the target airspeed and C_{risk} is the collision risk score associated with the given node. Given any two consecutive nodes in the global path i.e. (x_1, y_1, z_1, ψ_1) and (x_2, y_2, z_2, ψ_2) the connecting path is constrained by minimum turning radius, initial and final bearings. The 3D path connecting the two nodes can be decomposed into two orthogonal planes as shown in Fig.5.

Bearing and minimum turning radius constrains UAV's movement in the horizontal plane while max climb rate and direction of climb(ascent/descent) affect UAV's propagation in the vertical plane. 2D Dubins[12] curve is created for each of these orthogonal planes. Depending on the distance of separation between the two nodes, either one of CSC

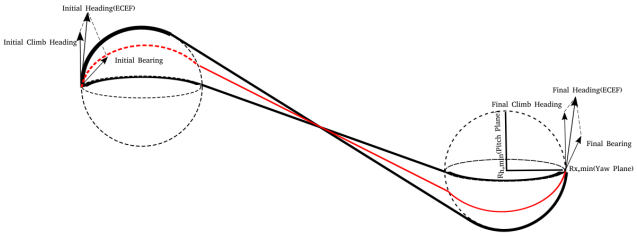

Fig. 5: 3D Dubins Path

or CCC trajectories[Fig.6] is chosen for the shortest path. The benefit of choosing Dubins curves to join the nodes is twofold as the initial and final headings are automatically aligned and it renders the shortest path given the radius curvature constraints.

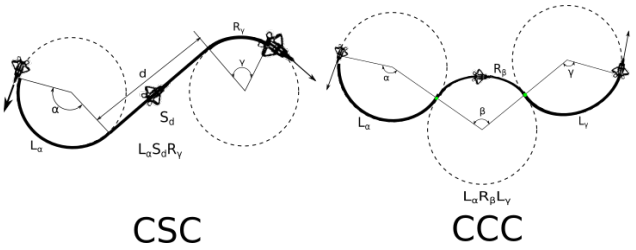

Fig. 6: 2D Dubins Path

2) Obstacle Path Adjustment: If an obstacle lies on the connecting path between the two consecutive nodes, then the Dubins path is modified to steer the UAV clear of obstruction with minimum deviation from the determined path. Depending on nature (static/dynamic) and radius of obstacle different path modification strategies are adopted. If the radius of the obstacle is less than the minimum turning radius of UAV, then its radius is taken to be equal to R_{min} for computation of viable curves in resultant Dubins path.

a) Static Obstacle: For a static obstacle multiple paths exist that can be generated for safe propagation of UAV, to ensure minimum deviation, path passing through tangentially closest point on the periphery of the obstacle is chosen, given that the change in steering angle for such a point is feasible.Assume that the UAV is initially at x_i, y_i, z_i and going towards next node at x_f, y_f, z_f,then the initial bearing and heading of the UAV is given as $\psi_{initial}$ and $\theta_{initial}$ where

$$\psi_{iniital} = \frac{\pi}{2} - \tan^{-1}(\frac{y_f - y_i}{x_f - x_i}) \tag{20}$$

$$\theta_{init} = \tan^{-1}(\frac{z_f - z_i}{y_f - y_i}) \tag{21}$$

Also consider a static obstacle that appears at x_o, y_o, z_o with radius R_{obst} and height h_{obst}.The obstacle can be dodged in two ways either by changing the current yaw or pitch angle.

The change in yaw angle($\Delta\psi_{yaw}$) is given as

$$\Delta\psi_{yaw} = \psi_{final} - \psi_{inital} \tag{22}$$

where ψ_{final} is expressed as

$$\psi_{final} = \cot^{-1}(\frac{y_{dodge} - y_i}{x_{dodge} - x_i}) \tag{23}$$

here x_{dodge}, y_{dodge} are x-y coordinates of the tangentially closest point on the periphery of the obstacle required to dodge the obstacle and can be given as

$$x_{dodge} = x_0 + R_{buff}\cos(\tan^{-1}(m_p)) \tag{24}$$

$$y_{dodge} = y_0 + R_{buff}\sin(\tan^{-1}(m_p)) \tag{25}$$

where

$$R_{buff} = R_{obst} + d_{buff} \tag{26}$$

and

$$m_p = \frac{(x_i - x_o)^2 - R_{buff}^2}{(x_i - x_o)(y_i - y_o) \pm R_{buff}((l^2 - R_{buff}^2)^{1/2}} \tag{27}$$

In Eq.26 d_{buff} is minimum safety clearance. l denotes the euclidean distance between (x_o, y_o) and (x_i, y_i). The z-axis is taken as the axis of rotation for yaw and hence there is no change in z coordinate.

Similarly the change in pitch angle is given as

$$\Delta\theta_{pitch} = \theta_{final} - \theta_{initial} \tag{28}$$

where θ_{fin} is expressed as

$$\theta_{fin} = \tan^{-1}(\frac{z_{dodge} - z_i}{y_{dodge} - y_i}) \tag{29}$$

here z_{dodge}, y_{dodge} are y-z coordinates of the tangentially closest point on the periphery of the obstacle required to dodge the obstacle and can be given as

$$z_{dodge} = h_{obst} + d_{buff} \tag{30}$$

$$y_{dodge} = y_0 - R_{buff} \tag{31}$$

The x-axis is taken as the axis of rotation for pitch and hence there is no change in x coordinate.The appropriate way to dodge the obstacle by changing pitch ot yaw is determined by wheather $\Delta\psi_{yaw}$ and $\Delta\theta_{pitch}$ are within UAV's constraints. If both are feasible the smaller change in angle requirement is followed.

b) Dynamic Obstacle: Consider the inital and target nodes as given in the previous section.Also consider a dynamic obstacle that appears at x_o, y_o, z_o and velocity $\overrightarrow{V}$.A similar procedure as followed to dodge the static obstacle is followed here with the difference being that x_o, y_o, z_o are not fixed and hence a sequence of dodge points are generated until the UAV steer clears of the obstacle.

Again the UAV can dodge by either changing the yaw or pitch to generate the next dodge point.At any instant the computation for the next dodge point as the result of the change in yaw angle is similar to that of the static obstacle and is given by Eq. 22,23,24,25.

The change required in pitch angle(heading) is given as in Eq. 28 but here

$$\theta_k = \tan^{-1}(\frac{z_{dodge}^{(k)} - z_{dodge}^{(k-1)}}{y_{dodge}^{(k)} - y_{dodge}^{(k-1)}}) \tag{32}$$

where

$$z_{dodge}^{(k)} = z_o + R_{buff}\sin(\tan^{-1}(m_q)\ ) \quad (33)$$

$$y_{dodge}^{(k)} = y_o + R_{buff}\cos(\tan^{-1}(m_q)\ ) \quad (34)$$

and

$$m_q = \frac{(y_{dodge}^{(k-1)} - y_o)^2 - R_{buff}^2}{(y_{dodge}^{(k-1)} - y_o)(z_{dodge}^{(k-1)} - z_o) \pm R_{buff}(l^2 - R_{buff}^2)^{1/2}} \quad (35)$$

Here $(y,z)_{dodge}^{(k)}$ is the k^{th} dodge point in the sequence,$(y,z)_{dodge}^{(k-1)}$ is the previous dodge point in the y-z plane and l is the euclidean distance between (y_o, z_o) and $(y_{dodge}^{(k-1)}, z_{dodge}^{k-1})$.The dodge point generation is terminated when the bearing from the current dodge point to the target point(x_f, y_f, z_f) is no longer intercepted by the obstacle.For more details on m_p and m_q refer to Appendix.

3) L1 Navigation Controller: A non-linear navigation controller based on[13] was used to guide the UAV along curved segments of the trajectory. The controller not only works like a PD controller for straight paths but also contains an anticipatory control element for minimizing drifts when following curved paths. The guidance logic works by selecting a reference point at a distance L_1 on the desired trajectory in front of the UAV. Then a lateral acceleration command is generated which gives it an adaptive capability to face external disturbances like winds. The expression for lateral acceleration command is given by

$$a_{cmd} = 2V^2\sin\tau/L_1 \quad (36)$$

Where V is the velocity of UAV, $L_1$is defined from current position to reference point, τ is the angle between V and L_1. Details regarding the calculation of the expression and error estimation are omitted due to space constraints and can be found in [13].

D. Markov Decision Process

Three sets of actions can be adopted to prevent a collision with obstacles. A control policy is needed for determining the efficacy of each action in a given state. The control policy determines whether variation in velocity, local path adjustment, global path amendment or a combination is required to evade an impending obstacle or tackle changes in the environment. The UAV control problem and decision process is modeled as a finite state Markov Decision Process[14].

K_1: if $D(UAV_{(x,y,z)}, O^i_{(x,y,z)}) < K_1$, do path adjustment rather than changing velocity for obstacle evasion.
K_2: if $C_{(x,y,z)} > K_2$, do global path adjustment rather than local path adjustment.
K_3,K_4: Max change in climb angle and steering angle.
K_5: if $C_{(x,y,z)} > K_5$ abandon destination milestone, execute emergency plan.

Fig. 7: Parameters learned by Desicion Process

We made use of the Policy Search algorithm as given in [15] to learn the critical parameters of our control policy. For the reasons of brevity, only a short description of each of the learned parameters is given in Fig. 7

IV. Results and Experiments

We validate our algorithm on the sig rascal model provided by JSBSim as a simulation platform for a fixed wing UAV. The on-board autopilot, control system and sensors are simulated using the ArduPilot platform with APM Planner as the ground control station. A custom C# .Net application was built for controlling and configuring the obstacles and Caesium was used for depicting the final scenarios in real-time. The kinematic constraints for the considered system are given in Table I.

TABLE I: Parameters for Simulation

Parameters	Values
Turning Radius	$22m$
Climb-Rate	$8ms^{-1}$
Cruise Speed	$30ms^{-1}$
Max. Climb-Angle	$30°$
Max. Roll Angle	$65°$
Max. Pitch Angle	$25°$
Min. Pitch Angle	$-20°$
NAV L1 Damping	0.75
NAV L1 Period	15.0
NAV L1 X TRAC I	0.2

We conducted over 44 full system simulations on a workstation equipped with an octa core intel i7, 2.50 Ghz CPU.In any typical mission there were 3-6 stationary obstacles of varying radii spread across the search space and 1-3 dynamic obstacles traversing along predetermined paths. The criterion involved in evaluating our system were the fraction of total search area (enclosed within the geofence boundary) surveyed, length of the path and distance of separation of UAV from the obstacles within the search space.

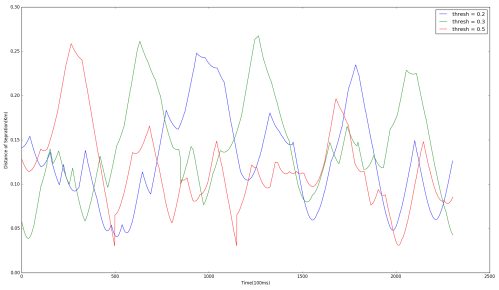

Fig. 8: Shows the average distance of separation of UAV from the obstacles during the course of the mission for different values of collision risk threshold with the number of milestones fixed at 10.

From Fig.8 and Fig.9 we conclude that the minimum distance of separation of UAV from obstacles decreases as collision risk threshold is increased from 0.2 to 0.8 at the same time the surveyed region increases from 72% to 94.7%.Hence an appropriate collision risk threshold has to

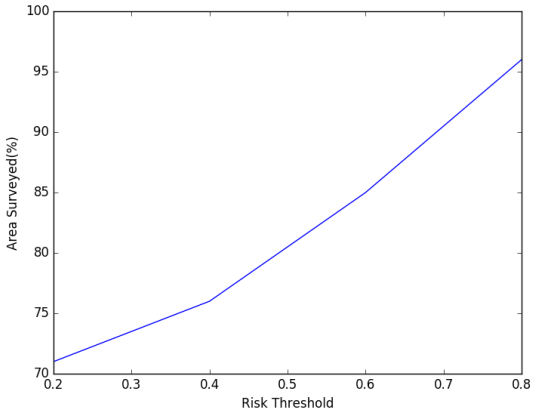

Fig. 9: Area Surveyed vs Collision Risk Threshold

be estimated experimentally for the desired UAV.Ideally the value lies between 0.4 - 0.7 depending on the mission profile.

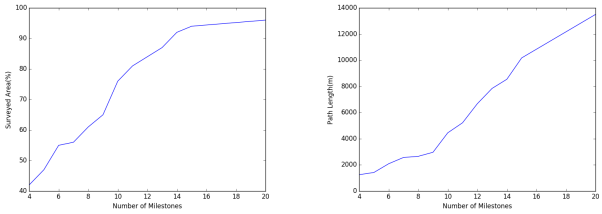

Fig. 10: (a)Area Surveyed vs Number of Milestones (b)Path Length vs Number of Milestones

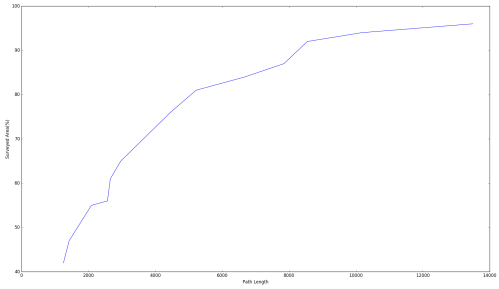

Fig. 11: Trade-off between Area Surveyed and Path Length for different Milestone count

The choice of number of milestone waypoints for mission also affects the expanse of search space surveyed. Fig. 10(a) shows the increase in the area covered with increase in number of milestones. From Fig.10(b) it is also noticed that the length of the tour also increases substantially.From Fig.11 it is noticed that there exists a trade-off between area surveyed and path length with respect to milestone count. In our simulations we found that for the geofence considered, there is a consistent increase in area surveyed with gradual increase in path length till 14 milestones, beyond which the path length increases without any appreciable growth in area surveyed. This is consistent with our heuristic as proposed in Eq.14 where for an area of dimensions 834x577m^2 the optimal milestone count should be 14 for a mission in which the on-board camera has fov 60^o and anticipated average altitude is $180m$.

TABLE II: Computation SpeedUp

C-Space Dim.	A*	A*-PRM	Speedup
25x30x27	27685	3109	8.90
40x30x30	31084	5942	5.23
50x50x50	52031	6232	8.95

Precomputation of a probabilistic roadmap from sample space greatly reduces planning time. Each node in PRM is extended by connecting to K-Nearest Neighbours and pruning those extensions which do not adhere to the dynamic and kinematic constraints of the system, then A* is used to find the optimal path between the milestone nodes in PRM. In comparison applying A* over the complete search space takes much longer to find a similar path with no added benefit. Table II shows the speedup in computation when a precomputed PRM is used instead of searching through the entire search space. On an average, the global path planning phase runs 7.69 times faster due to this optimization.

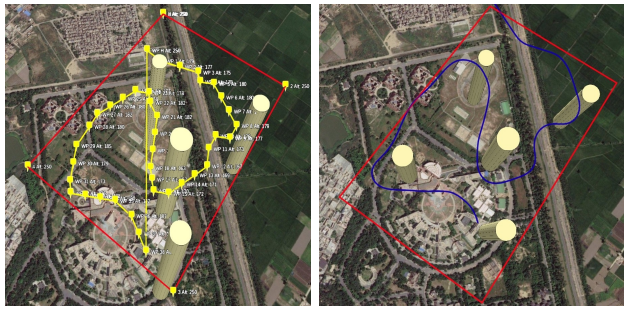

Fig. 12: (a)Red boundary represents the Geofence,Yellow curve depicts Initial Global Path (b)Blue curve is final Smooth Trajectory of the UAV followed in Simulation after Dubins smoothing

Fig.12, 13and 14 illustrate the results of simulations, in which a consistent wind blowing at 2 m/s with the bearing of 120° from North was considered. Non-linear L1 controller with the aforementioned parameters was used as the waypoint controller to ensure that the UAV does not drift considerably from its trajectory in presence of wind. For all the illustrations the boundary of geofence was demarcated at points A (28.754812 N, 77.115204 E), B (28.754812 N, 77.115204 E), C (28.755188 N, 77.119689 E) and D (28.748698 N,77.120161 E). The UAV after take-off enters the search space at coordinates at point (28.752088 N,77.116211 E). Fig.12 demonstrates the working of the global grid planner in the presence of obstacles , four stationary obstacles of radii 25,35,28 and 30 m are present at locations (28.7536640 N,77.1160412 E), (28.7522719

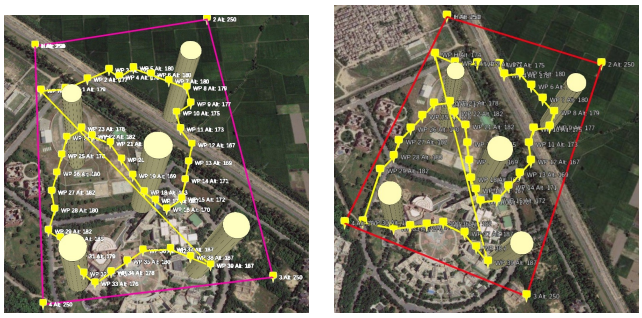

Fig. 13: (a)Fifth Obstacle appears intersecting the path of the UAV (b)Corrected path in response to the new obstacle

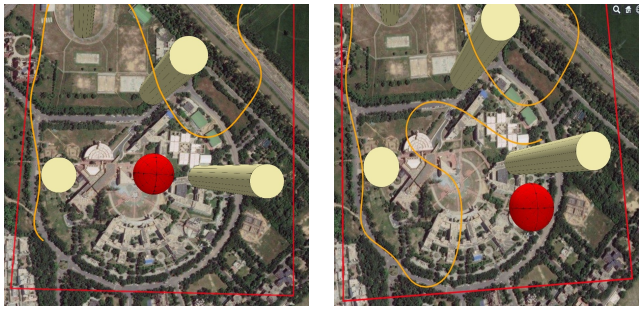

Fig. 14: (a)UAV detects the approaching dynamic obstacle(b)Final Path taken by the UAV:A sequence of dodge points is added tangentially by the local planner to evade the obstacle

N,77.1180367 E),(28.7547551,77.1193027) and (28.7503155 N,77.1195173 E). The global planner generates a kinematically feasible path represented by the yellow coarse path as shown in Fig.12(a).The local planner generates interconnecting motion primitives which result in a smooth dynamically feasible path which is traversed by the UAV as shown in Fig.12(b).

Fig.13 depicts the response of the local planner when an additional fifth obstacle appears unexpectedly at (28.7502026 N,77.1157837 E) of radius $32m$.The corrected path is shown in Fig.13(b).We see that an additional dodde point has been added to the current path so as to avert the collision.

Fig.14 illustrates the case where in addition to previous obstacles a dynamic obstacle of radius $30m$ approaches the path of the UAV with velocity $15m/s$ at distance of $105m$.A path alteration was made by the local planner to steer the UAV away safely from the oncoming obstacle. The UAV was able to stay clear of the obstacles and maintain a minimum separation of more than $3m$ which was taken as the safety clearance.

V. Conclusion

In this study, a dynamic motion planning approach has been presented for a fixed wing UAV surveying urban environment. The specialty of the proposed approach lies in its utility to work in partially known and updating environment.The computation involved in generating feasible trajectories for the UAV through the search space is greatly

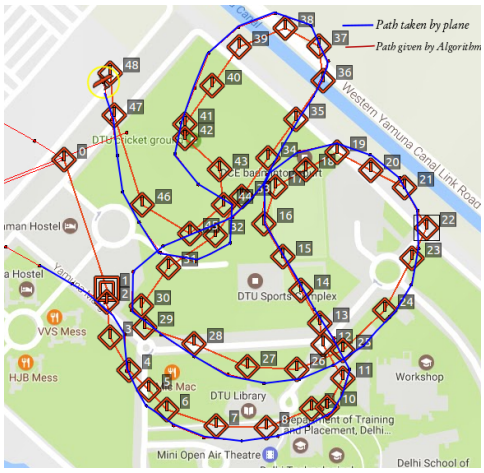

Fig. 15: The orange curve represents global path, blue curve depicts actual path followed during simulation in APM Planner.

reduced by the use of precomputed PRM.Voronoi Tessellation of search space and identification of key waypoints in the form of milestones leads to efficient mapping of the region to be surveyed.The changes in the environment are handled effectively by the decision process in the form of local or global planner.The application of 3D Dubins curve leads to smooth and dynamically feasible trajectories at runtime.The efficacy of the proposed approach is demonstrated in the complex simulation scenarios in highly cluttered environments comprising of both static and dynamic elements.In future, we plan on extending the capability of the proposed system by integrating an array of sensors to impart perception ability to our UAV platform.

References

[1] Karaman S, Frazzoli E. Incremental sampling-based algorithms for optimal motion planning. arXiv preprint arXiv:1005.0416, 2010

[2] Geraerts, Roland. "Planning short paths with clearance using explicit corridors."Robotics and Automation (ICRA), 2010 IEEE International Conference on. IEEE, 2010.

[3] Karaman S, Frazzoli E. Sampling-based algorithms for optimal motion planning[J]. The International Journal of Robotics Research, 2011, 30(7):846-894.

[4] DuToit R, Holt M, Lyle M, et al. UAV Collision Avoidance Using RRT* and LOS Maximization Technical Report# CSSE12-03[J].

[5] Anonymous,"World geodetic system 1984 (wgs-84)its definition and relationships with local geoderic systems," Defense Mapping Agency,Tech. Rep. NIMA TR 8350.2, 2000.

[6] M. Hwangbo, J. Kuffner and T. Kanade, "Efficient Two-phase 3D Motion Planning for Small Fixed-wing UAVs," Proceedings 2007 IEEE International Conference on Robotics and Automation, Roma, 2007, pp. 1035-1041. doi: 10.1109/ROBOT.2007.363121

[7] J. E. Bobrow, "Optimal robot path planning using the minimum-time criterion," IEEE Trans. on Robotics and Automation, vol. 4, no. 4, pp.443-450, 1988.

[8] Y. Kuwata and J. How, "Three dimensional receding horizon control for uavs," AIAA Guidance, Navigation, and Control Conference and Exhibit,Aug. 2004.

[9] Jin X., Han J.,"K-Medoids Clustering",Encyclopedia of Machine Learning, 2010, Springer US, Boston, MA, pp. 564-565, doi:10.1007/978-0-387-30164-8_426

[10] ltman, N. S."An introduction to kernel and nearest-neighbor nonparametric regression". The American Statistician, 1992,pp. 175?185. doi:10.1080/00031305.1992.10475879

[11] L. Tassiulas, "Worst case length of nearest neighbor tours for the Euclidean traveling salesman problem," SIAM J. Discrete Math ., Vol. 10, No. 2, pp 171-179, May 1997.
[12] L.E.Dubins, On curves of minimal length with a constraint on average curvature and with prescribed initial and terminal positions and tangents,? American Journal of Mathematics, vol. 79, no. 3, pp. 497-516, jul 1957.
[13] S. Park, J. Deyst, and J. P. How, "A New Nonlinear Guidance Logic for Trajectory Tracking," Proceedings of the AIAA Guidance, Navigation and Control Conference, Aug 2004. AIAA-2004-4900.
[14] Martin L. Puterman,"Markov Decision Processes: Discrete Stochastic Dynamic Programming (1st ed.)",1994, John Wiley & Sons, Inc., New York, NY, USA.
[15] Andrew Y. Ng, Michael I. Jordan, "Policy Search Method for Large MDPs and POMDPs", CoRR, 2013, Vol. abs/1301.3878

APPENDIX

Derivation of dodge point coordinates for Eq. 27 and 35.

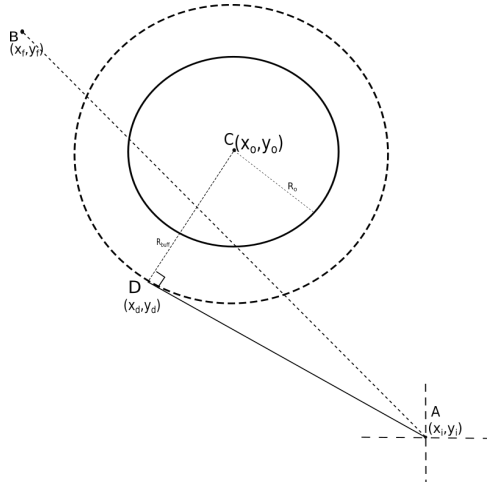

Fig. 16: A typical dodging scenario

Equation of the circle centered at (x_o, y_o) is given as:

$$(x - x_o)^2 + (y - y_o)^2 = R_{buff}^2 \tag{37}$$

Let the Equation of the tangent from point A be of the form

$$y = mx + c \tag{38}$$

then,after substituting y and c Eq. 37 can be written as:

$$(x - x_o)^2 + (mx + y_i - mx_i - y_o)^2 = R_{buff}^2 \tag{39}$$

Since line AD is a tangent to the circle, therefore both the roots of Eq. 39 are equal and hence the discriminant is zero. Using this we obtain the following quadratic relation in m:

$$m^2(Rbuff^2 - X^2) - 2m(Y)(X) - (Y)^2 + R_{buff}^2 = 0 \tag{40}$$

where

$$X = x_i - x_o \tag{41}$$

$$Y = y_i - y_o \tag{42}$$

Solving the quadratic Eq. 40 we get the roots as:

$$m = \frac{XY \pm R_{buff}(X^2 + Y^2 - R_{buff)^2})^{1/2}}{R_{buff}^2 - X^2} \tag{43}$$

where m is the possible values of the slope of line AD. The slope of line CD which is perpendicular to line AD is given by $-1/m$. Thus coordinates of the dodge points in the yaw plane are obtained as in Eq. 24 and 25 using parametric form equation of a line. Similar steps can be followed for pitch plane to obtain coordinates of dodge points.

Superlattices and Microstructures xxx (2017) 1–15

Contents lists available at ScienceDirect

Superlattices and Microstructures

journal homepage: www.elsevier.com/locate/superlattices

Effect of trench depth and gate length shrinking assessment on the analog and linearity performance of TGRC-MOSFET

Ajay Kumar

Electrical Engineering Department, Delhi Technological University, Delhi India

A R T I C L E I N F O

Article history:
Received 21 January 2017
Received in revised form 18 April 2017
Accepted 20 May 2017
Available online xxx

Keywords:
Analog
Distortions
Linearity
TGRC-MOSFET
Trench gate
Transconductance coefficients

A B S T R A C T

This paper discusses the impact of trench depth (Negative Junction Depth (NJD)) and gate length (L_G) shrinking on analog and linearity performance of Transparent Gate Recessed Channel (TGRC) MOSFET with an aim to achieve a reliable and high performance transistor. It is found that device enhances the I_{ON} by 38% and thereby improves the analog performance in terms of transconductance, device efficiency, output resistance, and gain. Moreover, linearity figure of merits are also enhanced at lower gate bias in TGRC MOSFET in comparison to conventional and Conventional Recessed Channel (CRC) MOSFET due to reduced harmonic distortions (g_{m3}). Thus, the improved analog and linearity performance at 5 nm NJD and 20 nm L_G of TGRC-MOSFET makes it suitable for low power linear RF amplifiers as a nano-scaled device. Thus, these results would serve as a worthy design tool for low power and high performance CMOS circuits.

© 2017 Elsevier Ltd. All rights reserved.

1. Introduction

For RFIC designing and high-frequency applications, CMOS devices are required with low intermodulation distortion to sustain linear operations when working with a weak signal. In modern communication systems, a high linearity is desired so as to exhibit less distortion. Intermodulation (IM) may induce when the system gives nonlinearity performance and generate different frequency signal at outputs compared to input signal frequency. This kind of interference may fall into the band of interest and distorted the desired output [1]. However, sub-nm MOSFET exhibit linear relation but short channel effects (SCEs) hinders its linearity. As the dimensions of the device are reduced, scaling the silicon-based MOSFET devices for barrier potential, critical electric field, oxide thickness, threshold voltage, etc., are becoming hardly increased [2]. To overwhelmed such scaling problems, various device engineering schemes (gate, channel and drain engineering, etc.) and numerous device structures such as multi-gate MOSFET by Barsan in 1981 [3], SOI MOSFET by An et al., in 2003 [4], Conventional Recessed Channel (CRC) MOSFET by Chaujar et al., in 2008 [5], GAA MOSFET by Auth et al., in 1997 [6], and Silicon Nanowire MOSFET by Gupta et al., in 2015 [7] etc., have already been reported in the literature. Among them, RC-MOSFET is most promising for extending the scaling limit of conventional CMOS technology due to tremendous gate controllability, lessened SCEs and ease of fabrication feasibility of RC MOSFET [8]. In CRC-MOSFET, two potential barrier are created at the two corners [9] owing to higher field lines due to which electrons are now required more energy to cross these barriers. Consequently, these barriers bounds device transport efficiency and thus, current driving capability (Ion) reduced. To overwhelm this limitation, there is a need of integration of engineering schemes onto RC MOSFET. Therefore, to enhance the current driving capability and

E-mail address: ajaykumar@dtu.ac.in.

http://dx.doi.org/10.1016/j.spmi.2017.05.045
0749-6036/© 2017 Elsevier Ltd. All rights reserved.

Please cite this article in press as: A. Kumar, Effect of trench depth and gate length shrinking assessment on the analog and linearity performance of TGRC-MOSFET, Superlattices and Microstructures (2017), http://dx.doi.org/10.1016/j.spmi.2017.05.045

improve the device performance for ULSI industry, gate metal engineering scheme is incorporated by some optically transparent and electrically conducting oxides (TCO). TCO is used for different applications in electronic devices due to various properties such as conductivity, thermal stability, transparency, mechanical durability, chemical durability, cost and toxicity [10]. Among all the TCO, indium tin oxide (ITO) has the highest conductivity and very good transparency as well so; it can be used as electrode material in flat panel display. ITO is a compound of In_2O_3 and SnO_2 and it needs lowest deposition temperature as well [11,12]. ITO has a high concentration in the order of 10^{21} cm^{-3} and a very low resistivity (10^{-5} Ω-cm) with higher Hall mobility (53.5 cm^2 $V^{-1}s^{-1}$) [13]. Due to these properties, ITO is frequently used in semiconductor devices and today silicon-based MOSFET devices having technology less than 30 nm are common. Shrinking the device sizes is the driving force towards circuit reduction, low cost, and portability [14]. It is found that the proposed design enhances the device performance in terms of electrical [15,16] and RF performances [17,18].

Therefore, in this work for the first time linearity and harmonic distortions of TGRC-MOSFET has been studied and concurrently compared with CRC MOSFET in terms of Voltage Intercept Point (VIP2, VIP3), IIP3, Distortions (IMD3, HD3) and transconductance and its higher order term (g_{m1}, g_{m3}) using ATLAS 3D device simulator [19]. In addition, effectiveness of geometry dependent parameters such as gate length (L_G) and recessed channel length (NJD) are also examined with an aim to optimize the device parameters so that TGRC MOSFET can be used as highly linear amplifiers with low distortions in communication systems.

2. Device designing and its description

Fig. 1 shows the simulated 3D device structure of TGRC-MOSFET. The source and drain region is highly doped with an n-type impurity of 5×10^{19} cm^{-3} and the substrate is doped with p-type impurity of 1×10^{17} cm^{-3} and thick oxide layer t_{ox} of 2.0 nm is embodied in it as shown in Fig. 1. Negative Junction Depth (NJD) is taken as 10 nm, gate bias (V_{gs}) is 0.7 V and drain bias (V_{ds}) is 0.5 V. Gate workfunction of TGRC-MOSFET (Φ_{ITO}) is 4.7eV and for CRC-MOSFET, it is 4.4eV. To equally analyze the device performances, both the devices (CRC and TGRC MOSFET) are optimized to have the similar threshold voltage, i.e., 0.3 V by adjusting the substrate doping. For this analysis, all the junctions of the device structure are assumed to be abrupt; the doping profiles are uniform, and the biasing conditions are considered at room temperature (T = 300 K). Further, to obtain the numerical solutions two numerical techniques Gummel and Newton have been considered [19] to obtain better convergence.

3. Simulation methodology and calibration

As we were considering a nanoscale MOSFET, the size of mesh nearly 0.003 or 0.004 units in the x and y-direction while 0.02 unit in z direction near the channel and in the active regions has been selected for more precise calculations [20]. The electron and hole currents are calculated by Poisson's equation and the continuity equations. All the simulations are based on the inversion layer Lombardi CVT mobility model to permit one to take account of carrier-carrier scattering, carrier velocity saturation, the influence of the vertical electric field and carrier diffusion at the interface. Auger recombination model and Shockley-Read–Hall (SRH) for minority carrier recombination were used. Further, the hydrodynamic energy transport model comprising of the continuity equations and momentum transport equations have also been used [19]. The equations and models utilized are listed below.

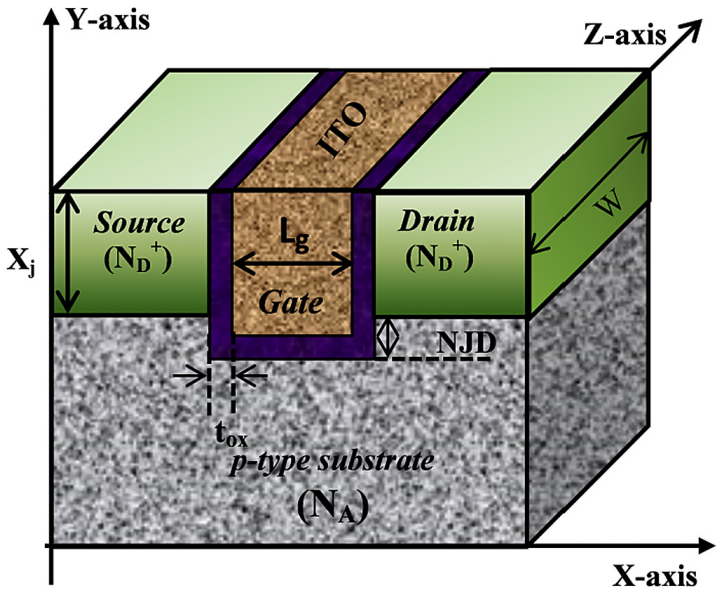

Fig. 1. 3-D device structure of TGRC-MOSFET.

Please cite this article in press as: A. Kumar, Effect of trench depth and gate length shrinking assessment on the analog and linearity performance of TGRC-MOSFET, Superlattices and Microstructures (2017), http://dx.doi.org/10.1016/j.spmi.2017.05.045

1. Poisson's equation

$$div(\varepsilon\nabla\phi) = -\rho \tag{1}$$

Where ε is local permittivity; φ is electrostatic potential and ρ is local space charge density.

2. Current continuity equation

For Holes,

$$\frac{\partial p}{\partial t} = \frac{1}{q} div\vec{J}_p + G_p - R_p \tag{2}$$

For Electrons,

$$\frac{\partial n}{\partial t} = \frac{1}{q} div\vec{J}_n + G_n - R_n \tag{3}$$

Where, $\vec{J}_p$ and $\vec{J}_n$ hole and electron current density respectively; G_p and G_n are the generation rate for holes and electrons;R_p andR_n is the recombination rate for holes and electrons respectively.

3 Recombination

3.1 SRH (Shockley Read Hall)

$$R_{SRH} = \frac{pn - n_{ie}^2}{\tau_p\left[n + n_{ie}e^{(-(E_{TRAP}/kT_L))}\right] + \tau_n\left[p + n_{ie}e^{(-(E_{TRAP}/kT_L))}\right]} \tag{4}$$

Where, E_{TRAP}, change between the trap energy level and the intrinsic Fermi level; τ_n and τ_p, and are the electron lifetime and hole lifetimes, respectively.

3.2 Auger recombination

$$R_{Auger} = AUGN\left(pn^2 - nn_{ie}^2\right) + AUGP\left(np^2 - pn_{ie}^2\right) \tag{5}$$

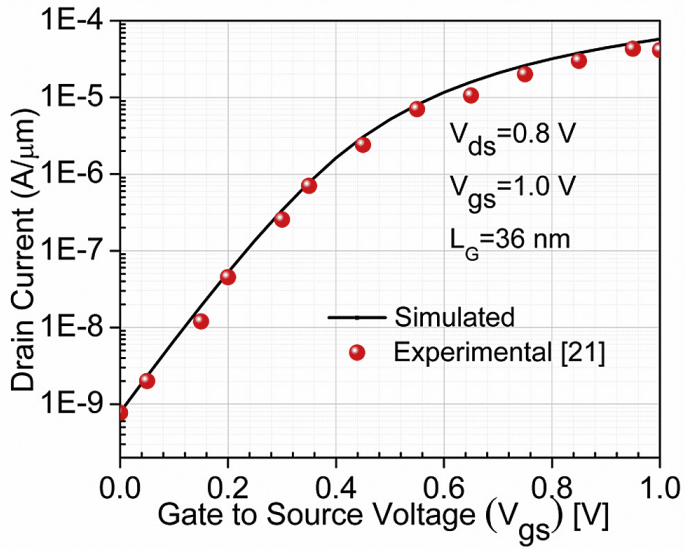

Fig. 2. Experimental and simulation of I_d-V_{gs} characteristics of 36 nm gate length recessed channel MOSFET.

Please cite this article in press as: A. Kumar, Effect of trench depth and gate length shrinking assessment on the analog and linearity performance of TGRC-MOSFET, Superlattices and Microstructures (2017), http://dx.doi.org/10.1016/j.spmi.2017.05.045

Table 1
Process flow [21,22,32] of TGRC MOSFET.

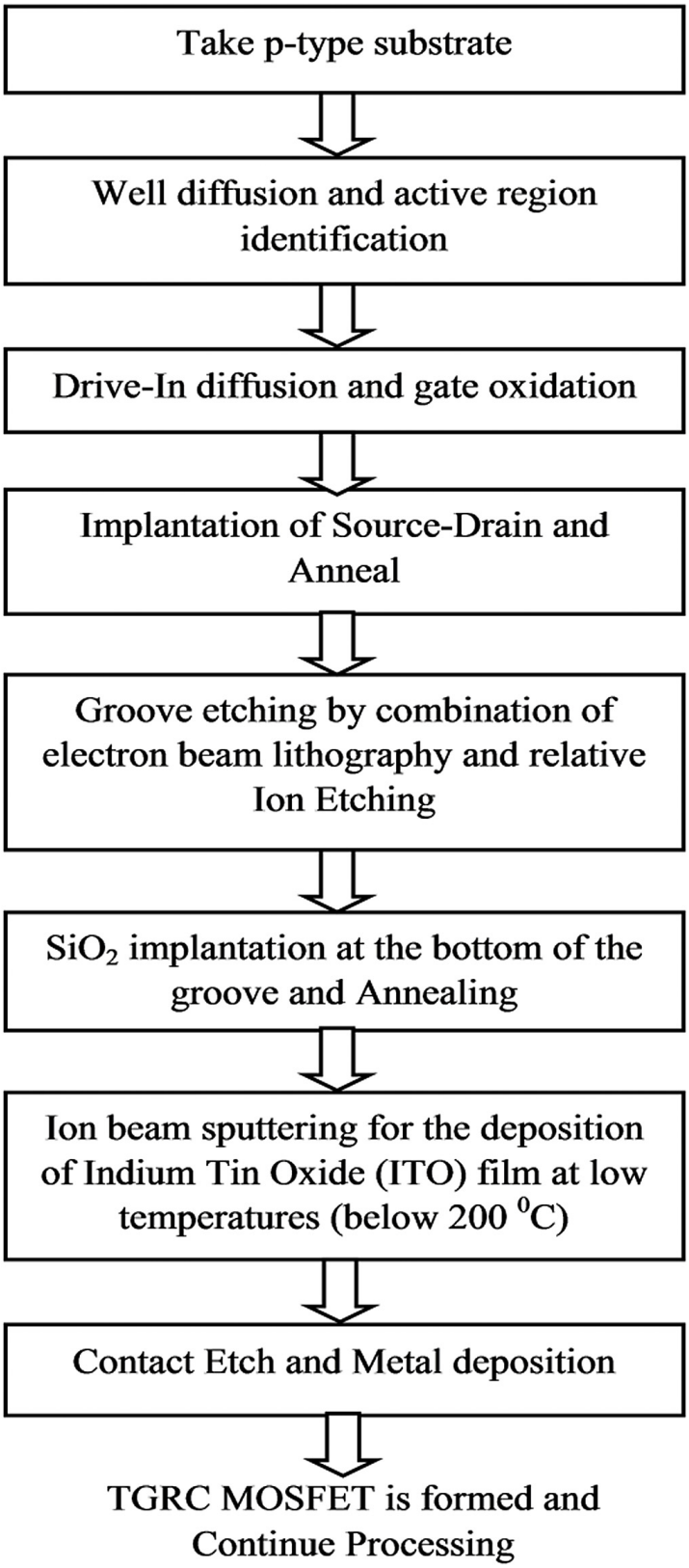

Please cite this article in press as: A. Kumar, Effect of trench depth and gate length shrinking assessment on the analog and linearity performance of TGRC-MOSFET, Superlattices and Microstructures (2017), http://dx.doi.org/10.1016/j.spmi.2017.05.045

AUGN and AUGP are user-definable and AUGN = 8.3×10^{-32} cm^6/s, AUGP = 1.8×10^{-31} cm^6/s.

4 Parallel electric-field-dependent mobility

$$\mu(E) = \mu_0 \left[\frac{1}{1 + (\mu_0 E / v_{sat})^{\beta}} \right]^{1/\beta} \tag{6}$$

Physical Model parameters which are used in device simulation have been calibrated according to the experimental results by Joerg Appenzeller et al., in 2002 [21]. In order to authenticate the simulations results, the data has been drawn-out [21] for 36 nm groove MOSFET and then plotted as shown in Fig. 2. It is evident from the figure that simulated results are in good agreement with the experimental results in sub-40 nm groove MOSFET thus validating the simulation models.

4. Fabrication feasibility of TGRC-MOSFET

The fabrication feasibility of TGRC-MOSFET is shown in Table 1. Moreover, the groove MOSFET has already been fabricated by different researchers such as Joerg Appenzeller et al., in 2002 [21] fabricated 36 nm groove gate and M. Xiao-Hua et al., in 2006 [22] fabricated 140 nm groove gate MOSFET. Thus, the TGRC MOSFET can be fabricated using the above device design schemes, in which the benefits of transparent gate engineering scheme have been combined with groove gate for accomplishing improved characteristics.

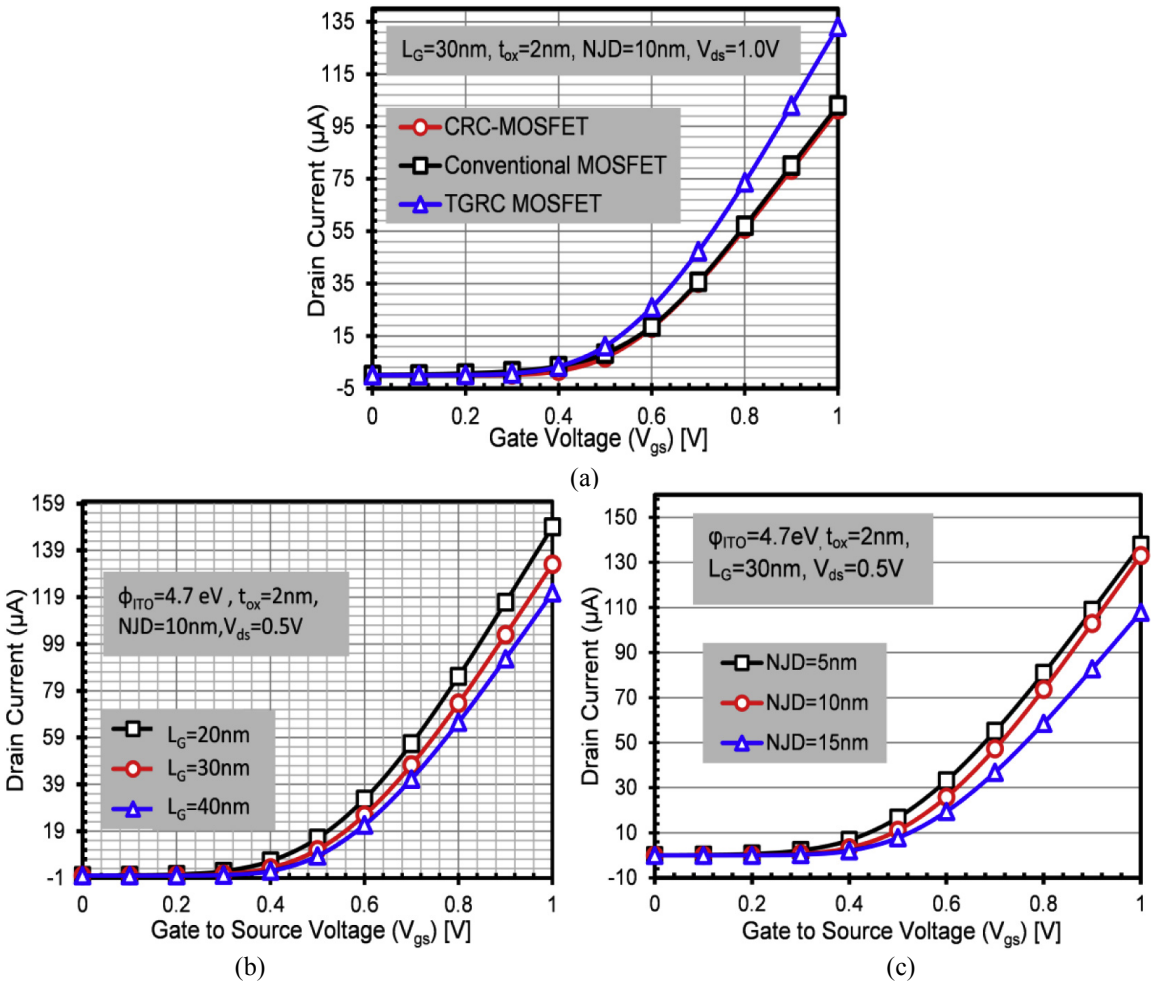

Fig. 3. (a) Drain current variations for TGRC-MOSFET, CRC-MOSFET, and Conventional MOSFET. (b) Drain current at different L_G. (c) Drain current variations at different NJDs as a function of applied V_{gs}.

Please cite this article in press as: A. Kumar, Effect of trench depth and gate length shrinking assessment on the analog and linearity performance of TGRC-MOSFET, Superlattices and Microstructures (2017), http://dx.doi.org/10.1016/j.spmi.2017.05.045

5. Results and discussion

5.1. Analog performance

This subsection describes and subsequently compared the analog performance of TGRC, CRC, and conventional MOSFET. Performances are studied in terms of transfer characteristics (I_{ds}/V_{gs}), transconductance (g_m), device efficiency (g_m/I_{ds}) and intrinsic gain (g_m/g_d). Transfer characteristics of Conventional, CRC, and TGRC-MOSFET, are shown in Fig. 3(a) and it is depicted that the current driving capability of conventional and CRC-MOSFET is approximately same, but TGRC-MOSFET shows higher current driving capability. This improvement is due to the incorporation of ITO which reduces electric field in drain side [15] and thereby improves carrier efficiency resulting in improvement in drain current (by 35%).

In addition, the effect of technology variations of TGRC-MOSFET such as L_G and NJD is also observed in the transfer characteristics. It is found as the L_G is scaled down from 40 nm to 20 nm, the drain current (I_{ON}) enhances as clearly shown in Fig. 3(b). This enhancement is due to the reduction of the gate length. Hence, charge carriers needed less time to reach drain from the source. Further, by varying the value of NJD, which greatly affects the performance of RC MOSFET [23], the current driving capability of TGRC is further improved due to the increment of charge carriers travelling from source to drain if NJD reduces as shown in Fig. 3(c). There is a limitation in the reduction of NJD and it should not be zero or less; if it is, then SCEs arises. Also, the transconductance increases with increase in gate voltage, and it is more prominent in TGRC-MOSFET as shown in Fig. 4(a) due to TCO at the gate in place of metal which gives high linearity performance because linearity is proportional to transconductance [24]. Further, the effect of variation of gate length on transconductance is observed in TGRC-MOSFET and found that if the gate length shrinks from 40 nm to 30 nm, then very small reduction (by 7.1%) in transconductance is observed while, major enhancement (by 23.37%) is observed when gate length reduces from 30 nm to 20 nm as evident from Fig. 4(b). Fig. 4(c) reflects the effect of technology variation on transconductance in terms of different NJDs

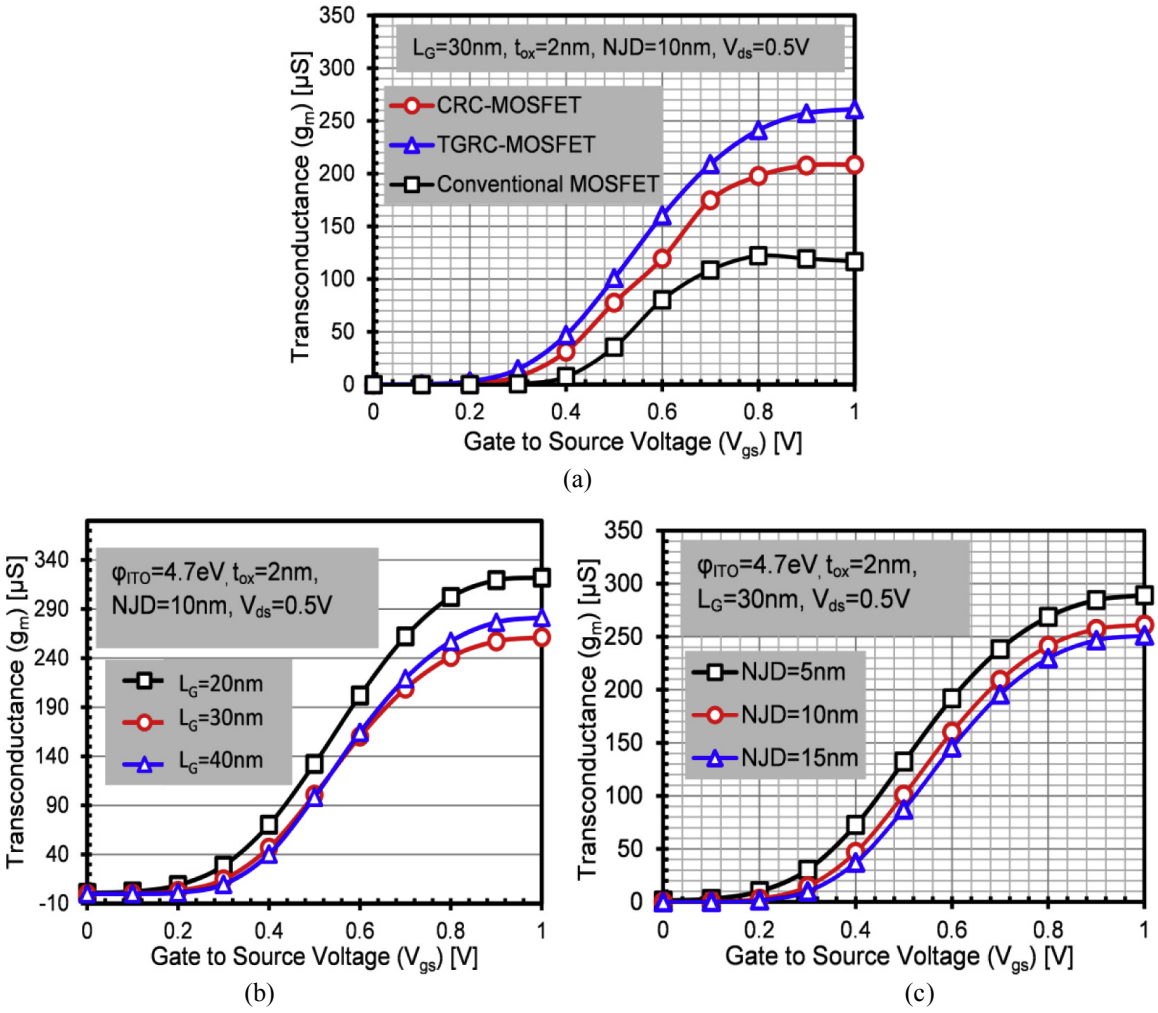

Fig. 4. (a) Variations of g_m for TGRC-MOSFET, CRC-MOSFET, and Conventional MOSFET, (b) Variation of g_m at different L_G, (c) Variation of g_m at various NJDs as a function of applied V_{gs}.

Please cite this article in press as: A. Kumar, Effect of trench depth and gate length shrinking assessment on the analog and linearity performance of TGRC-MOSFET, Superlattices and Microstructures (2017), http://dx.doi.org/10.1016/j.spmi.2017.05.045

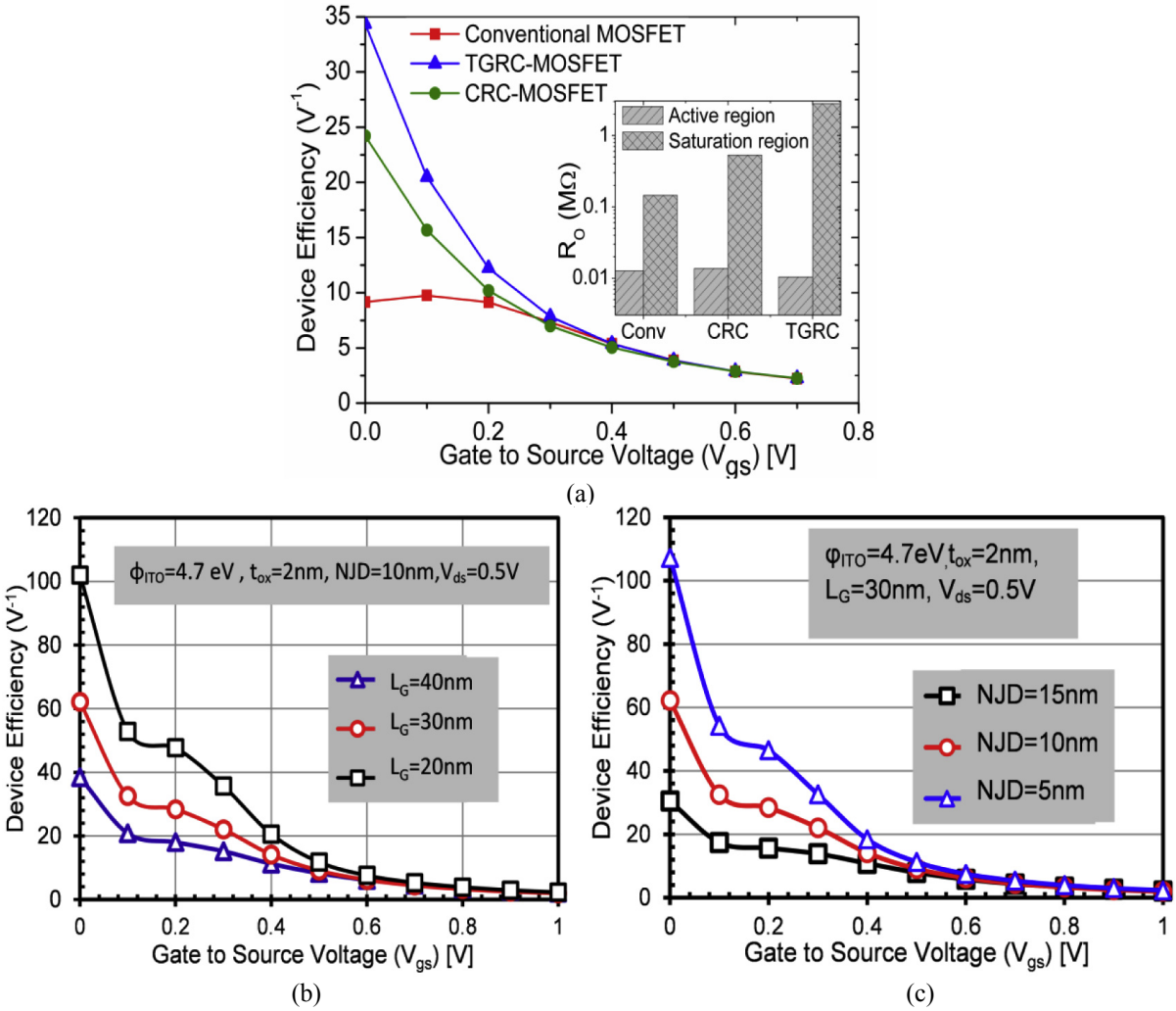

Fig. 5. (a) Variations of Device Efficiency for TGRC-MOSFET, CRC-MOSFET, and Conventional MOSFET. Inset: Output resistance. (b) Variation of Device Efficiency at different L_G, (c) Variation of Device Efficiency at various NJDs as a function of applied V_{gs}.

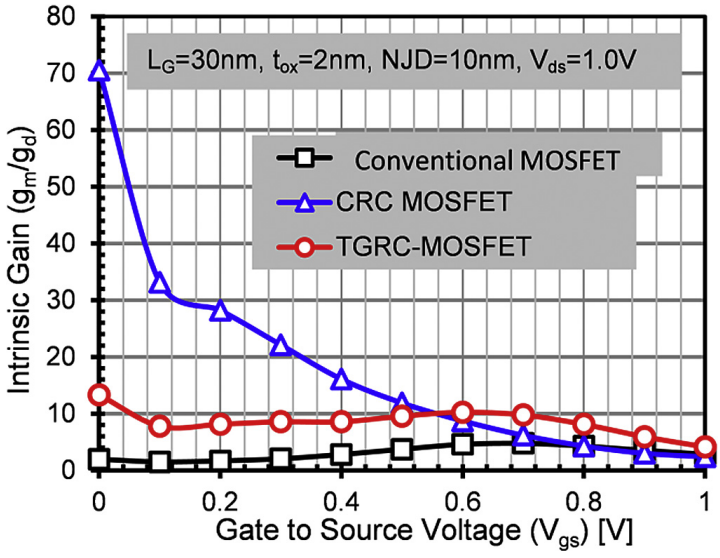

Fig. 6. Variations of Intrinsic Gain as a function of applied V_{gs} for TGRC-MOSFET, CRC-MOSFET, and Conventional MOSFET.

Please cite this article in press as: A. Kumar, Effect of trench depth and gate length shrinking assessment on the analog and linearity performance of TGRC-MOSFET, Superlattices and Microstructures (2017), http://dx.doi.org/10.1016/j.spmi.2017.05.045

and it is found that transconductance is more prominent which gives high linearity performance at 5 nm NJD while it degrades if NJD increases to 10 nm and 15 nm. Thus, improved analog performance of TGRC-MOSFET as such scaled dimensions make it suitable for 22 nm node technology [2] as per ITRS (International Technology Roadmap for Semiconductor) [25].

The transconductance to the current ratio (g_m/I_d) or device efficiency and output resistance have been evaluated for three different devices (Conventional, CRC, and TGRC MOSFET) as depicted in Fig. 5(a). Device efficiency is an important parameter in the design of analog circuits, which offers the measure of efficiency to convert power into speed. It is evident from Fig. 5(a) that the device efficiency is higher in TGRC-MOSFET as compared to conventional MOSFET and CRC-MOSFET due to improvement in g_m in comparison to I_d, which overall enhances g_m/I_d. The output resistance (R_o) of a MOSFET is the inverse of the output conductance. The most important characteristics of R_o in the circuit design is maximum R_o which decides the maximum available power gain for the device. R_o is low in active region while high in the saturation region in TGRC-MOSFET as compared to conventional counterparts (shown in Fig. 5(a) inset). The device efficiency further increases by 63% and 61.29% if the gate length shrinks from 40 nm to 30 nm and 30 nm–20 nm respectively in TGRC-MOSFET, as shown in Fig. 5(b).

In addition, in technology variation, the effect of NJD variation on device efficiency is also perceived for TGRC-MOSFET (shown in Fig. 5(c)). It is evident from Fig. 5(c) that the reduction in NJD enhances the device efficiency by 78.33% if NJD is scaled to 5 nm. Intrinsic gain one of the important characteristic of MOSFET which is defined as the ratio of transconductance (g_m) to output conductance (g_d) [26]. For better performance, intrinsic gain should be as high as possible and it is evident from Fig. 6 that the intrinsic gain is lower in subthreshold region (where device is off) and inactive region, and the intrinsic gain increases in TGRC architecture in comparison to conventional and CRC MOSFET. Thus TGRC-MOSFET shows promising analog performance for ULSI in comparison to conventional and CRC MOSFET.

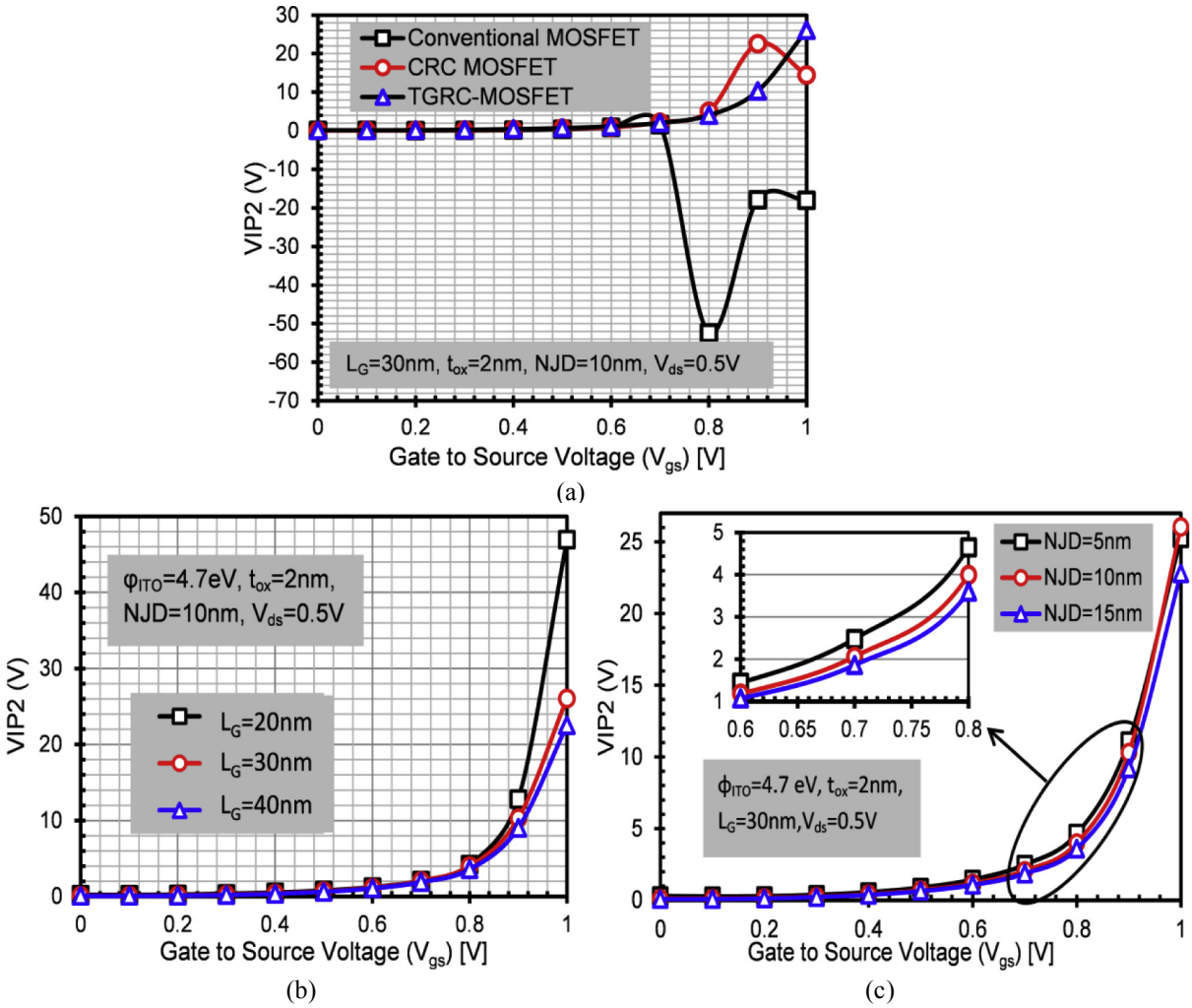

Fig. 7. (a) Variations of VIP2 for TGRC-MOSFET, CRC-MOSFET, and Conventional MOSFET. (b) Variation of VIP2 at different L_G. (c) Variation of VIP2 at different NJDs as a function of applied V_{gs}.

Please cite this article in press as: A. Kumar, Effect of trench depth and gate length shrinking assessment on the analog and linearity performance of TGRC-MOSFET, Superlattices and Microstructures (2017), http://dx.doi.org/10.1016/j.spmi.2017.05.045

5.2. Intermodulation and linearity performance

5.2.1. Linearity performance

In this sub-section, the linearity of our proposed device is studied and simultaneously compared with its conventional counterparts. Thereafter, technology variations in terms of gate length and NJD have also been studied with an aim to analyze the linearity performance of TGRC at scaled dimensions. The performance metrics used in this analysis are VIP2, VIP3, IIP3 and 1-dB Compression Point. The generalized input voltage (VIP2 and VIP3) represents input voltage at which first order harmonics and third order harmonics are same as shown in equations (7) and (8) [23].

$$VIP2 = 4\frac{g_{m1}}{g_{m2}} \tag{7}$$

$$VIP3 = \sqrt{24 \times g_{m1}/g_{m3}} \tag{8}$$

Where $g_{m1} = \frac{\partial I_d}{\partial V_{gs}}$ and$g_{m2} = \frac{\partial^2 I_d}{\partial V_{gs}^2}$.$g_{m3} = \frac{\partial^3 I_d}{\partial V_{gs}^3}$

Fig. 7(a) reflects the variation of VIP2 w.r.t. the V_{gs} for TGRC-MOSFET and it is also compared with conventional MOSFET and CRC-MOSFET. For higher linearity and lower distortion operation the value of VIP2 should be higher. From Fig. 7(a), it is analyzed that the TGRC device resembles to a higher value of VIP2 by 22.3% and 8.49% as compared to the conventional and CRC designs respectively, which is only due to the incorporation of ITO as a TCO in the TGRC design. The variation of VIP2 w.r.t. applied gate to source voltage for three different gate lengths of TGRC-MOSFET as shown in Fig. 7(b), and it is found that when the gate length shrinks from 40 nm to 30 nm and from 30 nm to 20 nm, then VIP2 increases which reflect higher value at

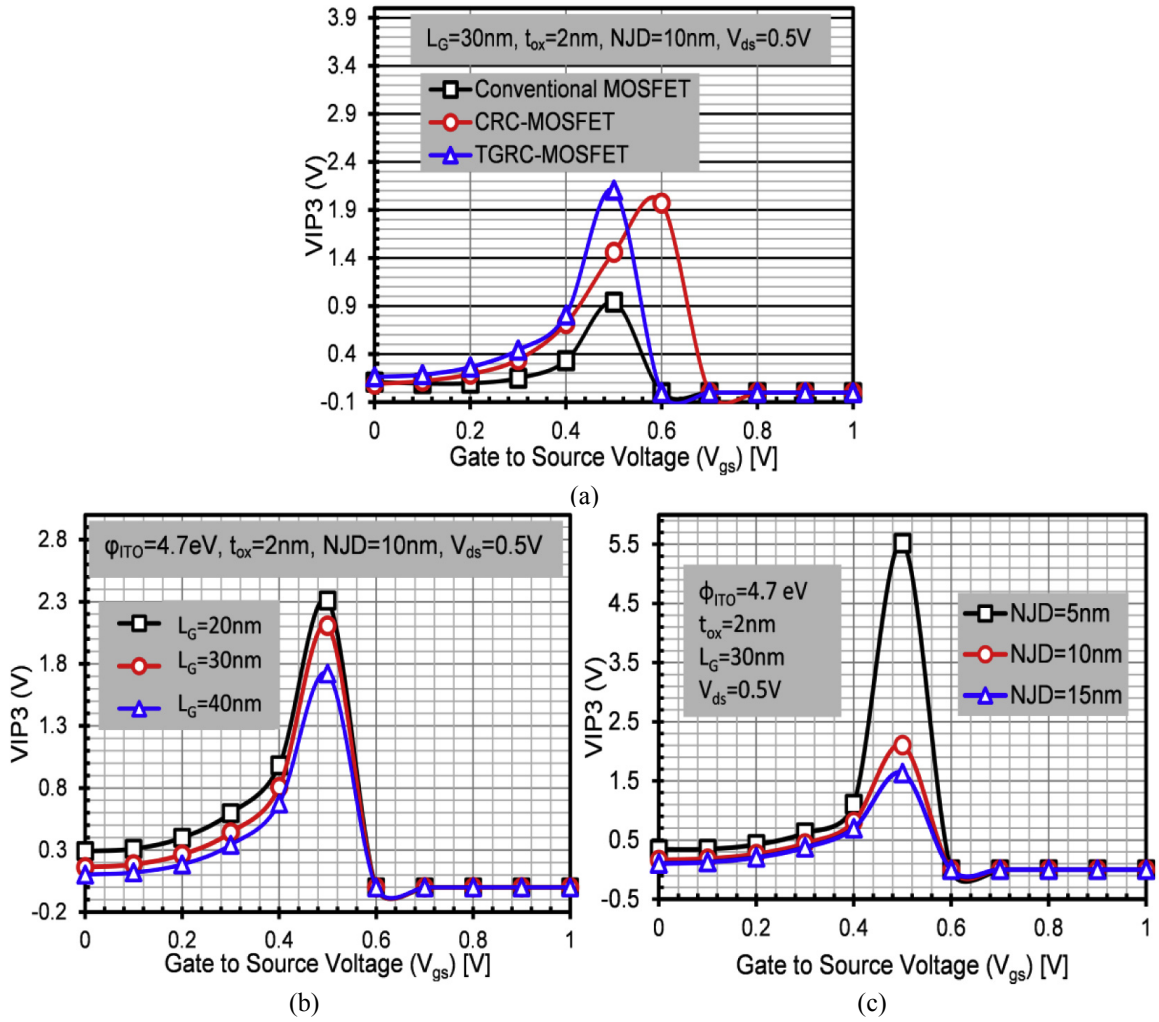

Fig. 8. (a) Variations of VIP3 for TGRC-MOSFET, CRC-MOSFET, and Conventional MOSFET. (b) Variation of VIP3 at different L_G. (c) Variation of VIP3 at various NJDs as a function of applied V_{gs}.

Please cite this article in press as: A. Kumar, Effect of trench depth and gate length shrinking assessment on the analog and linearity performance of TGRC-MOSFET, Superlattices and Microstructures (2017), http://dx.doi.org/10.1016/j.spmi.2017.05.045

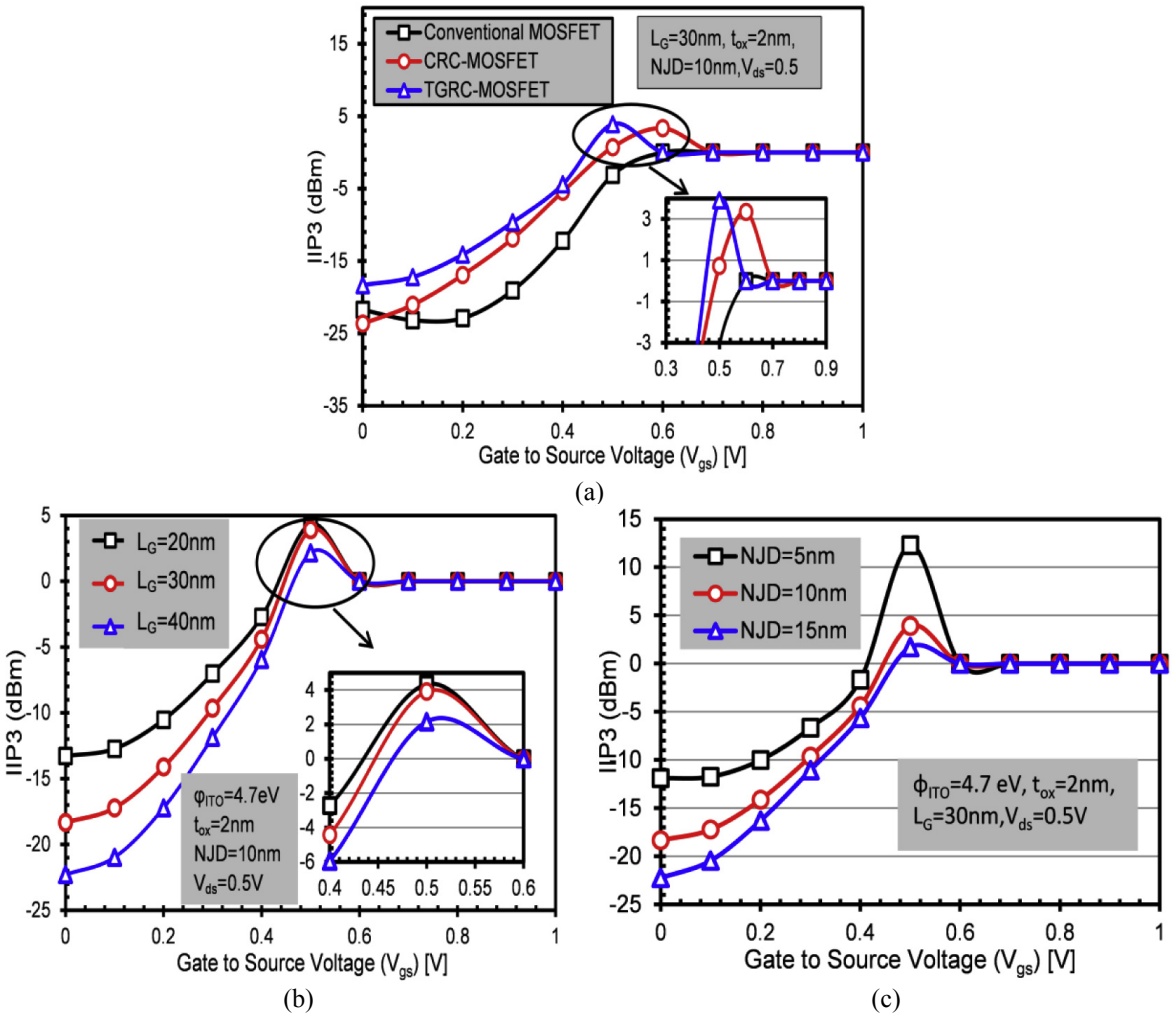

Fig. 9. (a) Variations of IIP3 for TGRC-MOSFET, CRC-MOSFET, and Conventional MOSFET. (b) Variation of IIP3 at different L_G. (c) Variation of IIP3 at different NJDs as a function of applied V_{gs}.

20 nm gate length. Thus, 20 nm TGRC architecture shows higher linearity performance. Similarly, by scaling down the NJD to 5 nm, TGRC shows the higher value of VIP2 owing to reduce SCEs, improves g_m and thus VIP2 as shown in Fig. 7(c).

Fig. 8(a) reflects the variation of VIP3 w.r.t. the V_{gs} for TGRC-MOSFET, CRC-MOSFET, and conventional MOSFET. VIP3 peak is perceived at low gate bias (i.e., 0.45 V) in TGRC architecture which is higher by 37.5%, 17.8% compared to conventional MOSFET and CRC MOSFET respectively, owing to ITO as a transparent gate design which enhances carrier velocity and thus transconductance. VIP3 peak is further enhanced by scaling down the gate length to 20 nm as clearly evident from Fig. 8(b). This enhancement is due to higher g_m (see Fig. 4(b)). Similarly, if NJD is scaled down to 5 nm from 15 nm, VIP3 peak increases significantly, reflected in Fig. 8(c), thus, signifies that scaled TGRC-MOSFET exhibit high linearity.

Moreover, there are two important FOMs which govern amplifier's efficiency and linearity i.e. third-order intercept point (IIP3) and 1-dB compression point (1 dB CP). In general for MOS based amplifiers, higher the output at the intercept, better the linearity. Third-order intercept is a theoretical point at which the third-order distortion signal amplitudes equal the input signals, and it is useful in determining the linearity condition of an amplifier. These two parameters are evaluated by equations (9) and (10) [23,27].

$$IIP3 = \frac{2}{3}\frac{g_{m1}}{g_{m3} \times Rs} \tag{9}$$

$$1 - dB\ Compression\ \text{Point} = 0.22 \times \sqrt{\frac{g_{m1}}{g_{m3}}} \tag{10}$$

where $R_S = 50\ \Omega$ for analog and RF applications.

Please cite this article in press as: A. Kumar, Effect of trench depth and gate length shrinking assessment on the analog and linearity performance of TGRC-MOSFET, Superlattices and Microstructures (2017), http://dx.doi.org/10.1016/j.spmi.2017.05.045

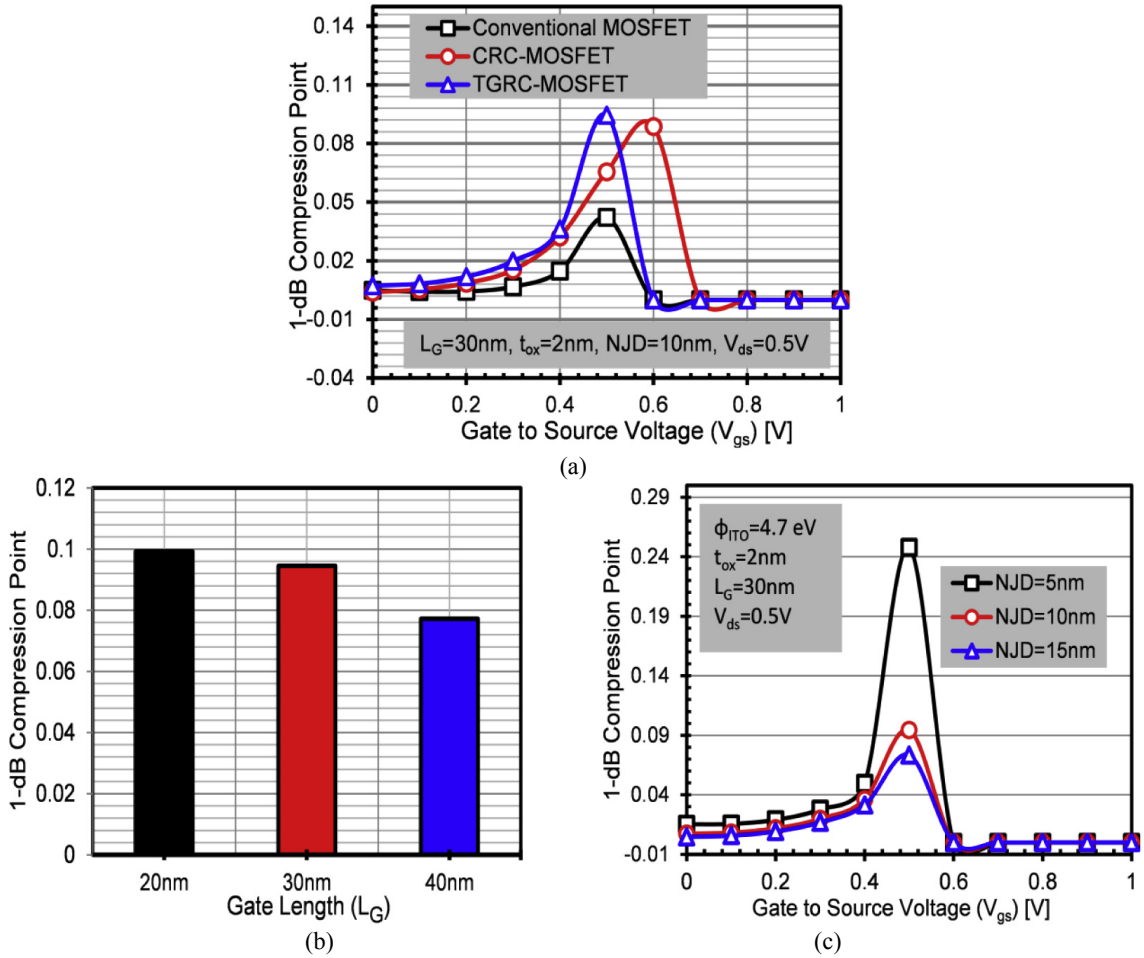

Fig. 10. (a) Variations of 1-dB Compression point for TGRC-MOSFET, CRC-MOSFET, and Conventional MOSFET. (b) Variation of 1-dB Compression point at different L_G. (c) Variation of 1-dB Compression at different NJDs as a function of applied V_{gs}.

Fig. 9(a) evidently reveals an improvement in IIP3 for the TGRC as compared to the conventional and CRC designs; this is due to the integration of the TGRC architecture, which is attributed to the high transconductance and lower value of g_{m3}, thus results in an enhancement in the carrier transport efficiency for well gate control over the channel. Moreover, the gate length and NJD variations w.r.t. the applied gate to source voltage are also shown in Fig. 9(b) and (c) and show enhancement in linearity of the device and, hence, desirable efficiency is observed. So, IIP3 can be enhanced by reducing the gate length (from 40 nm to 30 nm and from 30 nm to 20 nm) and decreasing the NJD (from 15 nm to 10 nm and from 10 nm to 5 nm). The 1-dB compression point is essential to identify at what point compression occurs so that input levels can be limited to prevent distortion. It is generally the input power that causes the gain to fall by 1 dB from the normal linear gain specification. This parameter signifies the maximum input power that the amplifier circuit can handle by providing a fixed amount of gain, and if the input power surpasses the compression point, the gain starts falling. Hence, it is desirable that a 1-dB compression point should be as high as possible for the high linear amplifier.

Fig. 10(a) shows peak value of 1-dB compression point in TGRC-MOSFET rises in comparison to its conventional counterparts. This improvement is due to the enhanced current driving capability of the device owing to high conductivity and transparency of ITO. Further, the gate length variation is observed for TGRC-MOSFET in terms of 1-dB compression point, and it is found that with the tuning of gate length and NJD, 1-dB compression point is significantly improved as shown in Fig. 10(b) and (c) owing to improved current driving capability of TGRC-MOSFET that enhances g_m and thus 1-dB compression point.

5.2.2. *Intermodulation distortion*

The previous subsection discusses linearity of TGRC-MOSFET and how its linearity improves if the device parameters scale down. In this subsection, distortion due to high order transconductance is studied to examine its efficacy on the performance of TGRC architecture. Fig. 11(a) reflects the variations of third derivative of transconductance (g_{m3}) w.r.t. the V_{gs} for conventional MOSFET, CRC-MOSFET, and TGRC-MOSFET. It is examined from Fig. 11(a) that the TGRC device has lower g_{m3} as compared to the CRC design; due to this lesser distortion is observed. Fig. 11(b) displays the variations of g_{m3}

Please cite this article in press as: A. Kumar, Effect of trench depth and gate length shrinking assessment on the analog and linearity performance of TGRC-MOSFET, Superlattices and Microstructures (2017), http://dx.doi.org/10.1016/j.spmi.2017.05.045

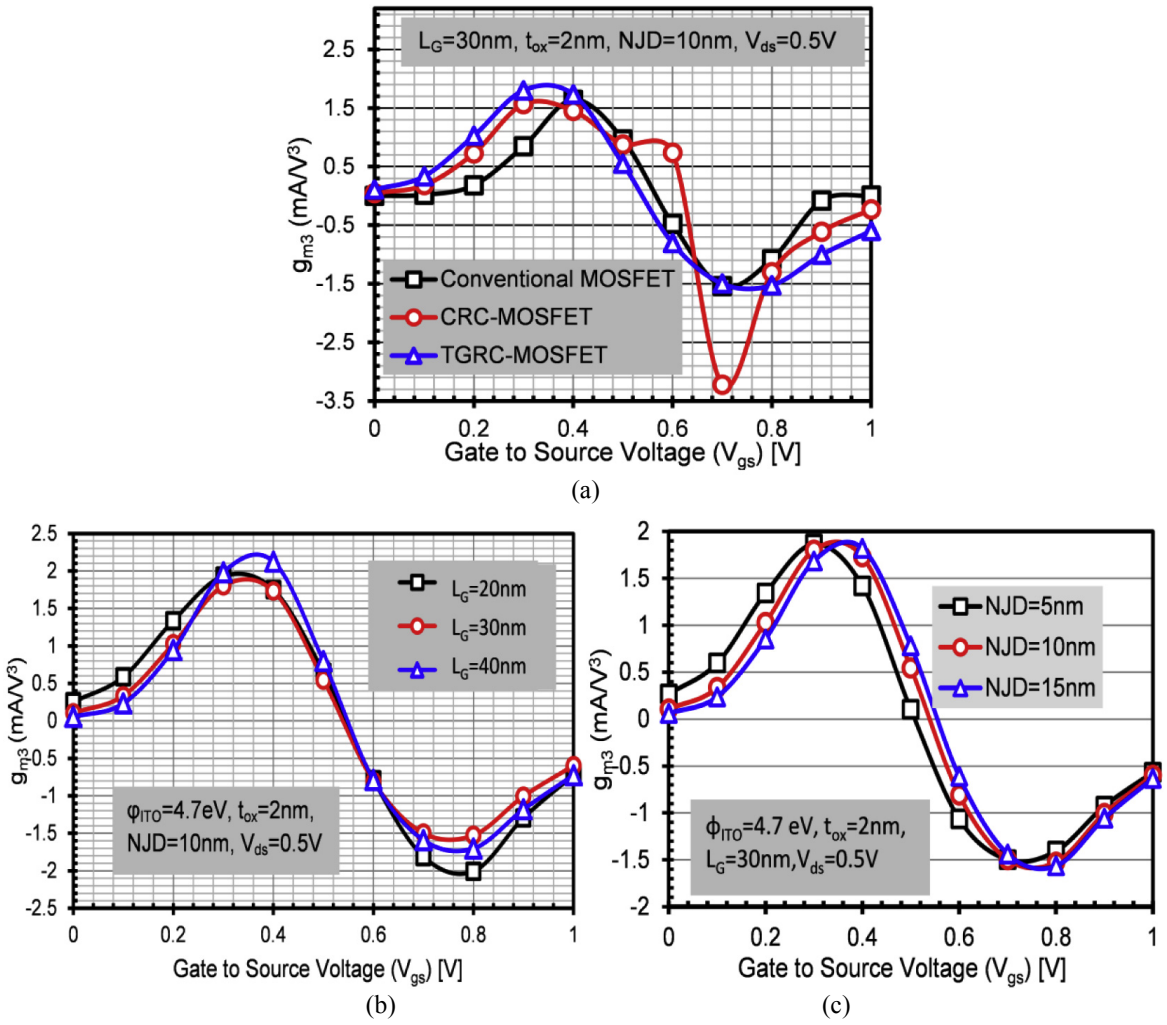

Fig. 11. (a) Variations of g_{m3} for TGRC-MOSFET, CRC-MOSFET, and Conventional MOSFET. (b) Variation of g_{m3} at different L_G. (c) Variation of g_{m3} at various NJDs as a function of applied V_{gs}.

w.r.t. the V_{gs} for three different gate lengths (20 nm, 30 nm, and 40 nm). It is found that the DC bias point moves towards higher V_{gs} with increase in L_G as clearly indicated by Fig. 11(b). This deviation is due to the amalgamation of ITO in TGRC-MOSFET.

Further, the variations of g_{m3} w.r.t. V_{gs} for different NJDs have been observed, and it is analyzed that, if NJD reduces then g_{m3} also reduces which indicates that when NJD is 5 nm, TGRC-MOSFET shows minimum distortion as depicted in Fig. 11(c).

In addition, IMD3 and HD3 (Third-order harmonic distortion) are major issues in linear amplifiers that arise owing to the nonlinearity performance of the device [28]. IMD3 signifies the intermodulation current at which first and third order intermodulation harmonic currents are equal. IMD3 is analyzed considering the effect of the transparent gate. The distortion has been calculated with the help of integral function method (IFM) since this approach allows the distortion extraction from DC measurements without an AC characterization, dissimilar to Fourier-based methods [29,30]. The approximate analytical expression for IMD3 and HD3 are given as:

$$IMD3 = \left(\frac{9}{2} \times (VIP)^3 \times g_{m3}\right)^2 \times R_s \tag{11}$$

$$HD3 = 0.25V_a^2 \frac{\left(\frac{d^2 g_{m1}}{dV_{GT}^2}\right)}{6g_{m1}} \tag{12}$$

Where V_a is the magnitude of AC signal and considered to be very small, of about 50 mV for IFM analysis. Fig. 12(a)–(d) shows the variation of IMD3 and HD3 w.r.t. the applied gate to source voltage for the conventional, CRC and TGRC

Please cite this article in press as: A. Kumar, Effect of trench depth and gate length shrinking assessment on the analog and linearity performance of TGRC-MOSFET, Superlattices and Microstructures (2017), http://dx.doi.org/10.1016/j.spmi.2017.05.045

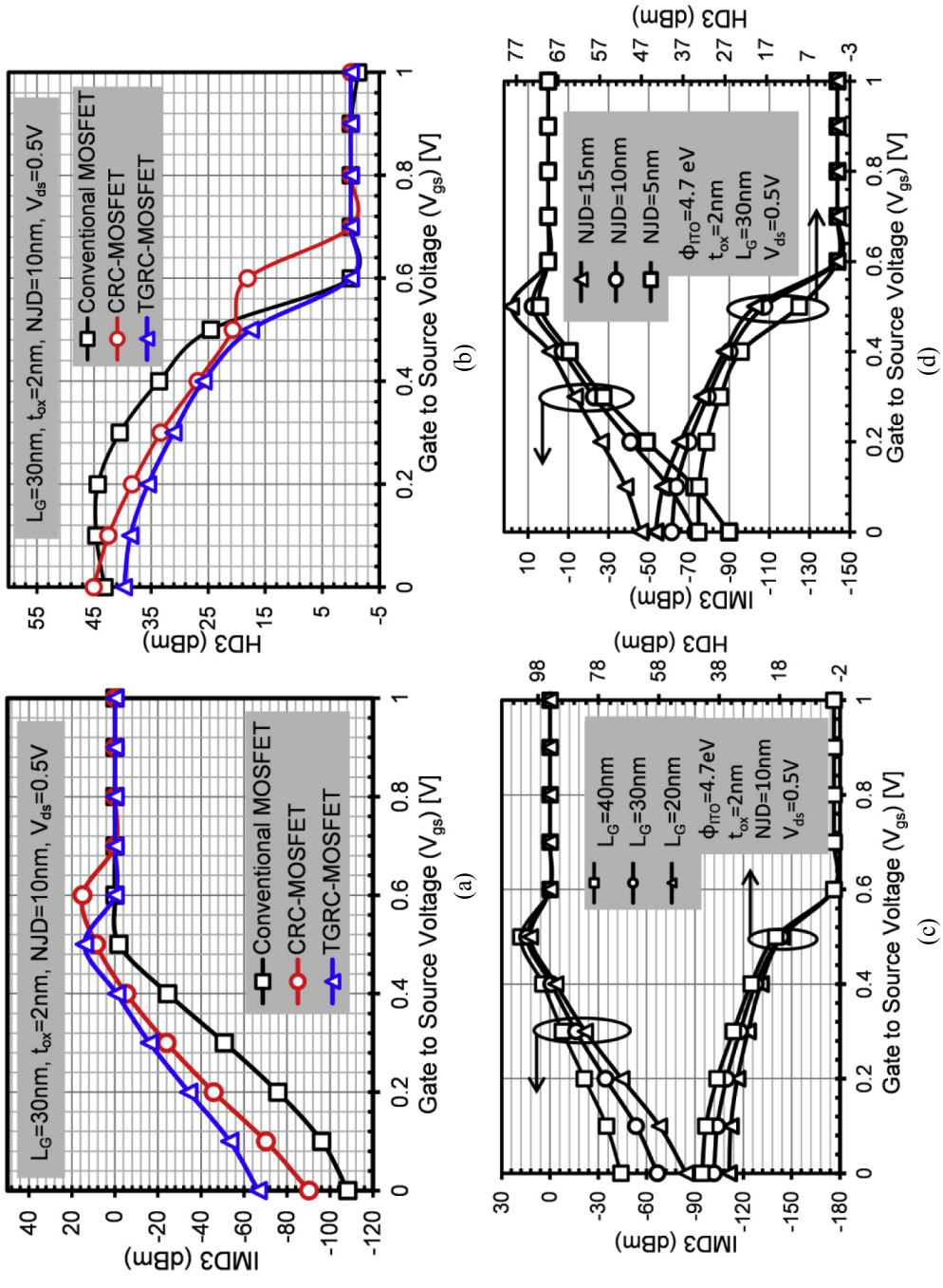

Fig. 12. (a) Variations of IMD3 for TGRC-MOSFET, CRC-MOSFET and Conventional MOSFET. (b) Variation of HD3 for TGRC-MOSFET, CRC-MOSFET, and Conventional MOSFET. (c) Variations of IMD3 and HD3 at different L_G. (d) Variation of IMD3 and HD3 at various NJDs as a function of applied V_{gs}.

Please cite this article in press as: A. Kumar, Effect of trench depth and gate length shrinking assessment on the analog and linearity performance of TGRC-MOSFET, Superlattices and Microstructures (2017), http://dx.doi.org/10.1016/j.spmi.2017.05.045

designs, for gate length variation, and for NJD variation, respectively. Degeneracy of signals in a wireless communication system is originated as IMD3 from the nonlinearity shown by the transistor static characteristics. By using a circuit with balanced topologies even-order harmonics can be reduced by 40–50 dB. Therefore, it is essential to diminish the third-order harmonics for decreasing the signal distortion [31]. Fig. 12(a) shows that the performance of IMD3 degrades in TGRC-MOSFET owing to the high peak value of VIP3 which dominates the value of IMD3 less in comparison to g_{m3} (Fig. 11(a)) as compared to its counterpart conventional and CRC-MOSFET. Meanwhile, HD3 is also reduced in TGRC architecture as compared to its conventional counterparts as shown in Fig. 12(b). Further, both the third order distortions have been reduced for TGRC-MOSFET if the gate length is reduced to 20 nm due to the reduction of g_{m3} as shown in Fig. 12(c). Fig. 12(d) also reflects the reduction in IMD3 and HD3 with reduced NJD. Thus, the scaling of the device architecture reduces the intermodulation and harmonic distortions, hence presenting TGRC-MOSFET as a favorable candidate for RFIC designing.

6. Conclusion

A complete study of the analog, linearity and intermodulation distortion analysis of TGRC-MOSFET has been explored with the impact of trench gate and gate length miniaturization at sub-nano level. From the investigation, it is found that TGRC-MOSFET is more linear device than its counterparts conventional MOSFET and CRC-MOSFET, due to the incorporation of the ITO as a transparent gate in TGRC design. It is found that TGRC-MOSFET reveals greater values of g_m (enhanced by 32.1% and 35% compared to conventional MOSFET and CRC-MOSFET respectively), lower g_{m3}, improved device efficiency and noteworthy improvement in peak values of VIP2, VIP3, 1-dB compression point, IIP3 and lesser values of the IMD3 and HD3 in comparison to its counterparts at 5 nm NJD and 20 nm gate length. Thus, TGRC-MOSFET delivered enriched analog and linearity performance in terms of superior input power and lesser signal distortion. Moreover, it is also analyzed that with the tuning of TGRC's parameters such as L_G and NJD, its linearity performance enhances appreciably owing to enhanced current driving capability and reduced g_{m3} (distortions). Therefore, the proposed TGRC-MOSFET is prominent for high scale integration, which can be developed for RFIC design and it is also a favorable candidate for ultra-low power, analog, and distortion-less application.

Acknowledgement

This work was supported by Microelectronics Research Lab, Department of Engineering Physics and Electrical Engineering Department Delhi Technological University (3507/(OBC)(NET-DEC.2015)).

References

[1] B. Razavi, R. Behzad, RF Microelectronics, Prentice Hall, New Jersey, 1998.
[2] H. Iwai, Roadmap for 22nm and beyond, Microelectron. Eng. 86 (2009) 1520–1528.
[3] R.M. Barsan, Analysis and modeling of dual-gate MOSFET's, Electron Devices IEEE Trans. 28 (1981) 523–534.
[4] X. An, R. Huang, B. Zhao, X. Zhang, Y. Wang, Design guideline of an ultra-thin body SOI MOSFET for low-power and high-performance applications, Semicond. Sci. Technol. 19 (2003) 347.
[5] R. Chaujar, R. Kaur, M. Saxena, M. Gupta, R. Gupta, TCAD assessment of gate electrode workfunction engineered recessed channel (GEWE-RC) MOSFET and its multilayered gate architecture—part I: hot-carrier-reliability evaluation, Electron Devices IEEE Trans. 55 (2008) 2602–2613.
[6] C.P. Auth, J.D. Plummer, Scaling theory for cylindrical, fully-depleted, surrounding-gate MOSFET's, Electron Device Lett. IEEE 18 (1997) 74–76.
[7] N. Gupta, A. Kumar, R. Chaujar, Impact of device parameter variation on RF performance of gate electrode workfunction engineered (GEWE)-silicon nanowire (SiNW) MOSFET, J. Comput. Electron. 14 (2015) 798–810.
[8] S. Veeraraghavan, J.G. Fossum, Short-channel effects in SOI MOSFETs, IEEE Trans. Electron Devices 36 (1989) 522–528.
[9] R. Chaujar, R. Kaur, M. Saxena, M. Gupta, R. Gupta, Laterally amalgamated DUal material GAte concave (L-DUMGAC) MOSFET for ULSI, Microelectron. Eng. 85 (2008) 566–576.
[10] H.T.D.J. Rogers, Criteria Choos. Conduct. 25 (2010).
[11] V. Singh, C. Suman, S. Kumar, Indium Tin Oxide (ITO) films on flexible substrates for organic light emitting diodes, Proc. ASID (2006) 388.
[12] R. Murali, J.D. Meindl, Modeling the effect of source/drain junction depth on bulk-MOSFET scaling, Solid-state Electron. 51 (2007) 823–827.
[13] T. Minami, Transparent conducting oxide semiconductors for transparent electrodes, Semicond. Sci. Technol. 20 (2005) S35–S44.
[14] G.E. Moore, Progress in digital integrated electronics, in: Electron Devices Meeting, 1975, pp. 11–13.
[15] A. Kumar, N. Gupta, R. Chaujar, Analysis of novel transparent gate recessed channel (TGRC) MOSFET for improved analog behaviour, Microsyst. Technol. 22 (11) (2015) 2665–2671.
[16] A. Kumar, N. Gupta, R. Chaujar, Effect of structured parameters on the hot-carrier immunity of transparent gate recessed channel (TGRC) MOSFET, Microsyst. Technol. (2016) 1–8.
[17] A. Kumar, N. Gupta, R. Chaujar, Power gain assessment of ITO based Transparent Gate Recessed Channel (TGRC) MOSFET for RF/wireless applications, Superlattices Microstruct. 91 (2016) 290–301.
[18] A. Kumar, N. Gupta, R. Chaujar, TCAD RF performance investigation of transparent gate recessed channel MOSFET, Microelectron. J. 49 (2016) 36–42.
[19] I. SILVACO, ATLAS User's Manual, Santa Clara, CA, Ver, 5, 2011.
[20] M. Rahimian, A.A. Orouji, Investigation of the electrical and thermal performance of SOI MOSFETs with modified channel engineering, Mater. Sci. Semicond. Process. 16 (2013) 1248–1256.
[21] J. Appenzeller, R. Martel, P. Avouris, J. Knoch, J. Scholvin, J.A. del Alamo, P. Rice, P. Solomon, Sub-40 nm SOI V-groove n-MOSFETs, IEEE Electron Device Lett. 23 (2002) 100–102.
[22] M. Xiao-Hua, H. Yue, S. Bao-Gang, G. Hai-Xia, R. Hong-Xia, Z. Jin-Cheng, Z. Jin-Feng, Z. Xiao-Ju, Z. Wei-Dong, Fabrication and characterization of groove-gate MOSFETs based on a self-aligned CMOS process, Chin. Phys. 15 (2006) 195.
[23] R. Chaujar, R. Kaur, M. Saxena, M. Gupta, R. Gupta, TCAD assessment of Gate Electrode Workfunction Engineered Recessed Channel (GEWE-RC) MOSFET and its multi-layered gate architecture, Part II: analog and large signal performance evaluation, Superlattices Microstruct. 46 (2009) 645–655.

Please cite this article in press as: A. Kumar, Effect of trench depth and gate length shrinking assessment on the analog and linearity performance of TGRC-MOSFET, Superlattices and Microstructures (2017), http://dx.doi.org/10.1016/j.spmi.2017.05.045

[24] T.W. Kim, B. Kim, K. Lee, Highly linear receiver front-end adopting MOSFET transconductance linearization by multiple gated transistors, IEEE J. Solid-State Circuits 39 (2004) 223–229.
[25] K. Jeong, A.B. Kahng, A power-constrained MPU roadmap for the International Technology Roadmap for Semiconductors (ITRS), in: SoC Design Conference (ISOCC), 2009 International, IEEE, 2009, pp. 49–52.
[26] R. Wang, J. Zhuge, R. Huang, Y. Tian, H. Xiao, L. Zhang, C. Li, X. Zhang, Y. Wang, Analog/RF performance of Si nanowire MOSFETs and the impact of process variation, IEEE Trans. Electron Devices 54 (2007) 1288–1294.
[27] P.H. Woerlee, M.J. Knitel, R. Van Langevelde, D.B. Klaassen, L.F. Tiemeijer, A.J. Scholten, A.T. Zegers-van Duijnhoven, RF-CMOS performance trends, IEEE Trans. Electron Devices 48 (2001) 1776–1782.
[28] N. Gupta, R. Chaujar, Optimization of high-k and gate metal workfunction for improved analog and intermodulation performance of Gate Stack (GS)-GEWE-SiNW MOSFET, Superlattices Microstruct. 97 (2016) 631–641.
[29] A. Cerdeira, M.A. Alemán, M. Estrada, D. Flandre, Integral function method for determination of nonlinear harmonic distortion, Solid-State Electron. 48 (2004) 2225–2234.
[30] R.T. Doria, A. Cerdeira, J.-P. Raskin, D. Flandre, M.A. Pavanello, Harmonic distortion analysis of double gate graded-channel MOSFETs operating in saturation, Microelectron. J. 39 (2008) 1663–1670.
[31] P. Ghosh, S. Haldar, R. Gupta, M. Gupta, An investigation of linearity performance and intermodulation distortion of GME CGT MOSFET for RFIC design, IEEE Trans. Electron Devices 59 (2012) 3263–3268.
[32] D. Kim, Y. Han, J.-S. Cho, S.-K. Koh, Low temperature deposition of ITO thin films by ion beam sputtering, Thin Solid Films 377 (2000) 81–86.

Please cite this article in press as: A. Kumar, Effect of trench depth and gate length shrinking assessment on the analog and linearity performance of TGRC-MOSFET, Superlattices and Microstructures (2017), http://dx.doi.org/10.1016/j.spmi.2017.05.045

Electronic properties and migration pathways of Cl functionalized zigzag graphene nanoribbons

Neeraj K. Jaiswal, Amit Kumar, Neha Tyagi, and Pankaj Srivastava

Citation: AIP Conference Proceedings **1832**, 090004 (2017); doi: 10.1063/1.4980557
View online: http://dx.doi.org/10.1063/1.4980557
View Table of Contents: http://aip.scitation.org/toc/apc/1832/1
Published by the American Institute of Physics

Electronic Properties and Migration Pathways of Cl Functionalized Zigzag Graphene Nanoribbons

Neeraj K. Jaiswal[*1], Amit Kumar[1], Neha Tyagi[2] and Pankaj Srivastava[3]

[1]*Discipline of Physics, Indian Institute of Information Technology, Design & Manufacturing, Jabalpur- India*
[2]*Department of Applied Physics, Delhi Technological University, Delhi-India*
[3]*Nanomaterials Research Group, ABV-Indian Institute of Information Technology & Management, Gwalior-India*

[*]*Corresponding Author: neerajkjaiswal@gmail.com*

Abstract. We have investigated the electronic properties of pristine and Cl functionalized zigzag graphene nanoribbons (ZGNR) by employing density functional theory (DFT) based calculations. The migration pathways of Cl adatom adsorption on Cl functionalized ZGNR are also discussed. It is revealed that Cl functionalization results in additional electronic states across the Fermi level which enhances the metallic character of ZGNR. Interestingly, it is predicted that migration of Cl adatom on ZGNR network is most likely to take place along the ribbon edges whereas migration across the ribbon width is found least energetically favorable.

Keywords: Graphene, nanoribbons, halogen, adsorption.
PACS: 71.15.Nc, 71.20.-b, 73.22.Pr

INTRODUCTION

Being first layered material and exhibiting unique chemical bonding of C, graphene is still dominating other 2-D materials [1]. However, some inorganic layered materials have also been explored [2, 3], but none of them could attract enough attention similar to graphene. Various techniques of synthesizing graphene [4] and the existence of sophisticated characterization have ignited the research to explore its potential for organic electronic application. Efforts have been made to use deliberate addition of impurities and various defects to tailor their properties [5, 6]. Previously, transition metal impurities were investigated in zigzag GNR (ZGNR) as well as in armchair GNR (AGNR) which predicted enhanced metallicity in GNR [7, 8]. Mao *et al.,* studied the adsorption of K on GNR [9]. It is worth to notice that most of the studies till date are devoted to ZGNR (passivated with H) due to their magnetic ground state. On the other hand, investigations on the functionalization with other elements are still limited. Halogens exhibit larger electro-negativity than that of H and are expected to form stable bonds with C. Therefore it would be interesting to study the functionalization of ZGNR with halogens. In the present work we have investigated functionalization of ZGNR with halogen taking Cl as a typical representative. Further, the migration pathways of Cl adatom adsorption are also discussed in Cl passivated edges of the ribbons.

METHODOLOGY

Density functional theory (DFT) based ab-initio approach has implemented to investigate the functionalization of AGNR via Cl adatoms using ATK-VNL package. We considered ZGNR having with N_Z= 4 and 6 to consider the width effects. The schematic of defining the nanoribbon width is depicted in Fig. 1. Supercell models, having periodicity along Z axis and confined in X and Y directions, were employed in the present study. The energy mesh cut off value equal to 70 Rydberg and k-point sampling of 1×1×50 was considered for the optimization of the structures. To calculate the electronic band structures and density of state (DOS) profiles, a dense grid of 1×1×100 was utilized. The exchange and correlation was accounted with the help of generalized gradient approximation (GGA) in the Perdew-Burke-Ernzerhof (PBE) form [10].

DAE Solid State Physics Symposium 2016
AIP Conf. Proc. 1832, 090004-1–090004-3; doi: 10.1063/1.4980557
Published by AIP Publishing. 978-0-7354-1500-3/$30.00

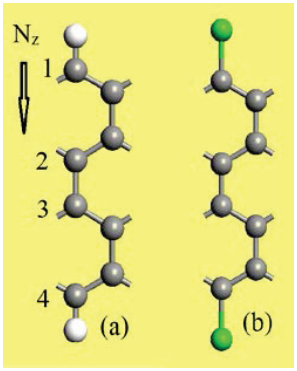

Fig. 1: The schematics of (a) pristine and (b) Cl passivated ZGNR (N_z =4). The grey, white and green spheres represent C, H and Cl atoms respectively

The artificial Coulombian interactions were avoided using 10 Å vacuum padding along non periodic directions. Norm conserving preudopotential and the double zeta polarized basis set has been employed in the present calculations.

RESULTS AND DISCUSSIONS

We have investigated the electronic properties of ZGNR functionalized with Cl. The considered ZGNR are shown in Fig. 2. To reveal the structural stabilities of the considered ribbons, binding energy (BE) analysis were performed. The BE per unit cell is calculated as $BE = E_T - nE_C - 2E_{Cl}$, where E_T, nE_C and E_{Cl} respectively represent total energies of the unit cell, isolated C atom and isolated Cl atom respectively. n is the number of C atoms in the unit cell and the coefficient 2 has been placed because there are two passivating Cl atoms (one at each edge of the ribbon) in a unit cell. The calculated BE values between ZGNR and the passivating Cl atoms are found to be -4.45 eV irrespective of the ribbon width which shows that Cl passivated ZGNR form stable geometries. The negative sign indicates that Cl passivation is exothermic in nature. Interestingly, Cl passivated ZGNR exhibit nonmagnetic (NM) ground state unlike pristine ribbons which prefer antiferromagnetic coupling between opposite edges. The electronic band structures of considered nanoribbons [Fig. 2] reveals that Cl passivated ZGNR are metallic in nature. Pristine (H-passivated) ribbon is also depicted for comparison basis. The corresponding DOS profiles as shown in Fig. 2(c)-(d) exhibit availability of electronic states across the Fermi level which further supports their metallic character.

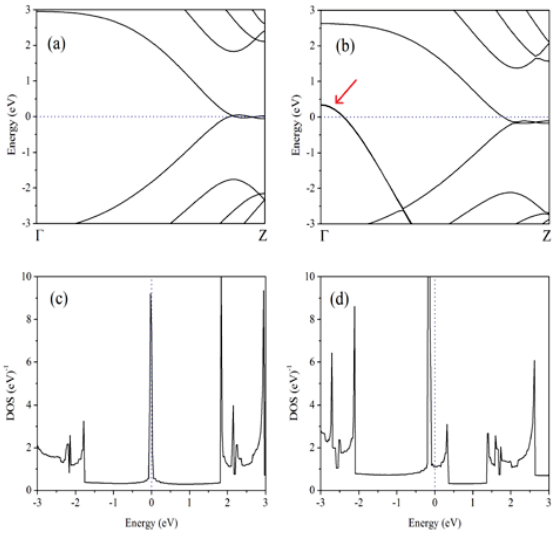

Fig. 2: The electronic band structures for (a) Pristine, (b) Cl-passivated ZGNR and density of states profiles for (c) Pristine and (d) Cl-passivated ZGNR. The Fermi level is set at 0 eV.

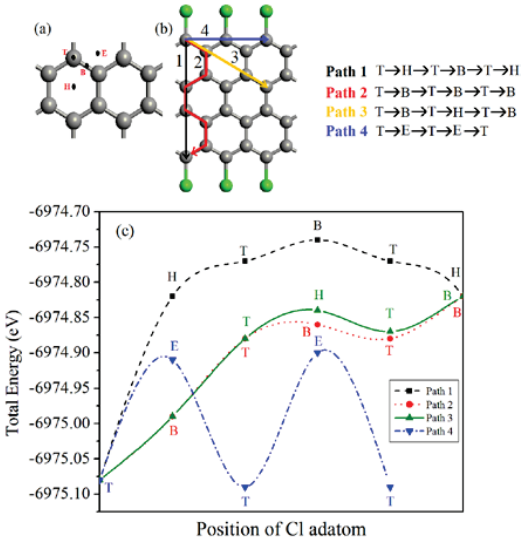

Fig. 3: (a) The considered adsorption sites (b) schematic of migration pathways and (c) migration of Cl adatom along various pathways.

Next, the migration paths of adsorbed Cl atom were explored to understand the effect of ribbon edges and feasibility of adatom (Cl) migration on ZGNR along various possible paths as shown in Fig. 3. The optimized heights of Cl adatom for T, B, H and E sites were found to be 2.6 Å, 2.6 Å, 2.8 Å and 2.6 Å respectively. It is observed that path 4 is the most preferred migration path for the adsorbed adatom.

On the other hand, the migration is least likely to take place along the ribbon width i.e. path 2. Further, pathways 2 and 3 do not have significant energy difference and are almost equally approachable. It is revealed that the energy difference between initial (T) and next (E) site of the most probable migration path is ~160 meV which is sufficiently higher than the room temperature excitation energy (25 meV). Therefore, the adsorption of Cl adatom on ZGNR is expected to be immune against migration at the room temperature.

CONCLUSIONS

DFT based ab-initio approach has been employed to study the electronic properties and migration pathways of Cl passivated ZGNR. It is noticed that Cl passivated ZGNR exhibit NM metallic character. Edge of the ribbon is regarded as the most preferred migration path amongst all considered pathways. However, the energy difference between adjacent sites suggests its immunity against migration of adsorbed Cl adatom at room temperature.

ACKNOWLEDGMENTS

This work was funded by DST-SERB Young Scientist Research Grant number **SB/FTP/PS-101/2014.** Authors are thankful to Indian Institute of Information Technology & Management Gwalior for providing Computational facilities.

REFERENCES

1. K. S. Novoselov , A. K. Geim, S. V. Morozov, D. Jiang, Y. Zhang, S. V. Dubonos, I. V. Grigorieva and A. A. Firsov, *Science* **306** (2004) 666-669.
2. P. Srivastava, N. K. Jaiswal and V. Sharma, *Microelectron. Eng.* **146** (2015) 62-67.
3. P. Liang, Y. Liu, S. Xing, H. Shu and B. Tai, *Solid State Commun.* **226**(2016) 19-24.
4. P. Nemes-Incze, L. Tapasztó, G. Z. Magda, Z. Osváth, G. Dobrik, X. Jin, C. Hwang and L. P. Biró, *Appl. Surf. Scie.* **291**(2014) 48-52.
5. Y. Wang, C. Cao and H. P. Cheng, *Phys. Rev. B* **82**(2010) 205429-1-5.
6. J. Zhao, H. Zeng, J. Wei, B. Li and D. Xu, *Phys. Lett. A* **378** (2014), 416-420.
7. N. K. Jaiswal and P. Srivastava, *Physica E* **54** (2013) 103-108.
8. N. Tyagi, N. K. Jaiswal, and P. Srivastava, *Mater. Today: Proceedings* **3** (2016) 2241-2246.
9. Y. Mao, W. Hao, X. Wei, J. Yuan and J. Zhong, *Appl. Surf. Sci.* **280** (2013) 698-704.
10. J. P. Perdew, K. Burke and M. Ernzerhof, *Phys. Rev. Lett.* **77** (1996) 3865-1-3865-4.

Applied Thermal Engineering 121 (2017) 1070–1079

Contents lists available at ScienceDirect

Applied Thermal Engineering

journal homepage: www.elsevier.com/locate/apthermeng

Research Paper

Energy and performance analysis of multi droplets shower cooling tower at different inlet water temperature for air cooling application

Mohammad Zunaid [a,*], Qasim Murtaza [b], Samsher Gautam [a]

[a] Department of Mechanical Engineering, Delhi Technological University, Bawana Road, Delhi 110042, India
[b] Department of Mechanical Engineering, Aligarh Muslim University, Aligarh 202002, India

HIGHLIGHTS

- Shower cooling tower can be used in hot and dry climates for human comfort.
- Ten different diameters water droplets are used for study.
- Rosin Rammler distribution is used to distribute ten different diameter droplets.
- As inlet water temperature increases shower cooling tower efficiency increases.
- Maximum amount of exergy of system destroy at the top of shower cooling tower.

ARTICLE INFO

Article history:
Received 26 August 2016
Revised 21 March 2017
Accepted 30 April 2017
Available online 3 May 2017

Keywords:
Shower cooling tower
Energy destruction
Multi droplets
Varying droplet diameter
Heat and mass transfer
Water temperature

ABSTRACT

This study present development of the two-dimension numerical model in MATLAB, in which mass, momentum, energy, exergy and water droplet trajectory equations are solved simultaneously for predicting the exit conditions of air and water for human comfort. Experimental data obtained from shower cooling tower (SCT) are used to validate numerical model. Ten different diameters water droplet are analyzed. The Rosin Rammler distribution is used to distribute ten different diameter droplets. In the parametric study, inlet water droplets temperature plays a significant role in water droplets and air exit temperature, the efficiency of SCT, convective and evaporative exergy of air, exergy of water and total exergy destruction of the system. Results show the efficiency of SCT increases with increase in the inlet water temperature and largest part of total exergy of the system destroyed at the top of SCT. The mathematical model developed has potential application in producing exit condition of air and water for human comfort.

© 2017 Elsevier Ltd. All rights reserved.

1. Introduction

Water sprays extensively used in several engineering applications, such as duct control, firefighting and nuclear reactor core cooling. The general disadvantage of the conventional cooling tower is fouling due to salt decomposition on the fills, and it is a major source of cooling tower performance deterioration. Replacement and cleaning of fills are tough. Therefore, to overcome these disadvantages, SCT has been developed where fills are eliminated entirely, and small water droplets replace the fill as the mode of simultaneous heat and mass transfer. For producing the comfortable indoor environment, SCT can be used for evaporative cooling of air in residential and commercial buildings when the weather is hot and dry. A 2-D mathematical model has been developed in MATLAB, in which mass, momentum, energy, exergy and multi droplets trajectories equation are solved simultaneously for predicting the exit conditions of air and water for human comfort. Air and water exergy variation has also been studied to explain the functioning of forced draft SCT. Multi droplet approach is advantageous over single droplet analysis as it is more close to experimental results.

Several works have reported their finding based on the conventional cooling tower. Muangnoi et al. [1] studied water jet cooling tower and validated their simulation results from experimental data. They observed that evaporation of water droplets influence the performance of cooling tower. Terblanche et al. [2] measured drop size distribution photographically below three different counter-flow wet-cooling tower fills. It observed that an increase in water mass velocity results in slightly larger Sauter means drop diameters. Nuyttens et al. [3] developed a test rig and protocol for the characterization of spray nozzles using a phase doppler particle analyzer (PDPA). This test rig was able to measure droplet sizes and

* Corresponding author.
E-mail addresses: mzunaid3k@gmail.com (M. Zunaid), qasimmurtaza@gmail.com (Q. Murtaza), sam6764@yahoo.com (S. Gautam).

http://dx.doi.org/10.1016/j.applthermaleng.2017.04.157
1359-4311/© 2017 Elsevier Ltd. All rights reserved.

Nomenclature

A	cross section area of test section (m^2)
A_s	surface area of droplet (m^2)
C_d	coefficient of drag
D_c	cross-sectional diameter of SCT (m)
d_n	outlet orifice diameter of nozzle (m)
g	gravitational force (m/s^2)
h	Specific enthalpy (kJ/kg)
h_{fg}	specific enthalpy of evaporation (kJ/kg)
h_g	specific enthalpy of saturated vapour (kJ/kg)
I	exergy destruction of system (W)
m	mass flow rate (kg/s)
R	drag force (N)
R_v	gas constant per unit molecular weight of water vapour (J/kg K)
S_g	specific entropy of saturated vapour (kJ/kg K)
T	Temperature (°C)
U	drop velocity (m/s)
X	exergy (W)
A_n	outlet orifice area of nozzle (m^2)
c	specific heat (kJ/kg K)
D	droplet diameter (m)
dm_d	change in mass flow rate of water vapour (kg/s)
E	internal energy (kJ/kg)
H	Height of SCT (m)
h_f	specific enthalpy of saturated water (kJ/kg)
$h_{fg,0}$	specific enthalpy of evaporation at 0 °C (kJ/kg)
h_m	mass transfer coefficient (kg/m^2 s)
Le_f	Lewis factor
N	number of droplets
q	heat transfer (kJ/kg)
R_a	gas constant for per unit molecular weight of dry air (J/kg K)
S_f	specific entropy of saturated water (kJ/kg K)
u	velocity (m/s)
W	relative velocity of drop w.r.t. air (m/s)

Greek letters

ρ	density (kg/m^3)
ϕ	relative humidity of air (%)
θ	inclination of water droplet from horizontal
η_{II}	second law efficiency (%)
ω	specific humidity (kg_w/kg_a)
ϕ_0	ambient humidity
η_{th}	thermal efficiency (%)

Subscripts

00	environment
a	air
c	convective
e	evaporative
l	evaporative loss
out	outlet
t	total
v	vapour
x	horizontal coordinate
0	restricted dead state
av	air vapour mixture
d	droplet
in	Inlet
m	Mean
p	Pressure
s	Saturated
w	Water
y	vertical coordinate

Abbreviations

DBT	dry bulb temperature
SCT	shower cooling tower
RLG	water to air mass flow ratio
SLE	second law efficiency

velocities based on light-scattering principles. It has been observed that nozzle type as well as nozzle size have an important effect on droplet size as well as on velocity spectra. Naphon [4] studied experimentally and theoretically about heat transfer characteristics of the cooling tower with water mass flow 0.01–0.07 kg/s, and 0.04–0.08 kg/s, respectively. The inlet air and inlet water temperatures were 23 °C, and 30–40 °C respectively. Kloppers and Kroger [5] gave a detailed procedure to solve the governing equations with their unique requirements for heat and mass transfer equations of evaporative cooling in wet-cooling towers. Xiaoni et al. [6] conducted the study on the cooling tower without fill packing and found that small Sauter mean droplet diameter is desirable for high performance of SCT. Qi et al. [7] designed tower with no tower packing and observed that both equivalent diameter of inlet water droplets and the initial air velocity affect the outlet water temperature. In a study of SCT, Yajima and Givoni [8] observed about 7 °C drop in DBT at the maximum ambient temperature. Givoni [9] developed a shower tower and compared its performance and found that system provided effective cooling even in an extreme desert climate. Pearlmutter et al. [10] developed and monitored a small-scale down draft evaporative cool tower in arid Negev Highlands of southern Israel. The results prove that there is a scope for substantial temperature reduction in the order of 10 °C under summer daytime conditions. Farnham et al. [11] carried out experiments by spraying water from varying heights in a large atrium and found that a single spray nozzle with Sauter mean droplet diameter of 41 μm can provide cooling of 0.7 K. Kachhwaha et al. [12] developed two-dimensional straightforward and efficient numerical model and observed that DBT decreases up to 9 °C by employing evaporative cooling during dry summer months. Kumar et al. [13] studied evaporative cooling of air by water sprays for two ambient conditions, viz., hot-dry and hot-humid, covering DBT from 35 to 47 °C, and relative humidity 10 – 60%. Kumar et al. [14] in another work have reported development of 1-D parallel flow heat and mass transfer model to solve air and water spray interaction for different combinations of drop diameter, air velocities, DBT and specific humidity. By using an optimum number of categories and velocity sub-classes, reasonably accurate predictions can be obtained with less computation time. Qureshi and Zubair [15] investigated full cooling tower which consists of three zones; namely, spray zone, filling and rain zones. In the cooling tower, a significant portion of the total heat rejected may occur in the spray and rain zones and fouling is a primary cause of cooling tower performance deterioration. Cui et al. [16] concluded that the droplet diameter had a great impact on the droplet temperature distribution and thermal performance of cooling tower. Bejan [17] expressed total exergy of air as the sum of convective and evaporative exergy of air. Sirok et al. [18] investigated that efficiency of cooling tower decreases with increase in the water to air mass flow ratio. Rotar et al. [19] presented experimental and numerical analysis of the natural-draft cooling tower. They sensed that the fill system mainly reduces the air mass flow rate, which results in a lower heat and mass-transfer from the water to the air.

Blain et al. [20] reported that the cooling tower approach are decreasing with increase in the ratio of mass flux of air to liquid. Huan et al. [21] observed that the heat rejection of cooling tower increases with increase in the crosswind velocity. Nasrabadi et al. [22] investigated that range of cooling tower decreases with decrease in the inlet water temperature. Sirena et al. [23] reported that the cooling tower efficiency increases with increase in the RLG. Jiang et al. [24] developed a closed wet cooling tower and investigated that the thermal efficiency of cooling tower got remarkably modified with change in the inlet water temperature and inlet air flow rate. Asvapoositkul et al. [25] developed a cooling tower model and analyzed that cooling tower range increased with increase in the inlet water temperature. Keshtkar [26] optimized cooling tower performance and found that the outlet water temperature of cooling tower increases with increase in the RLG. Singh and Das [27] studied mechanical draft cooling tower and found that heat rejection by water increases with increase in the inlet air flow rate. Gonzalez-Tello et al. [28], Lefebvre [29] and Masters [30] reported that the Rosin–Rammler distribution is most commonly used function for particle size distribution of spray droplets. Zunaid et al. [31,32] reported total exergy of air controlled by its convective and evaporative exergy, and evaporative exergy of air are major component present in total exergy of air. Murtaza et al. [33] found that the air enhances the break-up of the liquid sheet from an atomizer; air also disperses droplets and prevents its collision. Fisenko et al. [34] reported as water droplet diameter increases cooling tower outlet water temperature decreases.

The experimental and simulation studies to understand the heat and mass transfer phenomenon in the conventional cooling tower are sufficiently available in the literature. However, very limited published research on SCT can be seen. Simplicity and low maintenance of SCT motivated us to undergo an in-depth study to correlate heat and mass transfer analysis and to determine the factors which govern the performance of SCT. To the best of our knowledge no reports are available for multi-droplet diameter and air interaction analysis to predict the SCT performance for air cooling application till date.

In the present work heat and mass transfer model for multi-diameter droplets and air interaction in downward vertical parallel flow configuration in which diameter of water droplets are varying along the height of SCT has been developed in MATLAB. A parametric study has been performed to determine the effect of variation in inlet water droplet temperature along SCT height. Spray air model is represented by the differential equation of mass, momentum, and energy of multi droplets. The results from the experimental study have used for validation of numerical results.

2. Experimental facility

In this experiment downdraft parallel flow SCT is used as shown in Fig. 1. In this system the atmospheric air and multi droplets of water from impaction pin nozzles enter and mix at the top of the tower. During mixing of air and water droplets, air cools down by convective and evaporative heat transfer and leaves at the bottom of the SCT. Nozzle orifice diameter, pressure, nozzle discharge and nozzle exit water velocity were measured, and the results are given in Table 1. At the exit of SCT, air and water properties were measured.

3. Mathematical model

To describe the motion characteristics of the water droplets in mathematical model some critical simplifying assumptions concerning the water droplet was made. It was assumed that the water droplet is spherical in shape, and droplet temperatures are uniform. The possibility of collision or scattering of the water droplet during the motion process is neglected. The mass, momentum, and energy conservation equations for varying diameter of water droplets and air are derived with the help of Kloppers and Kroger [5], Xiaoni and Zhenyan [6] and Masters [30]. The thermal efficiency of cooling tower was derived with the help of Fisenko et al. [34]. The equations for air exergy, water exergy, system exergy, exergy destruction and second law efficiency were derived with the help of Bejan [17]. Mass flow of air is constant at the inlet of tower however velocity of air varying along the length of tower with varying its density. The following analysis considers the property variations in the vertical direction. The SCT height is divided into 'n' sections of finite thickness and finite volume.

3.1. Conservation of mass for water droplet

For drop of category '*i*', a control volume for air water droplet is shown in Fig. 2.

$$(m_{d,i})_{in} = (m_{d,i})_{out} + \frac{dm_{d,i}}{dy}dy \tag{1}$$

where mass flow rate of water is given as '$m_{d,i}$' = $N_i \cdot M_{d,i}$, here '$M_{d,i}$' is mass of single droplet.

$$\frac{dM_{d,i}}{dt} = -h_{m,i}(\omega_{s,i} - \omega_a)A_{s,i} \tag{2}$$

where $A_{s,i} = \pi D_i^2$ and '$\omega_{s,i}$' = specific humidity of water vapour at the drop surface.

$$\frac{dM_{d,i}}{dy} = -\frac{h_{m,i}}{U_{y,i}}(\omega_{s,i} - \omega_a)A_{s,i} \tag{3}$$

Since, $M_{d,i} = \frac{1}{6}\pi D_i^3 \rho_w$, then,

$$\frac{1}{6}\pi\rho_w \frac{d}{dy}\left(D_i^3\right) = -\frac{h_{m,i}}{U_{y,i}}(\omega_{s,i} - \omega_a)\pi D_i^2 \tag{4}$$

Variation of droplet diameter with tower height can be written as:

$$\frac{d(D_i)}{dy} = -\frac{2h_{m,i}}{U_{y,i}\rho_w}(\omega_{s,i} - \omega_a) \tag{5}$$

3.2. Conservation of momentum for water droplet

$$\text{Rosin Rammler function, } RR = 1 - \exp\left(-\left(\frac{D}{D_m}\right)^{uc}\right) \tag{6}$$

where 'D_m' is characteristic droplet size and 'uc' is uniformity constant.

For drop of category '*i*',

$$\text{Gravitational force, } G_i = M_{d,i}g = \frac{\pi D_i^3 \rho_w g}{6} \tag{7}$$

$$\text{Buoyancy force, } F_i = \frac{\pi D_i^3 \rho_a g}{6} \tag{8}$$

$$\text{Drag force, } R_i = \frac{\pi C_{d,i}\rho_a W_i^2 D_i^2}{8} \tag{9}$$

Velocities of droplet in *xandy* directions are given as:

$$W_{x,i} = W_i \cos\theta \tag{10}$$

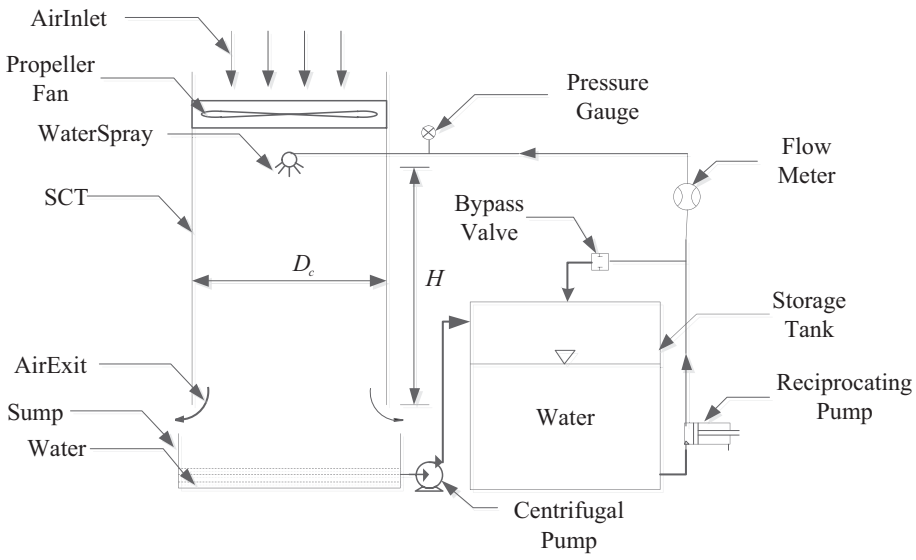

Fig. 1. Parallel flow downdraft evaporative SCT.

Table 1
Discharge characteristic of the nozzle.

Nozzle outlet orifice diameter (m)	Nozzle pressure (bar)	Discharge (l/min)	Nozzle exit water velocity (m/s)
2.03×10^{-3}	2	3.4	17.7
	3	4.2	21.7
	4	4.9	25.1

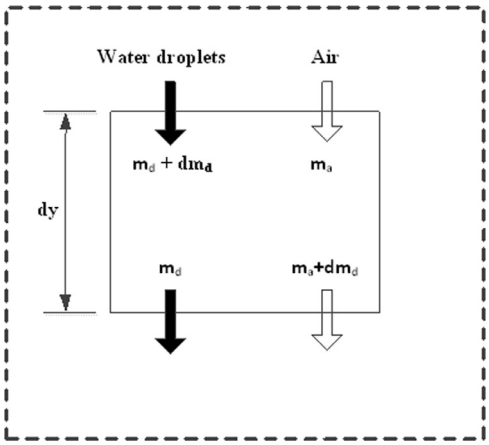

Fig. 2. Control volume for mass flow along tower height.

$$W_{y,i} = W_i \sin\theta \tag{11}$$

Resultant velocity of droplet and its inclination angle 'θ' from horizontal and it is given as:

$$W_i = \sqrt{(U_{y,i} - u_a)^2 + U_{x,i}^2} \tag{12}$$

$$\theta = \tan^{-1}\left(\frac{W_{y,i}}{W_{x,i}}\right) = \tan^{-1}\left(\frac{U_{y,i} - u_a}{U_{x,i}}\right) \tag{13}$$

Now the drag force in the *xandy* directions respectively we get:

$$R_{x,i} = R_i \frac{W_{x,i}}{W_i} = \frac{1}{8}\pi\rho_a C_{d,i} W_i D_i^2 W_{x,i} \tag{14}$$

$$R_{y,i} = R_i\left(\frac{W_{y,i}}{W_i}\right) = \frac{1}{8}\pi\rho_a C_{d,i} W_i D_i^2 W_{y,i} \tag{15}$$

For drop of category '*i*', the variation in momentum of the droplet in horizontal direction with tower height is expressed as:

$$\frac{d(M_{d,i}U_{x,i})}{dt} + \frac{\pi C_{d,i}\rho_a W_i D_i^2 W_{x,i}}{8} = 0 \tag{16}$$

Multiply and divide LHS of above equation by *dy*

$$\frac{d(M_{d,i}U_{x,i})}{dt} \times \frac{dy}{dy} + \frac{\pi C_{d,i}\rho_a W_i D_i^2 W_{x,i}}{8} = 0 \tag{17}$$

$$\frac{d(M_{d,i}U_{x,i})}{dy} + \frac{\pi C_{d,i}\rho_a W_i D_i^2 W_{x,i}}{8U_y} = 0 \tag{18}$$

Differentiate above equation with respect to *y*

$$M_{d,i}\frac{dU_{x,i}}{dy} + U_{x,i}\frac{dM_{d,i}}{dy} = -\frac{\pi C_{d,i}\rho_a W_i D_i^2 W_{x,i}}{8U_{y,i}} \tag{19}$$

$$\frac{\pi\rho_w D_i^3}{6}\frac{dU_{x,i}}{dy} + U_{x,i}\frac{\pi\rho_w}{6}\frac{dD_i^3}{dy} = -\frac{\pi C_{d,i}\rho_a W_i D_i^2 W_{x,i}}{8U_y} \tag{20}$$

$$\frac{\pi\rho_w D_i^3}{6}\frac{dU_{x,i}}{dy} = -\frac{\pi C_{d,i}\rho_a W_i D_i^2 W_{x,i}, i}{8U_y} - U_{x,i}\frac{\pi\rho_w}{6}\frac{dD_i^3}{dy} \tag{21}$$

$$\frac{dU_{x,i}}{dy} = -\frac{6}{\pi\rho_w D_i^3}\left[\frac{\pi C_{d,i}\rho_a W_i D_i^2 W_{x,i}, i}{8U_y} + U_{x,i}\frac{\pi\rho_w}{6}\frac{dD_i^3}{dy}\right] \tag{22}$$

Now conserving momentum for droplet in horizontal direction yield the variation of horizontal component of droplet velocity in *x* direction with height is.

$$\frac{dU_{x,i}}{dy} = -\frac{3\rho_a C_{d,i} W_i W_{x,i}}{4\rho_w D_i U_{y,i}} - \frac{3U_{x,i}}{D_i}\frac{dD_i}{dy} \tag{23}$$

For drop of category '*i*', variation in momentum of droplet in vertical direction with tower height is expressed as:

$$\frac{d(M_{d,i}U_{y,i})}{dt} = M_{d,i}g - \frac{\pi\rho_a g D_i^3}{6} - \frac{\pi C_{d,i}\rho_a W_i^2 D_i^2}{8}\frac{W_{y,i}}{W_i} \tag{24}$$

Multiply and divide LHS of above equation by *dy*

$$\frac{d(M_{d,i}U_{y,i})}{dt}\times\frac{dy}{dy}=M_{d,i}g-\frac{\pi\rho_a gD_i^3}{6}-\frac{\pi C_{d,i}\rho_a W_i^2 D_i^2}{8}\frac{W_{y,i}}{W_i} \tag{25}$$

$$\frac{d(M_{d,i}U_{y,i})}{dy}=\frac{M_{d,i}g}{U_{y,i}}-\frac{\pi\rho_a gD_i^3}{6U_{y,i}}-\frac{\pi C_{d,i}\rho_a W_i D_i^2 W_{y,i}}{8U_{y,i}} \tag{26}$$

Differentiate above equation with respect to y

$$M_{d,i}\frac{dU_{y,i}}{dy}+U_{y,i}\frac{dM_{d,i}}{dy}=\frac{M_{d,i}g}{U_{y,i}}-\frac{\pi\rho_a gD_i^3}{6U_{y,i}}-\frac{\pi C_{d,i}\rho_a W_i D_i^2 W_{y,i}}{8U_{y,i}} \tag{27}$$

$$\frac{\pi\rho_w D_i^3}{6}\times\frac{dU_{y,i}}{dy}+U_{y,i}\frac{\pi\rho_w}{6}\frac{dD_i^3}{dy}=\frac{\pi\rho_w D_i^3 g}{6U_{y,i}}-\frac{\pi\rho_a gD_i^3}{6U_{y,i}}-\frac{\pi C_{d,i}\rho_a W_i D_i^2 W_{y,i}}{8U_{y,i}} \tag{28}$$

$$\frac{\pi\rho_w D_i^3}{6}\times\frac{dU_{y,i}}{dy}=\frac{\pi\rho_w D_i^3 g}{6U_{y,i}}-\frac{\pi\rho_a gD_i^3}{6U_{y,i}}-\frac{\pi C_{d,i}\rho_a W_i D_i^2 W_{y,i}}{8U_{y,i}}-\frac{3\pi\rho_w U_{y,i}D_i^2}{6}\frac{dD_i}{dy} \tag{29}$$

$$\frac{dU_{y,i}}{dy}=\left[g(\rho_w-\rho_a)-\frac{3C_{d,i}\rho_a WW_{y,i}}{4D_i}\right]\frac{1}{\rho_w U_{y,i}}-\frac{3U_{y,i}}{D_i}\frac{dD_i}{dy} \tag{30}$$

3.3. Conservation of energy for water droplet

For '*ith*' category of droplet, Energy balance on control surface surrounding the water droplet yields following equations.

$$\frac{dE_i}{dt}=-(q_{c,i}+q_{e,i}) \tag{31}$$

where $E_i=M_{d,i}c_{pd,i}T_{d,i}$ (32)

$$q_{c,i}=h_i A_{s,i}(T_{d,i}-T_a) \tag{33}$$

$$q_{e,i}=h_{m,i}A_{s,i}(\omega_{s,i}-\omega_a)h_{fg,i} \tag{34}$$

where $h_{fg,i}=h_{fg0,i}+c_{pv,i}T_{d,i}$ (35)

Then, $M_{d,i}c_{p_{d,i}}\frac{dT_{d,i}}{dt}=-\left[h_i(T_{d,i}-T_a)+h_{m,i}(\omega_{s,i}-\omega_a)h_{fg,i}\right]A_{s,i}$ (36)

$$\frac{dT_{d,i}}{dt}=-\frac{6h_{m,i}}{\rho_w c_{pd,i}D_i}\left[\frac{h_i}{h_{m,i}}(T_{d,i}-T_a)+(\omega_{s,i}-\omega_a)h_{fg,i}\right]-\frac{3T_{d,i}}{D_i}\frac{dD_i}{dt} \tag{37}$$

where $T_{d,i}-T_a=\frac{(h_{s,i}-h_{av,i})-(\omega_{s,i}-\omega_a)h_{fg,i}}{c_{pav,i}}$ (38)

$$Le_{f,i}=\frac{h_i}{h_{m,i}c_{pav,i}} \tag{39}$$

and $c_{pav,i}=c_{pa}+\omega_a c_{pv,i}$ (40)

Here 'c_{pav}' is specific heat of air vapour mixture at constant pressure.

Then, $\frac{dT_{d,i}}{dt}=-\frac{6h_{m,i}\left[Le_{f,i}(h_{s,i}-h_{av})+(1-Le_{f,i})(\omega_{s,i}-\omega_a)h_{fg,i}\right]}{c_{pd,i}D_i\rho_w}-\frac{3T_{d,i}}{D_i}\frac{dD_i}{dt}$ (41)

$$\frac{dT_{d,i}}{dt}=\frac{dT_{d,i}}{dy}\frac{dy}{dt}=U_{y,i}\left[\frac{dT_{d,i}}{dy}\right]=-\frac{6h_{m,i}\left[Le_{f,i}(h_{s,i}-h_{av})+(1-Le_{f,i})(\omega_{s,i}-\omega_a)h_{fg,i}\right]}{c_{pd,i}D_i\rho_w}-\frac{3T_{d,i}}{D_i}\frac{dD_i}{dt} \tag{42}$$

Therefore, energy balance of drops is represented by

$$\frac{dT_{d,i}}{dy}=-\frac{6h_{m,i}\left[Le_{f,i}(h_{s,i}-h_{av})+(1-Le_{f,i})(\omega_{s,i}-\omega_a)h_{fg,i}\right]}{U_{y,i}c_{pd,i}D_i\rho_w}-\frac{3T_{d,i}}{D_i}\frac{dD_i}{dy} \tag{43}$$

3.4. Thermal balance equations in the SCT

A mass balance in the control volume is given as:

$$\sum_i dm_{d,i}=m_a d\omega_a \tag{44}$$

The energy balance in the control volume of the SCT

$$m_a dh_{av,i}=\sum_i m_d dh_{d,i}+h_{d,i}dm_{d,i} \tag{45}$$

Rearranging using above two equations

$$dT_{d,i}=\sum_i\frac{m_a}{m_{d,i}}\left(\frac{dh_{av,i}}{c_{pd,i}}-T_{d,i}d\omega_a\right) \tag{46}$$

Energy balance at water and air interface yields

$$dq_i=\sum_i dq_{c,i}+dq_{e,i} \tag{47}$$

$$dq_i=\sum_i\left[h_i(T_{d,i}-T_a)+h_{m,i}h_{fg,i}(\omega_{s,i}-\omega_a)\right]dA_i \tag{48}$$

$$dq_i=\sum_i\left[\frac{h_i}{C_{pav,i}}(h_{s,i}-h_{av,i})+(h_{m,i}-\frac{h_i}{c_{pav,i}})h_{fg,i}(\omega_{s,i}-\omega_a)\right]dA_i \tag{49}$$

The enthalpy transfer to air stream is $dh_{av}=\frac{dq}{m_a}$

$$dh_{av,i}=\sum_i\frac{dq_i}{m_a}=\sum_i\frac{h_{m,i}}{m_a}\left[Le_{f,i}(h_{s,i}-h_{av,i})+(1-Le_{f,i})h_{fg,i}(\omega_{s,i}-\omega_a)\right]dA_i \tag{50}$$

where $dA_i=\frac{m_{d,i}\pi D_i^2 dy}{M_{d,i}U_{y,i}}=\frac{6m_{d,i}dy}{\rho_w D_i U_{y,i}}$

Now change in air temperature due to mass and heat transfer interaction can be expressed as:

$$\frac{dh_{av,i}}{dy}=\sum_i\left(\frac{m_{d,i}}{m_a}\right)\frac{6h_{m,i}}{\rho_w D_i U_{y,i}}\left[Le_{f,i}(h_{s,i}-h_{av,i})+(1-Le_{f,i})h_{fg,i}(\omega_{s,i}-\omega_a)\right] \tag{51}$$

$$\frac{dT_a}{dy}=\sum_i\left(\frac{m_{d,i}}{m_a}\right)\frac{6h_{m,i}}{\rho_w D_i U_{y,i}C_{pav,i}}\left[Le_{f,i}(h_{s,i}-h_{av,i})+(1-Le_{f,i})h_{fg,i}(\omega_{s,i}-\omega_a)\right]-\frac{h_{fg,0}}{C_{pav,i}}\frac{dw_a}{dy} \tag{52}$$

3.5. Mass balance equation in the SCT

Mass balance equation for the control volume

$$\sum_i dm_{d,i} = m_a d\omega_a = \sum_i N_i \frac{dM_{d,i}}{dt} \tag{53}$$

Substituting, $N_i = \frac{m_{d,i}dy}{M_{d,i}U_{y,i}}$ and $M_{d,i} = \frac{1}{6}\pi D_i^3 \rho_w$,

$$dw_a = \sum_i \left(\frac{m_{d,i}}{m_a}\right) \frac{6h_{m,i}}{\rho_w U_{y,i} D_i} (\omega_{s,i} - \omega_a) dy \tag{54}$$

The mass transfer associated with the control volume expressed as:

$$\frac{dw_a}{dy} = \sum_i \frac{m_{d,i} h_{m,i} A_{s,i}}{m_a M_{d,i} U_{y,i}} (\omega_{s,i} - \omega_a) \tag{55}$$

3.6. Drop trajectory equation

Drop trajectory expressed in terms of the horizontal and vertical components of velocity.

$$\frac{dx}{dy} = \frac{U_{x,i}}{U_{y,i}} \tag{56}$$

3.7. Exergy formulation

Exergy of water is given as:

$$X_{d,i} = m_{d,i}((h_{fd,i} - h_{g0}) - T_0(s_{fd,i} - s_{g0}) - R_v \ln(\phi_0)) \tag{57}$$

Exergy of air due to the convective heat transfer

$$X_c = \sum_i m_a \begin{bmatrix} c_{pa}(T_a - T_0) - T_0 c_{pa} \ln\left(\frac{T_a}{T_0}\right) + \\ \omega_a \left\{ c_{pv}(T_a - T_0) - T_0 c_{pv} \ln\left(\frac{T_a}{T_0}\right) \right\} \end{bmatrix} \tag{58}$$

Exergy of air due to evaporative heat transfer

$$X_e = \sum_i m_a \begin{bmatrix} R_a T_0 \ln\left(\frac{1+1.608\omega_{a0}}{1+1.608\omega_a}\right) + \\ \omega_a R_v T_0 \ln\left(\frac{\omega_a(1+1.608\omega_{a0})}{\omega_{a0}(1+1.608\omega_a)}\right) \end{bmatrix} \tag{59}$$

Total exergy of system is given as:

$$X_t = \sum_i (X_{d,i} + X_c + X_e) \tag{60}$$

The total exergy destruction 'I' for discrete height of tower will be:

$$I = X_{t,y(j)} - X_{t,y(j+1)} \tag{61}$$

where $y(j+1) - y(j) = dy$

3.8. Equation for efficiency

Thermal efficiency of SCT gives as:

$$\eta_{th} = \frac{(T_{d,in} - T_{d,m,i})100}{T_{d,in} - T_{wb,in}} \tag{62}$$

where $T_{d,m,i} = \frac{\sum_i m_{d,i} T_{d,i}}{\sum_i m_{d,i}}$ (63)

Second law efficiency (SLE) of SCT given as:

$$\eta_{II} = \frac{X_{t,out} \times 100}{X_{t,in}} \tag{64}$$

3.9. Boundary conditions

The boundary conditions required for the solution of above formulation include tower geometry, spray characteristics, inlet air and multi droplets diameters. Tower geometry includes height, cross-section area, and shape of the tower. Spray characteristics are droplet velocity and temperature, the angle of projection, ten different droplets diameters, characteristic droplet size and uniformity constant. The initial air conditions required are air velocity, flow rate, relative humidity and different DBT.

4. Results and discussion

4.1. Model validation

The experimental data of a down draft SCT has been used for model validation. The model prediction with test data and test conditions is given in Table 2. Fig. 3(a) and (b) shows the comparison between the total data points of the outlet DBT of air and outlet specific humidity of air obtained from the experiment and those obtained from the model. It can be seen that the majority of the data fall within ±10% of the model.

Table 2
Comparison between experimental data and those obtained from mathematical model.

Test no.	1	2	3	4	5	6	7	8	9
Experimental inlet parameters									
Inlet air DBT (°C)	35.50	35.50	35.30	35.50	35.50	35.30	35.50	35.50	35.30
Inlet air relative humidity (%)	46.30	46.30	46.00	46.30	46.30	46.00	46.30	46.30	46.00
Inlet air velocity (m/s)	0.35	0.35	0.35	0.66	0.66	0.66	1.21	1.21	1.21
Inlet air volume flow rate (m^3/s)	0.10	0.10	0.10	0.19	0.19	0.19	0.35	0.35	0.35
Nozzle pressure (bar)	2	3	4	2	3	4	2	3	4
Inlet water droplet temp (°C)	31.50	31.50	31.90	31.50	31.50	31.90	31.50	31.50	31.90
Inlet diameter of water droplet (m)	421	311	205	421	311	205	421	311	205
Inlet water droplet velocity (m/s)	17.70	21.73	25.07	17.70	21.73	25.08	17.70	21.73	25.08
Water to air mass flow ratio (kg/kg)	0.46	0.57	0.66	0.24	0.30	0.34	0.13	0.16	0.19
Nozzle spray angle	89°	90°	91°	89°	90°	91°	89°	90°	91°
Experimental results									
Outlet air DBT (°C)	31.81	29.87	29.43	33.30	30.96	28.96	34.23	32.89	29.91
Outlet air specific humidity (kg/kg of dry air)	0.0231	0.0252	0.0264	0.0209	0.0225	0.0252	0.0195	0.0208	0.0230
Model predicted results									
Outlet DBT (°C)	31.59	29.43	29.03	33.11	30.83	28.44	34.12	32.67	29.45
Outlet air specific humidity (kg/kg of dry air)	0.0230	0.0248	0.0258	0.0207	0.0226	0.0245	0.0194	0.0206	0.0227

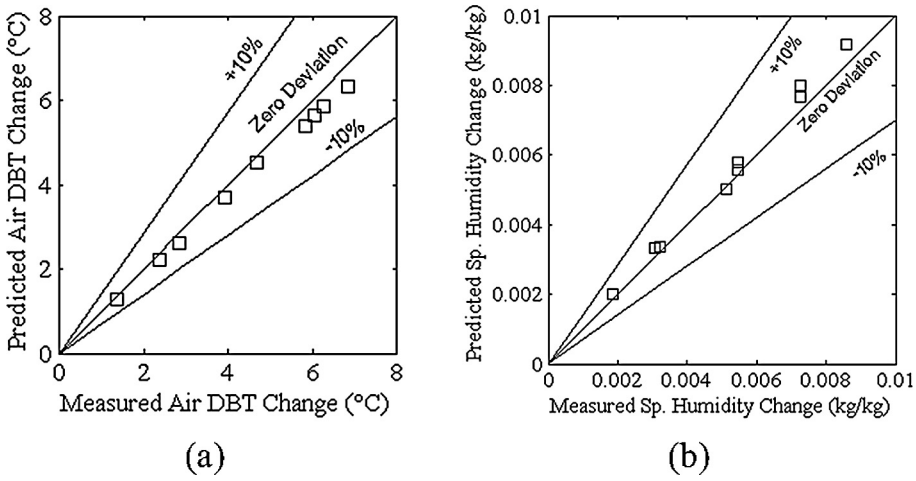

Fig. 3. Comparison of experimental data and model predictions (a) air DBT change and (b) air specific humidity change.

Table 3
Effect of inlet water temperature on model predicted results.

$T_{d,in}$ (°C)	$T_{a,out}$ (°C)	ω_{out} (kg/kg)	$T_{d,m,out}$ (°C)	$m_{d,l}$ (kg/s)	η_{th} (%)	$X_{c,out}$ (W)	$X_{e,out}$ (W)	$X_{air,out}$ (W)	$X_{d,out}$ (W)	$X_{t,out}$ (W)	I_t (W)	η_{II} (%)
28	25.49	0.0208	25.50	0.0014	44.93	44.76	80.19	124.95	13550.29	13675.24	22.37	98.47
30	26.25	0.0218	26.27	0.0015	49.29	40.18	93.52	133.70	13530.66	13664.36	29.71	98.16
32	27.00	0.0228	27.03	0.0016	51.98	35.92	108.00	143.92	13511.08	13655.00	38.54	97.83
34	27.74	0.0238	27.77	0.0017	53.85	31.96	123.63	155.59	13491.50	13647.09	48.96	97.46
36	28.46	0.0249	28.50	0.0019	55.28	28.30	140.44	168.74	13471.87	13640.61	61.10	97.06

4.2. Parametric study

Initial conditions used for computer simulation are inlet air DBT 40 °C; relative humidity 20%, inlet air volume flow rate 11.11×10^{-2} m^3/s, the ratio of mass flow rate of water to air 0.5. The distance between spray water inlet to the bottom of the tower (tower height 1.25 m along with the direction of y-axis) and tower diameter 0.61 m, droplet velocity 10 m/s and droplet angle of projection at inlet 45° was considered. Droplets of ten different diameters were used for study, and its distribution is based on Rosin Rammler distribution function. Inlet diameters of ten different droplets were 25.45, 50.90, 76.36, 101.81, 127.27, 152.72, 178.18, 203.63, 229.09, 254.54 μm, characteristic droplet size was 180 μm, and uniformity constant was 3.9342. Mass fractions of these ten droplets were 0.0005, 0.0066, 0.0273, 0.0685, 0.1274, 0.1859, 0.2139, 0.1894, 0.1238 and 0.0567. Effect of variation on inlet water temperature on various performance parameters was studied, and its exit conditions are shown in Table 3. The solution procedure has been outlined in Fig. 4.

4.3. Droplet trajectory and water loss due to evaporation along SCT height

Fig. 5(a) shows the trajectory of ten different diameter droplets whose diameter varies from 25.45 μm to 254.54 μm along tower height, the trajectory of droplet governed by Eq. (56). Smaller sized droplet covers longer path in comparison to larger size along the tower height. Fig. 5(b) and Table 3 show that as the water inlet temperature increases water loss due to evaporation increases along the height of SCT.

4.4. Effect of variation of water inlet temperature

Water inlet temperature varied from 28 to 36 °C with intervals of 2 °C. Fig. 6(a) shows that as inlet water temperature increases

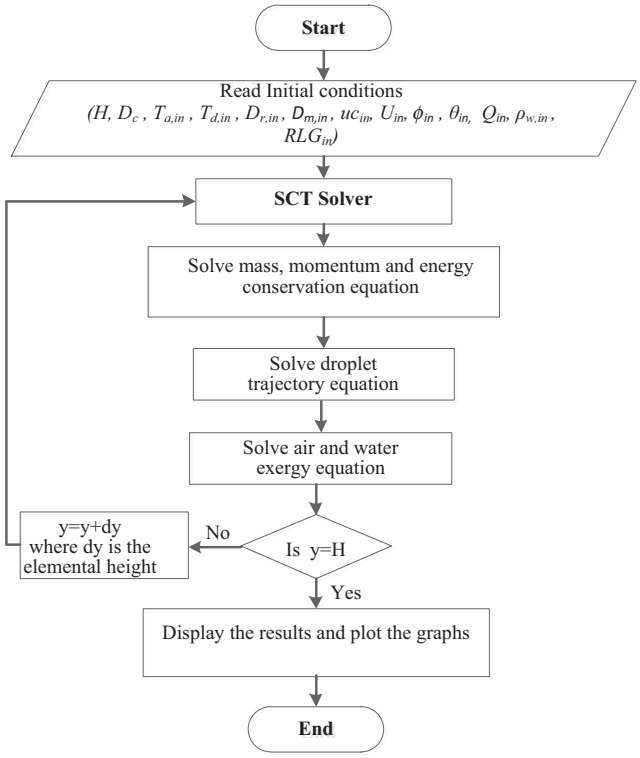

Fig. 4. Flow chart for the calculation of water-air conditions in SCT.

from 28 to 36 °C along the height of SCT, exit air DBT relatively increases. It also shows water at 28 °C produces maximum cooling, and air DBT reduces up to 14.35 °C and it is governed by Eq. (52). As inlet water temperature increases the convective and evaporative heat transfer decreases because the temperature difference

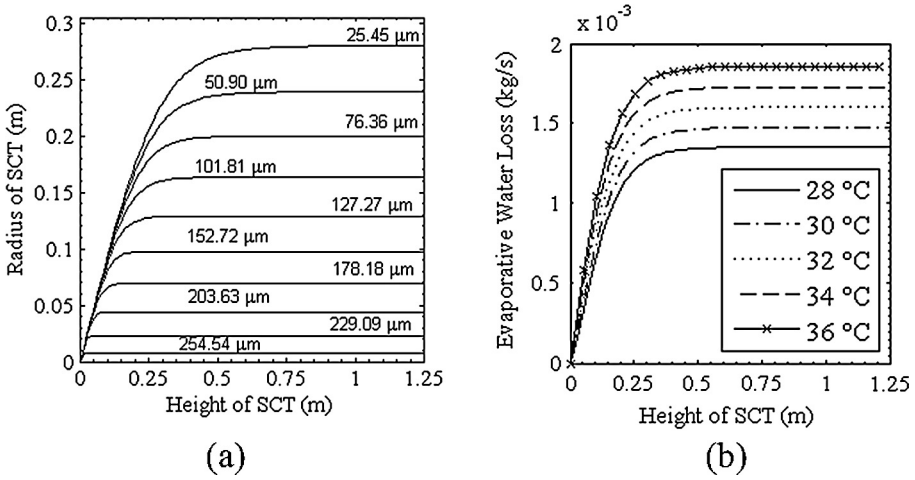

Fig. 5. Variation in trajectory of different water droplets (a) and evaporative water loss (b) along the tower height.

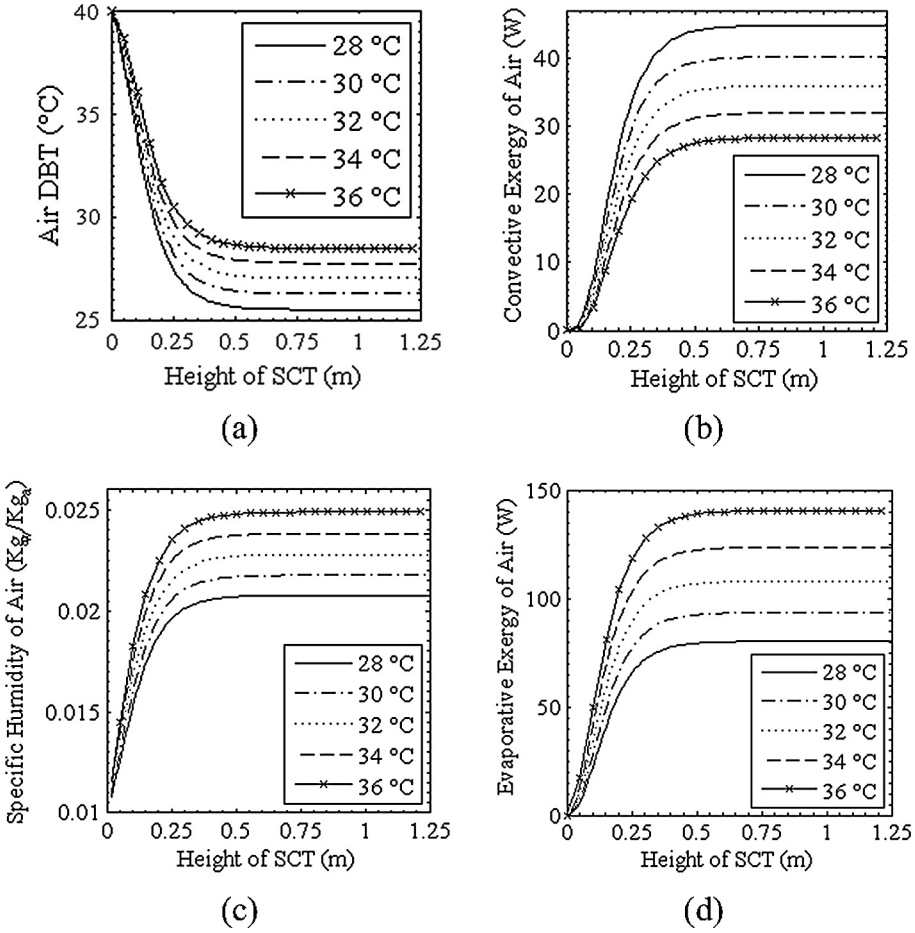

Fig. 6. Variation of different parameters along the tower height for different water inlet temperature (a) air DBT, (b) convective exergy of air, (c) specific humidity of air and (d) evaporative exergy of air.

between air and water decreases. Convective exergy of air as defined by Eq. (58) and plotted in Fig. 6(b), it is clear from figure as inlet water temperature increases exit exergy of air due to convective heat transfer relatively decreases because temperature difference between air and water droplet decreases. Fig. 6(c) and (d) shows specific humidity and evaporative exergy of exit air relatively increase with increase in the inlet water temperature defined by Eqs. (55), (59) because as inlet water temperature increases water molecules leave their surface and diffuse into the surrounding air. The total exergy of air which is the sum of convective and evaporative exergy of air increases with increasing the inlet water temperature (Table 3). Variation of inlet water temperature governed by Eq. (43) and it is also shown in Fig. 7(a), as inlet water temperature increases exit mean water droplet temperature relatively increases. This may occur because as the difference between inlet air and water temperature decreases convective

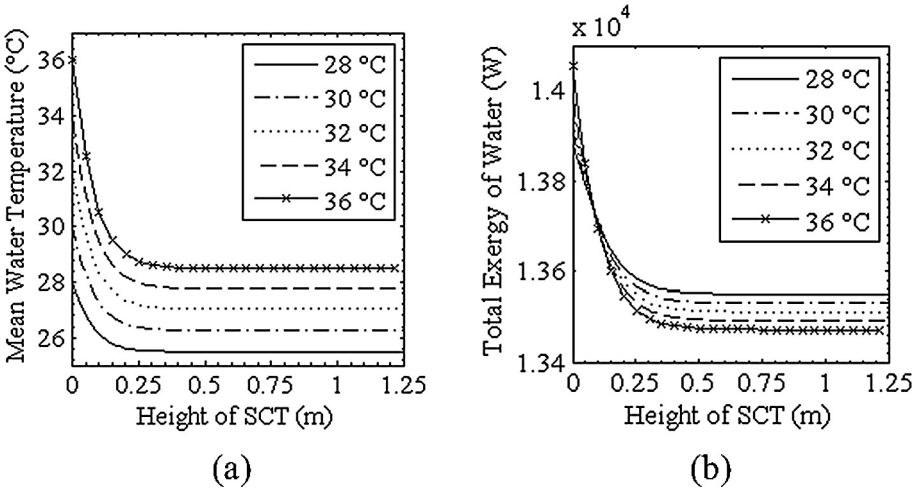

Fig. 7. Mean water droplet temperature (a) and exergy of water (b) along the tower height for different water inlet temperature.

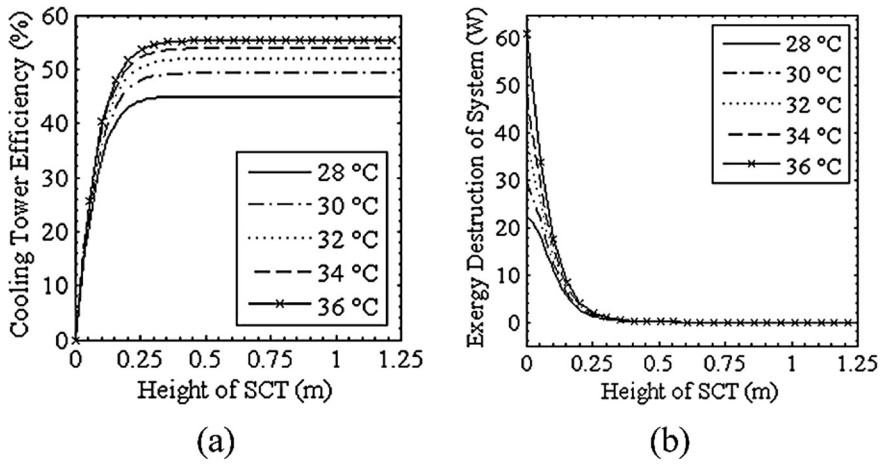

Fig. 8. Efficiency of SCT (a) and total exergy destruction (b) along the tower height for different water inlet temperature.

and evaporative heat transfer decreases. Eq. (57) and Fig. 7(b) represent deviation in water exergy along the tower height. Droplets loss its exergy faster along the height of SCT with increase in the inlet water temperature. Mean water droplet temperature reduces from top to bottom as a result of supplying its exergy to air. In total exergy of system contribution of water exergy component is more than total air exergy component (Table 3). Fig. 8(a) and Eq. (62) represent thermal efficiency of SCT. The efficiency of the cooling tower is increased relatively by increasing the inlet water temperature. Maximum efficiency of cooling tower achieved is 55.28% for 36 °C water. Total exergy of the system define by Eq. (60) is the sum of total exergy of air and water which is destroyed continuously from top to bottom of SCT. Maximum exergy of the system is destructed at the top of the tower and decreases along the height of the tower (Eq. (61) and Fig. 8(b)). Exergy destruction increases with increase in the inlet water temperature hence SLE of system defined by Eq. (64) decreases with increase in the inlet water droplet temperature (Table 3).

5. Conclusions

For finding out the outlet condition of air and water two-dimensional numerical model has been developed in MATLAB for reducing air DBT for human comfort. Convective and evaporative heat transfer between air and water droplets decreases by increasing the inlet water droplet temperature. Inlet water droplets of 28 °C reduce air DBT up to 14.35 °C, so this type of SCT can be used in hot and dry climates such as summer season in India and other parts of the world to cool air DBT for human comfort. Total exergy of the system is the sum of total exergy of air and water has been destroyed continuously from top to bottom of SCT. Cooling tower efficiency increases with increasing the inlet water temperature. Maximum efficiency of cooling tower achieved is 55.28% for 36 °C water. Total exergy of the system is the sum of total exergy of air and water that has been destroyed continuously from top to bottom of SCT. Maximum exergy of the system is destructed at the top of the tower and decreases along the height of the tower, and exergy destruction increases with increasing the inlet water droplet temperature. SLE of system decreases with increasing the inlet water droplet temperature. For same operating condition the optimum height of SCT can be reduced because maximum efficiency and maximum exergy destruction of SCT are achieved up to 0.5 m height of the tower.

Acknowledgements

This work was supported by Delhi Technological University, Delhi.

Appendix A. Supplementary material

Supplementary data associated with this article can be found, in the online version, at http://dx.doi.org/10.1016/j.applthermaleng.2017.04.157.

References

[1] T. Muangnoi, W. Asvapoositkul, P. Hungspreugs, Performance characteristics of a downward spray water-jet cooling tower, Appl. Therm. Eng. 69 (1) (2014) 165–176.
[2] R. Terblanche, H.C.R. Reuter, D.G. Kröger, Drop size distribution below different wet-cooling tower fills, Appl. Therm. Eng. 29 (8) (2009) 1552–1560.
[3] D. Nuyttens, K. Baetens, M. Schampheleire, B. Sonck, Effect of nozzle type, size and pressure on spray droplet characteristics, Biosys. Eng. 97 (3) (2003) 333–345.
[4] P. Naphon, Study on the heat transfer characteristics of an evaporative cooling tower, Int. Commun. Heat Mass Transf. 32 (8) (2005) 1066–1074.
[5] J.C. Kloppers, D.G. Kroger, A critical investigation into the heat and mass transfer analysis of counterflow wet-cooling towers, Int. J. Heat Mass Transf. 48 (3) (2005) 765–777.
[6] Xiaoni Qi, Zhenyan Liu, Dandan Li, Performance characteristics of a shower cooling tower, Energy Convers. Manage. 48 (2007) 193–203.
[7] X. Qi, Z. Liu, D. Li, Prediction of the performance of a shower cooling tower based on projection pursuit regression, Appl. Therm. Eng. 28 (8) (2008) 1031–1038.
[8] S. Yajima, B. Givoni, Experimental performance of the shower cooling tower in Japan, Renewable Energy 10 (2) (1997) 179–183.
[9] B. Givoni, Performance of the shower cooling tower in different climates, Renewable Energy 10 (2) (1997) 173–178.
[10] D. Pearlmutter, E. Erell, Y. Etzion, I.A. Meir, H. Di, Refining the use of evaporation in an experimental down-draft cool tower, Energy Build. 23 (3) (1996) 191–197.
[11] C. Farnham, M. Nakao, M. Nishioka, M. Nabeshima, T. Mizuno, Study of mist-cooling for semi-enclosed spaces in Osaka, Japan, Proc. Environ. Sci. 4 (2011) 228–238.
[12] S.S. Kachhwaha, P.L. Dhar, S.R. Kale, Experimental studies and numerical simulation of evaporative cooling of air with a water spray—I. Horizontal parallel flow, Int. J. Heat Mass Transf. 41 (2) (1998) 447–464.
[13] R. Sureshkumar, S.R. Kale, P.L. Dhar, Heat and mass transfer processes between a water spray and ambient air–I, experimental data, Appl. Therm. Eng. 28 (5) (2008) 349–360.
[14] R. Sureshkumar, P.L. Dhar, S.R. Kale, Effects of spray modeling on heat and mass transfer in air–water spray systems in parallel flow, Int. Commun. Heat Mass Transf. 34 (7) (2007) 878–886.
[15] B.A. Qureshi, S.M. Zubair, A complete model of wet cooling towers with fouling in fills, Appl. Therm. Eng. 26 (16) (2006) 1982–1989.
[16] H. Cui, N. Li, J. Peng, J. Cheng, S. Li, Study on the dynamic and thermal performances of a reversibly used cooling tower with upward spraying, Energy 96 (2016) 268–277.
[17] A. Bejan, Advanced Engineering Thermodynamic, third ed., John Wiley and Sons, 2006.
[18] B. Sirok, B. Blagojevic, M. Novak, M. Hocevar, F. Jere, Energy and mass transfer phenomena in natural draft cooling towers, Heat Transf. Eng. 24 (3) (2003) 66–75.
[19] M. Rotar, M. Sirok, B. Drobnic, B. Novak, B. Donevski, A numerical analysis of the local anomalies in a natural-draft cooling tower, Heat Transf. Eng. 26 (9) (2005) 61–72.
[20] N. Blain, A. Belaud, A.M. Miolane, Development and validation of a CFD model for numerical simulation of a large natural draft wet cooling tower, Appl. Therm. Eng. 105 (2016) 953–960.
[21] M. Huan, S. Fengqi, Y. Kong, Z. Kangping, Y. Wensheng Yan, A new theoretical method for predicating the part-load performance of natural draft dry cooling towers, Appl. Therm. Eng. 91 (2015) 1106–1115.
[22] M. Nasrabadi, P.F. Donal, Mathematical modeling of a low temperature low approach direct cooling tower for the provision of high temperature chilled water for conditioning of building spaces, Appl. Therm. Eng. 64 (1) (2014) 273–282.
[23] J.A. Sirena, Electrical-fluid dynamic performance of mechanical draft water cooling towers, Appl. Therm. Eng. 54 (1) (2013) 185–189.
[24] J.J. Jiang, X.H. Liu, Y. Jiang, Experimental and numerical analysis of a cross-flow closed wet cooling tower, Appl. Therm. Eng. 61 (2) (2013) 678–689.
[25] W. Asvapoositkul, S. Treeutok, A simplified method on thermal performance capacity evaluation of counter flow cooling tower, Appl. Therm. Eng. 38 (2012) 160–167.
[26] M.M. Keshtkar, Performance analysis of a counter flow wet cooling tower and selection of optimum operative condition by MCDM-TOPSIS method, Appl. Therm. Eng. 114 (2017) 776–784.
[27] K. Singh, R. Das, An improved constrained inverse optimization method for mechanical draft cooling towers, Appl. Therm. Eng. 114 (2017) 573–582.
[28] P. González-Tello, F. Camacho, J.M. Vicaria, P.A. González, A modified Nukiyama-Tanasawa distribution function and a Rosin-Rammler model for the particle-size-distribution analysis, Powder Technol. 186 (3) (2008) 278–281.
[29] A.H. Lefebvre, Atomization and Sprays, Hemisphere Publishing Corporation, New York, 1989.
[30] K. Masters, Spray Drying Handbook, fifth ed., Longman Scientific and Technical, UK, 1991.
[31] M. Zunaid, Q. Murtaza, S.S. Kachhwaha, Performance analysis of down draft parallel flow shower cooling tower, in: Proceedings of the 21st National & 10th ISHMT-ASME Heat and Mass Transfer Conference, IIT Madras, India, 2011.
[32] M. Zunaid, Q. Murtaza, S.S. Kachhwaha, Analysis of air and water spray interaction in downdraft parallel flow shower cooling tower, in: Proceedings of the 22th National and 11th International ISHMT-ASME Heat and Mass Transfer Conference, IIT Kharagpur, India, 2013.
[33] Q. Murtaza, J. Stokes, M. Ardhaoui, Computational fluid dynamics analysis of the production of bio-thermal spray hydroxyapatite powders, Int. J. Comput. Mater. Sci. Surf. Eng. 5 (1) (2012) 31–54.
[34] S.P. Fisenko, A.I. Petruchik, A.D. Solodukhin, Evaporative cooling of water in a natural draft cooling tower, Int. J. Heat Mass Transf. 45 (23) (2002) 4683–4694.

Sādhanā
DOI 10.1007/s12046-017-0643-7

© Indian Academy of Sciences

Estimation of stochastic environment force for master–slave robotic system

NEELU NAGPAL[1,*], BHARAT BHUSHAN[1] and VIJYANT AGARWAL[2]

[1]Department of Electrical Engineering, Delhi Technological University, Delhi 110042, India
[2]Division of Manufacturing Processes and Automation Engineering, Netaji Subhas Institute of Technology, New Delhi 110078, India
e-mail: nagpalneelu1971@gmail.com; bharatdce@yahoo.co.in; vijaynt.agarwal@gmail.com

MS received 15 August 2015; revised 10 December 2015; accepted 12 July 2016

Abstract. The aim of this work is to obtain the maximum likelihood estimate (MLE) of controller-gain parameters $\widehat{K}$ of the slave robot to determine the stochastic environment force. This is accomplished by measuring the joint positions of master and slave for a known master torque using stochastic difference equation. Here, the environmental force is modelled as a zero-mean white Gaussian random process. Therefore, the joint probability distribution function (pdf) of the slave angle over a given time duration can be computed as a function of the parameters 'K'. This pdf is maximized with respect to 'K' to obtain the MLE of controller-gain parameters. Subsequently, convergence analysis of error in the estimates is performed. Also, an expression of the Cramer–Rao lower bound (CRLB) is derived to measure accuracy of the estimation. Comparison of CRLB with variance of MLE supports that our estimates are asymptotically efficient. The estimation performance is validated analytically and through simulations carried out on a two-link master–slave robotic system.

Keywords. Environmental noise; parameter estimation; trajectories; MLE; CRLB; Fisher information matrix.

1. Introduction

There exists a wide spectrum of controllers to tackle the potential problems related to master–slave robotic systems [1, 2]. The problems of parameter uncertainty, time delay, disturbance, loss of information, transparency, etc. are the subject of present research and researchers have suggested various control techniques to tackle some of these problems. Model prediction adaptive controller [3], robust μ-synthesis controllers [4, 5], intelligent controllers [6–8], nonlinear and composite adaptive controller [7, 9] and disturbance observer [10] have been used to control such dynamical systems. Further, the environment, operator and task (EOT) adaptive controllers have been considered in [11] highlighting the importance of on-line information for the control. But many times, on-line information is not available due to various limitations and the researchers have to cope with the uncertainty. The designing of controllers seeks the evaluation of environmental force as all robots ultimately perceive the world through limited and improper sensors. Mostly, environmental force has been modelled as a spring–damper system and its variants [11–16]. Another approach is to regard it as an external disturbance [17] or environmental noise and disturbance observer has been suggested to estimate the environmental force. The dynamic environment effect is more realistically modelled with states of the robot and obstacle as random variables [18].

According to the central limit theorem, a large sum of small independent random effects of environmental noise converges to the Gaussian law. Therefore, in this work, environmental force has been assumed to follow the structure of Gaussian statistics. The whiteness of the environmental noise is based on the fact that usually the environmental kicks appear randomly and independent of each other, similar to a molecule that kicks a pollen particle in a fluid, leading to the pollen particle executing Brownian motion [19–22].

The technique of maximum likelihood estimation is optimal [23, 24] as compared with others under the condition of known trajectory. MLE works with the block processing method and acts as an efficient estimator since this estimation attains Cramer–Rao lower bound CRLB [25, 26].

Designing of a controller by considering the measured data as a joint PDF in combination with the estimation and convergence analysis of noise is not available in the literature. In this paper, this is attempted successfully. Furthermore, no work has been done on MLE of the proportional-derivative (PD) controller's coefficients of a robot, and there does not exist any computation of CRLB of the component vector comparing the matrix elements of the

*For correspondence
Published online: 26 April 2017

controller's gain parameters. The work presented in this paper is a novel application of MLE of nonlinear dynamics of master–slave robotics system. Moreover, the evaluation of CRLB from approximate statistics of the robot angular position and angular velocity perturbations is obtained from the correlation theory of the Gauss–Markov process.

Further, limited literature [27] exists on applications of stochastic methods in robots to model torque noise and no attempt has been made to estimate torque noise sample path trajectory from MLE.

In the proposed approach, stochastic environment force is introduced into the dynamics of slave robot, which adds formidable complexity into robotic systems dynamics. It requires reconfiguring the available PD controller gain parameters of master–slave robotic system by exploiting estimation methods. Hence, the joint PDF of the slave angle over a given time duration can be computed as a function of the unknown parameters K, where K is a vector whose components are linear combination matrices of PD parameter entries. In this work, MLE has been proposed for estimation of controller-gain parameters; and back-substituting these controller estimates into the dynamics leads to estimation of the sample trajectory of the environmental noise process.

Convergence analysis of the parameter estimates is performed by obtaining approximate expressions for the mean square parameters estimation error based on N data samples and the accuracy of environmental noise estimate is justified due to low signal to noise ratio (SNR).

Finally, an approximate expression is derived for the CRLB on the parameter estimation error covariance matrix. This lower bound sets a limit to the accuracy in estimating a parameter that influences probability density. It will be proved that as number of iterations i.e., $N \longrightarrow \infty$, the CRLB $\longrightarrow 0$, implying that efficient parameter estimates are consistent.

2. Master–slave dynamics

A block diagram illustrating the proposed optimal design of the PD controller's parameters and environmental noise estimation is shown in figure 1. The slave motion does not influence the master dynamics in this model since no error feedback is provided to the master. However, the slave dynamics is determined by (a) the environmental torque, $\tau_E(t)$, (b) the master process, $\theta_M(t)$ and (c) the PD controller coefficients K_p, K_d, which affect the error process $e(t)$ that gets fed into the slave torque.

The inverse dynamics takes the master angles, $\theta_m(t)$ and angular velocities $\theta'_m(t)$ as its other two variables and generates a torque (τ_I) that is used as input to the slave. As a result the slave tends to track the master. Assuming zero environmental torque, the PD feedback coefficients are designed based on optimal control theory to minimize the error energy between the master and slave angles for a master torque. This system is then handed over to the user, who does not know the exact values of the PD control gain parameters but wishes to use the system to determine the torque generated by a rapidly vibrating environment (environmental uncertainty). This is done by causing the slave to act on the environment and measure the angles of master and slave for a given master torque and random environmental torque (τ_E).

The angular measurement $\theta[.]$ by the forward dynamics is being utilized to form joint pdf as a function of the unknown value of controller-gain parameters (K). Maximizing the conditional pdf of the state vectors, $p(\theta_s[.], K)$ over a duration of time w.r.t. K is equivalent to minimizing the negative likelihood function $f(\theta_s[.], K)$. The estimated value $\widehat{K}$ is substituted in the linearized version of slave dynamics in place of K to estimate the enviornment noise trajectory, $\{W[n]\}_{n=0}^{N}$.

Remark 1 The dynamic equations of both two-link master and slave robots are identical except for the input torques.

The master equation is represented as

$$M_m(\theta_m)\theta''_m + N_m\left(\theta_m, \theta'_m\right) = \tau_{mo}(t) \tag{1}$$

where M_m represents the moment of inertia matrix, N_m combines the effects of damping Coriolis and centrifugal forces and gravitation and $\tau_{mo}(t)$ is torque [28]. The master equation (1) can be rearranged as

$$\theta''_m = \psi_1\left(\theta_m, \theta'_m\right) + \psi_2\left(\theta_m, \theta'_m\right)\tau_{mo}(t) \tag{2a}$$

$$\psi_1\left(\theta_m, \theta'_m\right) = -M_m(\theta_m)^{-1}N_m\left(\theta_m, \theta'_m\right) \tag{2b}$$

and

$$\psi_2\left(\theta_m, \theta'_m\right) = M_m(\theta_m)^{-1}. \tag{2c}$$

For a given torque process in discrete time $\tau_{mo}[n] = \tau_{mo}[n\Delta]$ (Δ being the discretization step size), the master robot angular position can be simulated as

$$\begin{aligned}(\theta_m[n+1] - 2\theta_m[n] + \theta_m[n-1])/\Delta^2 \\ = \psi_1(\theta_m[n], (\theta_m[n] - \theta_m[n-1])/\Delta) \\ + \psi_2(\theta_m[n], (\theta_m[n] - \theta_m[n-1])/\Delta)\tau_{mo}[n+1].\end{aligned} \tag{3}$$

The error dynamics is represented as

$$e(t) = K_p(\theta_m - \theta_s) + K_d\left(\theta'_m - \theta'_s\right) \tag{4}$$

The master robot controls the slave robot by inverse dynamics computation as shown in figure 1. The inverse dynamics block takes the input as the angular position (θ_m) and velocity (θ'_m) of master. The torque control law is computed using the angular acceleration of master (θ''_m) plus an error torque $(e(t))$ obtained by passing the position and velocity error through a PD controller. This error

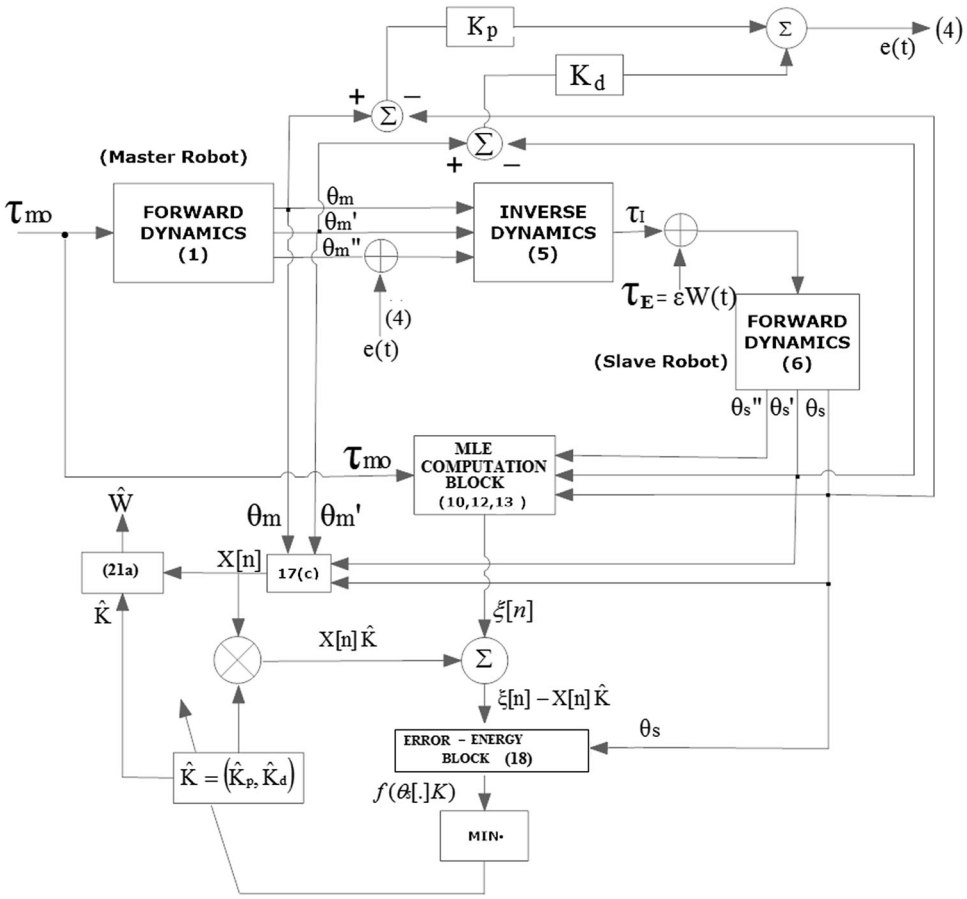

Figure 1. Block diagram for estimation process of PD controller gain parameters and environment force for master–slave system.

feedback guarantees that if the slave robot lags the master robot either in position or in velocity, then the acceleration input to the inverse dynamics block increases, thus causing the torque applied to the slave to increase so that its position and velocity approach more closely the master robot position and velocity, respectively. In the presence of environmental torque, τ_E, and torque from inverse dynamics, τ_I, the total torque applied to the slave robot is τ_s. Also τ_I is represented as

$$\begin{aligned} \tau_I(t) &= F\left(\theta_I, \theta_I', \theta_I''\right) \\ \text{where } \theta_I &= \theta_m, \quad \theta_I' = \theta_m' \\ \text{and } \theta_I'' &= \theta_m'' + e(t) \end{aligned} \tag{5}$$

The slave equations are represented as follows:

$$F\left(\theta_s, \theta_s', \theta_s''\right) = \tau_s = \tau_E + \tau_I \tag{6a}$$

$$= \tau_E + F\left(\theta_m, \theta_m', \theta_m'' + e(t)\right) \tag{6b}$$

$$= \tau_E + F\left(\theta_m, \theta_m', \theta_m'' + e(t)\right) \tag{6c}$$

or equivalently, the dynamics of slave robot interacting with environment is

$$\begin{aligned} \theta_s'' = & -M_s(\theta_s)^{-1} N_s\left(\theta_s, \theta_s'\right) + M_s(\theta_s)^{-1} M_m(\theta_m) e(t) \\ & + M_s(\theta_s)^{-1}(\tau_E + \tau_{mo}) \end{aligned} \tag{6d}$$

$$= \psi_1(\theta_s, \theta_s') + L(t, \theta_s, \theta_s')e(t) + \psi_2(\theta_s, \theta_s')(\tau_E + \tau_{mo})$$

$$\text{where } L(t, \theta_s) = M_s(\theta_s)^{-1} M_m(\theta_m(t)). \tag{6e}$$

Remark 2 Suppose τ_E is small, i.e., $\tau_E(t) = \epsilon W(t)$, where $W(t)$ is a standard 2-dimensional zero-mean white Gaussian random process and ϵ is a perturbation parameter attached to the noise term in the slave dynamics to keep track of terms having different order of smallness in the dynamics. This amounts to assuming that the noise term is of first order of smallness and enables expanding the solution in the powers of ϵ. Thus the solution of the dynamical system to any degree of smallness (i.e., power of ϵ) can be achieved by this process. At the end of the calculation, we may let $\epsilon = 1$. This appears when the slave robot hits a randomly vibrating wall.

Then from Eq. (6e) and [29], the stochastic difference equation representing the discretized dynamical model of slave can be expressed as

$$
\begin{aligned}
&(\theta_s[n+2]-2\theta_s[n+1]+\theta_s[n])/\Delta^2\\
&\quad=\psi_1(\theta_s[n],(\theta_s[n+1]-\theta_s[n])/\Delta)+L(n,\theta_s[n],\\
&\quad\quad(\theta_s[n+1]-\theta_s[n])/\Delta)e[n]+\psi_2(\theta_s[n],\\
&\quad\quad(\theta_s[n+1]-\theta_s[n])/\Delta)(\epsilon W[n+2]/\sqrt{\Delta}+\tau_{mo}[n+2])
\end{aligned}
\tag{7}
$$

In the above equation, $L[n,\theta_s,\theta_s']=L[n\Delta,\theta_s,\theta_s']$ and $W[n]$ is an independent and identically distributed (i.i.d.) $N(0,\sigma_w^2 I_2)$ sequence.

Remark 3 The factor $\dfrac{1}{\sqrt{\Delta}}$ is attached to $W[n+2]$ is based on the fact that if $B(t)$ is standard Brownian motion [30], then $\dfrac{dB(t)}{dt}$ is standard white Gaussian noise and in discrete time, can be approximated by $\dfrac{B(t+\Delta)-B(t)}{\Delta}$, which is a Gaussian random variable having zero mean and variance $\dfrac{1}{\Delta}$.

Equation (7) can be arranged as

$$
\begin{aligned}
\theta_s[n+2]&=2\theta_s[n+1]-\theta_s[n]+\Delta^2\psi_1(\theta_s[n],(\theta_s[n+1]-\theta_s[n])/\Delta)\\
&\quad+\Delta^2 L(n,\theta_s[n],(\theta_s[n+1]-\theta_s[n])/\Delta)(K_p(\theta_m[n]-\theta_s[n])\\
&\quad+(K_d/\Delta)(\theta_m[n+1]-\theta_m[n]-\theta_s[n+1]+\theta_s[n])\\
&\quad+\psi_2(\theta_s[n],(\theta_s[n+1]-\theta_s[n])/\Delta)\\
&\quad\times\left(\epsilon\Delta^{3/2}W[n+2]+\Delta^2\tau_{mo}[n+2]\right).
\end{aligned}
\tag{8}
$$

3. Estimation of controller's gain parameters with stochastic environmental Force

3.1 *Controller design*

It is assumed that designing of controller parameters, i.e., K_p and K_d is done so that $\{\sum_{n=0}^{N-1}||\theta_m[n]-\theta_s[n]||^2\}$ is a minimum in the presence of noise. Direct minimization of $\{\sum_{n=0}^{N-1}||\theta_m[n]-\theta_s[n]||^2\}$ w.r.t. K_p, K_d is equivalent to a maximum likelihood problem since the noise has been considered to be white Gaussian. This design can be achieved using stochastic optimal control methods like Bellman's stochastic dynamic programming method.

Remark 4 Having designed K_p and K_d, noise is introduced through the environment in the slave dynamics and the robot is handed over to a user who does not know values of gain parameters and the environment. This user takes measurements of noisy slave position $\delta\theta_s[n]=\theta_s[n]-\theta_m[n]$ over a finite time duration; then using MLE, he estimates the unknown controller's gain parameters K_p and K_d and after that estimates to determine the environmental noise.

The aim is to design K_p and K_d (2×2 matrices) so that

$$
\begin{aligned}
&\mathbb{E}\left\{\sum_{n=0}^{N-1}||\theta_m[n]-\theta_s[n]||^2\right\}\text{is minimum,}\\
&\text{where }\ \theta_s[n]-\theta_m[n]\approx\delta\theta_s[n]\ \text{ is of } O(\epsilon).
\end{aligned}
\tag{9}
$$

After linearizing Eq. (8) about $\theta_s^{(0)}[n]=\theta_m[n]$, the linear time-varying stochastic difference equation is represented as

$$
\begin{aligned}
\delta\theta_s[n+2]&=2\delta\theta_s[n+1]-\delta\theta_s[n]\\
&\quad+\Delta^2\Psi_{1,1}[n]\delta\theta_s[n]+\Delta\Psi_{1,2}[n](\delta\theta_s[n+1]-\delta\theta_s[n])\\
&\quad-\Delta^2 L[n](K_p\delta\theta_s[n]+K_d/\Delta(\delta\theta_s[n+1]-\delta\theta_s[n]))\\
&\quad+\Delta^2\Psi_{2,1}[n](\delta\theta_s[n]\otimes\tau_{mo}[n+2])\\
&\quad+\Delta\Psi_{2,2}[n](\delta\theta_s[n+1]-\delta\theta_s[n])\otimes\tau_{mo}[n+2])\\
&\quad+\Delta^{3/2}\Psi_2[n]W[n+2].
\end{aligned}
\tag{10}
$$

It may be noted that

$$
\begin{aligned}
\psi_1[n]&=\psi_1\left(\theta_m[n],\theta_m'[n]\right)\\
\psi_2[n]&=\psi_1\left(\theta_s[n],\theta_s'[n]\right)\\
\text{where }\psi_{1,1}[n]&=\frac{\partial\psi_1\left(\theta_m[n],\partial\theta_m'[n]\right)}{\left(\partial\theta_s[n]\right)}.\\
\text{Also, }\theta_m'[n]&=\frac{\theta_m[n]-\theta_m[n-1]}{\Delta}.\\
\text{Similarly, }\theta_s'[n]&=\frac{\theta_s[n]-\theta_s[n-1]}{\Delta}\\
\psi_{1,2}[n]&=\frac{\partial\psi_1\left(\theta_m[n],\partial\theta_m'[n]\right)}{\left(\partial\theta_s[n]\right)}\\
\psi_{2,1}[n]&=\frac{\partial\psi_2\left(\theta_m[n],\partial\theta_m'[n]\right)}{\left(\partial\theta_s'[n]\right)}\\
\psi_{2,2}[n]&=\frac{\partial\psi_2\left(\theta_m[n],\partial\theta_m'[n]\right)}{\left(\partial\theta_s'[n]\right)}.\\
\theta_m[n]&=\theta_m[n\Delta]\text{ is obtained by sampling}\\
&\quad\text{the continuous time master trajectory.}\\
\theta_s[n]&=\theta_s[n\Delta]\text{ is obtained by sampling the}\\
&\quad\text{continuous time slave trajectory.}\\
\text{Also, }L[n]&=L(n,\theta_m[n],(\theta_m[n+1]-\theta_m[n])/\Delta)=I_2.
\end{aligned}
$$

Applying elementary linear algebra techniques involving Kronecker product in Eq. (10), this can be derived as

$$
\begin{aligned}
\delta\theta_s[n+2]&=[2I_2+\Delta\Psi_{1,2}[n]-\Delta K_d\\
&\quad+\Delta\Psi_{2,2}[n](I_2\otimes\tau_{mo})[n+2])]\delta\theta_s[n+1]\\
&\quad+[I_2+\Delta^2\Psi_{1,1}[n]-\Delta\Psi_{1,2}[n]-\left(\Delta^2K_p-\Delta K_d\right)\\
&\quad+\Delta\Psi_{2,1}[n](I_2\otimes\tau_{mo}[n+2])-\Delta\Psi_{2,2}[n]\\
&\quad\times\left(I_2\otimes\tau_{mo}[n+2])\right]\delta\theta_s[n]\ +\Delta^{3/2}\Psi_2[n]W[n+2].
\end{aligned}
\tag{11}
$$

We can define

$$\Delta K_d = \alpha_d \in \mathbb{R}^{2\times 2}, \quad \Delta^2 K_p - \Delta K_d = \beta_d \in \mathbb{R}^{2\times 2} \tag{12a}$$

$$A[n] = 2I_2 + \Delta\Psi_{1,2}[n] + \Delta\Psi_{2,2}[n](I_2 \otimes \tau_{mo}[n+2]) \tag{12b}$$

$$\begin{aligned} B[n] = & -I_2 + \Delta^2\Psi_{1,1}[n] - \Delta\Psi_{1,2}[n] + \Delta\Psi_{2,1}[n] \\ & \times (\tau_{mo}[n+2] \otimes I_2) - \Delta\Psi_{2,2}[n](I_2 \otimes \tau_{mo}[n+2]) \end{aligned} \tag{12c}$$

$$C[n] = \Delta^{5/2}\Psi_2[n]. \tag{12d}$$

Then Eq. (11) can be rearranged as

$$\begin{aligned} \delta\theta_s[n+2] = & [A[n] - \alpha_d]I_2\delta\theta_s[n+1] \\ & + [B[n] - \beta_d]I_2\delta\theta_s[n] + C[n]W[n+2]. \end{aligned} \tag{13}$$

This equation is now in the right form required for applying the ML method to estimate α_d and β_d (or equivalently K_p and K_d).$\{\delta\theta_s[n]\}$ follows 2nd order difference equation with white-noise-driving term [31].

The pdf of $\{\delta\theta_s[n]\}$ parameterized by α_d and β_d can be calculated by the following process based on second order Markov model [32]:

$$\begin{aligned} & p(\delta\theta_s[n+2]|\delta\theta_s[n+1], \delta\theta_s[n]) \\ & = 1/2\pi|C[n]|exp\{-1/2\sigma^2(\delta\theta_s[n+2] - (A[n] - \alpha_d)\delta\theta_s[n+1] \\ & \quad - (B[n] - \beta_d)|\delta\theta_s[n]|^T(C[n]C[n]^T)^{-1}\delta\theta_s[n+2] \\ & \quad - (A[n] - \alpha_d)\delta\theta_s[n+1] - (B[n] - \beta_d)\delta\theta_s[n]\} \end{aligned} \tag{14}$$

$$\begin{aligned} & = 1/|C[n]|\Phi(C[n]^{-1}(\delta\theta_s[n+2] - (A[n] - \alpha_d) \\ & \quad \delta\theta_s[n+1] - (B[n] - \beta_d)\delta\theta_s[n])); \\ & \quad \text{where } \Phi(\xi) = \frac{1}{2\pi}\ \exp(-||\xi||^2/2), \quad \xi \in \mathbb{R}^2. \end{aligned} \tag{15}$$

Thus the ML estimates of α_d and β_d based on the measurements of $\{\delta\theta_s[n] : 0 \le n \le N\}$ are given by setting the variational derivative of the product of all terms in Eq. (14) over $0 \le n \le N$ w.r.t. α_d and β_d to zero and assuming $P[n] = (C[n]C[n]^T)^{-1}$. The resulting expression can be arranged in the following form using elementary properties of the Kronecker tensor product, especially $Vec(A \times B) = (B^T A) \otimes Vec(X)$ [33]:

$$\begin{aligned} & Vec\left\{\sum_n P[n]\xi[n+2]\delta\theta_s[n+1]^T\right\} \\ & + \left(\sum_n (\delta\theta_s[n+1]\delta\theta_s[n+1]^T) \otimes P[n])Vec(\widehat{\alpha}_d)\right) \\ & + \left(\sum_n (\delta\theta_s[n+1]\delta\theta_s[n]^T) \otimes P[n])Vec(\widehat{\beta}_d)\right) = 0 \end{aligned} \tag{16a}$$

$$\begin{aligned} & \text{and } Vec\left\{\sum_n P[n]\xi[n+2]\delta\theta_s[n]^T\right\} \\ & + \left(\sum_n (\delta\theta_s[n]\delta\theta_s[n+1]^T \otimes P[n])Vec(\widehat{\alpha}_d)\right) \\ & + \left(\sum_n (\delta\theta_s[n]\delta\theta_s[n]^T \otimes P[n])Vec(\widehat{\beta}_d)\right) = 0. \end{aligned} \tag{16b}$$

Equations (16a) and (16b) form a set of eight simultaneous linear equations for the unknown parameter vector $\begin{bmatrix} Vec(\alpha_d) \\ Vec(\beta_d) \end{bmatrix} \in \mathbb{R}^8$.

They can be expressed as follows and can be inverted immediately:

$$\begin{aligned} & \begin{bmatrix} \sum \delta\theta_s[n+1]\delta\theta_s[n+1]^T \otimes P[n] & \sum \delta\theta_s[n+1]\delta\theta_s[n]^T \otimes P[n] \\ \sum \delta\theta_s[n]\delta\theta_s[n+1]^T \otimes P[n] & \sum \delta\theta_s[n]\delta\theta_s[n]^T \otimes P[n] \end{bmatrix} \\ & \quad \times \begin{bmatrix} Vec(\widehat{\alpha}_d) \\ Vec(\widehat{\beta}_d) \end{bmatrix} \\ & = -\begin{bmatrix} Vec(\sum P[n]\xi[n+2]\delta\theta_s[n+1]^T) \\ Vec(\sum P[n]\xi[n+2]\delta\theta_s[n]^T) \end{bmatrix}. \end{aligned} \tag{16c}$$

Equation (16c) can be solved for the 4×1 vectors, i.e., $Vec(\widehat{\alpha}_d)$ and $Vec(\widehat{\beta}_d)$, i.e.,

$$K = \begin{bmatrix} Vec(\alpha_d) \\ Vec(\beta_d) \end{bmatrix} \text{ or equivalently for the } 8 \times 1 \text{ vector.}$$

The proposed maximum likelihood estimator of K, i.e., $\widehat{K}[N]$ based on slave linearization, has been expressed in the form $K + P^{-1}Q$ where Q is a bilinear vector function of $\{\delta\theta_s[n]\}$ and $\{W[n]\}$, and P is a quadratic function $\delta\theta_s[n]$. Here, $\{\delta\theta_s[n]\}$ is the master–slave angular error. In view of the linearized dynamics, P and Q are both quadratic functions of the environmental torque noise $W[n]$. Thus $\widehat{K} - K = ||\mathbb{E}P^{-1}||^2||\mathbb{E}Q||^2$ can be regarded as a "matrix ratio" of two quadratic functions of $W[n]$. The mean value of Q turns out to be zero in view of the system causality. The mean value of P is non-zero, and hence if approximation of $\mathbb{E}(\widehat{K} - K)$ by $(\mathbb{E}P^{-1})(\mathbb{E}Q)$ is done, result is zero. This justifies the PD estimator of the proposed work being nearly unbiased. Also, approximating $\mathbb{E}[||\widehat{K}[n] - K||^2]$ by $||(\mathbb{E}P)||^2\mathbb{E}[||Q||^2]$, it can be proven that this is small using the fact that Q is a sum of independent χ^2 random variables. We then substitute the estimated value $\widehat{K}[N]$ of K into the slave dynamics(non-linear) in place of K, and solve for $W[n]$ in terms of $\{\theta[n]\}_{n=0}^N$ and $\widehat{K}[n]$. The result is $\{W[n]\}_{n=0}^N$, an estimate of the environmental torque process. Then it can be shown that $\widehat{W}[n] - W[n]$ is a bilinear

function of $\delta\theta_s[n]$ and $\{\widehat{K}[n]-K\}$ and is therefore of second order of smallness, i.e., of $O(||W||^2)$. This justifies our accurate estimate of the environmental torque $\widehat{W}[n]$, from which the structure of the environment can be determined, and computations of this are presented in the following section.

3.2 *Environment noise estimation*

Using the general nonlinear dynamical model of slave given in Eq. (8), the aim is to compute the statistics of $(\widehat{K}[N]-K)$ and $(\widehat{W}[N]-W)$. We now present in brief the ML parameter estimates based on the exact nonlinear dynamics. However, for computation of the performance of these estimates, it is required that we linearize the dynamics otherwise the evaluation of the angular correlation becomes impossible. The expression given in Eq. (7) can also be written in the linear form as

$$\xi[n+2] = X[n]K + Y[n]W[n+2] \tag{17a}$$

where

$$\begin{aligned}\xi[n+2] &= \theta_s[n+2] - 2\theta_s[n+1] + \theta_s[n] \\ &\quad - \Delta^2\Psi_1(\theta_s[n]\theta_s[n+1) - \theta_s[n]/\Delta \\ &\quad - \Delta^2\Psi_1(\theta_s[n]\tau_{mo}[n+2])\end{aligned} \tag{17b}$$

$$X[n] = -\Delta^2 L[n,\theta_s[n]](\delta q[n]^T \otimes I_2) \tag{17c}$$

$$Y[n] = \epsilon\Delta^{3/2}\psi_2(\theta_s[n]) \tag{17d}$$

Remark 5 Recall that:

$$\begin{aligned}L[n,\theta_s[n]] &= M_s(\theta_s[n])^{-1}M_m[n]), \\ \delta q[n] &= \begin{bmatrix}\delta\theta_s[n] \\ \delta\omega_s[n]\end{bmatrix}, \\ \delta\theta_s[n] &= \theta_s[n] - \theta_m[n] \\ \delta\omega_s[n] &= \omega_s[n] - \omega_m[n].\end{aligned}$$

Based on the model (17a), we can immediately write down the ML estimate of K based upon samples up to time $N+2$.

Remark 6 After linearization, $L[n,\theta_s[n]] = I_2$ since $\theta_s \approx \theta_m$ and $M_m \approx M_s$

$$\widehat{K}[N] = argmin_K \sum_{n=0}^{N} ||Y^{-1}[n](\xi[n+2] - X[n]K)||^2 \tag{18a}$$

$$\begin{aligned}&= \left[\sum_{n=0}^{N} X[n]^T(Y[n]Y[n]^T)^{-1}X[n]\right]^{-1} \\ &\quad \left[\sum_{n=0}^{N} X[n]^T(Y[n]Y[n]^T)^{-1}\xi[n+2]\right]\end{aligned} \tag{18b}$$

$$= K + H[N]^{-1}\sum_{n=0}^{N} F[n]W[n+2] \tag{18c}$$

where

$$H[N] = \sum_{n=0}^{N} X[n]^T(Y[n]Y[n]^T)^{-1}X[n] \tag{18d}$$

$$F[n] = X[n]^T(Y[n]Y[n]^T)^{-1}Y[n] \tag{18e}$$

Up to $O(||\delta q||^2)$ in numerator and denominator, $(W[n] = O(||\delta q||))$, we then have $\widehat{K}[N] - K = P^{-1}Q$ as

$$\begin{aligned}\widehat{K}[N] - K = \lambda &\left(\sum_{n=0}^{N}(\delta q[n]\otimes I_2)R[n]^{-1}(\delta q[n]^T \otimes I_2)\right)^{-1} \\ &\left(\sum_{n=0}^{N}(\delta q[n]\otimes I_2)R[n]^{-1}\psi_2[n]W[n+2]\right) \\ &\text{where } \lambda = \Delta^{-4}x\omega(-\Delta^2)x\epsilon\Delta^{3/2} = -\epsilon\Delta^{-1/2},\end{aligned} \tag{19}$$

$$\begin{aligned}&R[n] = \Psi_2(\theta_m[n])\Psi_2(\theta_m[n])^T = \Psi_2[n]\Psi_2[n]^T \\ &\text{and } \Psi_2[n] = \Psi_2(\theta_m[n]).\end{aligned} \tag{20}$$

From Eqs. (18c) and (18d), the following is expressed as

$$\begin{aligned}&H[n] \propto \sum_{0}^{N}(\delta q[n]\otimes I_2)R[n]^{-1}(\delta q[n]^T\otimes I_2) \\ &\text{and linearization is around } \theta_m[n], \\ &\text{Also, } \sum_{0}^{N} F[n]W[n+2] \propto \sum_{0}^{N}(\delta q[n]\otimes I_2)R[n]^{-1}\psi_2[n]W[n+2].\end{aligned}$$

Remark 7 The numerator in Eq. (19) has mean zero since $\delta q[n]$ is uncorrelated with $W[n+2]$ and denominator has non-zero mean since $\mathbb{E}[\delta q[n]\delta q[n]^T] \neq 0$. Hence $\widehat{K}[N] - K$ is small in probability. This justifies our model.

The noise estimate from Eq. (19) is estimated as

$$\widehat{W}[n+2] = Y[n]^{-1}(\xi[n+2] - X[n]\widehat{K}[N]) \tag{21a}$$

$$= Y[n]^{-1}(X[n]K + Y[n]W[n+2] - X[n]\widehat{K}[N]). \tag{21b}$$

4. Convergence analysis

The aim is to determine the limiting mean square deviation $\lim_{n\to 0}\mathbb{E}\{||\delta\theta_s[n]||^2\}$, $\delta\theta_s[n] = \theta_s[n] - \theta_m[n]$ of the slave position, which requires linearization of the nonlinear slave dynamics in discrete time about the master position. The linearized equation has time-dependent matrix coefficients

and a driving white noise term coming from the environmental torque, which provides evaluation of correlation $\mathbb{E}\{\delta\theta_s[n]\delta\theta_s[n]^T\}$. Aiming that the master has a limiting angular position, derivation of a linear algebraic equation for the limiting error correlation matrix as a function of the feedback parameters K_p and K_d is done.

The limiting NSR is represented as $\dfrac{\mathbb{E}[||\delta\theta_s(\infty)||^2]}{||\delta\theta_m(\infty)||^2}$.

Approximate formulas for the PD parameter error $\widehat{K}[n]-K$ and the noise estimation error $\widehat{W}[n]-W[n]$ in terms of W[n] and $\delta q[n]=(\theta_s[n]-\theta_m[n]),\omega_s[n]-\omega_m[n])$ are obtained. Specifically, the expression for the approximate value of $\widehat{K}[n]-K$ is evaluated as a ratio of two quadratic functions of a Gaussian process, i.e., $\widehat{K}[n]-K=P^{-1}Q$, where $Q\in 8\times 1$ is a quadratic function of $\delta q[n]$. We show that Q has zero mean and P has non-zero mean and this justifies our approach that $\mathbb{E}\{\widehat{K}[n]-K\}$ is small. A recursive algorithm is derived for calculating the correlation $\mathbb{E}[\delta q[n]\delta q[n]^T]$ and $\mathbb{E}[\delta q[n]W[m^T]$ using linearized version of the dynamical model and this enables us to perform the above calculations.

The noise estimate error energy is given by

$$\begin{aligned}\widehat{W}[n+2]-W[n+2]&=Y[n]^{-1}X[n](K-\widehat{K}[N])\\&\approx\epsilon^{-1}\Delta^{-3/2}\Psi_2[n]^{-1}(-\Delta^2)(\delta q[n]^T\\&\quad\otimes I_2)(K-\widehat{K}[N])\\&=-\epsilon^{-1}\sqrt{\Delta}\Psi_2[n]^{-1}(\delta q[n]^T\otimes I_2)\\&\quad(K-\widehat{K}[N])\end{aligned}\tag{22}$$

The approximate expression for the absolute error $|\widehat{W}[n]-W[n]|$ is obtained as a bilinear function of $\delta q[n]$ and $\{\widehat{K}[n]-K\}$, showing that this is small in probability.

This analysis is based on substituting $\widehat{K}$ in place of K in Eq. (21a) and $\widehat{W}[n+2]$ in place of $W[n]$ in the same equation and substituting the resulting equation from Eq. (21b).

Since, in Eq. (22), $\widehat{W}[n+2]-W[n+2]$ is proportional to the tensor product of two small quantities $\delta q[n]$ and $K-\widehat{K}[N]$, $\widehat{W}[n+2]-W[n+2]$ is very small in probability. Thus an environmental noise estimate is highly accurate as also demonstrated in the simulations.

Remark 8 The random variables $\{\delta q[n]\otimes W[n+2]\}, n=0,1,2,\ldots$ are uncorrelated owing to the whiteness of $W(.)$ and hence the variance of the numerator in Eq. (22) grows with N as O(N). Equivalently, the mean modulus of the numerator is of $O(\sqrt{N})$. On the other hand, since $\mathbb{E}(\delta q[n]\delta q[n]^T)\neq 0$, the mean modulus of the denominator in Eq. (22) grows as O(N). Hence the mean modulus of Eq. (22) decreases with increasing N as $\dfrac{O(\sqrt{N})}{O(N)}=O\left(\dfrac{1}{\sqrt{(N)}}\right)$.

By considering the linearized model, the expression for the state equation for $q[n]$ is as a linear first-order difference equation with the white Gaussian input. This readily verifies the Gaussianity of $\delta q[n]$; standard methods can be used to derive recursive equations for its covariance evolution for calculating $\mathbb{E}||\widehat{K}[N]-K||^2$ using Eq. (19) can be done.

5. CRLB of estimation

The significance of obtaining the CRLB for controller-gain parameters estimates is that, since the estimates $\widehat{K_p}$ and $\widehat{K_d}$ are substituted in Eq. (22) to get an estimate of the environment noise process, these uncertainties in $\widehat{K_p}$ and $\widehat{K_d}$ will reflect as an error in the noise estimate $\widehat{W}-W$. Thus, the minimum variance in the noise estimate $\mathbb{E}(||\widehat{W}-W||^2)$ taken over all estimates of $\widehat{K_p}$ and $\widehat{K_d}$ will be lower bounded by a quantity proportional to the CRLB for K_p and K_d.

Evaluation of the CRLB for any unbiased estimator of the estimation problem under consideration requires the use of a linearized model. This is computed as a linear combination of the master–slave error angular position–velocity correlation matrix.

Remark 9 The diagonal entries of the CRLB determine the minimum possible variance/mean square estimation error $\mathbb{E}(K-\widehat{K}[N])^2$ of each component of $K[N]$. The angular position–velocity correlation matrix approximately satisfies a linear difference equation of slave dynamics and by solving this equation recursively, the Fisher information matrix and hence the CRLB is obtained.

Concrete approximations of the CRLB that give its order of magnitude are derived by assuming that the master angular position has stabilized as a constant value. In this case, the linearized slave dynamics is a linear time-invariant state variable system of the form

$$\begin{aligned}\delta q[n+1]&=A[K]\delta q[n]+GW[n+2],\text{ where }\delta q\\&=[\delta\theta_s,\delta\omega_s]^T.\end{aligned}$$

This state variable equation is easily solved using the state transition matrix in discrete time and an expression for the error angular position–velocity correlation matrix $R_q[n]=\{\delta q[n]\,\delta q[n]^T\}$ is immediately obtained.

Remark 10 For stability, we assume that all the eigenvalues of $A[K]$ have magnitude smaller than unity and then we derive, using the spectral norm, a bound on $||R_q[n]||$ in

term of the maximum eigenvalue magnitude of $A[K]$. This enables us to derive the order of magnitude of the CRLB and hence of the parameter variance estimate. We show that the CRLB $\longrightarrow 0$ as $N \longrightarrow \infty$, implying that efficient parameter estimates are consistent.

The expression for the Fisher inverse matrix (i.e., the CRLB) that is obtained in the special case when the robot vibrates noisily around a fixed point.

Computation of Fisher information matrix is presented as

$$J(K) = -\mathbb{E}\frac{\delta^2 \log}{\delta K \delta K^T} p(q(.)|K) \tag{23a}$$

$$= \sum_{n=0}^{N} \mathbb{E}X[n]^T (Y[n]Y[n]^T)^{-1} X[n] \text{ (see Eq. (17))} \tag{23b}$$

$$\approx \epsilon^{-2} \Delta^{-3} \Delta^4 \sum_{n=0}^{N} \mathbb{E}(\delta q[n] \otimes I_2) R[n]^{-1} (\delta q[n]^T \otimes I_2) \tag{23c}$$

$$= \epsilon^{-2} \Delta \sum_{n=0}^{N} \begin{bmatrix} \delta q[n] & 0 \\ 0^T & \delta q[n] \end{bmatrix} \begin{bmatrix} (R[n]^{-1})_{11} & (R[n]^{-1})_{12} \\ (R[n]^{-1})_{21} & (R[n]^{-1})_{22} \end{bmatrix} \begin{bmatrix} \delta q[n]^T & 0 \\ 0^T & \delta q[n]^T \end{bmatrix} \tag{23d}$$

$$= \epsilon^{-2} \Delta \sum_{n=0}^{N} \begin{bmatrix} (R[n]^{-1})_{11} \mathbb{E}\{\delta q[n] \delta q[n]^T\} & (R[n]^{-1})_{12} \mathbb{E}\{\delta q[n] \delta q[n]^T\} \\ (R[n]^{-1})_{21} \mathbb{E}\{\delta q[n] \delta q[n]^T\} & (R[n]^{-1})_{22} \mathbb{E}\{\delta q[n] \delta q[n]^T\} \end{bmatrix} \tag{23e}$$

$$\begin{aligned} &= \epsilon^{-2} \Delta \sum_{n=0}^{N} (R[n]^{-1} \otimes R_q[n]), \text{where } R_q[n] \\ &= \mathbb{E}\{\delta q[n] \delta q[n]^T\} \end{aligned} \tag{23f}$$

$$\begin{aligned} &\text{and the CRLB of } K \text{ is } J(K)^{-1} \\ &= \frac{\epsilon^2}{\Delta} \left(\sum_{n=0}^{N} R[n]^{-1} \otimes R_q[n] \right)^{-1}. \end{aligned} \tag{23g}$$

Remark 11 The diagonal entries of $J(K)^{-1} \in R^{2\times 2}$ give a lower bound for the variance of the corresponding entry of $\widehat{K}[N]$. For evaluating the CRLB, $J(K)^{-1}$, we require $R_q[n]$, which has been calculated in Appendix A.

Remark 12 If we assume that the master angle vector $\theta_m[n]$ has stabilized around some nominal value, say θ_m^*, then $\Psi_{1,1}[n]$ and $\Psi_{1,2}[n]$ are nearly constant matrixes, namely $\Psi_{1,1}(\theta_m^*, o)$ and $\Psi_{1,2}(\theta_m^*, o)$ and so is $\psi_2[n] = \psi_2(\theta_m^*)$.

Then $A[n,k] = A[K]$ is a constant matrix and so is $G[n] = G$ (say).

In this case we have $\delta q[n+1] = A[K]\delta q[n] + G\omega[n+2]$, the solution to which is obtained after assuming $\delta q[0] = 0$) and $\delta q[n] = \sum_{k=0}^{n-1} A[k]^{n-k-l} GW[k+2]$. Then, $R_q[n] = \mathbb{E}[\delta q[n] \;\; \delta q[n]^T] = \sum_{k=0}^{n-1} A[K]^{n-k-l} |GG^T (A[K]^T)^{n-k-l}|$ and this can be used to get an approximate expression for the CRLB.

$$G \approx \epsilon \sqrt{\Delta} \begin{bmatrix} o \\ \psi_2 \end{bmatrix}$$

$$GG^T = \epsilon^2 \Delta \begin{bmatrix} o & o \\ o & \psi_2 \psi_2^T \end{bmatrix} = \epsilon^2 \Delta \begin{bmatrix} o & o \\ o & R \end{bmatrix}.$$

Assumption Let $A[k] = \sum_{\alpha=1}^{4} \lambda_\alpha \vartheta_\alpha \vartheta_\alpha^T$ be the spectral representation of $A[k]$.

Then,

$$R_q[n] = \epsilon^2 \Delta \sum_{k=0}^{n-1} \sum_{\alpha,\beta=1}^{4} (\lambda_\alpha \lambda_\beta)^{n-k-1} \vartheta_\alpha \vartheta_\alpha^T \begin{bmatrix} (0 & 0 \\ 0 & R \end{bmatrix} \vartheta_\beta \vartheta_\beta^T$$

$$= \epsilon^2 \Delta \sum_{\alpha,\beta=1}^{4} \left(\frac{1 - (\lambda_\alpha \lambda_\beta)^n}{1 - \lambda_\alpha \lambda_\beta} \right) \vartheta_\alpha \vartheta_\alpha^T \begin{bmatrix} (0 & 0 \\ 0 & R \end{bmatrix} \vartheta_\beta \vartheta_\beta^T$$

As $n \to \infty$, it can be reduced to

$$= \epsilon^2 \Delta \sum_{\alpha,\beta=1}^{4} \left(\frac{1}{1 - \lambda_\alpha \lambda_\beta} \right) \vartheta_\alpha \vartheta_\alpha^T \begin{bmatrix} (0 & 0 \\ 0 & R \end{bmatrix} \vartheta_\beta \vartheta_\beta^T$$

Assuming $|\lambda_\alpha| < 1 \forall \alpha$, from Eq. (23g), we get,

$$\text{CRLB} = J^{-1} \approx \frac{1}{\Delta^2 N} R^{-1} \otimes \sum_{\alpha,\beta=1}^{4} \left(\frac{1}{1 - \lambda_\alpha \lambda_\beta} \right)$$

$$\vartheta_\alpha \vartheta_\alpha^T \begin{bmatrix} (0 & 0 \\ 0 & R \end{bmatrix} \vartheta_\beta \vartheta_\beta^T$$

$$\text{Then } R_q[n] = \epsilon^2 \Delta \sum_{k=0}^{n-1} A[K]^{n-k-1} \begin{bmatrix} (0 & 0 \\ 0 & R \end{bmatrix} A^T[K]^{n-k-1}$$

$$\text{and CRLB}\,(K) = \frac{1}{\Delta^2} \left[\sum_{n=0}^{N} R^{-1} \otimes \sum_{k=0}^{n-1} \left(A[K]^{n-k-1} \begin{bmatrix} (0 & 0 \\ 0 & R \end{bmatrix} A^T[K]^{n-k-1} \right) \right]^{-1}. \tag{24}$$

Remark 13 In Eq. (24), for a stable linearized system, eigenvalues of $A[k]$ will all be smaller than unity in magnitude and hence the inner sum will be upper bounded by a finite positive definite matrix, say P, as $n \to \infty$ and subsequently as $N \to \infty$, the CRLB(K) will converge to zero as

$$\text{CRLB}(K) \approx \frac{1}{N\Delta^2} (R^{-1} \otimes P)^{-1} = \frac{1}{N\Delta^2} (R \otimes P^{-1})$$

6. Simulation results

For simulation purpose the moment of inertia matrix of a unit length planner two-link manipulator (both master and slave) is

$$\text{M} = \begin{bmatrix} \cos(q_1 - q_2) + 5/3 & \cos(q_1 - q_2) + 1/3 \\ \cos(q_1 - q_2) + 1/3 & 1/3 \end{bmatrix}$$

We have taken PD gain parameters matrices as

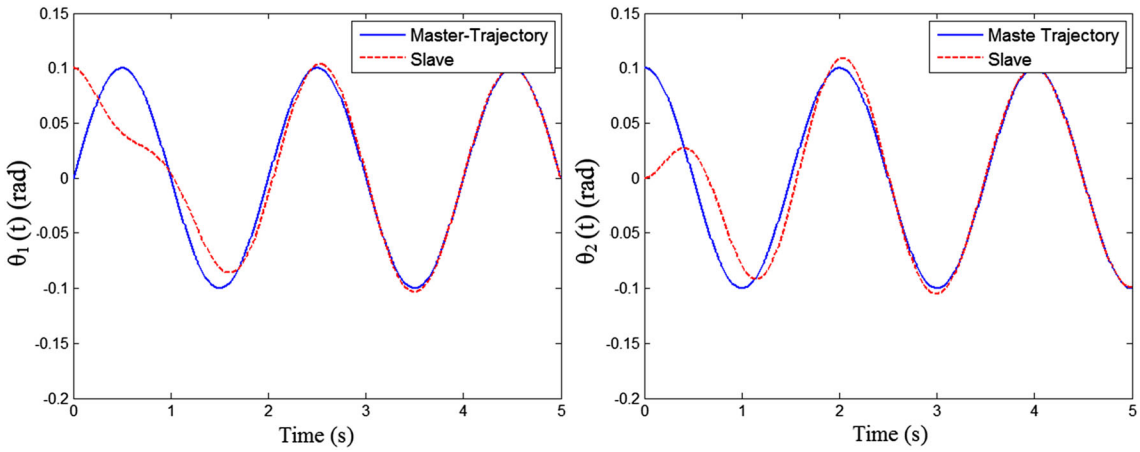

Figure 2. Trajectories of joint 1 and joint 2 of the Master–Slave System.

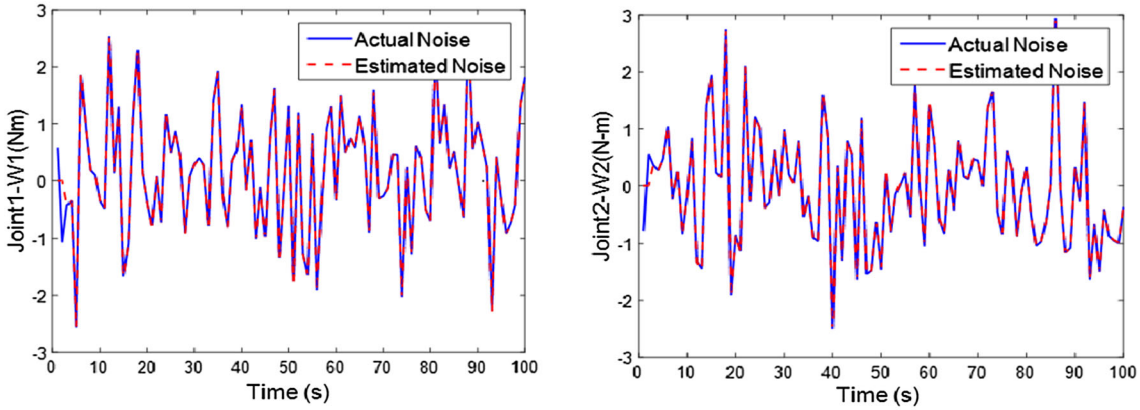

Figure 3. Estimation performance of environment noise of joint 1 and joint 2 of Slave robot.

$$\alpha_d = \begin{bmatrix} 20 & 0.01 \\ 0.01 & 20 \end{bmatrix} \text{ and } \beta_d = \begin{bmatrix} 2 & 0.01 \\ 0.01 & 2 \end{bmatrix}.$$

Then we add random environmental noise with 0.01 covariance. The deviation $\theta_s[n]$ of the slave angles due to this noise is measured and using this deviation, the estimation of α_d and β_d using MLE (from section 3.1) is

$$\widehat{\alpha_d} = \begin{bmatrix} 19.99 & -0.1 \\ 0.4 & 20 \end{bmatrix} \text{ and } \widehat{\beta_d} = \begin{bmatrix} 1.85 & 0.06 \\ -0.1 & 1.8 \end{bmatrix}.$$

With this PD controller's gain parameters, tracking plots of the slave robot are depicted in figure 2.

Error plot of this trajectory (figure 3) illustrates that error converges with the proposed technique.

Figure 4 illustrates that estimated environment force accurately tracks the actual environmental random force.

7. Conclusion

This paper has presented the algorithm of estimating environment force using MLE based on measurements of the slave position process over a given time range. The performance of parameter estimation has been explored through formulation of analytical expression of convergence and CRLB.

The success of algorithm is exemplified through convergence analysis that provides low noise to signal ratio for the parameter estimates as number of samples (N) increases. Computation of CRLB of parameter estimation has been carried out that indicates that as N tends to infinity, the CRLB variance approaches zero, which means that our parameter estimates are consistent.

The expressions for the parameter and noise estimation errors show via intuitive arguments that they are small in probability and decrease with increasing data length. The simulation results show the effectiveness of the estimation and encourage our contribution to recast the approach of conventional control in tracking of master–slave robotics system.

Acknowledgements

The authors acknowledge the discussion with Professor Harish Parthasarathy, Netaji Subhas Institute of

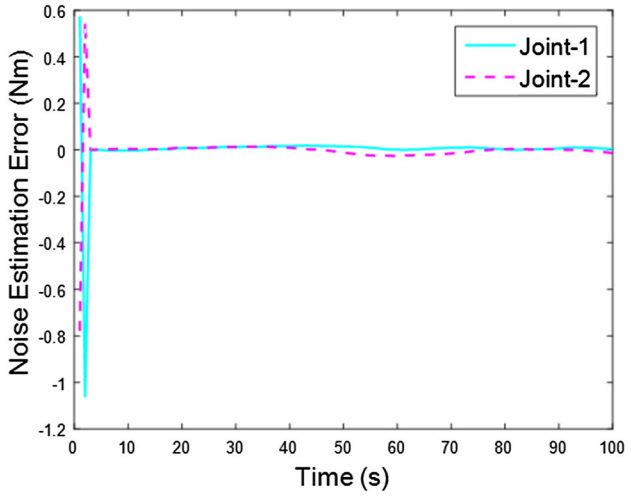

Figure 4. Time histories of estimation error of environment noise of Master–Slave system.

Technology, Delhi, India, who has helped in improving the quality of this paper.

Appendix

Computation of the statistics of $\delta q[n]$

$$\text{Define } \delta\theta_s[n] = \theta_s[n] - \theta_m[n], \tag{25a}$$

$$\delta\omega_s[n] = \omega_s[n] - \omega_m[n] \tag{25b}$$

$$\delta q[n] = \begin{bmatrix} \delta\theta_s[n] \\ \delta\omega_s[n] \end{bmatrix} \tag{25c}$$

The state equations satisfied by $\delta q[n]$ are

$$\delta\theta_s[n+2] - 2\delta\theta_s[n+1] + \delta\theta_s[n] = \Delta^2(\Psi_{1,1}[n]\delta\theta_s[n] + \Psi_{1,2}[n]\delta\omega_s[n]) - \Delta^2((\delta\theta_s[n]^T, \delta\omega_s[n]^T) \otimes I_2)K + \epsilon\Delta^{3/2}\Psi_2[n]W[n+2] \tag{26a}$$

$$\text{or } \delta\theta_s[n+1] = \delta\theta_s[n] + \Delta\delta\omega_s[n], \delta\omega_s[n+1] \tag{26b}$$

$$\begin{aligned} &= \delta\omega_s[n] + \Delta(\Psi_{1,1}[n]\delta\theta_s[n] + \Psi_{1,2}[n]\delta\omega_s[n]) \\ &\quad - \Delta((\delta\theta_s[n]^T, \delta\omega_s[n]^T) \otimes I_2)K \\ &\quad + \epsilon\sqrt{\Delta}\Psi_2[n]W[n+2]. \end{aligned} \tag{26c}$$

Note that $(\eta^T \otimes I)Vec(B) = B\eta$

Write K as the 2×4 matrix formed from $K = [K_p|K_d]$, where K_p and K_d are 2×2 matrices. We thus have

$$\begin{aligned} \delta\omega_s[n+1] &= \delta\omega_s[n] + \Delta(\Psi_{1,1}[n]\delta\theta_s[n] + \Psi_{1,2}[n]\delta\omega_s[n]) \\ &\quad - \Delta K_p\delta\theta_s[n] - \Delta K_d\,\delta\omega_s[n] \\ &\quad + \epsilon\sqrt{\Delta}\Psi_2[n]W[n+2] \end{aligned} \tag{27a}$$

$$\begin{aligned} &\text{or } \begin{bmatrix} \delta\theta_s[n+1] \\ \delta\omega_s[n+1] \end{bmatrix} \\ &= \begin{bmatrix} I_2 & \Delta I_2 \\ (\delta\Psi_{1,1}[n] - \Delta K_p) & (I + \Delta\Psi_{1,2}[n] - \Delta K_d) \end{bmatrix} \begin{bmatrix} \delta\theta_s \\ \delta\omega_s \end{bmatrix} \\ &\quad + \begin{bmatrix} \epsilon\sqrt{\Delta} \end{bmatrix} \begin{bmatrix} O \\ \Psi_2[n] \end{bmatrix} W[n+2]. \end{aligned} \tag{27b}$$

$$\text{Putting } A[n,K] = \begin{bmatrix} I_2 & \Delta I_2 \\ (\delta\Psi_{1,1}[n] - \Delta K_p) & (I + \Delta.\Psi_{1,2}[n] - \Delta K_d) \end{bmatrix} \text{ and } G[n] = \epsilon\sqrt{\Delta}\begin{bmatrix} O \\ \Psi_2[n] \end{bmatrix}$$

Equation (26b) can be expressed as

$$\delta q[n+1] = A[n,K]\delta q[n] + G[n]W[n+2]. \tag{28a}$$

$$\text{Let } \mathbb{E}[\delta q[n]\delta q[n]^T] = R_q[n]. \tag{28b}$$

$$\text{Then } R_q[n+1] = A[n,k]R_q[n]A^T[n,k] + G[n]G[n]^T. \tag{28c}$$

$$\text{Also } \mathbb{E}[\delta q[n]W[m]^T] = 0. \tag{28d}$$

$$\mathbb{E}[\delta q[n]W[m]^T] = A[n,k]\mathbb{E}[\delta q[n]W[m]^T], \quad n \geq m-1 \tag{28e}$$

$$\mathbb{E}[\delta q[m-1]W[m]^T] = \mathbb{E}[\delta q[n+1]W[n+2]^T] \tag{28f}$$

$$\begin{aligned} \mathbb{E}[\delta q[n+1]W[n+2]^T] &= A[n,k]\mathbb{E}[\delta q[n]W[n+2]^T] + G[n] \\ &= G[n] \end{aligned} \tag{28g}$$

Note that, $\delta q[n]$ is a Gaussian vector sequence and its correlation is determined from the above equations.

References

[1] Hokayem P F and Spong M W 2006 Bilateral teleoperation: an historical survey. *Automatica* 42(12): 2035–2057

[2] Islam S, Liu P X and El Saddik A 2013 Nonlinear control for teleoperation systems with time varying delay. *Nonlinear Dyn.* 76(2): 931–954

[3] Sirouspour S and Shahdi A 2006 Model predictive control for transparent teleoperation under communication time delay. *IEEE Trans. Robot.* 22(6): 1131–1145

[4] Polushina I G, Tayebib A and Marquezc H J 2006 Control schemes for stable teleoperation with communication delay based on IOS small gain theorem. *Automatica* 42: 905–915

[5] Namerikawa T, Ito S and Kawada H 2005 Robust control of master–slave robot system considering environment uncertainties. *Proc. SPIE* 60520F-1

[6] Agarwal V 2012 Trajectory planning of redundant manipulator using fuzzy clustering method. *Int. J. Adv. Manuf. Technol.* 61(528): 727–744

[7] Li Z and Su CY 2013 Neural-adaptive control of single-master multiple-slaves teleoperation for coordinated multiple mobile manipulators with time-varying communication delays and input uncertainties. *IEEE Trans. Neural Netw. Learn. Syst.* 24(9): 1400–1413

[8] Watcharin P-N 2013 Adaptive four-channel neuro-fuzzy control of a master–slave robot. *Int. J. Adv. Robot. Syst.* 10: 150. doi:10.5772/55591

[9] Kim B Y and Ahn H S 2013 A design of bilateral teleoperation systems using composite adaptive controller. *Control Eng. Pract.* 21: 1641–1652

[10] Mohammadi A, Tavakoli M and Marquez H J 2011 Disturbance observer-based control of non-linear haptic teleoperation systems. *IET Control Theory Appl.* 5(18): 2063–2074

[11] Passenberg C, Peer A and Buss M 2010 A survey of environment-, operator-, and task adapted controllers for teleoperation systems. *Mechatronics* 20: 787–801

[12] Cho C W S 2000 *Nonlinear random vibration, analytical techniques and applications*, 2nd ed. Boca Raton, FL: CRC Press

[13] Erickson D, Weber M and Sharf I 2003 Contact stiffness and damping estimation for robotic systems. *Int. J. Robot. Res.* 22(1): 41–57

[14] Hua C C and Liu P X 2009 Convergence analysis of teleoperation systems with unsymmetric time-varying delays. *IEEE Trans. Circuits Syst. II: Express Briefs* 56(3): 240244

[15] Love L J and Book W J 2004 Force reflecting teleoperation with adaptive impedance control. *IEEE Trans. Syst. Man Cybern. B Cybern.* 34(1): 159–165

[16] Yamamoto T, Bernhardt M, Peer A, Buss M and Okamura A M 2008 Techniques for environment parameter estimation during telemanipulation. In: *Proceedings of the 2nd Biennial IEEE/RAS-EMBS International Conference on Biomedical Robotics and Bio mechatronics*, USA

[17] Chan L, Naghdy F and Stirling D 2013 Extended active observer for force estimation and disturbance rejection of robotic manipulators. *Robot. Auton. Syst.* 61(12): 1277–1287

[18] Vitus M P and Tomlin C J 2011 Belief space planning for linear, Gaussian systems in uncertain environments. In: *18th World Congress of the International Federation of Automatic Control*, Milan, Italy

[19] Van Trees H L, Bell K L and Tian Z 2013 *Detection, estimation and modulation theory, part I: detection, estimation, and filtering theory*, 2nd ed. London: Wiley, ISBN: 978-0-470-54296-5

[20] Rao P B L S 1980 *Statistical inference for stochastic processes*. London: Academic Press

[21] Rao R C 2001 *Linear statistical interference and its applications*, 2nd ed. London: Wiley

[22] Singla R, Agarwal V and Parthasarathy H 2015 Statistical analysis of tracking and parametric estimation errors in a 2-link robot based on Lyapunov function. *Nonlinear Dyn.* 82(1): 217–238

[23] Jazwinski A H 1970 *Stochastic processes and filtering theory*. New York: Academic Press, ISBN 0-12-381550-9

[24] Myung I J 2002 Tutorial on maximum likelihood estimation. *J. Math. Psychol.* 47(2003): 90–100

[25] Moschitta A and Carbone P 2007 Noise parameter estimation from quantized data. *IEEE Trans. Instrum. Meas.* 56(3): 736–742

[26] Saatci E and Akan A 2010 Inverse modeling of respiratory system during noninvasive ventilation by maximum likelihood estimation. *EURASIP J. Adv. Signal Process.* 2010: 237562. doi:10.1155/2010/237562

[27] Phong L D, Choi J, Lee W and Kang S 2015 A novel method for estimating external force: simulation study with a 4-DOF robot manipulator. *Int. J. Precis. Eng. Manuf.* 16(4): 755–766

[28] Spong M W, Hutchinson S and Vidyasagar M 2005 *Robot modelling and control*, 1st ed., London: Wiley

[29] Mendel J M 1987 *Lessons in digital estimation theory*. Prentice Hall Signal Processing Series

[30] Rao P B L S 2002 Nonparametric inference for a class of stochastic partial differential equations based on discrete observations. *Indian J. Stat.* 64(Ser A, pt. 1): 1–15

[31] Ioannis K and Shreve S 1998 *Brownian motion and stochastic calculus*. Graduate texts in Mathematics, vol. 113, 2nd ed. 470 pp. New York: Springer, ISBN 978-1-4612-0949-2

[32] Smith L 2006 *Sequential Monte Carlo particle filtering for state estimation*. Thesis, Carleton University, Ottawa, Ontario

[33] Brewer J 1998 Kronecker products and matrix calculus in system theory. *IEEE Trans. Circuits Syst.* 25(9): 772–781

RIET-IJSET: International Journal of Science, Engineering and Technology
Volume 4, Number 1, January-June 2017 pp. 64-75
DOI: 10.5958/2395-3381.2017.00007.7

IndianJournals.com
A product of Diva Enterprises Pvt. Ltd.

Evaluation of Energy Ratios Using Life Cycle Analysis for Mahua, Jatropha and Neem Biodiesels

Mukesh Kumar[1]*, Onkar Singh[2] and Naveen Kumar[3]

[1]Research Scholar, Uttarakhand Technical University, Dehradun, Uttarakhand, India.
[2]VC, Madan Mohan Malaviya University of Technology, Gorakhpur, Uttar Pradesh, India.
[3]Professor, Mechanical Engineering Department, Delhi Technological University, Delhi, India.
*(*Corresponding author) email id: mukeshyadav1984@gmail.com*

www.IndianJournals.com
Members Copy, Not for Commercial Sale
Downloaded From IP - 14.139.251.107 on dated 23-May-2017

ABSTRACT

In the present energy crisis scenario of the world, biodiesels are the best alternatives to the mineral diesel fuel. Due to big climatic assortment, there are several nonedible oil bearing seed plants available in India. The energy is consumed in every stage of biodiesel production. Biodiesel production process involves various stages, i.e., nursery plantation, growth, seed collection, oil extraction, transesterification. For biodiesel production, mahua, jatropha and neem are the capable tree variety available in India. For this research work, a life cycle analysis technique is used in which cradle to grave analysis takes place. This research shows the organized evaluation of the energy consumed by mahua, jatropha and neem trees at each phase during the development cycle and conversion of its seed oils to bio-diesel fuels. Evaluated results verify that the total energy consumed during complete life of the plants in study is lower than the energy output through combustion in IC engine.

Keywords: Life cycle analysis (LCA), bio-diesel, energy ratio, energy consumption, Plantation, growth, yielding.

INTRODUCTION

As an alternative fuel, biodiesel has many good qualities. It is produced from domestic resources which are renewable in nature. Among all nonedible vegetable oils, mahua (*Madhuca indica*), jatropha (*Jatropha curcas*) and neem (*Azadirachta indica*) are the encouraging species as they can be developed in Indian variety of sands. Mahua and neem are long trees and underutilized while jatropha is a small tree with 4–6 mheight. Jatropha has highest yield of oil, an animal repellent and can be grown in areas of low rain fall. Life cycle analysis (LCA) method is used to assess the environmental impacts of a product during its life cycle [1–4]. Energy life cycle of the biodiesel starts with the extraction of raw material, i.e., plant nursery and ends with conversion to the biodiesels.

Jatropha curcas is drought-resistant plant which grows fine in marginal land of low to high rainfall areas and can be used as a commercial crop. It grows wild in many areas and even survives in infertile soil. The plant is easy to grow and produces seed for 50 years life span. The maximum oil

content that has been reported for jatropha seeds has been close to 47%. However, the accepted average is 37–40%.

The *Madhuca indica*tree grows up to 8–9 m and matures 9th year and yield fruits up to 60 years. It is a large deciduous tree and grows in semidry, tropical and subtropical areas, in altitude up to 1200m. It grows even on rocky, sandy, dry shallow soils and tolerates water logging conditions. *Madhuca indica*grows in South India, Bihar.

The scientific name of neem is *Azadirachta indica*. It is a large tree of around 3–4 m. The neem kernels have 35–55% of an acrid bitter greenish yellow to brown oil with strong garlic like smell.

LCA shows the inputs of extra energy needs to convert the energy present in the raw material in to useable energy of the fuel. The LCA calculates the net energy ratio which is evaluated by dividing the energy output of the system in the form of fuel energy delivered to the compression ignition engine by the cumulative energy demand of the system. The study analyses biodiesel production and identifies resource consumption and energy use for various life cycle stages and sub processes. In the present study, energy LCA for biodiesels obtained from three oils (mahua, jatropha and neem) is carried out. Variations in net energy ratios under different environmental conditions are analysed.

www.IndianJournals.com
Members Copy, Not for Commercial Sale
Downloaded From IP - 14.139.251.107 on dated 23-May-2017

METHODOLOGY

To find the consumed energy by mahua, jatropha and neem plants during the life cycle, a cradle to grave analysis is carried out for produced biodiesel used in CI engine, energy inputs at every stage of the cycle during plant nursery, plantation, growth, seed collection, oil extraction, transesterification and care and safety are calculated. The total energy input is calculated by adding up all energy heads of life cycle of plants and then it is compared with the total calorific value of the fuel. One hectare land area is considered as reference for this study. Energy considered in interaction during life cycle is indirect energy, given to the system and not direct energy such as energy contained in the soil and solar energy taken by plant (Fig. 1).

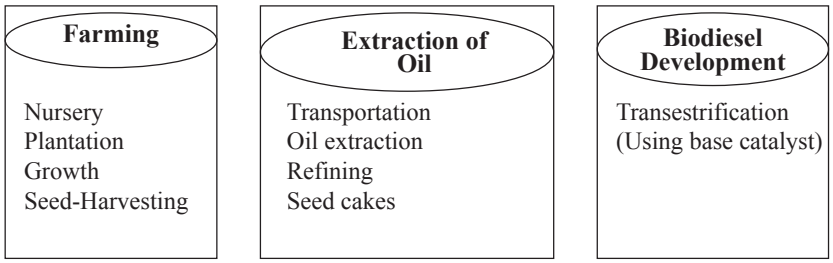

Fig. 1.System and types of energy interaction.

ASSUMPTIONS AND INPUT PARAMETERS

The study analyses biodiesel production and identifies resource consumption and energy use for the following life cycle stages and subprocesses:

(i) Mahua, jatropha and neem cultivation;

(ii) Mahua, jatropha and neem oil extraction; and

(iii) Biodiesel production from mahua, jatropha and neem oil via the transesterification.

The following assumptions are made for calculating energy ratios using LCA [9]:

(i) Cultivation of mahua, jatropha and neem starts since nursery.

(ii) Nursery plants per hectare are 200 trees for mahua, 2400 trees for jatropha and 400 trees for neem.

(iii) No chemicals are used in the cultivation or plantation and management process.

(iv) No pesticides, insecticides, or herbicides are applied to the crops.

(v) It is assumed that the amount of fertilizers used in the plantation equals the amount of the seed cak

(vi) No energy is considered for creating or manufacturing of machinery used in farming and ir rigation to help the production of biodiesels.

(vii) No other use of seed cake is taken into account.

(viii) The LCA of all biodiesels is done for the growth time up to first yielding.

Input Parameters

Jatropha tree starts yielding at the age of four years while it starts flowering at the age of one year. Neem and mahua trees start fruiting at the age of 5–6 years but after 9 years they starts yielding fully.Table1 shows the yielding age, seed pod yield, seed yield per plant, seed yield per hectare, oil yield per hectare and extraction efficiency of mahua, neem and jatropha plants.

Table 1. Yielding of mahua, neem and jatropha seed/seed pod/oil [5–8].

S.no.	Item	Mahua	Neem	Jatropha
1	Plant age at yielding (year)	9	9	4
2	Seed pod yield per plant (kg)	90	30	3.82
3	Seed yield per plant (kg)	40	16	1.8
4	Seed yield per hectare (t)	9	6	4
5	Oil yield per plant (t)	2.3	1.5	1.3
6	% Oil yield	34	29	36
7	Oil extraction efficiency	94	95	95

www.IndianJournals.com
Members Copy, Not for Commercial Sale
Downloaded From IP - 14.139.251.107 on dated 23-May-2017

MATHEMATICAL MODELLING OF INPUT PARAMETERS

For the LCA analysis, the numerical formulations are carried out for various processes involved in plant growth and biodiesel production. A ground survey is done to calculate the various coefficients involved in the mathematical analysis. In this modelling, the energy consumed in developing various machines, materials and manpower is not taken in considerations which are used in biodiesel production cycle. The energy input parameters starting from plant nursery to the transesterification process, i.e., biodiesel production are divided in seven categories detailed as follows [10].

Plant Nursery

It covers energy inputs in soil preparation, soil bag fillings, watering the soil bags, machinery and man power used, care and safety up to one month. Four type of energy inputs are involved, energy in machinery for ploughing, irrigation, manures and manpower for all the activities of plant nursery [11].

Ploughing

For nursery plantation, the soil is prepared by ploughing. A tractor is used to plough the soil. The energy used in ploughing is calculated by

$$E_{NP}=V_f\times SG\times CV\times K \quad \text{.....(1)}$$

where

K=1 for normal soil; K=1.1 for hard soil; and K=0.9 for soft soil.

Irrigation

The half-litre of water is required to irrigate the nursery plants in rainy season with a pump of one kWh which is capable to supply one thousand litre of water in one hour. The energy used in irrigation is calculated by

$$E_{NI}=60\times 60\times RP\times T\times D\times Kr \quad \text{.....(2)}$$

where

D=1 for normal depth up to 100 m ; D=0.2 for ground water; D=1.3 for depth more than 100 m; Kr=1, for average rainfall; Kr=3, for no rainfall; and Kr=0.4, for heavy rainfall.

Manpower Used

As per standards given by Sherwood, a human labour works at the rate of 1.0 kJ/h under normal working conditions, 0.84 kJ/h under soft working conditions and 1.2 kJ/h under hard working conditions. By using these parameters, the energy used as manpower in various stages of life span of plants is calculated by

www.IndianJournals.com
Members Copy, Not for Commercial Sale
Downloaded From IP - 14.139.251.107 on dated 23-May-2017

$$E_{NM}=E\times[(L_1\times T_1)+(L_2\times T_2)+(L_3\times T_3)+(L_4\times T_4)+(L_5\times T_5)] \quad \text{.....(3)}$$

where

L_1=1.1, for labour type used in ploughing; L_2=1.3, for labour type used in soil preparation using manures; L_3=1.3, for labour type used in filling soil bags; L_4=1.3, for labour type used in irrigation; and L_5=1.3, for labour type used in general manpower use.

Total energy consumed by plants nursery is the sum of all three energies from (1)–(3):

$$E_N=E_{NP}+E_{NI}+E_{NM}. \quad \text{.....(4)}$$

Plantation and Management

Factors such as land type, land preparation, irrigation, care and safety, etc., are analysed for energy use in plantation and caring up to the age of one year of the plant. Four type of energy inputs as required in plant nursery are involved here also, energy in machinery for ploughing, irrigation, manures and manpower for all the activities of plant nursery.

Total energy consumed in plantation and management is

$$E_{PL}=E_{PL1}+E_{PL2}+E_{PL3}+E_{PL4}. \quad \text{.....(5)}$$

Growth

After one year of plant age, growth is seenup to 3 years of age. So man power for safety and care is the input for the 2 years of growth. After this, no additional energy input is required. After 1 year plant age, normal rainfall and the biomass produced by plant itself is sufficient for plant growth [8]. Two hours working of a labour is needed daily for two years for safety and care of plants (i.e., after 12 months to 36 months). Few sprays of water are also given in a year.

Total energy consumed in growth can be calculated as

$$E_{GR}=E\times T+2.5\times E_{PL2}. \quad \text{.....(6)}$$

Seed Collection

No machines are used in fruit collection, fruit drying, dehusking of fruits and seed drying. These processes are carried out manually. Collected fruits are dried in open sunlight for 4–5 days and dehusking of fruits is carried out. Finally, the drying of seeds is done for another 2–3days. Energy consumed in seed collection is calculated as

$$E_{SC}=E\times(T_1+T_2+T_3+T_4)\times K \quad \text{.....(7)}$$

where

www.IndianJournals.com
Members Copy, Not for Commercial Sale
Downloaded From IP - 14.139.251.107 on dated 23-May-2017

T_1–time taken for fruit collection (hours); T_2– time taken for drying of fruits (hours); T_3– time taken for de-husking of fruits (hours); and T_4– time taken for seeds drying (hours).

Transportation of Seeds

Energy input is given to an IC engine tractor-trolley which is used to transport seeds from the field to the biodiesel production unit. Seeds are collected first and then dried there and then transported to the unit at the distance of 3–4 km where extractions of oil and esterification units are installed. The tractor consumes 3 litre diesel fuels and takes one hour. Two labours are engaged in loading and unloading of seeds for four hours.

Energy consumed in transportation of seeds is given by

$$E_{TP}=V\times SG\times CV+E\times T. \quad \text{.....(8)}$$

Oil Extraction

Oil is extracted from seeds by an oil expeller of capacity 1 t of seed/hour. Energy consumed in oil extraction is given by

$$E_{EX}=P\times M+E\times T \quad \text{.....(9)}$$

Where T is the time used of manpower in oil extraction.

Transesterification

A transesterification unit of capacity 50,000 t per annum is considered for analysis. In the transesterification process, energy of alcoholis not considered in analysis as during the chemical process equivalent amount of glycerine is produced as by-product.

The efficiency of this process is considered 90%:

$$E_{TE}=(P\times M)\times n+E\times T. \quad \text{.....(10)}$$

SYSTEM INPUT ENERGY

The total energy input in all the subprocesses gives the total energy demand of the biodiesel life cycle evaluation of energy ratios for mahua which is energy input (E_{input}) to the system. This energy input is indirect energy. Other energies such as solar energy, energy contained in soil are not considered:

$$E_{input}=E_N+E_{PL}+E_{GR}+E_{SC}+E_{TP}+E_{EX}+E_{TE}. \quad \text{.....(11)}$$

www.IndianJournals.com
Members Copy, Not for Commercial Sale
Downloaded From IP - 14.139.251.107 on dated 23-May-2017

SYSTEM OUTPUT ENERGY

Methyl esters of all three oils (biodiesels) contain the energy, which is given by

$$E' = CV_{BD} \times W \times 1000 \quad \text{.....(12)}$$

where

CV_{BD}=heating value of biodiesel (kJ/kg); W=Quantity of biodiesel (ton).

Consideringbrake thermal efficiency (BTE) of a CIengine as 25%, brake output energy will give the following amount:

$$E_{output} = 0.25 \times E' . \quad \text{.....(13)}$$

NET ENERGY RATIO

Net energy ratio can be calculated as

$$ER = E_{output} / E_{input} . \quad \text{.....(14)}$$

Table 2. Energy per hectare consumed by mahua, neem and jatropha biodiesel in LCA analysis.

S.no.	Items		Para meters	Mahua (kJ)	Neem (kJ)	Jatropha (kJ)
1	Plant Nursery(one month)	Ploughing, Water spray and Manpower	Normal soil	238	249	482
			Hard soil	273	296	574
			Soft soil	187	218	379
2	Plantation and care (up to one year)	Ploughing, Water spray and Manpower	Normal soil	1648	1829	2594
			Hard soil	1895	2196	3096
			Soft soil	1384	1469	2172
3	Growth and care (one to three years)		Normal soil	1016	1235	1503
			Hard soil	1138	1356	1696
			Soft soil	945	1109	1138
4	Seed collection		Machine and Manpower	1421	1527	1714
5	Transportation		Machine and Manpower	115	112	94
6	Oil extraction		Machine and Manpower	673	598	428
7	Transesterification		Machine and Manpower	204	192	164
8	Energy output from engine using biodiesel			9079	9281	8610

www.IndianJournals.com
Members Copy, Not for Commercial Sale
Downloaded From IP - 14.139.251.107 on dated 23-May-2017

RESULTS AND DISCUSSIONS

Table 1 shows the different energy life cycle parameters of the energy inputs and output for the three biodiesels. For different parameters, net energy ratios are evaluated of different soil conditions. Table 2 shows the results of different energy inputs and output for the LCAwith varying parameters. The total energy input essential to convert the energy contained in the raw material into useable form is lower than the energy output by the system. Table 2 also shows the energy received by biodiesel combustion in the CI engine. The energy shown in Table 1 is indirect energy given to the system and direct energy is not considered. The wood of mahua tree can be used in making wooden furniture which helps in permanent seizure of greenhouse gases [12,13]

In Figs. 2–4, the requirement of energy in plant nursery, plantation and management and growth is shown for different soil conditions.

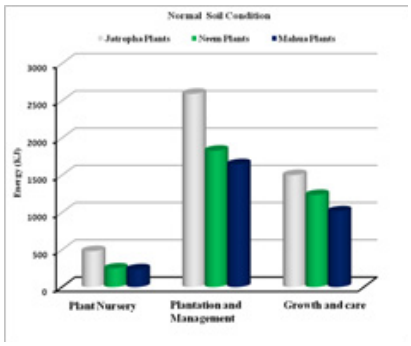

Fig. 2. Energy requirement for plant development up to 3 years under normal soil conditions.

Fig. 2 shows the variation of energy consumed in plant growth under normal soil conditions when energy life cycle of all three biodiesel is considered. Figure shows jatropha needs maximum energy for all life cycle stages while energy requirement for mahua is minimum for normal soil conditions. The highest energy consumed under normal soil condition is 2594 kJ for plantation and management of jatropha plant.

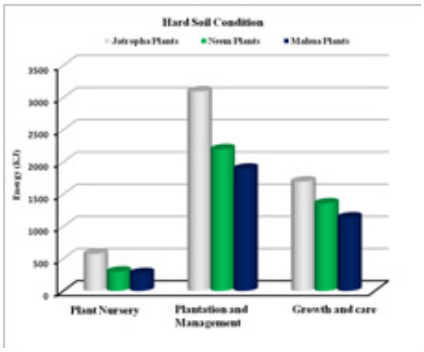

Fig. 3. Energy requirement for plant development up to 3 years under hard soil conditions.

www.IndianJournals.com
Members Copy, Not for Commercial Sale
Downloaded From IP - 14.139.251.107 on dated 23-May-2017

Fig. 3 shows the variation of energy consumed in plant growth under hard soil conditions when energy life cycle of all three biodiesel is considered. The highest energy consumed under hard soil condition is 3096 kJ for plantation and management of jatropha plant. Figure shows jatropha needs maximum energy for all life cycle stages while energy requirement for mahua is minimum for hard soil conditions.

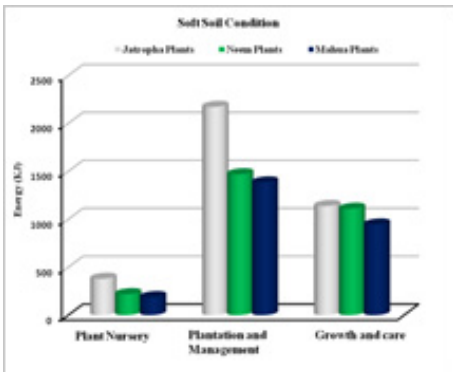

Fig. 4. Energy requirement for plant development up to 3 years under soft soil conditions.

Fig. 4 shows the variation of energy consumed in plant growth under soft soil conditions when energy life cycle of all three biodiesel is considered. Figure shows the energy requirement for mahua is minimum while jatropha needs maximum energy for all life cycle stages for normal soil conditions. The highest energy consumed under soft soil condition is 2172 kJ for plantation and management of jatropha plant.

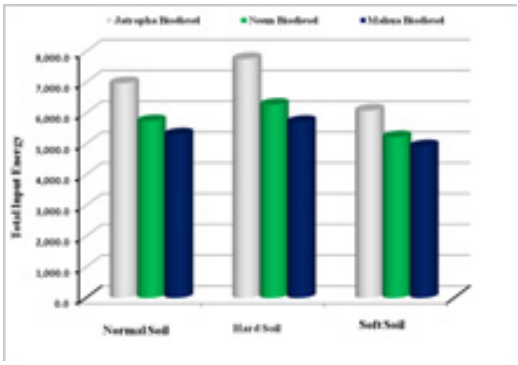

Fig. 5. Total input energy required for plant development.

Total energy input given to the plants is shown in Fig. 5 for all soil conditions. Maximum energy requirement is for jatropha plants under hard soil conditions while minimum energy requirement is for mahua plants under soft soil conditions.

www.IndianJournals.com
Members Copy, Not for Commercial Sale
Downloaded From IP - 14.139.251.107 on dated 23-May-2017

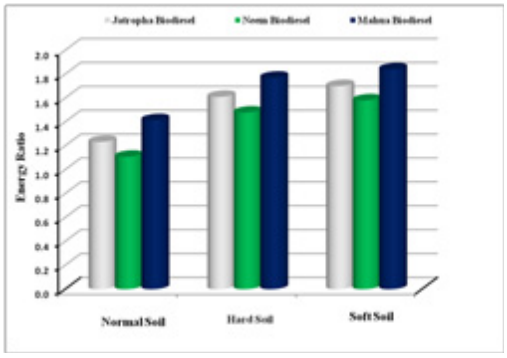

Fig. 6. Energy ratios for jatropha, neem and mahua biodiesels under different soil conditions.

The energy ratios are above unity. Mahua biodiesel shows highest energy ratio for soft soil conditions while neem biodiesel shows minimum energy ratio for normal soil conditions. Mahua biodiesel is to be a good renewable fuel for environment. Higher energy ratio means consumption of indirect energy is less during growth because mahua has the ability to with stand adverse conditions of soil condition and rainfall. Fig. 6 shows the variation of net energy ratio for all biodiesels considered for the LCA analysis.

CONCLUSIONS

Estimated life cycle energy ratio of biodiesels using LCA shows that all the three bio fuels are renewable. The energy output from all three methyl esters is more than input. Under normal soil conditions, mahua, neem and jatropha biodiesel life cycle have energy ratios, ER_M=1.7, ER_N=1.61 and ER_J=1.233, respectively. Under hard soil conditions, mahua, neem and jatropha biodiesel life cycle have energy ratios, ER_M=1.58, ER_N=1.478 and ER_J=1.108, respectively. Under soft soil conditions, mahua, neem and jatropha biodiesel life cycle have energy ratios, ER_M=1.84, ER_N=1.77 and ER_J=1.414, respectively.The highest variation in net energy ratio is among jatropha and mahua biodiesel (1.10–1.84). Mahua biodiesel has highest energy ratio under soft/sandy soil conditions. By using latest technologies and less use of manpower, the net energy ratios can be improved.

REFERENCES

[1] Yadav A, Singh O, Kumar N. Evaluation of energy ratios for karanja and neem biodiesel life cycles. *SAMRIDDHI–J Phys Sci Eng Technol*2010;1(1):55–9.

[2] Bhattacharya P, Joshi B. Strategies and institutional mechanisms for large scale cultivation of *Jatropha curcas* under agroforestry in the context of the proposed biofuel policy of India. *ENVIS Bull Grassland Ecosyst Agroforest*2003;1(2):58–72.

[3] Rao DG, Gupta RC, Goel AK, Yadav A. An integrated system of complete assessment of transesterified jatropha oil in CI engine starting from growth of the plant. In *Proceedings of the Joint International Conference on ASR - NSC New Delhi*; 2009.

www.IndianJournals.com
Members Copy, Not for Commercial Sale
Downloaded From IP - 14.139.251.107 on dated 23-May-2017

[4] Yadav A, Singh O.A comparative evaluation of compression ignition engine performance using preheated jatropha, karanja and neem oils. *J Power Energy* 2009;223–224(1):47–57.

[5] Deep A, Kumar N, Kumar M, Singh A, Performance and emission studies of diesel engine fuelled with orange peel oil and n-butanol alcohol blends. SAE Technical Paper 2015-26-0049; 2015. DOI:10.4271/2015-26-0049.

[6] Deep A, Kumar N, Gupta D, Sharma A, .Potential utilization of the blend of orange peel oil methyl ester and isopropyl alcohol in CI engine. SAE Technical Paper 2014-01-2778; 2014. DOI:10.4271/2014-01-2778.

[7] Deep A, Kumar N, Karnwal A, Gupta D, .Assessment of the performance and emission characteristics of 1-octanol/diesel fuel blends in a water cooled compression ignition engine. SAE Technical Paper 2014-01-2830; 2014.DOI:10.4271/2014-01-2830.

[8] Deep A, Singh A, Vibhanshu V, Khandelwal A, .Experimental investigation of orange peel oil methyl ester on single cylinder diesel engine. SAE Technical Paper 2013-24-0171; 2013. DOI: 10.4271/2013-24-0171.

[9] Yadav A, Singh O. Energy estimations for life cycle analysis of jatropha, neem and karanja biodiesels–a parametric study. J Power Energy2010;224(8):1049–57.

[10] Venkateswara Rao T, Prabhakar Rao G, Hema Chandra Reddy K. Experimental investigation of pongamia, jatropha and neem methyl esters as biodiesel on C.I. engine. Jordan J Mech Ind Eng 2008;2(2):117–22.

[11] Al-Hassana M, Mujafeta H, Al-Shannag M. An experimental study on the solubility of a diesel-ethanol blend and on the performance of a diesel engine fueled with diesel biodiesel – ethanol blends. Jordan J Mech Ind Eng 2012;6(2):147–53.

[12] Nanaki EA, Koroneos CJ. Comparative LCA of the use of biodiesel, diesel and gasoline for transportation. J Clean Prod2012;20(1):14–9.

[13] Liang S, Xu M, Zhang T. Life cycle assessment of biodiesel production in China. Bioresour Technol2013;129:72–7.

APPENDIX

Notation	
CV	Calorific value of diesel (MJ/kg)
CV_{BD}	Calorific value of biodiesel (MJ/kg)
SG	Specific gravity of diesel fuel
D	Constant for ground water
Kr	Constant for rainfall
RP	Rating of water pump(kWh)

www.IndianJournals.com
Members Copy, Not for Commercial Sale
Downloaded From IP - 14.139.251.107 on dated 23-May-2017

E_{NP}	Energy consumed in nursery ploughing
E_{NI}	Energy consumed in nursery irrigation
E_{NM}	Energy consumed in nursery manpower
E_{N}	Energy consumedin plant nursery
E_{PL}	Energy consumed in plantation and management
E_{GR}	Energy consumed in growth
E_{SC}	Energy consumed in seed collection
E_{TP}	Energy consumed in transportation of seeds is given by
E_{EX}	Energy consumed in oil extraction
E'	Energy contained in biodiesels
E_{output}	Total energy output
E_{input}	Total energy input
ER	Net energy ratio
V_{f}	Diesel fuel consumed per hectare
M	Total mass of oil

www.IndianJournals.com
Members Copy, Not for Commercial Sale
Downloaded From IP - 14.139.251.107 on dated 23-May-2017

RIET-IJSET: International Journal of Science, Engineering and Technology
Volume 4, Number 1, January-June 2017 pp. 40-54
DOI: 10.5958/2395-3381.2017.00005.3

IndianJournals.com
A product of Diva Enterprises Pvt. Ltd.

Experimental Analysis of Performance and Emissions of a Diesel Engine Fuelled With Biodiesels (Mahua and Neem)

Mukesh Kumar[1]*, Onkar Singh[2] and Naveen Kumar[3]

[1]Research Scholar, Uttarakhand Technical University, Dehradun, Uttarakhand, India.
[2]VC, Madan Mohan Malaviya University of Technology, Gorakhpur, Uttar Pradesh, India.
[3]Professor, Mechanical Engineering Department, Delhi Technological University, Delhi, India.
*(*Corresponding Author) email id: mukeshyadav1984@gmail.com*

www.IndianJournals.com
Members Copy, Not for Commercial Sale
Downloaded From IP - 14.139.251.107 on dated 23-May-2017

ABSTRACT

The use of nonedible vegetable oils as an alternative fuel for diesel engine is accelerated by the energy crisis due to depletion of resources, oil prices and increased environmental degradation, as well as the great need for edible oil as food and the reduction of biodiesel production cost, etc. Abundance of nonedible vegetable oils which can be exploited for substitute fuel as diesel fuel, two vegetable oils, i.e., mahua and neem oils, were selected for discussion in this paper. There exists a big difference in the fuel properties of two nonedible vegetable oils and its biodiesels considered in this research paper. The target of current research includes testing a medium capacity water-cooled diesel engine fuelled with different biodiesel/diesel fuel blends, i.e., MB10D90 (10% mahua biodiesel with 90% diesel) and NB10D90 (10% neem biodiesel with 90% diesel) which were prepared by volumetric ratio and analysing brake-specific energy consumption, brake thermal efficiency on the performance aspects while studying nitrogen oxides (NO_x), carbon monoxide (CO), hydro carbon (HC) and smoke opacity on the emission aspects with an objective to find out the optimum biodiesel/fuel blend to be run on diesel engine without any modifications. It is clear that during experiments, biodiesel generally causes an increase in NO_x emission and a decrease in HC, CO and smoke opacity emissions compared to diesel fuel.

Keywords: Biodiesel, Petro-Diesel, Mahua And Neem Oils, Engine Testing, Emissions, Performance, Energy.

Abbreviations : % = Percentage, ηth = Thermal efficiency, A = Ampere, Bhp = Brake horse power, BMEP = Brake mean effective pressure, BP = Brake power, BSEC = Brake specific energy consumption, BTE = Brake thermal efficiency, CO = Carbon monoxide, CO2 = Carbon dioxide, cSt = Centistokes, FC = Fuel consumption, h = hour, HC = Hydrocarbon, Hz = Hertz, kg = Kilogram, KGOE = Kilogram of oil equivalent, kJ = Kilo joule, kVA = Kilo volt ampere, kW = Kilo Watt, kWh = Kilo Watt Hour, L = Litre, D100 = Neat diesel, MB10D90 = 10% mahua biodiesel with 90% diesel, NB10D90 = 10% neem biodiesel with 90% diesel, mf = Mass flow rate, v/v = Volume by volume

INTRODUCTION

Energy is a necessary and fundamental input for sustainable socioeconomic growth of a country [1]. Ever since the industrial revolution, the energy consumption has increased exponentially and also led to the serious problem of environmental degradation. The gulf crisis was an eye opener for both developed and developing countries and it was then for the first time the world seriously started looking for alternative source of energy along with efficient utilization of energy. Although oil, coal and natural gas cover most of the world energy needs, nevertheless these fuels are not considered sustainable and are also questionable from an economic, ecological and environmental point of view. The recent volatility in petroleum prices and the growing awareness related to the clean environment have stimulated the recent interest in alternative energy sources.

Alternative fuels are considered very promising to play an important role in meeting the world's energy requirements. India is rich in coal and abundantly endowed with renewable energy in the form of solar, wind, hydro and bio energy; however, its hydrocarbon reserves represent only 0.3% of the global reserves and India is mainly dependent upon crude import to sustain its growth [2]. Moreover, India's per capita consumption is very low at 560 kg of oil equivalent (KGOE) as compared to the world average of 1790 KGOE in 2009 [3]. In 2010–11, India spent 82.89 billion US $ towards import of crude oil [4]. Recently, the use of diesel engines in India has increased by virtue of their low fuel consumption and high efficiencies due to higher compression ratio. These engines are extensively used in transportation, commercial, domestic, electric power generation, farming, construction and in many industrial activities for the generation of power/mechanical energy [5]. However, the exhaust emissions from diesel engines cause environmental pollution. Pollutants from diesel engines include carbon monoxide (CO), carbon dioxide (CO_2), hydro carbon (HC), nitrogen oxides (NO_x), particulate matter (PM) and smoke emissions and these have hazardous effects on air, water and soil as well as a global climatic change and human health.

Amongst the variety of alternative fuels for use in diesel engine, biofuels have the potential to mitigate the vulnerability and the adverse effects of use of fossil fuels. Several developed countries have introduced policies encouraging the use of biofuels to replace part of their fossil fuel use in order to achieve the following goals to prevent environmental degradation by using cleaner fuel, to reduce dependence on imported, finite fossil supplies by partially replacing them with renewable, domestic sources and to provide new demand for crops to support producer income and rural economics.

Within the gamut of biofuels, vegetable oils derived fuels are very promising and have the potential to meet growing energy demand in a sustainable manner. Vegetable oils in neat form are not suitable as a fuel in diesel engine due to high viscosity and need to be chemically modified to produce biodiesel. Biodiesel is a renewable diesel fuel defined as the mono-alkyl esters derived from vegetable oils or animal fats. It is largely competitive with petroleum diesel as far as technical issues are concerned and can be used as a substitute for mineral diesel without major engine modification. Its production and use have expanded exponentially in many countries around the world in recent years. In addition to being biodegradable and nontoxic, biodiesel is also essentially free of sulphur and aromatics, producing lower exhaust emissions than conventional diesel [6]. It

www.IndianJournals.com
Members Copy, Not for Commercial Sale
Downloaded From IP - 14.139.251.107 on dated 23-May-2017

is renewable in nature and safer to handle and helps to reduce the carbon dioxide emission in the atmosphere. It has no aromatic compounds and oxygen atoms in the molecule of fuel may reduce the emissions of CO, total HC and PM [7].

World wide biodiesel production is mainly from edible oils such as soybean, peanut, coconut, sunflower and canola oils. However, biodiesel production from edible oils is not sustainable in India as India is not self-sufficient in edible oil production and imports substantial amount of edible oil for meeting its requirement. In this context, nonedible oils are very promising for biodiesel production in India with abundance of forest and plant-based nonedible oils being available in India such as Pongamia (Karanja), Jatropha curcas (jatropha), Madhuca indica (mahua), Shorearobusta (sal), AzadirachtaIndica (neem), Schleicheraoleosa (Kusum) and Heveabrasiliensis (rubber) [8,9]. A significant amount of work has been done on conversion of vegetable oil into biodiesel [10–13] along with karanja oil [14–17]; however, production of biodiesel from mahua and neem seed oil is recently gaining considerable importance in India [18–20]. In this context, the present study was carried out on two nonedible oils (mahua and neem oil).

Mahua (Species: Madhuca indica, Family: Sapotaccac) is a forest-based tree-borne nonedible oil with annual production potential of 60 million tons in India. It has two major subspecies, i.e., Madhuca indica (latifolia) and Madhuca indica (longifolia) out of which the latter one is the predominant one in the subcontinent. Mahua is an Indian origin deciduous tree mostly found in the dry and arid climates of Northern and Eastern regions of the Indian subcontinent spreading over West Bengal, Bihar, Odisha, Madhya Pradesh, Punjab and Uttar Pradesh along with the submountainous Himalayas. These species, due to their multifaceted usage of flower, leaves, bark, seed oil, seed cake, etc., have been widely domesticated since the ancient times. Mahua grows well on a wide variety of soils such alluvial soil of Indo-gangetic plain, rocky and gravelly red soils, saline and sodic soils, soil between crevices of barren rock, shallow boulder, clay and calcareous soils and so on. However, deep or sandy-loam soils with good drainage are ideal footings for the rapid growth of the plant. It usually attains about 20 m height with the spreading crown. Mahua seeds contain 30–40 per cent oil by mass. The oil is obtained from the seed kernels and is pale yellow, semisolid at room temperature. Crude mahua oil generally contains high % free fatty acid [21–25]. It is well adapted in arid and semi-arid conditions and has low fertility and moisture demand. It can also grow on moderately sodic and saline, degraded and eroded soils. The ideal density of plants per hectare is 2500. It produces seeds after 12 months and reaches its maximum productivity by 5 years and can live 30–50 years. Depending on variety, the decorticated seed of Jatropha contains 43–59% of oil [26,27].

Neem oil is light to dark brown in colour, bitter in taste and has a strong odour. Neem oil can be obtained from solvent extraction of the neem seed, fruit, oilcake, or kernel. The neem oil remaining in the seed cake is extracted using hexane [28]. The neem tree is native to India and Burma [29,30] and almost the whole tree is usable for various purposes such as medicines, pesticides and organic fertilizer. Neem can be grown on every marginal soils which may be very rocky, shallow, dry, or pan forming. Neem tree can tolerate some extreme conditions such as temperature of 45°C and rainfall less than 35 cm per year [31]. Neem tree get full maturity in just 10 years and gives an average seed yield of around 5.25 tonnes per hectare and has oil content of 45%. As the energy

www.IndianJournals.com
Members Copy, Not for Commercial Sale
Downloaded From IP - 14.139.251.107 on dated 23-May-2017

ratio of neem biodiesel is around 1.64, it is considered as one of the best renewable fuels in view of environmental inputs. Azadirachtin is the main constituent of neem seed oil, which varies from 300 to 2500 ppm depending on the extraction technology and quality of the neem seeds crushed [32].

A wide range of exhaustive engine trials have been carried out so far on variety of biodiesel and a comprehensive review of some of the research findings is summarized as follows.

Soo-Young No studied the performance, emissions and applications of seven vegetable oils, i.e., jatropha, karanja, mahua, linseed, rubber seed, cottonseed and neem oils. He found that a diesel engine without any modification would run successfully on the blending of 20% vegetable oil with diesel fuel [33].

Puhan *et al*. produced five biodiesels from different vegetable oils tested on a diesel engine to study the effect of biodiesel fatty acid composition (FAC) specifically unsaturated composition on the engine combustion. The results from fuel analysis show that biodiesel with 45% saturated ester and 55% unsaturated ester composition shows a NO_x neutral fuel with a penalty of 1.75% in thermal efficiency. He was also found that the no significant differences in unburnt HC, CO and smoke emissions among the biodiesel fuels were noticed except for linseed oil methyl ester [34].

Rakopoulos *et al*. investigated comparative performance and emissions study of a direct injection (DI) diesel engine using blends of diesel fuel with vegetable oils or bio-diesels of various origins. Experiments were conduct on a four stroke, DI, Ricardo/Cussons 'hydra' diesel engine with blend ratios of 10/90 and 20/80. The results showed that CO emissions and NO_x emissions were reduced with the use of bio-diesel of various origins with respect to that of the neat diesel fuel, with this reduction being higher than the percentage of bio-diesel in the blend while the unburned HC emissions showed no definite trend, increasing or decreasing, with either the use of bio-diesel or vegetable oil blends of various origins or their percentage increase in the blends [35].

Haldar *et al*. studied the comparison of performance and emission characteristics of a diesel engine using three degummed nonedible vegetable oils. The experiments conducted on 10%, 20% 30% and 40% blends of degummed nonedible putranjiva, jatropha and karanja oils with diesel are used in a Ricardo variable compression engine to study and compare the performance and emission characteristics. During experiments, they found that the out of three nonedible oils, jatropha is promising to yield good performance and emissions (CO, CO2, NO_x and HC) at high loads for all tested blends with respect to diesel fuel [36].

Rakopoulos *et al*. conducted experimental study to evaluate the use of sunflower, cottonseed, corn and olive straight vegetable oils (SVO) of Greek origin, in blends with diesel fuel at proportions of 10% and 20% volume by volume in a fully instrumented, six-cylinder, turbocharged and after-cooled, heavy duty, DI, 'Mercedes-Benz', mini-bus engine. The tested results showed that the smoke opacity was reduced while NO_x emissions were slightly increased by the use of all vegetable oil blends with respect to neat diesel fuel. They also found that the HC and CO emissions were slightly increased for both blends as compared to pilot fuel [37].

www.IndianJournals.com
Members Copy, Not for Commercial Sale
Downloaded From IP - 14.139.251.107 on dated 23-May-2017

Alton *et al*. investigated the effects of vegetable oil fuels and their methyl esters (raw sunflower oil, raw cottonseed oil, raw soybean oil and their methyl esters, refined corn oil, distilled opium poppy oil and refined rapeseed oil) on a direct injected, four stroke, single cylinder diesel engine performance and exhaust emissions was investigated in this paper. The results showed that the particulate emissions of vegetable oil fuels were higher than those of diesel fuel, but on the other hand, NO_2 emissions were less. Vegetable oil methyl esters gave performance and emission characteristics closer to the diesel fuel. So, they seem to be more acceptable substitutes for diesel fuel [38].

Misra *et al*. studied SVOs usage in a compression ignition engine-A review. During their summarized studies, they found that the usage of pure vegetable oil, straight or in a blend with fossil diesel, in a compression ignition engine cannot be underrated. Certainly in tropical developing countries such as India the use of pure vegetable oil, straight or as a blend, is believed to have great potential. The results reveal that SVOs have the potential to reduce NO_x emissions which is one of the major concerns of the world today [39].

Atabani *et al*. conducted study on nonedible vegetable oils: A critical evaluation of oil extraction, FACs, biodiesel production, characteristics, engine performance and emissions production. They concluded that the numerous aspects linked to nonedible oil feedstocks such as nonedible oil resources, advantages of nonedible oils, problems in exploitation of nonedible oils, FAC of various nonedible oils, oil extraction techniques, technologies of biodiesel production, properties and characteristic of nonedible biodiesel and engine performance and emission characteristics have been studied. The determined properties beside the engine performance and emission characteristics of nonedible biodiesel covered in this review indicated that there is a huge chance to produce biodiesel from nonedible sources in the future [40].

Grabosk *et al*. have studied combustion of fat and vegetable oil derived fuels in diesel engines. They found that the lubricity of these fuels is superior to conventional diesel and this property is imparted to blends at levels above 20% volume by volume. Emissions of PM can be reduced dramatically through use of biodiesel in engines that are not high lube oil emitters. Emissions of NO_x increase significantly for both neat and blended fuels in both two- and four-stroke engines [41].

EXPERIMENTAL SET-UP

Fig. 1 shows the schematic diagram of the experimental set-up which is used in the present investigation. It is a Kirloskar made water-cooled single cylinder four-stroke diesel engine. Specification of engine is listed in Table 1.

Table 1. Technical specification of the engine.

Make	Kirloskar
Model	VCR test setup 234
Rated Brake Power (kW)	3.5

www.IndianJournals.com
Members Copy, Not for Commercial Sale
Downloaded From IP - 14.139.251.107 on dated 23-May-2017

Rated Speed (rpm)	1500
Number of Cylinder	One
Bore X Stroke (mm)	87.5 × 110
Compression Ratio	17.5:1
Variable Compression Ratio	12 to 18
Cooling System	Water Cooled
Dynamometer	Eddy current
Piezo Sensor	Range 5000 PSI, with low noise cable
Crank Angle Sensor	Resolution 1°, Speed 5500 rpm with TDC pulse
Load Sensor	Type strain gauge, range 0–50 kg
Cubic Capacity	661CC
Air flow transmitter	Pressure transmitter, Range (–) 250 mm WC
Inlet Valve Open (°)	4.5 BTDC
Inlet Valve Closed (°)	35.5 ABDC
Exhaust Valve Open (°)	35.5 BBDC
Exhaust Valve Closed (°)	4.5 ATDC
Fuel Injection Timing (°)	26 BTDC

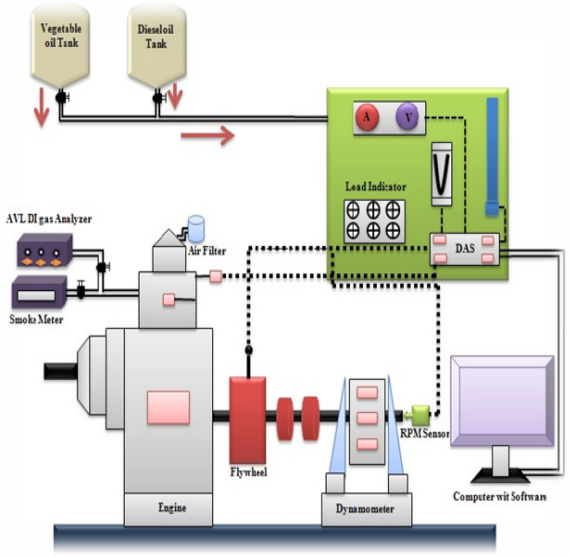

Fig. 1. Schematic diagram of experimental set-up.

www.IndianJournals.com
Members Copy, Not for Commercial Sale
Downloaded From IP - 14.139.251.107 on dated 23-May-2017

All three tests were conducted according to IS: 10,000. A single cylinder water-cooled diesel engine was encumbered by the eddy current dynamometer which was coupled with the use of rigid coupling. A water-cooled dynamometer was connected to a strain gauge type load cell for measurements of load which is applied during whole investigation. Applied loads were taken according to measuring standards, i.e., 0%, 20%, 40%, 60%, 80% and full load. The measurement of pressure time history was completed by a water-cooled piezo-electric pressure transducer which is cabled with the testing engine. To collect the use full information a data acquisition system NI USB-6210, 16-bit was used and stored in a PC for offline analysis. The parameters fed into the computer were cylinder pressure, crank angle, fuel flow rate data, engine speed, etc. The acquisition card could collect data at the rate of 250 kS/s. AVL DI Gas 4000 was used to measure the emission of NO_x, CO and HC. AVL 437 smoke meters were used to measure the opacity of the exhaust gas. The details of engine instrumentation are shown in Table 2.

Table 2. Test rig specifications.

Instrument name	**Range**	**Accuracy**	**Measurement technique**	**% Uncertainty**
Eddy current dyna-mometer	40 Nm	±0.25 N m	Opposing eddy current.	±0.25
Load indicator	0–50 kg	±0.1 kg	Strain gauge type load cell.	±0.2
Fuel flow sensor	0–50 cc	±0.1 cc	Volumetric type.	±0.1
Air flow meter	±100 kg/h	±0.01 kg/h	Turbine flow principle.	
Speed measuring unit	0–10,000 rpm	±10 rpm	Magnetic pick up type.	±0.1
Pressure sensor	0–200 bar	≤0.10	Transmission light principle	±0.25
Exhaust gas analyser				
Carbon Monoxide	0–9.99% vol.	±1%	NDIR principle (nondisper-sive infra-red sensor)	±0.20
Hydrocarbons	0–10,000 ppm	±20 ppm	Flame ionization detector-FID.	±0.20
Oxides of Nitrogen	0–10,000 ppm	±10 ppm	Chemiluminescence prin-ciple.	±0.20
Opacity	0–100% capacity in %0 –∞ absorption m-1	± 1% full scale reading	Selenium photocell Detector	±1%

www.IndianJournals.com
Members Copy, Not for Commercial Sale
Downloaded From IP - 14.139.251.107 on dated 23-May-2017

RESULT AND DISCUSSION

The experiments were conducted using each fuel sample thrice and average of the three reading was taken for further analysis. The performance of the engine was evaluated using parameters such as brake thermal efficiency (BTE) and brake specific energy consumption (BSEC) and emission characteristics such as CO, NO_x, HC and smoke opacity. No visible problem was observed during the experiment for any fuel samples. Characteristics of neem and mahua oil methyl ester are shown in Table 3.

Table 3. Characteristics of neem and mahua oil methyl ester.

Methyl Esters	Density g/cm^3	Kinematic Viscosity at 40°C (mm^2/s)	Cetane Number	Calorific Value (MJ/kg)
Diesel Fuel	0.841	3.35	40–50	42.50
Neem Oil Methyl ester	0.842	5.65	49	38.28
Mahua Oil Methyl ester	0.882	5.5	49	39.33

PHYSICO-CHEMICAL PROPERTIES

Physico-chemical properties of all methyl ester and its blend (in different volumetric proportion) with mineral diesel were evaluated using standard test facilities, straight mahua and neem oil biodiesel has lower calorific value than mineral diesel but has high viscosity and density (straight mahua, neem oil biodiesel has lower calorific value however having high viscosity and density than mineral diesel). The physico-chemical properties evaluated in respect to different blends are summarized in Table 4.

Table 4. Physico-chemical properties of different biodiesel and diesel blends.

Blends	Density (g/cm^3)	Kinematic Viscosity at 40°C (mm^2/s)	Calorific Value (MJ/kg)
MB10D90	0.844	3.57	42.18
NB10D90	0.841	3.58	42.07

BRAKE THERMAL EFFICIENCY (BTE)

The variation in BTE is shown in Fig. 2. It can be observed that BTE of all three biodiesel with diesel blends is lower than that of mineral diesel. At full load condition, the BTE of MB10D90, NB10D90 and D100 was found to be 23.67%, 22.51% and 25.87%, respectively. This is due to the fact that all two blends contain lower calorific value and higher kinematic viscosity as compared to mineral diesel fuel. Due to this, incomplete combustion takes place hence there is a slight decrease in the break thermal efficiency in case of biodiesel diesel blends. These results are in agreement with the result obtained by Kumar *et al*. [42] and Godiganur *et al*. [44].

www.IndianJournals.com
Members Copy, Not for Commercial Sale
Downloaded From IP - 14.139.251.107 on dated 23-May-2017

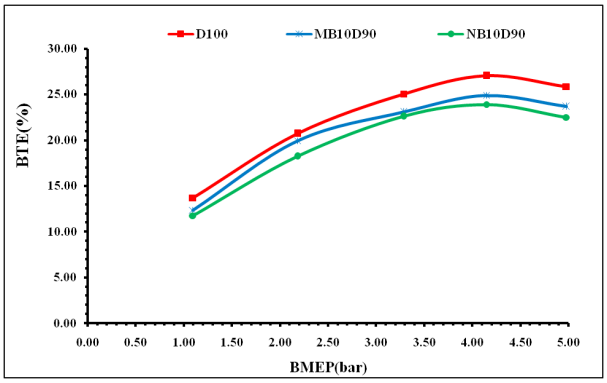

Fig. 2. Variations of BMEP with BTE.

www.IndianJournals.com
Members Copy, Not for Commercial Sale
Downloaded From IP - 14.139.251.107 on dated 23-May-2017

BRAKE SPECIFIC ENERGY CONSUMPTION (BSEC)

BSEC measures the amount of input energy required to develop one-kilowatt power. The BSEC is an important parameter of an engine because it takes care of both mass flow rate and heating value of the fuel (the BSEC takes care of both mass flow rate and heating value of the fuel so it is an important parameter of an engine). Basic specific energy consumption is an essential and ideal parameter for comparing engine performance of the fuels having different calorific value and density. Fig. 3 shows the variation of BSEC for neat diesel and mahua, neem oil biodiesel blends. It is observed that the BSEC is higher for all blends of biodiesels as compared to the mineral diesel fuel. At full load condition, the BSEC for NB10D90 blend is 30.64% higher than that of mineral diesel. These results are similar to the results obtained by Kumar *et al*. (2008) [42] and Adaileh *et al*. [45].

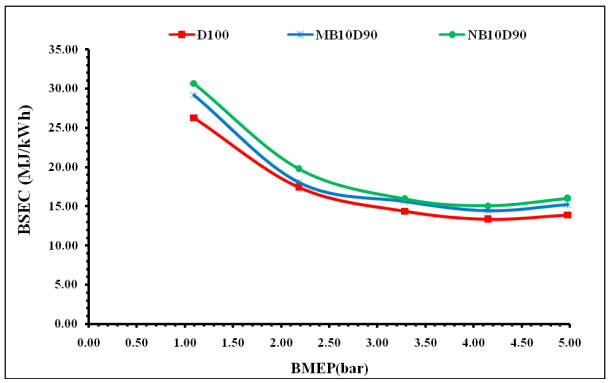

Fig. 3. Variations of BMEP with BSEC.

www.IndianJournals.com
Members Copy, Not for Commercial Sale
Downloaded From IP - 14.139.251.107 on dated 23-May-2017

CARBON MONOXIDE (CO)

The variation of CO emission of blends of diesel and all biodiesels are shown in Fig. 4. It has been observed that the CO emission is lower for all the blends of mahua, neem oil methyl ester than that of neat diesel. The CO emissions are found to be increasing with increase in load since the air–fuel ratio decreases with increase in load such as in internal combustion engines. The engine emits less CO using biodiesel blends as compared to that of diesel fuel under all loading conditions. Due to blending of biodiesel with diesel fuel, CO emission level decreases as amount of oxygen content in biodiesel helps in proper oxidation. The higher cetane number of blend as compared to that of mineral diesel is also one of the reasons of better combustion. These results are in confirmation with the result by Nabi *et al*. [46] and Godiganur *et al*. [44].

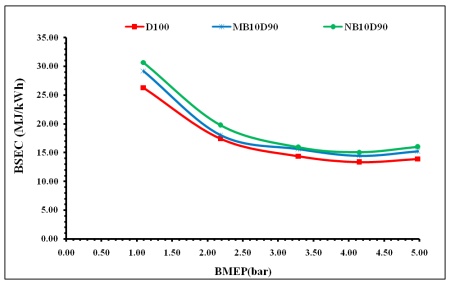

Fig. 4. Variations of BMEP with carbon monoxide.

HYDROCARBON (HC)

The HC emissions of different blends are shown in Fig. 5. It is found that the HC emission is lower for all the blends of mahua oil methyl ester as compared to neat diesel fuel. As the blending of biodiesels with diesel fuel, HC emission decreases. NB10D90 has 9.8% less hydrocarbon emission than that of mineral diesel fuel at full load condition but at part load condition HC emission of diesel is 10.8% more than that of biodiesel blends. The significant decrease in HC emission is due to the complete combustion of the fuels.

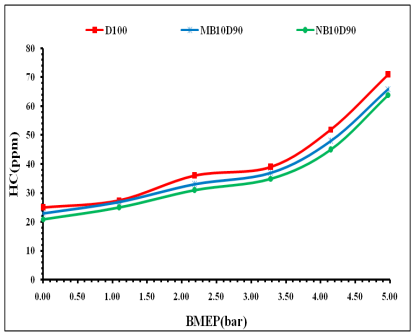

Fig. 5. Variations of BMEP with hydrocarbons.

NITROGEN OXIDE (NO_x)

The nitrogen oxide (NO_x) emissions for different biodiesels and diesel are shown in Fig. 6. The results show that the NO_x emission of biodiesel blends is quite high as compared to the neat diesel with maximum value for MB10D90 fuel. The emission of NO_x is determined by oxygen concentration, peak pressure, combustion temperature and time. The NO_x emission increases when the oxygen availability is increased in biodiesel. This result is in consistent with the results obtained by Adaileh *et al*. [45] and Nabi *et al*. [46].

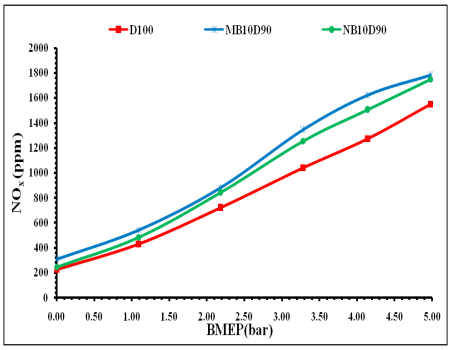

Fig. 6. Variations of BMEP with nitrogen oxide.

SMOKE OPACITY

Fig. 7 shows the variation of smoke opacity of mahua and neem oil methyl ester blends and diesel fuel. From the test results, it was found that the smoke opacity of neat diesel fuel is higher to that of biodiesel blends. At lower loads, the opacity difference is comparable but for full load condition NB10D90 shows lower smoke opacity than that of diesel fuel. The longer ignition delay period (keeping all parameters constant) causes for additional fuel injection before ignition, higher temperature in the cycle and earlier termination of the combustion process. The residence time is therefore increased. All these factors have found to reduce smoke opacity in exhaust. However, previous injection may result in extra combustion noise and nitrogen oxide emission.

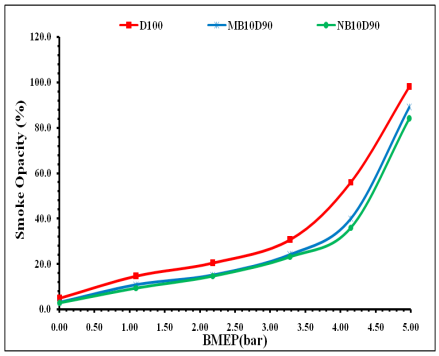

Fig. 7. Variations of BMEP with smoke opacity.

www.IndianJournals.com
Members Copy, Not for Commercial Sale
Downloaded From IP - 14.139.251.107 on dated 23-May-2017

CONCLUSIONS

In the present experimental investigation, a set of exhaustive engine trials were conducted on a naturally aspirated, single cylinder diesel engine fuelled with various blends of biodiesels and diesel. Several performance and emission characteristics of the engine trial and their comparative assessment with diesel baseline are described briefly as follows.

1. Full load BTE was found to decreases with blending of different biodiesels in the diesel fuel. At full load condition BTE of NB10D90 was found to be nearly 12.98% lower than diesel baseline.

2. Maximum peak load BSEC of 26.27 MJ/kWh was observed at the baseline data of diesel. With the blending of all three biodiesel in diesel fuel increasing in BSEC was reported. JB10D90 exhibited BSEC of 15.21 MJ/kWh where as that of NB10D90 showed a maximum BSEC of 15.99 MJ/kWh.

3. Emission of CO was found to reduce with blending of biodiesel in diesel fuel. At part loads CO emission was found to be low for all the test fuels; however, substantial increase was observed after 60% load. Reduction in CO emissions at higher blends may be attributed towards better combustion characteristics of high cetane oxygenated biodiesels.

4. MB10D90 exhibited parallel hydrocarbon emission tendencies as that of diesel baseline. However, other blends of biodiesel showed reduction in HC emission at all loads compared to that of diesel confirming better combustion characteristics.

5. Due to higher cetane rating of all biodiesels and improved combustion characteristics, the in-cylinder temperature was increased resulting in higher NO_x emission for blended fuels as compared to baseline data. Full load NO_x emission was steeply increased by 11.38% for MB10D90 as compared to diesel baseline.

6. Opacity of full load engine smoke was insignificant at lower loads for all the test fuels. However, at higher loads biodiesel blends showed reduction in smoke opacity as compared to neat diesel operation.

REFERENCES

[1] Harrington KJ. Chemical and physical properties of vegetable oil esters and their effect on diesel fuel performance. Biomass 1986;9:1–7.

[2] BP statistical review of world energy; 2012.

[3] Available from: http://data.worldbank.org/indicator/eg.use.pcap.kg.oe.

[4] Petstat, Ministry of Petroleum and Natural Gas, Government of India. Available from: ww.petroleum.nic.in/petstat.pdf [accessed Oct. 2011].

[5] Varde KS. Bulk modulus of vegetable oil-diesel fuel blends. Fuel 1984(63):713.

www.IndianJournals.com
Members Copy, Not for Commercial Sale
Downloaded From IP - 14.139.251.107 on dated 23-May-2017

[6] Srivastava A, Prasad R. Triglycerides-based diesel fuels. Renew Sustain Energy Rev 2000;4(2):111–33.

[7] Fernando BL, Gemma V, Rodríguez R, Pacheco M. Optimisation of FAME production from waste cooking oil for biodiesel use. Biomass Bio Energy 2009;33:862–72.

[8] Puhan S, Vedaraman N, Rambrahamam BV, Nagarajan G. Mahua (Madhuca indica) seed oil: a source of renewable energy in India. J Sci Ind Res 2005;64:890–6.

[9] Patil BS, Gosai DC, Patel AJ. Performance analysis of dual cylinder diesel engine fueled with mahua biodiesel. World J Sci Technol 2012;2(4):24–7.

[10] Deng X, Fang Z, Liu, Y-H, Yu C-L. Production of biodiesel from jatropha oil catalyzed by nanosized solid basic catalyst. Energy 2011;36(2):777–84.

[11] Deng X, Fang Z, Liu, Y-H, Yu C-L. Biodiesel production from jatropha oil by catalytic and noncatalytic approaches. Bioresour Technol 2011;102(2):452–60.

[12] JoonChing J, Agung KD, Yeong WT, Yun HT-Y. Biodiesel production from crude Jatropha curcas L. oil with trace acid catalyst. Chin J Chem Eng 2012;20(4):740–6.

[13] Liu Y, Lu H, Jiang W, Li D, Liu S, Bin L. Preparation of biodiesel from Jatropha curcas L. oil produced by two-phase solvent extraction. Bioresour Technol 2010;101(18):7025–31.

[14] Junfeng Q, Haixian S, Zhi Y. Ultrasonic transesterification of Jatropha curcas L. oil to biodiesel by a two-step process. Energy Convers Manage 2010;51(12):2802–7.

[15] Naik M, Meher LC, Naik SN, Das LM. Acid catalyzed esterification of karanja (Pongamiapinnata) oil with high free fatty acids for biodiesel production. Fuel 2012;98:1–4.

[16] Thiruvengadaravi KV, Nandagopal J, Baskaralingam P, Bala VSS, Sivanesan S. Development of biodiesel from karanja, a tree found in rural India. Fuel 2008;87(8–9):1740–2.

[17] Sharma YC, Singh B. Optimization of two step karanja biodiesel synthesis under microwave irradiation. Fuel Process Technol 2011;92(1):100–5.

[18] Venkatesh KH, Regupathi I, Saidutta MB. Methyl ester of karanja oil as alternative renewable source energy. Fuel 2008;87(8–9):1673–7.

[19] Srivastava PK, Verma M. Biodiesel production from mahua (Madhuca indica) oil having high free fatty acids. Biomass Bioenergy 2005;28(6)601–5.

[20] Ghadge SV, Raheman H. Process optimization for biodiesel production from mahua (Madhuca indica) oil using response surface methodology. Bioresour Technol 2006;97(3):379–84.

[21] Gupta A, Chaudhary R, Sharma S. Potential applications of mahua (Madhuca indica) biomass. Waste Biomass Valorization 2012;3(2):175–89.

www.IndianJournals.com
Members Copy, Not for Commercial Sale
Downloaded From IP - 14.139.251.107 on dated 23-May-2017

[22] Savariraj S, Ganapathy T, Saravanan CG. Experimental investigation of performance and emission characteristics of mahua biodiesel in diesel engine, Renew Energy 2011;2011. Art. ID. 405182. Doi:10.5402/2011\405182.

[23] Padhi SK, Singh RK. Optimization of esterification and transesterification of Mahua (Madhuca indica) oil for production of biodiesel. J Chem Pharm Res 2010;2(5):599–608.

[24] Syers JK, Wood D, Thongbai P. The proceedings of the international technical workshop on the ''feasibility of non-edible oil seed crops for biofuel production. Chiang Rai, Thailand: Mae Fah Luang University; 2007.

[25] Openshaw K. A review of Jatropha curcas: an oil plant of unful□lled promise. Biomass Bioenergy 2000;19(1):1–15.

[26] Balat M. Potential alternatives to edible oils for biodiesel production-a review of current work. Energy Convers Manag 2011;52(2):1479–92.

[27] Azam MM, Waris A, Nahar NM. Prospects and potential of fatty acid methyl esters of some non-traditional seed oils for use as biodiesel in India. Biomass Bioenergy 2005;29(4):293–302.

[28] No SY. Inedible vegetable oils and their derivatives for alternative diesel fuels in CI engines: a review. Renew Sustainable Energy Rev 2011;15(1):131–49.

[29] Knothe G. Biodiesel and renewable diesel: a comparison. Prog Energy Combust Sci 2010;36:364–73.

[30] Banapurmath NR, Tewari PG, Yaliwal VS, Kambalimath S, Basavarajappa YH. Combustion characteristics of a 4-stroke CI engine operated on Honge oil, neem and rice bran oils when directly injected and dual fuelled with producer gas induction. Renew Energy 2009;34:1877–84.

[31] Balaji G, Cheralathan M. Potential of various sources for biodiesel production. Energy Sources A Recover Util Environ Effects 2013;35:831–9.

[32] No S-Y. Inedible vegetable oils and their derivatives for alternative diesel fuels in CI engines: a review. Renew Sustain Energy Rev 2011;15:131–49.

[33] Kumar A, Sharma S. Potential non-edible oil resources as biodiesel feedstock: an Indian perspective. Renew Sustain Energy Rev 2011;15:1791–800.

[34] No S-Y. Inedible vegetable oils and their derivatives for alternative diesel fuels in CI engines: a review. Renew Sustainable Energy Rev 2011;15:131–49. Doi:10.1016/j.rser.2010.08.012.

[35] Puhan S, Gopinath A, Nagarajan G. Combustion, performance and emission characteristics of a DI CI engine using biodiesel with varied fatty acid composition. Int J Renew Energy Technol 2009;1(1). Art.ID. 024732.

www.IndianJournals.com
Members Copy, Not for Commercial Sale
Downloaded From IP - 14.139.251.107 on dated 23-May-2017

[36] Rakopoulos CD, Antonopoulos KA, Rakopoulos DC, Hountalas DT, Giakoumis EG. Comparative performance and emissions study of a direct injection diesel engine using blends of diesel fuel with vegetable oils or bio-diesels of various origins. Energy Convers Manag 2006;47:3272–87. Doi:10.1016/j.enconman.2006.01.006.

[37] Haldar SK, Ghosh BB, Nag A. Studies on the comparison of performance and emission characteristics of a diesel engine using three degummed non-edible vegetable oils. Biomass Bio-energy 2009;33:1013–8. Doi:10.1016/j.biombioe.2008.01.021.

[38] Rakopoulos DC, Rakopoulos CD, Giakoumis EG, Dimaratos AM, Founti MA. Comparative environmental behavior of bus engine operating on blends of diesel fuel with four straight vegetable oils of Greek origin: sun□ower, cottonseed, corn and olive. Fuel 2011;90:3439–46. Doi:10.1016/j.fuel.2011.06.009.

[39] Alton R, Cetinkaya S, Yucesu HS. The potential of using vegetable oil fuels as fuel for diesel engines. Energy Convers Manag 2001;42:529–538, PII: S0196-8904 (00)00080-7.

[40] Misra RD, Murthy MS. Straight vegetable oils usage in a compression ignition engine-a review. Renew Sustainable Energy Rev 2010;14:3005–13. Doi:10.1016/j.rser.2010.06.010.

[41] Atabani AE, Silitonga AS, Ong HS, Mahlia TMI, Masjuki HH, Badruddin IA, Fayaz H. Non-edible vegetable oils: a critical evaluation of oil extraction, fatty acid compositions, biodiesel production, characteristics, engine performance and emissions production. Renew Sustainable Energy Rev 2013;18:211–45. Available from: http://dx.doi.org/10.1016/j.rser.2012.10.013.

[42] Graboski MS, McCormick RL. Combustion of fat and vegetable oil derived fuels in diesel engines. Prog Energy Combust Sci 1998;24:125–64, PII:S0360-1285, 00034-8.

[43] Kumar KS, Velraj R, Ganesan R. Performance and exhaust emission characteristics of a CI engine fuelled with pongamiapinnata methyl ester (PPME) and its blends with diesel. Renewable Energy 2008;33:2294–302. Doi: 10.1016/j.renene.2008.01.011.

[44] Godiganur, Sharanappa BM, Suryanarayana CH, Reddy RP. 6BTA 5.9 G21 Cummins engine performance and emission tests using methyl ester mahua (Madhuca indica) oil/diesel blends. Renew Energy 2009;34:2172–7.

[45] Adaileh WM, AlQdah KS. Performance of diesel engine fuelled by a biodiesel extracted from a waste cocking oil. Energy Procedia 2012;18:1317–34, ISSN 1876-6102. Available from: http://dx.doi.org/10.1016/j.egypro.2012.05.149.

[46] Nurun NM, Mustafizur RM, Shamim AM. Biodiesel from cotton seed oil and its effect on engine performance and exhaust emissions. Appl Therm Eng 2009;29:2265–70. Doi: 10.1016/j.applthermaleng.2008.11.009.

www.IndianJournals.com
Members Copy, Not for Commercial Sale
Downloaded From IP - 14.139.251.107 on dated 23-May-2017

ResearchGate

See discussions, stats, and author profiles for this publication at: https://www.researchgate.net/publication/316472931

Experimental Analysis of Surface Roughness in CNC Taper Turning of Aluminum 6061 Using Taguchi Technique

Conference Paper · April 2017

CITATIONS
0

READS
19

5 authors, including:

Dr Ranganath Muttanna Singari
Delhi Technological University, Formerly Delhi college of Engineering, Delhi, India
83 PUBLICATIONS **165** CITATIONS

SEE PROFILE

Some of the authors of this publication are also working on these related projects:

Working in the area of Tribology (Engine tribology, bearing design, tribology by nano particles and tubes.
View project

Working with CNC Milling View project

All content following this page was uploaded by Dr Ranganath Muttanna Singari on 26 April 2017.

The user has requested enhancement of the downloaded file. All in-text references underlined in blue are added to the original document and are linked to publications on ResearchGate, letting you access and read them immediately.

Experimental Analysis of Surface Roughness in CNC Taper Turning of Aluminum 6061 Using Taguchi Technique

Sanchay Gupta, Vimanyu Chadha, Vishal Sardana, Viplav Setia, Ranganath M Singari
Department of Mechanical, Production and Industrial Engineering
Delhi Technological University
New Delhi, 110058, India
sanchay2303@gmail.com, vimanyuchadha@gmail.com, sardana.vishal.95@gmail.com, viplav.setia@gmail.com, ranganathdce@gmail.com

Abstract

The work and study presented in this paper aims to investigate the effect of various cutting parameters as well as nose radius on surface roughness, in CNC Taper Turning of Aluminum (6061) in dry condition. The effect of cutting conditions (speed, feed and depth of cut) and tool geometry (nose radius) on surface roughness has been studied and analyzed. For the experimentation Taguchi's L27 Orthogonal array has been employed. Analysis of Variance is performed to determine the significance for each parameter. The Nose Radius is identified as the most significant parameter followed by Feed Rate. It is observed that Surface Roughness value decreases with increase in Nose Radius and increases with increase in Feed Rate.

Keywords
ANOVA, Surface Roughness, S/N Ratios, Taguchi, Taper Turning

1. Introduction

Surface roughness is an essential attribute used to determine and evaluate the quality of a turned product. However, the study and optimization of surface roughness is not as easy as determining any other variable. The study of Surface Roughness is harder to achieve as it depends on both controllable and uncontrollable factors. The controllable variables include tool rake angle, feed rate, spindle speed, depth of cut etc. while wearing of tool, material friction, tool degradation etc. factors are much harder to control. Surface roughness of a machined product could affect several of the product's features such as surface friction, wearing, light reflection, heat transmission, ability of distributing and holding a lubricant, coating and resisting fatigue [1]. Hence, achieving optimal roughness response has become crucial for industries to improve their quality and merit. Identifying the most influential parameter allows proper selection of tool material that prolongs the life of tool and minimizes the surface roughness. Consequently, a recent advent in Design of Experiments has given vent to various methods such as Taguchi Method, Response Surface Methodology, etc., that have not only allowed scholars and industrialists to efficiently organize the process of optimizing roughness but has also given way to several techniques to reduce the number of trials that have to be carried out to obtain optimal response. Quality control is a process by the virtue of which businesses seek to ensure that product quality is maintained and improved and manufacturing errors are reduced or eliminated. Prajwalkumar M. Patil et al. [12] observed and analyzed the effect of cutting parameters on the surface roughness and hardness. Taguchi method was analyzed by the authors in the optimization of cutting parameters. L9 orthogonal array was employed to carry out the analysis. The analysis of means (ANOM) and Analysis of variance (ANOVA) were carried out to determine the optimal parameters level and obtain level of importance of each parameter. From the ANOVA, the feed had maximum significance in case of R_a and R_z. Murat Sarikaya et al. [11] used Taguchi design and Response Surface Methodology (RSM) Technique under Minimum Quantity Lubrication (MQL) for analyzing CNC turning parameters. The results were analyzed using 3D surface graphs, signal to noise ratios and main effect graphs of means. Also mathematical model output showed that the developed RSM model was statistically significant and suitable for all the cutting conditions because of higher R^2 value. Ilhan Asiltürk et al. [6] used the Taguchi method and L9 orthogonal array to reduce number of the experiments. Analysis of Variance (ANOVA) was applied to investigate effects of cutting speed, feed rate and depth of cut on surface roughness.

Results indicated that the feed rate had the most significant effect on R_a and R_z. The effects of two factor interactions of the feed rate-cutting speed and depth of cut-cutting speed appeared to be important. Chinnasamy Natarajan et al. [3] predicted and analyzed surface roughness factors of a non-ferrous material using Artificial Neural Network (ANN). A model was developed to predict the surface roughness of material (Brass C26000) through Artificial Neural Networks technique by utilizing feed-forward back propagation training algorithm using Matlab (2009a) software for the data obtained. As the spindle speed increases, for lower feed rates, the surface roughness decreases, for higher feed rates, the surface roughness changes considerably. The depth of the cut influences the surface roughness considerably for a given feed rate. The increase in feed rate causes the surface roughness to increase and then decrease. For lower depth of cut, surface roughness decreases and then increases. Ranganath M S et al. [14] presented a paper on analysis of the effect of the cutting speed, feed rate and depth of cut on surface roughness. The author employed an L27 orthogonal array to carry out the analysis. The ANOVA values proved that speed is the most significant factor; the next significant factor was depth of cut followed by feed.
This paper presents the experimental approach for studying the effects of cutting parameters and nose radius on the surface roughness of the tapered work-piece. Taguchi method was adopted for analyzing the surface roughness and Analysis of Variance (ANOVA) was used for finding the most significant factor that affects the surface response. For different levels of the factors, different output values of surface roughness were obtained. A systematic and organized study of the response values and the control factors in the experiment were tabulated. No significant interactions were observed among the control factors. Feed rate and Nose radius were found to be the most significant factors.

2. Taguchi's Methodology

The Taguchi method of quality control is an approach to engineering that emphasizes the roles of research and development, product design and product development in reducing the occurrence of defects and failures in products. This method considers design to be more important than the manufacturing process in quality control and tries to eliminate variances in production before they can occur. Because noise factors are also present in the process that cannot be controlled, this method identifies the values of controllable factors that minimizes the effect of noise factors and provide an optimal response. The concept of S/N ratio originated in the electrical engineering field. Taguchi effectively applied this concept to establish the optimum condition from the experiments. In an experiment there are number of factors which influence the response but are uncontrollable. These external factors are called the noise factors and their effect on the outcome of the quality characteristics under test is termed "noise." The signal to noise (S/N) ratio measures the sensitivity of the quality characteristics with respect to factors not under control. The S/N ratio indicates the degree of the predictable performance parameter of a product or process in the presence of noise factors.

Steps of Taguchi method are as follows:

1. Identification of main function, side effects and failure mode.
2. Identification of noise factor, testing condition and quality characteristics.
3. Identification of the main function to be optimized.
4. Identification of the control factor and their levels.
5. Selection of orthogonal array and matrix experiment.
6. Conducting the matrix experiment.
7. Analyzing the data, prediction of the optimum level and performance.
8. Performing the verification experiment and planning the future action.

3. Experimental Work

3.1 Work piece Material

Aluminum 6061 was selected as the work material. It is one of the most extensively used of the 6000 series aluminum alloys. This standard structural alloy, one of the most versatile of the heat-treatable alloys, is popular for medium to high strength requirements and has good toughness characteristics. Applications range from transportation components to machinery and equipment applications to recreation products and consumer durables. It is widely used for producing automotive components by turning process.

3.2 Cutting Tool Inserts

CNMG cutting tool inserts of nose radius 0.4 mm, 0.8 mm, 1.2 mm. The geometry of the tool is:

Table 1. Details of Cutting Inserts

Insert	Shape	Clearance Angle	Inscribed Circle Size	Thickness	Nose Radius
CNMG120404	Diamond	0^0	12.7 mm	4.76 mm	0.4 mm
CNMG120408	Diamond	0^0	12.7 mm	4.76 mm	0.8 mm
CNMG120412	Diamond	0^0	12.7 mm	4.76 mm	1.2 mm

3.3 Experimental Plan

The experimental work was carried out on Computer and Numeric Control (CNC) turning center LMW LL20TL3 shown in Fig. 1

Figure 1. CNC Turning- LMW LL20TL3

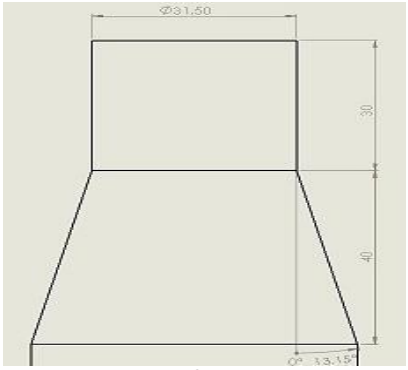

Figure 2. Sketch of Tapered Work piece

Surface Roughness of these machined surfaces has been measured by a Surface Roughness measuring instrument Talysurf Surtronic 3+. Surtronic 3+ is a self-contained, portable instrument for the measurement of surface texture and is suitable for use in both the workshop and laboratory. Parameter used for surface texture evaluation is average roughness (R_a). It is the arithmetic average of absolute roughness profile ordinates. The parameter evaluation and other functions of the instrument are microprocessor based. [13]

3.4 Experimentation and Analysis

Fig. 2 represents the dimensions of the machined work piece. Table 2 represents various Factors and their respective levels. The factors considered are speed, feed rate, depth of cut and Nose radius. Three levels for each factor were considered. The feasible orthogonal arrays for experimentation are L9 and L27. L27 orthogonal array was used as sufficient degrees of freedom could be allocated to each factor and residual error for complete analysis. Table 3 shows the experimental design table along with mean value of surface roughness and S/N ratio for each treatment. The First Four columns of the Table 4 include the coded values of control factors. The different units here are: speed-rpm, feed-mm/rev, depth of cut-mm and Surface Roughness Ra-µm. MINITAB 17 software has been employed for the Analysis.

Table 2. Factors and their Levels

LEVELS	1	2	3
Speed (rpm)	1600	1900	2200
Feed (mm/rev)	0.12	0.18	0.24
Depth (mm)	0.25	0.50	0.75
Nose Radius (mm)	0.4	0.8	1.2

Table 3. Design Table

EXPERIMENT NO.					SPEED (rpm)	FEED (mm/rev)	DEPTH OF CUT (mm)	NOSE RADIUS (mm)	Ra MEAN (µm)	S/N RATIO
	A	B	C	D						
1	1	1	1	1	1600	0.12	0.25	0.4	1.6000	-4.0824
2	1	1	2	2	1600	0.12	0.50	0.8	0.5945	4.5170
3	1	1	3	3	1600	0.12	0.75	1.2	0.5470	5.2403
4	1	2	1	2	1600	0.18	0.25	0.8	1.0150	-0.1293
5	1	2	2	3	1600	0.18	0.50	1.2	0.7635	2.3438
6	1	2	3	1	1600	0.18	0.75	0.4	2.8550	-9.1121
7	1	3	1	3	1600	0.24	0.25	1.2	1.4350	-3.1370
8	1	3	2	1	1600	0.24	0.50	0.4	4.5000	-13.0643
9	1	3	3	2	1600	0.24	0.75	0.8	2.0100	-6.0639
10	2	1	1	1	1900	0.12	0.25	0.4	1.7150	-4.6853
11	2	1	2	2	1900	0.12	0.50	0.8	0.5690	4.8978
12	2	1	3	3	1900	0.12	0.75	1.2	0.5595	5.0440
13	2	2	1	2	1900	0.18	0.25	0.8	1.0400	-0.3407
14	2	2	2	3	1900	0.18	0.50	1.2	1.0090	-0.0778
15	2	2	3	1	1900	0.18	0.75	0.4	3.2600	-10.2644
16	2	3	1	3	1900	0.24	0.25	1.2	1.4150	-3.0151
17	2	3	2	1	1900	0.24	0.50	0.4	4.3450	-12.7598
18	2	3	3	2	1900	0.24	0.75	0.8	2.1150	-6.5062
19	3	1	1	1	2200	0.12	0.25	0.4	1.6550	-4.3760
20	3	1	2	2	2200	0.12	0.50	0.8	0.6725	3.4462
21	3	1	3	3	2200	0.12	0.75	1.2	0.5085	5.8742
22	3	2	1	2	2200	0.18	0.25	0.8	1.0625	-0.5266
23	3	2	2	3	2200	0.18	0.50	1.2	1.1195	-0.9805
24	3	2	3	1	2200	0.18	0.75	0.4	2.7750	-8.8653
25	3	3	1	3	2200	0.24	0.25	1.2	1.3250	-2.4443
26	3	3	2	1	2200	0.24	0.50	0.4	4.4100	-12.8888
27	3	3	3	2	2200	0.24	0.75	0.8	2.1400	-6.6083

The main effect plot for means is shown in fig.3. They show the variation of response with considered parameters i.e. speed, feed and depth of cut and nose radius. In the plot x-axis represents the value of each process parameter and y-axis is response value. Horizontal line indicates the mean of the response. The main effect plots are used to determine the optimal design conditions to obtain the minimum surface finish. It is evident from Fig.3 that R_a is minimum at the first level of speed (A), first level of Feed (B), first level of Depth of cut (C) and third level Nose Radius (D).

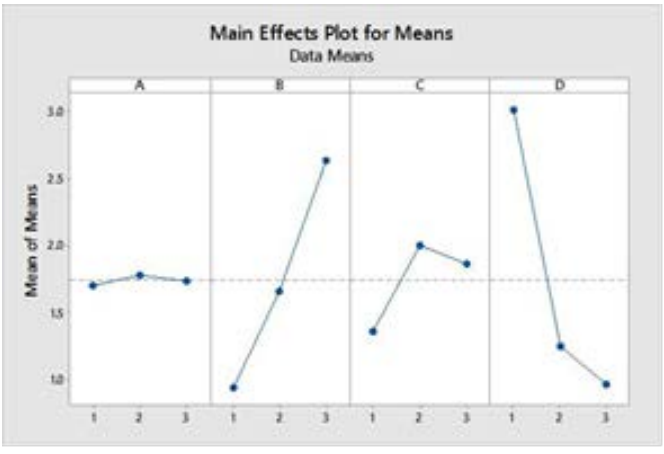

Figure 3. Main Effects Plot for Means

Fig.4 represents Main Effects Plot for S/N Ratio. The objective of using the S/N ratio as a performance measurement is to develop products and the processes insensitive to variance factors. [4] The aim of any experiment is always to determine the highest possible S/N ratio for the result. Process parameters setting with the highest S/N ratio always yield the optimum quality with minimum variance. Consequently, the level that has a larger value is the optimum level of each factor. In Fig.4 level one for speed (1600 rev/mm) has maximum S/N ratio value, which defines that the machining performance at such level gives minimum variation of the surface roughness. Hence, as indicated by main effect plots for S/N ratio, the ideal conditions for least surface roughness (R_a) are speed at level 1 (1600 rev/min), feed at level 1 (0.12 mm/rev), depth of cut at level 1 (0.25 mm)and nose radius at level 3 (1.2 mm).

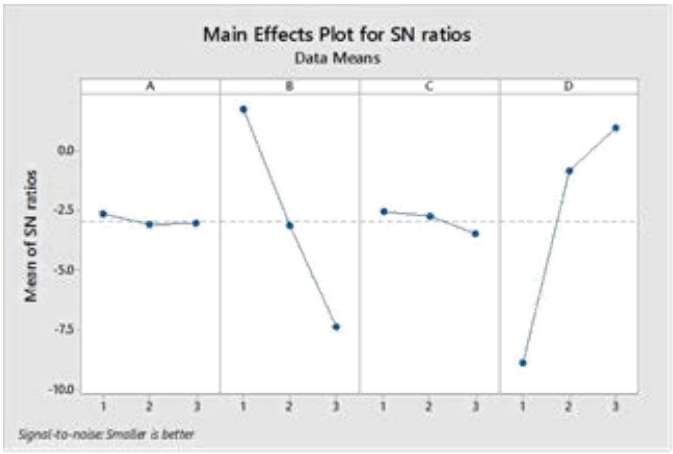

Figure 4. Main Effects Plot for SN Ratios

The purpose of the analysis of variance (ANOVA) is to investigate which design parameter significantly affects the surface roughness. [13] A better feel for the relative effect of the different factors can be obtained by the decomposition of the variance, which is commonly known as analysis of variance (ANOVA). [4] Table.4 and Table.5 shows the analysis of variance (ANOVA) for Means and S/N ratio respectively. In the present investigation, ANOVA and the F-test are applied to analyze the experimental data. Nose Radius and Feed are the most significant factors followed by depth of cut. The spindle speed has very less effect on the response in this experiment.

Table 4. Analysis of Variance (ANOVA) table for Means

SOURCE	DF	Adj SS	Adj MS	F Value	P Value
A	2	0.0278	0.0139	0.08	0.921
B	2	13.0603	6.5301	39.21	0.000
C	2	2.0190	1.0095	6.06	0.036
D	2	22.1818	11.0909	66.59	0.000
A*B	4	0.0515	0.0129	0.08	0.986
A*C	4	0.0572	0.0143	0.09	0.984
A*D	4	0.0362	0.0091	0.05	0.993
RESIDUAL ERROR	6	0.9993	0.1665		
TOTAL	26	38.4331			

Table 5. Analysis of Variance (ANOVA) table for SN Ratios

	DF	Adj SS	Adj MS	F Value	P Value
A	2	1.222	0.611	0.60	0.581
B	2	377.392	188.696	184.18	0.000
C	2	4.476	2.238	2.18	0.194
D	2	498.891	249.445	243.43	0.000
A*B	4	1.837	0.459	0.45	0.772
A*C	4	2.755	0.689	0.67	0.635
A*D	4	1.249	0.312	0.30	0.865
RESIDUAL ERROR	6	6.148	1.025		
TOTAL	26				

Table.6 and Table.7 are the response tables for S/N ratio and Mean. The response tables explain that the nose radius is the most dominant factor followed by feed, depth of cut and speed.

Table 6. Response Table for SN Ratio

LEVEL	A	B	C	D
1	-2.6098	1.7640	-2.5263	-8.8998
2	-3.0786	-3.1059	-2.7296	-0.8127
3	-3.0410	-7.3875	-3.4735	0.9831
Delta	0.4688	9.1515	0.9472	9.8829
Rank	4	2	3	1

Table 7. Response Table for Means

LEVEL	A	B	C	D
1	1.7022	0.9357	1.3625	3.0128
2	1.7808	1.6555	1.9981	1.2465
3	1.7409	2.6328	1.8633	0.9647
Delta	0.0786	1.6971	0.6356	2.0481
Rank	4	2	3	1

The diagnostic checking has been performed through residual analysis for the developed model. The Residual plots for surface roughness are shown in Fig.5 and Fig.6. These fall on a straight line implying that errors are distributed normally. From Fig.5 and Fig.6 it can be further concluded that all the values are within the control range, indicating

that there is no obvious pattern and unusual structure and also the residual analysis does not indicate any model inadequacy.

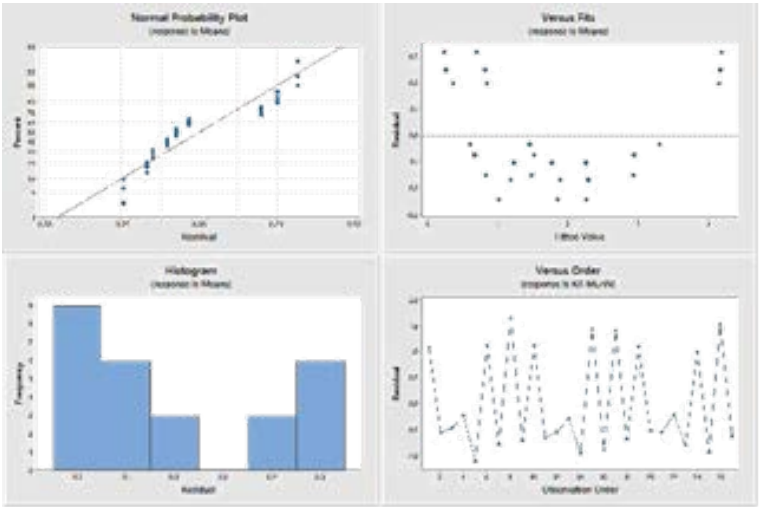

Figure 5. Residual Plots for Means

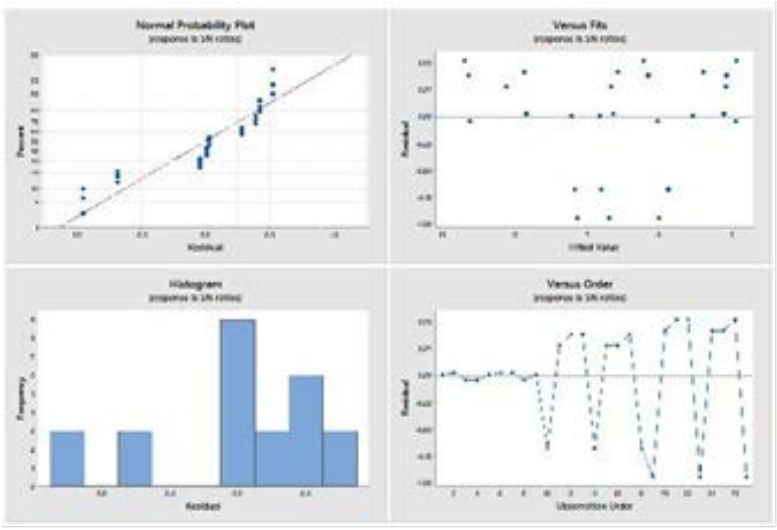

Figure 6. Residual Plots for SN Ratios

Regression Model:

Surface Roughness = 0.72 + 0.00001 * (speed) + 15.6 * (feed) + 0.96 * (doc) - 2.99 * (nose radius)
- 0.00076 * (speed*feed) + 0.00002 * (speed*doc) + 0.00022 * (speed*nose radius)

4. Conclusions

This research presents a way of optimizing cutting as well as tool parameters in a simple machining process of taper turning wherein the optimum setting of the control factors by main effects plots was found to be A1B1C1D3 (highest S/N Ratio) 1600 rpm, 0.12 mm/rev, 0.25 mm and 0.12 mm. This result is ideal when the prime requirement is to minimize surface roughness while machining Aluminum 6061-T6. The surface roughness decreased with increase in nose radius for the range 0.4-1.2 mm and increased with increase in feed rate for the range 0.12-0.24 mm/rev. ANOVA Table and F-statistic value showed that the percentage contribution of nose radius and feed were maximum followed by depth of cut. Taguchi gives a systematic and

efficient method for evaluating optimum operating conditions. The research can be extended to more number of responses for further increment in operational efficiency.

References

1. A. Agrawal, S Goel, W. B Rashidc, M. Price, "Prediction of surface roughness during hard turning of AISI 4340 steel (69 HRC)" ELSEVIER Applied Soft Computing 30, (2015), 279–286.
2. Ahmet Hasçalık, Ulaş Çaydaş, "Optimization of turning parameters for surface roughness and tool life based on the Taguchi method" The International Journal of Advanced Manufacturing Technology, Volume 38, Issue 9, (2008), 896-903
3. C. Natarajan, S. Muthu, P. Karuppuswamy, "Prediction and analysis of surface roughness characteristics of a non-ferrous material using ANN in CNC turning" International journal for Advanced Manufacturing Technology 57, (2011), 1043-1051.
4. Devesh Pratap Singh, R. N. Mall, "Optimization of Surface Roughness of Aluminum by ANOVA based Taguchi Method using Minitab15 Software" International Journal for Technological Research in Engineering Volume 2, Issue 11, (2015), 2782-2787.
5. E. García-Plazaa, P.J. Núñeza , D.R. Salgadob, J. García Sanz-Calcedob, I. Camberob, J.M. Herrera Olivenzab, "Surface Finish Monitoring in Taper Turning CNC Using Artificial Neural Network and Multiple Regression Methods" The Manufacturing Engineering Society International Conference, (MESIC), Science Direct, Procedia Engineering 63, (2013), 599 – 607.
6. I. Asilturk, Harun Akkus, "Determining the effect of cutting parameters on surface roughness in hard turning using the Taguchi method" ELSEVIER Measurement 44, (2011), 1697-1704.
7. Lin, W.S., Lee, B.Y., Wu, C.L., "Modelling the surface roughness and cutting force for turning" J. Mater. Process. Technol. 108, (2001), 286–293.
8. `Marinković Velibor et.al. "Optimization of surface roughness in turning alloy steel by using Taguchi method" Scientific Research and Essays Vol. 6(16), (2011), 3474-3484.
9. M. Nalbant, H. Gökkaya, G. Sur, "Application of Taguchi method in the optimization of cutting parameters for surface roughness in turning" Materials & Design, ELSEVIER Volume 28, Issue 4, (2007), 1379–1385.
10. Montgomery, D.C., 1997. "Design and Analysis of Experiments" 4th ed. Wi1ey, New York.
11. M. Sarikaya, A. Gullu "Taguchi design and response surface methodology based analysis of machining parameters in CNC turning under MQL" ELSEVIER Measurement 65, (2014), 604-616.
12. P.M. Patil, R.V. Kadi, S.T. Dundur, A.S. Pol, "Effect of cutting Parameters on Surface Quality of AISI 316 Austenitic Stainless Steel in CNC Turning" International Research Journal Of Engineering and Technology,Volume: 02 Issue: 04, (2015), 1453-1460.
13. Ranganath M. S., Vipin, Nand Kumar, R Srivastava, "Surface Finish Monitoring in CNC Turning Using RSM and Taguchi Techniques" International Journal of Emerging Technology and Advanced Engineering Website Volume 4, Issue 9, (2014), 171-179.
14. Ranganath. M. S., Vipin, R.S. Mishra, Prateek, Nikhil, "Optimization of Surface Roughness in CNC Turning of Aluminum 6061 Using Taguchi Techniques" International Journal of Modern Engineering research (IJMER), volume 5, Issue 5, (2015), 42-50.
15. Ranganath. M. S., Vipin, Sanchay Gupta, "Prediction of surface roughness in CNC turning of Aluminum 6061 using Taguchi method and ANOVA for the effect of tool geometry" International Journal of Advanced Production and Industrial Engineering (IJAPIE), volume 1, Issue 2, (2016), 22-27
16. S. Thamizhmanii*, S. Saparudin, S. Hasan, "Analyses of surface roughness by turning process using Taguchi method" Journal of Achievements in Materials and Manufacturing Engineering, VOLUME 20 ISSUES 1-2, (2007), 503-506.
17. Upinder Kumar Yadav, Deepak Narang, Pankaj Sharma Attri, "Experimental Investigation and Optimization Of Machining Parameters For Surface Roughness In CNC Turning By Taguchi Method" International Journal of Engineering Research and Applications (IJERA) Vol. 2, Issue4, (2012), 2060- 2065.
18. W.H. Yang,Y.S. Tarng, "Design optimization of cutting parameters for turning operations based on the Taguchi method" Journal of Materials Processing Technology, ELSEVIER Volume 84, Issues 1–3,(1998), 122–129.

Biography

Sanchay Gupta is a student at Delhi Technological University (Formerly Delhi College of Engineering) pursuing Bachelor of Technology in Mechanical Engineering and is currently in fourth (final) year. He is currently working on optimization method viz. Taguchi Technique. He has been a part of Deltech Baja, a prestigious society in the college that designs, manufactures and tests an off-road vehicle from the scratch and has published a research paper on effect of tool geometry on the surface roughness. He has worked as an intern in L&T Hydrocarbon Engineering and ISGEC Heavy Engineering Ltd.

Vimanyu Chadha is currently a fourth year Mechanical Engineering student of Delhi Technological University. He worked and captained a Technical Team HPVC of DTU. He interned at DRDO, India's Premier Defense Research Facility. There he worked on the state of the art new material, "Functionally Graded Material". He's always had the eagerness to pursue Research. He plans to pursue Master's in Material Science after his graduation.

Vishal Sardana is pursuing Bachelor of Technology (Mechanical) from Delhi Technological University, Delhi, India. He is currently working on the optimization of cutting parameters on surface roughness and evaluation of safety index for machining process. He is a member of ASME. He has published research paper in IOSR Journal of engineering. He has worked as an intern at Air India Ltd. and Daikin Air Conditioning India Pvt. Ltd. He has been felicitated with OP Jindal Engineering and Management Scholarship for being selected among top 100 scholars in India for year 2016.

Viplav Setia is a final year undergraduate student pursuing B.Tech in Mechanical engineering from Delhi Technological University, Delhi, India. He has been a part of HPVC team, which makes a recumbent bicycle and also of Deltech Baja, which makes an off road race car. He has also completed internships at International COIL limited, Maruti Suzuki India limited, and Audi Delhi South.

View publication stats

Experimental investigation of performance and emission characteristics of Palm oil

P. K. Chaudhary[1], A. Pal[2], Kunal Chauhan[3], Shailendra Nath Tiwari[4]

[1]*Associate Prof., School of Mechanical Engineering, Galgotias University, Greater Noida, U. P., India*

[2]*Department of Mechanical Engineering, Delhi Technological University, Delhi, India*

[3,4]*M.Tech. Scholar, School of Mechanical Engineering, Galgotias University, Greater Noida, U. P., India*

Abstract: *Today the world is at the state of war of consuming the fossil fuel. The developed countries are trying to capture the reservoirs of fossil fuel because they are nothing but zero without the fuel. Another problem with the petro diesel fuel is that the level of pollution is increasing day by day due to excess use in vehicle and machinery. The fossil fuels are available in limited amount to the world. The scientists are trying to find alternative sources of fossil fuel that are effective, environmental friendly and economically functional.This experiment is basically testing the performance and emission characteristics of biodiesel. This paper deals with the same thing. Basically this paper deals with finding of performance characteristics and emission characteristics of engine running with biodiesel and its various blends [B10, B20 and B30] at various conditions. Average brake thermal efficiency of the diesel is higher than biodiesel. There is an increase in brake thermal efficiency (BTE) with increase in load. CO emission by blends of biodiesel is higher than diesel [7]. There is relation between density and atomization. HC emission formed by the blends of biodiesel is greater than that of the diesel. There is less production of NOx from engine running with diesel and on the other hand the engine produces higher NOx running with Palm biodiesel.*

Keywords **– Bio-diesel, Parameter Design, Taguchi Methodology, Trans-esterification**

1. INTRODUCTION

It is unanimously accepted truth that the fossil fuel reservoir is depleting day by day and in coming generation certainly this reservoir will not be able to supply our demand. In view of this, the researchers have put their focus in search of the renewable energy sources. Out of the list of plenty renewable sources of energy, biodiesel is one of the important [1, 2]. Biodiesel may be categorized under the heading of renewable energy sources arguing that as it is mostly sourced from plants and the amount of carbon dioxide produced after burning of the biodiesel derived from a plant is almost less than that of the amount of the carbon dioxide required to nurture that plant from where that amount of biodiesel has been produced [4,5]. In this light, the biodiesel is a renewable source of energy. Further, researchers have been reported that the biodiesel can directly be used as fuel without any major modification in the modern CI (compression Ignition) engines either in pure form (100 % biodiesel) or mixing it with the existing diesel. Furthermore, the pollutants resulting from biodiesel combustion in CI engines are comparatively less harmful to environment and human health [9, 10] than that of the traditional

diesel oil. Additionally, emissions from road vehicles are major contributors to air pollution, which is a nagging issue of China regarding environmental point of view [6].

In the contemporary field of research, increased number of researchers has shown their interest in establishing the facts related to the use of biodiesel. In this regard Ramesh D et al. have reported the many facts after synthesizing a great number of publication related to the performance and emission characteristics of biodiesel (derived from various sources) which when used in an engine. They particularly mentioned that the parameters (content of biodiesel, properties of biodiesel and its feed stock, engine type, operating conditions and additives) are bitterly influences the engine power, fuel economy and emission characteristics[11].

A critical review of literature may revels that the biodiesel obtained from different feedstock yields different performance and shows different emission characteristics under different conditions. Noteworthy remarks remarked by the contemporary authors related to performance and emission characteristics of biodiesel sourced from different feed stocks is as follows.

Considering the viewpoint presented by the aforementioned authors, in this paper report their findings after analysis of the data pertaining to the performance and emission characteristics which has been obtained by running an IC engine using biodiesel harnessed from palm.

K. Suresh kumar et al. [15] put forward the investigated the performance and emission characteristics when diesel engine run using Pongamiapinnata methyl ester (PPME) and its blends with diesel. The conclusions came were that blends of PPME with diesel up to 40% by volume (B40) yields better Brake Specific Fuel Consumption and improved emission characteristics. Similarly, **S. Godiganur et al. [16]** used blends of methyl ester obtained from mahua oil and studied performance and emission characteristics in a cummins 6BTA 5.9 G2- 1, 158 HP rated power, turbocharged, DI, water cooled diesel engine. For this case, authors have observed a significant reduction in CO, HC emissions and fuel consumption with slight increase in NOx emission with increased in blend percentage but in contrast, brake specific energy consumption decreases and thermal efficiency of engine marginal increases at the specific operating condition when working with 20% biodiesel blend. For other authors for example **S. Puhan et al. [19]** (mahua oil), **XiangmeiMenget al. [29] (**waste cooking oil)and**Haiter Lenin A et al. [37]** (mahua oil)have carried out the similar experiments but with bio diesel obtained from diversified feed stoke.

2. METHODOLOGY

2.1 Fuel Properties

The role of properties of biodiesel on performance and emission characteristics have discussed by various authors [4]. It is noteworthy that the important properties parameters such as viscosities, flash point, cloud point, cetane number, ash content and chain of aromatic rings dictates the performance and emission characteristics and value of these parameters of a biodiesel is solely depends on the sources (feed stock) with which it is obtained. For example, viscosity,

cetane number and flash point of Palm oil is very higher than petro diesel. Also, it contains less percentage amount of ash and sulphur content. The cetane number is volume percent of n-hexadecane in the blend of n-hexadecane and 1-methylnaphthalene [4, 10].

2.2. Experiment Setup and Procedure

The experimental set up used in this work is shown in Figure 1 and with is set up there is also a provision to note the emission related data (CO, HC and NO_X) by attaching an extra set up as shown in Figure 2. Here, CO is expressed in terms of percentage whereas the HC and NO_X is presented in terms of ppm Basically, the set up used in this work is four strokes, four cylinders, Tata Indica, Diesel engine with eddy current dynamometer, Piezo sensor, engine cooling and calorimeter. The details of the specifications of engine set up and smoke analyzer parameters are presented in Table 1 and Table 2 respectively. The experiments are conducted at varying load conditions. Here, the load refers to the BHP. While taking the data, after starting the engine at a particular load is then set by gradually regulating the throttle valve. For a combination of load and blend, the corresponding value of CO, HC and NO_X is directly noted whereas, SFC, BTE is calculated using equation (1) and (2) by noting the fuel flow. Reading has been taken at the steady state condition. The level of load and blend is considered in this work as 10, 15, 20, 25, 30 KW and B0 (only Diesel), B10, B20, B30 respectively.

$$\text{Brake Specific fuel consumption } \left(\frac{\text{Kg}}{\text{kWh}}\right) = \text{BSFC}$$

$$\text{BSFC} = \frac{\text{fuel flow } \left(\frac{\text{kg}}{\text{h}}\right)}{\text{Brake power (kW)}} \quad (1)$$

$$\text{Brake Thermal Efficiency (\%)} = \text{BTE}$$

$$\text{BTE} = \frac{\text{Brake power (kW)} \times 3{,}600 \times 100}{\text{fuel flow } \left(\frac{\text{kg}}{\text{h}}\right) \times \text{calorific value(kj/kg)}} \quad (2)$$

Here,

Brake power (kW) = (2×π × Speed × Torque) / (60×1,000)

And

Torque (Nm) = Load (N) × Arm length (m)

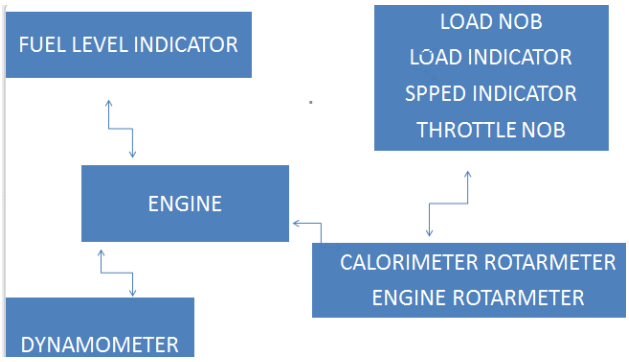

Figure 1. Engine Test Rig

Figure 2.AVL GAS Analyzer (AVL DIGAS 444)

Table 1.Technicalspecificationofthe testengine

Particulars	Specification
Make	TelcTel. Telco
Model	TataIndica,
Type	FourFourcylinders,fourstroke,dieselwater cooled
Ratedpower	39kWat5,000rpm,
Torque	85Nmat2,500rpm
Cylindervolume	1,405cc
Compressionratio	22:1
Dynamometer	Type eddy current, water cooled, with loading unit
Air box	M S fabricated with orifice meter and manometer
Fuel tank	Capacity 15 lit with glass fuel metering column
Calorimeter	Type Pipe in pipe
Piezo sensor	Range 5000 PSI, with low noise cable
Crank angle sensor	Resolution 1 Deg, Speed 550 RPM
Digital milivoltmeter	Range 0-200mV, panel mounted
Temperature sensor	Type RTD, PT100 and Thermocouple, Type K
Load indicator	Digital, Range 0-50 Kg, Supply 230VAC
Load sensor	Load cell, type strain gauge, range 0-50 Kg
Fuel flow transmitter	DP transmitter, Range 0-500 mm WC
Air flow transmitter	Pressure transmitter, Range (-) 250 mm WC
Rota meter	Engine cooling 100-1000 LPH; Calorimeter 25-250 LPH
Data acquisition card	Resolution12 bit, 8/16 input, mounting PCI slot
Software	"Engine soft" performance analysis software
Overall dimensions	W 2000 x D 2750 x H 1750 mm

Table 2: TechnicalspecificationofALV Analyser

S.NO.	PARAMETER	MEASURMENT	RESOLUTION
1	CO	0-10%	0.01% Vol
2	CO2	0-20%	0.1% Vol
3	HC	0-20000 ppm Vol	1 ppm
4	NOx	0-5000 ppm Vol	1 ppm
5	O2	0-25% Vol	0.01% Vol

2.3 Observation

Following the procedure mentioned in the Section 2.2, the data pertaining to the Brake thermal efficiency, Brake specific fuel consumption, CO %, HC, and $NO_x$are noted for different loading condition and are summarized in Table 4, 5, 6 and 7 for different blends of biodiesel. Also, for better visualization of the trends of the variation, the data is depicted graphically.

In order to have better visualization of the important trends regarding BSFC, BTE and emission related

characteristics for each blends, using the data obtained from the experimental investigation are plotted for increasing load condition. These plots are depicted in Figure 3, 4, 5 and 6. Also, the average of each performance (considering all load together) is plotted for all blends so as to visualize the trends of the average performance. This plot is depicted in Figure 8.

Results have been after carrying out the analysis considering variations depicted in Table 4 to Table 7 and graph plotted is displayed in Figure 3 to Figure 7. The important points of the analysis are elaborated in the subsequent subsection 2.4.

Table 3: Properties of biodiesel [14]

Name of oil	Kinematic viscosity (mm^2/s)	Cetane no.	Lower heating value (MJ/kg)	Cloud point (°C)	Pour point (°C)	Flash point (°C)	Density (kg/l)
Palm	5.7	62	33.5	13	-	164	0.88
Diesel	3.06	50	43.8	-	-16	76	0.855

Table 4: Observation Table for B0

LOAD	BTE	SFC	CO %	HC(PPM)	NO_X(PPM)
10	12.0	0.79	0.01	2.0	096
15	16.0	0.47	0.01	1.8	120
20	19.0	0.43	0.02	1.0	140
25	21.0	0.40	0.05	2.1	150
30	22.2	0.38	0.12	4.2	160
Average	18.0	0.49	0.04	2.2	133

Table 5: Observation Table for B10

LOAD	BTE	SFC	CO%	HC(PPM)	NO_X(PPM)
10	10.0	0.86	0.01	1.8	095
15	16.0	0.50	0.01	2.0	130
20	18.4	0.42	0.03	2.1	140
25	20.4	0.37	0.06	6.0	150
30	22.2	0.38	0.11	8.0	160
Average	17.4	0.51	0.04	4.0	135

Table 6: Observation Table for B20

LOAD	BTEE	SFC	CO%	HC(PPM)	NO_X(PPM)
10	10.0	0.86	0.01	1.8	096
15	15.8	0.50	0.02	2.3	135
20	18.5	0.43	0.04	2.0	155
25	20.0	0.40	0.06	4.1	175
30	21.8	0.38	0.13	6.2	160
Average	17.4	0.51	0.04	4.0	135

Table 7: Observation Table for B30

LOAD	BTE	SFC	CO%	HC(PPM)	NO_X(PPM)
10	08.8	0.97	0.01	2.0	095
15	16.0	0.57	0.01	2.0	125
20	18.0	0.43	0.04	4.0	145
25	19.6	0.41	0.05	5.1	165
30	21.2	0.40	0.11	5.8	155
Average	17.4	0.51	0.04	4.00	135

2.4 Discussion

Variation in brake thermal efficiency vs load

From the Figure 3 it can be noted that the brake thermal efficiency of pure diesel is better than bio diesel at respective loads. In contrast, irrespective of load that is average of the brake thermal efficiency has an improved value for all blends and this value (17.4) which is not much less than that of the pure diesel. This fact is displayed in Figure 8. It can also be noted that the maximum thermal efficiency is obtained at maximum loading condition irrespective of the type of blend.

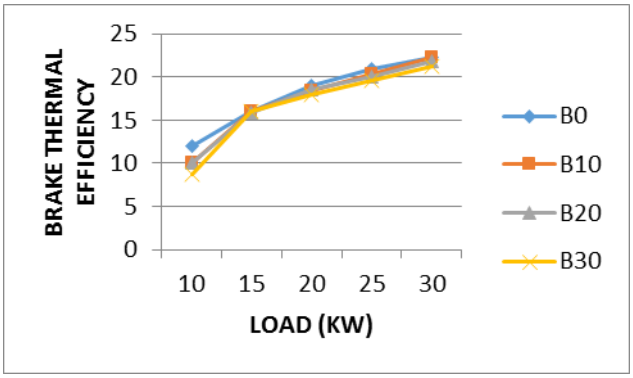

Figure: 3 BRAKE THERMAL EFFICIENCY Vs LOAD (KW)

Brake specific fuel consumption vs load

The comparison of specific fuel consumption for various blends of palm oil and diesel fuel is shown in Figure 4. The pure diesel yields the lowest fuel consumption at all loads. However, it is bit higher than palm oil blends at 25 kW and 30 kW. It seems that the combination effect of density and calorific value has led to this situation. In contrast, the average of the brake specific fuel consumption (Figure 8) is same for all blends of biodiesel and pure diesel.

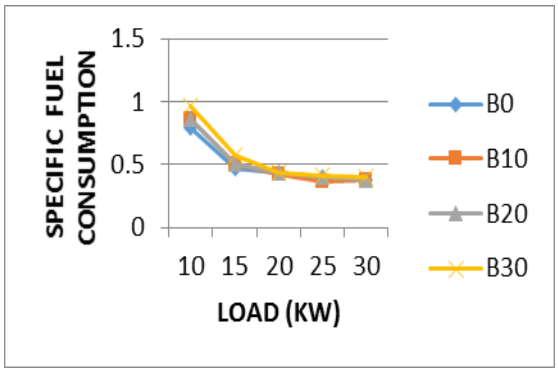

Figure: 4 SPECIFIC FUEL CONSUMPTION Vs LOAD (KW)

Variation of CO vs load

From the Figure 5, it may be noticed that carbon Monoxide emissions for B10, B20 and B30 are comparatively higher than diesel over a broad range. At high load (25 KW), the CO emission for is highest one. However, at the highest load, it has the lowest value. This situation reveals the fact of better combustion at the highest load condition. At low speed, the CO emission was almost equal for all the blends. If it is looked from the perspective of average (Figure 8), the CO emission has the same value for all blends.

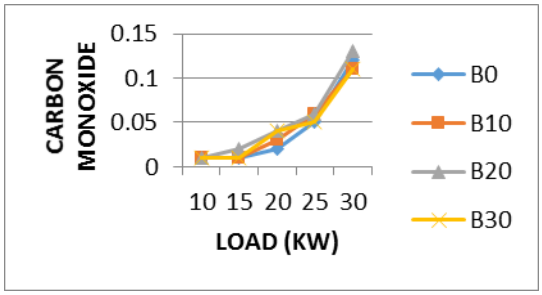

Figure: 5 CARBON MONOXIDE Vs LOAD (KW)

Variation in unburnt hydrocarbon vs load

Unburnt Hydrocarbon consists of incomplete combustion comprising of actual carbon and product of complex reaction. The variation in concentration of HC is shown Figure 6. Palm biodiesel blends produce

higher HC emission release compared to the diesel fuel at higher load (25 and 30 KW). It gives clear indication that HC emissions for blends are lower at partial engine load, however, higher at higher engine load. The highest HC emission is found with B10 at high loading condition. From Figure 8, it can be noticed that the HC emission is comparatively lower for the pure bio diesel.

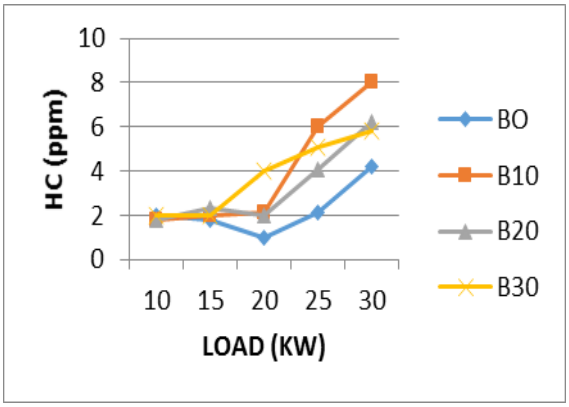

Figure: 6 HYDRO CARBON Vs LOAD (KW)

Variation of NO_x vs load

Figure 7 reveals that emission of NOx increases with increasing load due to higher combustion temperature, hence increase thermal efficiency and NOx emissions. The NOx emission for B20 and B 30 is much more than that of the diesel fuel. The NOx emission for B10 is slightly higher than that of diesel. However, the average, emission has of the blends of biodiesel is not much higher. This fact can be seen from Figure 8.

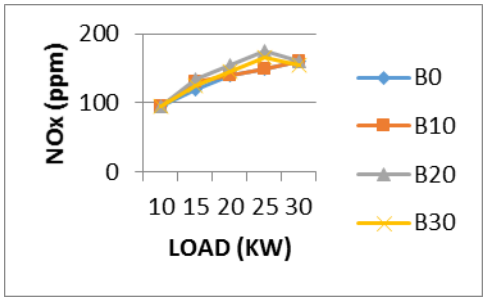

Figure: 7 OXIDES OF NITROGEN Vs LOAD (KW)

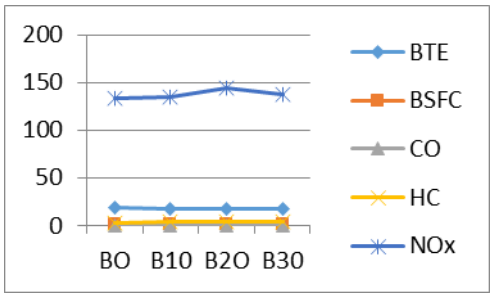

Figure: 8 AVERAGE OF PERFORMANCES AND EMISSIONS Vs LOAD (KW)

3. CONCLUSIONS

In the light of discussion made in aforementioned section the following conclusions can be made. The pure diesel performs well on almost all performance (brake thermal efficiency and specific fuel consumption) and emission characteristics (CO, HC and NO_x) at most of the loading conditions. However, the blend B10 has comparable performance and emission characteristics as that of pure diesel under varying loads and thus can be recommended as an alternative fuel for the CI engines. It may also be noted that the almost all blends yield a comparable performance and shows almost similar emission characteristics from the perspective of the data pertaining to the average of all the loads. Exceptionally, the B10 yields marginally better than that of the other blend.

1. Brake thermal efficiency increases with the increase in load and average brake thermal efficiency of the pure diesel is greater than for all most all blends of palm biodiesel.
2. Specific fuel consumption of pure diesel is less as compared to various blends of biodiesel at all loads. At high load the diesel gives low fuel consumption as compared to the other biodiesel blends.

3. CO emission for all types of blends is higher than diesel. The CO emission data shows correlation between density and atomization process.
4. HC emission produced by the blends of biodiesel is higher than that of the diesel. At low loads, the emission is close to the diesel. However at high load, the emission is much high.
5. Emission of NOx for pure diesel is lesser than Palm biodiesel and its blends. NOx emission increases with the increase of blend.

REFERENCES

[1] PintoA. C., Guarieiro L. L. N., Rezende M. J. C., Ribeiro N. M., Torres E.A., Lopes W. A., Pereira P. A. P. and Andrade J.B., 2005. "Biodiesel: An Overview", J. Braz. Chem. Soc., Vol. 16, No. 6B, pp. 1313-1330.

[2] Rasha, A. R., Isam, J., and Chaouki, G., 2012, "Transesterification of Biodiesel: Process Optimization and Combustion Performance", Int. J. of Thermal & Environmental Engineering, Vol. 4, No. 2, pp. 129-136.

[3] Saeikh, Z. H. and Madhu, V., 2014, "Parametric effects on kinetics of esterification for biodiesel production: A Taguchi approach", Chemical Engineering Science, Vol. 110, pp. 94–104.

[4]Ramadhas A.S.,JayarajS., andMuraleedharan C., "Theoriticalmodelingand experimental studieson biodiesel-fuelled engine". J. RenewableEnergy.31 (2006), pp. 1813-1826.

[5] M.Balatand H.Balat, "Acriticalreview of bio-dieselas avehicular fuel".EnergyConversionandManagement.,49(2008),pp.2727-2741.

[6] Yan XY, Crookes RJ. Energy demand and emissions from road transportation vehicles in China. Prog Energ Combust. 2010;36:651–76.

[7] A. K. Agrawal, "Biofuels (alcoholsand biodiesel) applications as fuels for internal combustion engines". Progress inEnergy and CombustionScience,33(2007), pp. 233-271.

[8]Demirbas,"Importanceofbiodieselastransportationfuel".Energy Policy,35 (2007),pp. 4661-4670.

[9] Khan AK. Research into biodiesel Kinetics and catalyst development, Individual inquiry A May(2002). www.mybiofuels.net/Pubs/Khan_Thesis_2002_Kinetics_Catalysts.pdf.

[10] S. Godiganur, C.H. S. Murthy, R. P. Reddy, "6BTA 5.9 G2-1 Cummins engine performance and emission tests using methyl ester mahua (Madhucaindica) oil/diesel blends", Renewable Energy, 34 (2009), 2172–2177.

[11] Ramesh D, Samapathrajan A, Venkatachalam P.Production of biodiesel from jatrophacurcasoil by using pilot biodiesel plant, July(2009).*www.jatropha.de/Journal/Pilot_Plant_for_Biodiesel-leaflet1.pdf.*

[12] Sarin R, Sharma M, Sinharay S, Malhotra RK. Jatropha–palm biodiesel blends: an optimum mix for Asia. Fuel 2007;86:1365–71.

[13] Ali Y, Hanna MA, Cuppett SL. Fuel properties of tallow and soybean oil esters. J Am Oil ChemSoc 1995;72:1557–64.

[14] B.K. Barnwal, M.P. Sharma, Prospects of biodiesel production from vegetable oils in India, Renewable and Sustainable Energy Reviews, 9 (2005) 363–378.

Available online at www.sciencedirect.com

ScienceDirect

Materials Today: Proceedings 4 (2017) 2470–2477

materialstoday: PROCEEDINGS

www.materialstoday.com/proceedings

5th International Conference of Materials Processing and Characterization (ICMPC 2016)

Fatigue failure prediction in spur gear pair using AGMA approach

Paras Kumar[a,*], Harish Hirani[b], Atul Agrawal[a]

[a]*Mechanical Enginering Department,Delhi Technological University, Delhi, India -110042*
[b]*Mechanical Enginering Department,Indian Institute of Technology, Delhi, India -110016*

Abstract

Gears predominantly fail in contact fatigue mode (pitting/spall) due to combined rolling and sliding motion. Pitting initiation has been experimentally investigated by many researchers under different loading and operating conditions. The present work attempts to predict pitting and bending fatigue crack initiation along gear tooth profile using American Gear manufacturing Association (AGMA) design approach. The effect of heat treatment process (Through hardened and Case hardened) on gear fatigue life is also studied.
The AGMA results for contact and bending stresses at pitch point are compared with FEA results and a close agreement is observed. The modeling results reveal that increase in load increases the chances of early pitting failure. Case hardening gears delays the pitting initiation on gear tooth surface, while it increases the chances of bending fatigue failure.The pinion addendum region shows better pitting resistance as compared with dedendum region. The highest probability of pitting /bending failure initiation is observed in single tooth contact region due to full load sharing andthe chance of contact fatigue failure is more in comparison to bending fatigue failure.

©2017 Elsevier Ltd. All rights reserved.
Selection and peer-review under responsibility of Conference Committee Members of 5th International Conference of Materials Processing and Characterization (ICMPC 2016).

*Keywords:*Spur gear; AGMA; Pitting; Contact pressure; Contact stress; Bending stress;Fatigue; Heat treatment

1. Introduction

Gear tooth normally fails due surface and bending fatigue failure. The most prevailing surface fatigue failure are pitting and spalling. These failures initiate when the induced stress is more than the material fatigue strength. Many studies have made in past to investigate surface/bending fatigue failure on gear tooth using different techniques

* Corresponding author. Tel.: +91-9560063121;
*E-mail address:*paraskum007@rediffmail.com

2214-7853©2017 Elsevier Ltd. All rights reserved.
Selection and peer-review under responsibility of Conference Committee Members of 5th International Conference of Materials Processing and Characterization (ICMPC 2016).

(vibration, wear debris analysis, and thermography etc.). Charkera et al. [1] presented the experimental and analytical techniques to characterize the role played by near-surface inclusions in the pitting of gears. Zakrajsek et al. [2]performed the experimentation on single mesh spur gear fatigue test rig to investigate naturally occurring pitting failure. They observed that the surface pitting was the primary failure mode. Glodejz et al. [3] presented a model forestimating pitting resistance of gear teeth flanks; they used Finite element method to find stresses in contact region and found a functional relationship between the stress intensity factorand crack length. They further performed computational simulation of the fatigue process leading to pitting theory for short cracks [4].Dempsey [5] compared the vibration and oil debris analysis to detect pitting damage. Aslantas and Tasgetiren [6] carried out a numerical prediction of pitting formation on spur gear (austempered ductile iron). Linear elastic fracture mechanics and the finite element method were used for numerical solutions.Duzcukog˘lu and Imrek [7] focused on the delay of pitting failure by increasing tooth width in single tooth contact region and assumed uniform contact pressure distribution.

Most of studies on gear tooth fatigue failure were experimental. The present work is an attempt to predict fatigue failure (contact and bending) initiation on spur gear tooth using American Gear manufacturing Association (AGMA) design procedure.The effect of heat treatment process (Through hardened and Case hardened) onfatigue initiation life is also investigated.The AGMA results of fatigue stresses are compared with Ansys result of bending and contact stresses. The spur gear meshing along line of action is modelled as two rolling cylinders in contact with varying radius. Transmitted force per unit width, contact pressure, induced bending/contact stresses, and fatigue life along tooth profile are computed using analytical expressions through a MATLAB code.

2. American Gear Manufacturing Association (AGMA) design

Gear teeth normally fail due to fatigue fracture or due to surface fatigue. The fatigue fracture theory for gears was formulated by W. Lewis in 1892; he designed each gear teeth as a cantilever beam and assumed that the transmitted load (F_t) is applied at the tip of the tooth. The application where the contact ratio is more than one, two gear teeth pairs are in contact to transmit the load during the start and the end of engagement. It is therefore conservative to apply the full transmitted load to the tip of the gear tooth [8]. In reality, the full load is applied somewhere in the middle of the tooth engagement, where the single tooth pair shares the load. A new gear design procedure proposed by AGMA is based on Lewis equation and considers new geometric factor(J) instead of Lewis form factor (Y)**;** it considers factors like non-conjugate gear meshing (transmission error), axial misalignment, fluctuation of driving and driven machine torque etc. Fatigue fracture occurs when induced bending stress is more than allowable bending fatigue strength of the gear material.

The meshing of gear teeth is a combination of rolling and sliding motion. During gear meshing, repeated stress are applied on gear tooth surface as a result of which surface fatigue phenomenon or pitting occurred on tooth surface. Pitting failure occurs when the contact stress between the meshing gears is greater than or equal to the surface endurance strength. The AGMA pitting resistance equation is based on Buckingham equation and factors like dynamic factor, load distribution factor, application factor, surface geometry factor, elastic coefficient and surface finish factor. AGMA design equations for contact and bending fatigue failure [8] are discussed as

2.1 Bending stress equation

$$\sigma_b = \frac{F_t}{mJ}\frac{K_a K_m}{K_v} K_S K_B K_I \tag{1}$$

where F_t - Transmitted load per unit width, m - module, J- Geometric factor, K_a - Application factor, K_m - load distribution factor, K_v- Dynamic factor, K_S- Size factor, K_B- Rim thickness factor and K_I- Idler factor.

2.2 Corrected bending strength equation

$$\sigma^{bc} = \frac{K_L}{K_T K_R}\sigma^{bfs} \tag{2}$$

where K_L – Life factor, K_T– Temperature factor, K_R- Reliability factor, σ^{bfs}- AGMA bending fatigue strength.

2.3 Contact stress equation

$$\sigma_C = C_p\sqrt{\frac{F_t}{Id}\frac{C_a C_m}{C_v}C_S C_f} \tag{3}$$

where F_t - Transmitted load per unit width, C_p - Elastic coefficient, I- Surface geometric factor, C_a - Application factor, C_m - load distribution factor, C_v- Dynamic factor, C_S- Size factor and C_f– Surface finish factor.

2.4 Corrected fatigue strength equation

$$\sigma^{fc} = \frac{C_L C_H}{C_T C_R}\sigma^{cfs} \tag{4}$$

where C_L – Surface life factor, C_H – Hardness ratio factor, C_T– Temperature factor, K_R- Reliability factor, σ^{cfs}- AGMA surface fatigue strength.

The bending and contact fatigue failures initiate, when the induced bending and contact stresses reach or exceed corrected bending and contact fatigue strengths of the gear materials. The bending (K_L) and surface life (C_L) factors used in corrected fatigue strength expressions are expressed in terms of number of load cycles (N) [8] as

$$(K_L) = \begin{cases} 2.7, & N \le 10^3 \\ 6.1514\,N^{-0.1192}, & 10^3 < N \le 10^6 \\ 1.6831\,N^{-0.0323}, & 10^3 < N \le 10^6 \ge 0 \end{cases} \tag{5}$$

and

$$(C_L) = \begin{cases} 1.5, & N \le 10^4 \\ 6.1514\,N^{-0.1192}, & 10^4 < N \le 10^{10} \end{cases} \tag{6}$$

Equations (5) and (6) predict the number of cycles required to initiate bending and contact fatigue crack along gear tooth.

3. Results and discussion

The effect of heat treatment process on bending and contact fatigue initiation of spur gear tooth is investigated. To study the fatigue initiation, tooth profile is segmented into 50 number of instantaneous point of contact. The point number '1' is on base circle, while the point '50' is at the tip of tooth. At each contact point bending and contact fatigue stresses are computed using AGMA equations. The instantaneous contact point is modelled as two cylinders in contact with varying radius. The gear /pinion specifications and AGMA factors used in present simulation are shown in Table-1 and 2 respectively.

Table-2 Spur gear specifications

Parameters	Unit	Pinion	Gear
Number of teeth (z)	-	27	53
Module (m)	mm	2	2
Pressure angle	Degree	20	20
Face width (w)	mm	33	33
Torque (t)	N-m	100	
Pinion speed (n)	RPM	2000	1000
Young's modulus (e)	N/mm^2	$2.1 * 10^5$	
Poisson's ratio (μ)	-	0.3	
Bending fatigue strength	MPa	450	
Surface fatigue strength	MPa	1275	

Table-3 AGMA factors

AGMA factors	Value
Application factor	1.25
Load distribution factor	1.158
Size factor	1.1
Quality class of gear set	6
Rim thickness factor	1
Idler factor	1
Surface finish factor	1
Temperature factor	1
Reliability factor	1
Hardness ratio factor	1
Geometric factor	0.37

The Ansys results for bending and contact fatigue stresses for pitch point loading are shown in Fig. 1(a) and (b). The fatigue stresses are also computed for similar loading using AGMA design equations for the parameters as listed in Table-1 and 2.

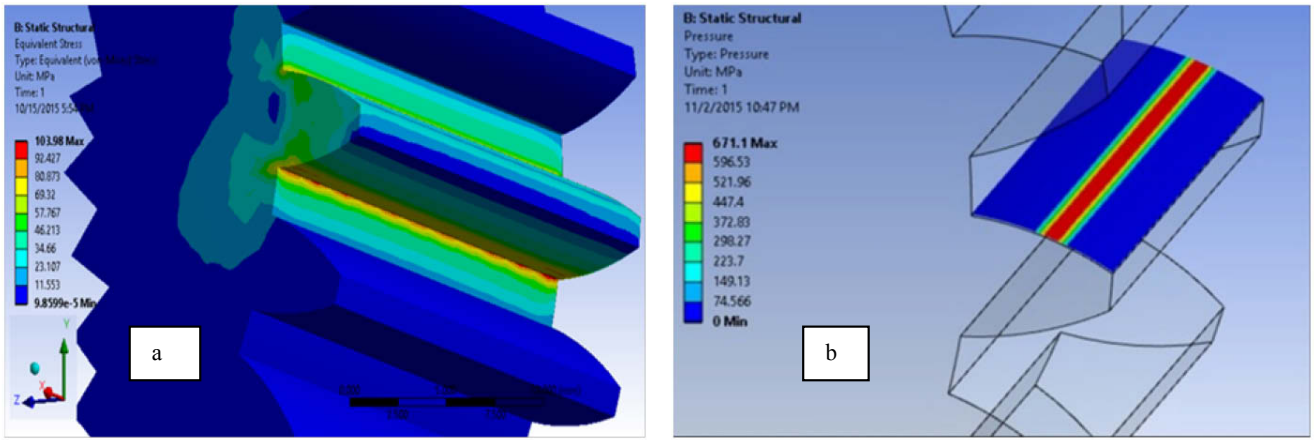

Fig. -1 (a) Bending stress (b) Contact stress

Table-3 shows the comparison in Ansys and AGMA result of bending and contact stresses at pitch point loading. The Ansys and AGMA results are very close to each other. It is also observed that the value of contact stress is higher for same loading, i.e. the probability of fatigue failure is higher as compared with bending fatigue failure.

Table-3 Ansys and AGMA results comparison (at Pitch point)

Stress	Ansys results	AGMA results	Percentage error (%)
Bending	103.98 MPa	106.1 MPa	2 %
Contact	671.1 MPa	704 MPa	4.6 %

The contact ratio for the given spur gear pair is 1.6 and the load per unit width is distributed on gear tooth as shown in Fig. 2. During tooth meshing, load on the gear tooth varies and the maximum load of 120 N/mm is applied during single tooth contact, which becomes half, i.e. 60 N/mm during double tooth contact. Double tooth contact takes place for 75 % of the teeth engagement time, while 25 % of time single tooth contact occurs. The Hertzian contact pressure in Fig.-2 is calculated by

$$p_{max} = \frac{2\,F_t}{\pi a_H} \tag{7}$$

where a_H is the semi-Hertzian contact width.

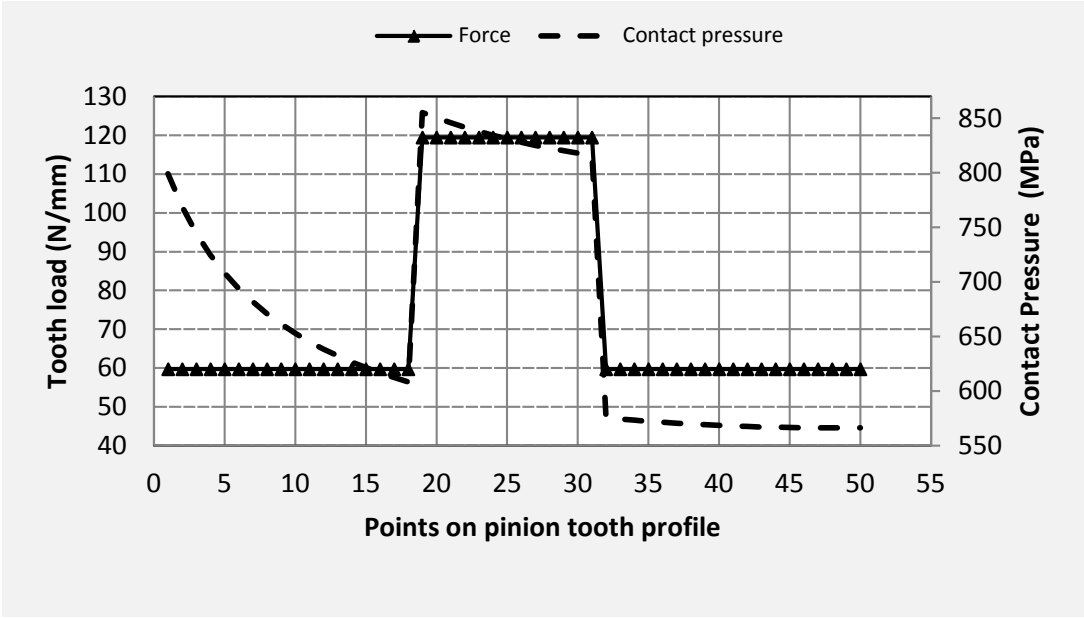

Fig.-2 Contact pressure and force distribution along tooth profile

The Hertzian contact pressure also varies as the transmitted load and attains the maximum value of 850 MPa at the lowest point of single tooth contact (LPSTC) followed by 800 MPa at the start of tooth contact. The highest contact pressure occurs in the single tooth contact, followed by the starting point of contact in dedendum. The lowest contact pressure is observed in addendum region. The contact pressure affects fatigue stresses. The induced contact and bending stress distribution, as shown in Fig. 3, follow the same patterns as the transmitted force and contact pressure. The maximum bending stress is 332 MPa, while the maximum contact stress is 1330 MPa in single tooth

contact zone.The bending stress shows almost same value in single and double tooth contact zones. The contact stress at the starting point in dedendum region is 1250 MPa and the smallest contact stress (886 MPa) occurs at the end of the contact. These developed induced stresses help to predict the number of pinion revolution (life) at which initiation of bending and contact fatigue failure start using Eq.-5 and 6.

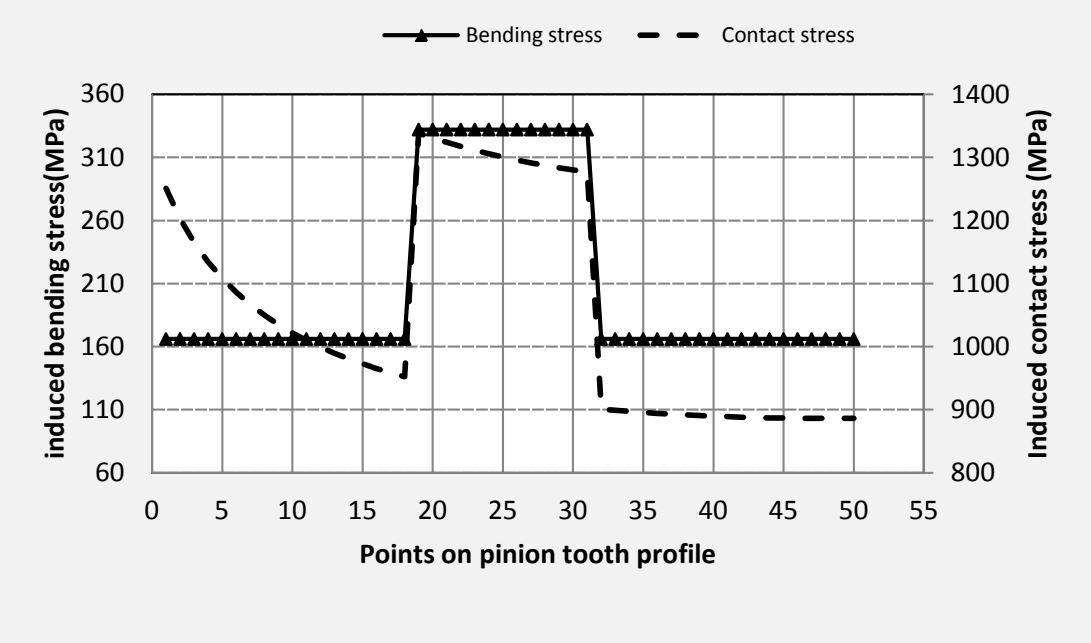

Fig. -3 Induced contact and bending stress along tooth profile

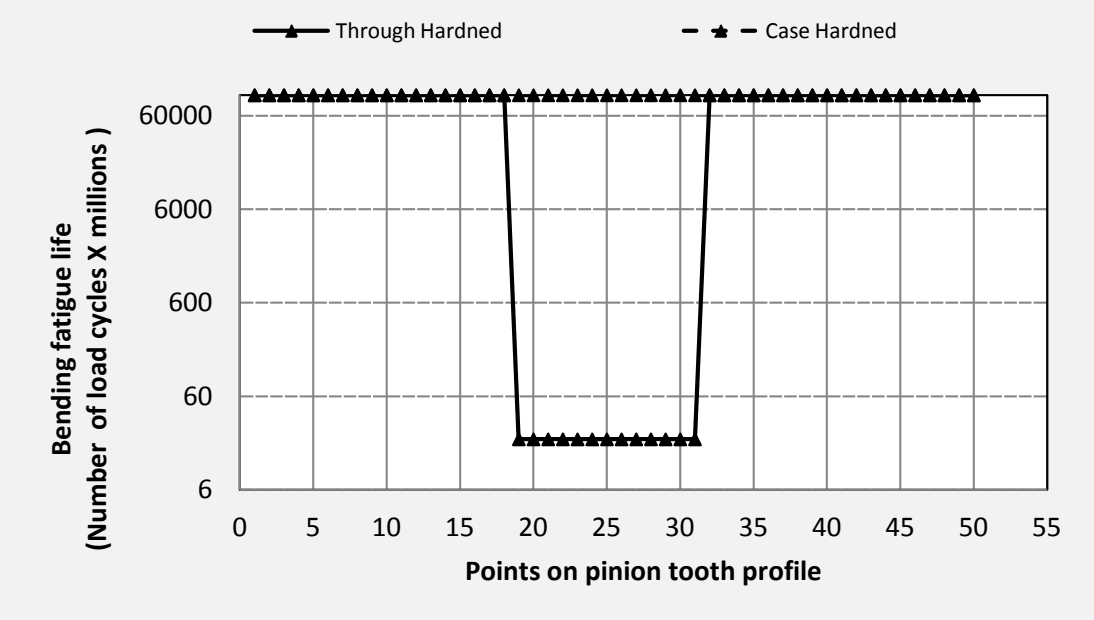

Fig. -4 Bending fatigue initiation (in million revolutions)

Fig. 4 shows the pinion life for bending fatigue failure along tooth profile. The chance of bending fatigue failure is more in single tooth contact in comparison to double tooth contact. Through hardened gear shows higher bending fatigue life in comparison to case hardened gear. Through hardened gear revolves 1 X 10^{11} cycles before bending fatigue failure, while the case hardened pinion life is 2.1 X 10^{7} revolutions in single tooth contact zone.

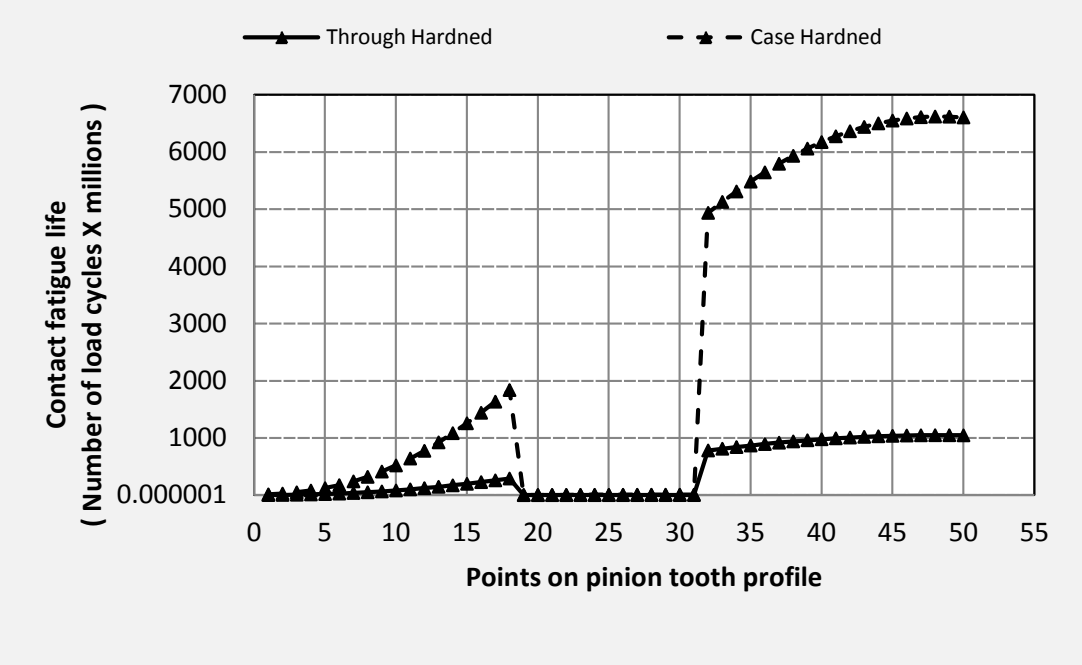

Fig. -5 Contact fatigue initiation (in million revolutions)

The contact fatigue life of case hardened gear is better in comparison to though hardened gearas shown in Fig. 5. The contact fatigue life in single tooth contact region for case hardened and through hardened gear are 4.2 X 10^{6} revolutions and 6.6 X 10^{5} revolutions respectively. The highest probability of contact fatigue failure occurs in single tooth region, followed by pinion dedendum and addendum region.

4. Conclusions

The bending and contact fatigue initiation of spur gear tooth profile is investigated using AGMA equations. The following conclusions are drawn:

- Transmitted force and contact pressure attain maximum value in single tooth contact region.
- The induced bending fatigue stress is higher and uniform in single tooth contact, while the induced contact fatigue stress shows maximum value at lowest point of single tooth contact (LPSTC).
- The bending fatigue life of through hardened gear (1 X 10^{11} revolutions) is better in comparison to case hardened gear. The opposite trend is observed for contact fatigue life. The contact fatigue life of case hardened gear (4.2 X 10^{6} revolutions) is better in comparison to through hardened gear.
- The maximum chance of contact/bending fatigue failure occurs in single tooth contact zone and the contact fatigue life is less in comparison to bending fatigue life.

References

[1] T.M. Clarke, G. R. Miller, L. M. Keer , H. S. Cheng, The role of near-surface inclusions in the pitting of gears, A S L E Transactions 28 (1)(1985) 111-116.
[2] J. J**.** Zakrajsek, D. P. Townsend, H. J. Decker, An analysis of gear fault detection methods as applied to pitting fatigue failure data, Prepared for the 47th Mechanical Failure Prevention Group Virginia Beach, Virginia,(1993) 13-15.
[3] S. Glodez, J. Flaskar, Z. Ren, A new model for the numerical determination of pitting resistance of gear teeth flanks,*Futigue Fruct. Engng Muter.* Struct. 20 (1) (1997) 71-83.
[4] S. Glodez, H. Winter, H.P. Stuwe, A fracture mechanics model for the wear of gear flanks by pitting,Wear 208 (1997) 177–183.
[5] P. J. Dempsey**,** A comparison of vibration and oil debris gear damage detection methods applied to pitting damage, NASA / TM--2000-210371 (2000) 1-10.
[6] K. Aslantas, S. Tasgetiren, A study of spur gear pitting formation and life prediction, Wear 257 (2004)1167–1175.
[7] H. Duzcukog˘lu, H. Imrek,A new method for preventing premature pitting formation on spur gears**,** Engineering Fracture Mechanics 75 (2008) 4431–4438.
[8] R. L. Norton, Machine design: An integrated approach, Pearson Education, 2004.

Environ Earth Sci (2017)76:341
DOI 10.1007/s12665-017-6679-5

ORIGINAL ARTICLE

Hydrochemical characterization and suitability assessment of groundwater in Baga–Calangute stretch of Goa, India

A. K. Haritash[1] · Karamveer Mathur[1] · Priyanka Singh[1] · S. K. Singh[1]

Received: 27 September 2016 / Accepted: 27 April 2017
© Springer-Verlag Berlin Heidelberg 2017

Abstract The present study is the first attempt to determine the suitability of groundwater for drinking and irrigation in the Baga–Calangute stretch of Goa. The suitability of groundwater for potable use was assessed by comparing observed values against standards prescribed by the Bureau of Indian Standards, and the quality was classified based on the Weighted Arithmetic Water Quality Index. Most of the groundwater samples (90%) were found to be suitable for drinking except for hardness, chlorides, and nitrates. The percent sodium (%Na), residual sodium carbonate, soluble sodium percentage, sodium adsorption ratio, Kelly's ratio, and Permeability Index were found to be within the prescribed limits for irrigation purposes. The major mechanism controlling groundwater chemistry, i.e., rock–water interaction, was also studied, and it was found that silicate weathering plays a major role in the dissolution of minerals. Based on the hydrochemical characterization, the water was observed to be of the Ca–Na–SO_4 composition type except for one sample which was of the Na–Cl composition type. Classification of the meteoric genesis suggested that the groundwater in surficial aquifers in the region had a deep meteoric percolation, and its chemistry is regulated by rock–water interaction.

Keywords Groundwater · Goa · Silicate weathering · Sodium adsorption ratio (SAR) · Meteoric genesis

✉ A. K. Haritash
akharitash@dce.ac.in

[1] Department of Environmental Engineering, Delhi Technological University, Bawana Road, Shahbad Daulatpur, Delhi 110042, India

Introduction

Groundwater is an important natural resource. Globally, around 2.5 billion people depend solely on groundwater for their basic daily needs (UNESCO 2012). Groundwater meets the drinking water needs of 50% of the world's population, and 43% of the water used for irrigated agriculture (FAO 2010). As per the available literature, 205 of world's aquifers are over-exploited (Gleeson et al. 2012) resulting in episodes of land subsidence and seawater intrusion (USGS 2013). Other factors which affect the quality of groundwater are land use practices, precipitation and infiltration rate, nature and type of underlying rock strata, runoff pattern, and other associated human activities. Water quality is, therefore, an outcome of the physiochemical state of water and any alteration in the characteristics owing to associated human activities (Venkateswaran et al. 2011; Haritash et al. 2016).

In the present study, an attempt has been made to interpret the drinking and irrigation water quality of groundwater in the area between Baga and Calangute in Goa, India, since no reports are available on the subject in the study area. The coastal zone of Goa had been exclusively used for tourism, agriculture, fishing, salt production, and recreation. Mining of iron and manganese ores is of chief economic importance in Goa. Mining and associated activities have greatly affected the natural landscape in and around the mined areas, which is characterized by the presence of pits and waste rejects. The environmental effects are more pronounced during the monsoon season resulting in a higher rate of runoff and erosion, leaching of pollutants, overflowing of mined pits, etc. The runoff adversely affects the quality of streams directly and agricultural fields

Published online: 05 May 2017

directly or indirectly. Percolation of contaminated water through the vadose zone into aquifers results in enhanced contamination of groundwater. Solar salt production in Goa is the other activity which significantly affects the surface and groundwater quality (Mani et al. 2012). Apart from it, recent large-scale and frenzied development of infrastructure has accelerated in last few decades and has affected the environmental quality adversely, particularly along the coastline (Mascarenhas 1998). As per the Department of Tourism, Goa, the tourist turnover in the region has increased from 2.64 million in 2010 to 4.0 million in 2014. There are a number of beaches in the state, but the Baga–Calangute stretch of coastline is the most popular destination. This region experiences intense tourism activity which may affect the availability and quality of groundwater and creates pressure on other natural resources. Impacts on groundwater quality may affect the health of population exposed, tourism, agriculture and may result in cultural changes. Therefore, the present study was undertaken to determine groundwater quality and characterize it for drinking and irrigation particularly in the Baga–Calangute area.

Materials and methods

Geomorphology of study area

Goa is one of the smallest states in India with an area of 3702 km^2 and is located in the western part of the country. It is bound by the state of Maharashtra to the north and by Karnataka to the south and east, while the Arabian Sea forms its western coast. The landscape in Goa is mostly hilly representing the features of Western Ghats. The coastline is dominated by sand dunes and sandy beaches with intermittent rocky headlands of basaltic and metamorphic formations. The headlands are capped by laterite and muscovite, kyanite and augite, and heavy mineral accumulations of zircon, monazite, and other opaque minerals occur in beach sands (Kidwai and Wagle 1975). The quantity of heavy minerals varies from 0.01 to 22.6% of the sediments, and opaques vary from 1 to 72% of the heavies. The major minerals found in Goa are iron ore, manganese ore, bauxite, and minor minerals like basalt, laterite stones, rubbles, river sand.

The Baga–Calangute region lies in North Goa and is located about 15 km from Panaji. Due to maritime influence, the diurnal range of temperature during the days is not large. Due to its proximity to the Arabian Sea, humidity throughout the year is more than 60% with a range from 80 to 90% during the monsoon period.

Hydrogeological profile of Goa

The groundwater bearing formations in Goa are laterites, coastal alluvium, iron ore bodies, and fractured rock aquifers in meta-sedimentary and meta-volcanic rocks, granites and gneisses, and weathered basement rocks. As per Central Ground Water Board (CGWB 2013), the thickness of the coastal alluvium varies from 5 to 22 m, and the depth to water level varies from 1 m to 6 m below ground level (bgl). Almost 70% of the area is covered by shallow lateritic aquifers which occur as belts covering the tablelands of coastal plains and hills and etch plains of midlands (Fig. 1). The laterites (5–30 m thick) are underlain by a thick layer of lithomarge clay followed by fractured basement rocks. Irrigation dug wells (3–10 m deep) tapping laterites are annually charged by rainfall, and the depth to water levels varies from 1 to 7 m bgl. Boreholes drilled on plateaus penetrating basement rock show a piezometric head of 20–25 m above mean sea level. The average annual rainfall in Goa is 2932 mm; net annual groundwater availability is 132 million cubic meters (MCM); and the annual groundwater draft is 43 MCM. The stage of groundwater development is 33%, and the entire state has been categorized under the "safe" category. In general, the groundwater has been classified as being of a calcium bicarbonate type.

Sample collection and analysis

The groundwater samples were collected at twenty (20) locations from open wells–dug wells in a residential area of the Baga–Calangute region. The samples were collected during June 2014 before the onset of the monsoon. Water samples were collected in distilled water rinsed fresh PET bottles. The coordinates of each location were noted to mark them on the map (Fig. 2), and site-specific activities were noted. Measurements of pH (precision $\pm$ 0.01), electrical conductivity (EC) (precision $\pm$ 1 µS/cm), total dissolved solids (TDS) (precision $\pm$ 2 mg/l), and salinity (as NaCl) were then taken on the site using an Orion make Star A320 model multi-parameter meter. The samples were stored in an icebox and were immediately transported to the laboratory for further analysis. Total hardness (TH), total alkalinity (TA) (as $CaCO_3$), and chloride (Cl^-) were determined by volumetric analysis; sulfate by the spectrophotometric method (Labtronics, India); and Na, K, Ca, and Mg were determined using a flame photometer (Systronics make 128 µc model) following the standard methods given by APHA (Eaton et al. 1995). The suitability of groundwater for drinking use was determined by comparing the observed value against the recommended concentration. Weighted Arithmetic Water Quality Index values (WQI) were also calculated to represent the quality of drinking based on the values of TDS, TH, total alkalinity

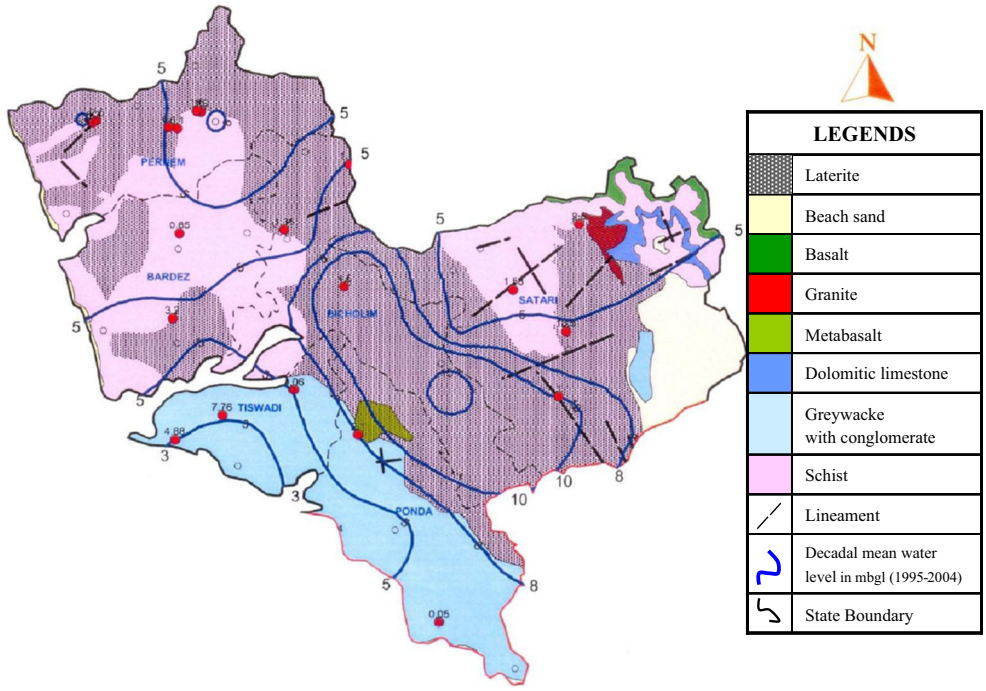

Fig. 1 Hydrogeological profile of North Goa (adapted from CGWB 2013)

(TA), Ca, Mg, Fe, Cl, SO_4^{2-}, and NO_3^-. The following equation was used to calculate WQI

$$\mathrm{WQI} = \sum W_i Q_i / \sum W_i$$

where Q_i—quality rating for each parameter [$Q_i = 100 * (V_i - V_o)/(S_i - V_o)$]; V_i—observed value of ith parameter; V_o—ideal value of the parameter in pure water (it is 0 for all parameters except pH—7.0); S_i is the recommended standard value of ith parameter; Wi—unit weight of each parameter ($W_i = K/S_i$); K is proportionality constant ($K = 1/\sum(1/S_i)$).

In order to determine the suitability for irrigation, following parameters were calculated.

Residual sodium carbonate (RSC) = $(HCO_3^- + CO_3^{2-}) - (Ca^{2+} + Mg^{2+})$	Eaton (1950)
Soluble sodium percentage (SSP) = $[Na^+/(Ca^{2+} + Mg^{2+} + Na^+)] \times 100$	Eaton (1950)
Sodium adsorption ratio (SAR) = $Na^+/(Ca^{2+} + Mg^{2+}/2)^{1/2}$	Richards (1954)
Percent sodium (% Na) = $[(Na^+ + K^+) \times 100]/(Ca^{2+} + Mg^{2+} + K^+)$	Wilcox (1955)
Permeability Index (PI) = $[Na^+ + (HCO_3^-)^{1/2}/(Ca^{2+} + Mg^{2+} + Na^+)] \times 100$	Doneen (1964)
Kelly's ratio (KR) = $Na^+/(Ca^{2+} + Mg^{2+})$	Kelly (1963)
Magnesium hazard (Mg Hazard) = $(Mg^{2+} \times 100)/(Ca^{2+} + Mg^{2+})$	Paliwal (1972)
Chlor-Alkali Index-1 (CAI-1) = $[Cl - (Na + K)]/Cl$	Schoeller (1977)

All ionic concentrations are in milli-equivalent per liter (meq/l)

In order to arrive at the weathering characteristics and hydrogeochemical classification, various ratios of cations and anions were studied as suggested in several other studies (Stallard 1980; Negrel et al. 1993; Gaillardet et al. 1999). A Piper trilinear diagram was also plotted using GW Chart software of USGS (Piper 1953).

Based on the values obtained during physicochemical analysis of collected samples of water (Table 1), its suitability for drinking and irrigation was assessed. The values were compared to the standards for drinking water prescribed by the Bureau of Indian Standards (BIS 2012) and the World Health Organization (WHO 2006). The suitability for irrigation was assessed by comparing the values of calculated parameters against the classification as suggested in different studies.

Results and discussion

Suitability for drinking

The average pH of groundwater in Baga–Calangute region was 6.7, ranging from 6.0 to 7.2. Slightly acidic pH of the water may be attributed to the dominance of acidic species like Cl^- and SO_4^{2-}, and lower concentrations of alkaline earth species like Ca^{2+} and Mg^{2+}. The dissolution of different chemical species in water primarily determines its quality. TDS had an average value of 151 mg/l ranging from 33 to 378 mg/l. Based on TDS, all water samples

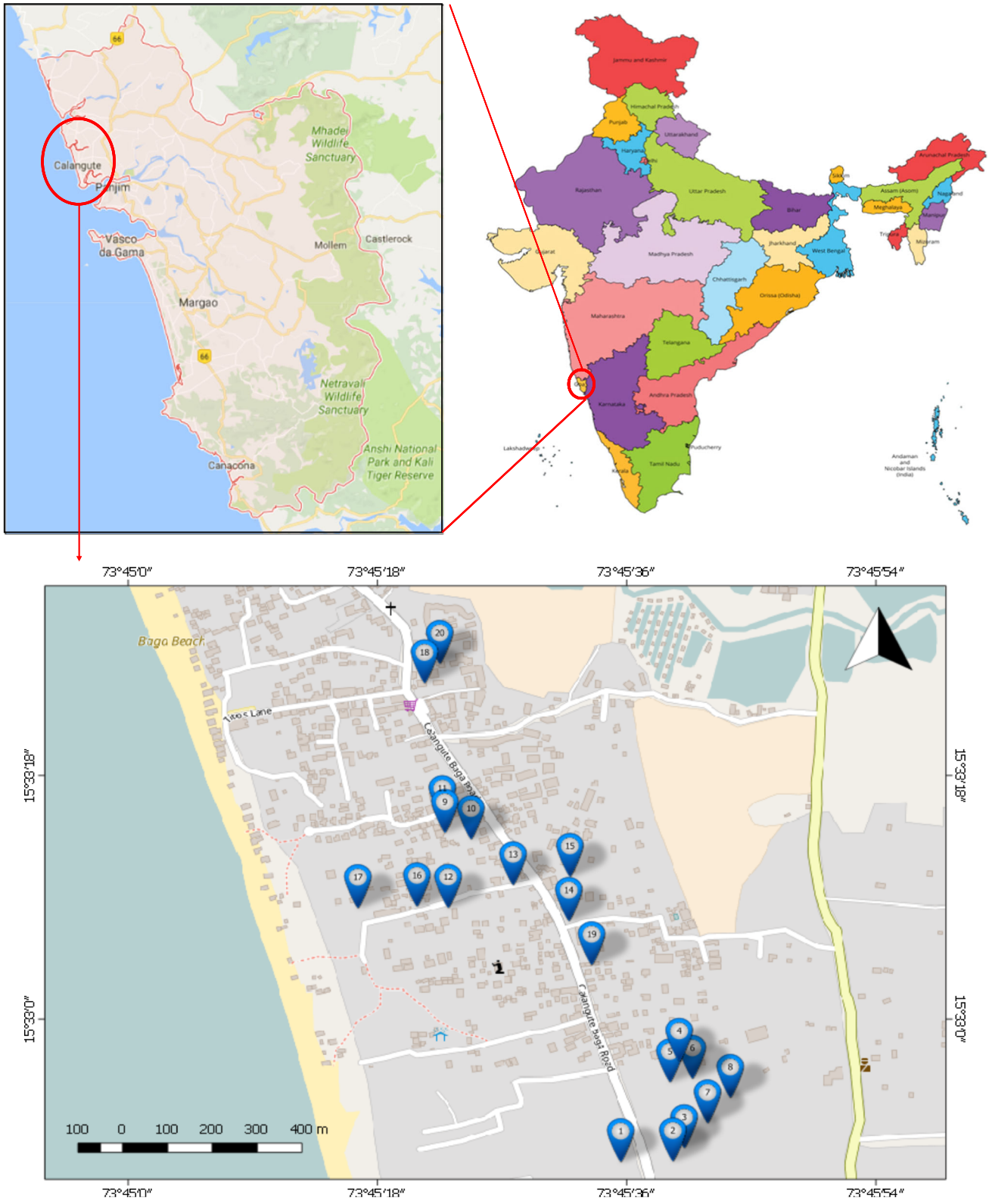

Fig. 2 Sampling locations in Baga–Calangute stretch

Table 1 Physicochemical characterization of groundwater samples of Baga–Calangute region

S. no.	Lat. (15°N)	Long. (73°E)	Temp. (°C)	pH	EC (μS/cm)	TDS	Total alkalinity	Total hardness	Na^+
1	32′49.52″	45′35.58″	28.8	6.8	771	378	129	282	46.6
2	32′49.57″	45′39.35″	27.7	6.4	706	346	124	254	57.9
3	32′50.55″	45′40.17″	27.7	6.0	300	148	76	90	40.7
4	32′56.94″	45′39.81″	28.6	6.5	125	68	42	54	11.2
5	32′55.42″	45′39.14″	27.7	6.9	84	42	42	42	6.7
6	32′55.68″	45′40.40″	27.8	6.8	109	54	34	38	10.2
7	32′52.39″	45′41.86″	27.8	6.7	220	108	49	58	19.9
8	32′54.27″	45′43.50″	27.8	6.4	66	33	59	42	35.7
9	33′13.87″	45′22.87″	27.7	6.3	336	165	44	94	25.9
10	33′13.38″	45′24.76″	27.7	6.6	318	156	61	100	26.4
11	33′14.52″	45′22.69″	27.9	7.2	419	201	63	118	33.7
12	33′08.32″	45′23.11″	28.0	7.0	245	120	63	80	19.0
13	33′09.99″	45′27.80″	28.0	6.4	394	193	73	84	34.6
14	33′09.35″	45′31.83″	28.0	6.9	118	59	71	64	9.2
15	33′10.61″	45′31.91″	28.3	7.0	75	37	49	52	4.6
16	33′08.43″	45′20.84″	27.8	6.0	491	241	83	174	32.5
17	33′08.30″	45′16.58″	28.2	6.7	512	253	127	176	38.3
18	33′24.92″	45′21.40″	27.9	7.2	498	244	73	160	36.5
19	33′04.09″	45′33.48″	29.1	7.0	207	102	71	88	13.5
20	33′26.37″	45′22.50″	28.5	6.9	138	68	51	54	11.7
Mean ± SD			28.1 ± 0.4	6.7 ± 0.4	307 ± 209	151 ± 102	69 ± 28	105 ± 70	25.7 ± 14.9

S. no.	K^+	Ca^{2+}	Mg^{2+}	Fe	CO_3^{2-}	HCO_3^-	Cl^-	SO_4^{2-}	$NO\bar{3}$	WQI[a]
1	8.9	106.4	3.9	0.00	0	129.3	15	32.9	48	2
2	7.5	37.6	38.9	0.00	0	124.4	477	43.8	63	3
3	6.8	27.2	5.4	0.00	0	75.6	124	40.3	64	1
4	0.4	16.0	3.4	0.00	0	41.5	285	18.7	62	1
5	2.1	10.4	3.9	0.04	0	41.5	297	4.9	56	14
6	3.3	12.8	1.5	0.00	0	34.2	878	7.3	47	1
7	4.2	16.8	3.9	0.00	0	48.8	278	12.1	59	1
8	0.6	9.6	4.4	0.00	0	58.6	164	16.0	48	1
9	6.6	27.2	6.3	0.00	0	43.9	296	24.5	56	1
10	6.4	25.6	8.8	0.00	0	61.0	132	23.5	51	1
11	8.3	33.6	8.3	0.04	0	63.4	181	31.7	72	15
12	5.1	19.2	7.8	0.00	0	63.4	328	28.1	48	1
13	16.5	23.2	7.3	0.00	0	73.2	62	31.1	48	1
14	2.2	12.8	7.8	0.00	0	70.8	30	10.6	86	2
15	0.9	16.0	2.9	0.00	0	48.8	470	3.2	51	1
16	7.4	44.0	15.6	0.00	0	83.0	136	44.2	96	2
17	6.7	44.0	16.1	0.01	0	126.8	35	33.7	87	5
18	8.1	44.8	11.7	0.00	0	73.2	154	38.9	52	2
19	2.7	27.2	4.9	0.02	0	70.8	288	11.4	72	8
20	2.3	9.6	7.3	0.00	0	51.2	469	7.5	83	2
Mean ± SD	5.5 ± 3.8	28.2 ± 21.8	8.5 ± 8.2	0.005 ± 0.01	0	69.2 ± 28.1	255 ± 206	23.22 ± 13.6	62.5 ± 15.3	

All the parameters are expressed in mg/l except pH, temperature (°C), and electrical conductivity (EC) (μS/cm); WQI[a] is for drinking water

were found to be suitable for drinking. The total hardness (as $CaCO_3$) of groundwater varied from 38 to 282 mg/l, with an average of 105 mg/l. As per classification for hardness, 35% samples were found to be soft (0–60 mg/l); 40% were moderately hard (61–120 mg/l); 15% were hard (121–180 mg/l); and 10% were very hard (>181 mg/l). Among the cations, sodium had an average concentration of 25.7 mg/l ranging from 4.6 to 57.9 mg/l; and potassium had an average concentration of 5.4 mg/l ranging from 0.4 to 16.5 mg/l. Calcium is an important species with respect to dissolved minerals and hardness, and it has the ability to affect the suitability of drinking water quality. Ca^{2+} had average concentration of 28.2 mg/l ranging from 9.6 to 106.4 mg/l. Only one sample in the study area had calcium concentration above the prescribed limit of 75 mg/l. Magnesium ions ranged from 1.5 to 38.9 mg/l with an average concentration of 8.5 mg/l, and only one sample exceeded the prescribed limit of 30 mg/l. Dissolved iron was present in only four samples, with concentration varying from 0.0 to 0.04 mg/l which was observed to be within the prescribed limit (0.3 mg/l) for drinking water. Among the anions, chloride was most prevalent with an average concentration of 255 mg/l. About 50% of the samples had chloride concentration above the prescribed limit of 250 mg/l. Carbonate was not reported in any of the samples owing to low average pH of 6.7; bicarbonate ranged from 34.2 to 129.3 mg/l with an average value of 69.2 mg/l. Sulfate was observed to be within the prescribed limit of 200 mg/l with an average concentration of 23.2 mg/l. But, the average concentration of nitrate was 62.5 mg/l ranging from 47 to 96 mg/l. Nitrate in all the samples was observed to be above the prescribed limit (45 mg/l) for drinking water. Based on the physicochemical parameters analyzed, groundwater of the study area was found to be suitable for drinking, but after disinfection, with a slight problem of nitrates, hardness, and dissolved chloride ions. Based on WQI, all the samples lie in grading A (WQI value 0–25) representing excellent water quality.

Suitability for irrigation

Agriculture is a dominant sector in the economic development of India and supports the majority of the population, contributing 46% to the gross national product (Kumarasamy et al. 2011). The criterion for suitability of groundwater for irrigation is entirely different from drinking purposes (Haritash et al. 2008). The water suitable for drinking may not be deemed suitable for irrigation; therefore, a number of indices have been suggested to infer the suitability on the basis of cations and anions primarily (Table 2). The observed values have been classified for suitability based on the criteria reported by different authors for designated parameters (Table 3). EC is the indirect inference of TDS present in groundwater. Based on EC, all the samples, but one, were considered to be suitable for irrigation (EC < 750 μS/cm) with an average of 307 μS/cm. Among the dissolved cations, Na^+ plays an important role with respect to factors including cation exchange capacity (CEC), percent sodium (%Na), SAR, RSC. High concentrations of sodium in irrigation water can enter cation exchange reactions with clay minerals in the soil which may reduce the soil permeability. Sodium adsorption ratio (SAR) values varied from 0.28 to 2.36 in the present study, with a mean value of 1.09 indicating that it would be unlikely that irrigation with the groundwater would affect soil structure and its permeability (Fig. 3). Similarly, unlike Ca^{2+} and Mg^{2+}, an excessive amount of SSP affects soil permeability and alters soil health. SSP values were observed in the range of 16.1 to 49.4% with a mean value of 34.6%, suggesting that concentration of sodium is high compared to other cations, but the water is safe for irrigation of soil with high permeability. In the same way, the percent sodium had an average concentration of 37.2% ranging from 17.6 to 64.9%. The values of RSC were observed to be negative for all the samples, signifying that it is unlikely that bicarbonate ions would react with calcium and magnesium ions to precipitate carbonate minerals in the soil. This may, otherwise, result in a relative increase in sodium posing the threat to the quality of irrigation water.

The presence of magnesium in soil is important to maintain its CEC and productivity, but excessive amounts can be harmful. If the magnesium hazard index is less than 50, the water is deemed fit for irrigation. In the present study, 90% of the samples were found to be safe for irrigation on the basis of their magnesium content. The average value of Mg hazard was 33.61 and ranged from 5.76 to 63.29.

The Kelly's ratio is another expression for calculation of sodium-related hazards. Based on KR, all the samples (95%), except one, were found to be free from salinity hazard. Apart from it, the permeability of the soil is affected by Na^+, Ca^{2+}, Mg^{2+}, and HCO_3^- content; and Permeability Index is a representation to designate water safe for use in agriculture. Based on the Permeability Index (PI: Doneen 1964), 80% of the samples were found fit for irrigation (class I and class II—75% of maximum permeability) and 20% in class III (25% of maximum permeability) which is deemed unfit for irrigation.

Weathering characteristics and hydrogeochemical classification

The chemical characteristics of water and relative abundance of chemical species may be used to determine the source from where majority of the ions originate and the

Table 2 Calculated values of various parameters to assess suitability for irrigation

S. no.	SAR	SSP	%Na	RSC	Mg hazard	KR	PI	CAI-1
1	1.21	26.41	28.54	−3.53	5.76	0.36	45.39	−4.34
2	1.57	32.95	34.60	−3.08	63.29	0.49	51.65	0.80
3	1.86	49.44	51.78	−0.57	24.86	0.98	80.54	0.44
4	0.66	31.01	31.46	−0.40	26.15	0.45	83.54	0.94
5	0.45	25.75	29.10	−0.16	38.46	0.35	98.23	0.96
6	0.72	36.70	40.84	−0.20	16.34	0.58	98.66	0.98
7	1.13	42.62	45.51	−0.37	27.90	0.74	86.67	0.88
8	2.39	64.71	64.93	0.11	43.31	1.83	105.56	0.66
9	1.16	37.40	40.73	−1.17	27.85	0.60	65.57	0.84
10	1.14	36.31	39.45	−1.01	36.42	0.57	67.94	0.65
11	1.35	38.19	41.44	−1.33	29.16	0.62	64.76	0.67
12	0.92	33.91	37.28	−0.57	40.37	0.51	75.76	0.90
13	1.60	45.97	52.15	−0.57	34.40	0.85	79.44	−0.10
14	0.50	23.67	26.13	−0.13	50.39	0.31	87.42	0.46
15	0.28	16.11	17.64	−0.24	23.20	0.19	88.14	0.98
16	1.07	28.76	31.41	−2.14	37.14	0.40	52.50	0.58
17	1.25	31.98	34.15	−1.46	37.88	0.47	59.67	−0.86
18	1.25	33.05	35.82	−2.02	30.33	0.49	55.86	0.59
19	0.62	24.92	27.06	−0.61	23.09	0.33	70.66	0.92
20	0.69	31.85	34.28	−0.25	55.90	0.47	89.22	0.96

SAR sodium adsorption ratio, *SSP* soluble sodium percentage, *%Na* percent sodium, *RSC* residual sodium carbonate, *Mg hazard* magnesium hazard, *KR* Kelly's ratio, *PI* Permeability Index, *CAI-1* Chlor-Alkali Index-1

Table 3 Criteria for classification of water quality for irrigation

Quality	EC range		% Na	RSC		KR	SAR	Mg hazard
Very good	250[a]	<1000[b]	20[a]	<0[c]	<1.25[d]	<1[g]	0–10[e]	<50%[f]
Good	250–750	1000–2000	20–40	0–2.5			10–18	
Marginal	750–2000	2000–4000	40–60	2.5–5.0	1.25–2.5	1–2	18–26	
Poor	2000–3000	4000–6000	60–80	5.0–7.5	>2.5	>2		>50%
Harmful	3000	>6000	80	>7.5			>26	

[a] Wilcox (1955), [b] Bhumbla and Abrol (1972), [c] Bishnoi et al. (1984), [d] Eaton (1950), [e] Richards (1954), [f] Paliwal (1972), [g] Kelly (1963)

mechanism controlling groundwater chemistry. The major sources of dissolved ions in inland water are atmospheric deposition, weathering of rock minerals, and anthropogenic inputs (Subramanian 1987). The rock–water interaction or precipitation-based effect can be predicted using Gibbs classification (Gibbs 1970). Gibbs "boomerang" plots suggest that the chemistry of groundwater is solely regulated by the dissolution of rock–minerals in the present study (Fig. 4). To further classify the source of ions as being from either silicate or carbonate weathering, ratios between (Ca + Mg)/(Na + K) can be used to infer relative contribution. The observed mean equivalent ratio of 2.04 in the present study suggests that water chemistry is primarily under the influence of silicate weathering (Taylor and McLennan 1985). Further, the average ratios between Ca/Na (1.44), Mg/Na (0.71), and HCO_3^-/Na (1.34) confirm that silicate weathering principally governs the water chemistry (Fig. 5), since the carbonate-dominated reservoirs have Ca/Na ratio around 50, Mg/Na around 10, and HCO_3^-/Na ratio near to 120 (Stallard 1980; Meybeck 1986; Negrel et al. 1993). On an average, the (Na + K)/TZ^+ (TZ^+ represents total cations) ratio of 0.37 also suggests that silicate weathering might be the major source of cations (Singh et al. 2005).

In order to arrive at the chemistry of groundwater, it is important to study its interaction with rocks–soil through which the water percolates. The Chlor-Alkaline Index (CAI-1) as suggested by Schoeller (1967) helps

determine the extent to which ion exchange takes place between groundwater and host environment. If the value of CAI-1 is observed to be positive, Na^+ and K^+ of water are exchanged with Ca^{2+} and Mg^{2+} of host rocks, and the value is negative if Ca^{2+} and Mg^{2+} of water are exchanged with Na^+ and K^+ of soil–rocks. In the present study, CAI-1 was observed to be positive for the majority (85%) of samples with a mean value of 0.39. It may be inferred that the direct base-exchange reaction is dominant factor governing groundwater chemistry in Baga–Calangute stretch.

A Piper trilinear diagram (Piper 1953) is a useful tool for the interpretation of the hydrochemical facies of groundwater and its classification based on normalized percentages of major cations and anions. In the present study, most of the samples belonged to mixed CaMgCl type and CaCl type, while three samples were observed as $CaHCO_3$ type and two samples as NaCl type. From the graphical representation of the Piper plot (Fig. 6), it may be inferred that alkaline earth (Ca^{2+} and Mg^{2+}) exceeds the alkaline (Na^+ and K^+) and the strong acid (Cl^- and SO_4^{2-}) exceeds weak acid (HCO_3^- and CO_3^{2-}). Based on the values of base exchange, the majority (95%) of the groundwater samples were found to be Ca–Na–SO_4 type (base exchange <1) except for one (sample 1) which was classified as being of NaCl type (Matthess 1982). Further, meteoric genesis indices suggested that the groundwater samples of Ca–Na–SO_4 type had deep meteoric percolation. Similar observations have been reported by Shedlock et al. (1993), stating that Ca–Na–SO_4-type water with deep meteoric percolation may be represented by surficial aquifers with unconsolidated sand as observed in open wells in Goa.

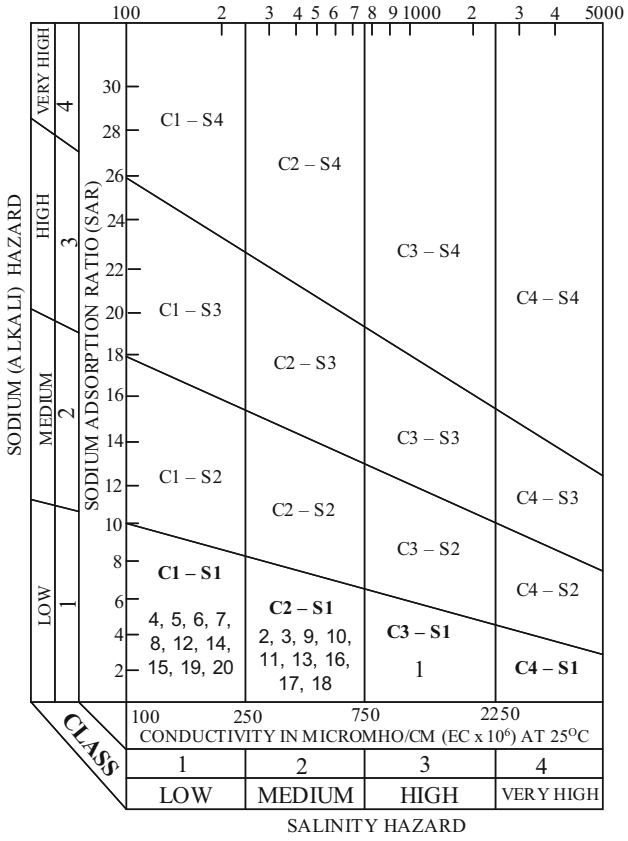

Fig. 3 US salinity diagram for calculated values of SAR

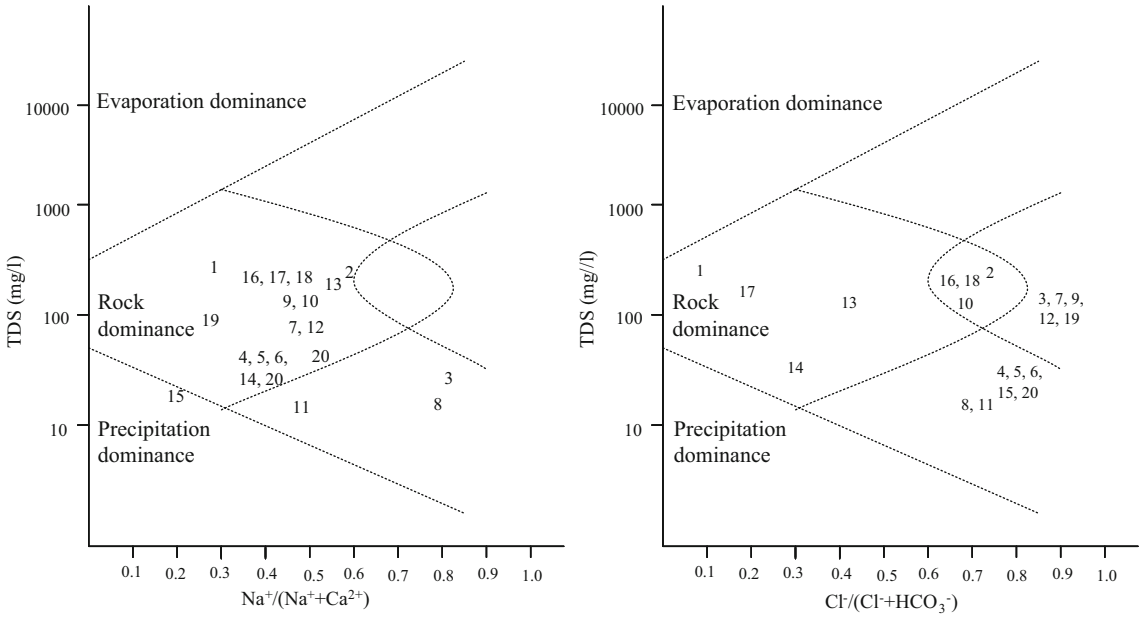

Fig. 4 Gibbs diagram for controlling factor of groundwater quality in the study area

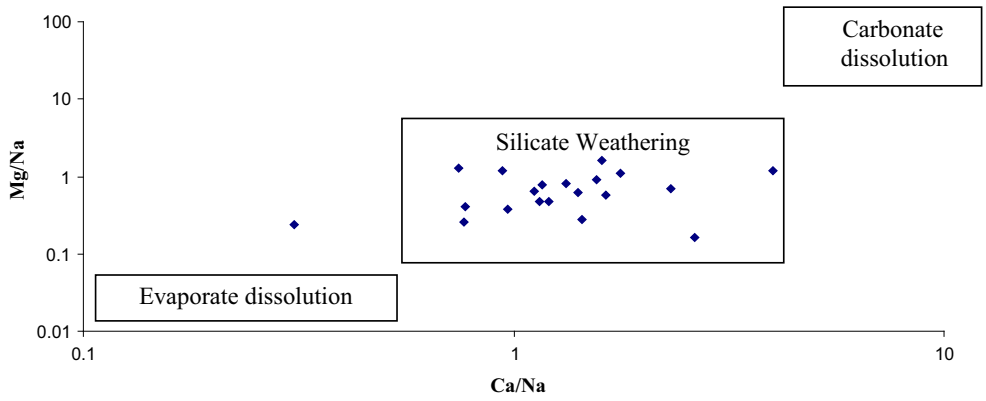

Fig. 5 Weathering type based on Na-normalized Ca and Mg

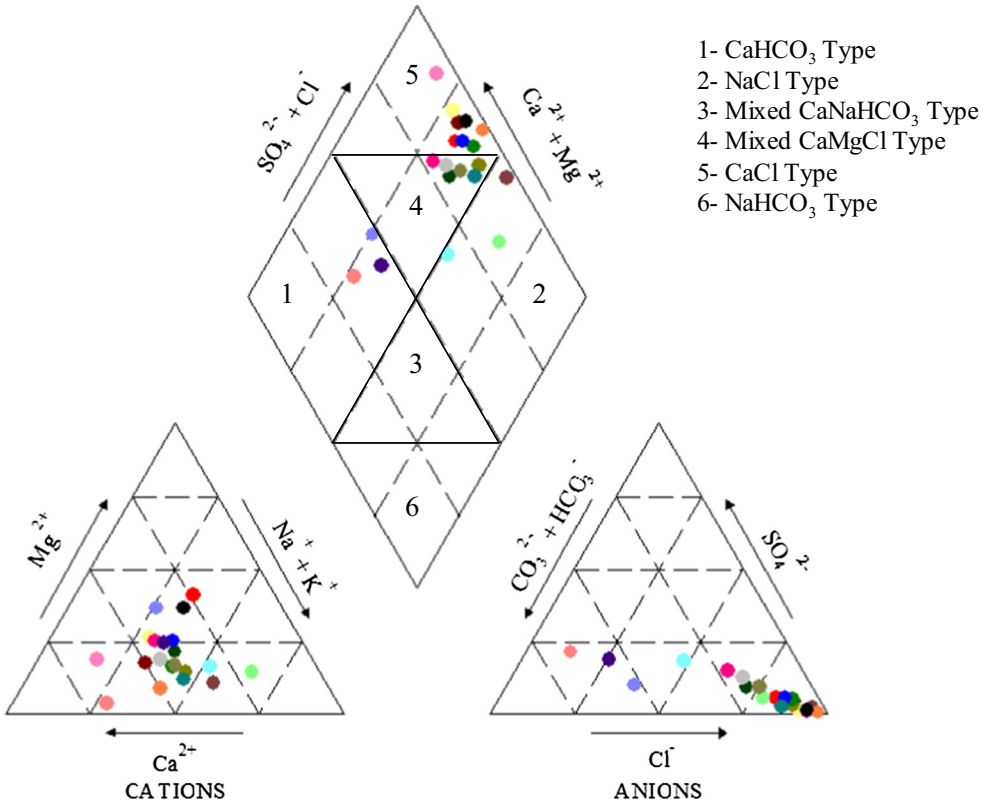

Fig. 6 Piper diagram for hydrogeochemical classification of groundwater in the present study

Conclusions

Based on the values observed in the present study, groundwater in Baga–Calangute area was found to be fit for drinking except for slightly elevated values of chlorides and nitrates. Therefore, it is likely that agriculture in Calangute–Baga stretch has had an impact on groundwater quality. An assessment of groundwater quality data suggests rock–water interactions in the form of direct base-exchange reactions and silicate weathering primarily govern the quality of groundwater. The only sample classified as NaCl type may be an outcome of seawater intrusion. Since most of the dug wells are shallow, groundwater can easily be affected by land use activities.

Given the increasing demand for the use of groundwater resources in the area due to tourism and population growth, it is likely that groundwater abstraction rates will also continue to increase. Although there is currently sufficient recharge from rainfall to maintain groundwater availability in the region, the quality of groundwater may be compromised by land use activities in the future since the tapped aquifers are surficial in nature. Therefore, it is necessary that groundwater quality in the region is monitored regularly, particularly at highly populated tourist destinations.

Acknowledgements The authors acknowledge the financial help from Delhi Technological University for conducting this study during the Survey-Camp, 2014.

References

Bhumbla DR, Abrol IP (1972) Is your water suitable for irrigation. Indian Farming 22:15–17

Bishnoi SR, Brar SPS, Kumar D (1984) Underground water quality of Dhuri block, district Sangrur, Punjab. Indian J Ecol 11(2):220–228

Bureau of Indian Standards (BIS) (2012) Indian standard drinking water specifications (2nd revision). BIS 10500: 2012, New Delhi

Central Ground Water Board (CGWB) (2013) Groundwater Information Booklet, North Goa District, Goa, Ministry of Water Resources. Government of India, South West Region-Bengaluru

Doneen LD (1964) Water quality for agriculture. Department of Agriculture, University of California, Davis, p 48

Eaton EM (1950) Significance of carbonate in irrigation water. Soil Sci 69:123–133

Eaton AD, Clesceri LS, Greenberg AE (1995) Standard methods for the examination of water and wastewater, 19th edn. APHA, New York

Food and Agriculture Organization of the United Nations (FAO) (2010) The wealth of waste: the economics of wastewater use in agriculture. FAO, Rome

Gaillardet J, Dupre B, Louvat P, Allegre CJ (1999) Global silicate weathering and CO_2 consumption rates deduced from the chemistry of large rivers. Chem Geol 59:3–30

Gibbs RJ (1970) Mechanism controlling world water chemistry. Science 17:1088–1090

Gleeson T, Wada Y, Bierkens MFP, VanBeek LPH (2012) Water balance of global aquifers revealed by groundwater footprint. Nature 488:197–200. doi:10.1038/nature11295

Haritash AK, Kaushik CP, Kaushik A, Kansal A, Yadav AK (2008) Suitability assessment of groundwater in some villages of Rewari district in Haryana. Environ Monit Assess 145(1–3):397–406

Haritash AK, Gaur S, Garg S (2016) Assessment of water quality and suitability analysis of River Ganga in Rishikesh, India. Appl Water Sci 6(4):383–392

Kelly WP (1963) Use of saline irrigation water. Soil Sci 95:355–391

Kidwai RM, Wagle BG (1975) Mineralogy of beach and dune sands of Morgin-Arambol beach on Goa coast. Indian J Mar Sci 4:128–130

Kumarasamy P, Alaguraja P, Deepasaraswathi M, Sekar M, Muthuveerran P, Yuvaraj D, Thirunavukkarasu A, Arthur J, Sames R (2011) Soil suitability and water quality study in Tirupur areas using geographic information system techniques. Int J Earth Sci Eng 4:85–97

Mani K, Salgaonkar BB, Das D, Bragança JM (2012) Community solar salt production in Goa, India. Aquat Biosyst 8(30):1–8

Mascarenhas A (1998) Study of Goa and its environment from space. A report on Coastal sand dune ecosystems of Goa: significance, uses and anthropogenic impacts. National Institute of Oceanography, Goa

Matthess G (1982) The properties of Groundwater, 1st edn. Wiley Publishers, New York

Meybeck M (1986) Compositiondes ruisseau non pollues de France. Sci Geo Bull 39:3–77

Negrel P, Allegre CJ, Dupre B, Lewin E (1993) Erosion sources determined by inversion of major and trace elements ratios and strontium isotopic ratios in river water: the Congo basin case. Earth Planet Sci Lett 120:59–76

Paliwal KV (1972) Irrigation with saline water. IARI Monograph No. 2 (New Series), New Delhi, p 198

Piper AM (1953) A graphic procedure in geochemical interpretation of water analysis. USGS Groundwater Note, No. 12

Richards LA (1954) Diagnosis and improvement of saline alkali soils. Agriculture Handbook no 60. US Department of Agriculture, Washington, p 160

Schoeller H (1967) Qualitative evaluation of groundwater resources. In: Schoeller H (ed) Methods and techniques of groundwater investigation and development. Water Research Series-33, UNESCO, Paris, pp 44–52

Schoeller H (1977) Geochemistry of groundwater. In: Brown RH, Konoplyantsev AA, Ineson J, Kovalevsky VS (eds) Groundwater studies—an international guide for research and practice. UNESCO, Paris, vol 15, pp 1–18

Shedlock RJ, Hamilton PA, Denver JM, Phillips PJ (1993) Regional groundwater quality assessment of Delmarva Peninsula. In: Alley WM (ed) Regional groundwater quality. VanNostrand Reinhold, New York, pp 563–588

Singh AK, Mondal GC, Singh PK, Singh S, Singh TB, Tewary BK (2005) Hydrochemistry of reservoirs of Damodar River Basin, India: weathering processes and water quality assessment. Environ Geol 48:1014–1028

Stallard RF (1980) Major elements geochemistry of the Amazon River System. Ph.D. thesis, WHOI-80-29, MIT/Woods Hole Oceanographic Institute USA

Subramanian V (1987) Environmental geochemistry of Indian River basins—a review. J Geol Soc India 29:205–220

Taylor SR, McLennan SM (1985) The continental crust: its composition and evolution. Blackwell, Oxford

UNESCO (United Nations Educational, Scientific and Cultural Organization) (2012) World's groundwater resources are suffering from poor governance. UNESCO Natural Sciences Sector News. UNESCO, Paris

USGS (United States Geological Survey) (2013) Land subsidence. http://ga.water.usgs.gov/edu/earthgwlandsubside.html

Venkateswaran S, Vijay Prabhu M, Mohammed Rafi M, Vallel LK (2011) Assessment of groundwater quality for irrigational use in Cumbum Valley, Madurai District, Tamil Nadu, India. Nat Environ Pollut Technol 10:207–212

Wilcox LV (1955) Classification and use of irrigation water. USDA, Circular 969, Washington, DC, p 19

World Health Organization (WHO) (2006) Guidelines for drinking water quality. First addendum to 3rd edn, vol 1. WHO, Geneva

ARTICLE IN PRESS

Ceramics International xxx (xxxx) xxx–xxx

Contents lists available at ScienceDirect

Ceramics International

journal homepage: www.elsevier.com/locate/ceramint

Improvement in dielectric, ferroelectric and ferromagnetic characteristics of $Ba_{0.9}Sr_{0.1}Zr_{0.1}Ti_{0.9}O_3$-$NiFe_2O_4$ composites

Aditya Jain[a], Amrish K. Panwar[a,*], A.K. Jha[b], Yogesh Sharma[c]

[a] Department of Applied Physics, Delhi Technological University (Formerly Delhi College of Engineering), Bawana Road Delhi 110042, India
[b] Department of Applied Science, A.I.A.C.T.R. Geeta Colony, Delhi 110031, India
[c] Department of Physics, Indian Institute of Technology, Roorkee 247667, India

ARTICLE INFO

Keywords:
Dielectric
Microstructure
Ferroelectric
Ferromagnetic
Perovskite

ABSTRACT

Multiferroic composites with the composition (1-x)$Ba_{0.9}Sr_{0.1}Zr_{0.1}Ti_{0.9}O_3$-($x$)$NiFe_2O_4$ (x=0.0, 0.05, 0.10, 0.20 and 0.30) were prepared by mechano-chemical activation technique. Rietveld refined X-ray diffraction pattern shows the formation of individual perovskite (BSZT) and inverse spinel (NFO) phases for all the four composite samples. Microstructural investigation reveals that the inhomogeneity in grains increases with addition of NFO as compared to bare BSZT sample. Dielectric studies show that all the samples exhibit a well-defined ferroelectric to paraelectric transition peak. Further, the diffuseness of the samples increases as NFO content increases. Ferroelectric properties were found to be superior for (1-x)BSZT-(x)NFO sample with x=0.05 and decreases on further increase in NFO content. Dielectric breakdown strength also shows the similar trend as ferroelectricity and shows a maximum for x=0.05 ferrite (NFO) fraction. Magnetic measurement of BSZT-NFO composite samples shows a gradual increase in saturation magnetization and coercive field (H_c) with increasing NFO content.

1. Introduction

ABO_3 type perovskite materials with their versatile multifunctional properties have attracted a lot of attention in past few decades because of their diverse range of applications in the field of microelectronics and communication [1]. Barium titanate based perovskite compounds like $A_xA'_{1-x}B_yB'_{1-y}O_3$ with $0 \le x,y \le 1$ are of utmost technological and commercial interest due to their superior electrical, optical and magnetic properties as well as better performance than the pristine ABO_3 perovskite compounds [2]. Cubic phase $BaZrO_3$ shows important properties for applications in piezoelectrics and substrate material for superconductors [3]. $SrTiO_3$, an important compound of perovskite family possesses high thermal and chemical stability combined with excellent optical properties making it a potential candidate for gas sensing, superconducting electronics and energy conversion applications [4]. $BaZr_{1-x}Ti_xO_3$ (BZT) has replaced $BaTiO_3$ in the production of multi-layered ceramic capacitors because Zr^{4+} is chemically more stable as compare to Ti^{4+}, in addition to this, BZT possess better dielectric properties compared to pure $BaTiO_3$ [5,6]. $NiFe_2O_4$ is a rare nickel iron oxide mineral and is known to be an important member of spinel family. Nickel ferrite has potential applications as ferromagnetic material in permanent magnets, telecommunications, computer peripherals, electronic and microwave devices [7].

Multifunctional materials which simultaneously exhibit coupled ferroelectric and ferromagnetic order are an important member of materials family due to their possible applications in the field of advanced electronic devices. The occurrence of magnetization/polarization on the application of electric field/magnetic field is known as magnetoelectric (ME) effect which is a highly useful phenomenon with a diverse range of applications namely magnetoelectric transducers, multiple-stage memories, spintronics, sensors and actuators, etc. [8]. The magneto-electric materials are either found in single phase or composite phase. There are some single phase magnetoelectric materials such as $BiFeO_3$ and few rare earth manganates namely $YMnO_3$, $TbMnO_3$, $BiMnO_3$, YMn_2O_5, etc. [9]. However, weak ME coupling and/or the low Curie temperature (below room temperature) of these single phase ME materials limits their application in electronic devices [10]. For this reason, the ME composites containing electrostrictive, magnetostrictive and piezoelectric materials as individual phases, have attracted a lot of attention of the researchers because of their better multiferroic properties as compared to single phase compounds. Further, the composites can be defined as the compounds having at least couple of phases with different chemical and physical properties. The overall properties of the end product, i.e. composites are controlled

* Corresponding author.
E-mail address: panwaramar@gmail.com (A.K. Panwar).

http://dx.doi.org/10.1016/j.ceramint.2017.05.053
Received 8 April 2017; Received in revised form 5 May 2017; Accepted 8 May 2017
0272-8842/ © 2017 Elsevier Ltd and Techna Group S.r.l. All rights reserved.

Please cite this article as: Jain, A., Ceramics International (2017), http://dx.doi.org/10.1016/j.ceramint.2017.05.053

by the type and volume ratio of the individual phases, solubility and interface properties as well as by the individual properties [11]. The multiferroic effect in composite materials is a combinational property, i.e. a particular effect could be absent in the individual materials but may be present in the composites as a consequence of coupling between the different material components.

Mechanochemical activation route of synthesis has been proved to be a viable method for the fabrication of barium titanate based materials and can be utilized to synthesize ultrafine particles with high purity, controlled morphology and uniform distribution. Such a uniform distribution combined with ultrafine particle size are very convenient and well suited for use in contemporary green fabrication technique namely inkjet printing, tape casting, etc. Moreover, the sintering temperature required in this method to synthesize the material are lower than those required for sintering conventionally produced materials (up to 100–200 °C lower in some cases) [12].

In the present work, the effect of addition of $NiFe_2O_4$ on the microstructural, dielectric, ferroelectric and magnetic properties of a multiferroic composite system $Ba_{0.9}Sr_{0.1}Zr_{0.1}Ti_{0.9}O_3$ – $NiFe_2O_4$ has been studied for the first time. $NiFe_2O_4$ (NFO), which is chosen as a ferromagnetic component of the multiferroic composite has been also synthesized by mechanochemical activation technique.

2. Experimental

Particulate composites with $Ba_{0.9}Sr_{0.1}Zr_{0.1}Ti_{0.9}O_3$ (BSZT) as ferroelectric phase and $NiFe_2O_4$ (NFO) as magnetic phase were synthesized by mechanochemical activation technique. $Ba_{0.9}Sr_{0.1}Zr_{0.1}Ti_{0.9}O_3$ was prepared by taking AR grade reagents (Sigma-Aldrich make) $BaCO_3$ (99.9%), $SrCO_3$ (99.8%), TiO_2 (99.9%) and ZrO_2 (99.9%) as the starting precursor materials. All precursor materials were taken in stoichiometric ratio and ground for effective 24 h in air atmosphere at 400 rpm. *Retsch PM100* planetary ball mill was used to carry out ball milling. A Zirconia jar with 45 mm diameter and 140 Zirconia balls with 5 mm diameter were used as milling medium. The ferroelectric phase BSZT was calcined at 1100 °C for 4 h followed by sintering at 1250 °C for 3 h. High purity AR grade NiO and Fe_2O_3 in stoichiometric ratio were milled with toluene to prepare the magnetic phase $NiFe_2O_4$ for 24 h in zirconia media. $NiFe_2O_4$ was calcined at 1150 °C for 5 h followed by sintering at 1300 °C for 12 h. Finally, the multiferroic composites $(1\text{-}x)Ba_{0.9}Sr_{0.1}Zr_{0.1}Ti_{0.9}O_3\text{-}(x)NiFe_2O_4$ (where x=0, 0.05, 0.1, 0.2 and 0.3) were obtained by thoroughly mixing the constituent phases BSZT and NFO in desired weight ratios by ball milling for 6 h. The resulting composite milled powder were then mixed with 2.5 wt% polyvinyl alcohol (PVA) and squeezed into cylindrical pellets of approximately 10 mm diameter and nearly 1 mm thickness by using a hydraulic press. The pellets of the composites were annealed at 800 °C with heating rate of 6 °C/min for 2 h in air atmosphere. Hereafter, these composites are referred to as BN0, BN5, BN10, BN20 and BN30 for x=0, 0.05, 0.1, 0.2 and 0.3, respectively.

The composite phase and crystal structure of BNx composite materials were examined by *Bruker D8 Advance* X-ray diffractometer coupled with $CuK_{\alpha 1}$ radiation having the wavelength of 1.541 Å. Lattice parameters and theoretical densities were evaluated with the help of XRD data using *X'Pert Highscore Plus* software followed by Rietveld analysis. The microstructural characteristics and surface morphology of high temperature sintered pellets were examined using *Hitachi S-3700N* scanning electron microscope. Grain size distribution analysis has been carried out using *ImageJ* software. TEM (FEISTWIN PF30) with 300 kV has been used to perform TEM/HRTEM and SAED analysis by using carbon coated copper grids. The sintered pellets of $(1\text{-}x)$BSZT-(x)NFO composites were polished to 1.2 mm thickness and slightly viscous silver paste was coated on both sides of pellets to form electrodes and then the pellets were heated at 160 °C for 15 min. Further, these pellet samples were used to carry out dielectric measurement by an *Agilent 4284A* LCR meter at various frequencies.

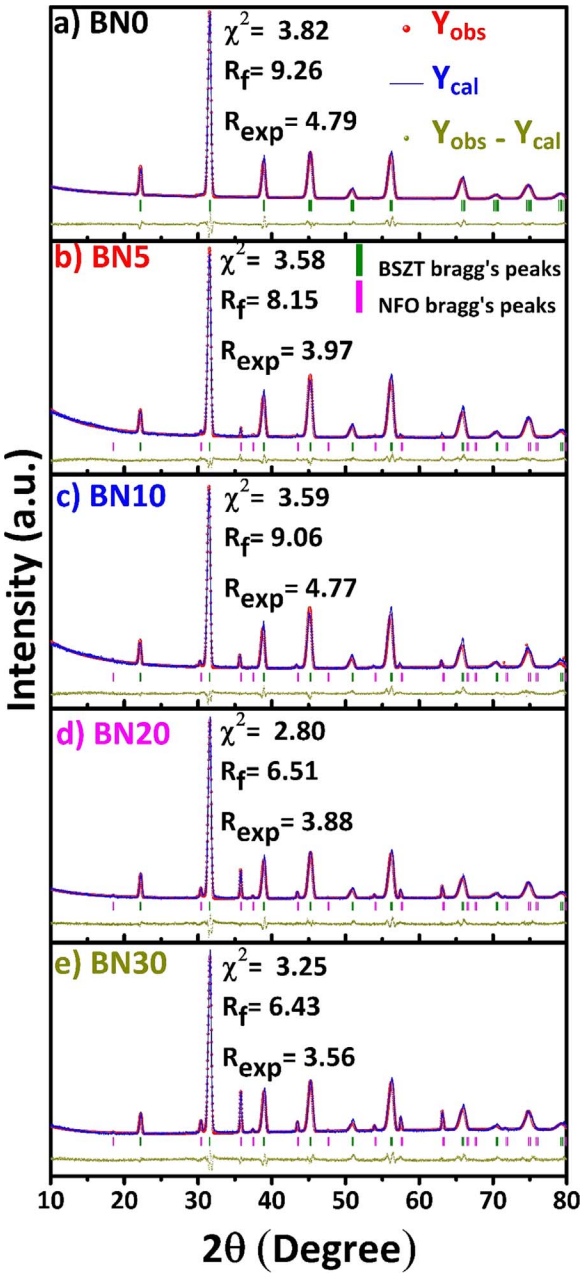

Fig. 1. Rietveld refined X-ray diffraction (XRD) patterns of (1-x)BSZT-xNFO composite ceramics: (a) x=0.0, (b) x=0.05, (c) x=0.10, (d) x=0.20 and (e) x=0.30.

Temperature dependent dielectric measurement was performed over the temperature range of 25–225 °C. The hysteresis loop measurement of the composites was performed using a Sawyer-Tower circuit based P-E loop equipment made by *M/s Marine Delhi, India*. Magnetic hysteresis loops of the composite samples at room temperature were recorded using a vibrating sample magnetometer (VSM). For Piezoelectric measurement, all the pellet samples were electrically poled for 1 h at E~20 kV/mm at a poling temperature of T_P~60 °C, at which finest piezoelectric properties were observed.

3. Result and discussion

3.1. X-ray diffraction (XRD)

In order to comprehend the structural variation on the addition of NFO in BSZT, we have performed structural refinement by Rietveld method using *X'Pert Highscore Plus* software. Fig. 1(a)-(e) shows the

Rietveld-refined X-ray diffraction pattern of (1-x)$Ba_{0.9}Sr_{0.1}Zr_{0.1}Ti_{0.9}O_3$ – $x$$NiFe_2O_4$ (x=0.0, 0.05, 0.10, 0.20 and 0.30). Barium titanate (JCPDS no. 01-074-1960) and nickel ferrite (JCPDS no. 00-010-0325) were taken as the reference patterns and the Pseudo-Voigt function has been used to refine diffraction peaks. A well-recognized tetragonal phase with *P4mm* space group is observed for BN0, however, as the NFO content is added, the peaks of nickel ferrite begin to appear (Fig. 1(b)-(e)). The (1-x)BSZT-(x)NFO composites have been prepared through the mechano-chemical activation technique, which exhibit a mixed perovskite-inverse spinel phase without any traces of impurities. The observed and calculated d values of all the diffraction lines in pure and NFO added BSZT compounds indicate that the basic crystal structure (i.e. tetragonal) does not change as x changes from 0.05 to 0.3. however, the slight changes in *'a'* and *'c'* values indicates a corresponding changes in tetragonality of the samples with the NFO addition. All the peaks of (1-x)BSZT-(x)NFO can be identified for the separate perovskite (BSZT) and inverse spinel (NFO) phases and no intermediate phase is observed during the formation of all the four composite samples. This confirms the successful preparation of the di-phase multiferroic composite material and it also suggests that both the constituent phases have retained their identity in the composites and no unwanted reaction has taken place between the ferroelectric BSZT and ferrite NFO phases during the final heat treatment process. The BSZT crystallizes in a tetragonal perovskite structure with space group *P4mm* and the NFO has a cubic inverse-spinel structure with space group *Fd-3m*. It is clearly noticed that the intensity of ferrite phase increases with increase in NFO concentration. Table 1 shows the detailed structural parameters estimated after Rietveld refinement analysis.

On observation of the X-ray diffraction pattern of composite samples, it can be inferred that limited reaction takes place between the ferroelectric-ferrite phase of BSZT and NFO, respectively. The reason being that, BSZT exhibit a perovskite structure and NFO has inverse spinel structure. So, these compounds have very little solid solubility with each other. These results are also confirmed by the c/a ratio which indicates a slight decrease with the increasing NFO concentration. Fig. 2(a)-(b) shows the crystal structure of BSZT and NFO. These structures were plotted by using VESTA software from the atomic positions obtained after the Rietveld analysis of BN5 sample. The atomic positions confirmed that the BSZT is present in tetragonal phase and NFO is existing in inverse spinel phase. In NFO crystal, the little white stripes in tetrahedral and octahedral positions of Fe and Ni atoms indicates the loss of occupancy which may be attributed to weight loss of the material during the calcination and sintering process.

3.2. Microstructural studies

The SEM images, shown in Fig. 3(a)-(e), demonstrate that composite materials are obtained with an overall good dispersion of the nickel ferrite inverse spinel phase in BSZT perovskite ferroelectric matrix. All the synthesized samples have shown the bimodal distribution with polygonal grain type morphology, where bigger and smaller grains are distributed randomly. The average grain size of the samples, calculated by ImageJ software was found to decrease slightly with an increase in NFO concentration. The average grain size of the samples are approximately 463, 424, 410, 390 and 388 nm for x=0.0, 0.05, 0.10, 0.20 and 0.30, respectively. The reason behind the non-homogeneous grain morphology may be attributed to three stage heating as well as high calcination and sintering temperature in solid state synthesis method which results in abnormal grain growth [13]. Moreover, it is a well-known fact that the grain size of ceramics is reliant on its sintering temperature, heating/cooling rate and soaking period at the highest temperature [14,15]. These three aspects do have a foremost effect on the microstructural properties of the final sintered specimen and therefore, they do affect the dielectric and ferroelectric properties of the ceramics. In composite materials, the presence of two different

Table 1
Rietveld refined XRD parameters for bare BSZT and BSZT-NFO composite samples.

Sample		Space group	Crystal structure	Lattice parameters (Å)	Cell volume (Å^3)	Theoretical density (gm/cm^3)	χ^2	R_{exp}	R_f	R_{Bragg}
BN0		*P4mm*	Tetragonal	a = 4.0038 c = 4.0250	64.5226	4.8963	3.82	4.79	9.26	3.03
BN5	**BSZT phase**	*P4mm*	Tetragonal	a = 4.0031 c = 4.0188	64.4035	4.8655	3.58	3.97	8.15	4.52
	NFO phase	*Fd-3m*	Cubic	a = 8.3103	573.920					6.70
BN10	**BSZT phase**	*P4mm*	Tetragonal	a = 4.0083 c = 4.0058	64.3673	4.7416	3.59	4.77	9.06	6.51
	NFO phase	*Fd-3m*	Cubic	a = 8.3322	578.470					3.67
BN20	**BSZT phase**	*P4mm*	Tetragonal	a = 4.0109 c = 3.9983	64.3254	4.7347	2.80	3.88	6.51	2.39
	NFO phase	*Fd-3m*	Cubic	a = 8.3341	578.881					2.54
BN30	**BSZT phase**	*P4mm*	Tetragonal	a = 4.0013 c = 4.0163	64.3044	4.7115	3.25	3.56	6.43	2.85
	NFO phase	*Fd-3m*	Cubic	a = 8.3346	578.967					2.68

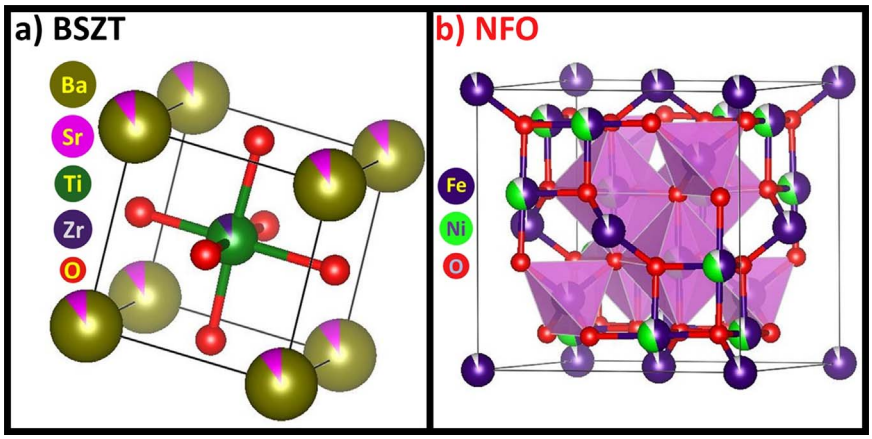

Fig. 2. Crystal structure of (a) BSZT and (b) NFO.

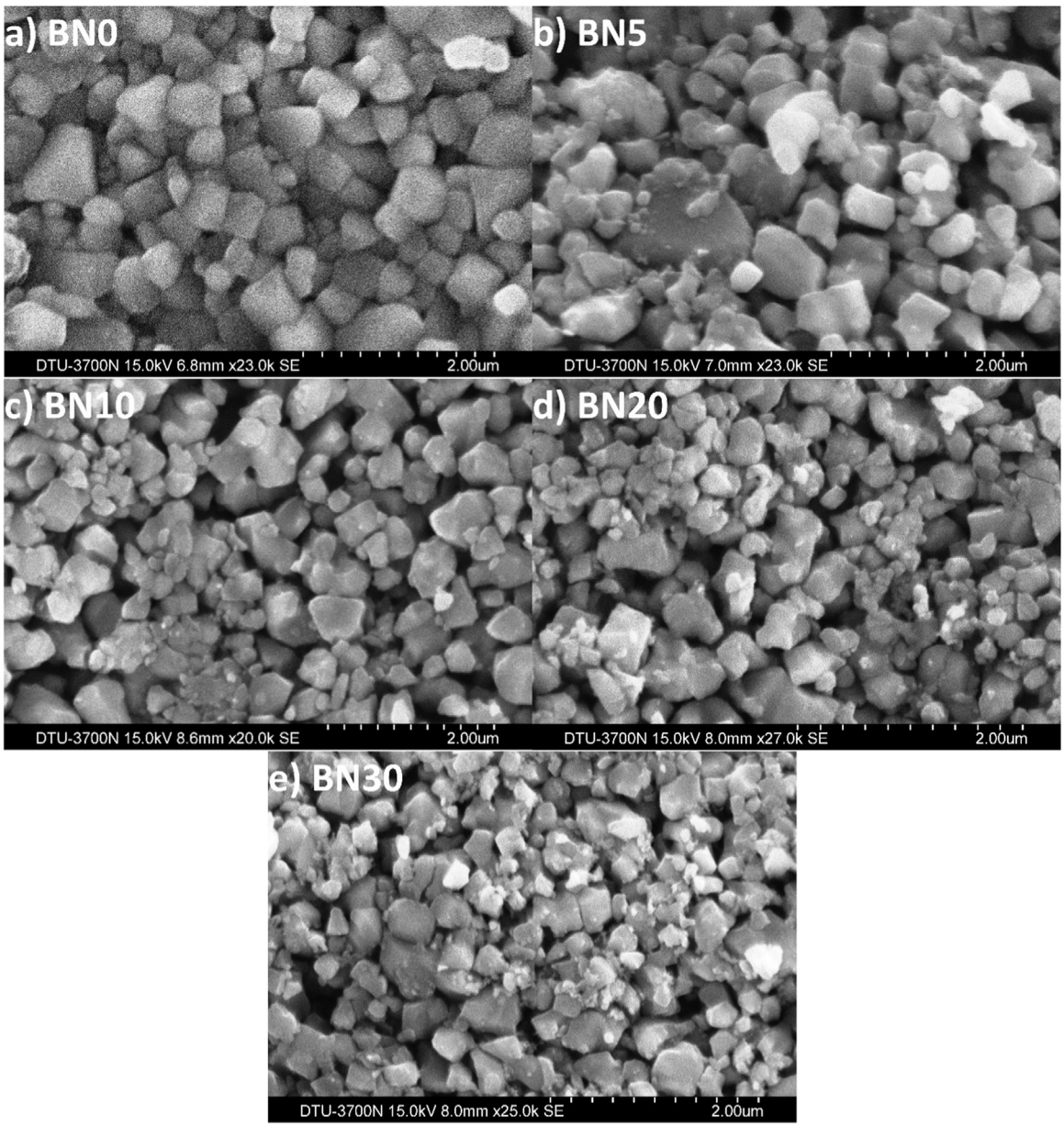

Fig. 3. SEM micrograph of sintered pellets of (1-*x*)BSZT- *x*NFO samples: (a) *x*=0.0, (b) *x*=0.05, (c) *x*=0.10, (d) *x*=0.20 and (e) *x*=0.30.

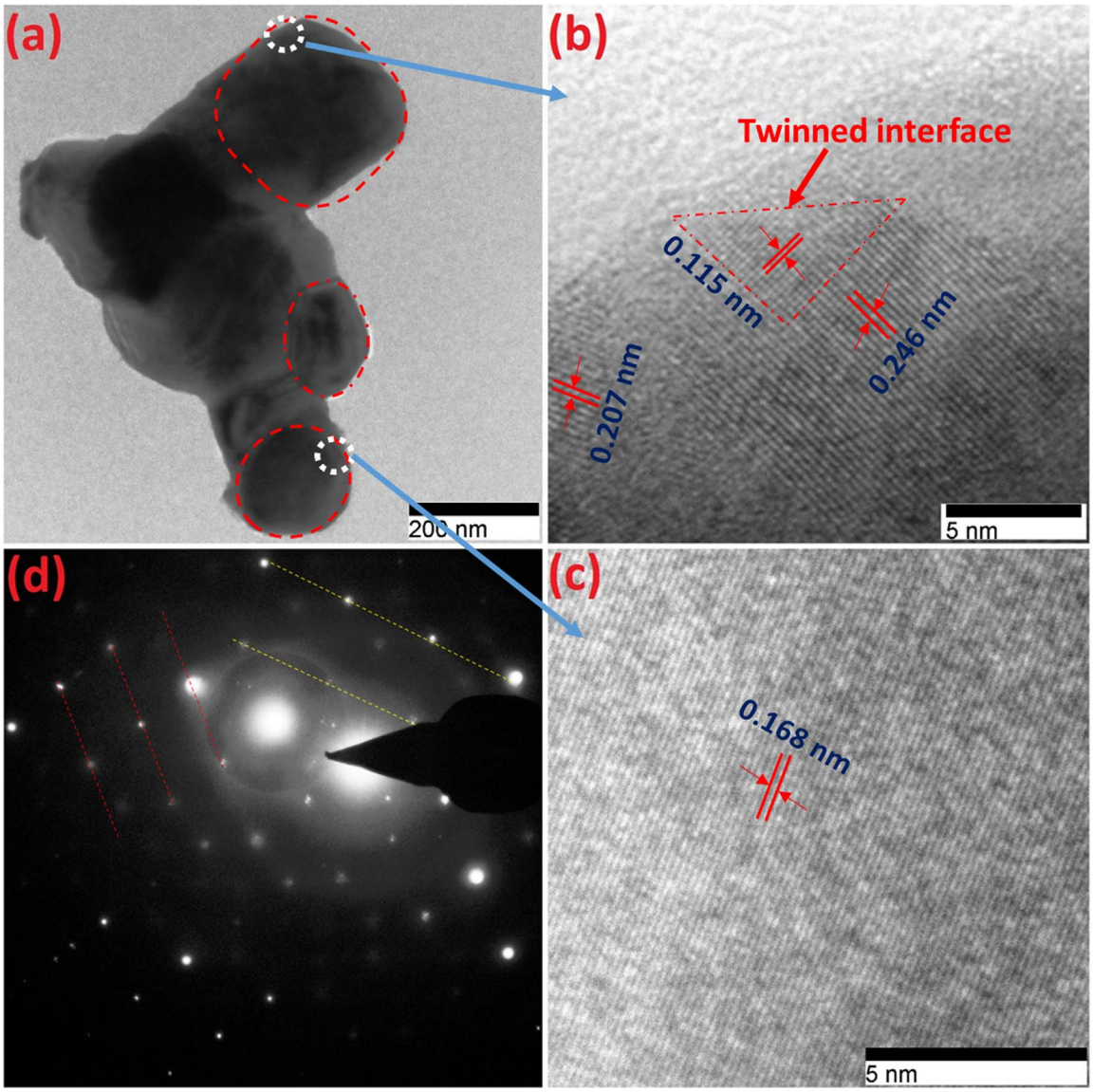

Fig. 4. TEM/HRTEM image of BN5: (a) TEM, (b) HRTEM, (c) SAED pattern.

types of grains may be ascribed to the fact that the grains of BSZT may have higher probability of growing as compared to NFO and therefore bigger grain grows at the cost of smaller grain. Moreover, in case of composites, it is hard to obtain a homogeneous microstructure due to the considerable difference in the sintering conditions and the thermal expansion coefficients of the BSZT and NFO phases.

TEM and HRTEM studies of BN5 have been performed since this sample shows overall superior structural and electrical properties among the five synthesized samples. The average particle size of BN5 powder from TEM analysis (Fig. 4(a)) is measured to be ~135 nm. The perfectly aligned lattice fringes in the HRTEM image of BN5 sample clearly suggest the formation of crystallized composite ceramic. The HRTEM image of BN5 particles is shown in Fig. 4(b) and (c) which depicts lattice fringes corresponding to different planes with an inter-fringe distance of 0.246 nm, 0.207 nm and 0.168 nm, respectively. Fig. 4(b) shows a twinned interface marked with a triangle, which may belong to an area where BSZT and NFO particles have diffused into each other resulting in the twinning of the lattice fringes. The continuous lattice fringes with an inter-fringe distance of 0.246 nm, 0.207 nm and 0.168 nm could be assigned to BSZT phase with corresponding (111), (002) and (112) planes with conventional d spacing of 0.243 nm, 0.208 nm and 0.162 nm, respectively. Further, the twinned lattice fringe with 0.115 nm inter-fringe spacing can be assigned to NFO phase with corresponding (533) plane having conventional d spacing of 0.119 nm. The selected area electron diffraction (SAED) pattern shown in Fig. 4(d), also confirms the crystalline nature of BN5 sample. The typical SAED pattern illustrates bright and dark spots that are assigned to different planes in the tetragonal and cubic crystal. SAED pattern was recorded for the twinned interface area of the HRTEM image which shows two groups of bright and dark spots showing the diffusion of BSZT and NFO phase in the selected area. Moreover, both the HRTEM and SAED pattern recorded for the selected sample indicate that there are no significant structural defects in the observed BN5 sample.

3.3. Dielectric studies

Fig. 5(a)-(e) shows the temperature dependencies of dielectric constant and loss tangent for $(1\text{-}x)Ba_{0.9}Sr_{0.1}Zr_{0.1}Ti_{0.9}O_3\text{-}(x)NiFe_2O_4$ composites at some chosen frequencies. The occurrence of a broad dielectric peak in the temperature vs. dielectric constant plot can be observed, which signifies the ferroelectric to paraelectric phase transition of the sample under study. It can be observed that the Curie temperature of the composite samples is slightly higher than the bare

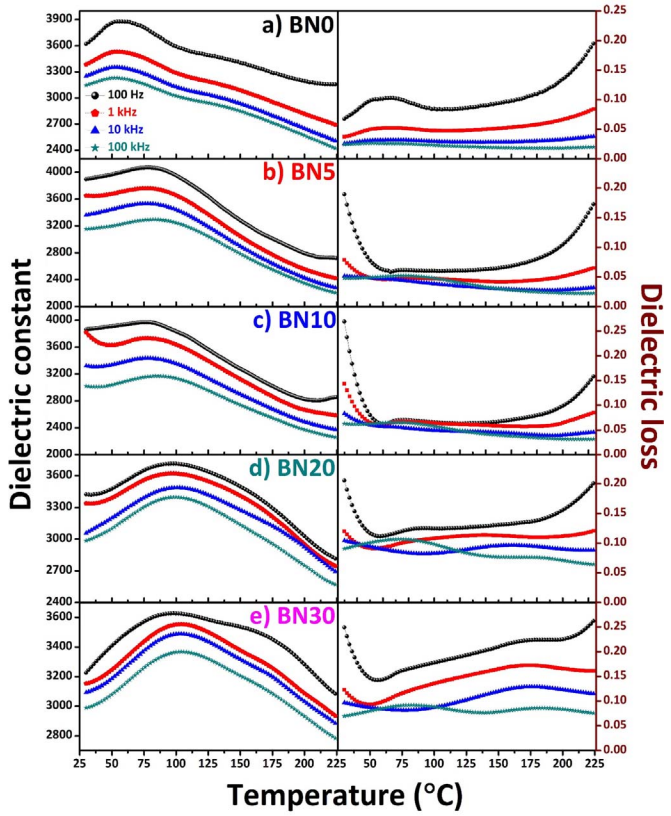

Fig. 5. Dielectric constant and dielectric loss as a function of temperature for the (1-*x*) BSZT- *x*NFO samples: (a) *x*=0.0, (b) *x*=0.05, (c) *x*=0.10, (d) *x*=0.20 and (e) *x*=0.30.

BSZT (BN0) sample. The transition temperature T_c corresponding to BN0, BN5, BN10, BN20 and BN30 were observed to be 57, 76, 81, 90 and 101 °C, respectively. For all the samples, a well-defined ferroelectric to paraelectric peak can be seen, which suggest that the dielectric characteristics are still dominated by BSZT phase even at samples containing higher concentration of NFO. The dielectric constant of the (1-*x*)BSZT-*x*NFO samples increases slightly up to x=0.05 (BN5) and then began to decrease on further addition of NFO. The higher value of dielectric constant for BN5 may be ascribed to the presence of optimum heterogeneity in the composite. In composites, heterogeneity signifies the boundary layer between the ferroelectric and ferrite phases that give rise to space charge/interfacial polarization and thus contributing to the higher value of dielectric constant. However, in the samples containing higher NFO amount, the effect of heterogeneity got hindered. Further, the decrease in dielectric constant for higher NFO content may be ascribed to an increasing amount of substitution of the Ti^{4+}/Zr^{4+} ions by Fe^{3+} in the BSZT lattice, resulting in weakening of bonding force between the oxygen atom and B-site ions of ABO_3 perovskite structure. In addition to this, the weakening of these bonds also leads to a shift of transition temperature towards high temperature side. From Fig. 5, it can be observed that dielectric constant decreases at higher frequency and thereby showing little dispersion in the dielectric constant maxima temperature. The observed dispersion can be explained by Maxwell-Wagner interfacial polarization model that plays a vital role in defining such systems [16,17]. At low frequency four types of polarization namely; (i) interfacial, (ii) dipolar, (iii) ionic and (iv) electronic polarization contribute to the total dielectric constant of the material. But at higher frequency, the dipoles inside the material are not able to align themselves with the alternating electric field and therefore contribution from different polarization decreases. Only electronic polarization has a substantial contribution to the dielectric constant at high frequency and consequently the dielectric constant decreases.

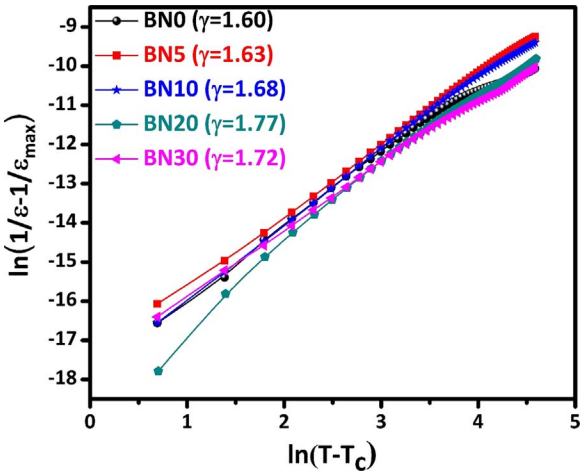

Fig. 6. Plot of $\ln(1/\varepsilon - 1/\varepsilon_m)$ as a function of $\ln(T-T_c)$ for the (1-*x*)BSZT- *x*NFO samples.

The dielectric anomaly at higher temperature, characterized by the flattening in the dielectric constant maximum curve at higher frequency and sharp increase of Tanδ with increase in temperature, arises due to Debye-type relaxation of space charge at the boundary between composite material and the electrodes, which is the characteristic for titanium containing oxide perovskites [18]. The dielectric loss in the vicinity of room temperature at 10 kHz has been slightly reduced in BN5 sample compared to NFO free BN0 sample. However, further increase in NFO concentration leads to an increase in dielectric loss, which may be attributed to introduction of $NiFe_2O_4$ phase. Another possibility for the slight reduction in dielectric loss of BN5 sample compared with BN0 may be the decrease in the concentration of Ti^{4+} ions and oxygen vacancies.

Another feature of these BSZT-NFO composites is the induction of diffuse phase. Fig. 6 shows the plot of diffuseness parameter for the five synthesized samples. The diffused dielectric peak at phase transition may be ascribed to polar structural distortion of TiO_6/ZrO_6 octahedra and disturbed localized dynamics due to the substitution of Sr and Zr at Ba and Ti-site of $BaTiO_3$ unit cell, respectively [19]. One more possibility for the diffused nature in BSZT-NFO composite samples is the random distribution of strain field in the material. Diffuseness constant can be calculated using the following expression [20]:

$$\frac{1}{\varepsilon} - \frac{1}{\varepsilon_m} = \frac{(T - T_c)^{\gamma}}{C'} \quad (1)$$

where, γ is the diffuseness parameter, T_c represents the Curie-Weiss temperature and C' signifies the Curie constant. The diffuseness parameter can provide information on phase transition nature of any ferroelectric material. The value of γ=1 corresponds to normal ferroelectric behavior and $1 < \gamma < 2$ resembles a diffuse phase transition [20]. By observing the dielectric properties, it can be reasonably concluded that the BN5 sample with large dielectric constant, small dielectric loss and good thermal stability over a broad temperature range is a suitable material for the fabrication of capacitors with operating temperature as high as 150 °C.

3.4. Ferroelectric studies

The ferroelectric hysteresis loop of pure and NFO containing BSZT composite ceramics at three different temperatures of 27, 60 and 100 °C are shown in Fig. 7(a)-(c). These hysteresis loops were measured using a maximum externally applied electric field of 50 kV/cm at a frequency of 20 Hz. All the samples exhibit clear hysteric behavior signifying ferroelectric nature of the synthesized samples. The room temperature saturation polarization ($2P_s$), remnant polarization ($2P_r$) and coercive field ($2E_c$) values for the studied samples are shown

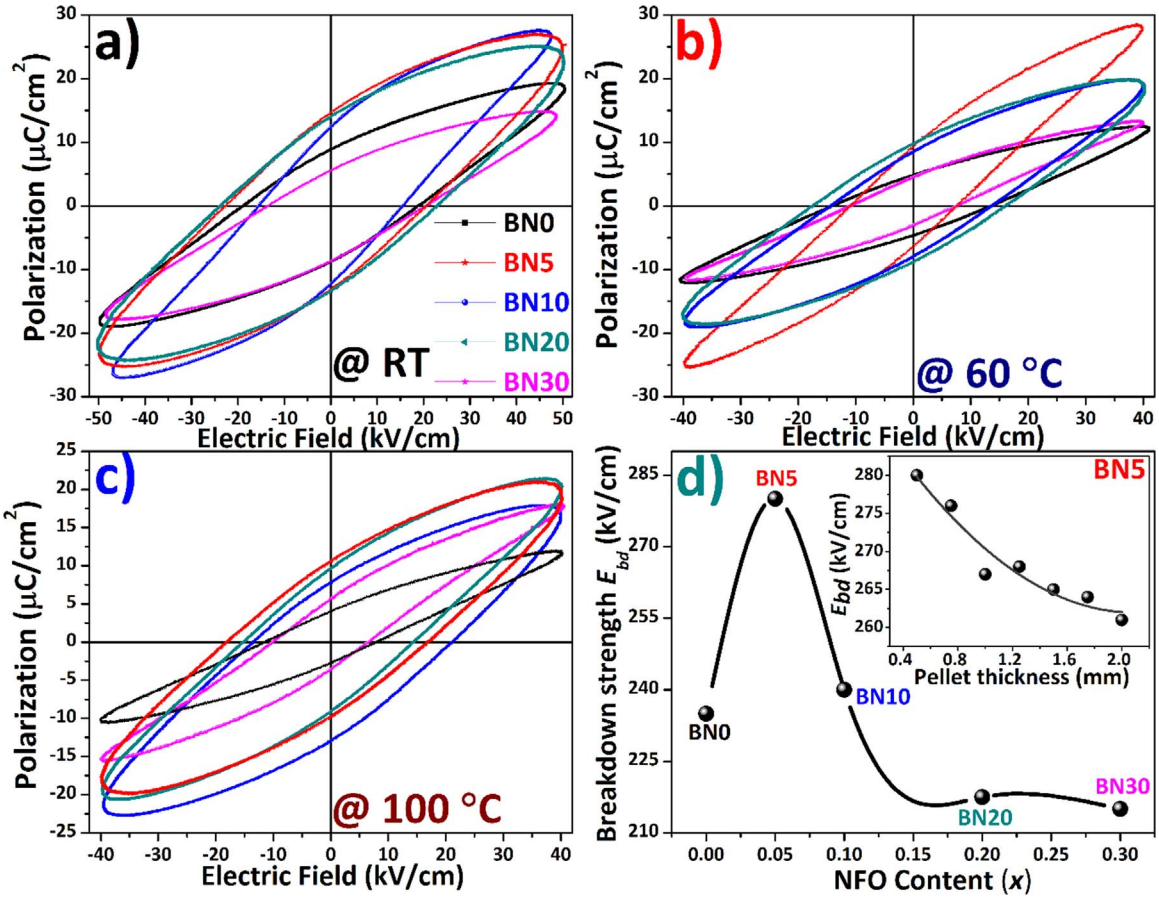

Fig. 7. Ferroelectric hysteresis loops of (1-*x*)BSZT- *x*NFO at three different temperatures: (a) at room temperature, (b) at 60 °C and (c) at 125 °C; (d) shows the variation of dielectric breakdown strength (E_{bd}) with different NFO content and inset shows the variation of E_{bd} for BN5 sample with different pellet thickness.

Table 2
Room temperature saturation polarization (P_s), remnant polarization ($2P_r$), coercive field ($2E_c$), breakdown strength (E_{bd}) and piezoelectric constant (d_{33}) for bare BSZT and BSZT-NFO composite samples.

Sample	$2P_s$ (μC/cm²)	$2P_r$ (μC/cm²)	$2E_c$ (kV/cm)	E_{bd} (kV/cm)	d_{33} (pC/N)
BN0	36.9	17.6	37.5	235	269
BN5	49.5	27.6	43.2	280	291
BN10	53.9	24.6	31.1	241	247
BN20	46.3	26.9	46.5	217	219
BN30	31.1	14.3	43.9	215	189

in Table 2. For all the five samples substantial ferroelectric character can be observed. This shows that at room temperature the crystal structure is in ferroelectric phase which is in good agreement with the temperature dependence of dielectric constant (ε_r) shown in Fig. 5. Under maximum applied electric field, the remnant polarization ($2P_r$) was found to be maximum for BN5 sample at all the three chosen temperatures. Further, NFO addition above x=0.05 leads to decrease in the remnant polarization. This indicates that appropriate amount of NFO concentration has evident effect in enhancing ferroelectric properties of BSZT. It is known that ferroelectric properties of ceramics are affected by their crystal phase, microstructure, composition and lattice defects like oxygen vacancies [21]. Moreover, structural transition occurring in the material also govern the stability of ferroelectric phase. It is known that superior ferroelectric properties result from the long-range polar ordering of the dipoles [22] and any disturbance in polar ordering would change the ferroelectric characteristics of the material.

The significant enhancement in remnant polarization for x=0.05 may be attributed to both structural distortion induced by NFO addition and reduction in leakage current [23]. Moreover, the improved polarization exhibited by the BN5 may also be due to the space charge effect, whose contribution to ferroelectricity increases as NFO content increases [24]. It may be observed from Fig. 7(a)-(c) that samples with higher NFO content are not fully saturated which may be due to much lower resistance of ferrite phase as compared to ferroelectric BSZT phase. Moreover, the polarization of composite materials becomes difficult as they can withstand lower electric field due to comparatively lower resistance [25]. At higher temperature of 60 °C and 100 °C, the remnant polarization shows nearly similar behavior but the loops were found to be shifted about the origin. This anomaly can possibly be explained by the presence of an internal electric field originating from the off-centering and inherent movement of bound electrons.

3.5. Breakdown strength measurement

The electrical breakdown strength (E_{bd}) of pure and NFO doped BSZT composite specimens have been measured and is illustrated in Fig. 7(d). Dielectric breakdown strength (E_{bd}) measurements were performed on the silver electroded specimens by dipping them in a bath containing silicon oil onto a baseplate of highly conductive copper connected to high voltage DC source. The external parameters such as the ramp rate of the applied electric field and frequency also affect the dielectric breakdown strength. In the present study, the ramp rate of externally applied electric field was kept constant at 1 kV/s. The electrical breakdown strength of ceramic materials also relies on electrode geometry, grain size of the material, density, area and thickness of the sample under study. Porosity in the material are one

of the main sources of electrical breakdown and hence, as the porosity in the material increases, electrical breakdown strength of materials decreases [26]. Mechanical defects such as micro-cracks can also result in dielectric breakdown. Generally, the intrinsic breakdown of a dielectric ceramic material is defined as the highest or the maximum value of the breakdown strength achieved after removing all the secondary effects that may affect the dielectric breakdown voltage.

The E_{bd} is found to be maximum for BN5 sample. Moreover, as the NFO content increases beyond x=0.05, the breakdown strength decreases and found to be minimum for BN30. In ceramic materials, under the application of applied DC electric field, as the number of weakly connected grains with higher porosity and lower density increases, the space displacement polarization also increases. This increase in space displacement polarization forces the micropores inside the material to offer small resistance to electrical breakdown and thus depreciates the dielectric strength value [27]. Further, the sample thickness can also influence E_{bd} value [28]. The dependence of the dielectric strength value on thickness for the BN5 sample is shown in the inset of Fig. 7(d). The curve displayed in the figure has been polynomial fitted and the E_{bd} value is found to decrease gradually with increase in thickness from 0.5 mm to 2 mm. Thick dielectric materials may contain a large number of defects, such as micro-pores and micro-cracks. These defective sites are much more susceptible to dielectric breakdown, which leads to a reduction in dielectric thickness resulting in corresponding increase in voltage per unit thickness, thus leading to avalanche breakdown and consequently failure of the material [29]. This analysis shows that for better electrical breakdown strength, it is preferable to design a high voltage ceramic device with a number of thin dielectric elements stacked up, rather than manufacturing a single piece of considerably thicker dielectric.

3.6. Ferromagnetic studies

The magnetic properties of BSZT-NFO composites have been studied by measuring the *M-H* loop at room temperature. Fig. 8 shows the *M-H* loops for the composites with varying NFO content and inset representing the variation of saturation magnetization with increasing NFO content. Here, the *M-H* loop of BN0 is not shown as it does not show a noteworthy magnetic behavior as compared to other NFO containing composites. All the composite materials demonstrate typical *M-H* loop at room temperature and thus confirming the existence of an ordered magnetic structure in the composite samples. All the loops display nearly saturated behavior above 1500 Oe. The magnetic characteristics of the BSZT-NFO composites is attributed to the ferrite phase [16]. It is to be noted that, the saturation magnetization and remnant magnetization shows an increasing tendency with as NFO content is increased. Moreover, the obtained values of saturation magnetization (M_s) are lower than that of pure NFO phase (M_s~60.87 emu/gm) [30]. The lower value of saturation magnetization may be due to the existence of ferroelectric BSZT phase, which is nonmagnetic, resulting in the dilution of magnetic properties. Further, the coercive field (H_c) of the composites is found to be much lower than of pure NFO (H_c~112.62 Oe) [30]. This indicates an easy magnetic domain wall motion and their rotation in these composites. It is observed that the coercive field in powder samples are highly dependent on the particle size. Moreover, the morphology of the particles, defects, disorders, etc. can also affect coercivity. The theory of size effect of coercivity in fine particles states that initially the magnetic coercivity increases with decrease of particle size and reaches a peak value at single domain particle size and afterward, below single domain size, the magnetic coercivity starts to decrease with decrease in particle size [31]. However, it is observed that, in micron grain sized materials prepared by using solid state synthesis have larger saturation magnetization and lower remanence and coercivity, which suggest that these samples exhibit multi-domain nature [32]. The observation of narrow saturated loops coupled with small remnant magnetization also indicates that the magnetism is an induced one and has its origin due to the alignment of the anti-ferromagnetically ordered spins. The observed values of saturation magnetization and coercive field are much more significant without much loss of ferroelectricity suggesting a multiferroic nature.

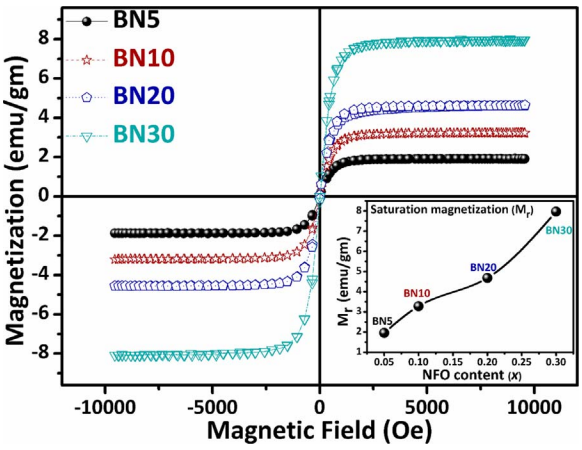

Fig. 8. Ferromagnetic hysteresis (*M-H*) loop of BSZT-NFO composite samples and inset shows the variation of remnant magnetization with increase in NFO content.

3.7. Piezoelectric studies

The piezoelectric response as a function of NFO content for the five synthesized samples have been recorded. The variation in piezoelectric constant (d_{33}), piezoelectric voltage coefficient (g_{33}) and electrostrictive coefficient (Q_{11}) as a function of NFO content is depicted in Fig. 9. Piezoelectric properties of any material are strongly influenced by the electrical poling conditions due to random orientation of domains in the as prepared material. In general, high electric field is required to obtain uniformly aligned domains, but at the same time the sample may get damaged due to electrical breakdown at high electric field. Further, the poling time and poling temperature also affect the piezoelectric properties and therefore the optimization of these poling parameters is very important. After the electrical poling, the polarized domains are oriented along the same direction as that of applied electric field [33]. In the present study, all the pellet samples were electrically poled for 1 h at E~20 kV/mm at a poling temperature of T_P~60 °C, at which finest piezoelectric properties were observed. The piezoelectric constant was found to saturate after 1 h of poling and there was no significant change in d_{33} value on increasing the poling

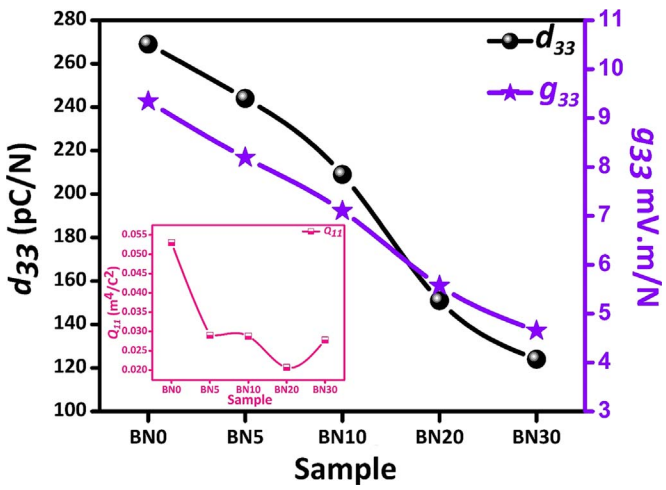

Fig. 9. Variation of piezoelectric constant (d_{33}), piezoelectric voltage coefficient (g_{33}) and electrostrictive coefficient (Q_{11}) (inset) as a function of different NFO content.

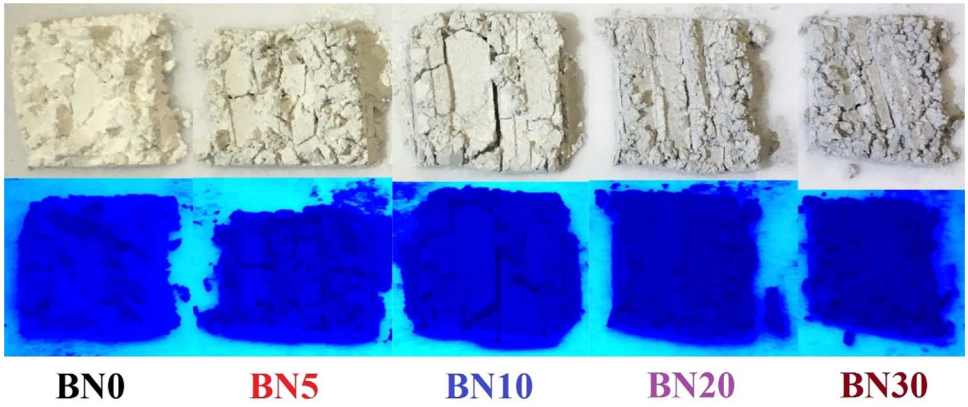

Fig. 10. Showing the comparison of light illumination when exposed to white light and UV light of 265 nm for the (1-*x*)BSZT- *x*NFO samples.

time. Further, poling of material at a suitable temperature helps in accumulation of charge carriers at the grain boundary introducing an internal electric field, which can increase the piezoelectric response of the poled sample [34,35]. The NFO addition did not show any increase in the longitudinal piezoelectric constant and is observed to be maximum for BN0. The d_{33} values of all the five BSZT-NFO samples are listed in Table 2. The higher value of BN0 may be ascribed to better crystallinity as well as larger grain size and higher density of the material. Ferroelectric domain structure also affects the piezoelectric properties of any material. Further, the piezoelectric properties of any ceramic material are closely related to microstructure i.e. grain size and grain uniformity of the material [36]. Previous literature on piezoelectric materials have indicated a parabolic relation between domain and grain sizes [37]. The piezoelectric voltage coefficient, g_{33} of any material can be calculated by dividing the piezoelectric coefficient by its dielectric permittivity, ε. According to the thermodynamic theory of ferroelectricity, the piezoelectric coefficient is related to electrostrictive coefficient as follows [38]:

$$d_{33} = 2Q_{11}P_r\varepsilon_{33} \quad (2)$$

where, Q_{11} is the electrostrictive coefficient, P_r denotes the remnant polarization and ε_{33} represents the dielectric permittivity of the material under study. Hence, it is likely that for any piezoelectric material with high remnant polarization and high dielectric constant will possess high piezoelectric constant. Electrostrictive coefficient (Q_{11}) was calculated using the Eq. (2) and is shown in the inset of Fig. 9.

3.8. Chromo-luminescence observation

After observing the improvement in various dielectric, ferroelectric and ferromagnetic properties of the synthesized specimens, an effort has been made to examine its optical response to UV exposure of 265 nm wavelength light. For this purpose, all the five samples shown in Fig. 10 were simultaneously exposed to UV light. It has been observed that pure as well as BSZT-NFO composite materials have shown dark blue emission. Moreover, samples BN20 and BN30 have shown stronger blue emission compared to other three samples. Based on this observation, it can be concluded that BSZT-NFO samples can also be used for the fabrication of optical device.

4. Conclusion

(1-*x*)BSZT-*x*NFO ($0 \le x \le 0.3$) composite ceramics have been successfully synthesized by the mechano-chemical activation technique. Rietveld refined X-ray diffraction patterns confirm the formation of diphasic compounds i.e. separate perovskite and inverse spinel phase for BSZT and NFO, respectively for all the four composite samples. Microstructural investigation reveals that the density of the ceramics decreases with NFO addition. The dielectric constant of BN5 composite sample is observed to be slightly higher than BN0 sample. However, it decreases on further increasing the NFO content. All the BSZT-NFO samples exhibit reasonably high dielectric constant, good thermal stability and low dielectric loss over a broad range of temperature. The similar trend was observed in ferroelectricity as well as dielectric breakdown strength and these parameters are observed to be maximum for BN5 sample. The *M-H* loop measurement of composite samples confirms the formation of ordered magnetic structure. Further, the saturation magnetization is found to increase with an increase in NFO content. The piezoelectric properties of composite samples do not show any improvement over the bare BSZT sample and found to decrease with NFO addition. Finally, it can be concluded that BN5 composite sample with high dielectric constant, low dielectric loss, large remnant polarization, enhanced dielectric breakdown strength and feeble saturation magnetization can be a potential material for multiferroic applications.

Acknowledgements

Authors are heartily thankful for the support of DST-SERB (Grant no. PS/039/2011), India to carry out this research.

References

[1] D.P. Dutta, A. Tyagi, Weak room temperature ferromagnetism and ferroelectric behavior in sonochemically synthesized bismuth and iron codoped $SrTiO_3$ nanoparticles, Mater. Lett. 164 (2016) 368–371.
[2] H. Tian, D. Wang, J. Qi, Y. Wang, H. Chan, C. Choy, Synthesis of $BaZr_{0.75}Hf_{0.25}O_3$ by a solid-state reaction technique and characterizations of dielectric properties, J. Alloy. Compd. 402 (1) (2005) 251–255.
[3] A. Erb, E. Walker, R. Flükiger, $BaZrO_3$: the solution for the crucible corrosion problem during the single crystal growth of high-T_c superconductors $REBa_2Cu_3O_7$–δ; RE=Y, Pr, Phys. C: Supercond. 245 (3) (1995) 245–251.
[4] A. Şale, S. Kazan, J.I. Gatiiatova, V. Valeev, R. Khaibullin, F. Mikailzade, Magnetic properties of Fe implanted $SrTiO_3$ perovskite crystal, Mater. Res. Bull. 48 (8) (2013) 2861–2864.
[5] M.D. Glinchuk, E.A. Eliseev, V.A. Stephanovich, Phase diagram of mixed ferroelectrics, Ferroelectrics 254 (1) (2001) 27–39.
[6] X. Tang, J. Wang, X. Wang, H. Chan, Effects of grain size on the dielectric properties and tunabilities of sol–gel derived $Ba(Zr_{0.2}Ti_{0.8})O_3$ ceramics, Solid State Commun. 131 (3) (2004) 163–168.
[7] N. Ponpandian, P. Balaya, A. Narayanasamy, Electrical conductivity and dielectric behaviour of nanocrystalline $NiFe_2O_4$ spinel, J. Phys.: Condens. Matter 14 (12) (2002) 3221.
[8] J. Rani, K. Yadav, S. Prakash, Dielectric and magnetic properties of $xCoFe_2O_4$–(1-x)[$0.5Ba(Zr_{0.2}Ti_{0.8})O_3$–$0.5(Ba_{0.7}Ca_{0.3})TiO_3$] composites, Mater. Res. Bull. 60 (2014) 367–375.
[9] C.R. Serrao, A. Sundaresan, C. Rao, Multiferroic nature of charge-ordered rare earth manganites, J. Phys.: Condens. Matter 19 (49) (2007) 496217.
[10] C.A. Vaz, J. Hoffman, C.H. Ahn, R. Ramesh, Magnetoelectric coupling effects in multiferroic complex oxide composite structures, Adv. Mater. 22 (26–27) (2010) 2900–2918.
[11] C.E. Ciomaga, M. Airimioaei, V. Nica, L.M. Hrib, O.F. Caltun, A.R. Iordan, C. Galassi, L. Mitoseriu, M.N. Palamaru, Preparation and magnetoelectric properties of $NiFe_2O_4$–PZT composites obtained in-situ by gel-combustion method, J.

Eur. Ceram. Soc. 32 (12) (2012) 3325–3337.
[12] I. MacLaren, C. Ponton, A TEM and HREM study of particle formation during barium titanate synthesis inaqueous solution, J. Eur. Ceram. Soc. 20 (9) (2000) 1267–1275.
[13] A. Zapata, G. Herrera, Effect of zinc concentration on the microstructure and relaxation frequency of Mn–Zn ferrites synthesized by solid state reaction, Ceram. Int. 39 (7) (2013) 7853–7860.
[14] A. Herabut, A. Safari, Processing and electromechanical properties of $(Bi_{0.5}Na_{0.5})_{(1-1.5x)}La_xTiO_3$ ceramics, J. Am. Ceram. Soc. 80 (11) (1997) 2954–2958.
[15] S. Sarraute, O.T. Sørensen, B.F. Sørensen, E.R. Hansen, Microstructure dependent thermophysical properties of Ni–Zn ferrite–$BaTiO_3$ functionally graded ceramics, J. Mater. Sci. 34(1), pp. 99–104.
[16] R. Sharma, P. Pahuja, R.P. Tandon, Structural, dielectric, ferromagnetic, ferroelectric and ac conductivity studies of the $BaTiO_3$–$CoFe_{1.8}Zn_{0.2}O_4$ multiferroic particulate composites, Ceram. Int. 40 (7, Part A) (2014) 9027–9036.
[17] H. Yang, H. Wang, L. He, L. Shui, X. Yao, Polarization relaxation mechanism of $Ba_{0.6}Sr_{0.4}TiO_3/Ni_{0.8}Zn_{0.2}Fe_2O_4$ composite with giant dielectric constant and high permeability, J. Appl. Phys. 108 (7) (2010) 074105.
[18] X.Y. Ye, Y.M. Li, J.J. Bian, Dielectric and energy storage properties of Mn-doped $Ba_{0.3}Sr_{0.475}La_{0.12}Ce_{0.03}TiO_3$ dielectric ceramics, J. Eur. Ceram. Soc. 37 (1) (2017) 107–114.
[19] D. Maurya, A. Kumar, V. Petkov, J.E. Mahaney, R.S. Katiyar, S. Priya, Local structure and piezoelectric instability in lead-free (1–x)$BaTiO_3$-xA$(Cu_{1/3}Nb_{2/3})O_3$ (A=Sr, Ca, Ba) solid solutions, RSC Adv. 4 (3) (2014) 1283–1292.
[20] P.A. Jha, P.K. Jha, A. Jha, R. Dwivedi, Dielectric behavior of (1–x) $BaZr_{0.025}Ti_{0.975}O_3$–(x)$BiFeO_3$ solid solutions, Mater. Res. Bull. 48 (1) (2013) 101–105.
[21] S.K. Das, R.N. Mishra, B.K. Roul, Magnetic and ferroelectric properties of Ni doped $BaTiO_3$, Solid State Commun. 191 (2014) 19–24.
[22] M. Kuehn, H. Kliem, The method of local fields: a bridge between molecular modelling and dielectric theory, J. Electrost. 67 (2) (2009) 203–208.
[23] Y. Wang, C.-W. Nan, Effect of Tb doping on electric and magnetic behavior of $BiFeO_3$ thin films, J. Appl. Phys. 103 (2) (2008) 4103.
[24] R. Zheng, J. Wang, S. Ramakrishna, Electrical and magnetic properties of multiferroic $BiFeO_3/CoFe_2O_4$ heterostructure, J. Appl. Phys. 104 (3) (2008).
[25] N. Adhlakha, K. Yadav, R. Singh, Effect of $BaTiO_3$ addition on structural, multiferroic and magneto-dielectric properties of $0.3CoFe_2O_4$–$0.7BiFeO_3$ ceramics, Smart Mater. Struct. 23 (10) (2014) 105024.
[26] A.L. Young, G.E. Hilmas, S.C. Zhang, R.W. Schwartz, Mechanical vs. electrical failure mechanisms in high voltage, high energy density multilayer ceramic capacitors, J. Mater. Sci. 42 (14) (2007) 5613–5619.
[27] W. Lei, R. Ang, X.-C. Wang, W.-Z. Lu, Phase evolution and near-zero shrinkage in $BaAl_2Si_2O_8$ low-permittivity microwave dielectric ceramics, Mater. Res. Bull. 50 (2014) 235–239.
[28] Q. Zhang, L. Wang, J. Luo, Q. Tang, J. Du, $Ba_{0.4}Sr_{0.6}TiO_3$/MgO composites with enhanced energy storage density and low dielectric loss for solid-state pulse-forming line, Int. J. Appl. Ceram. Technol. 7 (Suppl. 1) (2010) E124–E128.
[29] W. Lei, Y.-Y. Yan, X.-H. Wang, W. Lu, Z.-B. Yang, W.-Z. Lu, Improving the breakdown strength of $(Mg_{0.9}Zn_{0.1})_2(Ti_{1-x}Mn_x)O_4$ ceramics with low dielectric loss, Ceram. Int. 41 (1, Part A) (2015) 521–525.
[30] M. Kooti, A.N. Sedeh, Synthesis and characterization of $NiFe_2O_4$ magnetic nanoparticles by combustion method, J. Mater. Sci. Technol. 29 (1) (2013) 34–38.
[31] B. Neelima, N.V. Rama Rao, V.R. Chary, S. Pandian, Influence of mechanical milling on structure, particle size, morphology and magnetic properties of rare earth free permanent magnetic Zr_2Co_{11} alloy, J. Alloy. Compd. 661 (2016) 72–76.
[32] P.C.R. Varma, R.S. Manna, D. Banerjee, M.R. Varma, K.G. Suresh, A.K. Nigam, Magnetic properties of $CoFe_2O_4$ synthesized by solid state, citrate precursor and polymerized complex methods: a comparative study, J. Alloy. Compd. 453 (1–2) (2008) 298–303.
[33] W. Choi, K. Choi, G. Yang, J.C. Kim, C. Yu, Improving piezoelectric performance of lead-free polymer composites with high aspect ratio $BaTiO_3$ nanowires, Polym. Test. 53 (2016) 143–148.
[34] S. Su, R. Zuo, S. Lu, Z. Xu, X. Wang, L. Li, Poling dependence and stability of piezoelectric properties of $Ba(Zr_{0.2}Ti_{0.8})O_3$-$(Ba_{0.7}Ca_{0.3})TiO_3$ ceramics with huge piezoelectric coefficients, Curr. Appl. Phys. 11 (3) (2011) S120–S123.
[35] J. Wu, D. Xiao, W. Wu, Q. Chen, J. Zhu, Z. Yang, J. Wang, Composition and poling condition-induced electrical behavior of $(Ba_{0.85}Ca_{0.15})(Ti_{1-x}Zr_x)O_3$ lead-free piezoelectric ceramics, J. Eur. Ceram. Soc. 32 (4) (2012) 891–898.
[36] C.A. Randall, N. Kim, J.P. Kucera, W. Cao, T.R. Shrout, Intrinsic and extrinsic size effects in fine-grained morphotropic-phase-boundary lead zirconate titanate ceramics, J. Am. Ceram. Soc. 81 (3) (1998) 677–688.
[37] W. Cao, C.A. Randall, Grain size and domain size relations in bulk ceramic ferroelectric materials, J. Phys. Chem. Solids 57 (10) (1996) 1499–1505.
[38] J.P. Praveen, T. Karthik, A. James, E. Chandrakala, S. Asthana, D. Das, Effect of poling process on piezoelectric properties of sol–gel derived BZT–BCT ceramics, J. Eur. Ceram. Soc. 35 (6) (2015) 1785–1798.

Volume 5, Issue 1 (2017) 117-121 ISSN 2347 - 3258
International Journal of Advance Research and Innovation

Major ions chemistry of surface water in Bhindawas wetland

Vandana Shan*, SK Singh, AK Haritash
Department of Environmental Engineering, Delhi Technological University,Bawana Road ,Delhi

Article Info
Article history:
Received 25 January 2017
Received in revised form
20 February 2017
Accepted 28 February 2017
Available online 15 March 2017

Keywords
Irrigation, Water Quality, Sodium Absorption Ratio, Soluble Sodium Percentage

Abstract
Water samples were taken from different locations in Bhindawas wetland during summer season for analysing major ion chemistry of surface water and its suitability for irrigation and domestic purpose. Along with some major ions, other general water quality parameters like temperature, pH, TDS, EC and Total Hardness were also analysed. Irrigation quality parameters Sodium Absorption Ratio (SAR), Soluble Sodium Percentage (SSP), Residual Sodium Carbonate (RSC), Kelly's Ratio(KR) were also investigated. The study was carried out in the month of May, 2016. The results showed that majority of samples were suitable for domestic purpose due to low and medium hardness. The values of pH ranges from 6.5 to 7.4, indicating slightly acidic to alkaline nature of surface water. Total dissolved solids ranges from166 to 344 mg/l. All the sampling locations have SAR value and KR value below 10 and 2 respectively, which indicates excellent water quality of lake for irrigation purposes. Also the values of SSP at each sampling locations is below 50 indicating good water for irrigation. Also RSC value for all the samples range below 2.5 and also suitable for irrigation. According to present study it was found that all the parameters were found within the permissible range and suitable for irrigation and domestic purpose.

1. Introduction

A large number of problems are associated with occurrence, use and control of water resources in developed as well as in developing nations which may cause direct impact on the sustainable development of these resources. Although three fourth earth surface is covered with water even then we have only 1% usable water in rivers, lake and subsoil aquifers. A large number of people are dependent on freshwater aquatic ecosystems for their personal and domestic needs such as drinking water, washing, cooking, watering animals, and irrigating fields. At a global level 70% of water is used for agriculture about 25% for industry and only 5% for domestic use (Bharucha 2004). Industrialized countries consume greater percentage of water resources as compared to other countries.90% of water is used for agriculture in India and only 7% for industry and 3% for domestic use. A high pressure on all water bodies have been exerted due to fast growth in industrialization, urbanization and agricultural revolution along with population growth, which is prime reason for all these developmental activities. And unfortunately all these developmental activities are responsible for fast depletion and deterioration of these available water resources (Gangwar 2013). Also point as well as nonpoint sources are responsiblefor impaired conditions of freshwater bodies. Pollutants from wastewater, municipal, domestic and industrial effluents are point sources which continuously add organic, inorganic and toxic pollutants respectively in surface water bodies. And pollutants from non-point sources are nutrients through fertilizers, toxic pesticides and other chemicals, mainly from agriculture runoff (Aenab and Singh 2013, Ravi kumar et al. 2013).Bhindawas lake is situated in between agricultural fields and surrounded by more than five villages so its water may be used for irrigation and domestic use. So it is necessary to check suitability of lake water for irrigation purpose. Major ions (cations and anions) Sodium Absorption Ratio (SAR),Soluble Sodium Percentage (SSP), Residual Sodium Carbonate (RSC), Kelly's Ratio(KR) and some other physicochemical parameters like conductivity, temperature, total dissolved solids, alkalinity, acidity, and hardness of the water was determined. The main objective of present study is to assess the major ion chemistry and irrigation water quality parameters of water in Bhindawas lake for its suitability for irrigation and domestic purpose. Time to time water quality monitoring has a high priority for the determination of current status and long term trends for effective management of water resources.

2.Site Area for study

The present study area is located from 80 kms west of Delhi and 20 km from Jhajjhar, on the Jhajjar-Kosli road. Bhindawas Lake is situated 28 37' 29" N and 76 40' 60" E coordinates and is at an altitude of 200 m. The lake is spread over an area of 1074 acres and larger than the Sultanpur Bird Sanctuary. The peripheral embankment is man-made and basically constructed to store the escaped water of Jawaharlal Nehru canal through an escape channel at the time of power failure of Lift Canal System. The Bhindawas lake is being used by the migratory and resident birds of about 250 species. This sanctuary is situated in between a number of villages namely Kanwah, Bilochpura, Nawada, Redhuwas, Shanjhanpur and Chadwana. The periphery of the sanctuary is 12 km.The temperature varies between 14℃ in Winter and 47 ℃ is summer. Average annual rainfall is 800 mm. Bhindawas Sanctuary is surrounded by agricultural crop fields.

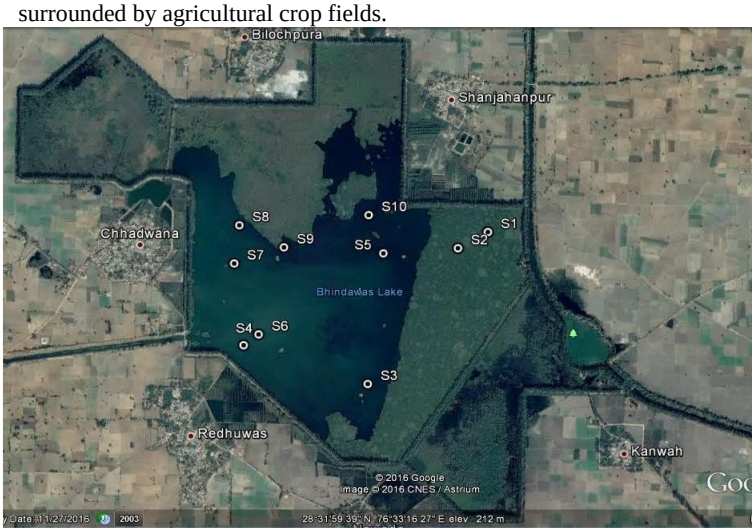

Fig.1 Sampling locations in Bhindawas Lake

3.Materials and Methods:

Surface water samples were collected in pre-cleaned polyethylene bottles from ten different locations in Bhindawas lake during summer (Post monsoon) season as per the standard procedures.(APHA 2005). The location of these samples is shown in Figure 1. The water samples were analyzed at Microbiology Lab, DTU, Delhi. Samples of post-monsoon were studied for various physico-chemical parameters which include pH, EC, TDS, TH, major ions, cations such as Ca^{2+}, Mg^{2+}, Na^{+}, K^{+} and anions Cl^{-}, $SO4^{2-}$, $PO4^{-}$, $NO3^{-}$ and $HCO3^{2-}$. The pH was measured using the digital pH meter, EC and TDS was determined on site with the help of multi meter and standard titration method was used for Total Hardness, $HCO3^{2-}$ and Cl^{-} .Na^{+}, Ca^{2+}, and K^{+} were analyzed by flame photometry. Sulfate was estimated by the Barium chloride method, $PO4^{-}$ by Stannous chloride method and Nitrate was analyzed by Brucine method by using UV-visible

Corresponding Author,
E-mail address: vandanashan@dce.ac.in
All rights reserved: http://www.ijari.org

Table 1. Analytical data of surface water samples in Bhindawas lake during Summer season

Sample no. / Parameters	S1	S2	S3	S4	S5	S6	S7	S8	S9	S10	Min	Max	Mean
pH	6.9	7.1	7.1	6.8	7.4	6.7	7	7.3	6.5	7.1	6.5	7.4	6.99
Temp (℃)	33.1	32	33.2	36.2	35.8	37.3	34.7	35.7	26.5	34.3	26.5	37.3	33.88
EC (ds/m)	0.338	0.337	0.341	0.348	0.700	0.353	0.353	0.343	0.416	0.347	0.337	0.700	0.388
TDS(mg/l)	166	166	168	171	344	173	176	169	204	170	166	344	190.7
TH(mg/l)	170	170	150	170	160	180	150	180	190	180	150	190	170
Cl^-(meq/l)	1.41	0.85	0.85	1.13	0.85	1.13	1.13	1.13	1.69	1.41	0.85	1.69	1.15
$SO4^2$(mg/l)	86.21	85.17	82.46	75.97	774.48	75.78	77.25	82.74	101.7	86.92	75.78	774.48	152.87
$PO4,^-$ (meq/l)	0.03	0.03	0.19	0.04	0.05	0.06	0.03	0.12	0.22	0.20	0.03	0.22	0.10
$NO3^-$(meq/l)	0.30	0.20	0.40	0.23	0.16	0.17	0.30	0.24	0.17	0.41	0.16	0.41	0.26
$HCO3^2$(meq/l)	2.4	2.6	4	4.2	2.2	2.2	2.6	2.2	3	2.6	2.2	4	2.8
Ca^{2+}(meq/l)	0.70	0.70	0.69	0.70	0.69	0.69	0.69	0.67	0.88	0.68	0.67	0.88	0.71
Mg^{2+}(meq/l)	1.40	1.40	1.60	1.40	1.40	1.40	1.20	2	1.20	2	1.20	2	1.50
Na^+(meq/l)	0.38	0.38	0.35	0.36	0.36	0.35	0.36	0.35	0.72	0.37	0.35	0.72	0.40
K^+(meq/l)	0.01	0.01	0.01	0.01	0.01	0.01	0.01	0.01	0.02	0.01	0.01	0.02	0.01

Table 2: Irrigation Water quality parameters

Sample no / Parameters	S1	S2	S3	S4	S5	S6	S7	S8	S9	S10	Min	Max	Mean
SAR	0.135	0.134	0.107	0.123	0.123	0.118	0.137	0.092	0.492	0.102	0.092	0.137	0.156
SSP(%)	15.17	15.08	13.21	14.58	14.58	14.34	15.92	11.56	25.41	12.08	11.56	25.41	15.19
RSC(meq/l)	0.30	0.50	1.71	2.10	0.11	0.11	0.71	-0.47	0.92	-0.08	-0.08	2.10	0.59
KR	0.18	0.18	0.15	0.17	0.17	0.17	0.19	0.13	0.34	0.14	0.13	0.34	0.18

Table3.Guidelines for Interpretations of Water Quality for Irrigation (UCCC, 1974)

Potential Irrigation Problem	Units	Degree of restrictions on use		
		None	Slight to moderate	Severe
Salinity (affect crop water availability				
EC_w	ds/m	<0.7	0.7-3.0	> 3.0
Or				
TDS	mg/l	< 450	450-2000	> 2000
Infiltration (affect infiltration of water into the soil				
Evaluate using EC_w and SAR together)				
SAR = 0-3	And EC_w	0.7	0.7-0.2	<0.2

= 3-6	=	> 1.2	1.2-0.3	<0.3
= 6-12	=	> 1.9	1.9-0.5	<0.5
= 12-20	=	> 2.9	2.9-1.3	<1.3
= 20-40	=	> 5.0	5.0-2.9	<1.9
Specific Ion Toxicity				
Sodium	meq/l	< 3.0	3.0-9.0	>9.0
Chloride	meq/l	< 4.0	4.0-10.0	>10.0
Boron	meq/l	< 0.7	0.7-3.0	>3.0
Miscellaneous effect				
Nitrogen(NO_3-N)	meq/l	< 5	5-30	>30
Bicarbonate (**HCO_3^2**)	meq/l	0-120	120-180	180-600
Carbonarte(**CO_3^2**)	meq/l			
pH		Normal Range	6.5 – 8.4	

spectrophotometer. Sodium Adsorption Ratio (SAR), the Soluble Sodium Percentage(SSP), the Residual Sodium Carbonate (RSC) and Kelly's ratio were determined by the methods described by Richards (1954), Todd (1980), Eaton (1950) and Kelly (1953) respectively.

4.Results and Discussion

The analytical data of surface water samples are presented in Table 1.

4.1 Temperature,pH and EC

The temperature, pH and EC ranged from the highest of 37.3ºC,7.4 and 0.700ds/m to the lowest of 26.5ºC, 6.5 and 0.337ds/m respectively. According to UCCC (1974),all the parameters, temperature and EC and pH are within the acceptable range. Electrical Conductivity measures the capacity of a substance/solution to conduct electric current. Total dissolved salts are directly related to EC of water. (Hari lal et al. 2004) and is used as an index to represent the total concentration of soluble salts in water (Gupta et al. 2008). As the lake is surrounded by many villages and agricultural land so man made activities such as waste disposal, and agricultural runoff may be the cause for addition of organic and inorganic waste. (Pandit 2002). The irrigation water of the Bhindawas lake is suitable for domestic and irrigation purpose as it falls under category 'slight to moderate' in terms of degree of restriction on use of EC.

4.2 Total Hardness and Total Dissolved Solids

Total Hardness in water is due to presence of carbonates and bicarbonates of calcium and magnesium ions. Total hardness values of surface water in lake was investigated from 150 mg/l to 190 mg/l with average value of 170 mg/l. According to WHO standards the water of Bhindawas lake is very hard and unsuitable for domestic use. Total Dissolved Solids(TDS) is most important parameter which plays major role in the determination of irrigation water quality, because many of the toxic(organic or inorganic solids) substances may be found in the water, Matthess, 1982 investigated that presence of toxic substances dissolved in water may affect the plants.TDS and EC are indicative of saline water (Michael 1992).TDS values ranged from 166mg/l to 344mg/l with average value of 190.7mg/l at sample locationsS1,S2(166mg/l),S5(344 mg/l). This indicates the category of'none' according to the degree of restriction on use (Table 3).An adequate amount of salinity is required by plants for their growth.Very high acidic and very high saline, both these conditions affects the productivity as well as survivality of plants.Irrigation water with high sodium (Na^+) can bring about a displacement of exchangeable cations Ca^{2+} and Mg^{2+} from the clay minerals of the soil.

4.3 Alkalinity and Chlorides

Alkalinity is a measure of the ability of water to neutralize acids. Bicarbonates, car-bonates and hydroxide of calcium, magnesium, sodium, potassium and salts of weak acids and strong bases as borates, silicates, phosphates, etc are responsible for alkalinity of surface water. Alkalinity of surface water of Bhindawas lake is mainly due to presence of bicarbonates which ranged from 2.2 meq/l to 4 meq/l which falls in none category according to degree of restriction on use by guidelines from UCCC,1974. Due to presence of excess alkalinity in water a bitter taste was felt. Excess amount of Alkalinity is harmful for irrigation as it damages soil and hence reduces crop yields (Sundar and Saseetharan 2008). In terms of degree of restriction on use of $HCO3^-$ and $CO3^{2-}$ they fall under category 'none'. High chloride content indicates heavy pollution. It can be due to the uses of inorganic fertilizer,leachates from landfills, industrial and irrigation drainage. Chloride concentrations in the study area have a range from 0.85meq/l to 1.69 meq/l in the surface water samples during post-monsoon periods at sampling locations S2 and S9 respectively.The value of chlorides is below the range and have no harmful impact and suitable for domestic and irrigation use.

4.4 Sulphate,Phosphate and Nitrates

$SO4^{2-}$ concentration is possibly contributed by the type of precipitation and excess use of fertilizers in paddy cultivation. The sulphate in the surface water ranged from 75.78 mg/l to 774.48 mg/l with a mean of 152.87 mg/l during the post-monsoon season. Similar results were observed by Deepika and Singh, 2015 in Bhalswa lake during premonsoon season. The maximum permissible limit $SO4^{2-}$ was 250 mg/l. The highest (774.48mg/l) value was observed at sample location S5.This could be due to high microbial degradation in summer season. Phosphate and nitrate are major anions, which are very important water quality parameters of lake water. Their excess concentration can have harmful impact on flora and fauna of lake ecosystem. Excess runoff of phosphates and nitrates cause eutrophication of lake. (Vyas et al. 2006). The phosphate in surface water found in range between 0.03meq/l to 0.22 meq/l with mean valueo.10 meq/l and value of nitrates were observed in range between0.16meq/l to 0.41meq/l with mean value0.26meq/l.The permissible limit of phosphate is 0.3 mg/l(0.01meq/l) in water.And all of sampling locations have value beyond this limit, which indicates the eutrophic nature of lake.But the values of nitrates are below permissible limits.

4.4 Calcium and Magnesium

All the surface water samples have lower Ca^{2+} than permissible limits of < 200 mg/l as per standards WHO standards. The S8 sampling station have minimum value, 0.67meq/l and high value Ca^{2+} was observed at sample locationS9 of Bhindawas lake. Mg^{2+} in surface water for post-monsoon periods varies from 2 to 1.20 meq/l . The average amount of magnisium present in water samples of the post-monsoon season is 1.50 meq/l. It seems that the average values of Ca^{2+} & Mg^{2+} are within the permissible limits as per WHO.All the analyzed water samples at each sampling locations have values suitable for drinking purposes, since the values of Mg^{2+} are within the permissible limits (<150 mg/l) as per the BIS standards .

4.5 Irrigational quality parameters

The base criteria for evaluating the irrigation water quality are calculations of SAR (Sodium Absorption Ratio), which is the measure of sodicity of the water, SSP (sodium soluble percentage), RSC (Residual sodium carbonate), KR (Kelly ratio), cations and anions.

4.6 Sodium absorption ratio

If the SAR ratio of the water samples in the study area is less than 10, it is excellent for irrigation purposes. The SAR values for each water sample was calculated using the following equation (Richards 1954).

$$SAR = \frac{Na}{\frac{Ca + Mg}{2}}$$

The sodium or alkali hazard in the use of water for irrigation is determined by the absolute and relative concentration of cations and is expressed in terms of sodium adsorption ratio (SAR). A significant relationship between SAR values of irrigation water and extent to which sodium adsorbed by the soil. High sodium and low calcium in water raises the cation exchange between water and soil and is responsible for saturated sodium in an irrigated area. The values of SAR of the water samples from the study area ranged from 0.092 to 0.137 with an average value of 0.156. According to Richards (1954), for salinity classification, all the irrigation water samples fell under no sodium hazard and no salinity hazard.

Table 4. Classification of irrigation water based on SAR

Sr. No.	Types of water and SAR value	Quality	Suitability for irrigation
1	Low sodium water (S1) SAR value: 0–10	Excellent	Suitable for all types of crops and all types of soils, except for those crops which are sensitive to sodium
2	Medium sodium water(S2) SAR value :10-18	Good	Suitable for coarse textured or organic soil with good permeability. Relatively unsuitable in fine textured soils.
3	High sodium water(S3) SAR value :18-26	Fair	Harmful for almost all types of soil, Requires good drainage, high leaching gypsum addition
4	Very High sodium water(S4) SAR value >26	Poor	Unusable for irrigation

Irrigation water rich in HCO3- tends to precipitate insoluble Ca^{2+} and Mg^{2+} in the soil which ultimately leaves higher proportion of Na+ and increase the SAR value (Michael, 1992) as shown in eq (1):

$$2HCO_3^- + Ca^{2+} \rightarrow CaCO_3 + H_2O + CO_2\uparrow \quad (1)$$

4.7 Percent Sodium

It has been recommended that percentage of sodium in irrigation water should not exceed 50–60, this is in order to avoid its harmful effects on soil. When the percent sodium exceeds 60, the water is considered to be unsuitable for irrigation purposes. It is considered, that water is of excellent quality if the % sodium is less than 20 % and beyond 80% water is of poorest quality.

$$SSP = Na \times 100/(Ca + Mg + Na)$$

All values of Na,Ca and Mg is in meq/l.

Table 5. Sodium percent water class (Wilcox 1995)

Sodium Percentage	Water Class
20	Excellent
20-40	Good
40-60	Permissible
60-80	Doutful
>80	Unsuitable

The average Soluble Sodium Percentage (SSP) value was found to be 15.19% with minimum value,11.56% at sampling station S8 and maximum value,25.41% at sampling station S9 indicating that all the sapling stations have percentage value excellent except sampling station S9.Based on water class we concluded lake water is highly suitable for domestic as well as irrigation use.

4.8 Residual sodium carbonate

If the water contains a high concentration of bicarbonate ion, then it is responsible for increase in sodium hazard . As the soil solution becomes more concentrated, there is a tendency for calcium and magnesium to precipitate as carbonates thus, increasing the relative proportion of sodium . RSC can be calculated using the equation below employing data of alkalinity, calcium and magnesium.

$RSC = (CO3 + HCO3 - (Ca + Mg))$

Where all ionic concentrations are expressed in meq/L.

The mean RSC concentration in Bhindawas lake water was 0.59 meq/l with minimum value of -0.08 meq/l at sampling location S10 and maximum, 2.10meq/l at sampling location S4.Lake water showed maximum RSC value 2.10 at sampling location S4, illustrating that these waters are marginal/Doubtful for irrigation purpose. A positive RSC value indicates that the contents of dissolved Ca^{2+} and Mg^{2+} ions is less that of $CO\ 3^{2-}$ and $HCO\ 3^{-}$ (Raihan and Alam, 2008). RSC is not satisfied in the study area. To be considered satisfactory, irrigation water should have RSC value <5 meq/l (Gupta and Gupta, 1987).

Table 6. Water quality based on RSC (after Richards 1954)

RSC(meq/l)	Water Quality
<1.25	Safe/good
1.25-2.50	Marginal/Doubtful
>2.50	Unsuitable

4.9 Kelly's Ratio (KR)

The concentration of Na^+ measured against Ca^{2+} and Mg^{2+} is known as Kelly's ratio, based on which irrigation water can be rated(Kelly 1946 and Paliwal 1967). The concentration of Na^+ is considered to be one of the prime concern in making the water unsuitable if Kelly's ratio is >1. As per the Kelly's ratio water from the study area are categorized into suitable if KR is <1, marginal, when KR is 1-2 and unsuitable if KR is >2. The majority of surface water samples were suitable for irrigation (Table 7) with average value of 0.156 indicated suitable water for irrigation.

Table 7. Water quality based on Kelly's Ratio

Range of Kelly's ratio	Category
<1	Suitable
1-2	Marginal
>2	Unsuitable

5 Conclusions

The quality of surface water in the present study area has been assessed for domestic and irrigation purposes using varies hydrochemical parameters and irrigation quality parameters that are suited for domestic and irrigation applications. The surface water from the study area has pH slightly acidic to alkaline in nature and are within permissible limits for drinking purposes. The EC values of the surface water in the study area reveal that the low sodium and low salinity hence the surface water is suitable for irrigation. In context of TDS value, concentration of dissolved solids is below permissible limits and quality of water is suitable for domestic and irrigation use but the range of Total hardness (TH) of the Bhindawas lake water is beyond permissible values and water is denoted very hard water and unfit for domestic use.water indicates that the majority of samples are unsuitable for domestic purposes due to high hardness; and therefore these are described as very hard and unsuitable for domestic, drinking and irrigation purposes. The major cations (Ca2+, Mg2+) from the surface water water samples shown considerable variation during post monsoon season. In spite of the variation in their concentration during study period, the majority of samples have values within the permissible limits. The major

cations in surface water distinctly exhibit decreasing order of their averages abundance as Mg2+>Ca2+>Na2+.>K Similarly anions also have varying concentrations in decreasing order of their mean values as HCO3- > SO42-> Cl > NO3 > PO4 during post-monsoon periods. The anionic concentration of Chloride is different from other anionic groups, since it is coherent with Na ion in the study area. Nitrates and phosphates are due to excess uses of fertilizers and organic material. The surface water of the study area are classified on the basis of Irrigation quality parameters like SAR, KR, RSC, SSP. The different physico-chemical parameters suggest that surface water in Bhindawas lake is good for irrigation use. But due to very high values of hardness at some sampling stations, restricts its use for domestic purpose. All the sampling locations have SAR value and KR value below 10 and below 2 respectively, which indicates excellent water quality of lake for irrigation. Also the values of SSP at each sampling locations is below 50 indicating good and safe water for irrigation. Also RSC value for all the samples range below 2.5 and also suitable for irrigation. According to present study it was found that all the parameters were found within the permissible range and suitable for irrigation and domestic purpose.

References

[1.] Aenab AM, SK Singh. Al-Masab Al-Aam River (Third River) and Surface Water Pollution within Baghdad Division, International Journal of Engineering Innovation & Research (IJEIR), 3(4), 2014, 444-451.

[2.] Aenab AM, SK Singh. Evaluating Water Quality of Ganga River Within Uttar Pradesh by Water Quality Index Analysis Using C++ Program, Intl. Journal of Civil & Environment Research, 3(1), 2013, 57-65.

[3.] American Public Health Association (APHA). Standard method for examination of water and wastewater, 21st edn. APHA, AWWA, WPCF, Washington 2005.

[4.] Bureau of Indian Standards (BIS). Drinking water specifica-tions (revised 2003), IS:10500, 1998.

[5.] Bharucha E. Textbook for Environmental Studies for Undergraduate Courses, University Grants Commission, New Delhi, 2004.

[6.] Deepika, SK Singh. Water Quality Index Assessment of Bhalswa Lake, New Delhi, International Journal of Advanced Research 3(5), 2005, 1052-1059

[7.] Eaton FM. Significance of carbonate in irrigation waters. Soil Science 95,1950, 123-133.

[8.] Gangwar S. Water Quality Monitoring in India:A Review,International Journal of Information and Computation Technology,3(8), 2013, 851-856

[9.] Garg RK, Rao RJ, Uchchariya D. Seasonal variations in water quality and major threats to Ramsagar reservoir,India.African Journal of Environmental Science and Technology 4(2), 2010, 061-076

[10.] Gupta S, Maheto A, Roy P, Datta JK, Saha RN. Geochemistry of groundwater Burdwan district, West Bengal India. Environ Geol 53, 2008, 1271–1282.

[11.] Harilal CC, Hashim A, Arun PR, Baji S. Hydro geochemistry of two rivers of Kerala with special reference to drinking water quality. J Ecol Environ Conserv 10(2), 2004, 187–192

[12.] Harilal CC, Hashim A, Arun PR, Baji S. Hydro geochemistry of two rivers of Kerala with special reference to drinking water quality. J Ecol Environ Conserv 10(2), 2004, 187–192

[13.] Kelly WP. Permissible composition and concentration for irrigation waters. In: Proceedings of ASC, 1946, 607.

[14.] Kelly WP. Use of Saline Irrigation Water. Soil Science,95, 1953, 355-391

[15.] Matthess G. The Properties of Ground Water, John Wiley and Sons, New York, U.S.A., 1982, 397.

[16.] Michael AM. Irrigation Theory and Practices. Vikash Publishing House Pvt. Ltd.,New Delhi, India. 1992, 686- 740

[17.] Paliwal KV. Effect of gypsum application on the quality of irrigation water. Madras Agric J 59, 1967, 646-647.

[18.] Paliwal KV. Irrigation with saline water. IARI, Monograph No. 2. New Science, New Delhi, 1972.

[19.] Pandit AK. Topical evolution of lakes in Kashmir Himalaya. In: Pandit AK (ed) Natural resources of western Himalaya. Valley Book House, Srinagar J&K, 2002, 213–242

[20.] Raihan F, Alam JB. Assessment of groundwater quality in Sunamganj of Bangladesh.Iranian Journal of Environmental Health Science & Engineering 5, 2008, 155-166

[21.] Ravikumar P, Mehmood MA, Somashekar RK. Water quality index to determine the surface water quality of Sankey tank and Mallathahalli lake, Bangalore urban district, Karnataka, India Appl Water Sci 3, 2013, 247–261

[22.] Richards LA. Diagnosis and Improvement of Saline and Alkali Soils, U. S. Department of Agriculture Handbook, Vol. 60, Washington DC, USA, 1954, 160

[23.] Satyanarayana E, Ratnakar D and Muralidhar M (2016),Major Ion Chemistry of Groundwater and Surface Water in Parts of Mulugu-Venkatapur Mandal, Warangal District, Telangana State, India,Hydrol Current Res 2016, 7:3

[24.] Shashank Shekhar Singh, SK Singh. Evaluating Water Quality of River Yamuna in Delhi by Regression Analysis International journal of Engineering and Management Research 5(3), 2015, 218-221

[25.] Sundar ML, Saseetharan MK. Ground water quality in Coimbatore, Tamil Nadu along Noyyal River. J Environ Sci Eng 50(3), 2008, 187–190

[26.] Todd DK. Ground Water Hydrology. 2ed., John Wiley and Sons Inc. New York, USA. 14, 1980, 10-138.

[27.] UCCC (University of California Committee of Consultants), Guidelines for Interpretations of water Quality for Irrigation. Technical Bulletin, University of California Committee of Consultants, California, USA , 1947, 20-28.

[28.] Vyas A, Mishra DD, Bajapai A, Dixit S, Verma N. Environment impact of idol immersion activity lakes of Bhopal, India. Asian J Exp Sci 20(2), 2006, 289–296

[29.] WHO. Guidelines for drinking water quality. Vol. 1. World Health Organization, Geneva 1980

[30.] Wilcox LV. Classification and Use of Irrigation Waters.US Department of Agriculture.Cire. 969, Washington DC, USA, 19, 1995.

Accepted Manuscript

Multicolor and white light emitting Tb^{3+}/Sm^{3+} doped zinc phosphate barium titanate glasses via energy transfer for optoelectronic device applications

Kaushal Jha, Amit K. Vishwakarma, M. Jayasimhadri, D. Haranath

PII: S0925-8388(17)31662-6

DOI: 10.1016/j.jallcom.2017.05.076

Reference: JALCOM 41806

To appear in: *Journal of Alloys and Compounds*

Received Date: 18 March 2017

Revised Date: 25 April 2017

Accepted Date: 7 May 2017

Please cite this article as: K. Jha, A.K. Vishwakarma, M. Jayasimhadri, D. Haranath, Multicolor and white light emitting Tb^{3+}/Sm^{3+} doped zinc phosphate barium titanate glasses via energy transfer for optoelectronic device applications, *Journal of Alloys and Compounds* (2017), doi: 10.1016/j.jallcom.2017.05.076.

This is a PDF file of an unedited manuscript that has been accepted for publication. As a service to our customers we are providing this early version of the manuscript. The manuscript will undergo copyediting, typesetting, and review of the resulting proof before it is published in its final form. Please note that during the production process errors may be discovered which could affect the content, and all legal disclaimers that apply to the journal pertain.

ACCEPTED MANUSCRIPT

Multicolor and white light emitting Tb^{3+}/Sm^{3+} doped zinc phosphate barium titanate glasses via energy transfer for optoelectronic device applications

Kaushal Jha[1], Amit K. Vishwakarma[1], M. Jayasimhadri*[,1], D. Haranath[2]

[1]*Luminescent Materials Research Lab (LMRL), Department of Applied Physics, Delhi Technological University, Delhi 110 042, India*

[2]*CSIR-National Physical Laboratory, Dr. K.S. Krishnan Road, New Delhi 110 012, India*

Abstract:

A series of Tb^{3+}/Sm^{3+} co-doped ZPBT glasses have been successfully prepared via melt quenching technique and their photoluminescence properties and energy transfer mechanism were investigated. Tb^{3+} doped glass exhibits dominant emission peak at 544 nm corresponding to $^5D_4 \rightarrow {}^7F_5$ transition under 375 nm excitation whereas Sm^{3+} doped glass exhibit intense emission peak at 599 nm corresponding to $^4G_{5/2} \rightarrow {}^6H_{7/2}$ under 399 nm excitation. The CIE chromaticity coordinates (0.259, 0.590) and (0.570, 0.428) are located in pure green and orange region for Tb^{3+} and Sm^{3+} doped glasses, respectively. The Tb^{3+}/Sm^{3+} co-doped glasses under 375 nm excitation emits a combination of blue, green and orange-red light while under 484 nm excitation emits green and red-orange emission light. The energy transfer occurs from Tb^{3+} to Sm^{3+} via dipole-dipole interaction, which was confirmed by applying Dexter and Reisfeld's theory and Inokuti Hirayama (I-H) model. Moreover, the energy transfer efficiencies and probabilities were calculated from the decay curves. The color tone of these glasses can be modulated from yellowish-green to warm-white via greenish-yellow emission by appropriate tuning of Sm^{3+} concentrations and excitation wavelengths. These results indicate that the prepared glasses can be a potential candidate for white light as well as solid state lighting applications.

Keywords: Glass, Photoluminescence, Rare Earths, Energy Transfer Studies, w-LEDs

***Corresponding author:** *Tel.:* +91-9013553360

E-mail: jayaphysics@yahoo.com (M. Jayasimhadri)

ACCEPTED MANUSCRIPT

1. Introduction

In recent years, white light emitting diodes (w-LEDs) are considered to be the next generation lighting sources as compared to the conventional incandescent and fluorescent lamps due to their longer lifetime, lower power consumption, higher energy efficiency and environmental friendly characteristics. Currently, w-LEDs are fabricated by using GaN LED chip with yellow phosphor (YAG:Ce^{3+}) encapsulated in an epoxy resin [1]. There are numerous problems with this approach such as white light emission is unstable with input power, poor color rendering index (*Ra*), high correlated color temperature (CCT), poor heat resistance and lack of red component. To overcome these significant issues, another approach utilizes n-UV LED chip with blue, green and red phosphors contained within an epoxy resin, offers high *Ra* and luminous efficiency but different degradation rate of the phosphors is a major issue [2,3]. In both the approaches, an epoxy resin is required to encapsulate the phosphor, which is made of polymer material. This epoxy gets deteriorated at high temperature and by high energy excitation and/or power sources. To overcome these shortcomings, it is essential to devise epoxy free luminescent converter for white LED, which can directly convert the light from n-UV LED chip into white light. In this context, inorganic glass is considered to be the best alternative due to salient features such as homogenous light emission, low production cost, ease of fabrication, high thermal, chemical and mechanical stability. Glasses serve for both the purposes of wavelength conversion as well as an encapsulant, which eliminates the need of epoxy resin [4–6].

Among different glass forming oxides, phosphate glasses have certain unique characteristics such as low melting and softening temperature, high transparency in the wide spectral region, excellent solubility for rare-earths and transition metal ions, high mechanical and

thermal stability [7,8]. However, the hygroscopic nature of phosphate glass limits its practical usage in devices. To overcome this nature, zinc oxide (ZnO) has been incorporated to make these phosphate glasses moisture resistant, which can act as both glass former and modifier depending on whether it is in four-fold or six-fold coordination [9,10]. These characteristics make zinc-phosphate glasses suitable for diverse applications such as lasers, optical displays, optical sensors, waveguides, solid state lighting and glass greenhouses [11–16]. The addition of TiO_2 provides stabilization to the glass structure and helps in further improving the chemical durability. BaO acts as a flux to zinc phosphate glass batch and helps in lowering the melting temperature [17,18]. Among various rare earths, Sm^{3+} is an excellent activator for producing orange/red-orange emission [19,20] while Tb^{3+} doped materials exhibit emission in the blue and green spectral region for multi-color emitting LEDs, display devices, etc. [21,22]. The appropriate rare earths can be co-doped in the host lattice to obtain the desired luminescent properties [23–25]. Thereafter, by appropriately adjusting the Sm^{3+} and Tb^{3+} concentrations in single host material, there is a possibility of obtaining multicolor as well as white light emission.

In the present work, the Tb^{3+}, Sm^{3+} doped and a series Tb^{3+}/Sm^{3+} co-doped zinc phosphate barium titanate (ZPBT) glasses were prepared for the first time. The luminescence properties and energy transfer mechanism between Tb^{3+} and Sm^{3+} and lifetime studies have been discussed in detail. Multi-color and white light emission were obtained by tuning Sm^{3+} concentration and the excitation wavelengths.

2. Experimental Procedure

The starting chemicals were analytical reagent (A.R) grade $NH_4H_2PO_4$, ZnO, TiO_2, $BaCO_3$, high purity Sm_2O_3 and Tb_4O_7. The ZPBT glasses were prepared by using a conventional melt quenching method. The chemical compositions are as follows:

(1) (40-X)ZnO-35P_2O_5-20BaO-5TiO_2-XSm_2O_3

(2) (40-X)ZnO-35P_2O_5-20BaO-5TiO_2-XTb_4O_7

In both the case, the value of X was kept equal to 1 mol %. Along with this, a series of glasses were doped with Sm_2O_3 and Tb_4O_7 in the molar composition as follows:

(3) (40-X-Y)ZnO-35P_2O_5-20BaO-5TiO_2-XTb_4O_7-YSm_2O_3

The value of X was fixed at 1 mol%, and the values for Y are 0.25, 0.50, 1.0 and 1.5 and 2.0 mol%. The chemical composition and the corresponding glass sample names are specified in Table 1. The chemicals were weighed as per stoichiometry and were grounded in an agate mortar for 1 hour using acetone as the wetting medium. The mixture was then placed in the muffle furnace at 1150 ℃ for 1 hour to obtain bubble free and transparent melt. The melt was then poured on the preheated brass plate and annealed at 400 ℃ for 3 hours to remove mechanical and thermal stress. Finally, colorless and transparent glasses were obtained.

The optical absorption studies were performed by Shimadzu-Solid Spec 3700 UV-VIS-NIR spectro-photometer. The photoluminescence (PL) properties were measured using Shimadzu RF-5301PC spectrofluorophotometer fitted with xenon flash lamp. The decay analysis were performed using an Edinburgh FLS920, where xenon lamp was used as an excitation source.

3. Results and Discussion

3.1 Absorption spectra and Optical Band gap:

The absorption spectra for SM01 (1.0 mol% Sm^{3+}), TB01 (1.0 mol% Tb^{3+}) and TS03 (1.0 mol% Tb^{3+} and 1.0 mol% Sm^{3+}) are shown in Fig. 1. For TB01 glass, two transitions originating from the $^7F_6$ ground state to excited state $^5D_3$ and $^5D_4$ are observed at 375 and 484 nm [26]. The SM01 glass represents four different bands originating from the ground state $^6H_{5/2}$ to different

excited states at $^6P_{7/2}$, ($^4F_{7/2}$), $^6P_{5/2}$ and $^4I_{13/2}$+$^4I_{11/2}$+$^4M_{15/2}$ at 372, 399, 418 and 467 nm [27]. The absorption spectrum of TS03 glass sample depict bands originating due to both the Sm^{3+} and Tb^{3+} ions at 372, 375, 399, 418, 467 and 484 nm corresponding to the $^6H_{5/2}\rightarrow{}^6P_{7/2}$, $^7F_6\rightarrow{}^5D_3$, $^6H_{5/2}\rightarrow{}^4F_{7/2}$, $^6H_{5/2}\rightarrow{}^6P_{5/2}$, $^6H_{5/2}\rightarrow{}^4I_{13/2}$+$^4I_{11/2}$+$^4M_{15/2}$ and $^7F_6\rightarrow{}^5D_4$ transitions, respectively. This indicates that TS03 glass exhibiting absorption peaks arising from both Sm^{3+} and Tb^{3+}.

The optical band gap (E_{opt}) for the TM01, SM01 and TS03 glasses were estimated from the absorption spectra near the optical absorption edge by Davis and Mott relation [28]:

$$\alpha h\nu = B(h\nu - E_{opt})^n \qquad (1)$$

where α is the absorption coefficient, ν is the frequency of light, h is the Planck's constant, and B is constant related to band tailing parameter, E_{opt} is the optical band gap energy. The value of n depends on the type of transition, which is 1/2, 2, 1/3 and 3 for direct allowed, indirect allowed, direct forbidden and indirect forbidden transitions, respectively. The value of the absorption coefficient was calculated using the following relation [29]:

$$\alpha(\nu) = \frac{1}{d}\, ln(\frac{I_0}{I_t}) \qquad (2)$$

where α (ν) is the absorption coefficient, d represents the thickness of the glass sample in cm and I_0 and I_t are the intensities of the incident and transmitted radiation, respectively. The E_{opt} energies for indirect allowed transitions were calculated from Tauc's plot [30,31] by extrapolating the linear region of the plot $(\alpha h\nu)^{1/2}$ versus $h\nu$ and is represented in the inset of Fig.1. The optical band gap (E_{opt}) value is the intercept on the energy axis. The E_{opt} values for the TB01, SM01 and TS03, were found to be 3.564, 3.594 and 3.596 eV, respectively.

3.2 Photoluminescence properties of Tb^{3+} and Sm^{3+} doped ZPBT glasses

The excitation spectrum of TB01 glass is represented in the inset of Fig. 2(a). The spectrum gives rise to three excitation bands located at 351, 375 and 484 nm corresponding to the transition from the ground state $^7F_6$ to different excited states $^5D_2$, $^5D_3$ and $^5D_4$, respectively. Under, the most intense n-UV excitation of 375 nm corresponding to $^7F_6 \rightarrow {}^5D_3$ transition, the emission spectrum measured within the range from blue to red region as a result of the transitions from $^5D_3$ and $^5D_4$ levels to the different ^7F_J levels of Tb^{3+} as shown in Fig. 2(a). The emission peaks were observed at 415 and 437 nm corresponds to $^5D_3 \rightarrow {}^7F_5$ and $^5D_3 \rightarrow {}^7F_4$ transitions, respectively. The other emission bands at 489 nm (blue), 544 nm (green), 585 nm (yellow) and 622 nm (red) corresponds to the $^5D_4 \rightarrow {}^7F_6$, $^5D_4 \rightarrow {}^7F_5$, $^5D_4 \rightarrow {}^7F_4$ and $^5D_4 \rightarrow {}^7F_3$ transitions, respectively. Among these peaks, the intense transition $^5D_4 \rightarrow {}^7F_5$ is magnetic dipole and $^5D_4 \rightarrow {}^7F_6$ is forced electric dipole in nature governed by the selection rule $\Delta J = \pm 1$ and $\Delta J = 2$, respectively [32–34]. The intensity of the yellow and red emission is much weaker than that of green emission, and the blue emission is one-third of green emission [22,35]. Fig. 2(b) represents both the emission and excitation spectra of the SM01 glass sample. The excitation spectrum consists of seven peaks at 343, 359, 372, 399, 413, 437 and 467 nm arising from the ground state $^6H_{5/2}$ to different excited state $^4H_{9/2}$, $^4D_{3/2}$, $^6P_{7/2}$, $^4F_{7/2}$, $^6P_{5/2}$, $^4G_{9/2}$, and $^4I_{13/2} + {}^4I_{11/2} + {}^4M_{15/2}$ [36]. The emission spectrum was recorded by fixing the most intense n-UV excitation of 399 nm and is represented in Fig. 2(b). The emission spectrum revealed three peaks at 563, 599 and 645 nm attributed to $^4G_{5/2} \rightarrow {}^6H_{5/2}$, $^4G_{5/2} \rightarrow {}^6H_{7/2}$ and $^4G_{5/2} \rightarrow {}^6H_{9/2}$ transitions, respectively. The $^4G_{5/2} \rightarrow {}^6H_{5/2}$ transition arises due to the MD transition, whereas the $^4G_{5/2} \rightarrow {}^6H_{9/2}$ is attributed to forced electric dipole (ED) transition. The $^4G_{5/2} \rightarrow {}^6H_{7/2}$ transition comes in play due to both the MD and forced ED transition. The intensity ratio of ED to MD transition is used to measure the symmetry of the local environment of trivalent 4f ions. The greater the value of

forced ED transition, more is the asymmetric nature. In the present case, the value of MD transition is dominant which suggests more symmetric nature [36,37].

The CIE chromaticity coordinates for TB01 and SM01 glasses were calculated based on the emission spectra and is represented in Fig. 3. The chromaticity coordinates for TB01 glass were found to be (0.259, 0.590) under 375 nm excitation, which lies in the green region. The chromaticity coordinates are in excellent agreement with well-known green phosphors (Zn,Cd)S:Ag (0.260, 0.600) and $ZnS:Au_{0.05},Cu_{0.01}$ (0.267, 0.582) [35]. The correlated color temperature (CCT) for TB01 was found to be 6663 K. For SM01 glass, the chromaticity coordinates were found to be (0.570, 0.428) under 399 nm excitation, which lies in the pure orange region and matches closely with the amber LED NSPAR 70 BS (0.575, 0.425) developed by Nichia corporation [36]. The CCT value was found to be 1848 K. The above mentioned results revealed the suitability of Tb^{3+} and Sm^{3+} doped ZPBT glasses for applications in the field of lighting and display devices.

3.3 Luminescent properties of Tb^{3+}/Sm^{3+} co-doped ZPBT glasses

The energy transfer between two rare earth ions can take place based on the Dieke's energy level. The energy transfer takes place from the rare earth (RE) ion with the high fluorescent state (excited state) to another RE ion having the lower state. In the case of Tb^{3+} and Sm^{3+} ion, Tb^{3+} has the higher fluorescent excited state in comparison with the Sm^{3+} ion. Therefore, the energy transfer might take place from Tb^{3+} to Sm^{3+}. One of the most important criteria for energy transfer is the spectral overlap between acceptor (Sm^{3+}) absorption with the donor (Tb^{3+}) emission [7,38]. In Fig. 4(a), the absorption band centered at 467 nm corresponding to $^6H_{5/2} \rightarrow {}^4I_{13/2} + {}^4I_{11/2} + {}^4M_{15/2}$ of Sm^{3+} ions overlaps with the emission band of Tb^{3+} centered at 489

nm corresponding to $^5D_4 \rightarrow {}^7F_6$ transition. This overlapped region suggest, that Tb^{3+} act as donor/sensitizer whereas Sm^{3+} act as acceptor/activator.

The excitation spectra of TS03 glass by monitoring emission at 599 and 544 nm were recorded and is represented in Fig 4(b). The excitation spectrum of TS03 by monitoring emission at 599 nm revealed the excitation lines of Sm^{3+}, while by monitoring emission at 544 nm revealed peaks due to the Tb^{3+}. The different excitation lines of Sm^{3+} and Tb^{3+} are discussed in detail in the preceding section. Based on the excitation spectra for TS03, 375 and 484 nm were considered as the appropriate excitation line for the series of co-doped glasses: TS01 (1.0 mol% Tb^{3+} and 0.25 mol% Sm^{3+}), TS02 (1.0 mol% Tb^{3+} and 0.50 mol% Sm^{3+}), TS03 (1.0 mol% Tb^{3+} and 1.0 mol% Sm^{3+}), TS04 (1.0 mol% Tb^{3+} and 1.5 mol% Sm^{3+}) and TS05 (1.0 mol% Tb^{3+} and 2.0 mol% Sm^{3+}).

The emission spectra of the Tb^{3+}/Sm^{3+} co-doped glasses (TS01, TS02, TS03, TS04 and TS05) were recorded at 375 and 484 nm and are represented in the Fig. 5(a) and (b) respectively. The emission spectra under 375 nm excitation revealed eight different peaks centered at 415, 437, 489, 544, 563, 585, 599 and 645 nm. While, the emission spectra measured under 484 nm excitation gives rise to five different emission bands centered at 544, 563, 585, 599 and 645 nm. The bands observed at 415, 437, 489, 544 and 585 nm are attributed to $^5D_3 \rightarrow {}^7F_5$, $^5D_3 \rightarrow {}^7F_4$, $^5D_4 \rightarrow {}^7F_6$, $^5D_4 \rightarrow {}^7F_5$ and $^5D_4 \rightarrow {}^7F_4$ transitions, respectively of Tb^{3+} ions, whereas the bands 563, 599 and 645 nm corresponding to the $^4G_{5/2} \rightarrow {}^6H_{5/2}$, $^4G_{5/2} \rightarrow {}^6H_{7/2}$ and $^4G_{5/2} \rightarrow {}^6H_{9/2}$ transitions, respectively of Sm^{3+} ions as discussed in the preceding section. It can be clearly observed from the Fig. 6(a) and (b) that the emission intensity of the Tb^{3+} bands decreases with an increase in the Sm^{3+} concentration under 375 and 484 nm, respectively. The intensity of the Sm^{3+} bands increases with an increase in Sm^{3+} concentration up to 1 mol% (optimized concentration of Sm^{3+}) and decreases after that due to the concentration quenching phenomenon. The variation in

the emission intensity for both the Sm^{3+} and Tb^{3+} is due to the interaction and energy transfer among the rare-earths. The concentration quenching phenomenon is due to self-quenching effect, as the energy is transferred from one Sm^{3+} to another Sm^{3+}, which in turn decreases the probability of radiative transition. The decrease in Tb^{3+} emission intensity is due to the energy transfer from Tb^{3+} to Sm^{3+} [36]. Fig. 7 represents the energy level for Tb^{3+} and Sm^{3+} doped glasses to explain the phenomenon of energy transfer. In case of TB01 and SM01 glasses, the rare earth ions (Tb^{3+} and Sm^{3+}) absorbs the excitation energy which in turns excites the electron from the ground state to the higher excited state. The excited electrons then quickly relaxes to lower lying states (Tb^{3+}:$^5D_3$, $^5D_4$ and Sm^{3+}:$^4G_{5/2}$) by non-radiative relaxation, and then falls to the lower states (Tb^{3+}:^7F_J (J= 3 to 6) and Sm^{3+}:^6H_J (J=5/2, 7/2 and 9/2) releasing energy in the form of visible radiation. However, the energy level of Sm^{3+} ($^4G_{5/2}$) is slightly lower than the energy level of Tb^{3+} ($^5D_4$) in the Tb^{3+}/Sm^{3+} co-doped glasses as shown in Fig. 7. Therefore, it is possible that a part of the energy from Tb^{3+} is non-radiatively transferred to the Sm^{3+}, which results in the decrement of Tb^{3+} emission. The smaller energy difference between the $^5D_4$ and $^4G_{5/2}$ makes the energy transfer possible via phonon assisted non-radiative transition. This indicates that Tb^{3+} act as efficient sensitizer for the Sm^{3+} [7].

The energy transfer from the sensitizer (Tb^{3+}) to an activator (Sm^{3+}) may take place via multipolar or exchange interaction. Based on Dexter's energy transfer formula for multipolar interaction and Reisfeld's approximation, a relation can be as [39]

$$\frac{\eta_0}{\eta} \propto C^{n/3} \qquad (3)$$

where η_0 and η are the luminescent quantum efficiency of the Tb^{3+} in the absence and in the presence of the Sm^{3+}, C represents the sum of the mole percent of the Tb^{3+} and the Sm^{3+}, and n equals to 6, 8 and 10 corresponding to dipole-dipole, dipole-quadrupole and quadrupole-

quadrupole interaction, respectively. The η_0/η value can be approximately calculated by the ratio of related luminescence intensities as:

$$\frac{I_{s0}}{I_s} \propto C^{n/3} \qquad (4)$$

where I_{s0} is the intrinsic emission intensity of Tb^{3+} and I_s is the emission intensity of Tb^{3+} in the presence of Sm^{3+}. The graph between the I_{s0}/I_s versus $C^{n/3}$ was plotted and the best fit was obtained for n=6, under both the 375 and 484 nm excitations as represented in Fig. 8(a) and (b), respectively. This indicates that the energy is transferred from the Tb^{3+} to Sm^{3+} due to the non-radiative dipole-dipole interaction.

3.4 Lifetime and energy transfer efficiency:

The decay profiles were recorded for the glasses (TB01, TS01, TS02, TS03, TS04 and TS05) by monitoring the emission at 544 nm corresponding to $^5D_4 \rightarrow {}^7F_5$ transition under the excitation of 375 and as represented in Fig. 9(a). The decay curves were fitted with different exponential equations. The best fit was obtained for single exponential function for TB01, TS01 and TS02 glasses under 375 nm excitation and bi-exponential fit was observed for remaining glasses (TS03, TS04 and TS05). A similar observation was obtained under 484 nm excitation wavelength also. The single and bi-exponential equations are as follows [40]:

$$I = I_0 + A_1 exp(-\frac{t}{\tau}) \qquad (5)$$

$$I = I_0 + A_1 exp\left(-\frac{t}{\tau_1}\right) + A_2\, exp\left(-\frac{t}{\tau_2}\right) \qquad (6)$$

where I and I_0 represent the luminescence intensities at time t and 0, τ_1 and τ_2 represents the two components of the lifetime, corresponding to the fast and slow lifetimes for exponential components, respectively; A_1 and A_2 are the fitting constant, and t is the time. The value of

lifetime for single exponential equation is the value of τ and the value for bi-exponential equations is given by formulae [40]

$$\tau = \frac{A_1\tau_1^2 + A_2\tau_2^2}{A_1\tau_1 + A_2\tau_2} \qquad (7)$$

The lifetimes are presented in Table 2. A deeper insight on the energy transfer process from the Tb^{3+} to Sm^{3+} can be realised by the decay time. It can be clearly seen from Table 2, the average value of the lifetime of Tb^{3+} decreases with an increase in the Sm^{3+} concentration, which is strong evidence of energy transfer from Tb^{3+} to Sm^{3+}. The value of energy transfer efficiency (η_T) from the Tb^{3+} to Sm^{3+} can be calculated by the formulae [41] as mentioned below:

$$\eta_{T(Tb\rightarrow Sm)} = 1 - \left(\frac{\tau_d}{\tau_{d0}}\right) \qquad (8)$$

The energy transfer probability rate in terms of lifetime can be expressed by the equation mentioned below[7]

$$P_{T(Tb\rightarrow Sm)} = \frac{1}{\tau_d} - \frac{1}{\tau_{d0}} \qquad (9)$$

where τ_{d0} and τ_d represents the decay time of the Tb^{3+} in the absence of the Sm^{3+} and in the presence of the Sm^{3+}, respectively. The values of the energy transfer efficiencies (η_T) and energy transfer probabilities (P_T) are represented in the Table 2. The energy transfer efficiency v/s Sm^{3+} concentration are plotted in Fig 10 (a) and (b) under 375 and 484 nm excitation, respectively. The value of both η_T and P_T increases with an increase in the Sm^{3+} concentration, which indicates that with an increase in Sm^{3+} more energy is transferred from Tb^{3+} to Sm^{3+}. Also, under 375 nm excitation, the energy transfer value is more than 484 nm excitation. This indicates that 375 nm is more prominent excitation for the efficient energy transfer.

The Inokuti- Hirayama (I-H) model gives a deeper insight about the multipolar interaction involved in the energy transfer process based on the decay curves. The decay of the luminescence of a donor (Tb^{3+}) - acceptor (Sm^{3+}) is given by equation [38,42]

$$I_t = I_0 \exp\left\{\frac{-t}{\tau_0} - Q\left(\frac{t}{\tau_0}\right)^{\frac{3}{s}}\right\} \qquad (10)$$

where, I_t is the luminescence intensity at time t, t is time after excitation, τ_0 is the intrinsic decay time of the donors in the absence of the acceptors. Q is the energy transfer parameter, S is the multipole interaction parameter and take the value 6, 8 and 10 for dipole-dipole, dipole-quadrupole and quadrupole-quadrupole interaction, respectively. The I-H model was applied for TS03 glass under 375 nm and 484 nm excitation with emission fixed at 544 nm as shown in Fig. 9(b) and (c). The value of S was obtained to be 5.87 and 5.68 under 375 and 484 nm, respectively and which is close to 6. Therefore, by applying I-H model it is confirmed that the interaction is of dipole-dipole nature. The results obtained from Dexter energy transfer formula and Reisfeld's approximation is in agreement with the I-H model.

3.5 Colorimetry calculations

The CIE chromaticity coordinates were calculated based on the emission spectra for TS01, TS02, TS03, TS04 and TS05 samples under the excitation of 375 and 484 nm and are represented in Fig. 11(a) and (b). The value of the CIE chromaticity coordinates are given in Table 1. The CIE chromaticity coordinates calculated under 375 nm excitation suggests that the color tone varies from yellowish-green to warm-white light with different Sm^{3+} concentration. In this case, warm white light emission is observed for TS03 glass. While, under 484 nm excitation the color tone varies from yellowish-green to greenish-yellow with high color purity, as the chromaticity coordinates falls on the perimeter of CIE diagram. A schematic representation of

light emission in the prepared glasses for the present work is show in Fig. 12. Under, n-UV excitation, Tb^{3+} doped glass (TB01) gives green emission while Sm^{3+} doped glass gives orange emission. When the co-doped samples were excited by n-UV excitation, tunable emission is obtained from yellowish-green to warm white light. Further, when excited by 484 nm (blue) it color tone varies from greenish-yellow to yellowish-green. For application of w-LEDs, CCT is an important parameter and the value should be below 5000K [43]. In the present case for TS03 glass sample, the value of CCT is 3944 K, which indicates warm white light emission. Also an important observation is that the CCT value decreases with an increase in Sm^{3+} concentration up to 1 mol % and beyond that it increases, which might be due to fact that after 1 mol% is concentration quenching comes into play and the intensity of Sm^{3+} bands decreases.

4. Conclusions

Tb^{3+}, Sm^{3+} doped and a series of Tb^{3+}/ Sm^{3+} co-doped ZPBT glasses have been successfully prepared via melt quenching technique. The optical band gap of the glasses were calculated based on the absorption spectra. The Tb^{3+} doped glasses revealed intense emission peak at 544 nm under 375 nm excitation. The CIE chromaticity coordinates were found to be (0.259, 0.590), which lies in pure green region and suggests its utility as a green component for w-LEDs and display devices. While, for Sm^{3+} doped glass intense emission peak was observed at 599 nm under 399 nm excitation. The CIE chromaticity coordinates (0.570, 0.428) lie in the pure orange region indicating its potential application for fabrication in orange LEDs and display devices. The emission color of Tb^{3+}/Sm^{3+} co-doped glasses tuned from yellowish-green to warm-white via greenish-yellow by varying Sm^{3+} concentration and excitation wavelengths. The emission spectra show a self-quenching phenomenon for Sm^{3+} and the optimized concentration was 1 mol%. The energy transfer occurs from Tb^{3+} ($^5D_4$) to Sm^{3+} ($^4G_{5/2}$) occurs via dipole-dipole

interaction which was confirmed by applying Dexter and Reisfeld's theory based on the emission spectra and Inokuti Hirayama (I-H) model based on decay curves. The energy transfer efficiencies and probabilities were calculated, which indicate that n-UV excitation is more efficient for energy transfer process. The above mentioned results strongly suggest the potential applicability of Tb^{3+}/Sm^{3+} glasses for white light and tunable emission under n-UV excitation based LED chips.

Acknowledgements

Kaushal Jha is grateful to the University Grants Commission (UGC) for providing financial support in the form of Junior Research Fellowship (JRF). The author (M. Jayasimhadri) is grateful to DST-SERB, Govt. of India for the sanction of a research project (No. SB/FTP/PS-082/2014, dt. 02/03/2015).

References

[1] S.P. Denbaars, D. Feezell, K. Kelchner, S. Pimputkar, C.-C. Pan, C.-C. Yen, S. Tanaka, Y. Zhao, N. Pfaff, R. Farrell, M. Iza, S. Keller, U. Mishra, J.S. Speck, S. Nakamura, Development of gallium-nitride-based light-emitting diodes (LEDs) and laser diodes for energy-efficient lighting and displays, Acta Mater. 61 (2013) 945–951.

[2] M. Shang, C. Li, J. Lin, How to produce white light in a single-phase host?, Chem. Soc. Rev. 43 (2014) 1372–86.

[3] R. Xie, N. Hirosaki, M. Mitomo, K. Takahashi, K. Sakuma, R. Xie, N. Hirosaki, M. Mitomo, Highly efficient white-light-emitting diodes fabricated with short-wavelength yellow oxynitride phosphors Highly efficient white-light-emitting diodes fabricated with short-wavelength yellow oxynitride phosphors, 101104 (2011) 2004–2007.

[4] X. Zhang, L. Huang, F. Pan, M. Wu, J. Wang, Y. Chen, Q. Su, Highly thermally stable

single-component white-emitting silicate glass for organic-resin-free white-light-emitting diodes, ACS Appl. Mater. Interfaces. 6 (2014) 2709–2717.

[5] H. Masai, Y. Yamada, Y. Suzuki, K. Teramura, Y. Kanemitsu, T. Yoko, Narrow energy gap between triplet and singlet excited states of Sn2+ in borate glass., Sci. Rep. 3 (2013) 3541.

[6] K. Jha, M. Jayasimhadri, Structural and emission properties of Eu^{3+} -doped alkaline earth zinc-phosphate glasses for white LED applications, J. Am. Ceram. Soc. (2017).

[7] D. Rajesh, K. Brahmachary, Y.C. Ratnakaram, N. Kiran, A.P. Baker, G.-G. Wang, Energy transfer based emission analysis of Dy^{3+}/Eu^{3+} co-doped ZANP glasses for white LED applications, J. Alloys Compd. 646 (2015) 1096–1103.

[8] Z.A. Talib, W.M. Daud, Y.N. Loh, H.A.A. Sidek, Optical and electrical characteristics of $(LiCl)_x$ $(P2O5)_{1-x}$ glass, Ionics (Kiel). 15 (2009) 369–376.

[9] N. Deopa, A.S. Rao, S. Mahamuda, M. Gupta, M. Jayasimhadri, D. Haranath, G.V. Prakash, Spectroscopic studies of Pr^{3+} doped lithium lead alumino borate glasses for visible reddish orange luminescent device applications, J. Alloys Compd. 708 (2017) 911–921.

[10] Y. Xiang, J. Du, L.B. Skinner, C.J. Benmore, A.W. Wren, D.J. Boyd, M.R. Towler, Structure and diffusion of ZnO–SrO–CaO–Na_2O–SiO_2 bioactive glasses: a combined high energy X-ray diffraction and molecular dynamics simulations study, RSC Adv. 3 (2013) 5966.

[11] G. Tripathi, V.K. Rai, S.B. Rai, Spectroscopy and upconversion of Dy^{3+} doped in sodium zinc phosphate glass, Spectrochim. Acta Part A Mol. Biomol. Spectrosc. 62 (2005) 1120–1124.

[12] L. Mishra, A. Sharma, A.K. Vishwakarma, K. Jha, M. Jayasimhadri, B.V. Ratnam, K.

Jang, A.S. Rao, R.K. Sinha, White light emission and color tunability of dysprosium doped barium silicate glasses, J. Lumin. 169 (2016).

[13] C. Pérez-Rodríguez, L.L. Martín, S.F. León-Luis, I.R. Martín, K.K. Kumar, C.K. Jayasankar, Relevance of radiative transfer processes on Nd^{3+} doped phosphate glasses for temperature sensing by means of the fluorescence intensity ratio technique, Sensors Actuators B Chem. 195 (2014) 324–331.

[14] L.B. Fletcher, J.J. Witcher, N. Troy, S.T. Reis, R.K. Brow, D.M. Krol, Effects of rare-earth doping on femtosecond laser waveguide writing in zinc polyphosphate glass, J. Appl. Phys. 112 (2012) 23109.

[15] C. Ming, F. Song, L. An, X. Ren, Turning ultraviolet-green into red light in transparent phosphate glasses for greenhouses, Appl. Phys. Lett. 102 (2013) 20–23.

[16] N. Vijaya, P. Babu, V. Venkatramu, C.K. Jayasankar, S.F. León-Luis, U.R. Rodríguez-Mendoza, I.R. Martín, V. Lavín, Optical characterization of Er^{3+}-doped zinc fluorophosphate glasses for optical temperature sensors, Sensors Actuators B Chem. 186 (2013) 156–164.

[17] D.V.R. Murthy, A.M. Babu, B.C. Jamalaiah, L.R. Moorthy, M. Jayasimhadri, K. Jang, H.S. Lee, S.S. Yi, J.H. Jeong, Photoluminescence properties of Er^{3+}-doped alkaline earth titanium phosphate glasses, J. Alloys Compd. 491 (2010) 349–353.

[18] A. Kiani, J. V Hanna, S.P. King, G.J. Rees, M.E. Smith, N. Roohpour, V. Salih, J.C. Knowles, Structural characterization and physical properties of P_2O_5-CaO-Na_2O-TiO_2 glasses by Fourier transform infrared, Raman and solid-state magic angle spinning nuclear magnetic resonance spectroscopies., Acta Biomater. 8 (2012) 333–40.

[19] M.G. Ha, J.-S. Jeong, K.-R. Han, Y. Kim, H.-S. Yang, E.D. Jeong, K.S. Hong, Characterizations and optical properties of Sm^{3+}-doped Sr_2SiO_4 phosphors, Ceram. Int. 38

(2012) 5521–5526.

[20] S. Sailaja, C. Nageswara Raju, C. Adinarayana Reddy, B. Deva Prasad Raju, Y.-D. Jho, B. Sudhakar Reddy, Optical properties of Sm^{3+}-doped cadmium bismuth borate glasses, J. Mol. Struct. 1038 (2013) 29–34.

[21] C. Zuo, Z. Zhou, L. Zhu, A. Xiao, Y. Chen, X. Zhang, Y. Zhuang, X. Li, Q. Ge, Luminescence properties of Tb^{3+}-doped borosilicate scintillating glass under UV excitation, Spectrochim. Acta Part A Mol. Biomol. Spectrosc. 147 (2015) 324–327.

[22] M. Reza Dousti, R.J. Amjad, Spectroscopic properties of Tb^{3+}-doped lead zinc phosphate glass for green solid state laser, J. Non. Cryst. Solids. 420 (2015) 21–25.

[23] Z. Feng, H. Xia, C. Wang, Z. Zhang, D. Jiang, J. Zhang, S. He, Q. Tang, Q. Sheng, X. Gu, Y. Zhang, B. Chen, H. Jiang, 1.8 μm luminescent properties and energy transfer of Yb^{3+}/Tm^{3+} co-doped α-NaYF4 single crystals, J. Alloys Compd. 680 (2016) 26–30.

[24] Z. Feng, S. Yang, H. Xia, C. Wang, D. Jiang, J. Zhang, X. Gu, Y. Zhang, B. Chen, H. Jiang, Energy transfer and 2.0μm emission in Tm^{3+}/Ho^{3+} co-doped α-$NaYF_4$ single crystals, Mater. Res. Bull. 76 (2016) 279–283.

[25] H. Hu, H. Xia, P. Wang, J. Peng, Y. Zhang, H. Jiang, B. Chen, Near and Mid-Infrared Emission Characteristics of Er^{3+}/Tm^{3+}/Ho^{3+}-Doped $LiYF_4$ Single Crystals Excited by Laser Diode, J. Nanosci. Nanotechnol. 16 (2016) 526–531.

[26] J.F.M. dos Santos, I.A.A. Terra, N.G.C. Astrath, F.B. Guimarães, M.L. Baesso, L.A.O. Nunes, T. Catunda, Mechanisms of optical losses in the $^5D_4$ and $^5D_3$ levels in Tb^{3+} doped low silica calcium aluminosilicate glasses, J. Appl. Phys. 117 (2015) 53102.

[27] A. Mohan Babu, B.C. Jamalaiah, T. Sasikala, S.A. Saleem, L. Rama Moorthy, Absorption and emission spectral studies of Sm^{3+}-doped lead tungstate tellurite glasses, J. Alloys Compd. 509 (2011) 4743–4747.

[28] E.A. Davis, N.F. Mott, Conduction in non-crystalline systems V. Conductivity, optical absorption and photoconductivity in amorphous semiconductors, Philos. Mag. 22 (1970) 0903–0922.

[29] A. Agarwal, V.P. Seth, S. Sanghi, P. Gahlot, D.R. Goyal, Optical band gap studies and estimation of two photon absorption coefficient in alkali bismuth borate glasses, Radiat. Eff. Defects Solids. 158 (2003) 793–801.

[30] K. Rawat, H.-J. Kim, P.K. Shishodia, Synthesis of Cu_2ZnSnS_4 nanoparticles and controlling the morphology with polyethylene glycol, Mater. Res. Bull. 77 (2016) 84–90.

[31] K. Rawat, P.K. Shishodia, Structural and optical properties of sol gel derived Cu_2ZnSnS_4 nanoparticles, Adv. Powder Technol. 28 (2017) 611–617.

[32] N. Yaiphaba, R.S. Ningthoujam, N.R. Singh, R.K. Vatsa, Luminescence Properties of Redispersible Tb^{3+}-Doped $GdPO_4$ Nanoparticles Prepared by an Ethylene Glycol Route, Eur. J. Inorg. Chem. 2010 (2010) 2682–2687.

[33] M. Jayasimhadri, K. Jha, B.V. Ratnam, H.-J. Woo, K. Jang, A.S. Rao, D. Haranath, Single NUV band pumped $PbO\text{-}GeO_2\text{-}TeO_2:Tb^{3+}$ yellowish green emitting glass material for tricolor white LEDs, J. Alloys Compd. 711 (2017) 395–399.

[34] Y.-C. Fang, X.-R. Huang, Y.-D. Juang, S.-Y. Chu, Color-Tunable Blue to Green $Ca_{4-1.5x}Ta_2O_9$: xTb^{3+} Phosphor: Cross-Relaxation Mechanism and Thermal Stability, J. Am. Ceram. Soc. 95 (2012) 1613–1618.

[35] B.V. Ratnam, M. Jayasimhadri, G. Bhaskar Kumar, K. Jang, S.S. Kim, Y.I. Lee, J.M. Lim, D.S. Shin, T.K. Song, Synthesis and luminescent features of $NaCaPO_4:Tb^{3+}$ green phosphor for near UV-based LEDs, J. Alloys Compd. 564 (2013) 100–104.

[36] A.K. Vishwakarma, M. Jayasimhadri, Pure orange color emitting Sm^{3+} doped $BaNb_2O_6$ phosphor for solid - state lighting applications, J. Lumin. 176 (2016) 112–117.

[37] T. Suhasini, J. Suresh Kumar, T. Sasikala, K. Jang, H.S. Lee, M. Jayasimhadri, J.H. Jeong, S.S. Yi, L. Rama Moorthy, Absorption and fluorescence properties of Sm^{3+} ions in fluoride containing phosphate glasses, Opt. Mater. (Amst). 31 (2009) 1167–1172.

[38] M. Inokuti, F. Hirayama, Influence of Energy Transfer by the Exchange Mechanism on Donor Luminescence, J. Chem. Phys. 43 (1965) 1978.

[39] G. Li, D. Geng, M. Shang, C. Peng, Z. Cheng, J. Lin, Tunable luminescence of Ce^{3+}/Mn^{2+}-coactivated $Ca_2Gd_8(SiO_4)_6O_2$ through energy transfer and modulation of excitation: potential single-phase white/yellow-emitting phosphors, J. Mater. Chem. 21 (2011) 13334.

[40] K. Li, X. Liu, Y. Zhang, X. Li, H. Lian, J. Lin, Host-Sensitized Luminescence Properties in $CaNb_2O_6$: Ln^{3+} (Ln^{3+} = Eu^{3+} / Tb^{3+} / Dy^{3+} / Sm^{3+}) Phosphors with Abundant Colors, Inorg. Chem. 54 (2015) 323–333.

[41] W.J. Yang, L. Luo, T.M. Chen, N.S. Wang, Luminescence and energy transfer of Eu- and Mn-coactivated $CaAl_2Si_2O_8$ as a potential phosphor for white-light UVLED, Chem. Mater. 17 (2005) 3883–3888.

[42] S. N Rasool, L. R Moorthy, C.K. Jayasankar, Spectroscopic Investigation of Sm^{3+} doped phosphate based glasses for reddish-orange emission, Opt. Commun. 311 (2013) 156–162.

[43] L. Wu, Y. Zhang, M. Gui, P. Lu, L. Zhao, S. Tian, Y. Kong, J. Xu, Luminescence and energy transfer of a color tunable phosphor: Dy^{3+}, Tm^{3+}, and Eu^{3+} coactivated KSr4(BO3)3 for warm white UV LEDs, J. Mater. Chem. 22 (2012) 6463.

ACCEPTED MANUSCRIPT

Table 1

Chemical Composition	**Sample name**	**Excitation wavelength(nm)**	**Colorimetric properties**	
			Chromaticity coordinates	**CCT (K)**
39ZnO-35P_2O_5-20BaO-5TiO_2-1Tb_4O_7	TB01	375	(0.259, 0.590)	6663
39ZnO-35P_2O_5-20BaO-5TiO_2-1Sm_2O_3	SM01	399	(0.570, 0.428)	1848
38.75ZnO-35P_2O_5-20BaO-5TiO_2-1Tb_4O_7-0.25Sm_2O_3	TS01	375	(0.338, 0.521)	5391
		484	(0.384, 0.609)	4722
38.50ZnO-35P_2O_5-20BaO-5TiO_2-1Tb_4O_7-0.50Sm_2O_3	TS02	375	(0.370, 0.513)	4757
		484	(0.420, 0.574)	4141
38ZnO-35P_2O_5-20BaO-5TiO_2-1Tb_4O_7-1Sm_2O_3	TS03	375	(0.401, 0.445)	3944
		484	(0.474, 0.521)	3230
37.50ZnO-35P_2O_5-20BaO-5TiO_2-1Tb_4O_7-1.50Sm_2O_3	TS04	375	(0.394, 0.460)	4152
		484	(0.464, 0.531)	3393
37ZnO-35P_2O_5-20BaO-5TiO_2-1Tb_4O_7-2.0Sm_2O_3	TS05	375	(0.396, 0.484)	4213
		484	(0.456, 0.539)	3542

ACCEPTED MANUSCRIPT

ACCEPTED MANUSCRIPT

Table 2.

Glass samples	Excitation wavelengths (nm)	Lifetime (ms)	Energy transfer efficiency (η_T)	Energy transfer probability rate (P_T)
TB01	375	2.256	0.00	0.00
	484	1.940	0.00	0.00
TS01	375	1.995	11.57	5.79
	484	1.767	8.90	5.05
TS02	375	1.752	22.33	12.74
	484	1.624	16.28	10.01
TS03	375	1.610	28.62	17.77
	484	1.491	23.16	15.53
TS04	375	1.490	33.91	22.70
	484	1.357	30.07	22.15
TS05	375	1.327	41.18	31.03
	484	1.233	36.45	29.55

ACCEPTED MANUSCRIPT

Fig. 1.

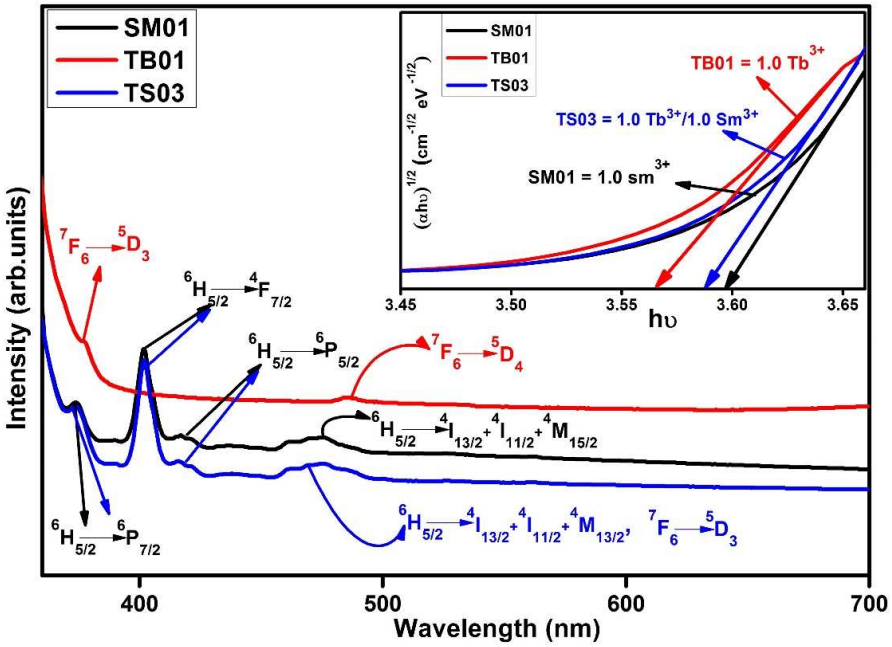
SM01
TB01
TS03
Intensity (arb.units)
Wavelength (nm)
400
500
600
700
$^7F_6 \rightarrow {}^5D_3$
$^6H_{5/2} \rightarrow {}^4F_{7/2}$
$^6H_{5/2} \rightarrow {}^6P_{5/2}$
$^7F_6 \rightarrow {}^5D_4$
$^6H_{5/2} \rightarrow {}^4I_{13/2} + {}^4I_{11/2} + {}^4M_{15/2}$
$^6H_{5/2} \rightarrow {}^6P_{7/2}$
$^6H_{5/2} \rightarrow {}^4I_{13/2} + {}^4I_{11/2} + {}^4M_{13/2}$, $^7F_6 \rightarrow {}^5D_3$
SM01
TB01
TS03
$(\alpha h\upsilon)^{1/2}$ ($cm^{-1/2}$ $eV^{-1/2}$)
TB01 = 1.0 Tb^{3+}
TS03 = 1.0 Tb^{3+}/1.0 Sm^{3+}
SM01 = 1.0 sm^{3+}
3.45
3.50
3.55
3.60
3.65
hυ

Fig. 2.

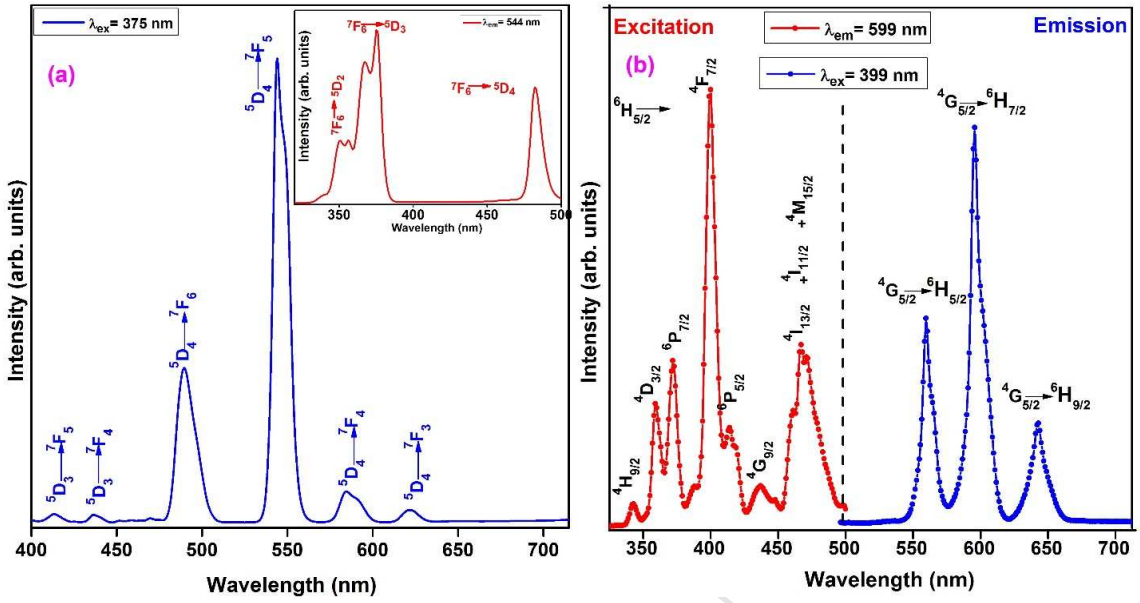

ACCEPTED MANUSCRIPT

Fig. 3.

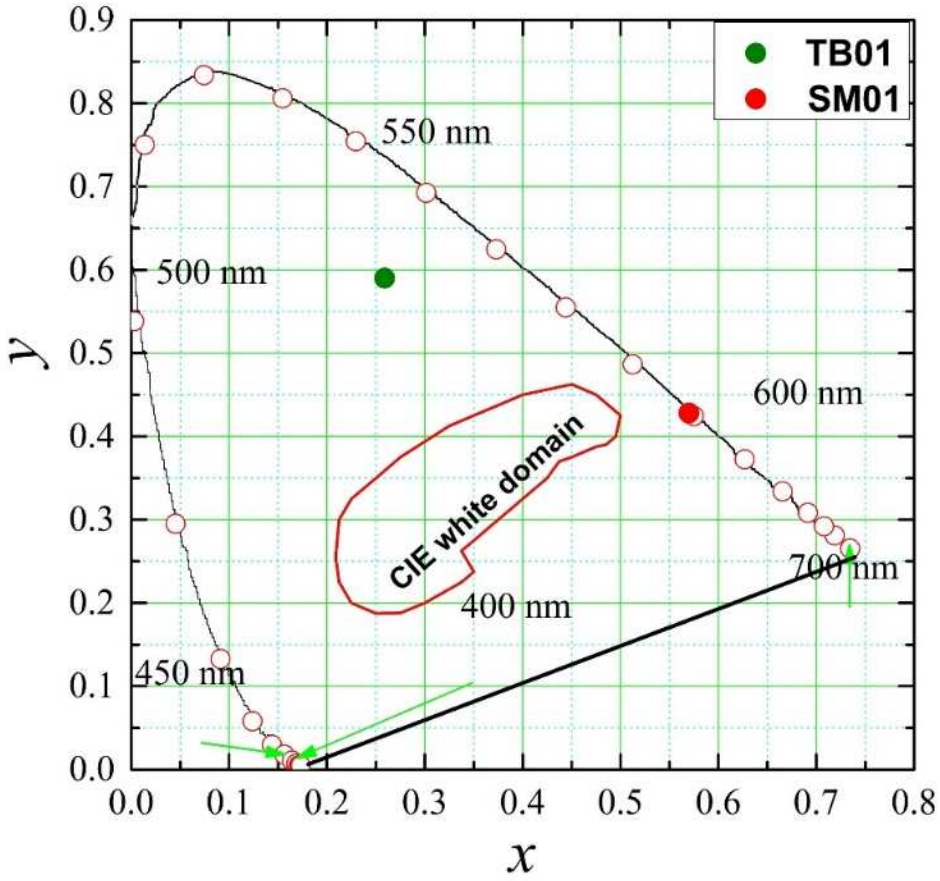

ACCEPTED

Fig. 4.

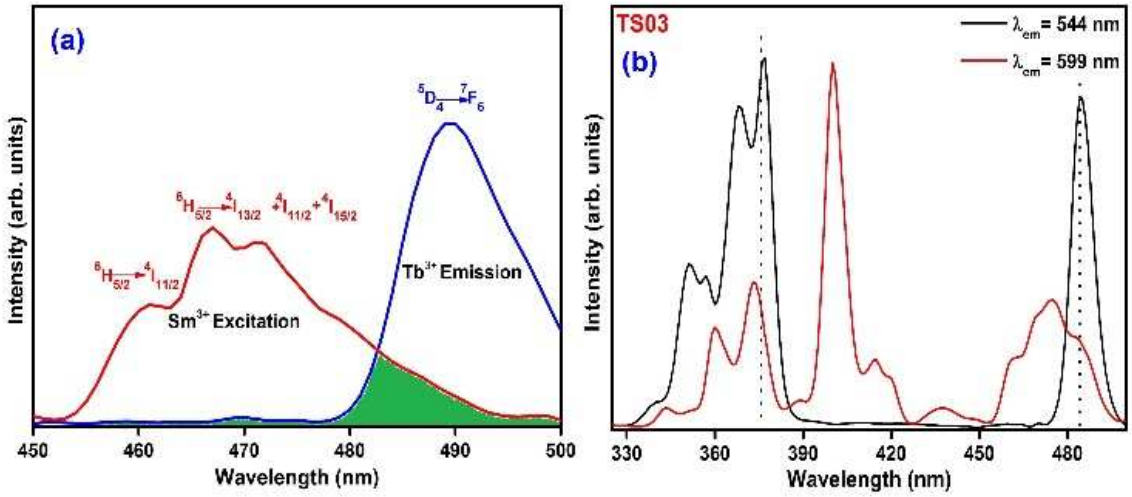

ACCEPTED MANUSCRIPT

Fig. 5.

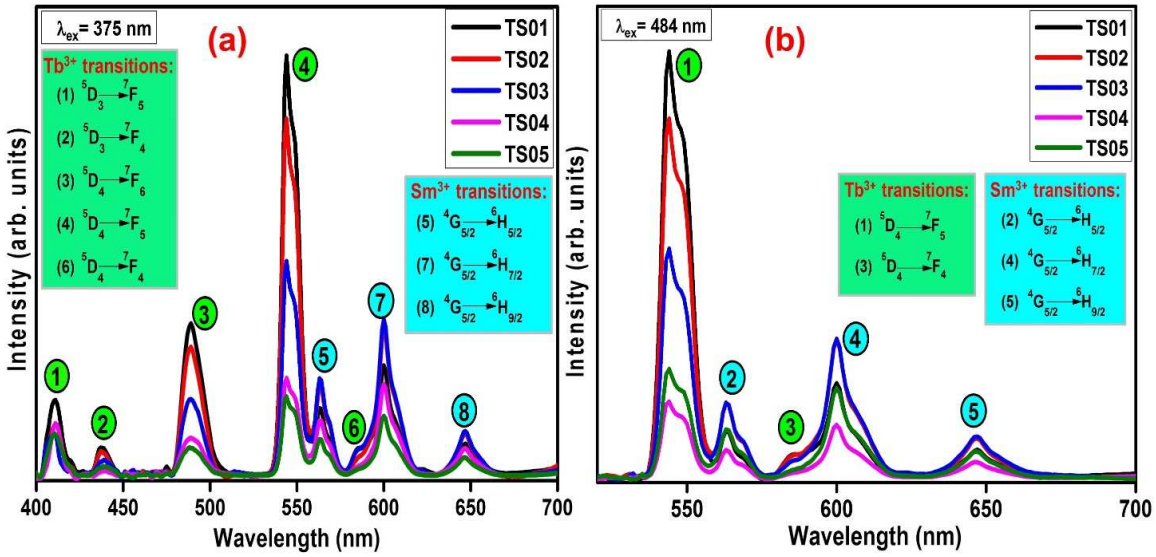

ACCEPTED MANUSCRIPT

Fig. 6.

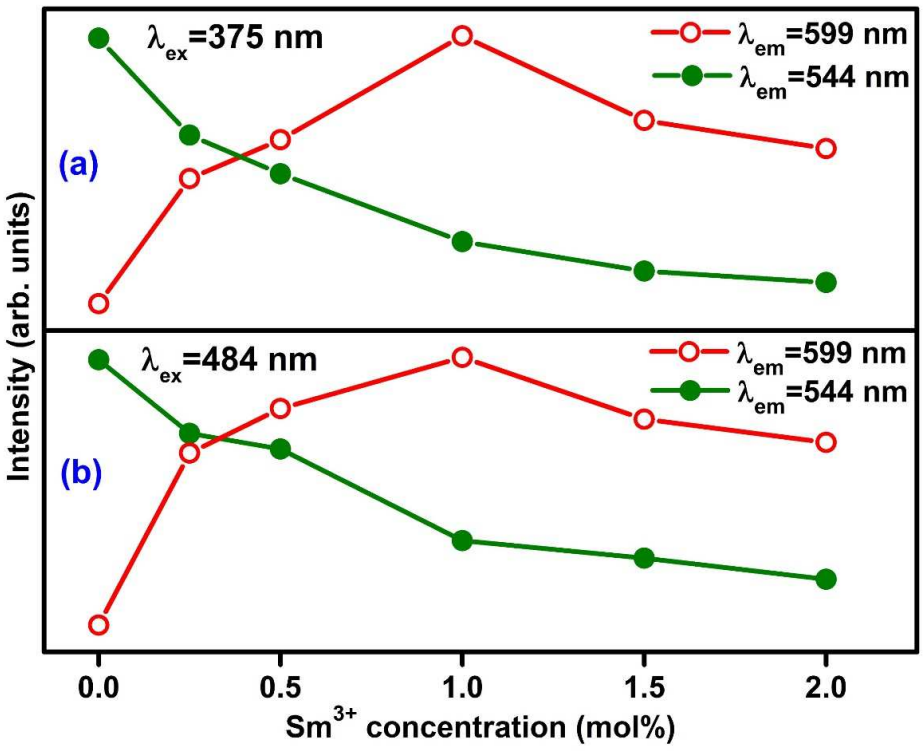

ACCEPTED

Fig. 7.

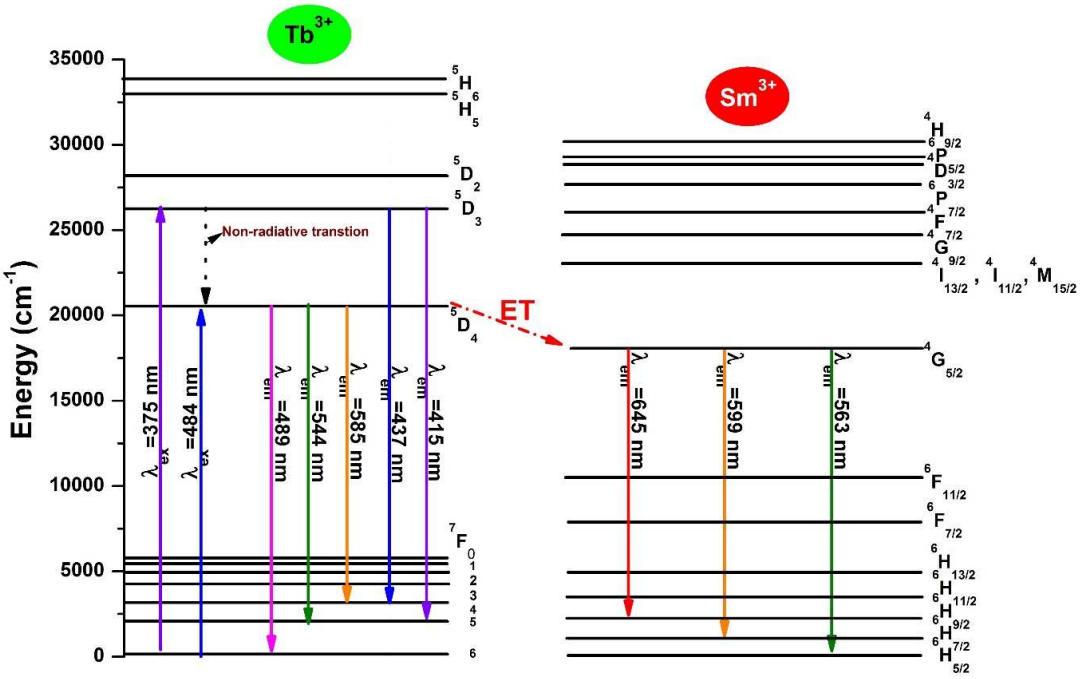

Fig. 7: Energy level diagram showing energy transfer involved in Tb^{3+}/Sm^{3+} co-doped glasses.

ACCEPTED MANUSCRIPT

Fig. 8.

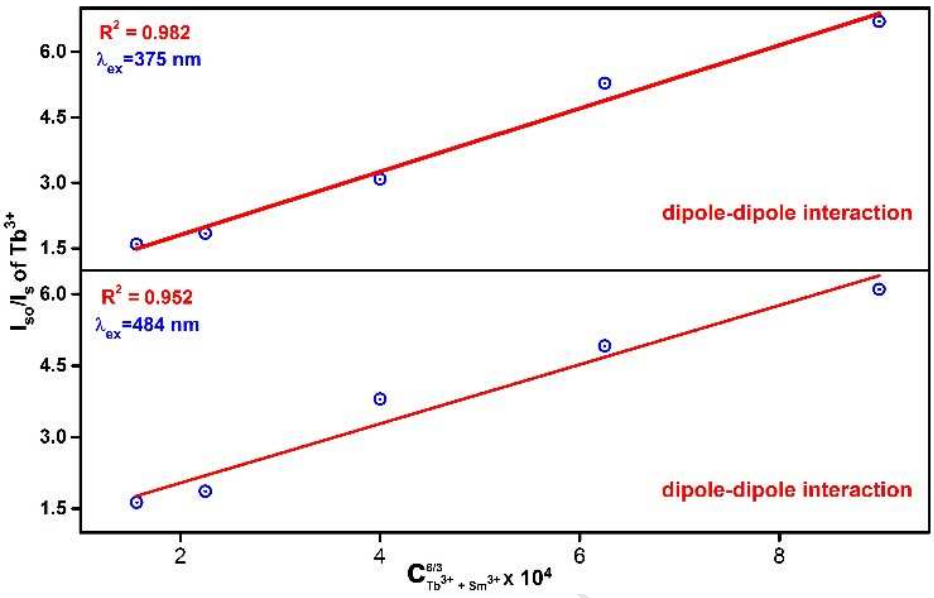

ACCEPTED MANUSCRIPT

Fig. 9.

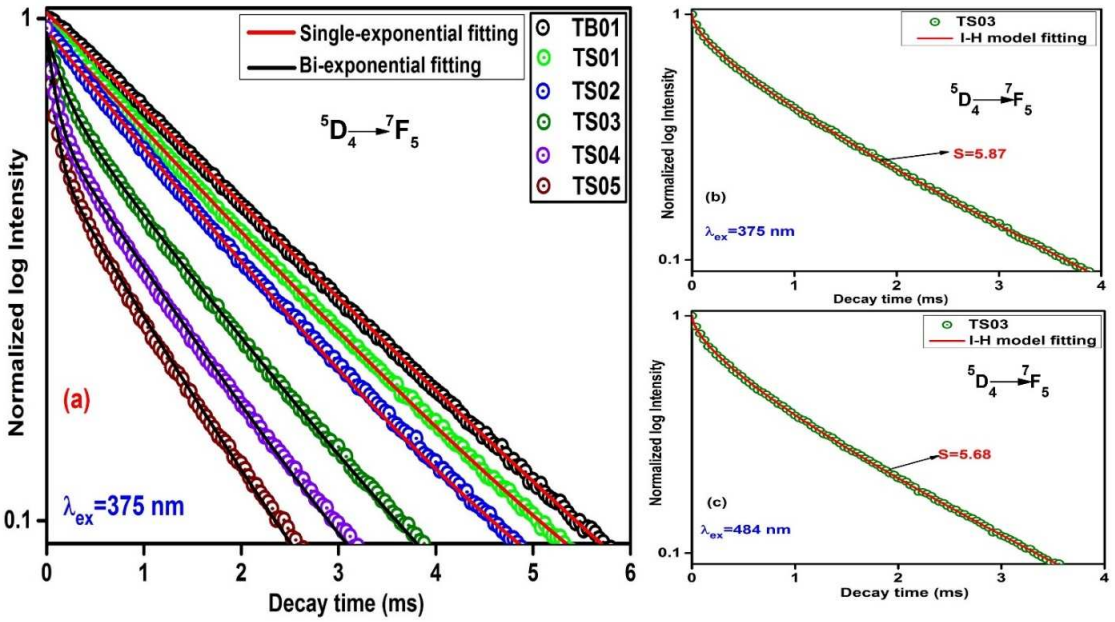

ACCEPTED MANUSCRIPT

Fig. 10.

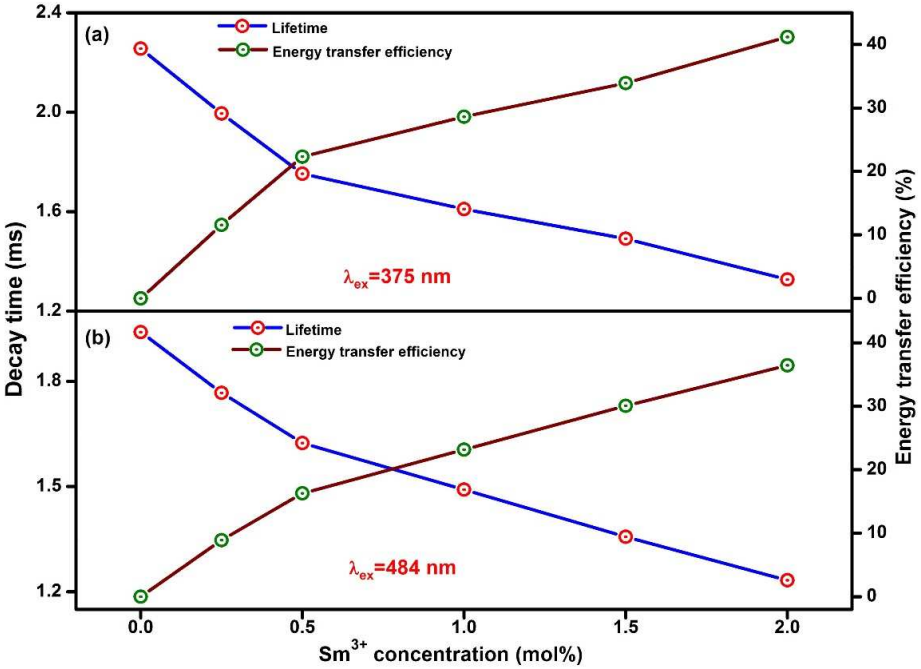

ACCEPTED MANUSCRIPT

Fig. 11.

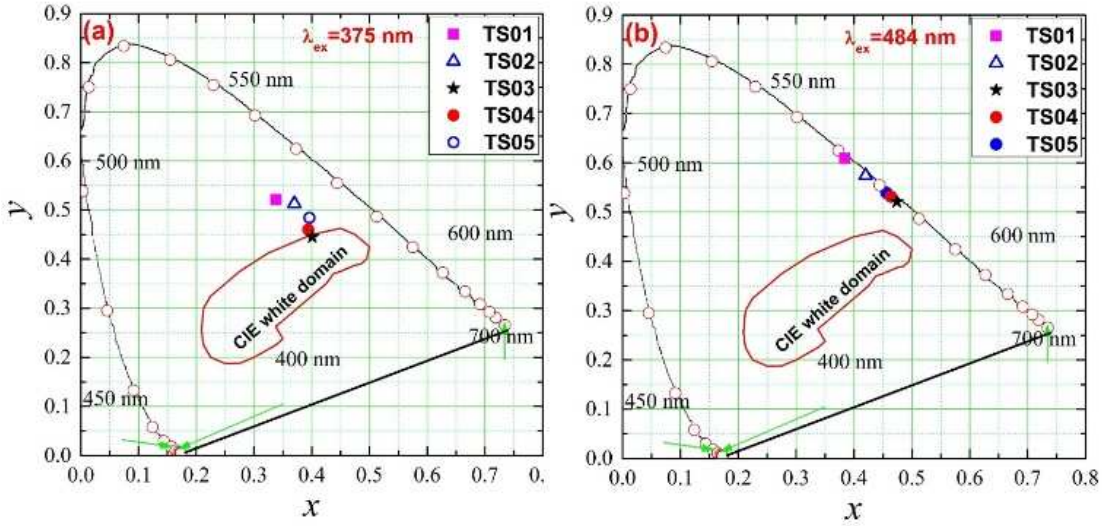

ACCEPTED MANUSCRIPT

Fig. 12.

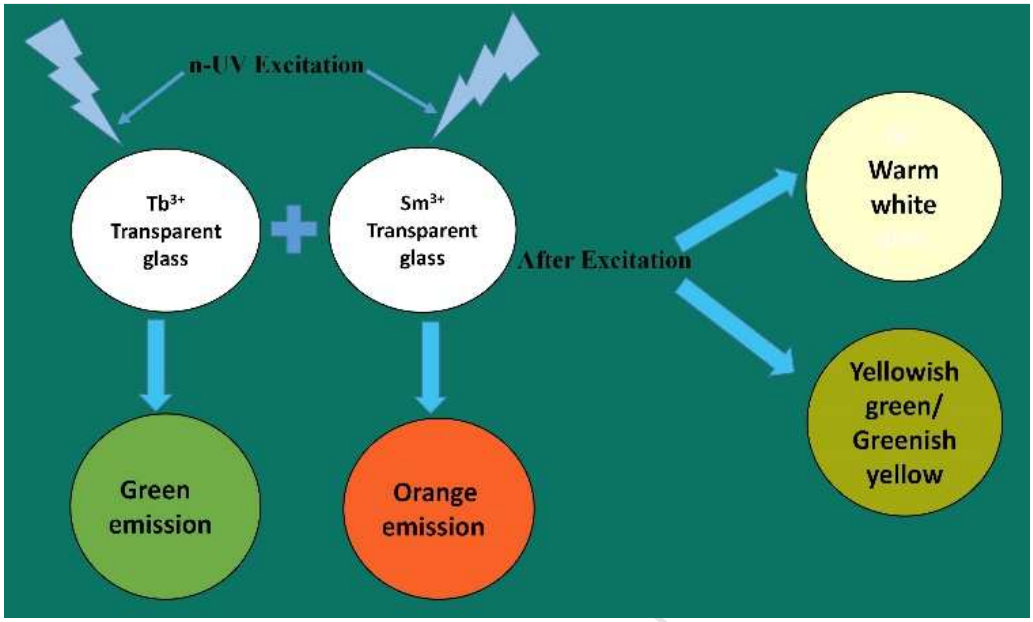

ACCEPTED MANUSCRIPT

ACCEPTED MANUSCRIPT

Highlights of the work

- Tb^{3+}/Sm^{3+} co-doped ZPBT glasses prepared by melt quenching technique
- The glasses exhibit intense green and orange emission under n-UV excitation
- Energy transfer properties analyzed via Dexter and Reisfeld's theory and I-H model
- White light and tunable emission observed in Tb^{3+}/Sm^{3+} co-doped ZPBT glasses
- Suggest that this glass may be useful for manufacturing organic resin free w-LEDs.

ACCEPTED MANUSCRIPT

Accepted Manuscript

Title: Numerical simulations of novel SiGe-based IBC-HJ solar cell for standalone and mechanically stacked tandem applications

Authors: Rahul Pandey, Rishu Chaujar

PII: S0025-5408(17)30752-3
DOI: http://dx.doi.org/doi:10.1016/j.materresbull.2017.05.006
Reference: MRB 9321

To appear in: *MRB*

Received date: 25-2-2017
Revised date: 28-4-2017
Accepted date: 2-5-2017

Please cite this article as: Rahul Pandey, Rishu Chaujar, Numerical simulations of novel SiGe-based IBC-HJ solar cell for standalone and mechanically stacked tandem applications, Materials Research Bulletinhttp://dx.doi.org/10.1016/j.materresbull.2017.05.006

This is a PDF file of an unedited manuscript that has been accepted for publication. As a service to our customers we are providing this early version of the manuscript. The manuscript will undergo copyediting, typesetting, and review of the resulting proof before it is published in its final form. Please note that during the production process errors may be discovered which could affect the content, and all legal disclaimers that apply to the journal pertain.

ACCEPTED MANUSCRIPT

Numerical simulations of novel SiGe-based IBC-HJ solar cell for standalone and mechanically stacked tandem applications

Rahul Pandey and Rishu Chaujar *

Department of Engineering Physics, Delhi Technological University, New Delhi, India

Shahbad Daulatpur, Main Bawana Road, New Delhi, Delhi 110042

E-mail: Rishu.phy@dce.edu*

Graphical abstract

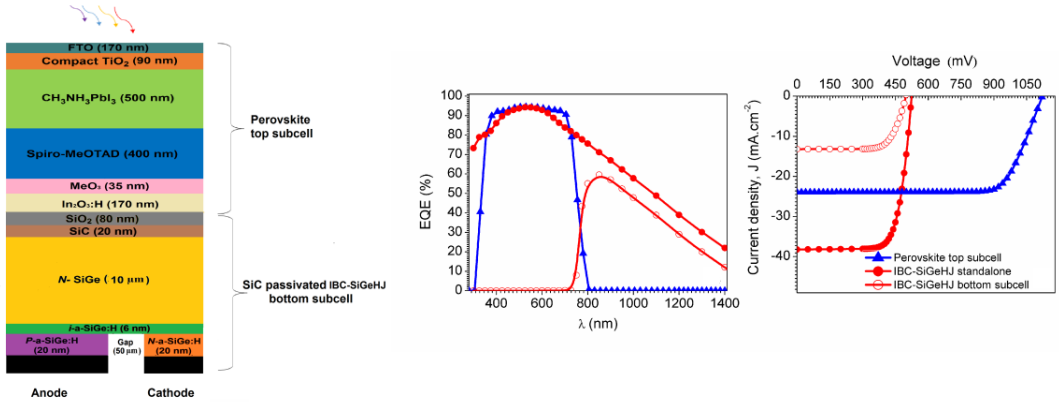

Highlights

- Innovative $Si_{0.75}Ge_{0.25}$ based IBC-HJ solar cell been proposed and simulated.
- Optimization has been done for 10 µm thick IBC-SiGeHJ.
- 15.4% PCE has been simulated under standalone operating condition
- In combination with perovskite top subcell, we further demonstrate 25.7% PCE.
- Results shows, proposed design, can be a good candidate to obtained ultra-high efficiencies.

Abstract- In this study, a novel 10 microns thick interdigitated back contact silicon-germanium heterojunction (IBC-$Si_{1-x}Ge_xHJ$) solar cell device has been designed and simulated for standalone and four-terminal mechanically stacked tandem applications. Optimization of i-a-SiGe: H thickness, the width of n-a-SiGe: H region, p-a-SiGe: H region and gap along with composition fraction (x) lead to 15.5% power conversion

ACCEPTED MANUSCRIPT

efficiency (PCE) in a stand-alone configuration. Whereas in combination with perovskite top subcell we further demonstrate 25.7% PCE in four-terminal tandem configuration. In mechanical stacking, top and bottom subcells are fabricated individually and then assembled in a module, which avoids the need for current matching between subcells, thereby giving greater process and design flexibility. The proposed IBC-SiGeHJ solar cell is ~ (25-30) times thinner than conventional Si solar cells which are used as bottom subcell in perovskite/silicon tandem solar cell. The results reveal that the proposed 4-terminal mechanically stacked perovskite/IBC-SiGeHJ tandem device may open new doors for the energy efficient applications. All the simulations have been done using Silvaco technology computer aided design (TCAD) simulator.

Keywords- Perovskite, solar cell, tandem, IBC-SiGeHJ, energy.

1. Introduction

Sunlight is the major source of renewable energy, about 4.3×10^{20} J/hr [1], is radiated because of a nuclear fusion reaction in the sun. Therefore, solar energy is one of the good renewable sources of energy substituting fossil fuels [2-3]. Photovoltaic (PV) devices are used for direct conversion of sunlight energy into electrical energy. The crystalline silicon (c-Si) solar cells have been dominating the PV market for several decades, with a current market share of 90% [4]. The efficiency of the crystalline silicon solar cell has only marginally improved during the last 15 years. The wafer size efficiency as high as 25.6% was obtained with amorphous silicon (a-Si) / c-Si heterojunction technology [5], and recently record of 26.3% has been achieved on 180 cm^2 crystalline silicon solar cell [6] which is close to the theoretical maximum efficiency of 29.4% [7].The increase in the PV market needs the new development and design to compete with conventional sources of energy fully. Hence, energy efficient modules are required. Further, to make PV system feasible at large scale, module cost should be <$0.5/W [8]. Therefore, to obtain high efficiency at a lower cost, tandem approaches have been proposed, which combines small band-gap and large band-gap solar technologies. In tandem approach, to utilize the solar spectrum, the large bandgap solar cell has been used as top subcell, and small bandgap solar cells are used as bottom subcell, respectively. One of the most exciting top subcell candidates is perovskite solar cell. In a liquid based dye-sensitized solar cell (DSSC), optical absorption of methylammonium-lead-halide on nanocrystalline TiO_2 surface produces the PCE of 3-4%, as first discovered in 2009 [9]. The methylammonium-lead-halide, $CH_3NH_3PbX_3$ (X=Br, I) perovskite has a tunable bandgap, ranging from (1.6-2.3) eV depending on halide composition. In recent years, to obtain the higher efficiency at

ACCEPTED MANUSCRIPT

lower cost perovskite/silicon-based tandem approaches have been proposed, which combine a silicon cell with a low-cost cell with wide-bandgap (1.6-1.9 eV) absorber material to form a tandem cell [10-11]. Moreover, in perovskite/silicon tandem solar cell, the perovskite top cell utilize the lower wavelength photons. Whereas, to absorb the photons of higher wavelength i.e. > 800 , thickness more than 250 µm is required since the absorption coefficient (α) of silicon is small at a higher wavelength [12-13]. The requirement of large volume and high-quality silicon in tandem solar cell significantly increases the module cost. These issues can be fixed by using a different material which has higher optical absorption compared to silicon at higher wavelengths. The use of SiGe cell as a bottom cell is a possible solution to enhance the absorption at a higher wavelength. The experimentally available data shows, the absorption coefficient (α) of SiGe is greater than Si in the higher wavelength region [14]. SiGe processing is simple since physical and electrical properties of silicon and germanium are similar [15]. The band gap of SiGe can be modified by changing the Ge content, and hence, the optical absorption [16, 17]. Moreover, recent simulation work shows that the SiGe-based solar cell could be a good candidate to obtain higher PCE [18-20].

This work presents, a novel 4- terminal perovskite/SiGe-based tandem solar cell where the use of SiGe instead of Si is a possible solution to minimize the absorption loss at higher wavelengths. 10µm thick SiGe solar cell has been used as bottom subcell, which is ~ (25-30) times thinner than conventional Si solar cell which is used as bottom subcell in perovskite/silicon tandem solar cell. This indicates that the proposed device significantly saves the material required for the fabrication. However, the cost of germanium doped wafer is higher compared to a silicon wafer, though present work shows a tandem device made using SiGe cell can be a good candidate for energy efficient applications. Moreover, future development of cost effective energy efficient methods may decrease the overall dollar per watt ($/W) of the device. The tandem architectures of perovskite are mainly divided into three categories: monolithically integrated, mechanically stacked, and spectrally split [21]. Mechanical stacking results in a 4-terminal tandem solar cell which mean that the top subcell and bottom subcell is fabricated independently, and then combined in the module. The 4-terminal perovskite/SiGe device simulated in this work is the mechanically stacked type. The overall work reported in this work has been divided into two parts: first, designing and optimization of the 10µm thick IBC-SiGeHJ standalone solar cell, and second, analyses of 4-terminal perovskite/IBC-SiGeHJ tandem solar cell. The IBC-SiGeHJ solar cell combines the advantages of the back contact that eliminates contact shading, leading to a higher short-circuit current (J_{SC}) and SiGe heterojunction solar cells with high open circuit voltage (V_{OC}) due to the better surface passivation with the help of the deposited i-a-SiGe: H layer. Further, to prevent the front surface recombination, SiC-based front surface passivation has been used as discussed in [22].

2. Device structures, models, and methods

The device simulation has been done using Silvaco ATLAS device simulator. The perovskite top subcell, IBC-SiGeHJ bottom subcell, and 4-terminal tandem cell have been shown in Fig. 1(a-c). The devices have been designed using ATHENA process simulator. The doping of *n-type* SiGe and *n-type* a-SiGe:H is 2.14×10^{16} cm^{-3} and 4.8×10^{18} cm^{-3}, respectively and that of *p-type* a-SiGe:H is 2×10^{19} cm^{-3}. The gap width is 50 µm and width of *p-type* a-SiGe: H, *n-type* a-SiGe: H are 100µm and 25µm respectively. Moreover, for top subcell, fluorine-doped tin oxide (FTO) has been used as a top contact for perovskite solar cell. The Spiro-MeOTAD and $CH_3NH_3PbI_3$ are *p-type* with a doping density of 3×10^{18} cm^{-3} and 2.14×10^{17} cm^{-3} respectively, whereas compact TiO_2 is *n-type*, with a doping density of 5×10^{19} cm^{-3}. In the mechanically stacked tandem configuration, the top subcell requires two transparent contacts. Hence, indium oxide (In_2O_3: H) based transparent rear electrode has been used for perovskite top subcell as reported in [23]. The electron-hole continuity equation is solved along with Poisson equation to obtain the current density (J) - voltage (V) curve under AM1.5 illumination. Top subcell has been simulated based on the recombination dynamics in $CH_3NH_3PbI_3$ with the help of SRH, Auger, and radiative recombination models to account for the

ACCEPTED MANUSCRIPT

monomolecular, bimolecular and trimolecular recombinations in the perovskite top subcell [24]. The second and third order charge carrier decay constant 1.5×10^{-10} $cm^3.s^{-1}$ and 3.4×10^{-28} $cm^6.s^{-1}$ have been used for perovskite cell as suggested in [25]. In the bottom IBC-SiGeHJ cell, Fermi statistics is used for carriers and drift-diffusion combined with Bohm Quantum Potential to account for quantum correction. The concentration dependent SRH (CONSRH), concentration dependent mobility (CONMOB) and Auger recombinations are activated for bottom IBC-SiGeHJ solar cell [26]. The band to band recombination in SiGe is negligible since it is an indirect bandgap semiconductor and hence, radiative recombination model has been ignored for bottom subcell. The description of semiconductor equations and models has been shown in Table 1 whereas material parameters used in the simulation is shown in Table 2. The material parameters for perovskite cell have been obtained from [27].

The Poisson equation, electron and hole continuity equation.	$\frac{d}{dx}\left(-\varepsilon(x)\frac{d\Psi}{dx}\right) = -q\left[\begin{matrix} n(x) - p(x) + N_a^-(x) - N_d^+(x) + \\ n_t(x) - p_t(x) \end{matrix}\right]$ $\frac{dn_p}{dt} = D_n \frac{d^2 n_p}{dx^2} + n_p \mu_n \frac{d\xi}{dx} + \mu_n \xi \frac{dn_p}{dx} + G_n - \frac{n_p - n_{p0}}{\tau_n}$	Where q the electron charge, D the diffusion coefficient, ε is the permittivity and G the generation rate. The n_s, n_t, p_s and p_t are the free electron, trapped electron, free hole, and trapped hole, respectively. ψ is the electrostatic potential. N_a^- the ionized n and N_d^+ are ıcentration. ξ e the carrier
Auger recombinatic		x10^{-32} $cm^6.s^{-1}$ een used for ely, at 300K efficient for btained from are the d holes at

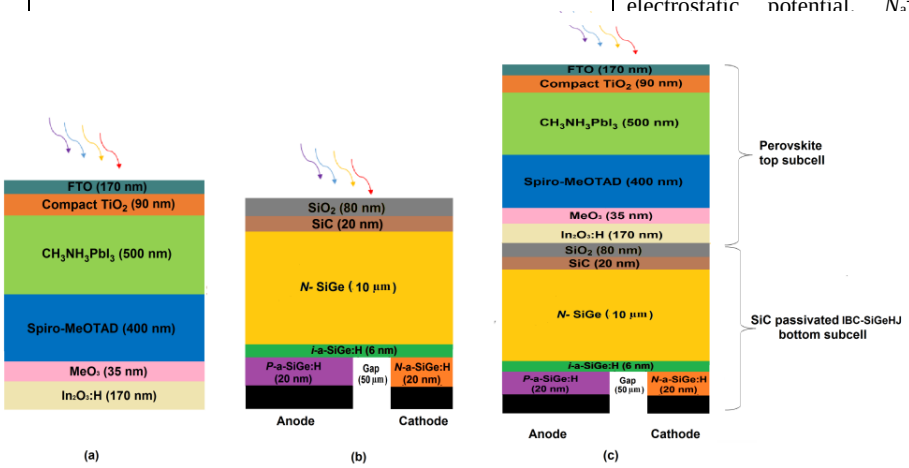

Figure 1. Device structures used in simulations (a) semitransparent perovskite top subcell, with FTO and In_2O_2: H based front and rear contact (b) IBC-SiGeHJ bottom subcell, and (c) 4-terminal mechanically stacked tandem solar cell

ACCEPTED MANUSCRIPT

Table 2. Materials parameters used in the simulation [26-27]

Table 1. Equations and models used in simulations [23]

Shockley-Read-Hall (SRH) recombination.	$R_{SRH} = \frac{pn - n_{ie}^2}{\tau_{n0}\left[p + n_{ie}\exp(\frac{E_i - E_t}{k_b T})\right] + \tau_{p0}\left[n + n_{ie}\exp(\frac{E_t - E_i}{k_b T})\right]}$	n_{ie} is the effective intrinsic carrier concentration and its value for perovskite and silicon are $1.97\times10^{7} cm^{-3}$ an $4.51\times10^{10} cm^{-3}$, respectively. K_b is Boltzmann's constant and E_i and E_t are the intrinsic fermi level and trap energy level, respectively. T is the lattice temperature in degree Kalvin. n and p are the electron and hole concentrations. Basic for the SRH model are the assumptions of one trap level in the forbidden band i.e. $E_t = E_i$ and corresponds to the most efficient recombination center. τ_{n0} and τ_{p0} are the electron and hole bulk lifetimes, $2x10^{-5}$ has been used for SiGe. N is the doping concentration of SiGe
Radiative recombination	$R_{np}^{OPT} = C_c^{OPT}(np - n_{ie}^2)$	The radiative rate coefficient for perovskite film has been obtained from experimental data [25].
Surface recombination	$R_{surface} = \frac{pn - n_{ie}^2}{\tau_n^{eff}\left[p + n_{ie}\exp(\frac{E_i - E_t}{k_b T})\right] + \tau_p^{eff}\left[n + n_{ie}\exp(\frac{E_t - E_i}{k_b T})\right]}$ $\frac{1}{\tau_n^{eff}} = \frac{1}{\tau_n^{i}} + \frac{d_i}{A_i} S_{n0}$ and $\frac{1}{\tau_p^{eff}} = \frac{1}{\tau_p^{i}} + \frac{d_i}{A_i} S_{p0}$ With $S_{p0} = \sigma_p \nu_{th} \mathrm{N}_{st}$ and $S_{n0} = \sigma_n \nu_{th} \mathrm{N}_{st}$	Where, A_i and d_i are the area and the length of the interface node i and τ_n^i is the bulk lifetime calculated at a node i along the interface. S_{p0}, S_{n0}, σ_p and σ_n are the surface recombination velocities parameters and capture cross section for holes and electrons respectively. N_{st} is the surface states per unit area and ν_{th} is the thermal velocity of the charge carrier (~ 10^7 cm.s^{-1}). The surface recombination effect incorporated in the bottom silicon solar cell using interface statement in ATLAS software and $S_{p0} = S_{n0}$ =100 cm.s^{-1} have been used.

ACCEPTED MANUSCRIPT

Material		A	B	C	D	E	F	G	H	I
Dielectric Constant		100	30	3	12.9	11.9	11.9	11.9	9.72	
Band Gap (eV)		3.2	1.5	2.91	0.94	1.60	1.60	1.60	2.2	0.99
Electron Affinity (eV)		4	3.93	2.2	4.17	4.0	4.0	4.0	4.2	
Thickness (µm)		0.09	0.5	0.4	10	0.02	0.006	0.02	0.02	0.001
Electron, Hole mobility ($cm^2/V{\cdot}s$)		0.006, 0.006	50,50	0.0001, 0.0001	1430, 480	20, 2	20, 2	20, 2	100, 50	
Effective conduction band (DOS) (cm^{-3})		1×10^{21}	2.5×10^{20}	2.5×10^{20}	2.36×10^{19}	2.5×10^{20}	2.5×10^{20}	2.5×10^{20}	6.4×10^{18}	
Effective valence band (DOS) (cm^{-3})		2×10^{20}	2.5×10^{20}	2.5×10^{20}	9.30×10^{18}	2.5×10^{20}	2.5×10^{20}	2.5×10^{20}	1.6×10^{18}	
Conduction tail states	$N^{c\text{-}tail}$ A (cm^{-3})	10^{14}	10^{14}	10^{14}	n/a	10^{21}	10^{18}	10^{21}	n/a	0
	$E^{c\text{-}tail}$ A (eV)	0.01	0.015	0.01	n/a	0.07	0.09	0.07	n/a	0.07
Valence tail states	$N^{v\text{-}tail}$ D (cm^{-3})	10^{14}	10^{14}	10^{14}	n/a	10^{21}	10^{18}	10^{21}	n/a	0
	$E^{v\text{-}tail}$ D (eV)	0.01	0.015	0.01	n/a	0.12	0.09	0.12	n/a	0.12
Acceptor-like (A) dangling bond states	N^{db} A (cm^{-3})	10^{17}	10^{14}	10^{16}	n/a	10^{19}	10^{16}	10^{19}	n/a	2.4×10^{16}
	E^{db} A (eV)	1.1	1.2	1.1	n/a	0.7	1.1	1.3	n/a	0.5
	σ^{db} A (eV)	0.1	0.1	0.1	n/a	0.2	0.15	0.2	n/a	0.2
Donor-like (D) dangling bond states	N^{db} D (cm^{-3})	10^{17}	10^{14}	10^{16}	n/a	10^{19}	10^{16}	10^{19}	n/a	2.4×10^{16}
	E^{db} D (eV)	1.1	1.2	1.1	n/a	0.45	0.9	1.1	n/a	0.5
	σ^{db} D (eV)	0.1	0.1	0.1	n/a	0.2	0.15	0.2	n/a	0.2

A= Compact TiO_2 , *B*= $CH_3NH_3PbI_3$, *C*= Spiro-MeOTAD, *D*=$Si_{0.85}Ge_{0.15}$, *E*= *n*- type a- $Si_{0.85}Ge_{0.15}$:H, *F*= Buffer a- $Si_{0.85}Ge_{0.15}$:H, *G*= *p*- type a- $Si_{0.85}Ge_{0.15}$:H, H=SiC, I=Interface defects

3. Results

3.1 Optimization of 10 microns thick IBC-SiGeHJ bottom subcell.

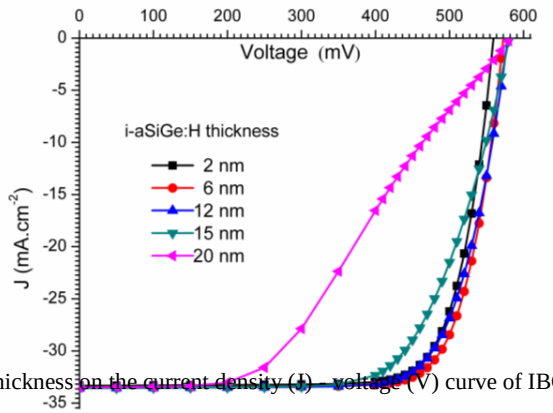

Figure 2. Impact of i-a-SiGe: H thickness on the current density (J) – voltage (V) curve of IBC-SiGeHJ solar cell.

ACCEPTED MANUSCRIPT

This section deals with the optimization of IBC-SiGeHJ bottom subcell i.e. the thickness of i-a-SiGe: H, the width of n-type (BSF), the width of p-type (emitter), gap width, and composition fraction have been optimized for improved efficiency. The simulation of the IBC-SiGeHJ solar cell has been performed, and the current density-voltage (J-V) curve with different i-a-SiGe: H thicknesses has been reported in Fig. 2. Result shows, increasing the thickness of a-SiGe: H layer leads to decrease in the fill factor (FF). Intrinsic a-SiGe: H prevents the recombination at the a-SiGe/SiGe region. However, it also reduces the conduction of generated carriers and hence leads to low FF. This has been verified in Fig. 2 that increasing the thickness of i-a-SiGe: H leads to decrease in the FF. Results also show that at a thickness of 20 nm, "S" shaped J-V curve with low FF has been obtained, which is confirmed by the already available results of 200-micron thick silicon-based device with the same architecture as reported in [28]. The impact of i-a-SiGe: H thickness on the photovoltaic parameters are shown in Fig. 3a (i-iv).

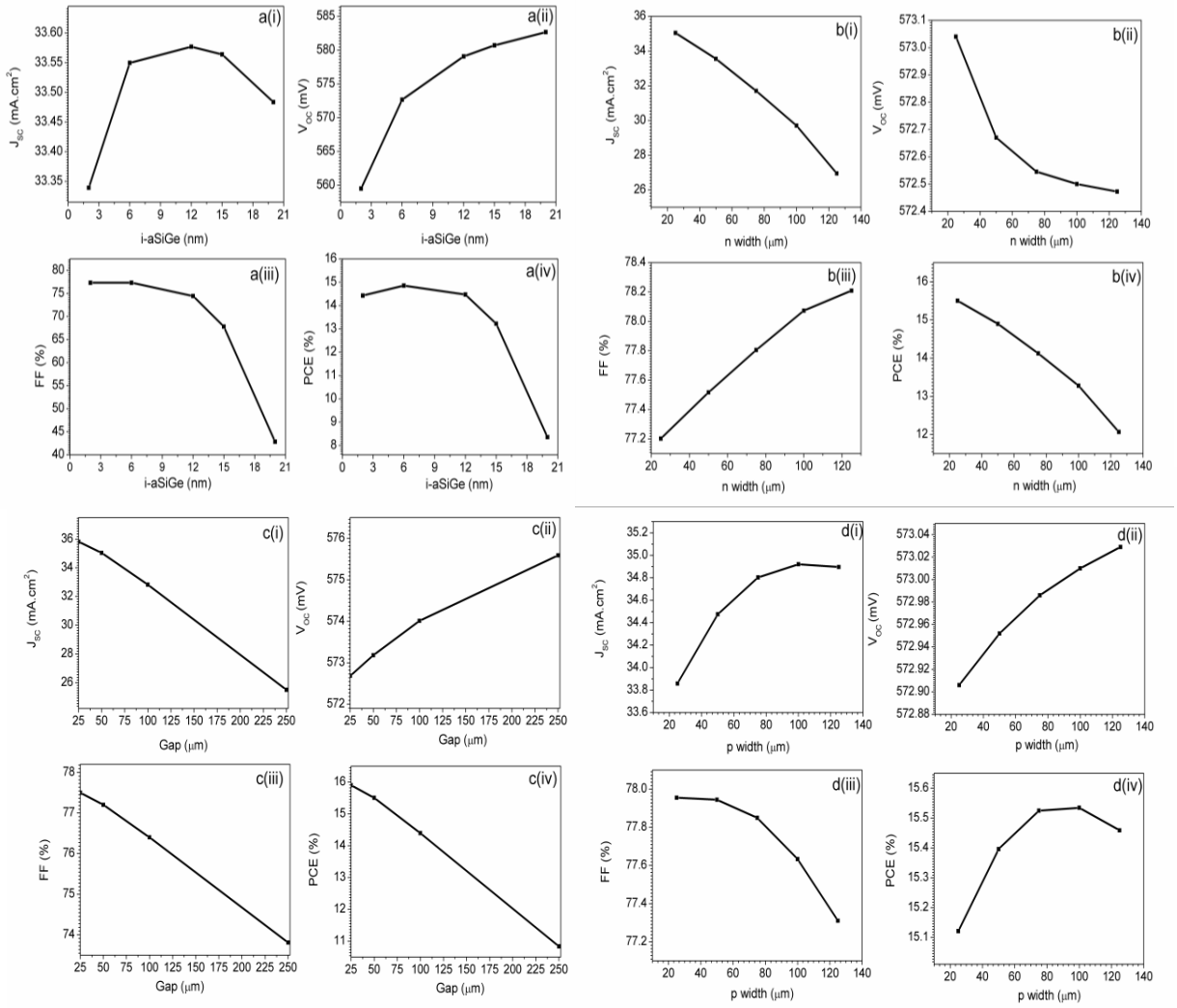

Figure 3. Optimization of IBC-SiGeHJ solar cell (a) thickness of i-a-SiGe: H layer, (b) width of n- type region (BSF), (c) Gap width, and (d) width of p- type region (emitter).

ACCEPTED MANUSCRIPT

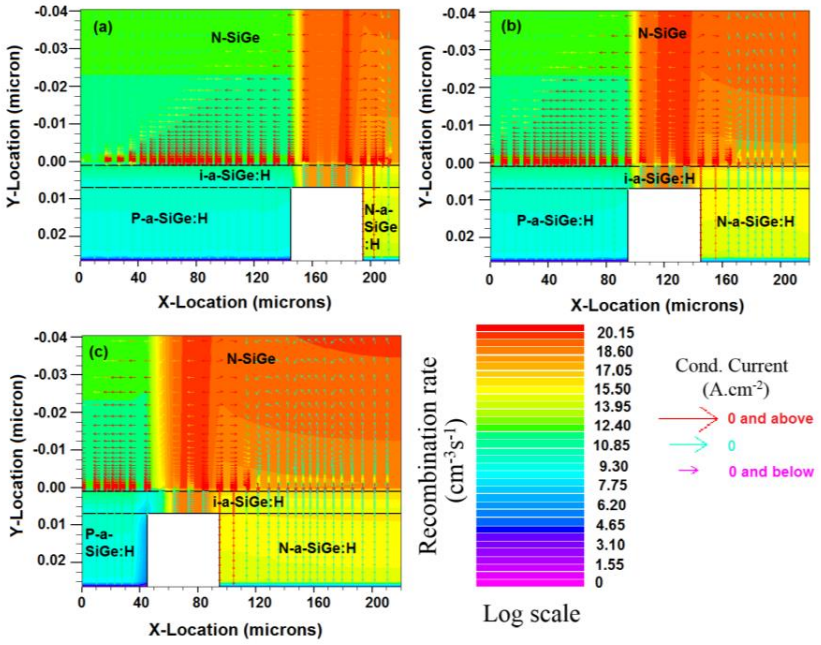

Figure 4. Contour representation of recombination rate with different N-strip widths (a) 25 micron, (b) 75 micron, and (d) 125 micron.

Moreover, Fig. 3a (ii) shows a slight improvement in V_{OC} on increasing the thickness of i-a-SiGe: H, which is supported by comparing with the already published results [29]. However, an increase in V_{OC} is not sufficient to compensate the decrease in FF, and hence the overall PCE reduces by increasing the thickness of i-a-SiGe: H, as shown in Fig. 3a (iv). Moreover, the width of BSF (n-strip), the emitter (p-strip), and the gap was also optimized, and the results are shown in Fig. 3(b-d). The J_{SC} vs. n-strip width is reported in Fig. 3b (i), increasing n-strip width considerably reduces J_{SC}, to understand the effect of n- strip width, contour representation of recombination rate; and the vector representation of conduction current have also been obtained and shown in Fig. 4. To obtain the results, a very small region near the back side of the device is exaggerated as shown in Fig. 4(a-c). Increasing n-strip width will decrease the carrier collection probability of p-strip region. Since the minority carriers that are generated near or at n-strip region requires to travel not only vertical to the rear junction but also laterally to arrive at the collecting junction i.e. p-strip. Increasing n-width results in longer traveling distance for minority carrier, and hence the probability of carrier recombination is higher, as shown in Fig. 4(a-c). Higher the recombination rate, lower will be the conduction current density, and the direction of the conduction current density is shown in Fig. 4(a-c). The FF and V_{OC} remain almost unaffected due to good surface passivation quality. Further, the impact of gap width is studied in Fig. 3c. Increasing the gap width will increase the lateral distance and series resistance for minority carrier that is generated at or near the BSF region. Therefore, increasing the gap width will decrease J_{SC} and FF. Furthermore, at the end of the optimization process, the impact of p-strip width has also been obtained, and results show that the 100-micron thick p-strip is optimum to give a good performance, as shown in Fig. 3d (iv). Concluding the section gives the optimized dimensions for 10 microns thick IBC-SiGeHJ solar cell i.e. width of BSF, gap, and emitter regions are 25 micron, 50 microns, and 100 microns respectively.

ACCEPTED MANUSCRIPT

3.2 Analysis of semitransparent Perovskite/IBC-SiGeHJ mechanically stacked tandem solar cell.

In this section, the potential of semi-transparent perovskite/IBC-SiGeHJ mechanically stacked tandem solar cell, a novel photovoltaic device for ultra-high conversion efficiency has been simulated. The organic-inorganic halide semitransparent perovskite solar cells are potential candidates to be used as top subcell, due to its suitable bandgap. A 20.9% efficient perovskite top subcell as reported in [30] has been used as top subcell. Whereas 10-micon thick IBC-SiGeHJ solar cell has been used as bottom subcell. The optical properties of perovskite solar cell used in simulations are identical to the properties reported in [30]. Four-terminal device simulated in this work is shown in Fig. 1c. In mechanical stacking, the top and bottom subcell are fabricated independently and then organized in the module. Hence, top subcell has been simulated individually, whereas bottom subcell has been simulated by placing perovskite as a filter. All the materials used in perovskite solar cell has been placed as a filter over IBC-SiGeHJ solar cell when simulating IBC-SiGeHJ solar cell as bottom subcell. The addition of the PCE of perovskite top subcell and IBC-SiGeHJ bottom subcell in tandem configuration gives the overall PCE of the tandem device. In the previous section, the optimization of IBC-SiGeHJ solar cell for a standalone application, i.e. optimization has been done under the full AM1.5 spectrum. Moreover, in this section fresh optimization for IBC-SiGeHJ has been done under filtered spectrum by top subcell, and results are reported in Fig. 5 (a-d). Results show that the behavior of bottom subcell device is identical as obtained in standalone condition. However, the magnitude of photovoltaic parameters is lower, particularly J_{SC} as shown in Fig. 5a (i). This is due to reduced light intensity in the presence of perovskite top subcell. Results reported in Fig. 5 shows that optimized dimensions under filtered spectrum are same as obtained for the stand-alone case. This validates that optimized dimensions i.e. the width of BSF, gap, and emitter regions 25 microns, 50 microns, and 100 microns respectively, hold good for both standalone as well as bottom subcell conditions.

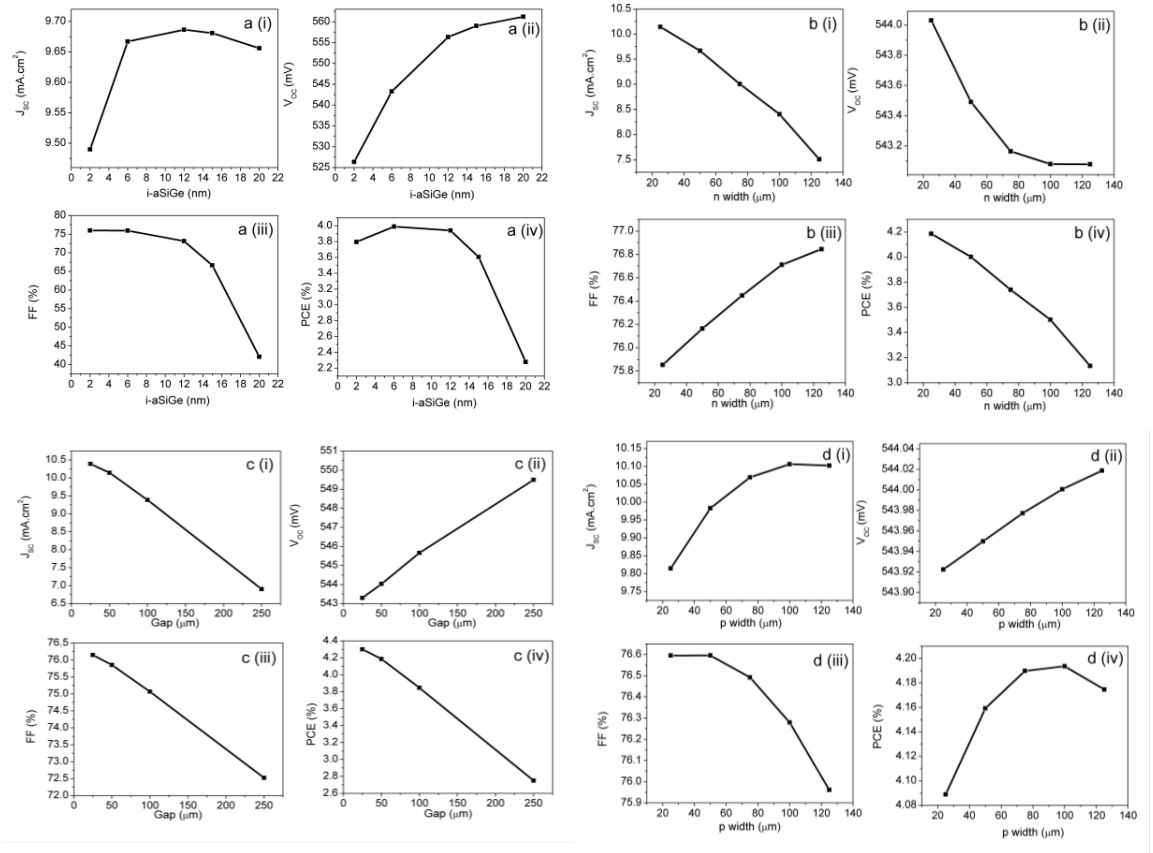

Figure 5. Optimization of IBC-SiGeHJ solar cell under filtered spectrum (a) thickness of i-a-SiGe: H layer, (b) width of n- type region (BSF), (c) Gap width, and (d) width of p- type region (emitter).

ACCEPTED MANUSCRIPT

Further, the impact of composition fraction (x) on the performance of bottom IBC-$Si_{1-x}Ge_x$HJ solar cell has been studied for both standalone as well as tandem configuration. The performance of bottom subcell device has been obtained with three different composition fractions i.e. x=0, 0.15, and 0.25. The optical properties i.e. complex reflective indices used in the simulation have been obtained from sopra database of ATLAS library [26] and reported in Fig. 6a. The J-V curves for different composition fraction are shown in Fig. 6b. Increasing the composition fraction results in higher optical absorption, and hence results in higher J_{SC} .However, bandgap also reduces which further results in lower V_{OC}. This has been verified in the J-V curve reported in Fig. 6b. Bottom subcell in standalone condition shows the J_{SC} values 26.4 mA.cm^{-2}, 34.9 mA.cm^{-2}, and 38.2 mA.cm^{-2} with x=0, 0.15, and 0.25 composition fractions, respectively. Whereas, the V_{OC} values 674mV, 573mV, and 524mV, respectively has been obtained. This results in 14.4%, 15.5%, and 14.9% PCEs for composition values of 0, 0.15, and 0.25, respectively, in standalone configuration. This concludes that under the standalone condition the optimum performance has been obtained for the composition fraction of 0.15. Moreover, under tandem configuration with x=0, 0.15, and 0.25 the bottom subcell shows J_{SC} values of 1.4 mA.cm^{-2} , 10.1 mA.cm^{-2}, and 13.2 mA.cm^{-2} and V_{OC} values of 640 mV, 544mV, and 498 mV, respectively. Photovoltaic parameters of bottom subcell in standalone and bottom subcell operating conditions with different x values are reported in Table 3. Improved optical absorption at a higher wavelength in $Si_{0.75}Ge_{0.25}$ leads to higher J_{SC} under bottom subcell. In order to verify this contour representation of photon absorption rate has been obtained in the bottom subcell device under tandem configuration and reported in Fig. 7(a-b). Fig. 7(a-c) shows higher photon coupling in bottom subcell for x value of 0.25, due to superior optical absorption in $Si_{0.75}Ge_{0.25}$ compared to other two composition fraction values.

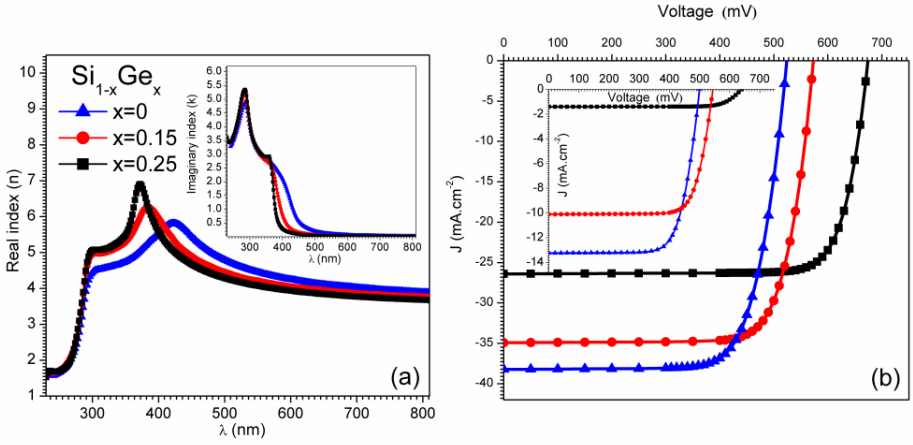

Figure 6 (a) Optical properties i.e. real and imaginary indices of $Si_{1-x}Ge_x$ as a function composition fraction and (b) The standalone J-V curve under AM1.5 illumination: Insect shows the J-V curve under filtered spectrum by top sub cell.

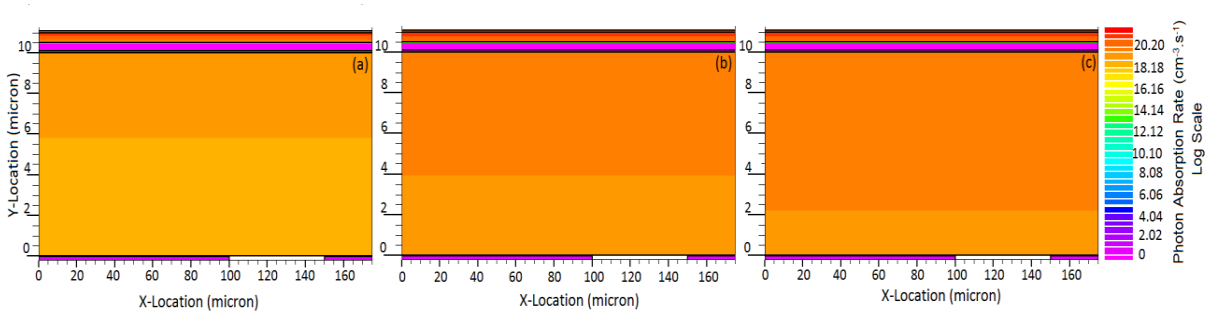

Figure 7 Photon absorption rate (cm^{-3}.s^{-1}) in bottom subcell under filtered spectrum by perovskite top subcell, with different x values. (a) x=0, (b) x=0.15, and (c) x=0.25. Regions above 10 µm in Y-locations represents perovskite top filter, and below 10 µm represents bottom IBC-SiGeHJ solar cell.

ACCEPTED MANUSCRIPT

Simulation results show that IBC-$Si_{0.85}Ge_{0.15}$HJ solar cell shows optimum performance in standalone condition, whereas IBC-$Si_{0.75}Ge_{0.25}$HJ solar cell superior performance under tandem configuration. Further, simulation results are obtained for the final tandem device and reported in Fig. 8(a-b). The spectrum response i.e. EQE of the perovskite top subcell, IBC-$Si_{0.75}Ge_{0.25}$HJ standalone, and IBC-$Si_{0.75}Ge_{0.25}$HJ as a bottom subcell in the tandem configuration are shown in Fig. 8a. The perovskite top subcell shows the EQE up to 800 nm, which is in good agreement with already published experimental results [31-33]. Bottom subcell operated standalone shows EQE in the lower wavelength as well as higher wavelength region. However, when operated in tandem configuration as a bottom subcell, the EQE at lower wavelengths disappears, due to the presence of perovskite top subcell. Since, up to 800 nm, top subcell absorbs the solar spectrum. However, a wavelength greater than 800 nm will be available for bottom subcell, as shown in Fig. 6a. J-V curve of the final tandem device is shown in Fig. 8b and corresponding photovoltaic parameters are shown in Table 3.

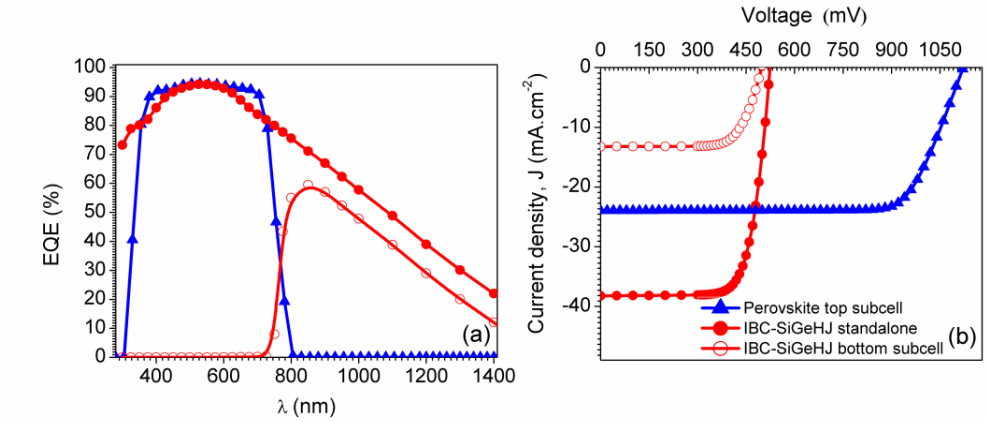

Figure 8. (a) Spectrum response i.e. EQE of perovskite top subcell and IBC-$Si_{0.75}Ge_{0.25}$HJ bottom subcell in tandem and standalone configuration. (b) The J-V curve of top subcell and bottom subcell under illumination.

Table 3 Photovoltaic parameters of IBC-SiGe bottom subcell with different composition fraction

IBC-$Si_{1-x}Ge_x$HJ		J_{SC} (mA.cm^{-2})	V_{OC} (mV)	FF (%)	PCE (%)
x=0	standalone	26.4	674	81.1	14.4
	under tandem	1.4	640	79.6	0.7
x=0.15	standalone	34.9	573	77.4	15.5
	under tandem	10.1	544	76.9	4.2
x=0.25	standalone	38.2	524	74.5	14.9
	under tandem	13.2	498	73.2	**4.8**
Pervoskite top subcell		23.9	1121	77.8	**20.9**
Mechanically stacked perovskite/IBC-$Si_{1-x}Ge_x$HJ tandem solar cell					20.9+4.8=25.7

ACCEPTED MANUSCRIPT

4. Conclusion

This work investigates the efficiency potential of a novel semitransparent perovskite/ IBC-SiGeHJ mechanically stacked tandem solar cell through numerical simulations. The first, optimization of IBC-SiGe solar cell has been performed for both standalone as well as bottom subcell operating conditions. Under tandem configuration, 4.8% PCE has been simulated in bottom subcell, which combines with 20.9% PCE of perovskite top subcell to gives overall conversion efficiency of 25.7% (20.9% top subcell + 4.8% bottom subcell). 10µm thick SiGe solar cell has been used as bottom subcell in perovskite/SiGe tandem solar cell which is ~ (25-30) times thinner than conventional Si solar cell which is used as bottom subcell in perovskite/silicon tandem solar cell. This indicates that proposed design can significantly save the material requirements. Mechanical stacking discussed in this work avoids the need for current matching between the top and bottom subcell. In perovskite-based tandem devices, the spectrum till 800 nm wavelength will be absorbed by perovskite top subcell whereas wavelength greater than 800 nm will be available for bottom subcell. Therefore the use of SiGe ensures higher absorption compared to Si-based IBC solar cell since the presence of Ge increases the optical absorption at higher wavelengths, which results in higher J_{SC}. The spectrum, as well as the electrical behavior of the devices, has been obtained to understand the device operation in both tandem as well as standalone conditions. Results reveal that proposed design will be a good candidate for energy efficient application.

Acknowledgments

The authors would like to thank Microelectronics Research Laboratory at Delhi Technological University to carry out this work and University Grant Commission (UGC), Government of India, for providing research fellowship. Rahul Pandey acknowledges Dr. Rishu Chaujar for her continuous guidance during this research work.

References

[1] N. S. Lewis, "Basic research needs for solar energy utilization," *in Proceedings of the Basic Energy Sciences Workshop on Solar Energy Utilization Chair, California Institute of Technology, September 2005.*, 2005.

[2] M. Wang, X. Gu, P. Ma, W. Zhang, D. Yu, P. Chang, X. Chen, D. Li, Microstructured superhydrophobic anti-reflection films for performance improvement of photovoltaic devices, *Materials Research Bulletin*, 91 (2017) 208-213.

[3] Zhiyong Liu, Tielin Shi, Zirong Tang, Guanglan Liao, A large-area hole-conductor-free perovskite solar cell based on a low-temperature carbon counter electrode, *Materials Research Bulletin* http://dx.doi.org/10.1016/j.materresbull.2017.03.069.

[4] ITRPV, "<ITRPV Seventh Edition Vers 2.pdf>," 2016.

[5] K. Masuko, M. Shigematsu, T. Hashiguchi, D. Fujishima, M. Kai, N. Yoshimura, *et al.*, "Achievement of More Than 25% Conversion Efficiency With Crystalline Silicon Heterojunction Solar Cell," *IEEE Journal of Photovoltaics*, vol. 4, pp. 1433-1435, 2014.

[6] Kaneka corporation. Available online. http://www.kaneka.co.jp/kanekae/images/topics/1473811995/1473811995_101.pdf

[7] A. Richter, M. Hermle, and S. W. Glunz, "Reassessment of the Limiting Efficiency for Crystalline Silicon Solar Cells," *IEEE Journal of Photovoltaics*, vol. 3, pp. 1184-1191, 2013.

[8] S. Jeong, M. D. McGehee, and Y. Cui, "All-back-contact ultra-thin silicon nanocone solar cells with 13.7% power conversion efficiency," *Nature communications*, vol. 4, pp. 2950-2950, 2013.

[9] Rahul, B. Bhattacharya, Z.H. Khan, Effect of crystal and powder of CH3NH3I on the CH3NH3PbI3 based Perovskite sensitized solar cell, *Materials Research Bulletin* 89 (2017) 292-296.

[10] J. P. Mailoa, C. D. Bailie, E. C. Johlin, E. T. Hoke, A. J. Akey, W. H. Nguyen, *et al.*, "A 2-terminal perovskite/silicon multijunction solar cell enabled by a silicon tunnel junction," *Applied Physics Letters*, vol. 106, 2015.

ACCEPTED MANUSCRIPT

[11] J. Werner, C.-H. Weng, A. Walter, L. Fesquet, J. P. Seif, S. De Wolf, *et al.*, "Efficient Monolithic Perovskite/Silicon Tandem Solar Cell With Cell Area > 1 cm 2," *The Journal of Physical Chemistry Letters*, vol. 7, p. acs.jpclett.5b02686, 2015.

[12] M. A. Green and M. J. Keevers, "Optical properties of intrinsic silicon at 300 K," *Progress in Photovoltaics: Research and Applications*, vol. 3, pp. 189-192, 1995.

[13] M. A. Green, "Self-consistent optical parameters of intrinsic silicon at 300K including temperature coefficients," *Solar Energy Materials and Solar Cells*, vol. 92, pp. 1305-1310, 2008.

[14] "NSM Archive - Silicon Germanium (SiGe) - Optical properties."

[15] "Springer Handbook of Electronic and Photonic Materials," 2007.

[16] H. Povolny, P. Agarwal, S. Han, and X. Deng, "Comparison Study of a-SiGe Solar Cells and Materials Deposited Using Different Hydrogen Dilution," *MRS Proceedings*, vol. 609, p. A30.3, 2011.

[17] C. C. Wang, D. S. Wuu, S. Y. Lien, Y. S. Lin, C. Y. Liu, C. H. Hsu, *et al.*, "Characterization of nanocrystalline SiGe thin film solar cell with double graded-dead absorption layer," *International Journal of Photoenergy*, vol. 2012, 2012.

[18] R. Pandey and R. Chaujar, "Rear contact SiGe solar cell with SiC passivated front surface for >90-percent external quantum efficiency and improved power conversion efficiency," *Solar Energy*, vol. 135, pp. 242-252, 2016.

[19] R. Pandey and R. Chaujar, "Novel back-contact back-junction SiGe (BC-BJ SiGe) solar cell for improved power conversion efficiency," *Microsystem Technologies*, vol. 22, pp. 2673-2680, 2016.

[20] R. Pandey, A. Jain, and R. Chaujar, "impact of minority carrier lifetime and temperature on SiC based rear contact sige solar cell for concentrator photovoltaic (cpv) applicationS," *32nd European Photovoltaic Solar Energy Conference and Exhibition*, p. 4, 2016.

[21] C. D. Bailie and M. D. McGehee, "High-efficiency tandem perovskite solar cells," *MRS Bulletin*, vol. 40, pp. 681-686, 2015.

[22] R. Pandey and R. Chaujar, "Numerical simulation of rear contact silicon solar cell with a novel front surface design for the suppression of interface recombination and improved absorption," *Current Applied Physics*, vol. 16, pp. 1581-1587, 2016.

[23] F. Fu, T. Feurer, T. Jäger, E. Avancini, B. Bissig, S. Yoon, *et al.*, "Low-temperature-processed efficient semi-transparent planar perovskite solar cells for bifacial and tandem applications," *Nature Communications*, vol. 6, p. 8932, 2015.

[24] C. Wehrenfennig, G. E. Eperon, M. B. Johnston, H. J. Snaith, and L. M. Herz, "High Charge Carrier Mobilities and Lifetimes in Organolead Trihalide Perovskites," *Advanced Materials*, vol. 26, pp. 1584-1589, 2014.

[25] Y. Yang, M. Yang, Z. Li, R. Crisp, K. Zhu, and M. C. Beard, "Comparison of Recombination Dynamics in CH3NH3PbBr3 and CH3NH3PbI3 Perovskite Films: Influence of Exciton Binding Energy," *Journal of Physical Chemistry Letters*, vol. 6, pp. 4688-4692, 2015.

[26] D. S. Software, "ATLAS User ' s Manual," pp. 567-1000, 2013.

[27] F. Liu, J. Zhu, J. Wei, Y. Li, M. Lv, S. Yang, *et al.*, "Numerical simulation: Toward the design of high-efficiency planar perovskite solar cells," *Applied Physics Letters*, vol. 104, p. 253508, 2014.

[28] S. B. Meijun Lu, Ujjwal Das, and Robert Birkmire, "A-SI/C-SI HETEROJUNCTION FOR INTERDIGITATED BACK CONTACT SOLAR CELL " *Pro. 22nd European PVSEC*, vol. 22, p. 4, 2007.

[29] D. Thibaut, D. V. Sylvain, S. Flore

ACCEPTED MANUSCRIPT

nt, D. Djicknoum, M. Delfina, G.-F. Marie, *et al.*, "Development of Interdigitated Back Contact Silicon Heterojunction (IBC Si-HJ) Solar Cells," *Energy Procedia*, vol. 8, pp. 294-300, 2011/01/01 2011.

[30] R. Pandey and R. Chaujar, "Numerical simulations: Toward the design of 27.6% efficient four-terminal semi-transparent perovskite/SiC passivated rear contact silicon tandem solar cell," *Superlattices and Microstructures*, vol. 100, pp. 656-666, 2016.

[31] X. Yin, P. Chen, M. Que, Y. Xing, W. Que, C. Niu, *et al.*, "Highly Efficient Flexible Perovskite Solar Cells Using Solution-Derived NiOx Hole Contacts," *ACS Nano*, vol. 10, pp. 3630-6, Mar 22 2016.

[32] Q. Lin, A. Armin, R. C. R. Nagiri, P. L. Burn, and P. Meredith, "Electro-optics of perovskite solar cells," *Nat Photon*, vol. 9, pp. 106-112, 02//print 2015.

[33] W. S. Yang, J. H. Noh, N. J. Jeon, Y. C. Kim, S. Ryu, J. Seo, *et al.*, "High-performance photovoltaic perovskite layers fabricated through intramolecular exchange," *Science.*, p. science.aaa9272, 2015.

ACCEPTED MANUSCRIPT

Figures

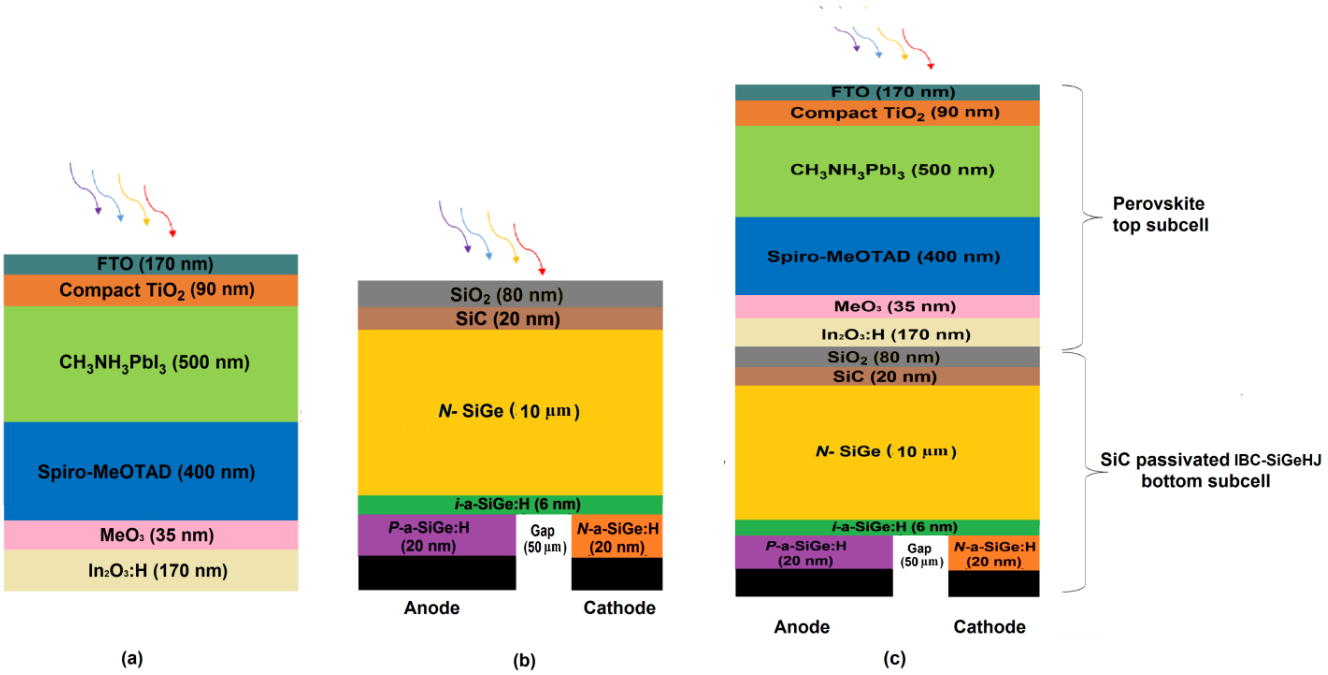

Figure 1. Device structures used in simulations (a) semitransparent perovskite top subcell, with FTO and ln_2O_2: H based front and rear contact (b) IBC-SiGeHJ bottom subcell, and (c) 4-terminal mechanically stacked tandem solar cell

ACCEPTED MANUSCRIPT

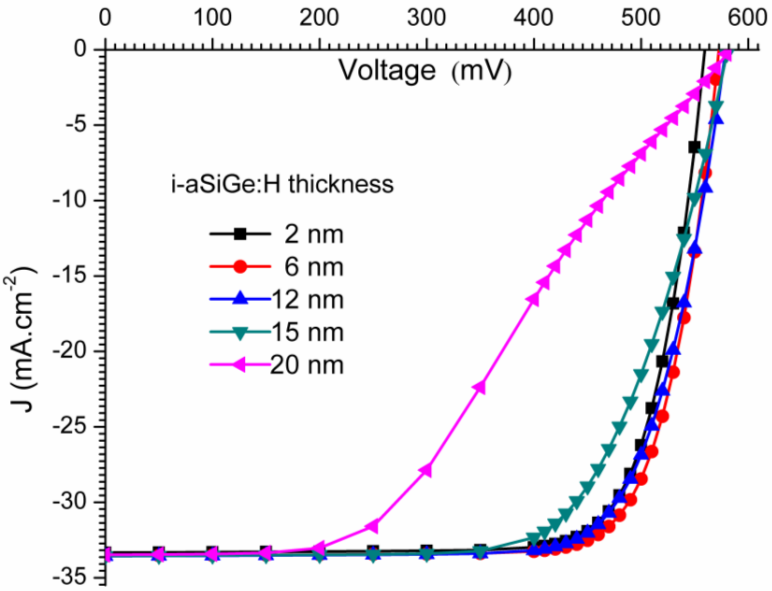

Figure 2. Impact of i-a-SiGe: H thickness on the current density (J) - voltage (V) curve of IBC-SiGeHJ solar cell.

ACCEPTED MANUSCRIPT

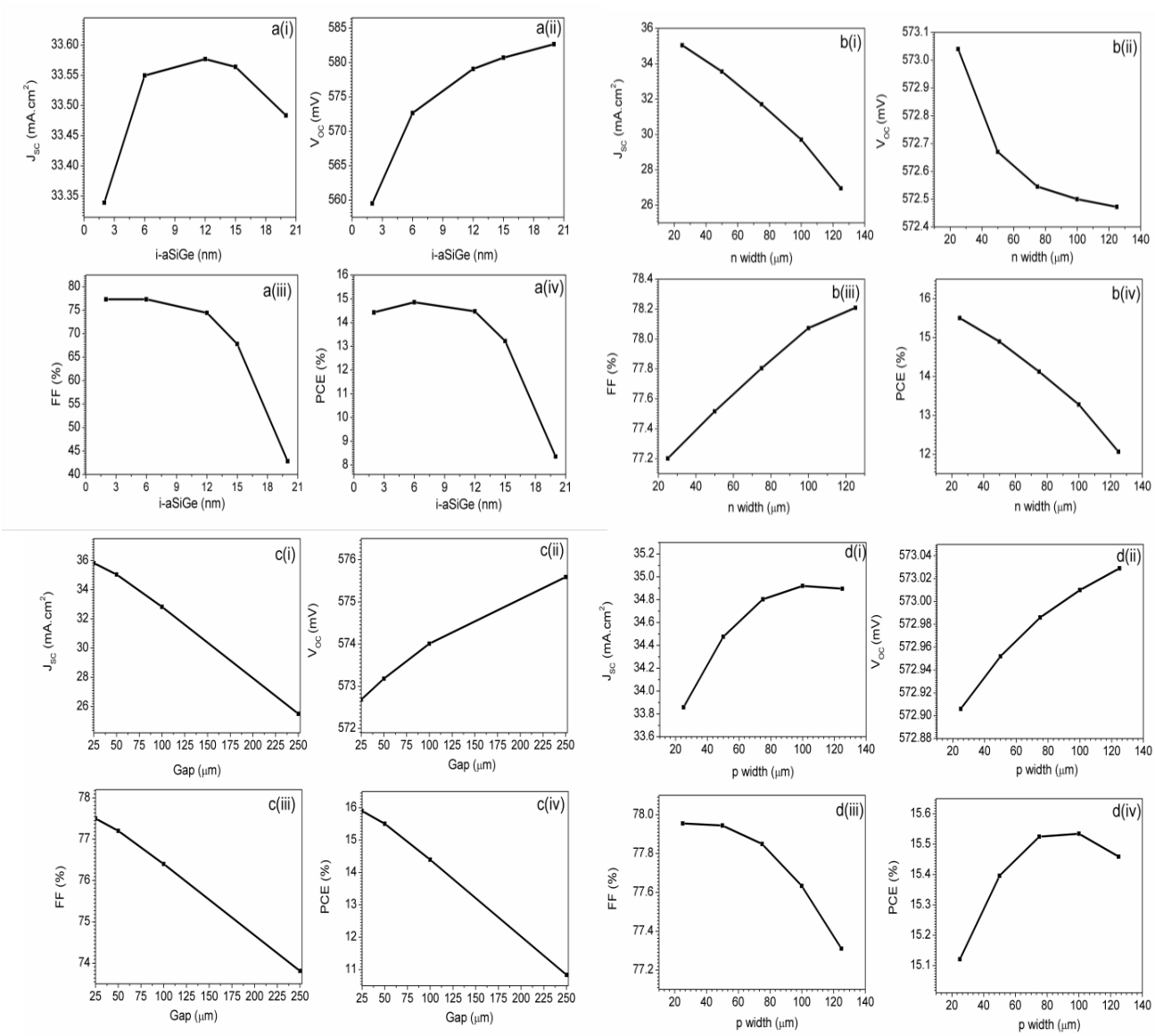

Figure 3. Optimization of IBC-SiGeHJ solar cell (a) thickness of i-a-SiGe: H layer, (b) width of n- type region (BSF), (c) Gap width, and (d) width of p- type region (emitter).

ACCEPTED MANUSCRIPT

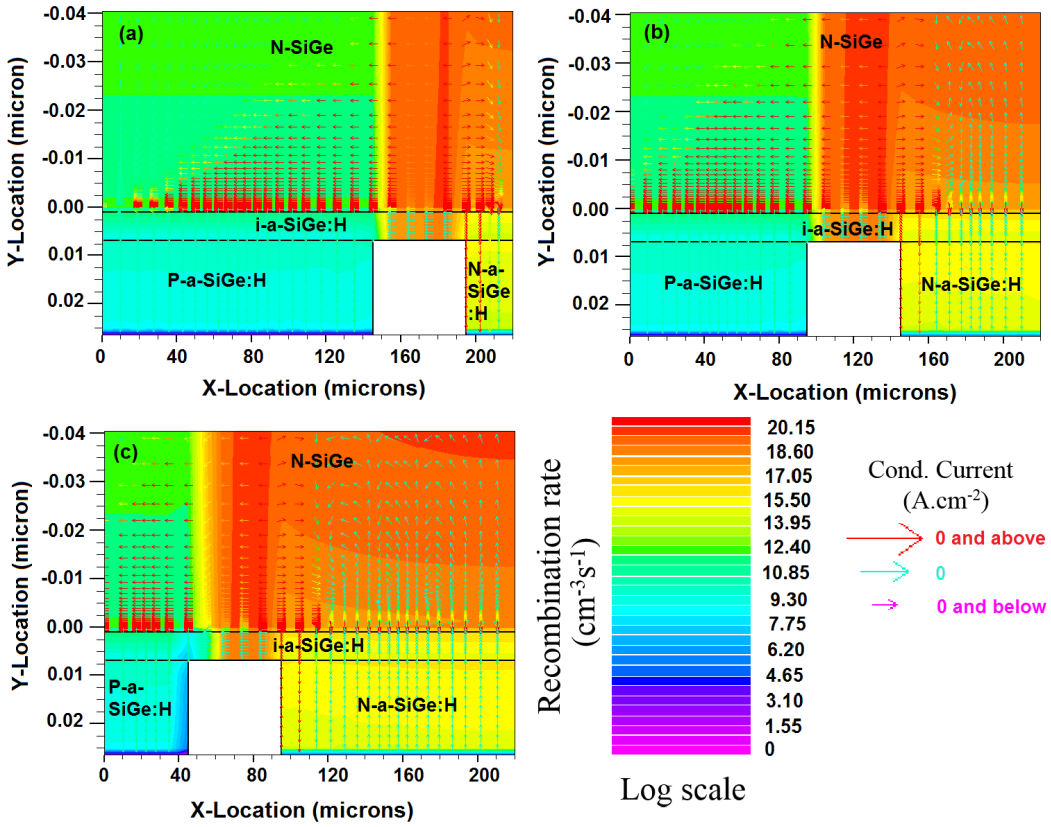

Figure 4. Contour representation of recombination rate with different N-strip widths (a) 25 micron, (b) 75 micron, and (d) 125 micron.

ACCEPTED MANUSCRIPT

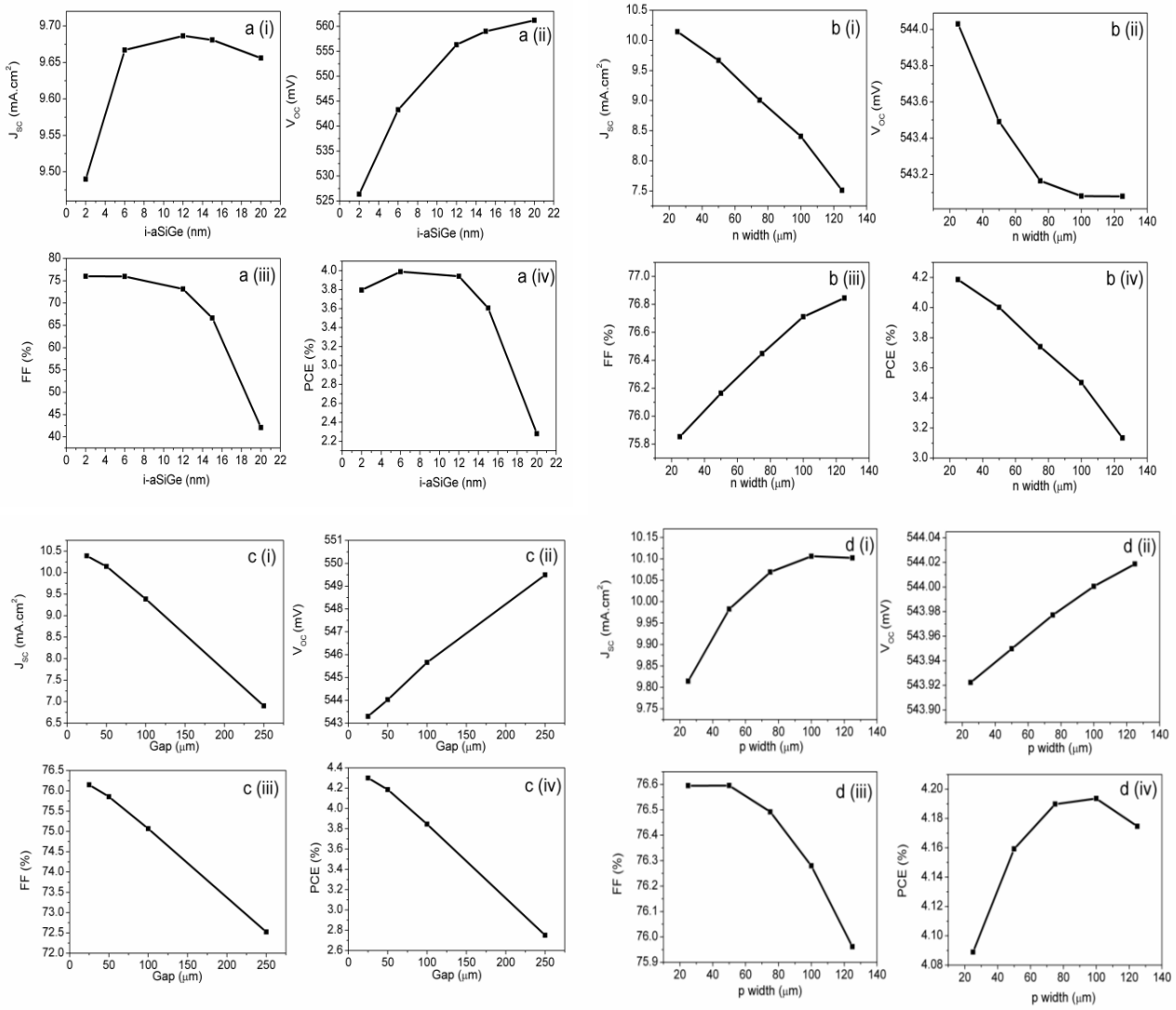

Figure 5. Optimization of IBC-SiGeHJ solar cell under filtered spectrum (a) thickness of i-a-SiGe: H layer, (b) width of n- type region (BSF), (c) Gap width, and (d) width of p- type region (emitter).

ACCEPTED MANUSCRIPT

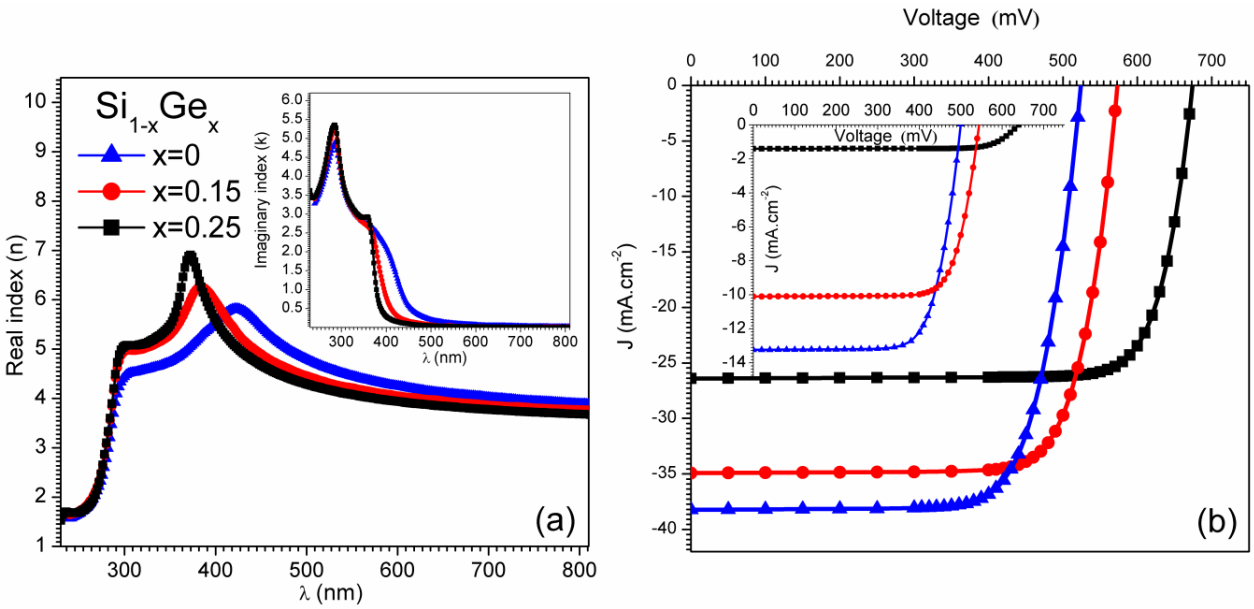

Figure 6 (a) Optical properties i.e. real and imaginary indices of $Si_{1-x}Ge_x$ as a function composition fraction and (b) The standalone J-V curve under AM1.5 illumination: Insect shows the J-V curve under filtered spectrum by top sub cell.

ACCEPTED MANUSCRIPT

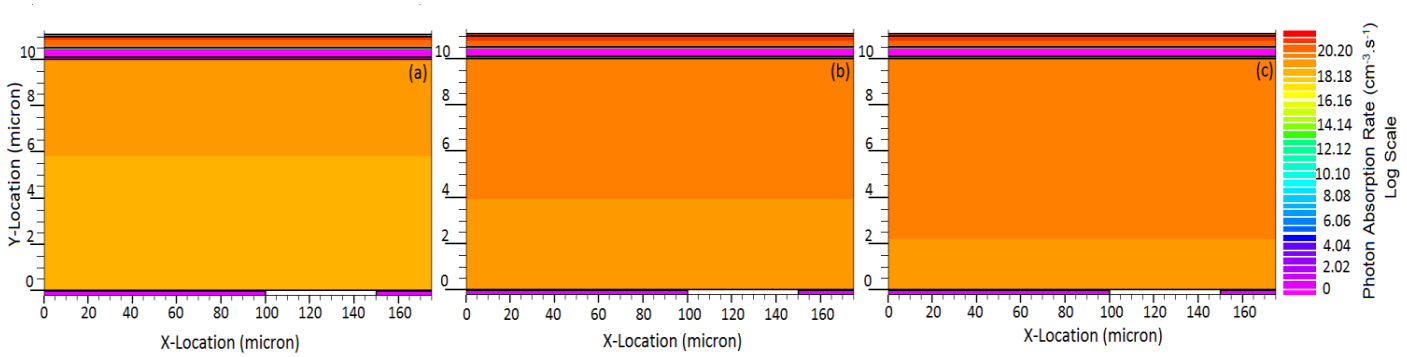

Figure 7 Photon absorption rate ($cm^{-3}.s^{-1}$) in bottom subcell under filtered spectrum by perovskite top subcell, with different x values. (a) x=0, (b) x=0.15, and (c) x=0.25. Regions above 10 µm in Y-locations represents perovskite top filter, and below 10 µm represents bottom IBC-SiGeHJ solar cell.

ACCEPTED MANUSCRIPT

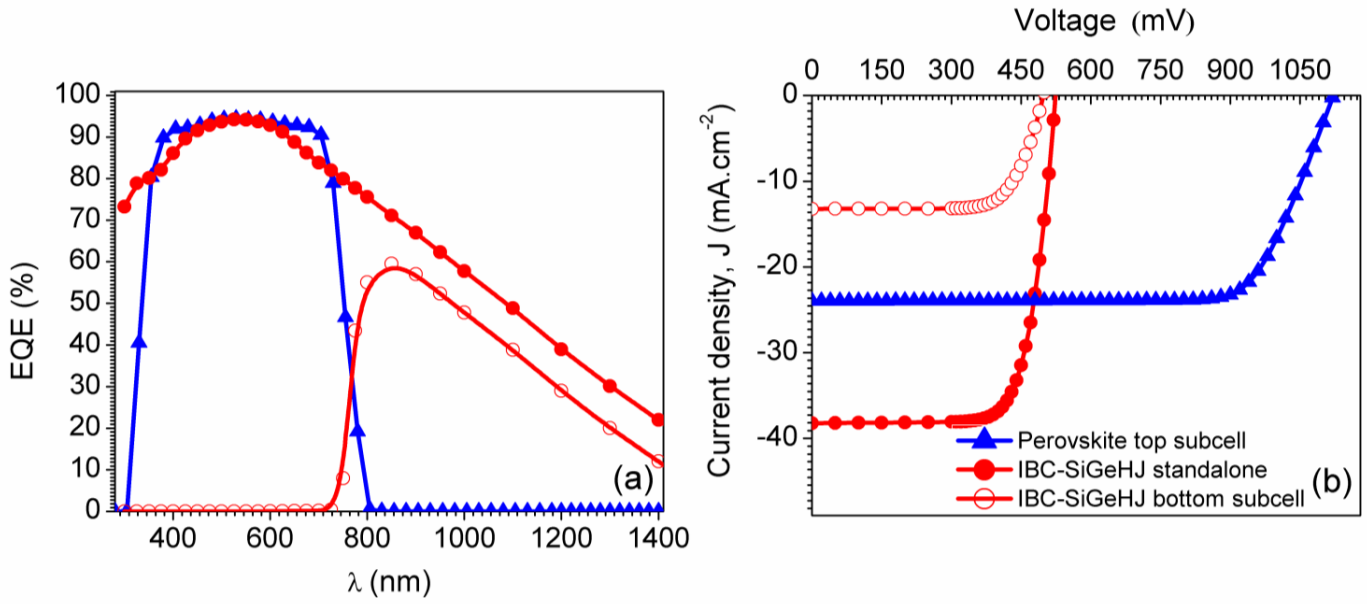

Figure 8. (a) Spectrum response i.e. EQE of perovskite top subcell and IBC-$Si_{0.75}Ge_{0.25}$HJ bottom subcell in tandem and standalone configuration. (b) The J-V curve of top subcell and bottom subcell under illumination.

Asian Journal of Convergence in Technology *Volume III, Issue III*
ISSN No.:2350-1146, I.F-2.71

Object picking using robotic arm mounted with a camera for detection using image processing

Vikas Kumar Singh
Department of Electrical Engineering
Delhi Technological University
Delhi, INDIA
kumarvikas15995@gmail.com

Sugandha Singh
Department of Electronics and Communication
Jaypee Institute of Information Technology
NOIDA, INDIA
sugandha0908@gmail.com

Abstract- **In lieu of making today's world working environment better for humans, the field of robotics has taken up new challenge these days with devices like humanoid type robot which works on human command. Robotic arm is one of the most important parts of the humanoid. In this paper, the design of robotic arm that can be used to pick up objects of given shape and color is described. The robotic arm works with a voice command from user. This arm is realized using servo motor for joints of robotic arm, Bluetooth module, Arduino Uno, MATLAB software and a mounted camera. The designed robotic arm is practically implemented to demonstrate its effectiveness such that it is able to pick objects of given shape and color using voice command from user. The task is completed using control of servo motors via Arduino board/ MATLAB software and a camera.**

Keywords—Bluetooth*; image processing; robotic arm; servo motor; voice control.*

I. INTRODUCTION

Robots suffer major shortcomings because of their limited abilities for manipulation and interaction with human [1]. Human being has always tried to make machine which can behave like human on commands. The world is progressing day by day and we have come up with various types of innovations to make the human dream possible thus making world a better place.

Robot executes different task repeatedly with high precision, thereby many functions like collecting information and studies about the hazardous sites where it is too risky to send human inside [2]. Humanoid robots which seem to be future today is one such innovation which can not only solve daily life problems but can also be helpful in case of calamities. Voice recognition is the process of taking the spoken word as an input to a computer program. This process is important to virtual reality because it provides a fairly natural and intuitive way of controlling the simulation while allowing the user's hands to remain free [3]. One such solution for the common aim is provided in this paper proposing a voice controlled robotic arm which is capable of identifying a structure of given color and shape using artificial intelligence provided. Projects have been made which mainly focuses on how to control or interface the robotic arm by human's voice commands to do a particular task that is to pick an object by detecting and classify it accordingly [4].The voice recognition feature in [3] was improved as user can command arm using only a single instruction. With the development of robotic arm discussed in [4], image processing was introduced and artificial intelligence was implemented for automatic functioning of color and shape detection. This hand can be used to defuse bombs using color detection and many such applications thus saving human resource from danger. The robotic arm consists of servo motors for arm movement, a Bluetooth module with a certain range for real time analysis, a Camera mounted in the claw Arduino Board as brain of the entire working mechanism. The working of the arm starts by taking a voice command from the user then processing it through the Arduino to MATLAB thereby moving the arm using servo motors and serving the purpose to identify the correct figure.

II. MECHANICAL STRUCTURE

The mechanical structure of robotic arm is based on robotic manipulator with similar functionality and design as human arm. The arm consists of 3 links and 4 joints as shown in Fig.1.

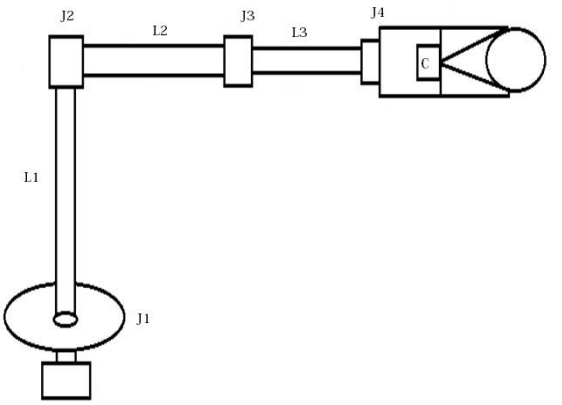

Fig.1 Structure of Robotic arm

A. Joints

The robotic arm consists of four joints which can be seen from Fig.1. The joint J1 namely base joint is analogous to body joint of human which lets them rotate in either direction with 180° rotation similarly the servo motor attached to the base allows whole arm system to move from left to right.

Second joint or J2 is called the shoulder joint which is analogous to shoulder movement of human body; it consists of servo motor which controls the next two joints and camera of the robotic arm.

Elbow joint i.e., J3 is the joint with 180° rotation as possible with human body which connects two links L2,L3 and also controls the position of camera mounted on wrist joint along with claw.

Last joint J4 is called wrist joint which is mounted with a camera and gear coupled claw. The gears move with the movement of servo resulting in opening and closing of claws. The mounted camera C (Fig.1) sends signal to MATLAB which in turn is connected to servo via Arduino for various positions of camera.

Fig.2 Gear coupled claws

B. Links and Claws

From the Fig.1 it can be seen that there are mainly three links in the arm. L1 connects base joint (J1) to shoulder joint (J2); it has been manufactured to withstand torque calculated using [5][6] of all the other links and the camera. It acts like the spinal cord for the whole system.

Now shoulder joint (J2) and elbow joint (J3) are connected via link 2 (L2); its length is less as compared to L1 to reduce the torque acting on J2 for more stability. Third link L3 connects joints elbow joint (J3) to wrist joint (J4).

Claws are coupled to motors through gears Fig.3 then one of the gears is connected to servo motor where clockwise motion of servo results in opening of claw and anti clockwise results in closing of claw thus grabbing the object.

III. ELECTRICAL COMPONENTS

The electronics for making the mechanism running includes Arduino Board, Bluetooth module, Servo motors and camera as shown in Fig.3 Thick arrow shows the data flow via electrical connections of the components. Single lined dual arrow between Arduino and MATLAB represents two way connections simultaneously. Dotted line between servo motor and camera represents mechanical coupling between them.

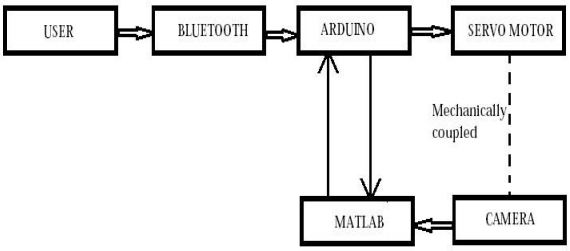

Fig.3 Methodology of robotic arm

A. *Bluetooth module*

Bluetooth is a wireless technology standard for exchanging data over short distances. It uses short-wavelength radio waves in the band from 2.4 to 2.485 GHz, from fixed and mobile devices, and building personal area networks. The module is used for connectivity between the user and the Arduino. The activating command input for the arm is given in the form of voice from the user and then send to Arduino using android application.

B. *Arduino*

The board used for this robotic arm is Arduino UNO. The Uno board consists of a microcontroller based on the ATmega328P. The various factors to choose and work on Arduino include its nominal cost, clear and easy programming and the extensive availability of the hardware as well as the software. Only one UNO board is used for controlling the entire mechanism therefore it acts as the brain of the working structure. The board has taken various controls in the entire process to serve the purpose which includes the process of collecting the command from the user via Bluetooth, then coding the input in a form that is usable by MATLAB and feeding it to the latter, thereafter moving the servos to align the camera with the object of desired color and shape and moving the gears to hold the object finally.

C. *Servo Motors*

These are the actuator that are specialized for high-response, high-precision positioning. It is best known for its capability of accurate rotation angle and speed control . There are 5 servo motors that have been used in the complete robotic arm. Servos are being controlled by the intellect of the arm i.e. the Arduino as per the position of the camera with the object.

D. *Camera*

A camera in today's world is an optical instrument for capturing images that can be stored locally or transmitted to another location for future use. The functioning of the camera in this project is similar to that of a human eye i.e. detecting things around or sensing objects without any physical contact. The task of this device in the arm is locate the instructed object of a specified color and shape so that the geared claws that are being moved with the help of servo and controlled by Arduino, are able to pick the correct object. The camera is connected to MATLAB/Arduino Uno.

IV. IMAGE PROCESSING

The image processing takes place using MATLAB, the flow chart for image processing has been shown in Fig.4. MATLAB has been used for detection of desired object from set of various different objects using image processing. Initially the camera captures the view Fig.5 (a) and is stored in MATLAB and is converted into grayscale image Fig.5 (b). The obtained image is processed for a single color (Red in this case) using RGB filter for red color such that only red objects are visible in binary format Fig.5(c).

Now bounding box and extent function of MATLAB is used for shape detection (square in this case) Fig.5 (d). After the desired object of given shape and color is detected, then centroid of contour is compared to centroid of camera view to calculate position and distance of claw from object and sent to Arduino (dark filled arrow Fig.4).

Thus for various position of camera image is captured and processed until the contour and camera view centroid matches Fig 6(a). Then claw moves forward with the help of servo until the contour covers around 65% of camera view.

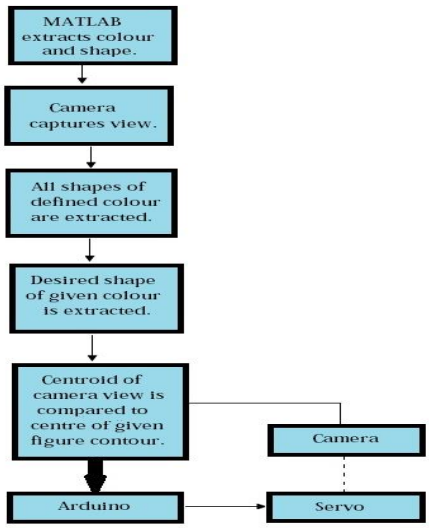

Fig.4 Flow chart of Image Processing

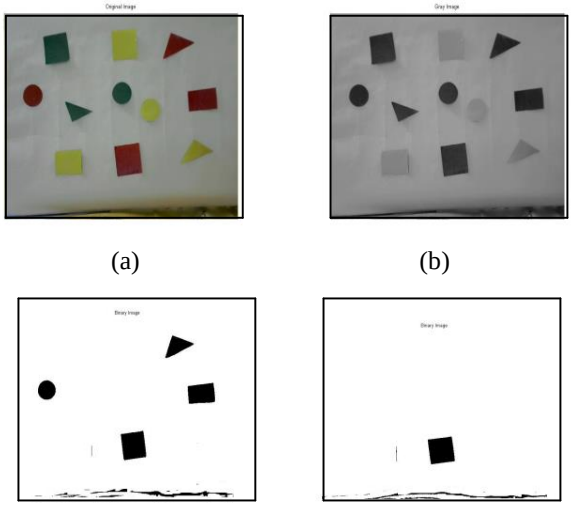

Fig.5 Different levels of image processing
(a)Original Image (b)Grayscale Image
(c)All red objects in binary
(d)Red Square in binary

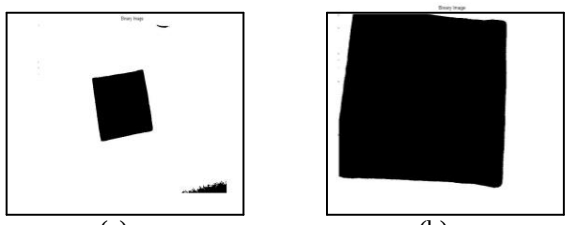

Fig.6 (a) Centroid matching (b) Final image

V. Experimental Implementation of Developed Robotic Arm

A voice controlled robotic arm is designed and developed to identify to a structure of given shape and color. The experimental setup for the same is shown in Fig.7. The developed robotic arm is used to pick object and its working is explained with the help of a flow chart shown in Fig.8. The process is initiated from the voice command given by the user let's say "Red Square" in this case. The voice command goes to Arduino via Bluetooth module. Arduino extracts the words from the received signal "Red", "Square". A code is assigned to this combination which is then sent to MATLAB.

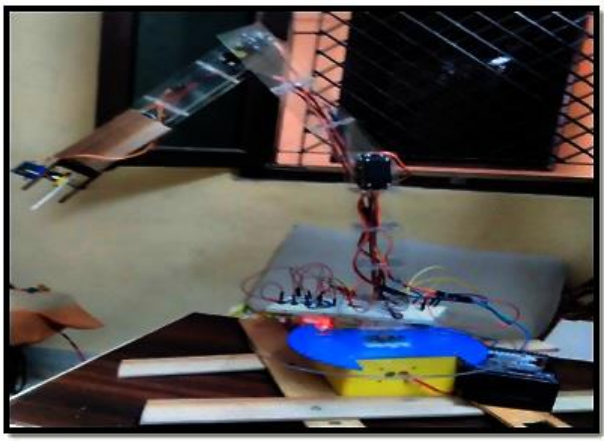

Fig.7 Robotic Arm

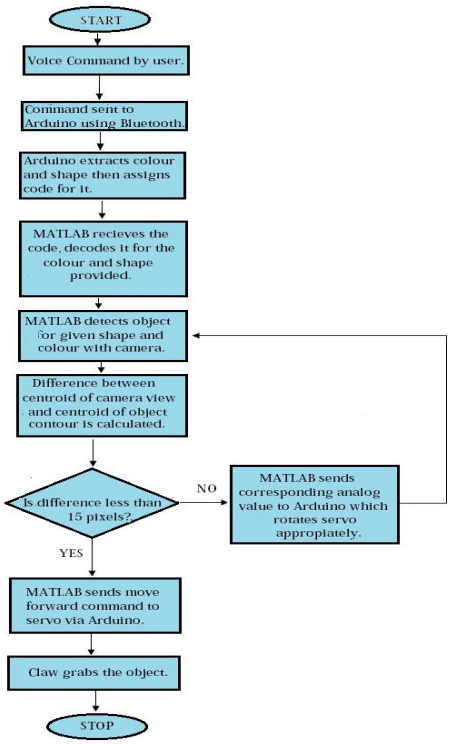

Fig.8 Flow chart of robotic arm working

MATLAB decodes the information received and starts the camera for processing. Camera captures the view and stores it in the form of image which is then converted into grayscale by MATLAB. Appropriate RGB filters are applied for colored detection i.e. Red, such that the next image shows only the red figures from the view. Bounding box and extent method of MATLAB is used for shape detection (i.e. Square).

So, now the new image shows red square in binary format where black represents object and white is the background. Now centroid of object contour is calculated and its difference is calculated from centroid of camera view. The pixel difference is passed on to Arduino in form of analog signal. Arduino moves the servos of joint J1 and J2 in order to reduce the difference between two centroids.

Again, the camera captures image from new position and difference is estimated again until the difference is less than 15 pixels. Now again the difference is sent to Arduino which moves servos from joint 3 & 4, in order to approach the target .Again a new image is captured and sent to MATLAB which calculates the contour area and send command to Arduino when the contour area is more 65% of total area. All the motors stop and grabbing mechanism starts to work.

VI. CONCLUSION

In this paper, a voice controlled object picking based on color and shape robotic arm was implemented practically using Arduino/MATLAB, servo, camera and Bluetooth. The robotic arm works with a voice command from user. The robotic arm is realized using servo motor for joints of robotic arm, Bluetooth module, Arduino Uno, MATLAB software and a mounted camera. The designed robotic arm is experimentally implemented to demonstrate its effectiveness such that it is able to pick objects of given shape and color using voice command from user. This hand can be used to defuse bombs using color detection and many such applications thus saving human resource from danger. The robotic arm consists of servo motors for arm movement, a Bluetooth module with a certain range for real time analysis, a camera mounted in the claw Arduino Board as brain of the entire working mechanism.

REFERENCES

[1] Pramod Arvind Kulkarni , Vaijanath V Yerigeri, "Robot by Haptic Technology", Vol.07,Issue.02, February-2015, Pages:0258-0262,IJATIR
[2] Shyam.R.Nair, Shalini.R.Nair, "Design of a Voice Controlled Robotic Arm for Picking and Placing an Object", Apr. 2012, Vol. 2(4) pp: 670-673, IOSR Journal of Engineering.
[3] Aishwarya Patil, Anilkumar Daharwal, Ankur Harshe, Mohnish Gakare, Monika Sajjanwar, " Haptic Robotic Arm Using Voice & Gesture Recognition", Vol. 2, Issue 3, March 2013, IJARCCE
[4] Vishnu Prabhu S and Dr. Soman K.P, "Voice Interfaced Arduino Robotic Arm for Object Detection and Classification ", Volume 4, Issue 7, July-2013, International Journal of Scientific & Engineering Research
[5] Md. Anisur Rahman, Alimul Haque Khan, Dr. Tofayel Ahmed, Md. Mohsin Sajjad, "Design, Analysis and Implementation of a Robotic Arm- The Animator", Volume-02, Issue-10, pp-298-307, American Journal of Engineering Research (AJER)
[6] Amon Tunwannarux, and Supanunt Tunwannarux, "Design of a 5-Joint Mechanical Arm with UserFriendly Control Program", World Academy of Science, Engineering and Technology 27 2007

Ontology Driven Sentiment Analysis on Social Web for Government Intelligence

Akshi Kumar
Department of Computer Science & Engineering
Delhi Technological University
New Delhi, India
akshikumar@dce.ac.in

Arunima Joshi
Department of Computer Science & Engineering
Delhi Technological University
New Delhi, India
j.arunima@yahoo.com

ABSTRACT
The World Wide Web as a global information medium has evolved radically from the first 'read only web' generation to the next participative- collaborative 'read and write' social web to the intelligent generation of web referred to as Semantic Web, the 'Read Write and Execute Web'. As a novel facet, digital governance intends to ensure and assure that stakeholders (government and citizens) have greater access and control over the governance mechanism which leads to a more transparent, accountable and efficient governance. Social media can be used to facilitate interaction between people and can offer a substantial, unparallel platform for extensive involvement of citizens in the governance measures. We propose using an ontology-based analytics on social media that expounds an intelligent governance model where sentiment can be mined for extracting views of citizens towards government practices, policies, rules and monitoring performance. The idea is to deploy ontology based techniques to determine the subjects/ topics discussed in the tweets, which are related to Ministries of India: their policies, rules, schemes, and analyzing the sentiment (positive, negative and neutral) for tweets retrieved (based on the concepts defined in Ontology). The proposed tool SentIndiGov–O proffers a sentiment analysis application model based on ontologies, where the ontology IndiGov-O is created for "Ministries of Government of India" to reinforce the feature selection task in a Naïve Bayesian classification paradigm. The preliminary results with performance accuracy of ~77% are encouraging and foster the need to exploit hybrid of concept based techniques and machine learning for sentiment analysis.

CCS Concepts
• **Applied computing~E-government**

Keywords
Sentiment Analysis; Digital Governance; Ontology

1. INTRODUCTION
As a global information source, the Web has evolved substantially from the first "read only web" or "static web" generation where there was no user interaction or content contribution to the next "Read and Write Web" or "social or dynamic web" generation which focussed on participation and collaboration of information amongst users, to the absolute intelligent generation of web referred to as Semantic Web, the "Read Write and Execute Web".

Permission to make digital or hard copies of all or part of this work for personal or classroom use is granted without fee provided that copies are not made or distributed for profit or commercial advantage and that copies bear this notice and the full citation on the first page. Copyrights for components of this work owned by others than ACM must be honored. Abstracting with credit is permitted. To copy otherwise, or republish, to post on servers or to redistribute to lists, requires prior specific permission and/or a fee. Request permissions from Permissions@acm.org.

ICEGOV '17 SCII, March 07-09, 2017, New Delhi, AA, India
© 2017 ACM. ISBN 978-1-4503-4930-7/17/03...$15.00
DOI: http://dx.doi.org/10.1145/3055219.3055229

The paradigm shift from Social to Semantic Web has significantly changed the perception of users towards the Internet and the Web. The Social Web (Web 2.0) improves information sharing among the users, the participation and collaboration of users, Semantic Web emphasises on the improvement of structure and representation of data. With the growth of Web 2.0, the way people express their views and opinions has changed prominently, ideas, comments, views, suggestions, feedbacks pertaining to specific and identifiable issues are shared by the users on the social media platforms, such as Facebook, Twitter etc. Sentiment Analysis or Opinion Mining [1], as an intelligent mining technique, helps to capture and determine attitudes, opinions, and emotions from text, speech, and database sources, which correspond to how users retort to a particular issue or event. Sentiment Analysis is a complex task and encompasses several separate tasks, viz: Sentiment Identification; Feature Selection; Sentiment Classification; Sentiment Polarity [1]. The first step in this classification problem is to identify and extract text features. Apposite feature selection techniques in sentiment analysis have a significant role in identifying relevant attributes and increasing the classification accuracy. Due to the high- dimensional, un-structured characteristics of the social media content, this problem of text classification manifolds, thus fostering the need to look for improved techniques for feature selection.

Sentiment analysis has turned out as an exciting new trend in social media with a gamut of practical applications that range from applications in business(marketing intelligence; product and service bench marking and improvement), applications as sub component technology(recommender systems; summarization; question answering) to applications in politics [2]. As a novel facet, digital governance intends to ensure and assure that stakeholders (government and citizens) have greater access and control over the governance mechanism which leads to a more transparent, accountable and efficient governance. Government intelligence has emerged as one radical and potential application for sentiment analysis. The emergence of the social web and the exponential data generated consequently can be analysed to give an intellectual facet to governance. All government organizations can mobilize this social facet of web with a view to reach out to more citizens in order to analyse the reaction of public to grasp the social buzz and retort to issues. It can be used for efficient rule making, by automatically analyzing the opinions of people about pending policies or government-regulation proposals or for tracking the citizen's opinion about a new scheme, predicting the likelihood of the success of a new legislative reform to be introduced and gauging the mood of the public towards a scandal or controversy. Thus, to ensure a greater access and control over the governance

mechanism, the need of the hour is to analyse the opinions of stakeholders (government and citizens) endorsing a transparent, accountable and efficient governance. Social media can be used to facilitate interaction between people and can offer a substantial, unparalleled platform for extensive involvement of citizens in the governance measures. We propose an ontology-based analytics on social media that expounds an intelligent governance model where sentiment can be mined for extracting views of citizens towards government practices, policies, rules and monitoring performance. The idea is to deploy ontology based techniques to determine the subjects/ topics discussed in the tweets, which are related to Ministries of India: their policies, rules, schemes, and analyzing the sentiment (positive, negative and neutral) of tweets retrieved (based on the concepts defined in Ontology). The proposed tool SentIndiGov–O proffers a sentiment analysis application model based on ontologies, where the ontology IndiGov-O [3] is created for "Ministries of Government of India" to reinforce the feature selection task in a Naïve Bayesian sentiment classification paradigm. The work is also a step towards building an intelligent social governance model as proposed in [4]. The preliminary results with performance accuracy of ~77% are encouraging and foster the need to exploit hybrid of concept based techniques and machine learning for sentiment analysis.

The rest of the paper is structured as: Section 2 tells about the related work in direction. Section 3 expounds the specifics of the proposed SentIndigov-O, the ontology based tool for sentiment analysis. Section 4 discusses the results and analysis for Indian Government. Finally, the conclusion is presented in Section 5.

2. RELATED WORK

Pertinent literature review depicts limited use of ontology based methods for sentiment analysis. Kontopoulos et.al. [5] proposed an approach of using ontologies for representing data and for extracting the features based on which tweets are extracted for sentiment analysis of smartphone reviews. The authors have used web service, OpenDover, to classify the tweets with sentiment grade. Iwanaga et.al. [6] presented a method to populate an existing ontology for earthquake evacuation with tweets instances. In their approach, some information related to earthquake like evacuation centers, product offered at the centers, time at which the tweet was posted are extracted. Thakora and Sasib [7] proposed the approach of identifying only the negative comments related to United States Postal Service and performing sentiment analysis on those negative comments. Ontology has been deployed in order to identify the problem area e.g. the deliver type- mail or letter etc. Also, the negative sentiments have been analyzed using SentiStrength tool. Wei and Gulla [8] proposed an approach of building ontology in form of sentiment ontology tree which is in terms of hierarchy defining positive side and negative side. An algorithm was defined to identify sentiments according to the threshold values and weights of the words in the product reviews. Wang et.al. [9] presented methodology in order to classify the product reviews of Chinese products. The reviews were first pre-processed and POS Tagging was performed. Then, fuzzy domain ontology is built by identifying the relationship between features and the reviews. Similarity between sentiment orientation words in reviews and a set of sentiment words in fuzzy domain ontology was then calculated and accordingly polarity was given. Freitas and Renata [10] presented a methodology for analyzing sentiments of Portuguese movie reviews and hotel reviews. It used domain specific ontology for feature extraction and after tagging of the words, SentiWordNet was used to classify the reviews. To our best knowledge, there is no work related to text classification of Twitter posts for Ministries of Government of India: their schemes, policies, rules, regulations etc. Moreover, the initiative of "Digital India" was recently proposed by Government of India, the use of concept based techniques for sentiment analysis is an innovative, pioneer direction of research.

3. SentIndiGov-O: ONTOLOGY BASED TOOL FOR SENTIMENT ANALYSIS

Sentiment Analysis is inherently a text classification problem, as its first and most important step is to identify and extract the precise set of apposite text features. The high- dimensional, un-structured characteristics of the social media manifold this problem, thus fostering the need to look for improved techniques for feature selection. The proposed tool takes advantage of concept based techniques by building an ontology which contains features, their attributes and components, mostly discussed by people who are actively giving opinions on social web. If we have ontology, it is easy and time efficient task to obtain the features desired and their inter-dependencies. The developed ontology is used for extracting the features from a domain for in Sentiment Analysis. Our work intends to accurately cover the topics which are defined by concepts and retrieve the relevant tweets from twitter. These tweets, after pre-processing are classified into positive, negative or neutral, thus accomplishing the sentiment classification task. The basic flowchart of the proposed approach is given in Fig. 1 below.

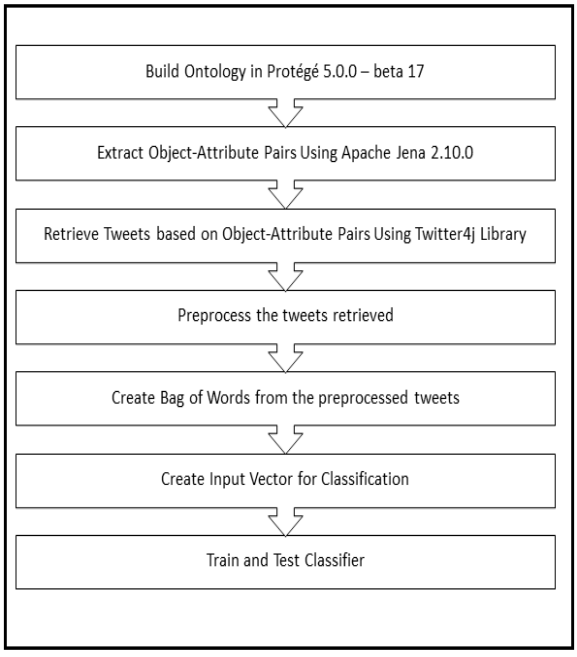

Fig. 1 System Flow

The following steps explain the details of the tool:

Step 1: Building Ontology: The basic building block of semantic web is ontology. So, the development of ontology is the preliminary step. The ontology of Ministries of Government of India, "IndiGov-O" [3], is developed in Protégé 5.0.0 – beta 17. It is a 4-level hierarchy which conceptualizes all the ministries of India, their departments and the functions of the departments. It includes 51 ministries, one independent department and one independent office [11]. This ontology is developed in Web Ontology Language (OWL). The consistency of this ontology model has been validated by the classifiers.

Step 2: Extracting Object-Attribute Pairs: The Web Ontology Language can be manipulated using Apache Jena Library. In order to perform sentiment analysis of Twitter posts, there is an obvious need to extract tweets from Twitter and in order to extract tweets, there is a requirement of some features on which related tweets are extracted. If performed manually, only 1 feature can be used at a time to retrieve tweets. But the use of Apache Jena and ontology easies the process of retrieval of tweets. It triggers the retrieval automatically using not just 1 but a list of features. So, these features in the form of object-attribute pair is extracted from ontology using Apache Jena 2.10.0.

Step 3: Retrieval of tweets: After the feature extraction, tweets are retrieved using Twitter4j library. It is a Java library for the Twitter API.

Step 4: Pre-Processing of Tweets: The tweets retrieved in the previous process needs to be pre-processed for analyzing the sentiments of these tweets. Pre-processing mainly includes removing unwanted things from the lot of tweets which will not do any positive contribution to the sentiment. It includes removing of URL, usernames, additional whitespaces, retweets, converting letters to lowercase, replacing #word with word, deleting stop words, stripping punctuation marks for feature vector.

Step 5: Creating Bag-of-Words: After pre-processing the tweets, in order to create input vector for the classification process, a bag of words is created. Bag of words contains all the words from the tweets. All the duplicated words are removed and so unique set of words is built.

Step 6: Creating Input Vector: After creating bag of words, a vector needs to be created which will serve as input to the classifier. This vector called as input vector depends on the bag of words and the individual tweets. Creation of input vector takes into account the number of the words which are common in each tweet and bag of words.

Step 7: Training and Testing: The classifier used in here is Naïve Bayes Classifier. It uses the input vector as training data and classifies the testing data into three classes i.e. positive, negative and neutral. The distribution of Naïve Bayes used in this work is Gaussian.

4. RESULT AND ANALYSIS

The tool SentIndiGov-O has been trained and tested with 1019 and 503 tweets. This tool has been evaluated by calculating accuracy of the system as how many tweets are correctly classified. The results according to the steps defined in the proposed framework are:

Step 1: Building Ontology:

The ontology IndiGov-O developed using Protégé is shown below:

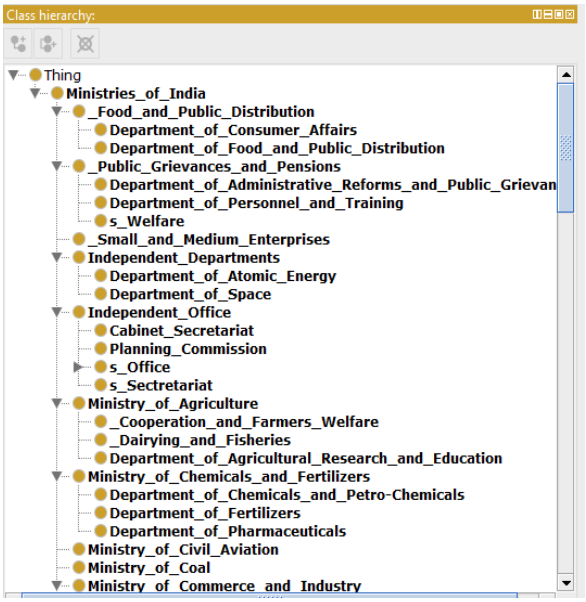

Fig. 2 Ontology for Ministries

The Fig.3 below depicts the OntoGraf illustrating various ministries of India.

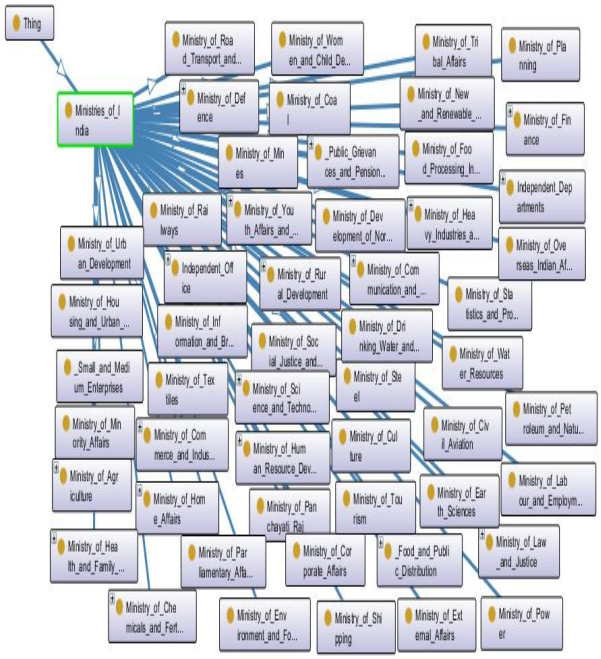

Fig. 3 OntoGraf of Ministries

Step 2: Extracting Object-Attribute Pair:

The following image shows some of the object- attribute pairs extracted from the above ontology.

```
Portals  OpenGovData
Portals  MyGov.in
Portals  India.gov.in
Portals  DigitialIndia
Portals  DiscussionForum
Portals  Contests
Portals  Quiz
Portals  Pillars
Portals  e-Governance
Portals  eKranti
Portals  ITforJobs
Portals  BroadbandHighways
Portals  PublicInternetAccessProgramme
Portals  AccesstoMobileConnectivity
Portals  InformationforAll
Portals  EasilyHarvestProgrammes
Portals  ElectronicsManufacturing
Portals  Blog
Portals  GOIDirectory
Portals  e-governance
Portals  Webcasts
Portals  Calendar
Portals  OnlineServices
Portals  e-greetings
Portals  Poll
Portals  Groups
Portals  Discuss
Portals  Blogs
Portals  Tasks
Portals  MannKiBaat
Ministry_of_Finance  Department_of_Revenue
Ministry_of_Finance  Department_of_Financial_Services
Ministry_of_Finance  Department_of_External_Affairs
Ministry_of_Finance  Department_of_Expenditure
Ministry_of_Finance  Department_of_Disinvestment
Ministry_of_Defence  Department_of_Ex-servicemen_Welfare
```

Fig. 4 Object-Attribute Pair

Step 3: Retrieving Tweets Based on Object-Attribute Pairs:

The following figure shows some of the tweets retrieved from Twitter using Twitter4j:

```
#Opendata should be the default in our gov't. That's why we joined 50 groups in supporting the #OPENGovData Act: https:/…"
 #OPENGovData Act requires federal agencies to publish their info online, using non-proprietary, #opendata formats! https…"
 Want to learn all about the #OPENGovData Act? Explore here: https://t.co/UC15SLhved #opendata https://t.co/p7q7e1rO…"
Does anyone know whether there is a API for election results (not just for the US)? #api #opengov #elections #OPENGovData"
RT @mygovindia: #WomenTransform Story-25: Muskan, being the change at a young age. Support her cause https://t.co/o4qosyy1I6 https://t.co/I…"
 Ecomaterionics shud be followed for rational use &amp;amp; recuperation of resources frm water to grains b4 its too late.\nhttps://t.co/7401TFCA9U"
 RT @NITIAayog: Read about the work of the 25 finalists of Women Transforming India! Vote for them: https://t.co/q0L9lyca2y https://t.co/zEhL"
RT @UNinIndia: 104-yr-old sold her goats to build a toilet &amp;amp; inspired all. Vote 4 Kuwarbai: https://t.co/elcKBBirTi #WomenTransform https:/…"
RT @vijaymaroo: Spl drive for cleanliness in govt offices/ bldgs fr 16-31 May. Photos can be uploaded on https://t.co/bAwiifRqZVn. States mu…"
RT @brijmohanJi: #NaMoDevelopingIndia :Direct Benefit Transfer (DBT) Paradigm-reaching d correct beneficiary. https://t.co/HH2SpUppo7 https…"
RT @mygovindia: This month's #MannkiBaat is on 22nd May.There are multiple ways in which you can contribute: https://t.co/NDuBIyRFwP https:…"
RT @UNinIndia: They said she won't walk. She became an athlete instead! Vote 4 Deepa Malik: https://t.co/elcKBBirTi #WomenTransform https:/…"
RT @mygovindia: #WomenTransform Story-14: Phani Trivedi aims for zero waste! Support her with your vote https://t.co/o4qosyPO6G https://t.c…"
RT @mygovindia: #WomenTransform Story-9: Roshni, one among \"100 women achievers\". Support her with your vote https://t.co/o4qosyPO6G https:…"
RT @mygovindia: #TransformingIndia: Quantum jump in FDI in telecom sector in the last two years. https://t.co/cjKSFPvCUB https://t.co/3oR9H…"
RT @mygovindia: Prime Minister @narendramodi on the #TransformingIndia website - A portal for positive news: https://t.co/O5ULJYpfTZ https:…"
RT @mygovindia: #WomenTransform Story-5: Moriam Toppo,securing land rights. Vote for her on MyGov or via SMS https://t.co/o4qosyPO6G https:…"
RT @mygovindia: #WomenTransform Story-6: Lata Mane,instilling hope for a better tomorrow. Vote for her here https://t.co/o4qosyPO6G https:/…"
RT @mygovindia: #WomenTransform Story-10: Kuwarbai Yadav, an inspiration to us. Vote for her on MyGov  https://t.co/o4qosyPO6G https://t.co…"
RT @mygovindia: #WomenTransform Story-12: Pavithra YS, enabling the disabled. Vote for her on MyGov or SMS https://t.co/o4qosyPO6G https://…"
RT @mygovindia: #WomenTransform Story-13: Naheed Aqueel, transforming many lives. Vote for her here https://t.co/o4qosyPO6G https://t.co/cC…"
RT @mygovindia: #WomenTransform Story-14: Phani Trivedi aims for zero waste! Support her with your vote https://t.co/o4qosyPO6G https://t.c…"
RT @mygovindia: #WomenTransform Story-18: Indiritta,making quality healthcare accessible. Click here to vote https://t.co/o4qosyPO6G https:…"
RT @DONational: #TransformingIndia: Features of #PMUjjwalaYojna launched by PM Modi-LPG to all BPL families. https://t.co/CeDzsAI3Ix https:…"
 #TransformingIndia: Parliament passes bill to repeal additional 1053 redundant laws. https://t.co/cjKSFPNdM9 https://t.co/u…"
#E-Health #Laws And #Regulations #In #India Are #Needed For #Businesses And #Digital #India Project https://t.co/SEUG8kvFPG"
Growth Of Technology Business #In #India Could Be #Impacted If Shortcomings Of Digital #India Project Are #Not Urge https://t.co/NiWMjuY4vI"
RT @sunit_goenka: #eKranti initiative by @_DigitalIndia;led by @srpsrasad; is surely the need of the hour! Digital transformation is certain…"
 RT @MoneyOial: Passport, Pension and OL will be #eDelivered under #eKranti.\n#aadhaarcard #itr #Mumbai\n@ https://t.co/Cd02v1BC2q https://t.c…"
 RT @MoneyOial: Passport, Pension and OL will be #eDelivered under #eKranti.\n#aadhaarcard #itr #Mumbai\n@ https://t.co/Cd02v1BC2q https://t.c…"
RT @FinancialXpress: #DigitalIndia's #eKranti to offer #passports, pension online https://t.co/gzGxk22fMk | https://t.co/3uuGL6OnU6 https:/…"
 Looking Forward to the Passport option.. How different would it be from the existing? @CPVIndia \xed %\xed¹\u008f #EKranti  https://t.co/CwznZ3Haak"
RT @mygovindia: This Mother's Day, share your favourite e-greetings with your mother and make the best design win. Click to share - https:/…"
Congratulations Winners! The results of EGreetings Baisakhi Contest is announced. Check your name on the list. Visit https://t.co/F23DXBdx7G"
fckfckshktimaan: RT @loosebool: #NGOIndia\n4. \" Paul Foundation \" is funding organisation to most of these 71195 NGOII am surprised\xed %\xed.³U can
Check out the National portal of India \nhttps://t.co/OWfNEWFxOv https://t.co/eea4kmblLt"
```

Fig. 5 Tweets Retrieved

Step 4: Pre-Processing the Tweets:

The tweets retrieved above are not pre-processed yet. The following figure shows the tweets after pre-processing phase:

```
opendata default gov't. that's joined 50 supporting opengovdata act
opengovdata act requires federal agencies publish info online, using non-proprietary, opendata formats
learn opengovdata act? explore here: opendata
api election results (not us)? api opengov elections opengovdata
womentransform story-25: muskan, change age. support cause
ecomaterionics shud followed rational &amp recuperation resources frm water grains b4 late
read 25 finalists women transforming india! vote them
104-yr-old sold goats build toilet &amp; inspired all. vote 4 kuwarbai: womentransform
spl drive cleanliness govt offices/ bldgs fr 16-31 may. photos uploaded mu
namodevelopingindia :direct benefit transfer (dbt) paradigm-reaching correct beneficiary
month's mannkibaat 22nd may.there multiple contribute
won't walk. athlete instead! vote 4 deepa malik: womentransform
womentransform story-14 phani trivedi aims zero waste! support vote
womentransform story-9 roshni 100 women achievers support vote
transformingindia: quantum jump fdi telecom sector years
prime minister transformingindia website - portal positive news:
womentransform story-5 moriam toppo,securing land rights. vote mygov via sms
womentransform story-6 lata mane,instilling hope tomorrow. vote
womentransform story-10 kuwarbai yadav, inspiration us. vote mygov
womentransform story-12 pavithra ys, enabling disabled. vote mygov sms
womentransform story-13 naheed aqueel, transforming lives. vote
womentransform story-18 indiritta,making quality healthcare accessible. click vote
transformingindia: features pmujjwalayojna launched pm modi-lpg bpl families.
transformingindia: parliament passes bill repeal additional 1053 redundant laws.
e-health laws regulations india businesses digital india project
growth technology business india impacted shortcomings digital india project urge
ekranti initiative surely hour! digital transformation certain
passport, pension dl edelivered ekranti aadhaarcard itr mumbai
digitalindia's ekranti offer passports pension online |
looking forward passport option existing ekranti
mother's day, share favourite e-greetings mother design win. click share
congratulations winners! results egreetings baisakhi contest announced. check name list. visit
fckfckshktimaan: ngoindia n4 paul foundation funding organisation 71195 ngo i am surprised u check too
check national portal india
ngoindia 1 according govt.india website 71195 ngo's registered partnership scheme
ngoindia 4 paul foundation funding organisation 71195 ngo i am surprised u check too
```

Fig. 6 Pre-processed Tweets

Step 5: Creating Bag of Words:

The list of words created after pre-processing is shown below:

```
opendata
default
joined
supporting
opengovdata
opengovdata
act
requires
federal
agencies
publish
info
online
using
opendata
learn
opengovdata
act
explore
opendata
api
election
results
api
opengov
elections
opengovdata
womentransform
muskan
change
age
support
cause
ecomaterionics
shud
followed
```

Fig. 7 Bag of Words

Total number of attributes in bag is 2872.

Step 6: Creating Input Vector:

The input vector of the tweets thus created is shown:

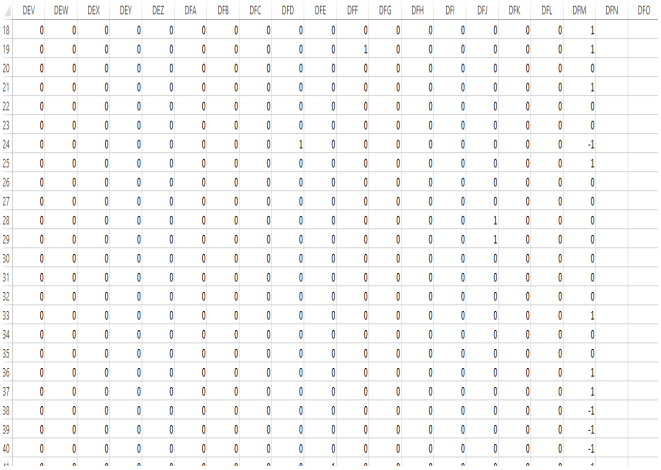

Fig. 8 Input Vector

The last column in above matrix is the sentiment value/ class value given to each tweet (row in above matrix).

Step 7: Training and Testing Classifier:

The following table shows some sample tweets with expected values of sentiments and the predicted values of sentiments as outputs from the classifier.

Table 1 Sample Tweets and their Predicted Values

S. No.	Tweets	Expected Value	Predicted Value
1.	school agarwal vidhya vihar surat guj school launched beti bachao beti padhao providing free education daughters .	1	1
2.	railways ;one iron chair signal lamp record book & loneliness journey...pathetic	-1	-1
3.	women child development director renu phulia 'beti bachao beti padhao': via	0	0
4.	seelampur: india's digital underbelly phones die	-1	0
5.	1.55 lakh pregnant women extended financial assistance janani suraksha yojana 2yrsofgatisheelgujarat Gujarat	1	0
6.	national health mission jish se hume job milta tha wo close ho gaya plzz modiji hume job chahiye homoeopathy dr. job	-1	0

The proposed tool achieved a performance accuracy of ~77%, which was encouraging and demonstrates that novel concept based techniques can further be investigated for improved sentiment analysis. The accuracy of the system calculated using the testing data is shown below:

Fig. 9 Accuracy

5. CONCLUSION

For any government, the stakeholders involved are the government itself and its citizens. Social media can be used to facilitate interaction between people and can offer a substantial, unparalleled platform for extensive involvement of citizens in the governance measures. With the rise of Web 2.0 and its related services and technologies like social networking sites, wikis and blogs, opinion mining has become one of the rapidly growing research area. The recent extensive use of micro-blogging services, especially Twitter, has given a lot of attention to sentiment analysis of micro-blogging posts. Though various machine learning techniques are used to analyze the sentiment of tweets, clear disadvantage appear as each tweet is treated as a uniform sentence and assigned score according to sentiment of the post. The SentIndiGov–O tool proposed in this research exploits ontology based techniques in order to determine the subjects/ topics discussed in the tweets, which are related to Ministries of India: their policies, rules, schemes, and analyzing the sentiment (positive, negative and neutral) of tweets retrieved (based on the concepts defined in Ontology). The tool depicts the integration of features of Semantic web on Web 2.0 (Twitter) for an automated and improved Sentiment analysis process. The preliminary results with performance accuracy of ~77% are encouraging and foster the need to exploit concept based techniques for sentiment analysis. As a potential direction of future work, we intend to explore the use of other machine learning techniques like SVM and Maximum Entropy for the classification of tweets and also optimize the performance by using neural networks and other soft computing techniques. The paradigm can be tested for other Web 2.0 technologies such as Facebook posts and/or comments.

6. REFERENCES

[1] Pang, B. and Lee, L., 2008. Opinion mining and sentiment analysis. *Foundations and trends in information retrieval*, *2*(1-2), pp.1-135.

[2] Kumar, A. and Teeja, M.S., 2012. Sentiment analysis: A perspective on its past, present and future. *International Journal of Intelligent Systems and Applications*, *4*(10), p.1-14, September 2012, MECS Publisher.

[3] Kumar, A. and Joshi, A., 2016. IndiGov-O: An ontology of Indian Government to empower Digital Governance, *India International Conference on Information Processing (IEEE), 2016, Accepted to be published.*

[4] Kumar, A. and Sharma, A., 2016, September. Paradigm shift from E-governance to S-governance. In *The Human Element of Big Data: Issues, Analytics, and Performance, Taylor and Francis, CRC Press*, September 2016.

[5] Kontopoulos, E., Berberidis, C., Dergiades, T. and Bassiliades, N., 2013. Ontology-based sentiment analysis of twitter posts. *Expert systems with applications*, *40*(10), pp.4065-4074.

[6] Iwanaga, I.S.M., Nguyen, T.M., Kawamura, T., Nakagawa, H., Tahara, Y. and Ohsuga, A., 2011, November. Building an earthquake evacuation ontology from twitter. In *Granular Computing (GrC), 2011 IEEE International Conference on* (pp. 306-311). IEEE.

[7] Thakor, P. and Sasi, S., 2015. Ontology-based Sentiment Analysis Process for Social Media Content. *Procedia Computer Science*, *53*, pp.199-207.

[8] Wei, W. and Gulla, J.A., 2010, July. Sentiment learning on product reviews via sentiment ontology tree. In *Proceedings of the 48th Annual Meeting of the Association for Computational Linguistics* (pp. 404-413). Association for Computational Linguistics.

[9] Wang, H., Nie, X., Liu, L. and Lu, J., 2013. A fuzzy domain sentiment ontology based opinion mining approach for chinese online product reviews. *Journal of Computers*, *8*(9), pp.2225-2231.

[10] Freitas, L.A. and Vieira, R., 2013, May. Ontology based feature level opinion mining for portuguese reviews. In *Proceedings of the 22nd International Conference on World Wide Web* (pp. 367-370). ACM.

[11] Ministries of India http://goidirectory.nic.in/union_categories.php?ct=E002

Opportunistic Self Organizing Migrating Algorithm for Real-Time Dynamic Traveling Salesman Problem

Shubham Dokania*, Sunyam Bagga†, and Rohit Sharma‡
*shubham.k.dokania@gmail.com, †sunyambagga@gmail.com, ‡deltechrs2119@gmail.com
†‡Department of Computer Science, *Department of Applied Mathematics
Delhi Technological University
New Delhi, India

***Abstract*—Self Organizing Migrating Algorithm (SOMA) is a meta-heuristic algorithm based on the self-organizing behavior of individuals in a simulated social environment. SOMA performs iterative computations on a population of potential solutions in the given search space to obtain an optimal solution. In this paper, an Opportunistic Self Organizing Migrating Algorithm (OSOMA) has been proposed that introduces a novel strategy to generate perturbations effectively. This strategy allows the individual to span across more possible solutions and thus, is able to produce better solutions. A comprehensive analysis of OSOMA on multi-dimensional unconstrained benchmark test functions is performed. OSOMA is then applied to solve real-time Dynamic Traveling Salesman Problem (DTSP). The problem of real-time DTSP has been stipulated and simulated using real-time data from Google Maps with a varying cost-metric between any two cities. Although DTSP is a very common and intuitive model in the real world, its presence in literature is still very limited. OSOMA performs exceptionally well on the problems mentioned above. To substantiate this claim, the performance of OSOMA is compared with SOMA, Differential Evolution and Particle Swarm Optimization.**

Keywords*—Dynamic Traveling Salesman Problem, Evolutionary Algorithms, Optimization, Self Organizing Migrating Algorithm.

I. Introduction

Optimization is a mathematical process to obtain the best solution out of a pool of certain possible solutions. Over the years, several algorithms inspired from natural phenomena have been proposed to efficiently solve various optimization problems. Evolutionary Algorithms are classified as meta-heuristic search algorithms, where possible solution elements span the n-dimensional search space to find the global optimum solution. These algorithms perform efficiently on various real-world problems. Most of these algorithms involve the creation of new solutions and discard those which fail to produce suitable results. Bacterial Foraging Optimization Algorithm (BFOA) [1] [2] explains a variety of bacterial swarming and social foraging behavior and dictates how foraging should proceed in E. coli. Ant Colony Optimization (ACO) [3] deals with the complex social behavior of ants which provides models for solving difficult combinatorial optimization problems. Particle Swarm Optimization (PSO) is a swarm intelligence algorithm based on the social behavior of a group of individuals such as flocking behavior of birds, school of fishes [4]. These individuals, called particles, move through an n-dimensional search space and share their information in order to find the global optimum. Differential Evolution (DE) is a stochastic, population based meta-heuristic algorithm in which random candidate solutions are generated [5]. SOMA is another evolutionary algorithm which was proposed by Zelinka et al. in 2000 [6]. It follows a cooperative-competitive behavior which differs from other algorithms in its approach to find new solutions. There are various strategies used for SOMA such as All-to-One and All-to-All. In All-to-One approach, the leader acts as a reference point for all other active individuals. In All-to-All approach, each individual moves towards all other agents which may lead to higher computational complexity [7]. All-to-One approach has been considered in this paper.

These nature-inspired algorithms do not yield an exact solution for an optimization problem but a close-to-optimal solution can be achieved. So, there is always scope for improvement in the efficiency of such algorithms. Kusum Deep et al. [8] proposed a binary coded Self Organizing Migrating Genetic Algorithm which is a hybridization of simple binary coded GA with real coded SOMA. Dipti et al. have developed a hybridization of SOMA with Quadratic Approximation crossover operator and Log Logistic mutation operator to maintain the diversity of the population and increase the search capability [9].

Traveling Salesman Problem (TSP) is a well known NP-hard problem in combinatorial optimization which was first studied in the 1930s by Karl Menger in Vienna and Harvard. Dynamic Traveling Salesman Problem is an extension of the traditional TSP which involves dynamic-cost allocation between the cities. This may include, but is not limited to, inclusion and exclusion of certain cities at any given time. It was proposed by Psaraftis [10] in 1988. DTSP is widely applicable in real-time scenarios than TSP but is arguably more difficult to solve. Usually, the algorithms used to solve Static TSP turn out to be inefficient for DTSP. In this paper, a real-time DTSP has been stipulated by using real time traffic data feed from Google Maps [11].

II. Self Organizing Migrating Algorithm

SOMA is based on the cooperation among a population of individuals (agents) where a stochastic search technique is employed for achieving global optimization. It is classified as an evolutionary algorithm; however, no new individuals are created during the search process. The robustness of this algorithm is evident from its fast convergence to the global extreme.

Each iteration in SOMA is called a migration loop, in which each individual locates the best position by competing against other individuals. The individual with the best fitness value becomes the leader and active individuals travel in the search space by following the leader. They exchange information

978-1-5090-4780-2/17/$31.00 ©2017 IEEE

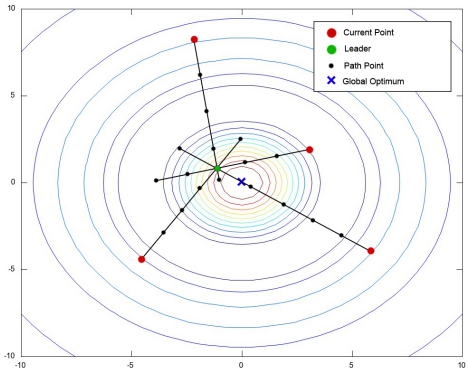

Fig. 1: Movement of individuals in a migration loop in SOMA

(cooperate) to update their leader after each migration loop. Thus, individuals in SOMA follow cooperative-competitive behavior. In each migration loop, all active individuals move towards the leader as shown in Fig. 1. It is a contour plot of how the individuals traverse the search space in a particular migration loop. The black solid points on the path of an individual represent the set of possible positions available in SOMA. The red points represent the current position of the individuals; the leaders position is represented by the green point which influences the path of other individuals. The global optimum is represented by the blue cross. The pseudo code for SOMA is shown in Algorithm 1. Movement of individuals is governed by eq. (1) as shown:

$$x_{i+1} = x_i + (x_L - x_i) * \phi * L \tag{1}$$

$$\phi = \begin{cases} 1, & \gamma < PR \\ 0, & otherwise \end{cases} \tag{2}$$

where, x_i is the current position of the individual,
x_{i+1} is the next position of the current individual,
x_L is the position of the leader,
L is the Path Value or displacement from the initial position for the current individual,
ϕ is the perturbation vector,
PR is the probability of perturbation,
$\gamma \in U(0, 1)$ is a random number from a uniform distribution.

Algorithm 1 Self Organizing Migrating Algorithm

```
procedure START
    Build initial population P.
    Initialize all parameters.
    while termination criteria is not met do
        for each individual x_i in P do
            Evaluate objective Z for x_i.
        end for
        Choose leader using Z.
        for each individual x_i in P do
            Generate φ using (2).
            Update position using (1).
        end for
    end while
end procedure
```

III. Opportunistic Self Organizing Migrating Algorithm

SOMA is a relatively new stochastic optimization algorithm based on the social behavior of cooperating individuals. Active individuals in SOMA move towards the leader based on the value of perturbation vector. In each dimension, they can either move a full step-size or not move at all. In our modified approach, an opportunistic strategy for generating the perturbation vector is proposed. The uniqueness of this algorithm is that it enhances the capability of an individual by providing it with a higher number of choices than SOMA. This allows OSOMA to exploit the search space and thus, yield better solutions. The individuals in OSOMA have their motion governed by a strategy which prohibits them to attain a stationary state. This strategy is quantitatively expressed as shown in eq. (3)

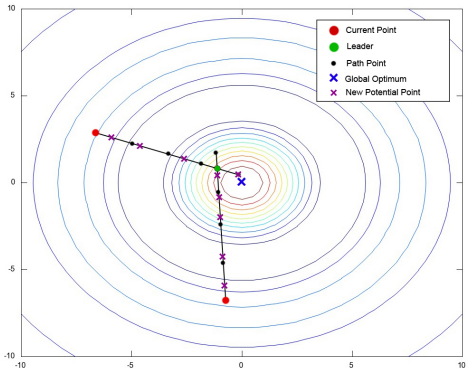

Fig. 2: Movement of individuals in a migration loop in OSOMA

$$x_{i+1} = x_i + (x_L - x_i) * \phi * L \tag{3}$$

$$\phi = \begin{cases} 1, & \gamma < PR \\ \lambda / D_n, & otherwise \end{cases} \tag{4}$$

where, x_i is the current position of the individual,
x_{i+1} is the next position of the current individual,
x_L is the position of the leader,
L is the Path Value or displacement from the initial position for the current individual,
ϕ is the perturbation vector,
PR is the probability of perturbation,
$\gamma \in U(0, 1)$ is a random number from a uniform distribution,
$\lambda \in U(0.60, 0.85)$ is a random number from uniform distribution, where limits have been obtained by experimental analysis,
D_n is the dimensionality of the problem.
The expression λ / D_n returns a small positive value which allows the individual to search through a higher number of potential solutions. D_n is the dimensionality of the objective function which stabilizes the perturbation value. The pseudo code for OSOMA is shown in Algorithm 2.

Fig. 2 is an illustration of how the individuals traverse the search space in a particular migration loop. The solid points on the path of an individual represent the set of possible positions available in SOMA. OSOMA follows the migration loop as shown in eq. (3). The set of crosses represents the new potential positions generated in OSOMA which were not available to individuals in SOMA. This set represents a particular case and these crosses can be present anywhere along the direction

Algorithm 2 Opportunistic Self Organizing Migrating Algorithm

```
procedure START
    Build initial population P.
    Initialize all parameters.
    while termination criteria is not met do
        for each individual x_i in P do
            Evaluate objective Z for x_i.
        end for
        Choose leader using Z.
        for each individual x_i in P do
            Generate φ using (4).
            Update position using (3).
        end for
    end while
end procedure
```

of traversal. Hence, the proposed algorithm allows individuals to effectively exploit the given search space. The number of dimensions plays an important role in this approach. When the number of dimensions increases, the average perturbation value returned decreases. Hence, performance of OSOMA approaches that of SOMA at higher dimensions.

IV. Real-Time Dynamic Traveling Salesman Problem

Traveling Salesman Problem is an intensively studied problem in graph theory, and is used as a benchmark for various optimization problems. The problem statement for the Traveling Salesman Problem is as follows: "A traveling salesman has to find the shortest tour to visit N number of cities, with each city being visited exactly once except the first city, which is visited twice.". It belongs to the class of NP-Hard problems and no effective solution method is yet known for the general case.

Real Time Dynamic Traveling Salesman Problem is an extension of the Traveling Salesman Problem where the cost matrix is time-varying. The cost of traveling from city i to city j changes with time or with an addition of a new city in the network. The expression for the dynamic cost matrix is given in eq. (5).

$$D(t) = [d_{ij}(t)] \tag{5}$$

where,
$D(t)$ represents the time dependent cost matrix,
$d_{ij}(t)$ represents the cost to travel from city i to city j as a function of time t.

In real-world, external factors such as traffic may lead to a change in the traveling time of the salesman. Hence, the cost matrix is dynamically updated resulting in an even more complex problem than the Traveling Salesman Problem. The dynamic nature of this problem requires a continuous evaluation due to the updates in the cost matrix. The path to be followed by the salesman is dynamic in nature i.e. bound to change continuously.

OSOMA has been applied on real-time DTSP using a special type of encoding proposed by Hadia et al. [12]. They introduced a new concept of Swap Operations to solve the city routing problem. This concept has been used in the application of OSOMA on real-time DTSP. Their concept of swap is presented with the help of an example:

Let M represent a possible tour, then $N = M \oplus MO(i, j)$ provides a new tour generated on application of operator $MO(i, j)$. For example:
Let $M = (3, 4, 5, 6, 8)$.
Then, $M' = M \oplus MO(2, 3) = (3, 4, 5, 6, 8) \oplus MO(2, 3) = (3, 5, 4, 6, 8)$
A Swap Sequence can be defined as the sequence of Swap Operators.
Let $A = (5, 6, 7, 8, 9)$ and $B = (6, 7, 5, 9, 8)$.
As $A(1) = B(3) = 5$, so first swap operation will be $MO(1, 3)$; $B' = B \oplus MO(1, 3) = (5, 7, 6, 9, 8)$
Now, $A(2) = B(3) = 6$, so second swap operation will be $MO(2, 3)$; $B'' = B' \oplus MO(2, 3) = (5, 6, 7, 9, 8)$.
Now, $A(4) = B(5) = 8$, so third swap operation will be $MO(4, 5)$; $B''' = B'' \oplus MO(4, 5) = (5, 6, 7, 8, 9)$
Hence, the final Swap Sequence $MM = A - B = [MO(1, 3), MO(2, 3), MO(4, 5)]$.
Using the above encoding method, the migration loop update equation of OSOMA (3) can be rewritten as follows:

$$x_{i+1} = x_i \oplus (x_L - x_i) * \phi * L \tag{6}$$

Where,
$\oplus$ and $-$ are the operators as shown in the above example, and the rest of parameters are same as in (3). The value obtained from $\phi * L$ is used to model the probability which picks the elements from $(x_L - x_i)$ to participate in the sequence update procedure, hence making $\phi * L$ a probabilistic decision factor.

V. Results and Discussions

All the evaluations were performed in python (2.7.6) using Scipy and Numpy [13] frameworks for scientific computations and Matplotlib [14] package for graphical representation of the results. This section has been divided into two subsections: V-A discusses the results obtained on standard benchmark test functions, V-B presents the results obtained on applying OSOMA to real-time DTSP.

A. Standard benchmark Test Functions

Table I [15] lists the test functions under consideration. It should be noted that all test functions have a global minima of 0.0 except Easom which has a global minimum of -1.0. Tables II and III show the average values obtained for these functions by OSOMA, SOMA, PSO and DE. The results have been obtained for dimensions $(d = 2, 5)$. Although OSOMA works on higher dimensions as well, only lower dimensions have been taken into account due to the nature of real-time DTSP under consideration.

Table II shows the results of considered algorithms on 11 two-dimensional test functions. SOMA, DE and PSO fail to converge to global minima in many cases while OSOMA attains the optimum value each time. In f2 test function, SOMA fails to converge to global optimum (attaining $4.365e-16$) while OSOMA achieves 0.0. Similarly, all the other algorithms are outperformed by OSOMA. In f3, DE, PSO and OSOMA get stuck at the same local minima with value $1.183e-30$ as shown in Table III. Here, SOMA is also stuck at a local minimum but with a worse value. This is because f3 is a relatively complex multimodal minimization test function.

The graphs in Fig. 3 show the objective value attained in initial iterations by PSO, DE, SOMA and OSOMA on f1 for

TABLE I: Test Functions

Name	Problem Function	Interval
Sphere (f1)	$f(x) = \sum_{i=1}^{d} x_i^2$	$[-5.12, 5.12]$
Ackley (f2)	$f(x) = -20\exp(-0.2\sqrt{\frac{1}{a}\sum_{i=1}^{d} x_i^2}) - \exp(\frac{1}{a}\sum_{i=1}^{d}\cos(cx_i)) + 20 + e$	$[-32, 32]$
Qing (f3)	$f(x) = \sum_{i=1}^{d}(x_i^2 - i)^2$	$[-500, 500]$
3^{rd} De Jong (f4)	$f(x) = \sum_{i=1}^{d} \lvert x_i \rvert$	$[-2.048, 2.048]$
4^{th} De Jong (f5)	$f(x) = \sum_{i=1}^{d} ix_i^4$	$[-1.28, 1.28]$
Rosenbrock (f6)	$f(x) = \sum_{i=1}^{d}[100(x_{i+1} - x_i^2)^2 + (x_i - 1)^2]$	$[-100, 100]$
Schwefel (f7)	$f(x) = (\sum_{i=1}^{d} x_i^2)^{\pi}$	$[-100, 100]$
Booth (f8)	$f(x) = (x + 2y - 7)^2 + (2x + y - 5)^2$	$[-5, 5]$
Matyas (f9)	$f(x) = 0.26(x_1^2 + x_2^2) - 0.48x_1x_2$	$[-10, 10]$
Easom (f10)	$f(x) = -\cos(x_1)\cos(x_2)\exp(-(x_1 - \pi)^2 - (x_2 - \pi)^2)$	$[-100, 100]$
Bohachevsky (f11)	$f(x) = x_1^2 + 2x_2^2 - 0.3\cos(3\pi x_1) - 0.4\cos(4\pi x_2) + 0.7$	$[-100, 100]$

TABLE II: Objective Function Value of DE, PSO, SOMA, OSOMA for $D_n = 2$

Function	DE	PSO	SOMA	OSOMA
f1	9.355e-155	6.738e-146	4.409e-144	0.0
f2	0.0	0.0	4.365e-16	0.0
f3	0.0	1.972e-31	1.131e-270	0.0
f4	3.077e-77	6.182e-59	8.073e-43	0.0
f5	9.815e-298	1.747e-235	1.131e-270	0.0
f6	0.0	1.573e-10	0.0	0.0
f7	1.196e-271	1.317e-205	2.854e-270	0.0
f8	0.0	0.0	0.0	0.0
f9	6.187e-66	3.182e-120	2.162e-144	0.0
f10	0.0	0.0	0.0	0.0
f11	-8.11e-05	-1.0	-1.0	-1.0

dimensions $d = 2, 5$. It can be seen that the convergence rate of DE is the worst among considered algorithms. OSOMA reaches the optimal value of 0.0 each time and at a considerably faster rate than the other algorithms. Hence, the accuracy of OSOMA is substantially higher than that of PSO, DE and SOMA as seen in Tables II and III. This can be attributed to the opportunistic nature of perturbations generated in OSOMA which enhances the ability of an individual to explore the search space efficiently. It is evident from the discussion above that OSOMA performs well as compared to the other algorithms.

TABLE III: Objective Function Value of DE, PSO, SOMA, OSOMA for $D_n = 5$

Function	DE	PSO	SOMA	OSOMA
f1	2.654e-86	5.648e-86	3.031e-77	0.0
f2	0.0	7.395e-11	6.579e-12	3.552e-15
f3	1.183e-30	1.183e-30	8.221e-25	1.183e-30
f4	7.821e-57	1.867e-43	1.326e-08	2.436e-60
f5	1.782e-136	3.778e-162	4.495e-163	0.0
f6	5.784e-04	7.858e-02	1.693e-06	2.288e-04
f7	7.809e-196	1.081e-148	3.396e-103	0.0

B. Real-Time Dynamic Traveling Salesman Problem

Dynamic Traveling Salesman Problem has been studied extensively in the past. A real-time DTSP deals with a dynamic

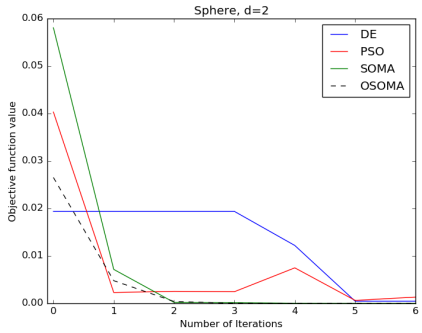

(a)

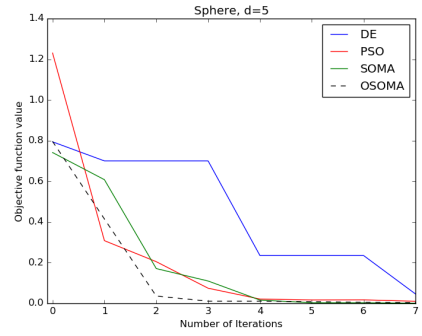

(b)

Fig. 3: Objective function value vs. Number of iterations for $f1$ in: (a) $D_n = 2$, (b) $D_n = 5$

cost matrix depending on conditions such as: Addition of new cities to the tour, Change in the 'cost' to travel from one city to another etc. The comprehensive discussion in this section covers the above-mentioned conditions. In the Initial Case, the graph is initialised with 11 cities as shown in Fig. 4a. In Case 1, a new city is added to the graph while the salesman has partially completed his tour. Case 2 considers the possibility of a change in cost incurred to travel from one location to another.

1) Initial Case: The initial case is analogous to the Static Traveling Salesman Problem. OSOMA, SOMA, DE and PSO

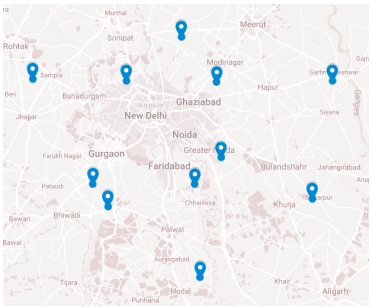

(a) Initial set of 11 cities.

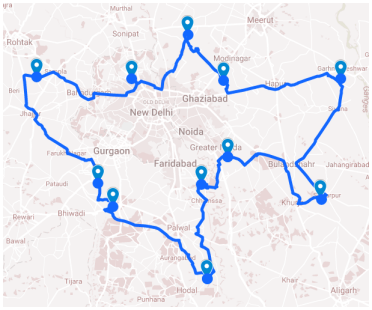

(b) Optimal Tour for the 11 cities.

Fig. 4: Maps depicting initial set of 11 cities and its optimal path

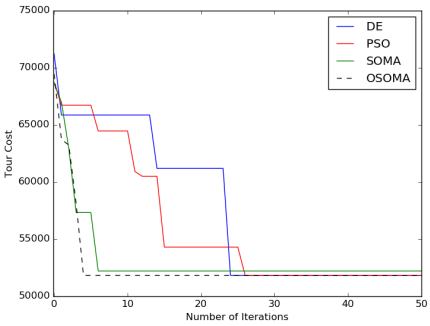

Fig. 5: Tour cost vs. Number of iterations for initial set of 11 cities (for 50 iterations).

are applied on this set of 11 cities and the numerical results obtained have been presented in Table IV. OSOMA outperforms the other meta-heuristics considered as it reaches the optimal value in just 4 iterations while the other algorithms take more than 20 iterations. Fig. 4b shows the final optimal tour for this set of 11 cities. Fig. 5 depicts the tour cost of each algorithm as a function of the number of iterations.

2) Case I: In this case, a new city is added to the tour while the salesman is traveling. When the salesman was at city (shaded red), a new city (shaded green) is added to the initial set of 11 cities as can be seen in Fig. 6a. This results in an update in the cost matrix. Now, the salesman needs to take this change into account and re-evaluate the possible tours in order to find the new optimal tour. The opportunistic nature of OSOMA enables it to better adapt to this change as compared to SOMA, PSO and DE. This is evident from the numerical values in Table V. Fig. 6b presents the new optimal tour found for this augmented set of 12 cities. Fig. 7 depicts the tour cost of each algorithm as a function of the number

TABLE IV: Tour Cost of DE, PSO, SOMA, OSOMA as a function of Number of Iterations

Iterations	SOMA	DE	PSO	OSOMA
0	68701	71224	68725	69459
5	57332	65869	66728	51837
10	52214	65869	64473	51837
15	52214	61196	54307	51837
20	52214	61196	54307	51837
25	52214	51837	54307	51837
30	52214	51837	51837	51837
35	52214	51837	51837	51837
40	52214	51837	51837	51837
45	52214	51837	51837	51837

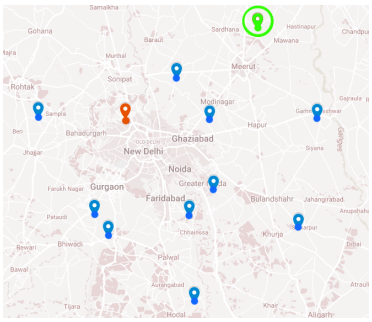

(a) Augmented set of 12 cities.

(b) Optimal Tour for the 12 cities.

Fig. 6: Maps depicting augmented set of 12 cities and its optimal tour.

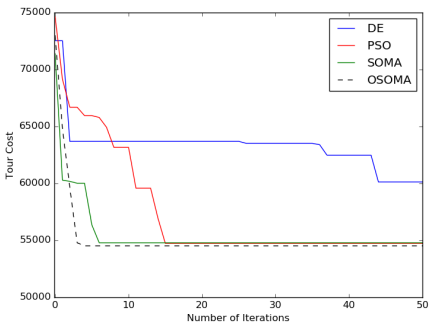

Fig. 7: Tour cost vs. Number of iterations for augmented set of 12 cities (For 50 iterations).

of iterations. It can be easily seen that OSOMA attains the optimal value in only 3 iterations. This substantiates the claim

that OSOMA achieves a higher accuracy solution at a faster speed as compared to the other algorithms.

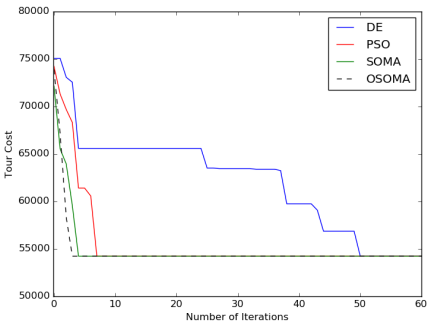

Fig. 8: Tour cost vs. Number of iterations for augmented set of 12 cities (for 60 iterations).

TABLE V: Tour Cost of DE, PSO, SOMA, OSOMA as a function of Number of Iterations (Case I)

Iterations	SOMA	DE	PSO	OSOMA
0	71390	72531	74650	73011
5	56364	63697	65959	54526
10	54794	63697	63168	54526
15	54794	63697	54741	54526
20	54794	63697	54741	54526
25	54794	63697	54741	54526
30	54794	63523	54741	54526
35	54794	63523	54741	54526
40	54794	62484	54741	54526
45	54794	60133	54741	54526
50	54794	60133	54741	54526

TABLE VI: Tour Cost of DE, PSO, SOMA, OSOMA as a function of Number of Iterations (Case II)

Iterations	SOMA	DE	PSO	OSOMA
0	72162	75078	74234	73913
5	54237	65590	61412	54237
10	54237	65590	54237	54237
15	54237	65590	54237	54237
20	54237	65590	54237	54237
25	54237	65590	54237	54237
30	54237	63519	54237	54237
35	54237	63462	54237	54237
40	54237	63396	54237	54237
45	54237	59754	54237	54237
50	54237	56867	54237	54237
55	54237	54237	54237	54237

3) Case II: This case considers the possibility of dynamic changes in the cost between any two cities, leading to an updation in cost matrix. Now, the salesman needs to take this change into account and re-evaluate the possible tours in order to find the new optimal tour. Table VI presents the performance of the considered algorithms with updated edge costs. The final optimal tour attained is the same as shown in Fig. 6, while the tour cost changes owing to the dynamic nature of the cost-matrix, as reflected in Table VI. Opportunistic nature of OSOMA allows it to adapt to this change in cost matrix efficiently. This is evident from Fig. 8 where OSOMA is able to reach the global minima in only 3 iterations. It should be noted that the optimal value attained has changed from 51,837 (in the Initial Case) to 54,237 (in this case).

VI. Conclusion

SOMA is one of the most recent evolutionary optimization algorithms. A modified SOMA- Opportunistic SOMA has been presented which introduces a novel strategy to generate perturbations. This strategy enhances the capability of an individual by providing it with a higher number of choices than SOMA. This allows OSOMA to exploit the search space to a greater extent and thus, yield better solutions. It has been tested on several unconstrained benchmark test functions. The numerical results clearly show that OSOMA outperforms the other metaheuristic algorithms under consideration. The application of OSOMA on real-time DTSP further substantiates this claim. However, each algorithm has its own limitations and cannot be universally accepted to perform well on all optimization problems. Hence, in future work, it is intended to further improve the performance of this algorithm and apply it to various other practical problems.

References

[1] G. C. Onwubolu and B. Babu, *New optimization techniques in engineering*. Springer, 2013, vol. 141.

[2] K. M. Passino, "Biomimicry of bacterial foraging for distributed optimization and control," *IEEE control systems*, vol. 22, no. 3, pp. 52–67, 2002.

[3] M. Dorigo and T. Stützle, "Ant colony optimization: overview and recent advances," in *Handbook of metaheuristics*. Springer, 2010, pp. 227–263.

[4] R. C. Eberhart, J. Kennedy *et al.*, "A new optimizer using particle swarm theory," in *Proceedings of the sixth international symposium on micro machine and human science*, vol. 1. New York, NY, 1995, pp. 39–43.

[5] R. Storn and K. Price, *Differential evolution-a simple and efficient adaptive scheme for global optimization over continuous spaces*. ICSI Berkeley, 1995, vol. 3.

[6] I. Zelinka and J. Lampinen, "Soma - self organizing migrating algorithm," in *Proceedings of the 6th International Mendel Conference on Soft Computing*. Brno, Czech Republic, 2000, pp. 177–187.

[7] P. Kadlec and Z. Raida, "A novel multi-objective self-organizing migrating algorithm," *Radioengineering*, vol. 20, no. 4, pp. 804–816, 2011.

[8] K. Deep *et al.*, "A new hybrid self organizing migrating genetic algorithm for function optimization," in *2007 IEEE Congress on Evolutionary Computation*. IEEE, 2007, pp. 2796–2803.

[9] D. Singh and S. Agrawal, "Log-logistic soma with quadratic approximation crossover," in *Computing, Communication & Automation (ICCCA), 2015 International Conference on*. IEEE, 2015, pp. 146–151.

[10] H. N. Psaraftis, "Vehicle routing: Methods and studies," *Dynamic Vehicle Routing Problems. North Holland, Amsterdam, The Netherlands*, pp. 223–248, 1988.

[11] Google, "Google maps api, accessed on august 2016," *http://code.google.com/apis/maps/*, Accessed on August 2016.

[12] S. K. Hadia, A. H. Joshi, C. K. Patel, and Y. P. Kosta, "Solving city routing issue with particle swarm optimization," *International Journal of Computer Applications*, vol. 47, no. 15, 2012.

[13] S. Van Der Walt, S. C. Colbert, and G. Varoquaux, "The numpy array: a structure for efficient numerical computation," *Computing in Science & Engineering*, vol. 13, no. 2, pp. 22–30, 2011.

[14] J. D. Hunter *et al.*, "Matplotlib: A 2d graphics environment," *Computing in science and engineering*, vol. 9, no. 3, pp. 90–95, 2007.

[15] S. Surjanovic and D. Bingham, "Virtual library of simulation experiments: test functions and datasets," *Simon Fraser University, in: http://www. sfu. ca/~ ssurjano/optimization. html [Links]*, 2013.

Accepted Manuscript

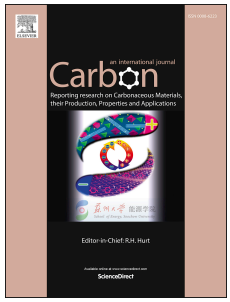

Optical effective mass of photon in single and bilayer graphene in 10 MHz–26.5 GHz frequency range

Kamlesh Patel, Pawan K. Tyagi

PII: S0008-6223(17)30505-5

DOI: 10.1016/j.carbon.2017.05.057

Reference: CARBON 12033

To appear in: *Carbon*

Received Date: 11 February 2017

Revised Date: 23 April 2017

Accepted Date: 16 May 2017

Please cite this article as: K. Patel, P.K. Tyagi, Optical effective mass of photon in single and bilayer graphene in 10 MHz–26.5 GHz frequency range, *Carbon* (2017), doi: 10.1016/j.carbon.2017.05.057.

This is a PDF file of an unedited manuscript that has been accepted for publication. As a service to our customers we are providing this early version of the manuscript. The manuscript will undergo copyediting, typesetting, and review of the resulting proof before it is published in its final form. Please note that during the production process errors may be discovered which could affect the content, and all legal disclaimers that apply to the journal pertain.

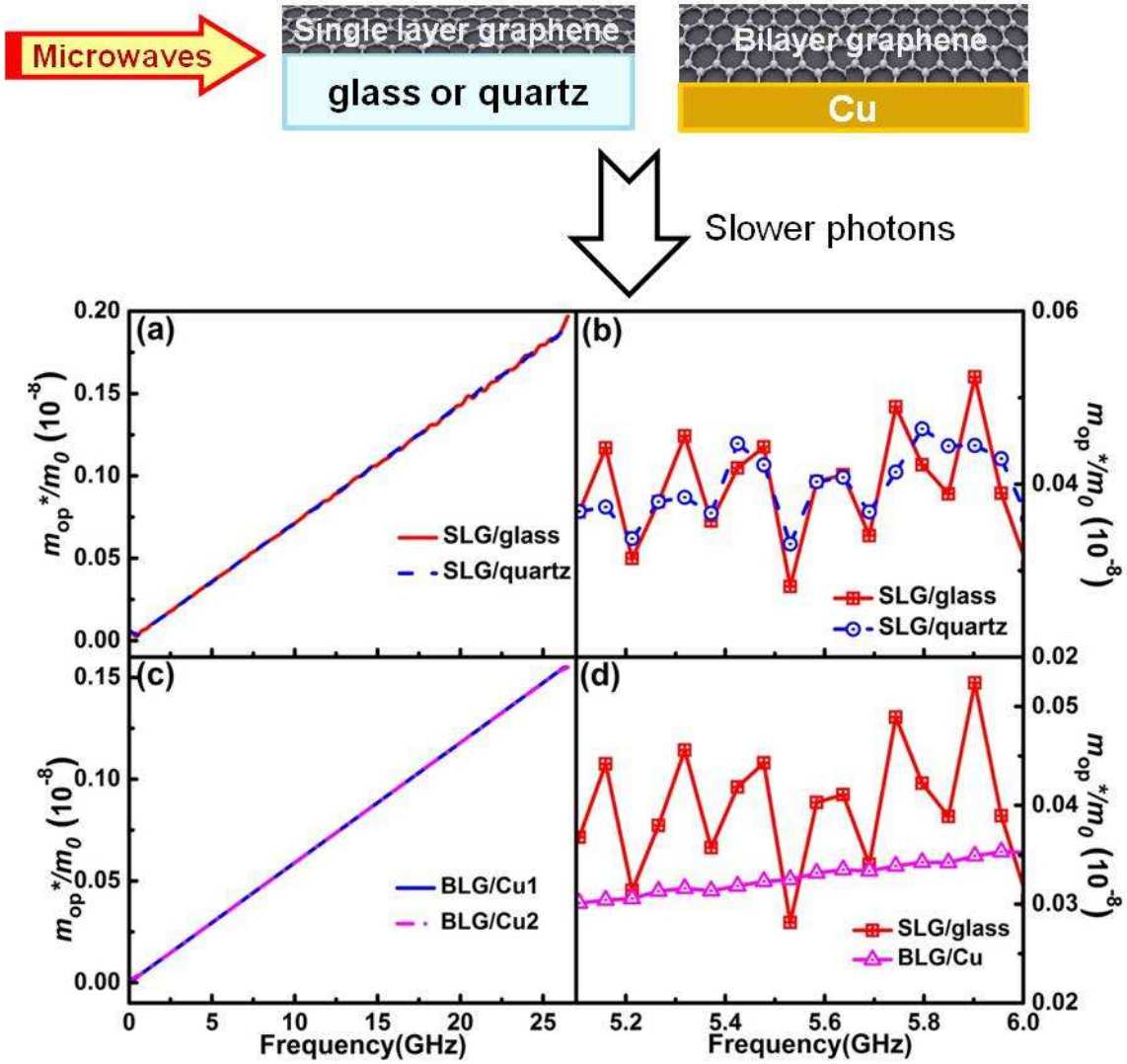

Photon's effective mass

ACCEPTED

ACCEPTED MANUSCRIPT

Optical effective mass of photon in single and bilayer graphene in 10 MHz to 26.5 GHz frequency range

Kamlesh Patel[1,2] and Pawan K. Tyagi[1#]

[1]Department of Applied Physics, Delhi Technological University, Delhi 110042, India

[2]Department of Electronic Science, University of Delhi South Campus, New Delhi 110021, India

Abstract

The present study has been carried out to experimentally determine the optical effective mass of photon in single layer graphene transferred on glass and quartz substrates, and bilayer graphene as-grown on Cu foil. Measurements have been performed in microstrip line based test fixture where first real and imaginary parts of complex relative permittivity have been obtained, then the refractive index is used to estimate the phase velocity in single and bilayer graphene, this index were found to be higher at lower frequency below 1.5 GHz. The phase velocities are found to be ~ 1.04×10^8 ms^{-1} and ~ 1.11×10^8 ms^{-1} in single and bilayer graphene, respectively and little high group velocities are found in range of 2 to 26.5 GHz. In single and bilayer graphene, the optical effective mass has been found to vary from ~ 0.72×10^{-10} m_0 to ~ 0.2×10^{-8} m_0 in a frequency range between 1 and 26.5 GHz. We envision that reported results can help to understand the transport behaviour of photons in as-grown graphene layer in microwave frequency range.

Keywords: Graphene, optical effective mass, dispersion, microwave absorption, group and phase velocity.

Email: pawankumartyagi@gmail.com, pawan.phy@dce.edu (Pawan K. Tyagi)

1. Introduction

In recent reports, it has been reported that few layer graphene (FLG) exhibits carrier mobility as high as 10^5 $cm^2V^{-1}s^{-1}$ at room temperature [1], controllable sheet resistance from 100 to 8.8 Ω/sq (ohms per square), sheet carrier density as high as 8.9×10^{14} cm^{-2} and carrier mean free path as large as ~0.6 μm [2], impressive flexibility and controllable conductivity. Furthermore, graphene is considered as a massless and gapless Dirac quasi-particle system with rough linear energy dispersion [3]. These outstanding properties make the graphene a potential candidate for application in sensors to terahertz (THz) devices. Recently, occurrence of anomalous dispersion in single layer graphene has been reported by determining effective relative permittivity, phase velocity and group velocity of the multilayer microstrip line [4]. Previously, strong anomalous optical dispersion was also reported with the complex refractive index $\tilde{n} = 2.98 - 1.44\hat{\imath}$ for single layer graphene (SLG) and around $\tilde{n} = 2.7 - 1.45\hat{\imath}$ for bilayer graphene (BLG) at 633 nm using Picometrology [5]. In further advances, anomalous dispersion has also been probed by using the broadband spectrophotometery and spectroscopic ellipsometry [6, 7]. It was reported that anomalous dispersion occurred due to interparticle interaction, impurities, lattice deformation [8]. Till date, only effective electron mass (m_e^*) was reported to be $0.012\, m_0$ [3] and $0.041\, m_0$ [9] in single layer and bilayer graphene, respectively using Shubnikov-de Hass (SdH) oscillations, where free electron mass (m_0) is 9.107×10^{-31} kg. Recently, Ariel and Natan [10] have presented a theoretical method to calculate the particle effective mass in graphene considering wave-particle duality and semi-classical definition of the particle momentum. In the present work, in order to experimently deduce the optical effective mass we have studied both single or bilayer graphene exhibiting roughly linear dispersion and determined the in-plane optical effective mass of photon in these as-grown layer in the microwave frequency range. This

is achieved by systematically evaluating the effective mass taking the phase and group velocity into account. In order to determine these velocities, first complex relative permittivity and complex refractive index have been obtained by characterizing the graphene using microstrip line measurement. Observed variations in effective mass with frequency are discussed which might be helpful to understand the interactions of electron and impurities under microwave exposure.

2. Experimental Section

2.1 Single and double layer graphene samples

In the present study, single layer graphene transferred on both glass and quartz of thickness 0.7 mm and 1.0 mm, respectively having area 1″×1″ were used which was procured from Graphene Industries, USA. Bilayer graphene was grown by using Hot Filament Chemical Vapor Deposition (HFCVD) System. Commercially available Cu sheet with a thickness of 25 μm were cut into 1/2″×1/4″ pieces to be used as substrate. Initially, Cu foil was ultrasonicated in acetone for 10 min, acetic acid for 10 min, and then washed with DI water. After drying the foil, it was placed in the chamber. Schematic presenting the process parameters has been shown in **Fig.1**.

ACCEPTED MANUSCRIPT

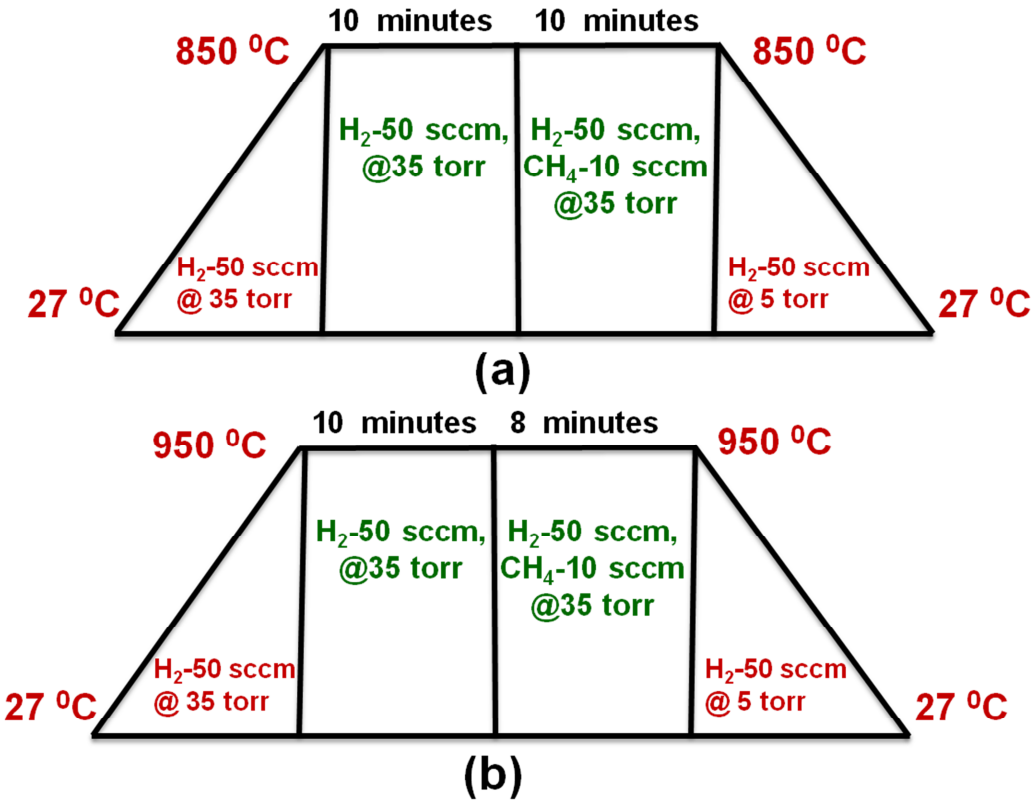

Figure. 1. Schematic diagram of the process parameters for (a) BLG/Cu_1 and (b) BLG/Cu_2.

2.2 Microwave characterization of graphene transferred on various substrates:

A 50.8 mm long microstrip line of width (w) 3.024 mm was fabricated on FR-4 substrate (relative permittivity 4.4 and thickness 1.5 mm). As shown in **Fig. 2**a**,** the microstrip line with sample holder was connected between ports (A and B) of calibrated vector network analyzer model N5227A of Keysight Technologies Inc. and S-parameters were measured for unloaded microstrip line from 10 MHz to 26.5 GHz. Then microstrip line was loaded by SLG/glass, SLG/quartz, BLG/Cu_1 and BLG/Cu_2 one by one and then S-parameters were measured individually**.** After loading, microstrip line has three parts, Part 1 (unloaded), Part 2 (loaded) and Part 3 (unloaded). In **Fig. 2**a, Z_i, γ_i and l_i represent the characteristic impedance, propagation constant and physical length of the respective microstrip line parts, i = 1, 2, 3. For Part 2 of microstrip line, S-parameters were obtained by using standard transmission line (ABCD)

parameters based de-embedded method (A MATLAB program is given in the supplementary material as SP1) [11].

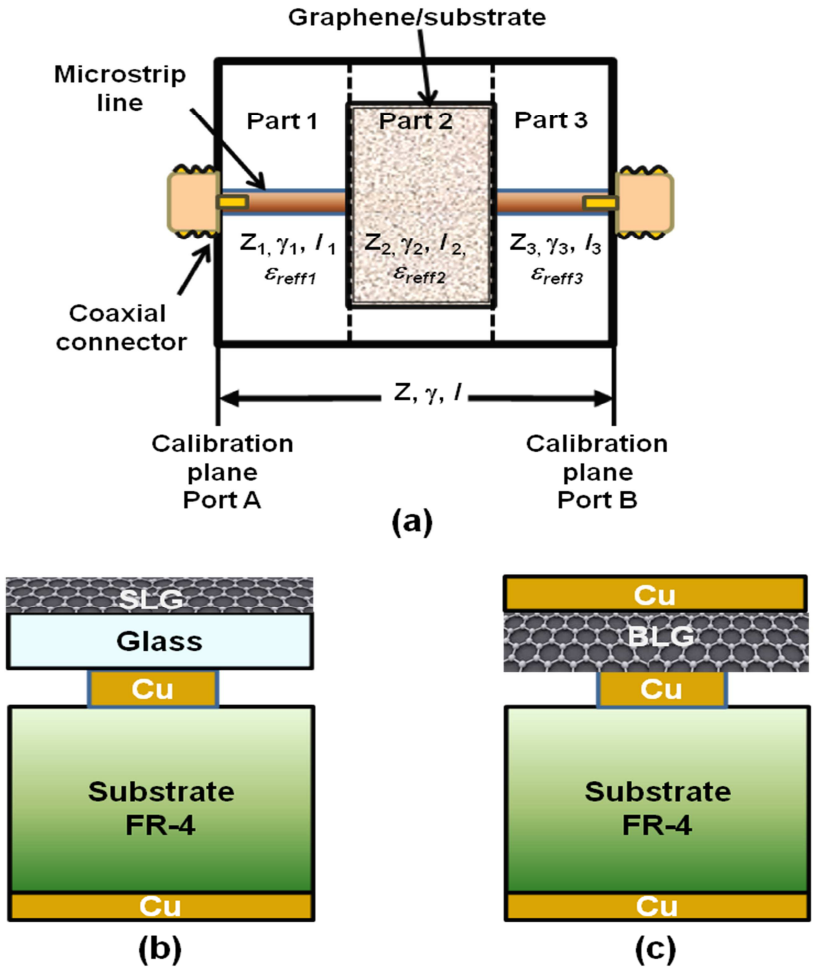

Figure. 2. Loading of microstrip line by sample, (a) schematic representation of center part loaded with (b) single layer graphene (SLG)/glass, and (c) bilayer graphene (BLG)/Cu.

Furthermore, in reported work, perturbation in electromagnetic fields which is caused due to SLG or BLG loadings when quasi-transverse electromagnetic (TEM) mode propagates in microstrip line will not be much [12]. This can be understood as: since thickness of both BLG and SLG is much less as compared to thick FR4 substrate as well as the sample length which is half than the length of microstrip line. Therefore, we can presume that EM fields distribution will

not be much perturbed after BLG/SLG loadings. In addition, as glass and quartz are low-loss materials with known properties in microwave frequencies, hence properties of SLG can be extracted from the measured S-parameters with capacitively perturbed EM fields. This perturbation caused due to loaded microstrip line depends on the properties of the graphene samples and the extent of their interaction with the electric fields in quasi-TEM mode where graphene is presumed to be a non-magnetic material.

After loaded with BLG/Cu, asymmetric stripline structure will be formed with near-TEM mode rather than planar waveguide. Formed structure has ultrathin BLG layer not a dielectric sandwitched between top and bottom conductors like in planerr waveguide. Since, thickness and relative permitivity of BLG and FR4 are different therefore, electric field lines will emerge from the center conductor Cu (in microstrip line) and will get terminated in outer part of Cu conductor after penetrating the BLG (**Fig. 2**c), whereas the magnetic field lines will surround the center conductor (microstrip) only. These both fields have direction which is perpendicular to the direction of propagation [12].

3. Results and discussion

3.1 Raman Spectra of graphene/Cu

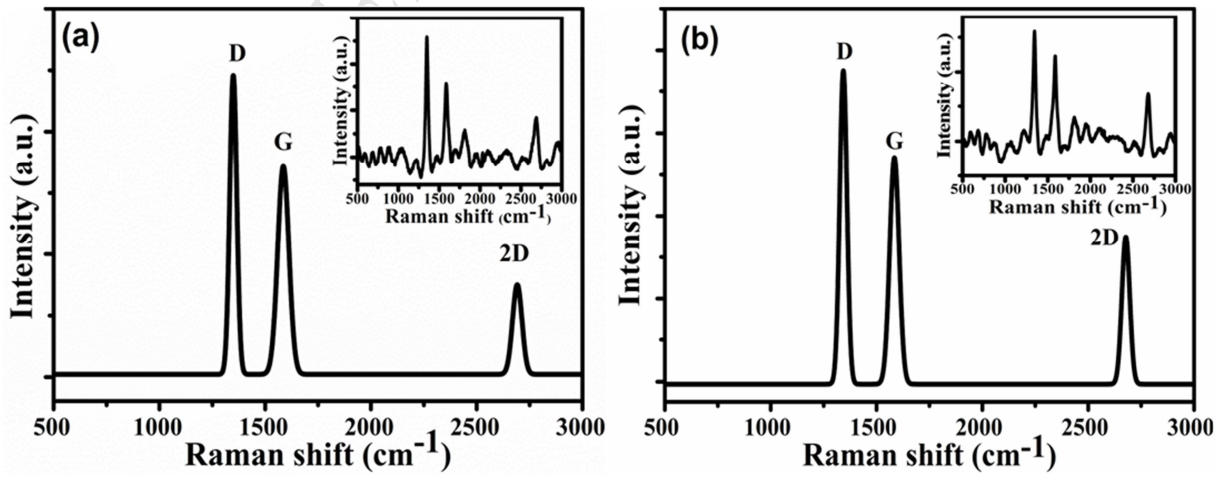

Figure. 3. Raman Spectra of as- grown graphene films on Cu substrate after smoothing of plot shown in inset for (a) BLG/Cu_1 and (b) BLG/Cu_2

In the Raman spectra shown in **Fig. 3**, three sharp peaks were indexed as D, G and 2D bands for as-grown graphene samples after curve fitting. The peak positions for BLG/Cu_1 are found at ω_D ~1342 cm^{-1}, ω_G ~1588 cm^{-1}, and ω_{2D} ~ 2713 cm^{-1}, and for BLG/Cu_2, these values are at ω_D ~1341cm^{-1}, ω_G ~1586 cm^{-1} and ω_{2D} ~2680 cm^{-1}. The 2D to G-band ratio (I_{2D}/I_G) is evaluated as ~0.55 and ~0.64, respectively for BLG/Cu_1 and BLG/Cu_2, which confirms that a bilayer graphene is present on both Cu substrates.

3.2 Microwave reflection and transmission of bilayer graphene/Cu

Both unloaded microstrip line and the ones loaded with BLG/Cu_1 and BLG/Cu_2, measured reflected (S_{11}, S_{22}) and transmitted (S_{12}, S_{21}) parameters have been shown in **Fig. 4**a-h. As shown in **Fig. 4**a, input reflection coefficient (S_{11}) is found to be high for BLG/Cu_1 and BLG/Cu_2 loading on the microstrip line in the lower frequency range up to 11 GHz. This may have happened due to confinement of electromagnetic fields into FR4 substrate and bilayer graphene as covered by Cu, which changes the effective impedance of microstrip line at lower frequency [12]. BLG/Cu_2 has been found to be more reflective than BLG/Cu_1 in lower frequency range. At higher frequency, fields are more concentrated in FR4 substrate, so S_{11} for both loadings is similar to the unloaded microstrip line from 11 GHz to 26.5 GHz. The phase of S_{11} also has recurrent shifts at lower frequencies, whereas only one lower shift near 20 GHz in range of 15 to 26.5 GHz is observed in **Fig. 4b**. For BLG/Cu_1, a minor difference in phase has been observed in comparison to BLG/Cu_2, indicating both have similar material properties.

In **Fig. 4**c & e, the magnitudes of forward (S_{21}) and reverse (S_{12}) transmission parameters are found to be decreased as frequency increased, due to the lossy nature of microstrip line. Compared to unloaded microstrip line, lower values of S_{21} and S_{12} for BLG/Cu_1 and BLG/Cu_2, indicate loss of transmission power on loading of microstrip line. In lower frequency range upto 13 GHz, BLG/Cu_2 exhibited higher loss than BLG/Cu_1 except near 9 GHz, and then both S_{21} and S_{12} decreased with frequency up to 26.5 GHz. In addition, high values > -15 dB of S_{11} and S_{22} suggest that unloaded microstrip line turned to be more reflecting at frequencies above 9 GHz. **Fig. 4**d & f show the minor shift of transmission phase for BLG/Cu_1 and BLG/Cu_2 in comparison to unloaded microstrip line. In **Fig. 4**g, S_{22} has high values for both loadings than unloaded microstrip line. The reflection (S_{22}) phase has values analogous to that of S_{11} as shown in **Fig. 4**h. For both loadings, minor variations in S_{11} (and S_{22}) and identical S_{21} (and S_{12}) suggested that BLG can offer a reciprocal and moderate dielectric loss from 2 to 5 dB compared to the unloaded case at higher frequency. In order to minimize the measurement error, multiple measurements have been taken. We compared the three measurement results and estimated the maximum measurement errors were found to be ~ 6.8 % and 11 % in magnitude and phase values, respectively. More details of multiple measurements (see Fig. S1-7 in supplementary material) and associated maximum standard deviation with each S-parameters are given Table S1 in the supplementary material.

ACCEPTED MANUSCRIPT

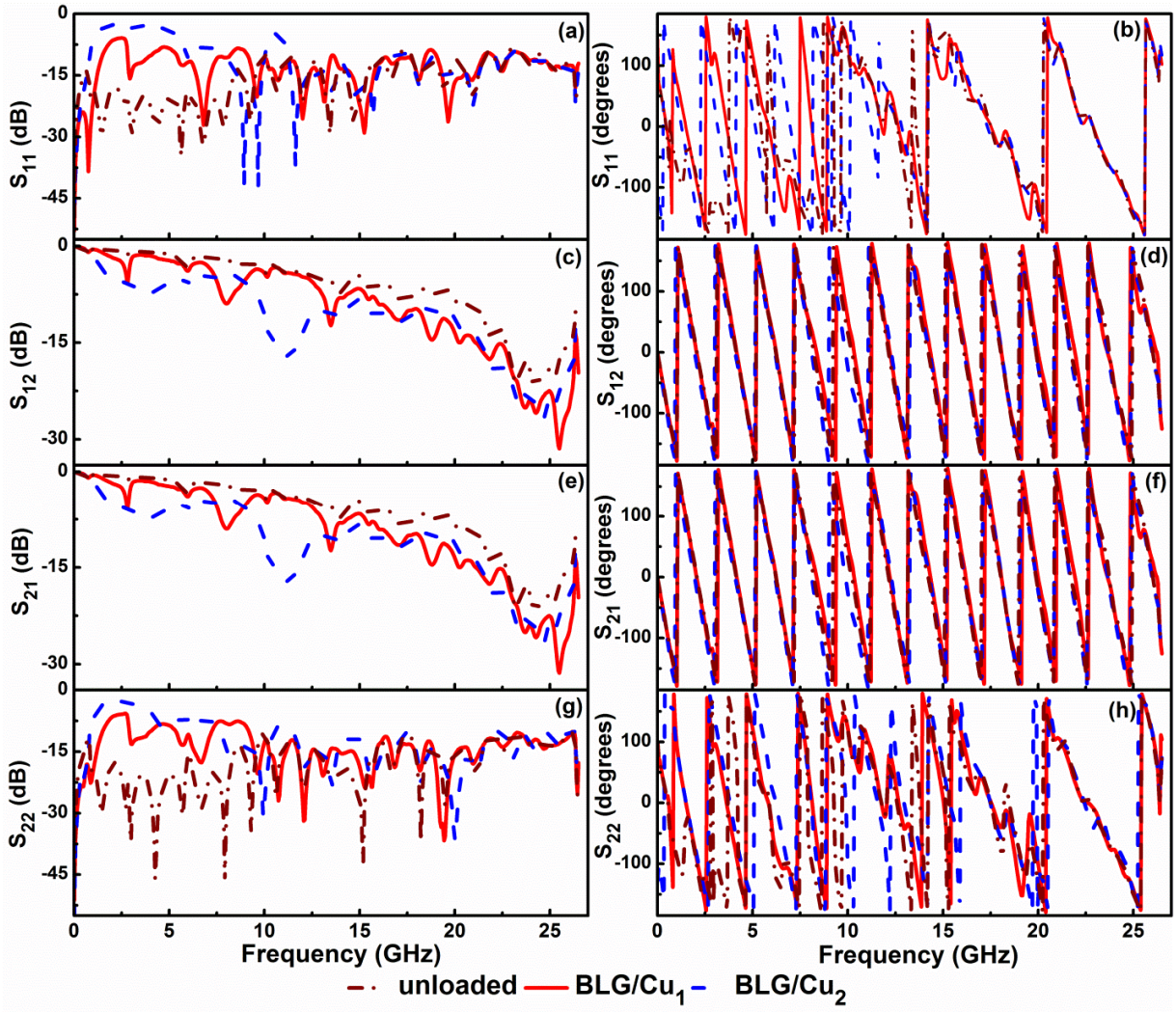

Figure. 4. Complex S-parameters of microstrip line unloaded, loaded with BLG/Cu_1 and BLG/Cu_2, (a) magnitude of S_{11}, (b) phase of S_{11}, (c) magnitude of S_{12}, (d) phase of S_{12}, (e) magnitude of S_{21}, (f) phase of S_{21}, (g) magnitude of S_{22} and (h) phase of S_{22}.

3.3 Complex relative permittivity and refractive index of Single and bilayer graphene

From the de-embedded S-parameters for microstrip line loaded with SLG/glass, SLG/quartz, BLG/Cu_1 and BLG/Cu_2, the complex propagation constant ($\gamma = \alpha + j\beta$) was determined [13], where α is the attenuation constant and β is the phase constant. The effective relative permittivity ε_{reff2} of multilayer microstrip line (Part 2) was determined as $(\gamma_2/\gamma_0)^2$ [14],

where $\gamma_0 = j2\pi f/c$, f is operating frequency in Hz and c is the velocity of light in ms^{-1}. When microstrip line is loaded with SLG/glass and SLG/quartz, it becomes three-layer line and when loaded with BLG/Cu$_1$ and BLG/Cu$_2$ makes it two-layer line which has metallic cover i.e. Cu. By applying the conformal mapping technique [15, 16, 17], we can obtain the complex relative permittivity (ε_r^*) of both SLG and BLG using formulas which have given in supplementary material S1. Since, we have assumed that BLG/Cu makes two-layer line, therefore obtained (ε_{r2}^*) by using Eq.S1 will be intrinsic value for BLG. These parameters were extracted using MATLAB program for two-layer and three-layer given in the supplementary material as SP2 &3. Afterward, we continue to assign SLG and BLG by SLG/glass, SLG/quartz, BLG/Cu$_1$ and BLG/Cu$_2$ to distinguish among them based on the substrate. In order to verify our measurement and evaluation process, we compared with the relative permittivity obtained for glass substrate, which was second layer in loading with SLG/glass.

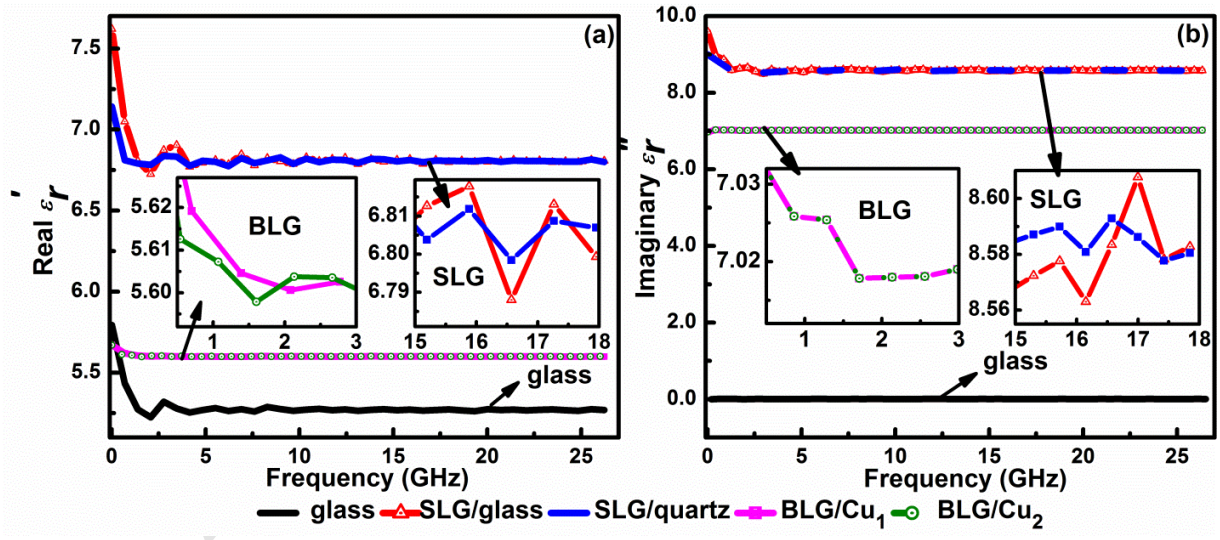

Figure. 5. (a) Real (ε_r') and (b) imaginary (ε_r'') parts of complex relative permittivity (ε_r) for SLG and BLG on various substrates.

The complex relative permittivity (ε_r^*) consists of real part ($\varepsilon_r^{'}$) and imaginary part ($\varepsilon_r^{"}$) have shown in **Fig. 5** for all studied materials. The real part ($\varepsilon_r^{'}$) for glass substrate has been found in 5.17 – 5.30 range and imaginary part was in the range of 0.0001- 0.01. Both parts have reduced at lower frequency range up to ~2.4 GHz and then exhibit insignificant variations as frequency increases further. These values are in agreement with the specifications provided by the manufacturer for supplied Corning glass substrate of ε_r^* = 5.27 – 0.009î. This agreement validates accuracy of adopted evaluation process to obtain the complex relative permittivity of the graphene layers, which was loaded on the microstrip line. The real part ($\varepsilon_r^{'}$) of SLG/glass and SLG/quartz has been found to reduce from 7.62 @ 10 MHz to ~ 6.71 @ 1.92 GHz and remains almost constant ~ 6.80 at frequency above 5 GHz, whereas the imaginary part ($\varepsilon_r^{"}$) decreased from ~ 9.58 @ 10 MHz to 8.47 @ 1.92 GHz. Both parts of ε_r were found to have slightly higher variations in SLG/glass than SLG/quartz over most of the frequencies as seen in the insets of **Fig. 5**a and b. This might be due to strong van der Waals attraction between SLG/quartz than that in SLG/glass. For BLG/Cu_1 and BLG/Cu2, $\varepsilon_r^{'}$ and $\varepsilon_r^{"}$ are found to be same in the range of 5.58 – 5.67 and 6.97 – 7.025, respectively. These real and imaginary parts become constant ~5.60 and ~7.02 at frequency > 2 GHz, as shown in the insets of panels **5**a and b, where insignificant variations with frequency have been observed. We found that SLG has higher value of both $\varepsilon_r^{'}$ and $\varepsilon_r^{"}$ than that of BLG. This indicates that BLG synthesized by HFCVD can absorb nearly same amount of microwave energy as by SLG without much dissipation (lesser $\varepsilon_r^{"}$) as a heat. Such frequency independent behaviour of BLG suggests that it can be utilized as a high power microwave absorber as well as substrate material for planar microwave passive components in the broadband frequency range. The FR4 substrate used was DURAVER®-E-Cu quality 104, which has very low profile Cu foil having a surface roughness of about 0.6 μm. It

was estimated that this roughness may affect the relative permittivity of studied materials only up to 3% in 10 MHz to 26.5 GHz [18].

In order to study dispersion behaviour, we have obtained the refractive index (n) and extinction coefficient (κ) by using a relation in Eq. 1 & 2 where $\varepsilon_r^{'}$ and $\varepsilon_r^{"}$ are real and imaginary parts of complex relative permittivity, respectively [19] and obtained results have been shown in **Fig.6**.

$$n = \left(\frac{\sqrt{\varepsilon_r^{'2} + \varepsilon_r^{"2}} + \varepsilon_r^{'}}{2} \right)^{\frac{1}{2}} \quad (1)$$

$$\kappa = \left(\frac{\sqrt{\varepsilon_r^{'2} + \varepsilon_r^{"2}} - \varepsilon_r^{'}}{2} \right)^{\frac{1}{2}} \quad (2)$$

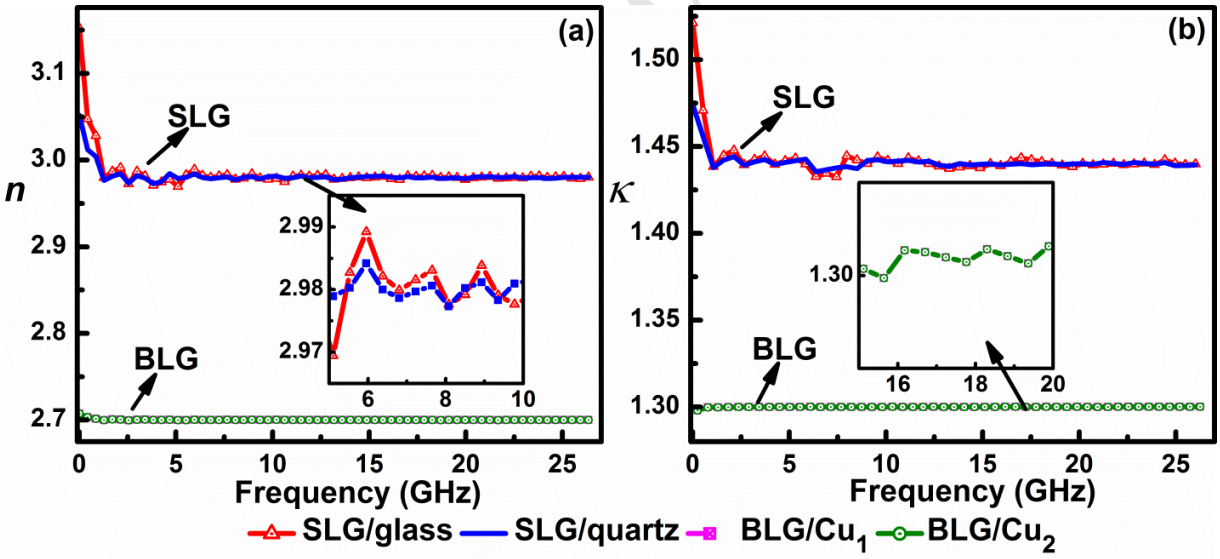

Figure. 6. (a) Refraction coefficient (n) and (b) extinction coefficient (κ) of SLG and BLG on various substrates.

In SLG, it was observed that as frequency increased, n decreased from 3.15 @ 10 MHz to 2.95 @ 6.5 GHz whereas, κ decreased from 1.52 to 1.43 as shown in **Fig. 6**a & b, respectively.

These values are slightly higher in SLG/glass than that in SLG/quartz. For both samples BLG/Cu_1 and BLG/Cu_2, same n and κ were obtained and found to be ~ 2.69 and ~ 1.28, respectively. SLG is found to be more dispersive at frequency below 1 GHz. Since, phase velocity (v_p) is expressed as, $v_p = c/n$ where c = 2.99 × 10^8 ms^{-1}, the velocity of the light in a vacuum and wavelength (λ) was obtained by using relation $\lambda = \frac{\lambda_0}{\sqrt{\varepsilon_r}}$. The group velocity ($v_g$) is then deduced by using relation,$v_g = v_p - \lambda . dv_p/d\lambda$. Both v_p and v_g have been analysed and results have been shown in **Fig. 7a** and **Fig. 7b**, respectively.

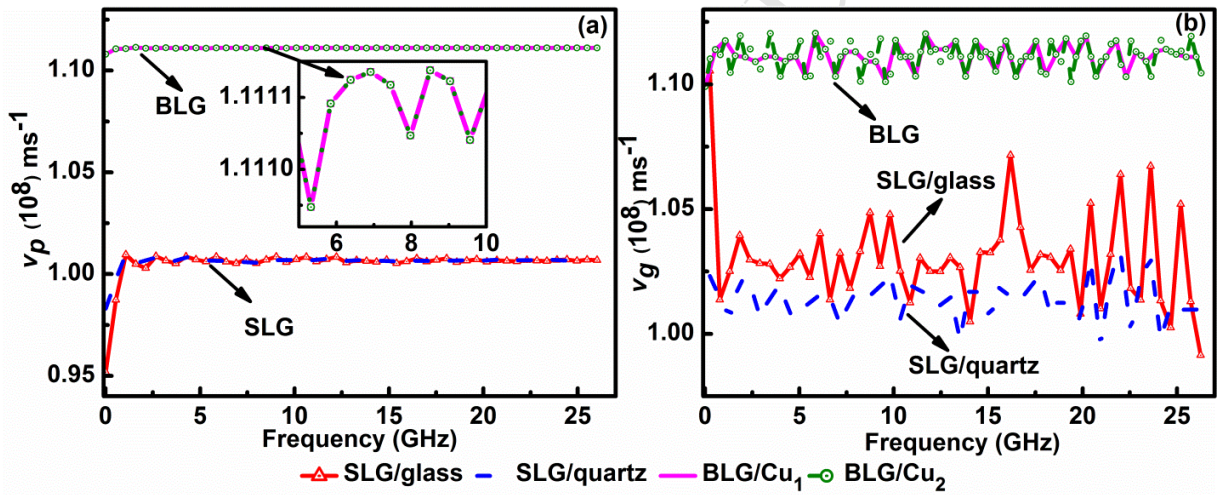

Figure. 7. (a) Phase velocity v_p (ms^{-1}) and (b) group velocity v_g (ms^{-1}) in SLG and BLG on various substrates.

With the frequency, the phase velocities in SLG slightly increased from 0.95 × 10^8 ms^{-1} @ 10 MHz to 1.04 × 10^8 ms^{-1} @ 1.2 GHz and then become stable at 10^8 ms^{-1} at higher frequency with minor variations. In BLG, the phase velocity is found to be near ~ 1.11 × 10^8 ms^{-1} with frequency as shown in the inset of **Fig. 7**a. High v_p in BLG indicates that the waves propagate faster than in SLG/glass or SLG/quartz suggesting that the propagation of the waves are

becoming faster with increasing number of graphene layers and has fairly constant velocity at higher frequencies. As shown in **Fig. 7**b for SLG/glass, group velocity (v_g) has been reduced from ~1.11×10^8 ms^{-1} @ 10 MHz to 1.02×10^8 ms^{-1} @ 1.1 GHz and then it varies significantly within 4%. In SLG/quartz, v_g has smaller variations with frequency. The peaks and falls at certain frequencies were observed in v_g for SLG, due to corresponding variations in the phase velocity (v_p) with frequency. In comparison to SLG, v_g is higher in BLG and it is found to be around 1.11×10^8 ms^{-1} in BLG. As, v_g has been found to be slightly higher than v_p at most of frequencies, it can be concluded that SLG has little anomalous dispersive behaviour than BLG. For BLG, v_p and v_g have similar values and thus confirmed linear dispersion. This might be due to lower inter-electron and electron-photon interactions in the measured frequency range in BLG [8]. High values of v_{p} and v_g also confirmed that BLG may have charge carriers to carry the energy than SLG in the frequency range of study and their interaction may lead to decrease the optical effective mass of photons with graphene layers. We have determined the optical effective mass by using the relation $m_{op}^{*} = \hbar k / v_g$[10], where $\hbar = 1.054 \times 10^{-34}$ J.s, and k is the momentum ($k = n\omega/c$). The values of m_{op}^{*} for SLG and BLG are normalized with the free electron mass, $m_0 = 9.107 \times 10^{-31}$ kg and plotted in **Fig. 8**.

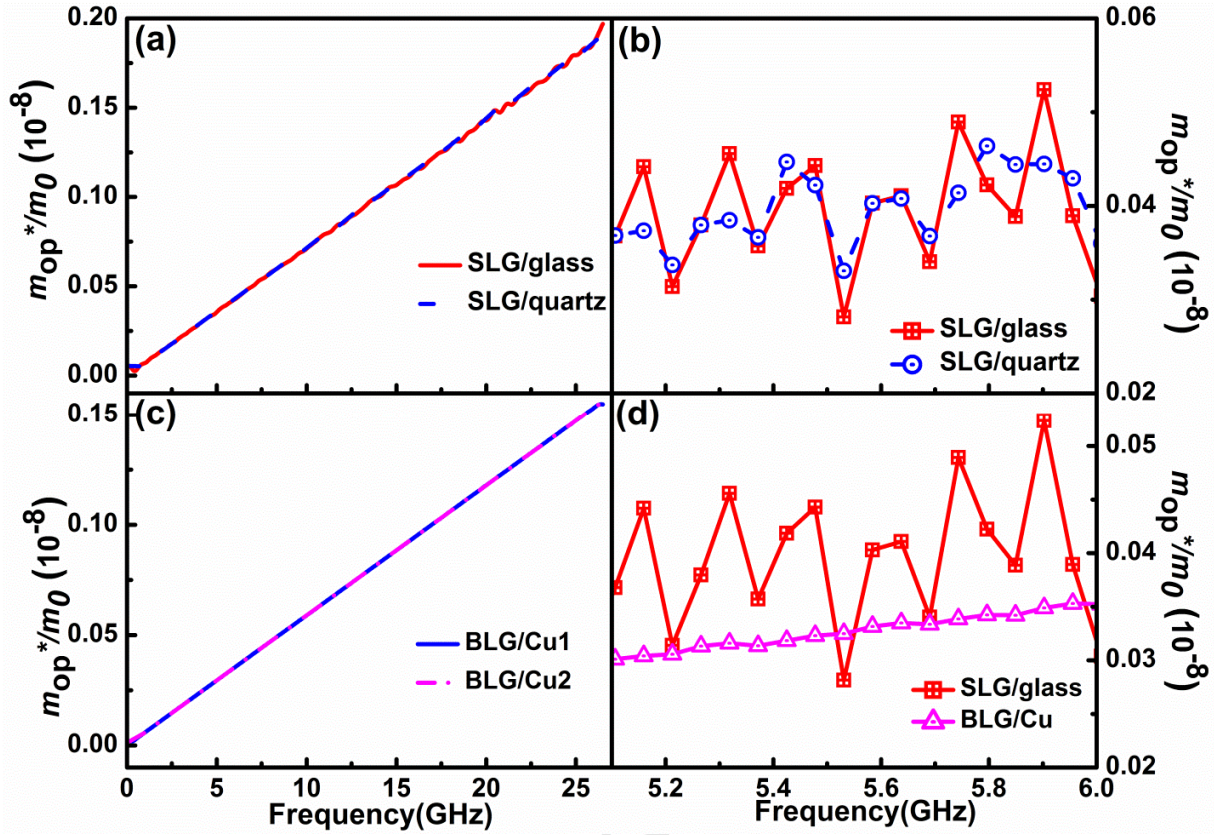

Figure. 8. Variation of optical effective mass m_{op}^*/m_0 in SLG and BLG on various substrates.

In SLG and BLG, the mass ratio starts from value around ~10^{-10} at 10 MHz and increases linearly to ~ 0.2×10^{-8} and ~ 0.16×10^{-8}, respectively at 26.5 GHz. The frequency dependence behaviour of m_{op}^* is governed by the momentum (k), which was found to vary with frequency, although group velocity (v_g) exhibits lower frequency dependence behaviour. The obtained m_{op}^* seems to have same values irrespective of the substrate (glass or quartz) for SLG or processing conditions for BLG. For verification, we have plotted the mass ratio for 5 to 6 GHz and it was observed (**Fig. 8**b**)** that m_{op}^* has larger variation for SLG/glass than SLG/quartz as well as BLG/Cu (**Fig. 8**d). Thus, it can be said that small variations in m_{op}^* make BLG a good candidate for the substrate material in the microwave components in broadband frequency applications.

The quantitative information on BLG provided by our analysis will guide the future study for effective utilization of graphene.

4. Conclusions

Transmission, dielectric and optical properties of as-grown BLG on Cu and SLG transferred on glass and quartz have been studied and compared in frequency range of 10 MHz to 26.5 GHz. Measured S-parameters for BLG confirmed that it is a better dielectric material than the SLG as it dissipates less microwave energy and can be utilized in developing reciprocal microwave passive components. In BLG, high phase velocity and group velocity represent faster propagation of energy and their relation suggests the linear dispersion. However, the lower effective mass of photons in BLG resulted owing to smaller refractive index, which in turn suggests minor interaction between photon-charge carriers. The present study would help to utilize the graphene in the microwave passive and reciprocal components as a substrate material in broad frequency range.

Acknowledgements

This work is supported by DST-SERB, fast track Program (SR/FTP/PS-055/2012) and DST-FCT, Portugal bilateral Program (INT/PORTUGAL/P-13/2013). We thank Ms. Geetanjali for her help in plotting Raman spectra. K. Patel thanks the R & D Scheme 2014-15 granted by University of Delhi.

References

[1] A. S. Mayorov, R. V. Gorbachev, S. V. Morozov, L. Britnell, R. Jalil, L. A. Ponomarenko, et al. Micrometer-scale ballistic transport in encapsulated graphene at room temperature, Nano Lett 2011; 11:2396–99.

[2] I. Khrapach, F. Withers, T. H. Bointon, D. K. Polyushkin, W. L. Barnes , S. Russo, and M. F. Craciun, Novel highly conductive and transparent graphene-based conductors, Adv. Mater. 2012;24:2844 – 49.

[3] E. Tiras, S. Ardali, T. Tiras, E. Arslan, S. Cakmakyapan, O. Kazar, et al. Effective mass of electron in monolayer graphene: Electron-phonon interaction, J. Appl. Phys. 2013;113: 43708.

[4] K. Patel and P. K. Tyagi, Single layer graphene possessing anomalous dispersion with exotic microwave transmission and dielectric properties, J. of Alloys and Compounds (under review).

[5] X. Wang, Y. P. Chen and D. D Nolte, Strong anomalous optical dispersion of graphene: complex refractive index measured by Picometrology, Optics Express 2008;16(26): 22105.

[6] A. Gray, M. Balooch, S. Allegret, S. D. Gendt, and W. E. Wang, Optical detection and characterization of graphene by broadband spectrophotometry, J. Appl. Phys. 2008; 104:053109.

[7] F. J. Nelson, V. K. Kamineni, T. Zhang, E. S. Comfort, J. U. Lee and A. C. Diebold, Optical properties of large-area polycrystalline chemical vapor deposited graphene by spectroscopic ellipsometry, Appl. Phys. Lett. 2010;97:253110.

[8] Z. Z. Alisultanova and R. P. Meilanov, On the theory describing graphene in an anomalous-dispersion region, Journal of Surface Investigation. X-ray, Synchrotron and Neutron Techniques 2013; 7(1): 46–50.

[9] K. Zou, X. Hong, and J. Zhu, E□ective mass of electrons and holes in bilayer graphene: electron-hole asymmetry and electron-electron interaction, Phys. Rev. B 2011;84:085408.

[10] V. Ariel and A. Natan, Electron Effective Mass in Graphene, e-print arXiv:1206.6100v2 [physics.gen-ph], (2012)].

[11] J. C. Rautio, A De-Embedding Algorithm for Electromagnetics, Int. J. Microwave Millimeter Wave Compter-Aided Engg. 1991;1(3):282-287.

[12] D. M. Pozar, *Microwave Engineering* (John Wiley & Sons, Inc., USA, 2012), 4th ed pp.147.

[13] A. Koul, P. K. R. Anmula, M. Y. Koledintseva, J. L. Drewniak, S. Hinaga, Improved Technique for Extracting Parameters of Low-Loss Dielectrics on Printed Circuit Boards, in Proceedings of IEEE EMC Symposium, Austin, USA, 2009, p.191-196.

[14] Y. Wu, Y. Xu, Z. Wang, C. Xu, Z. Tang, Y. Chen, R. Xu, Microwave transmission properties of chemical vapor deposition graphene, Appl Phys Lett 2012;101(5):053110.

[15] J. Sva˘cina, Analysis of multilayer microstrip lines by a conformal mapping method, IEEE Trans. Microwave Theory Tech. 1992;40 (4):769-772.

[16] J. Sva˘cina, A simple quasistatic determination of basic parameters of multilayer microstrip and coplanar waveguide, IEEE Microwave Guided Wave Lett. 1992;2(10):385-387.

[17] C. Wan and A. Hoorfar, Improved Design Equations for Multilayer Microstrip Lines, IEEE Microwave Guided Wave Lett. 2000;10 (6): 223-224.

[18] A. F. Horn, J. W. Reynolds and J. C. Rautio, Conductor profile effects on the propagation constant of microstrip transmission lines, in Proceedings of IEEE MTT-S International Microwave Symposium, Anaheim, CA, 2010, p. 868-871.

[19] Mira Naftaly, *Terahertz Metrology* (Artech House Publishers, New York, USA, 2015), pp. 35.

ACCEPTED MANUSCRIPT

Figure Captions:

Figure. 1. Schematic diagram of the process parameters for (a) BLG/Cu_1 and (b) BLG/Cu_2.

Figure. 2. Loading of microstrip line by sample, (a) schematic representation of center part loaded with (b) single layer graphene (SLG)/glass, and (c) bilayer graphene (BLG)/Cu.

Figure. 3. Raman spectra of as- grown graphene films on Cu substrate after smoothing of plot shown in inset for (a) BLG/Cu_1 and (b) BLG/Cu_2.

Figure. 4. Complex S-parameters of microstrip line unloaded, loaded with BLG/Cu_1 and BLG/Cu_2, (a) magnitude of S_{11}, (b) phase of S_{11}, (c) magnitude of S_{12}, (d) phase of S_{12}, (e) magnitude of S_{21}, (f) phase of S_{21}, (g) magnitude of S_{22} and (h) phase of S_{22}.

Figure. 5. (a) Real ($\varepsilon_r^{'}$) and (b) imaginary ($\varepsilon_r^{"}$) parts of complex relative permittivity (ε_r) for SLG and BLG on various substrates.

Figure. 6. (a) Refraction coefficient (n) and (b) extinction coefficient (κ) of SLG and BLG on various substrates.

Figure. 7. (a) Phase velocity v_p (ms^{-1}) and (b) group velocity v_g (ms^{-1}) in SLG and BLG on various substrates.

Figure. 8. Variation of optical effective mass m_{op}^*/m_0 in SLG and BLG on various substrates.

Volume 5, Issue 1 (2017) 78-82 ISSN 2347 - 3258
International Journal of Advance Research and Innovation

Optimization of Machining Parameters in CNC Turning of Hybrid Metal Matrix Composites Using Different Techniques: A Review

Vaibhav Sharma, Ravi Butola*
Department of Mechanical Engineering, Delhi Technological University, Bawana Road, New Delhi-110042, India

Article Info
Article history:
Received 25 January 2017
Received in revised form
20 February 2017
Accepted 28 February 2017
Available online 15 March 2017

Keywords
Analysis of Variance (ANOVA), Metal Removal Rate (MRR), Taguchi Design

Abstract
Metal Matrix Composites is a subject of interest from last 6 decades and it is finding wide applications in many fields like Aerospace, Automobile, Spaceship, Piston and Sports Equipment etc. Adding a new element in the Metal Matrix Composite makes it Hybrid. HMMC's provide better machinability and tribological properties. In CNC turning process, Surface Roughness and MRR are two main parameters. The Objective of the present paper review is to determine the optimum machining parameters in CNC turning of HMMC using different algorithms and techniques. This can be achieved by finding the optimum cutting parameters by Minimizing the Surface Roughness and Maximizing the Metal Removal Rate. For this we have reviewed Taguchi's Design experiment. The main cutting parameters considered are Cutting Speed, Feed rate and Depth of Cut. Also we have reviewed Response Surface Methodology and Grey-Fuzzy Algorithm.

1. Introduction

Turning is defined as the machining process which is used to produce rotational parts by removal of unwanted material from the work piece. It requires a turning machine (lathe machine), work piece and cutting tool in position with its fixture. The cutting tool used is basically a single point cutting tool and it is fed either linearly in the direction parallel or perpendicular to the axis of rotation of the work piece or along a certain path to make complex rotational shapes. For material removal in Turning process, the primary motion is the rotation of workpiece and the secondary motion is the feed motion. CNC machines are highly accurate and precise for machining different materials. An appropriate setting of CNC machine depends on Operator's experience and manufacturer guidelines. However, manufacturer guidelines are not meant for recently developed HMMC's and thus the cutting parameters are required to be optimized. This is also required because in developing nations, the machines in the manufacturing industries are not working at their optimal operating conditions. In these industries, handbooks are being used at the process of planning level due to which due to which productivity decreases as a result of partially optimal use of machining capability [1].There is a direct relation between change in surface roughness and the cutting conditions and thus Surface Roughness is one of the main parameter which needs to be monitored [2]. The tool and the work piece are subjected to specific deformation due to relative motion between them, both in the cutting speed direction. Thus, as a result the tool is under thermal loads on those faces which are in contact with the workpiece and the chip. When chips are formed, the work piece is under compression and undergoes plastic deformation. The main objective of metal cutting is to solve the practical problems related to efficient metal removal in the process. Therefore, knowledge of principle of metal cutting process is essential for selecting optimum machining conditions for different cases [3].

The most often applied techniques for optimization of machining parameters are Taguchi technique, Response Surface Methodology, Artificial Neural Network (ANN), Grey Relational approach, Fuzzy Logic approach, Scatter Search technique and Genetic algorithm [4]. The main machining parameters taken into consideration for optimization of CNC turning operation are Cutting speed, Depth of cut and Feed Rate. Daniel applied Taguchi technique for optimization of surface roughness obtained by CNC turning. The machining parameters considered were spindle speed, feed rate and depth of cut. From the experiment, he concluded that the feed rate was most significant parameter followed by spindle speed and depth of cut had insignificant effect in machining [5]. Nalbant used Taguchi's experimental method and L_9 orthogonal array for optimizing surface roughness in turning of AISI 1030 carbon steel. The parameters used were insert radius, feed rate and depth of cut. The results revealed that insert radius and feed rate are more significant parameter affecting surface roughness of AISI 1030 carbon steel [6].Yanda studied the optimization of MRR, Surface Roughness and Tool life in the process of conventional dry turning by FCD700. The conclusion was that optimum MRR is achieved when cutting speed and feed rate are high while the optimum surface roughness was obtained at high cutting speed and low feed rate. For optimum tool life, cutting speed and feed rate were less [7]. Palani kumar observed the characteristics of surface roughness on Al-HMMC. Input parameters considered for machining were feed rate, cutting speed and depth of cut. The results revealed that surface roughness increases with increase in feed rate and decreases with increase in cutting speed [8].Krishnamurthy and Venkatesh experimented on TiB_2 particles reinforced Al6063 metal matrix composites to optimize surface roughness and MRR. The results showed that cutting speed is affects surface roughness while in MRR, cutting speed and feed rate are important parameters [9]. Vikas performed experiment on EN8 steel to optimize machining parameters by using Taguchi and ANOVA. The results revealed that normal tool shape, medium cutting speed, lowest feed and lower depth of cut are the optimum machining parameters [10]. Senthil Kumar and Rajendran optimized CNC turning parameters on Al-HMMC using Taguchi's Design. They concluded that for better surface finish feed rate is the most significant parameter followed by cutting speed as the second significant parameter and depth of cut as the third significant parameter. For optimum MRR the order of significance decreases from feed rate to cutting speed to depth of cut [11].

Response Surface Methodology was introduced by G.E.P. Box and K.B. Wilson in 1951. It helps in relating independent input variables with output response variables.The principal approach of RSM is to apply a sequence of designed experiment to obtain an optimum response. For this, a second degree polynomial model is used. Suresh made a second order quadratic model of surface roughness. Using RSM technique, he concluded that optimum machining parameters of Al-SiC-Gr composite for minimum surface roughness is at 113 m/min of cutting speed, 0.250 mm/rev of feed rate and 0.2 mm of depth of cut [12].

Deng used Grey Relational analysis to work with incomplete and uncertain output [13]. It helped in solving complex inter relationships in multiple responses. The basic purpose of Grey relational analysis is to optimize multiple responses to determine the appropriate input parameters according to the conditions [14]. P. Suresh used Grey-fuzzy algorithm to minimize surface roughness and flank wear of the tool and to maximize the material removal rate. This logic provided optimum input machining parameters with multi performance characteristics [15]. Paulo Davim concluded that surface roughness during turning is directly proportional to an

Correspoding author,
E-mail address:ravibutola33855@gmail.com
Phone No--+91-8750305182
All rights reserved: http://www.ijari.org

increase in feed rate and inversely proportional to cutting speed [17].

2. Methodology Analysis

2.1Taguchi's Design

In this method, CNC turning was performed on Aluminium hybrid metal matrix composite workpiece by a Ceramic tool. The workpiece composition of Al-SiC-Gr is 80% Al 7015, 17% SiC and 3% Gr by weight. In the papers reviewed, mostly L_{27} orthogonal array is used which is based on Taguchi's Technique. The input machining parameters considered were Cutting speed, Feed rate and Depth of cut while the output machining parameters considered were Surface roughness and Metal Removal Rate. Instruments like Surftest 211 Mitutoyo was used to measure Surface Roughness while MRR was evaluated using Analytical Method. For this, the input parameters were allocated based on 3 different levels such as minimum, medium and maximum. S/N ratio was evaluated to determine optimum machining parameter and ANOVA was used to determine significance of the parameter based on Taguchi design and helped to establish the relationship between input and output machining parameters.

Table 1. Chemical Composition of Aluminium 7015 [11]

Al	91.3-93.9%	Other each	<=0.050%
Cu	0.060-0.15%	Other total	<=0.15%
Cr	<=0.15%	Si	<=0.20%
Fe	<=0.30%	Ti	<=0.10%
Mg	1.3-2.10%	Zn	4.6-5.20%
Mn	<=0.10%	Zr	0.10-0.20%

Table 2. Different Symbols and Levels of Parameter [11]

S.NO.	SYMBOL	INPUT MACHINING PARAMETER	LEVELS 1, 2, 3
1.	A	Cutting Speed (S)	100,125,150
2.	B	Feed Rate (F)	0.1,0.2,0.3
3.	C	Depth of Cut (DoC)	0.5,0.75,1.0

2.1.1 Results

(a)For Surface Roughness

To determine significant parameters through ANOVA, signal to noise ratio needs to be calculated first. According to Taguchi's technique, Lower value of S/N ratios indicates better the surface roughness.

The following equation was used to determine S/N ratio:

$$ratio(S/N) = -10\log(1/r\sum yi\text{^}2)$$

From the observations, following response graph is Obtained in figure 1.

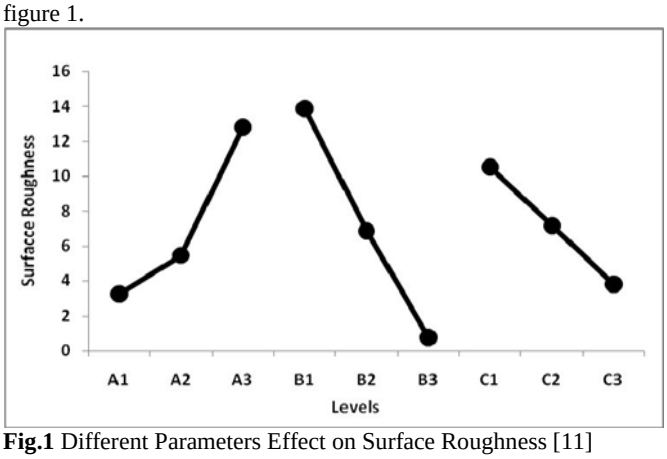

Fig.1 Different Parameters Effect on Surface Roughness [11]

Therefore it can be stated that minimum surface roughness is achieved when machining parameters combination used are A3, B1 and C1 i.e, 150 m/min cutting speed, 0.1 mm/rev feed rate and 0.5 mm depth of cut respectively. Thus it is the optimal combination for given experimental review.

The purpose of the ANOVA is to determine the significant machining parameter for minimum surface roughness. ANOVA was performed to evaluate contribution of different parameters affecting surface roughness of Al-HMMC during Turning Operation. F-test was performed with 95% confidence level to identify the significant parameter. The result is shown in following pie chart in fig.2.

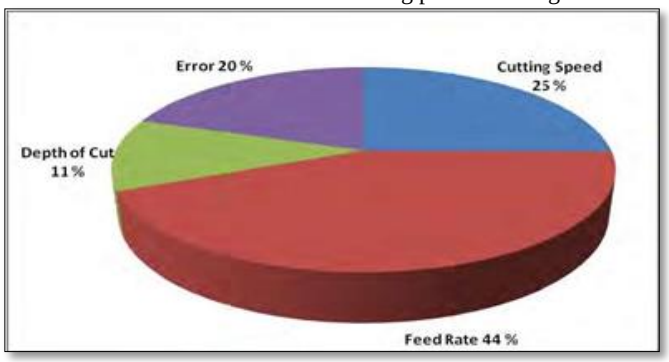

Fig. 2 Percentage Contribution for surface roughness [11]

(b) For Metal Removal Rate

The S/N ratio is used to evaluate MRR through ANOVA to identify significant parameter. Higher value of this ratio indicates higher MRR.The equation used to find this ratio is:

$$ratio(S/N) = -10\log(1/r\sum 1/yi\text{^}2)$$

The Optimum combination of parameters for maximum MRR can be concluded from fig.3. and it clearly shows that A3, B3 and C3 i.e., 150 m/min cutting speed, 0.3 mm/rev feed rate and 1 mm depth of cut respectively.

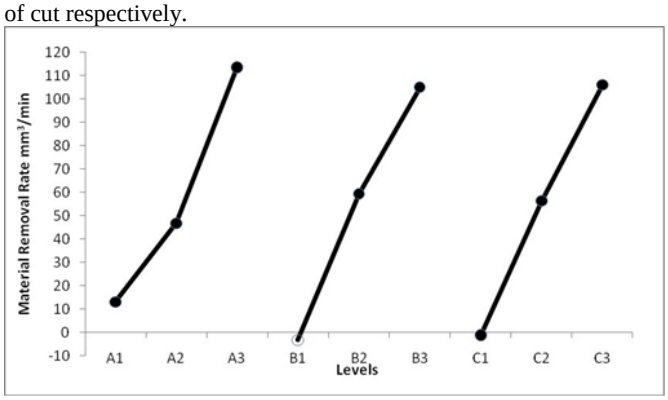

Fig.3 Main Parameter effect on MRR [11]

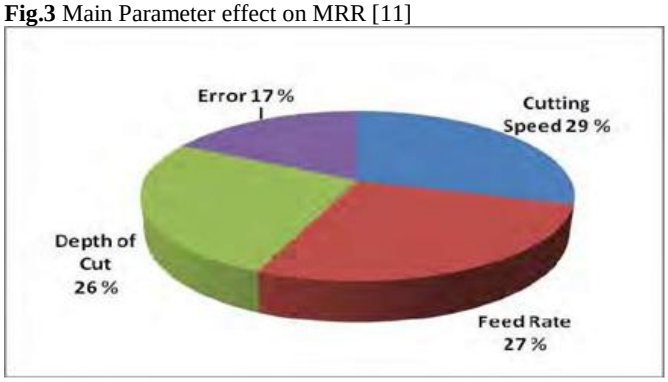

Fig.4 Percentage contribution of parameters on MRR [11]

ANOVA results are represented in fig.4.The contribution of different parameters for optimum MRR is calculated. Again F-test with 95% confidence level was used to determine significant parameter for optimum MRR.

2.2 Response Surface Methodology

RSM is used to establish relationship between input machining variables with output response variables. The principal approach of RSM is to apply a sequence of designed experiment to obtain an optimum response. The Workpiece material is Al-HMMC with Al6061 as the base material reinforced with 10% SiC and 3% Gr by weight. Final Design Matrix can be developed using RSM. The RSM can be used to find optimum parameters of turning for output responses like surface roughness and MRR. In RSM, Central Composite Design was selected to perform experiment and to

evaluate the impact of process parameters. In this experimental study review, we have selected four parameters i.e, speed, feed, depth of cut and tool material (insert). To determine the parameter which significantly affected the responses surface roughness and MRR, certain perturbation graphs were drawn. From these graphs, we observed that MRR and surface roughness were directly influenced by feed, depth of cut and TNMG2000 tool insert [16]. For optimization of which tool insert had maximum MRR and minimum surface roughness, 3-D graphs were drawn to correlate process parameter with response variables. The following inferences can be made from study review:

2.2.1 Effect of Speed with Tool insert on MRR and surface roughness:

From fig.5 we can observe that both MRR and surface roughness decreases linearly with increase in speed.

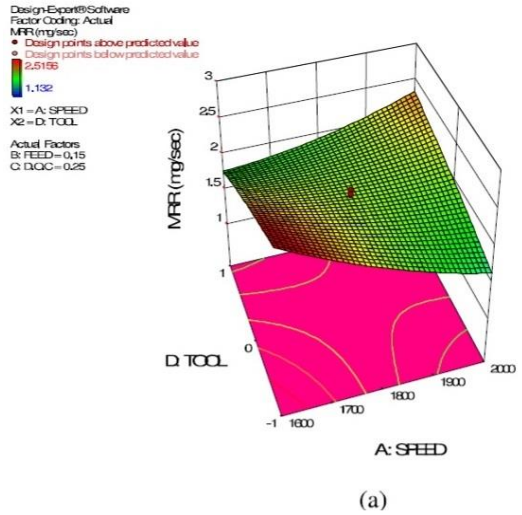

Fig. 5 3-D graph (a) MRR (b) SR(surface roughness) [16]

2.2.2Effect of feed with tool insert on MRR and SR

From fig.6 we observed that MRR increases immediately as the value of feed increases while SR decreases slightly with increase in feed.

2.2.3 Effect of depth of cut with tool insert on MRR and SR

From fig.7, it is observed that MRR increases linearly with increase in depth of cut while surface roughness decreases with increase in depth of cut.

From these graphs we observed that maximum MRR was obtained on TNMG160408 Tool insert while minimum Surface Roughness was obtained on TNMG2000 Tool insert.

Confirmation test runs were carried out by the suggested model.

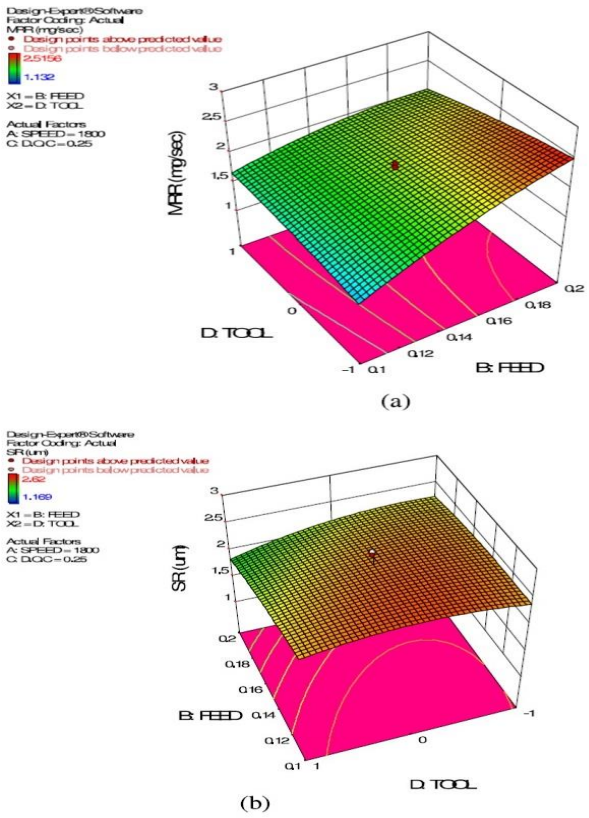

Fig.6 3-D graph (a) MRR (b) SR(surface roughness) [16]

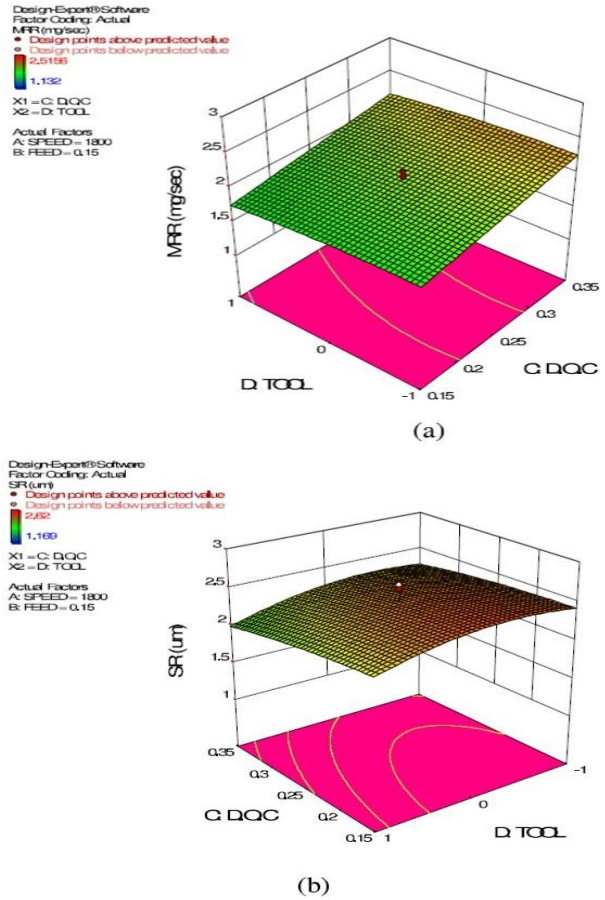

Fig.7 3-D graph (a)MRR and (b)SR(surface roughness) [16]

2.3 Grey-Fuzzy Algorithm Analysis

When grey-fuzzy output is obtained by integrating grey relational coefficients with fuzzy approach is termed a grey-fuzzy reasoning analysis. MATLAB tool was used for this analysis. Work piece material is Al-SiC-Gr hybrid metal matrix composite.Surface roughness, material removal rate and flank wear are assigned with triangular membership resulting into nine grey output. For fuzzy interference system activation, rules are evaluated. Since there is reduction in uncertainty in data found by grey relational approach. Due to reduced fuzziness, grey-fuzzy reasoning grade is higher in comparison with grey relational grade. The relation between average fuzzy reasoning grade with different levels of machining parameter is shown in fig8.In this experimental review, results reveal that feed rate has a greater influence when compared with other parameters. At high cutting speed surface roughness is reduced and increased flank wear of tool. The highest value of grey-fuzzy reasoning grade indicates optimal level machining parameters. The optimal setting should be: cutting speed at level 3 (200 m/min), feed rate at level 1 (0.075mm/rev) and mass fraction of SiC-Gr at level 3(10%)[15].

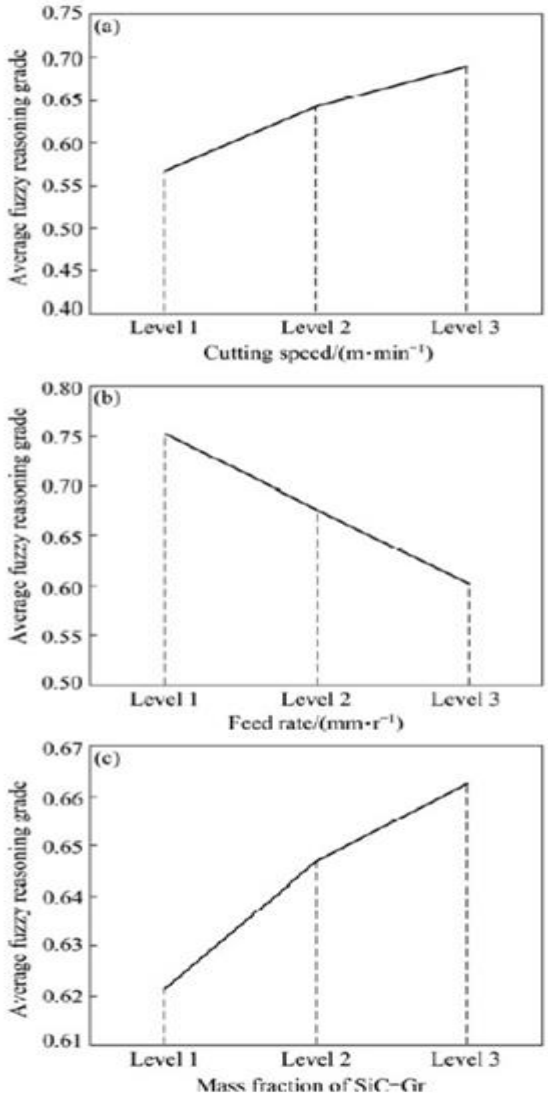

Fig 8. Response Graph for different level of machining parameters: (a)Cutting Speed; (b)Feed Rate; (c)MassFraction of SiC-Gr [15].

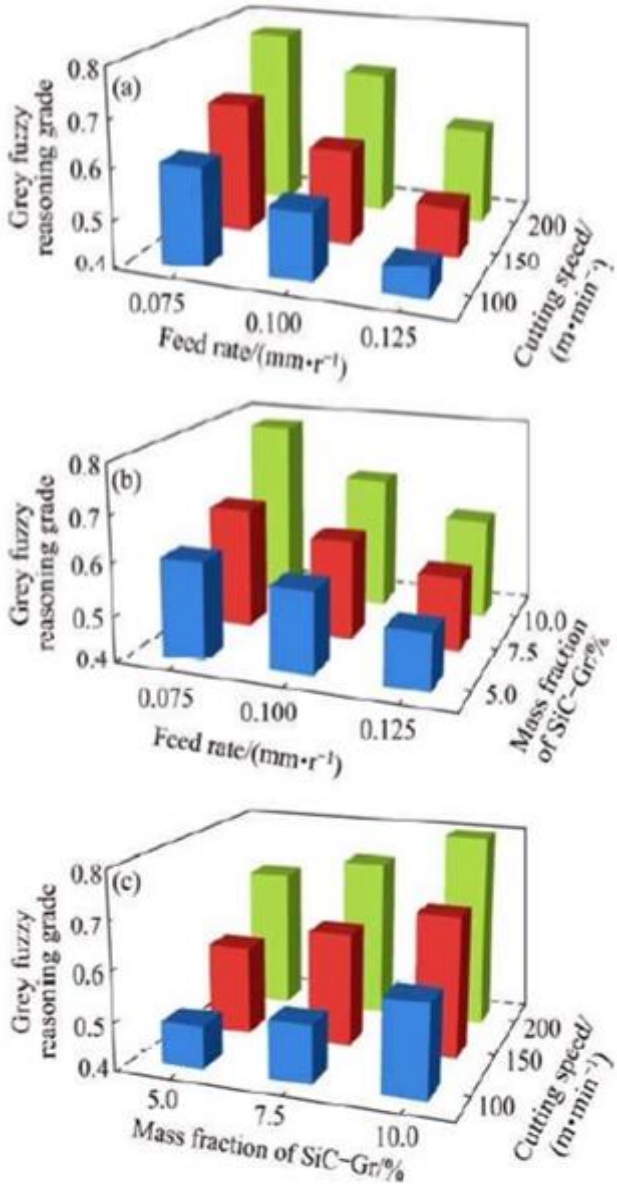

Fig.9 Effect of Grey-fuzzy reasoning gradeon machining parameters:
(a) feed rate and cutting speed
(b) feed rate and mass fration of SiC-Gr
(c)mass fraction of SiC-Gr and Cutting speed[15].

3. Conclusions

From this paper review, effect of machining parameters on HMMC's can be concluded as following:

1. In Taguchi's technique to determine the significance of each of the cutting parameters on Surface Roughness and MRR, we have used Signal to Noise Ratio (S/N) and Analysis of Variance (ANOVA). It was found that feed rate was most significant parameter followed by cutting speed as second and depth of cut as third significant parameter on surface roughness.For optimization of MRR, it was found as feed rate as most significant parameter followed by cutting speed and depth of cut as second and third significant parameter respectively.

2.Using Response Surface Methodology, 3-D graphs were plotted and effect of process parameters were analysed:

(i)Metal Removal Rate increases with increase in feed and depth of cut while it decreases with increase in speed.

(ii)Surface Roughness decreases with increase in speed while it decreases with increase in feed and depth of cut.

3.Using Grey-Fuzzy logic approach, uncertainty in output was reduced. Increase in grey fuzzy reasoning grade indicated optimization of parameters.It was found that Al-10%(SiC-Gr) provided improved machinability with minimum surface roughness and flank wear, and maximum metal removal rate as compared with 5% and 7.5% mass fraction of SiC-Gr. The optimal parameter setting was having cutting speed at level 3,feed rate at level 1 and mass fraction of SiC-Gr at level 3 at a constant depth of cut (1 mm) throughout the turning process.

Acknowledgment

V Sharma thanks R Butola for their efforts in work to make it possible.

References

[1] HM Somashekara, NLakshmana. Optimizing Surface Roughness in Turning Operation using TAGUCHI Technique and ANOVA, International Journal of Engineering Science and Technology, 4(5), 2012

[2] Ilhan, Ali. Development of a Neural Network Based Surface Roughness Prediction System using cutting Parameters and an Accelerometer in Turning, Department of Mechanical Education, Faculty of Technical Education, University of Seljuk, Turkey, IEEE, 2010.

[3] Rakesh K Patel, HR Prajapati. Parametric Analysis of Surface Roughness and Material Removal Rate of Harden Steel on CNC Turning using ANOVA Analysis. International Journal of Engineering Science and Technology, 4(7), 2012.

[4] Aman A, Hari S. Optimization of machining techniques–A retrospective and literature review, Sadhana, 2005.

[5] Daniel Kirby E. A Parameter Design Study in a Turning Operation Using the Taguchi Method, Industrial technology program, Department of Agricultural and Biosystems Engineering, The technology Interface 2006.

[6] Nalbant M , Gokkaya H ,Sur G. Application of Taguchi Method in the Optimization of Cutting parameters for surface roughness in Turning; Materials and Design, 28, 2007, 1379-1385.

[7] Yanda, JA Ghani, MNAM Rodzi, K. Othman, CHC Haron. Optimization of Material Removal Rate, Surface Roughness and Tool Life on Conventional Dry Turning of FCD700, International Journal of mechanical and Materials Engineering , 5(2), 2007, 182-190.

[8] Sasimurugan T, Palanikumar K. Analysis of Machining Characteristics on Surface Roughness of a Hybrid Aluminium Metal Matrix Composite (Al6061-SiC-Al_2O_3), Journal of Minerals and Materials Characterization and Engineering, 10(13), 2011, 1213-1224.

[9] Krishnamurthy K, Venkatesh J. Assessment of surface roughness and material removal rate on machining of TiB_2 reinforced Al-6063: A Taguchi's Approach, International Journal of Scientific and Research Publications, 3(1), 2013, 1-6.

[10] Vikas B Magdum, Vinayak R Naik. Evaluation and Optimization of Machining Parameter for Turning of EN 8 Steel, International Journal of Engineering Trends and Technology, 4(5), 2013, 1564-1568.

[11] Senthil Kumar, Rajendran. Optimization of CNC Turning Parameters on Aluminium 7015 Hybrid Metal Matrix Composite Using Taguchi Robust Design, International Journal of Engineering and Technology, 6(4), 2014.

[12] Suresh P, Marimuthu K, Ranganathan S, Arunkumar G. Evaluation of Parameters Influencing Surface Roughnesson Turning of Al-SiC-Gr Hybrid Composites, International Journal of Advanced Engineering Applications, 2(3), 2013.

[13] Deng J L. Introduction to grey system, J Grey System, 1989.

[14] Ranganathan S, Senthilvelan T. Multi-response Optimization of Machining Parameters in hot turning using grey analysis, Int J Adv Manuf Technol, 2011.

[15] P Suresh, K Marimuthu, S Ranganathan, T Rajmohan, Optimization of Machining Parameters in Turning of AL-SiC-Gr Hybrid Metal Matrix Composites using Grey-Fuzzy Algorithm,2014.

[16] A Kumar, H Singh, HK Garg. Optimization of MRR and SR while Turning of Hybrid Aluminium Metal Matrix Composite on CNC lathe using Response Surface Methodology, International Journal on Emerging Technologies, 2016.

[17] Paulo Davim J. Design of Optimization of cutting parameters for turning metal matrix composite based on the orthogonal arrays, J Mater Process Technol, 132, 2003, 340-344.

Computational Materials Science 136 (2017) 102–108

Contents lists available at ScienceDirect

Computational Materials Science

journal homepage: www.elsevier.com/locate/commatsci

Potential application of multilayer n-type tungsten diselenide (WSe_2) sheet as transparent conducting electrode in silicon heterojunction solar cell

Pranjala Tiwari [a], Kamlesh Patel [a,b], Lucky Krishnia [a], Reetu Kumari [a], Pawan K. Tyagi [a,*]

[a] Department of Applied Physics, Delhi Technological University, New Delhi 110042, India
[b] Department of Electronic Science, University of Delhi, South Campus, Delhi 110021, India

ARTICLE INFO

Article history:
Received 21 February 2017
Received in revised form 18 April 2017
Accepted 25 April 2017

Keywords:
Heterojunction silicon solar cell
Tungsten diselenide
Transparent conducting electrode
AFORS-HET

ABSTRACT

In this paper, structure of n-type WSe_2/p-type Si heterojunction solar cell has been simulated by using AFORS-HET software version 2.5 at AM1.5. In order to get maximum power conversion efficiency (PCE), parameters of both tri-layer tungsten diselenide (WSe_2) and Si have been optimized. In the present study, tri-layer WSe_2 has been considered as 3-D in nature instead of the reported 2-D nature. After optimizing the parameters of both tri-layer WSe_2 and silicon wafer, PCE of nearly 13.09 % has been achieved which decreases to 8.9 % as number of layers of WSe_2 increases from 3 to 40. Furthermore, maximum value PCE has been found to be 6.8 % when parameters of commercial available silicon wafer were taken for simulation. We have also analyzed the effect of temperature as well as the spectral response in order to make the best optimized solar cell. In the present work, we have demonstrated that n-type tri-layered WSe_2 has an immense potential to be used as an excellent transparent conducting electrode.

© 2017 Elsevier B.V. All rights reserved.

1. Introduction

In heterojunction solar cells, transparent conducting electrode (TCE) is responsible for separation as well as transport of photo-generated charge carriers to the cell terminals. This happens due to the formation of a Schottky barrier at the interface between the electrode and silicon and TCE also serving as anti-reflector [1–3]. To carry out this task successfully, TCE should have low sheet resistance, for example in ITO, typically order of 20 Ω/sq with 85 % optical transmission and mobility as high as > 20 cm^2/V s [1,4]. Recently, graphene has been emerged as a novel TCE material owing to its extraordinary properties such as high transparency [5], sheet resistance as low as 8.8 Ω/sq [4] and carrier mobility exceeding 7350 cm^2/Vs [5]. However, its emergence as a TCE material is limited due to low photo responsivity and poor external quantum efficiency which originate from the zero band gap and low light absorption coefficient [6,7]. These limitations of graphene can be overcome by taking atomically thin 2-D transition metal dichalogenides (TMDs), as they posses relatively large band gap (1–2 eV) and carrier mobility as high as 1800 cm^2/V s [8,9]. These properties ensure that ultrathin sheet of TMD can be utilized in the TMDs/silicon heterojunction solar cells as a new TCE material and tungsten diselenide (WSe_2) is one of them. Furthermore, in recent advances carrier mobility as high as 500 cm^2/V s (in bulk) and 250 cm^2/V s (in single layer) was reported in WSe_2 [10,11] which is due to low electron/hole effective mass. It has been reported that charge carriers in ultrathin TMDs are weakly screened and their carrier mobility is sensitive to the interfaces on both the ends of the semiconductor which causes variation in mobility [12]. In contrast to the other 2D materials, quantum confinement in WSe_2 can be observed by studying the valleys in charge of electron and hole conduction and observed that as the number of layers reduces, these valleys are raised up/down. This effect is only apparent if layer number is lower than three [11]. Furthermore, single layer WSe_2 does not exhibit the gapless nature as well as linear dispersion relation in spite of having graphene-like hexagonal lattice structure. This happens due to the lack of inversion symmetry [11]. Recently, p-type behavior of as-grown monolayer WSe_2 with mobility of ~0.2 cm^2/Vs and carrier concentration of nearly 1×10^{18} cm^{-3} has been confirmed [13]. In further advances, possibility of both n-and p-doping in WSe_2 has been demonstrated [14]. Lee *et al.* have reported that by treating with hydrazine p-type WSe_2 can be converted to n-type with enhanced electron conduction as well as reduced work function [15]. Having such extraordinary properties, to the best of our knowledge experimentally or theoretically, no heterojunction solar cell using WSe_2

* Corresponding author.
E-mail addresses: pawan.phy@dce.edu, pawankumartyagi@gmail.com (P.K. Tyagi).

http://dx.doi.org/10.1016/j.commatsci.2017.04.026
0927-0256/© 2017 Elsevier B.V. All rights reserved.

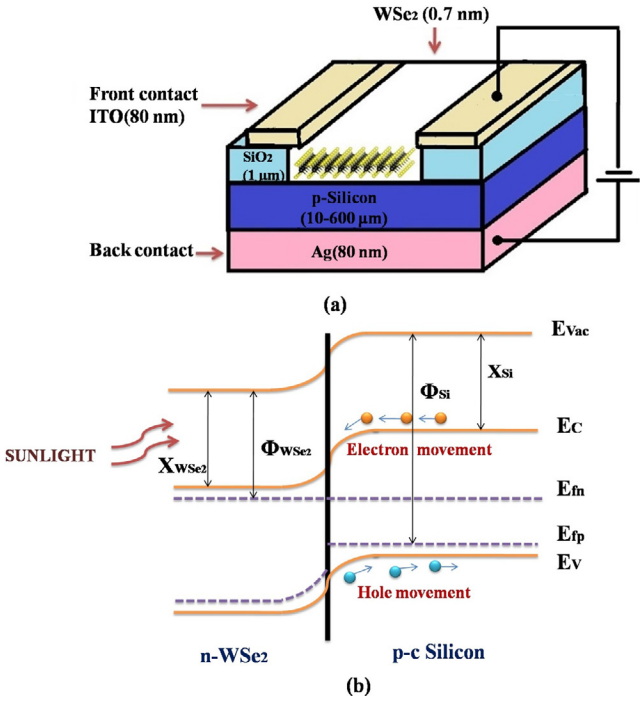

Fig. 1. Tungsten diselenide/silicon heterojunction cell (a) schematic of proposed WSe_2-pcSi heterojunction solar cell (b) schematic of band diagram after the formation of heterojunction showing hole and electron movement after the EHP generation.

as a TCE has yet been reported therefore, in the present work, we have simulated a n-WSe_2/p-silicon heterojunction solar cell. Since mono or multi layer WSe_2 can be directly deposited on silicon substrate either by using CVD method or vapor phase deposition [13,16], this motivated us to optimize the parameters of proposed heterojunction solar cell. Thus, we have simulated the n-WSe_2/p-silicon structure under air mass 1.5 (AM1.5) illuminations with power density of 100 mW/cm^2 using AFORS-HET version 2.5 (Automat For Simulation of Hetero-structures) software [17]. This software uses 1-D semiconductor equations related to Shockley–Reed–Hall statistics solver and Lambert–Beer law based optical model to obtain the optimized cell parameters. In simulation, n-type WeS_2 film is assumed to be 3-D in nature instead of 2D and taken as cathode. Thereafter, parameters of both WeS_2 and crystalline silicon (c-Si) layers are optimized in order to achieve highest efficiency. The present simulation aims to study the independent effects of both the layer parameters on the performance of the cell and to analyze simulated results. After simulation, we have achieved power conversion efficiency (PCE) as high as 13.09 % (100 μm thick p-type silicon).

2. Simulation structure

High mobility with transparency of about 95 % in WSe_2 has motivated us to use it as a new TCE material [18]. In heterojunction solar cell, at the interface formation of strong rectifying junction is mandatory whereas ohmic front and back contacts with low resistance are highly desirable in order to reduce series resistance of solar cell. Wei Liu *et al.* have reported that ohmic contact with small contact resistance between WSe_2 and indium due to the high work function of indium [10]. In our work, indium tin oxide (ITO) is taken as transparent conductive oxide (TCO) and basic structure of proposed cell is configured as ITO/n-WSe_2/p-cSi/Ag as shown in Fig. 1(a) where ITO taken as TCO in front contact and Ag metal as back contact. Here, Ag metal not only passivates silicon back but also avoids the band bending and other details of the contacts were given in Table 2. The thickness of WSe_2 tri-layer is fixed at 2.1 nm since monolayer thickness is reported to be 0.7 nm and then the six parameters i.e. the donor concentration (N_D), band gap (E_g), effective conduction and valance band densities (N_C/N_V), electron affinity (χ), relative permittivity (ε_r) and electron mobility (μ_n) were varied in feasible ranges [19–21]. After optimizing these parameters, layer number was also optimized and maximum efficiency of 9.055 % has been achieved. In second step, we have extended our simulation in order to further optimize the parameters of p-type crystalline Si (p-cSi) by varying acceptor concentration (N_A), effective conduction and valance band densities (N_C/N_V), the electron affinity (χ) and thickness. Other parameters like relative permittivity (ε_r), electron mobility (μ_n) and band gap (E_g) were fixed at their standard previously reported values [22–24]. The various material parameters and their feasible ranges are mentioned in Table 1.

3. Results and discussion

3.1. Optimization of n-WSe_2 layer parameters

It is well known that if two semiconductors are brought together, either Schottky or ohmic junction forms depending on mismatch of their work functions. The formation of heterojunction in present case can be explained as, when n-type WSe_2 and p-cSi

Table 1
Ranges of various material parameters of tungsten diselenide and p-c Silicon as previously reported.

Input parameters	n-WSe_2	p-cSi
Relative permittivity, ε_r	6.9–7.5	11
Electron mobility, μ_n (cm^2/V s)	250	1350
Hole mobility, μ_p (cm^2/V s)	215	450
Electron affinity, (χ)	3.97–4.15	3.2–4.6
Band gap, E_g (eV)	0.9–1.6	1.12
Acceptor concentration, N_A (cm^{-3})	0	1×10^{12}–1×10^{21}
Donor concentration, N_D (cm^{-3})	1×10^{7}–1×10^{17}	0
Effective conduction band density, N_c (cm^{-3})	1×10^{17}–1×10^{22}	3×10^{18}–3×10^{25}
Effective valance band density, N_v (cm^{-3})	1×10^{17}–1×10^{22}	3×10^{18}–3×10^{25}
Thermal velocity of electrons (cm s^{-1})	1×10^{7}	1×10^{7}
Thermal velocity of holes (cm s^{-1})	1×10^{7}	1×10^{7}
Thickness (cm)	7×10^{-8}	2×10^{-4}–200×10^{-4}
Mid band gap density of states (cm^{-3} eV^{-1})	0	Single acceptor
Switch-over energy (eV)	0	0.56
Auger recombination coefficient for electron (cm^6 s^{-1})	0	0
Auger recombination coefficient for hole (cm^6 s^{-1})	0	0
Direct band-to-band recombination coefficient (cm^3 s^{-1})	0	0

Table 2
Detailed front contacts and back contacts characteristics.

Contact parameters	Front contact	Back contact
Width (cm)	8×10^{-6}	0.001
File	ITO.nk	Ag.nk
Metal work function	Yes (flatband)	Yes (flatband)
Absorption loss	ITO.abs	0
External reflection constant	aSicSi_ITO.ref	0
Surface condition	Plane	Plane
Internal reflection constant	0	0

are brought in contact, due to mismatch of work functions ($\Phi_{WSe2} < \Phi_{Si}$) electrons flow from WSe_2 to p-type silicon in order to occupy lower energy empty states in valence band. This further resulted in upward curvature of energy bands. As a consequence chemical potential of p-cSi comes in equilibrium with the Fermi level of n-type WSe_2 as shown in Fig. 1(b). This in turn creates a region which is depleted of holes and a potential barrier, commonly known as Schottky barrier to reach the interface and then recombine with an electron. Potential barrier (Φ_{bi}) is given by the relation:

$$\Phi_{bi} = \Phi_{Si} - \Phi_{WSe_2} = \chi_{Si} + k_B T \ln\left(\frac{N_A}{N_V}\right) - \chi_{WSe_2} - k_B T \ln\left(\frac{N_C}{N_D}\right) \quad (1)$$

where Φ_{WSe_2}, χ_{WSe_2}, Φ_{Si} and χ_{Si} are the work function and affinity of WSe_2, and work function and affinity of the silicon, respectively. N_D and N_C are the donor doping concentration and effective conduction band density of WSe_2, whereas N_A and N_V are acceptor doping concentration and effective valence band density of the p-cSi, respectively. When n-WSe_2/p-cSi junction is illuminated, electron-hole pairs (EHP) generate and then get separated due to the built-in voltage (V_{bi}). These free minority carriers move to the opposite sides of barrier and get collected at the respective electrodes. When the cell is operated in open circuited conditions, the separated photogenerated carriers at respective regions result in an open circuit voltage (V_{OC}) whereas when short circuited, the carriers exit the device terminal and generate current known as short circuit current (I_{SC}). The charge carrier transport can be explained by the drift-diffusion model across the barrier. However, due to ultrathin layer of WSe_2, a thin depletion layer was formed which may facilitate the tunneling of carriers. Therefore, transport of carriers may occur via both drift-diffusion as well as tunneling [25]. In AFORS-HET, we have presumed Schottky junction at WSe_2/Si interface and transport of the carrier through drift-diffusion, neglecting the tunneling effects.

In the proposed simulation, first the optimization of N_D was carried out while keeping the other parameters as previously reported values and results have been plotted in Fig. 2(a-d). As N_D increased from 10^7 cm^{-3} to 10^{19} cm^{-3}, there is an upward shift in the positions of Fermi level and level moves closer to conduction band edge and this results in increase of barrier height which in turn increases both V_{bi} and V_{OC} as it linearly depends on V_{bi} [26]. For low doping concentrations, mobility is almost constant and limited by the phonon scattering, while at higher N_D, mobility decreases due to the scattering with ionized doping atoms. Hence, the current density remains constant initially below 10^{11} cm^{-3}, while at higher values of N_D, it decreases due to decrease in mobility as well as lifetime of carriers [27]. But the percentage increment in open circuit voltage dominates the percentage decrement in short circuit current and hence the overall efficiency increases to 6.267 % at $N_D = 5 \times 10^{16}$ cm^{-3}. Also, the fill factor of solar cell is determined by its series resistance, shunt resistance as well as ideality factor. Increase in the doping concentration is inversely proportional to the resistivity, which consequently increases the fill factor values [28].

After optimizing N_D to 5×10^{16} cm^{-3}, we have optimized the values of N_c/N_v as shown in Fig. 2(e-h). Initially, V_{OC} decreases sharply along with J_{SC} as N_C/N_V varies from 10^{17} to 10^{19} cm^{-3}. Above 10^{19} cm^{-3}, only V_{OC} decreases whereas J_{SC} becomes constant at 24.14 mA/cm^2. This decrement in V_{OC} can be explained by taking in account of Eq. (1) which shows that density of conduction band as well as valence band state inversely vary V_{OC} and the equilibrium concentration of electrons and holes depends on these state densities. Any deviation from equilibrium disturbs the rate of generation as well as recombination which are equal at equilibrium. If $n_o \cdot p_o > n_i^2$, where n_o and p_o equilibrium electron and hole concentration and n_i being intrinsic concentration, then the diode will experience more recombination which leads to reduction in J_{SC} [29]. Due to reduction in V_{OC} as well as J_{SC}, cell efficiency (η) reduces from 9.609 % to 2.34 % at $N_C/N_V = 10^{22}$ cm^{-3}. Hence, we have optimized value of N_C/N_V to 5×10^{17} cm^{-3}. It has been reported that bulk WSe_2 has indirect band gap of 0.9 eV whereas monolayer WSe_2 has direct band gap of about 1.6 eV [15]. Therefore, as layer number reduces, band gap increases and band transition (from indirect to direct) is also observed if layer number is below three. Hence, we have considered tri-layer WSe_2 as bulk and 3-D in nature because quantum confinement can only occur in single or double layer. The same effect could be directly seen while optimizing the band gap as shown in Fig. 2(i-l). As band gap increases from 0.9 eV to 1.2 eV, there is a sharp increase in device performance. This change can be explained as if band gap is small and indirect in nature then some of the frequencies of photon are hindered and higher E_g reduces n_i exponentially consequently V_{OC} increases linearly with E_g [30]. On the other hand, as E_g increases to 1.3 eV and above, it becomes transparent for all incoming photons and results in increase of η as well as J_{SC}. On further increasing E_g, η becomes constant at 11.71 % due to the

Table 3
Summary of the best optimized solar cell parameters.

Cell parameters	n-WSe_2 layer optimized cell	n-WSe_2 and p-cSi wafer optimized solar cell		p-cSi wafer optimized cell for commercially available silicon cell
		(@100 μm p -cSi)	(@ 600 μm p-cSi)	
V_{oc} (mV)	472.4	546.1	550.8	474.2
J_{sc} (mA/cm^2)	24.23	26.07	29.72	18.24
FF (%)	79.07	79.64	79.96	78.65
Efficiency (%)	9.055 (@100 μm p-cSi) (@ triple layer WSe_2 at $N_D = 5 \times 10^{16}$ cm^{-3}, $N_C/N_V = 5 \times 10^{17}$ cm^{-3}, $E_g = 0.9$ eV, $\chi = 3.95$ eV, $\varepsilon_r = 7.2$, $\mu_n = 250$ cm^2/V s and p-cSi at $N_A = 1 \times 10^{16}$ cm^{-3}, $N_C/N_V = 3 \times 10^{19}$ cm^{-3} and $\chi = 4$ eV)	11.34 (@ triple layer WSe_2 at $N_D = 5 \times 10^{16}$ cm^{-3}, $N_C/N_V = 5 \times 10^{17}$ cm^{-3}, $E_g = 0.9$ eV, $\chi = 3.95$ eV, $\varepsilon_r = 7.2$, $\mu_n = 250$ cm^2/V s and @ p-cSi at $N_A = 1 \times 10^{17}$ cm^{-3}, $N_C/N_V = 1 \times 10^{18}$ cm^{-3} and $\chi = 4$ eV)	13.09 (@ triple layer WSe_2 at $N_D = 5 \times 10^{16}$ cm^{-3} at $N_C/N_V = 5 \times 10^{17}$ cm^{-3}, $E_g = 0.9$ eV, $\chi = 3.95$ eV, $\varepsilon_r = 7.2$, $\mu_n = 250$ cm^2/V s and @ p-cSi at $N_A = 1 \times 10^{17}$ cm^{-3}, $N_C/N_V = 1 \times 10^{18}$ cm^{-3} and $\chi = 4$ eV)	6.803 @100 μm p-cSi) (@triple layer WSe_2 at $N_D = 5 \times 10^{16}$ cm^{-3}, $N_C/N_V = 5 \times 10^{17}$ cm^3 and $E_g = 0.9$ eV, $\chi = 3.95$ eV, $\varepsilon_r = 7.2$, $\mu_n = 250$ cm^2/V s @ p-cSi N_A at 5×10^{16} cm^{-3}, N_C/N_V at 2.8×10^{19} cm^{-3},χ at 4.05 eV, $\mu_n = 365.2$ cm^2/V s, $\mu_p = 192.3$ cm^2/V s, $\varepsilon_r = 11.9$

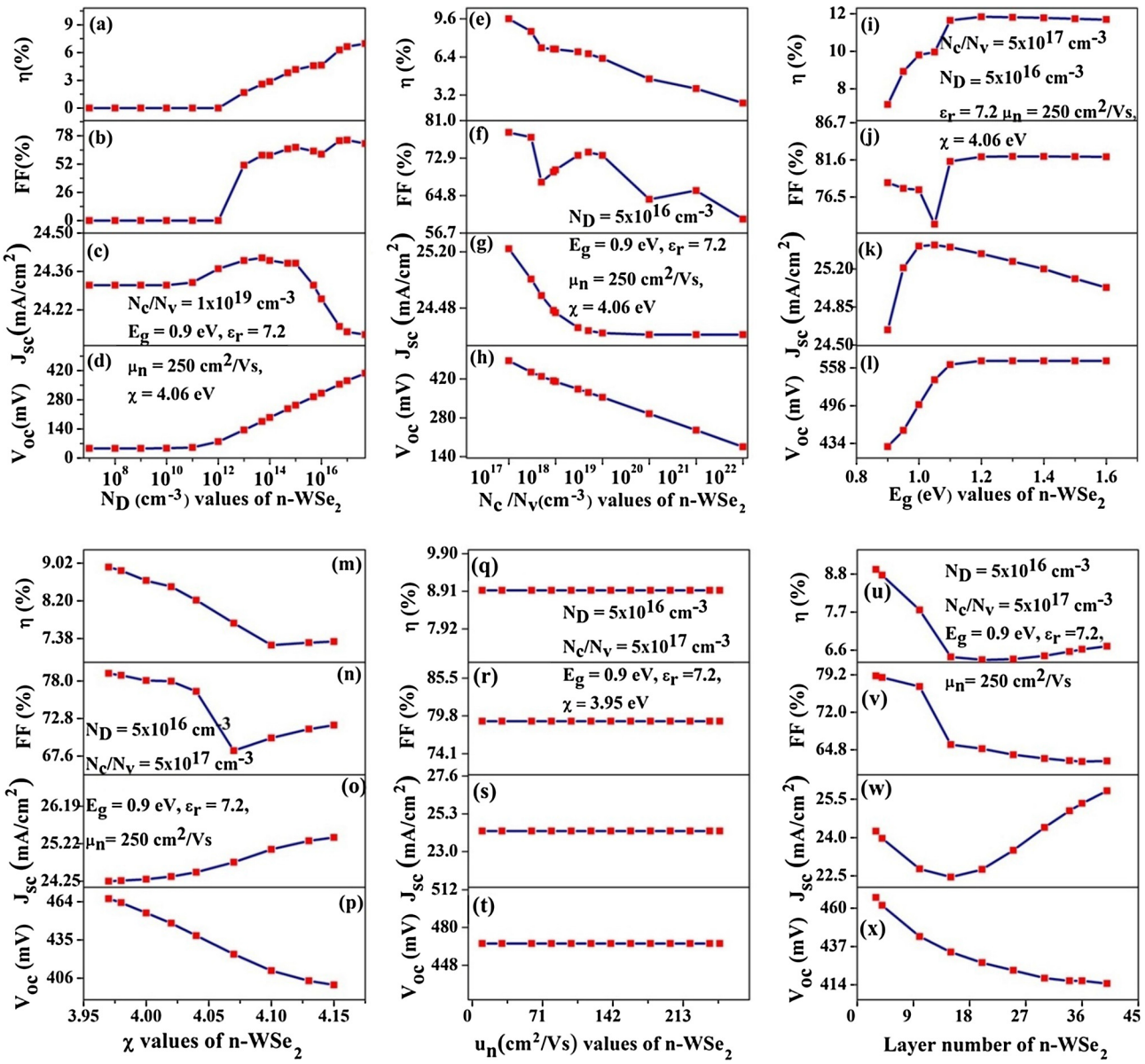

Fig. 2. Optimization of n-WSe_2 layer parameters (a-d) donor concentration (N_D), (e-h) effective density of CB and VB states N_C/N_V (cm^{-3}), (i-l) the band gap energy E_g (eV), (m-p) electron affinity χ (eV), (q-t) electron mobility μ_n (cm^2/V s) and (u-x) layer number while keeping p-cSi layer parameters as, $N_A = 1 \times 10^{16}$ cm^{-3}, $N_C/N_V = 3 \times 10^{19}$ cm^{-3}, χ = 4.0 eV and thickness 100 μm. The other parameters are given in Table 1.

absorption of maximum of photonic waves. It was also observed that if E_g is above 1.2 eV then J_{SC} decreases which is due to large photon absorption at low E_g leading to maximal J_{SC}.

While optimizing χ_{WSe_2} as shown in Figs. 2(m-p), we have observed that V_{OC} decreases from 472.7 eV to 400.8 eV whereas J_{SC} increases slightly. These changes can be understood as χ_{WSe_2} increases conduction band moves downward and facilitates EHP generation as well as carriers flow across the load and thus J_{SC} increases from 24.64 mA/cm^2 to 25.03 mA/cm^2. Furthermore, possible decrease in V_{OC} can be explained by Eq. (1) where Φ_{bi} decreases as Φ_{WSe2} increases which in turn decreases V_{OC}. Since, percentage decrement in V_{OC} is higher as compared to increment in J_{SC} as seen in Fig. 2(m-p), hence η is also reduced to 7.311 % at χ_{WSe_2} = 4.15 eV. Therefore, χ_{WSe_2} is optimized to be 3.95 eV. Relative permittivity (ε_r) and electron mobility (μ_n) were also analyzed and found to be unaffected as shown in Fig. 2(q-t). This can be explained as total current in cell is sum of both photogenerated as well as dark current and η is limited due to recombination of carriers. For organic solar cells, it has been reported that near the short circuit conditions as mobility increases, the photogenerated carrier recombination decreases whereas in open circuited conditions dark carrier recombination increases [31]. Hence, these two opposite effects balance each other and thus performance parameters of cell remain constant over a range of mobility.

In order to further analyze that in the proposed solar cell whether WSe_2 is only functioning as a transparent conducting electrode or actively contributing in photogeneration process too, we have varied layer numbers from 3 to 40. Resulted cell performance parameters have been shown in Fig. 2(u-x) and it was observed that J_{SC}, FF, V_{OC} and η change with layer number. As the layer number increases, mobility is enhanced [11] and thus surface recombination became higher which decreases V_{OC} [32]. This may also be one of the reasons for low J_{SC} and another reason for this decrement in J_{SC} might be the increase of optical absorption

in WSe_2 layer which does not contribute to J_{SC}. Hence, lesser number of photons will reach to silicon and results in lesser photogenerated carriers, as a consequence J_{SC} decreases. Later, J_{SC} increases which may be due to the fact that as layer number increases sheet resistance reduces which in turn improves η as well as J_{SC}. Furthermore, fill factor is also directly affected by series resistance of solar cell [28]. So, the overall efficiency decreases with increase of layer numbers up to 32 and then slightly improves. After optimizing all parameters of n-type tri-layer of W_{Se2}, the maximum η has been achieved to be 9.055 %.

3.2. Optimization and simulation of p-cSi wafer

In order to further improve the efficiency, parameters of p-type silicon layer have been optimized whereas parameters of n-WSe_2 are fixed at optimized ones. When the acceptor concentration (N_A) has been increased from 10^{12} cm^{-3}, χ_{Si} decreases, in turn V_{OC} decreases as shown in Fig. 3(a-d). η is found to be increased at high doping levels. When N_A increases, Fermi level starts moving down and the acceptor band widens and starts overlapping the valence band. This increases the Schottky barrier height (SBH) and consequently V_{bi} and V_{OC} enhance. As it is clear from Eq. (1) that the V_{bi} is directly proportional to N_A which in turn affects V_{OC} which increases from 278.9 mV to 457 mV at N_A of 10^{17} cm^{-3}. Under high doping conditions, lifetime of minority carrier is increased whereas both surface recombination as well as SRH recombination are minimized [27]. High doping in silicon absorber layer makes it act as a Back Surface Field (BSF) layer [32]. As a consequence, both J_{sc} and η increased and η of 9.349 % has been achieved at optimized N_A (1×10^{17} cm^{-3}). After optimizing N_A, N_C/N_V is optimized in the range of 1×10^{18} to 1×10^{25} cm^{-3}. During the optimization process V_{OC} was found to be decreased linearly. It has been further observed that with the increase in N_C/N_V and V_{OC} also decreases from 566.4 mV to 8.549 mV at N_C/N_V of 10^{25} cm^{-3} and the overall η decreases with similar rate. However, J_{SC} is slightly increased from 26.06 mA/

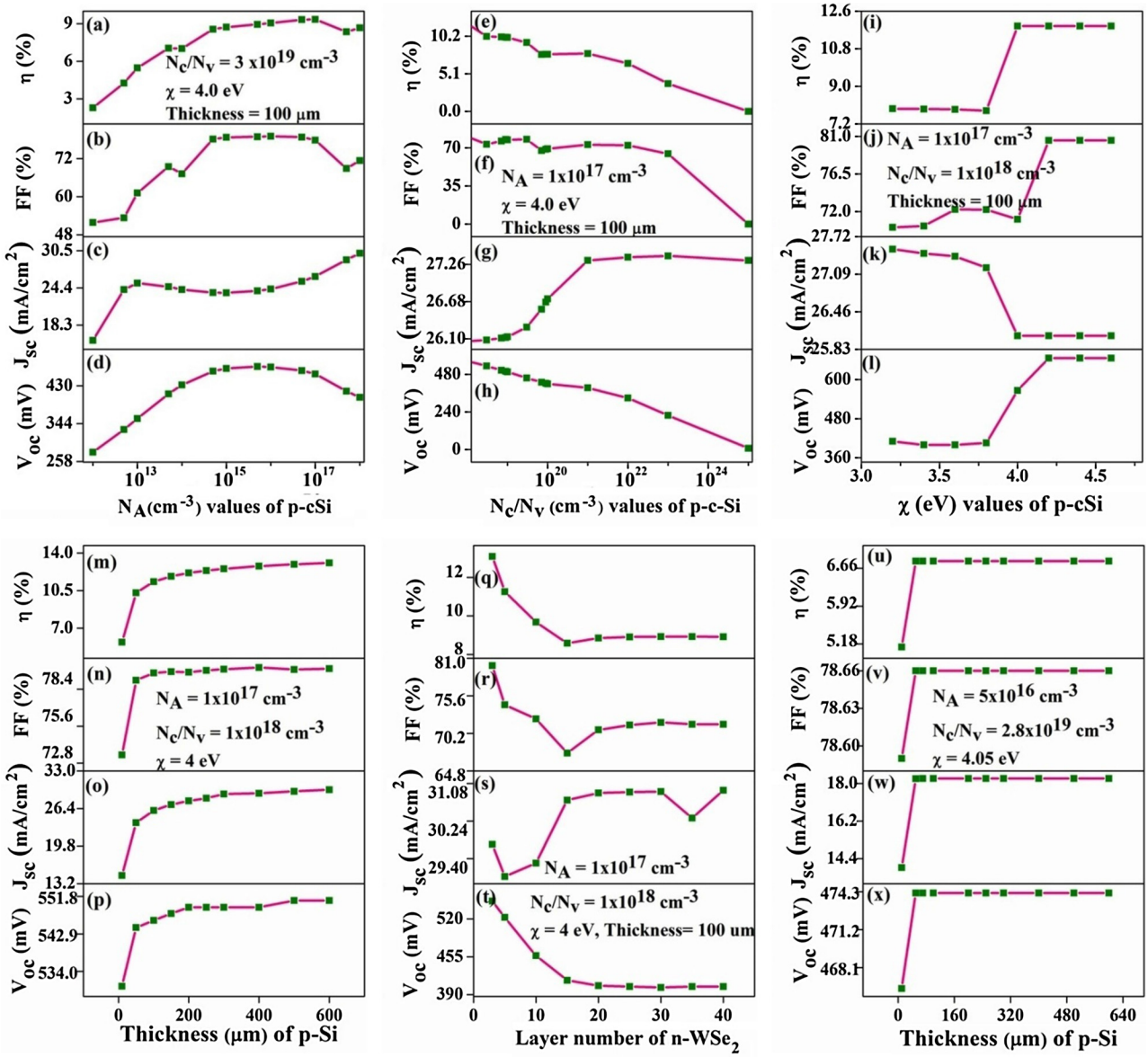

Fig. 3. Graphical representation for the optimization of the parameters of p-cSi wafer.(a-d) the acceptor concentration N_A (cm^{-3}), (e-h) the effective density of states N_C/N_V (cm^{-3}), (i-l) the electron affinity χ (eV), and (m-p) thickness (μm), (q-t) layer number of WSe_2 and (u-x) thickness keeping rest of the parameters fixed as same as that of commercially available silicon. Optimized parameters of n-WSe_2 are taken as: $N_D = 5 \times 10^{16}$ cm^{-3}, $N_C/N_V = 5 \times 10^{17}$ cm^{-3}, $E_g = 0.9$ eV, $\chi = 3.95$ eV, $\varepsilon_r = 7.2$, $\mu_n = 250$ cm^2/V s.

cm^2 to 27.32 mA/cm^2 as N_C/N_V increases due to low recombination across the interface. χ_{Si} has also been optimized and found to be 4 eV as shown in Fig. 3(i-l).

The most important parameter in determining efficiency of cell is the thickness of absorber layer. To study the effect of thickness variation, we have varied the thickness of p-cSi from 50 μm to 600 μm and noticed an appreciable change in all the performance parameters of the cell. As the thickness increases, more number of photons get absorbed which results in large EHP generation and as a consequence J_{SC} as well as other parameters increase [33]. However, while optimizing thickness, diffusion length of generated carriers has to be taken in to account along with absorbance coefficient. When thickness of Si increases, probability of minority carriers to reach either the depletion region or the back surface of Si layer also reduces. Hence, recombination in the Si layer might occur and as a consequence J_{SC} decreases. As thickness is increased from 100 μm to 600 μm, J_{SC} is found to increase from 25.34 mA/cm^2 to 29.72 mA/cm^2 and maximum efficiency 13.09 % has been achieved. After optimizing the parameters of Si layer, cell performance was further analyzed by varying layer number of n-WSe_2 as shown in Fig. 3(q-t). We found that η was reduced to 8.584 % as layer number increased and then reached to a constant value of 8.914 %. After optimizing the parameters of p-Si layer, simulation was further performed considering the parameters of standard commercial available silicon as shown in Fig. 3(u-x). η was found to be increased initially and then becomes constant if Si thickness was above 50 μm. The maximum value of η in case of commercial silicon comes out to be 6.8 %. Optimized cell parameters have been summarized in Table 3. Later, simulation was further carried out by varying both front and back contact. We have simulated the cell by changing the front contact from ITO to aluminum (n = 1.0972, k = 6.7943) and back contact from silver to chromium/silicon (n = 3.0504, k = 4.2504) as used by Tsai et al. [34] and lower work function material like Titanium (n = 1.906, k = 3.0606). No change in the simulated results was observed by doing so.

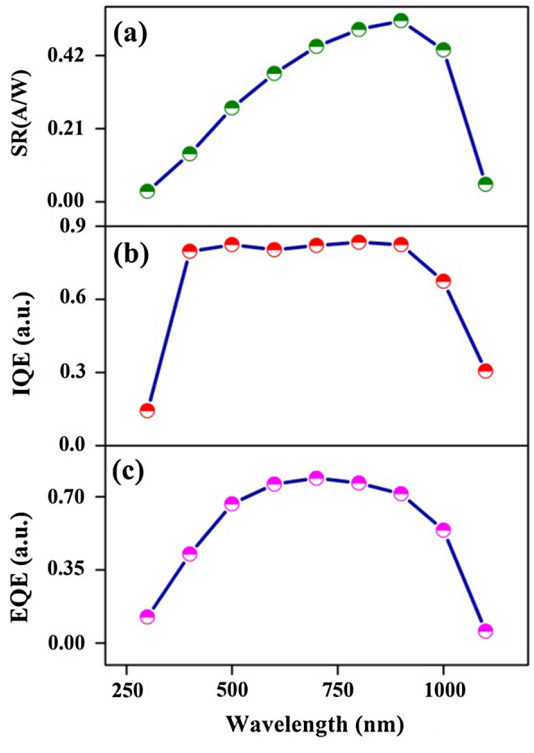

Fig. 4. (a) Spectral response, (b) Internal quantum efficiency (IQE), (c) External quantum efficiency (EQE) of the tri-layer WSe_2-pcSi optimized solar cell at PCE 13.09 %.

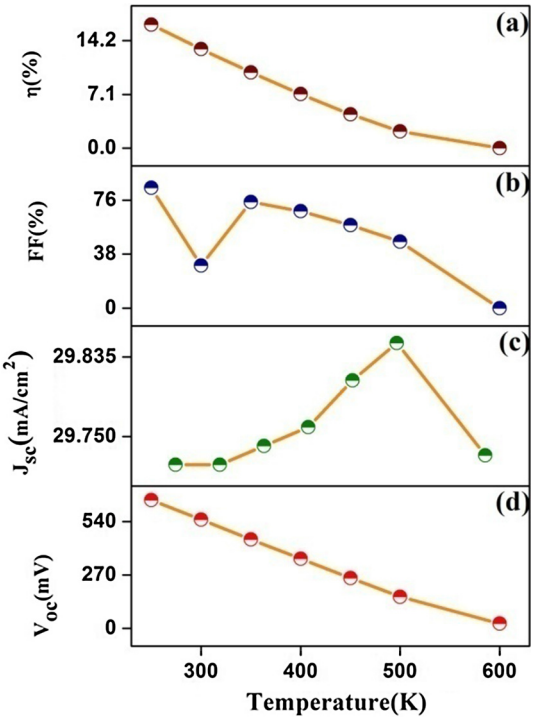

Fig. 5. Variation in solar cell output parameters (a) efficiency (b) fill factor (c) J_{SC} (d) V_{OC} with temperature change.

4. Quantum efficiency, spectral response and temperature dependence

The internal quantum efficiency (IQE) is always either high or equal to the external quantum efficiency (EQE) due to recombination at the interface. The wavelength dependent characteristics IQE, EQE and spectral response (SR) for the optimized simulated solar cell are shown in Fig. 4(a-c). IQE and EQE have shown quite a similar response with wavelength. EQE and IQE started with value of nearly 0.12 and 0.14 at 300 nm and increased to 0.78 and 0.83, respectively in the wavelength range of 300–800 nm. After 800 nm, both are reduced exponentially and become zero at 1100 nm. SR is found to be 0.03 at 300 nm and then increased to 0.51 at 900 nm. Further, SR linearly decreases at higher wavelengths which happens due to the inability of semiconductor to absorb photons with energies lesser than the semiconductor band gap [35]. For analyzing solar cell response under various temperature fluctuations, simulation was performed for best optimized cell in a given temperature range of 200–600 K as shown in Fig. 5(a-d). V_{OC} linearly decreased with increase in temperature which is in accordance with the fact that Voc is directly related to reverse saturation current [36,37]. Increase in temperature reduces the band gap of silicon and thus increases the reverse saturation current whereas V_{OC} decreases. J_{SC} is found to be constant while the overall η decreases with temperature.

5. Conclusions

We have simulated the proposed ITO/n-WSe_2/p-cSi/Ag heterojunction solar cell using AFORS-HET v2.5 and studied the effect of various material parameters on solar cell output independently. Among all the parameters, N_A/N_D, N_C/N_V, thickness of layers and the layer number of WSe_2 were the ones which influenced the cell efficiency. After analyzing n-WSe_2 layer parameters, the maximum η of 9.055 % has been achieved. While after optimizing p-c silicon

layer parameters, we found that the η was greatly enhanced by increasing thickness and reached to 13.09 % maximum at 600 μm. Efficiency 6.8 % was achieved in case commercial silicon of 100 μm thickness. Present results demonstrated that multilayer WSe_2 has potential to act as an efficient transparent conducting electrode material.

Acknowledgement

We thank the financial support from DST-SERB, fast track Program (SR/FTP/PS-055/2012). The authors gratefully acknowledged Helmholtz-Zentrum Berlin for providing AFORS-HET simulation software.

References

[1] S. DeWolf, A. Descoeudres, Z.C. Holman, C. Ballif, High-efficiency silicon heterojunction solar cells: a review, Green 2 (2012) 7–24.
[2] Y. Lin, X. Li, D. Xie, et al., Graphene/semiconductor heterojunction solar cells with modulated antireflection and grapheme work function, Energy Environ. Sci. 6 (2013) 108–115.
[3] X. Li, H. Zhu, K. Wang, et al., Graphene-on-silicon Schottky junction solar cells, Adv. Mater. 22 (2010) 2743–2748.
[4] I. Khrapach, F. Withers, T.H. Bointon, et al., Novel highly conductive and transparent graphene-based conductors, Adv. Mater. 24 (2012) 2844–2849.
[5] S. Bae, H.K. Kim, et al., 30 in roll-based production of high-quality graphene films for flexible transparent electrodes, Nat. Nanotechnol. 5 (2010) 574–578.
[6] R.R. Nair, P. Blake, et al., Fine structure constant defines visual transparency of graphene, Science 320 (2008) 1156965.
[7] F. Xia, T. Mueller, et al., Photocurrent imaging and efficient photon detection in a graphene transistor, Nano Lett. 9 (2009) 1039–1044.
[8] Cheng Gong, Hengji Zhang, et al., Band alignment of two-dimensional transition metal dichalcogenides: application in tunnel field effect transistors, Appl. Phys. Lett. 103 (2013) 053513.
[9] K. Ghosh, U. Singisetti, et al., Thermoelectric transport coefficients in monolayer MoS_2 and WSe_2: role of substrate, interface phonons, plasmon, and dynamic screening, Appl. Phys. 118 (2015) 135711.
[10] W. Liu, J. Kang, et al., Role of metal contacts in designing high-performance monolayer n-type WSe_2 field effect transistors, Nano Lett. 13 (2013) 1983–1990.
[11] W. Liu, W. Cao, et al., High-performance field-effect-transistors on monolayer WSe_2, ECS Trans. 58 (2013) 281–285.
[12] D. Jariwala, V.K. Sangwan, et al., Band-like transport in high mobility unencapsulated single-layer MoS_2 transistors, App. Phy. Lett. 102 (2013) 173107.
[13] J. Huang, L. Yang, et al., Large-area synthesis of monolayer WSe_2 on SiO_2/Si substrate and its device applications, Nanoscale 7 (2015) 4193–4198.
[14] H.J. Chuang, X. Tan, et al., High mobility WSe_2 p- and n-type field-effect transistors contacted by highly doped graphene for low-resistance contacts, Nano Lett. 14 (2014) 3594–3601.
[15] I. Lee, S. Rathi, et al., Non-degenerate n-type doping by hydrazine treatment in metal work function engineered WSe_2 field-effect transistor, Nanotechnology 27 (2016) 225201.
[16] G. Clark, S. Wu, et al., Vapor-transport growth of high optical quality WSe_2 monolayers, Appl. Phy. Lett. 2 (2014) 101101.
[17] R. Stangl, M. Kriegel et al., AFORS-HET, Version 2.2, a Numerical Computer Program for Simulation of Heterojunction Solar Cells and Measurements, IEEE 2, 2006, pp. 1350–1353.
[18] A. Pospischil, M.M. Furchi, et al., Solar-energy conversion and light emission in an atomic monolayer p–n diode, Nat. Nanotech. 9 (2014) 257–261.
[19] Kam, Kam-Keung, Electrical properties of WSe_2, WS_2, $MoSe_2$, MoS_2, and their use as photoanodes in a semiconductor liquid junction solar cell, Retrospective Thesis and Dissertations, Paper 8356,1982.
[20] K. Kim, S. Larentis, et al., Band alignment in WSe_2-graphene heterostructures, ACS Nano 9 (2015) 4527–4532.
[21] H. Fang, S. Chuang, et al., High performance single layered WSe_2 p-FETs with chemically doped contacts, Nano Lett. 12 (2012) 3788–3792.
[22] S. Zhong, X. Hua, W. Shen, et al., Simulation of high-efficiency crystalline silicon solar cells with homo–hetero junctions, IEEE Trans. Electron Dev. 60 (2013) 2104–2110.
[23] U. Gangopadhyay, S. Roy, S. Garain, et al., Comparative simulation study between n- type and p- type silicon solar cells and the variation of efficiency of n- type solar cell by the application of passivation improvement layer with different thickness using AFORS HET and PC1D, IOSR J. Eng. 2 (8) (2012) 41–48.
[24] Z. Zhang, T. Cui, et al., Improved efficiency of graphene/Si heterojunction solar cells by optimizing hydrocarbon feed rate, J. Nanomater. 2014 (2014) 359305.
[25] T. Georgiou, R. Jalil, et al., Vertical field-effect transistor based on graphene–WS_2 heterostructures for flexible and transparent electronics, Nat. Nanotech. 8 (2013) 100–103.
[26] D. Cheyns, J. Poortmans, et al., Analytical model for the open-circuit voltage and its associated resistance in organic planar heterojunction solar cells, Phys. Rev. B 77 (2008) 165332.
[27] G.J.H.M. Wilfried, V. Sark, et al., Physics and Technology of Amorphous-Crystalline Heterostructure Silicon Solar Cells, 1997, 197–395.
[28] M. Dadu, A. Kapoor, et al., Effect of operating current dependent series resistance on the fill factor of a solar cell, Sol. Energy Mater. Solar Cells 71 (2002) 213–218.
[29] S. Sokolic, S. Amon, Modelling heavy doping effects for low temperature device simulations, J. Phys. IV Colloque 04 (C6) (1994) 133–138.
[30] R.R. King, R.A. Sherif, et al., Bandgap engineering in high-efficiency multijunction concentrator cells, in: 3rd International Conference on Solar Concentrators (ICSC-3), Scottsdale, AZ, May 2005.
[31] J.T. Shieh, C. Hua Liu, et al., The effect of carrier mobility in organic solar cells, J. Appl. Phys. 107 (2010) 084503.
[32] J.M. Gee, M.D. Bode, et al., Boron-doped back-surface fields using an aluminum-alloy process, in: 26th IEEE PVSC, 1997, pp. 275–278.
[33] Haque, KASM Ehetshamul, et al., An analysis of efficiency variation in an Al0. 7Ga0. 3As/Al0. 48In0. 52As heterojunction solar cell with change in device parameters using adept 1D software, Electron. Mater. Lett. 9.1 (2013) 47–52.
[34] M.L. Tsai et al., Monolayer MoS_2 heterojunction solar cells, ACS Nano 8 (8) (2014) 8317–8322.
[35] S. Chander, A. Purohit, et al., A study on spectral response and external quantum efficiency of mono-crystalline silicon solar cell, Int. J. Renew. Energy Res. 5 (2015) 1.
[36] A. El-Shaer, M.T.Y. Tadros, et al., Effect of light intensity and temperature on crystalline silicon solar modules parameters, Int. J. Emerg. Technol. Adv. Eng. 4 (2014) 2250–2459.
[37] P. Kumar, S.C. Jain, et al., Effect of illumination intensity and temperature on open circuit voltage in organic solar cells, Appl. Phy. Lett. 94 (2009) 183505.

Quantum Key Distribution Simulation

Suhail Akhtar
Department of CS&IT
Maulana Azad National Urdu University, Hyderabad

Pradeep Kumar
Department of CS&IT
Maulana Azad National Urdu University, Hyderabad

Abdul Wahid
Head, Department of CS&IT
Maulana Azad National Urdu University, Hyderabad

***Abstract*— Quantum cryptography is a new type of cryptographic system. In the traditional system we use mathematic properties in the algorithm to make them strong but these type of algorithms are vulnerable by high computation power computers such as Quantum computer because the security of these algorithms are based on unproven mathematical formula which is thought to be secure and it is thought that currently available computers will take a very long time to break these types of security. So the Quantum cryptography uses the solid concept of Quantum mechanics to secure the data and theoretically it is impossible to crack it. In this technique, data is sent as Quanta which is polarized light.**

***Index Terms*—Cryptography, Quantum Cryptography, Highly Secure cryptography, Light based cryptography, Quantum mechanics**

I. INTRODUCTION

Quantum Cryptography is a new type of cryptography in which polarized light is used to generate the secret key for the encryption/decryption algorithm. This technique helps both parties in the generation of the secret key and it also tells them if someone is trying to snoop the communication and they can take the required measures to protect the communication from the attack.

This study is to understand the alternative of classic cryptography algorithms to generate the cryptographic secret keys for the encryption-decryption algorithm.

This study explores the BB84 algorithm for generation of cryptographic keys on two cases: with and without the attack by an attacker Eve.

II. IMPLEMENTATION (SIMULATION)

Phase 1: BB84 Quantum Transmission

The first step in the algorithm is to prepare a sequence of qubits so Alice create a sequence of 500 qubits by randomly choosing a basis for each qubit,rectilinear polarization (horizontal/0 degrees and vertical/90 degrees) or a diagonal polarization (+45 degrees and -45 degrees shifted) and then by using a quantum channel she sends it to Bob. Then she does the mapping of basis to qubit states. Horizontal and vertical are mapped to qubit states |0> and |1>, and +45 degrees and -45 degrees shifted with the states |+> and |->, respectively.

- Alice selects basis randomly with a basis selection bias of 0.5 which means 50% probability for choosing the basis.
- An eavesdropper Eve is also in between the communication, trying to steal the key. Eve is eavesdropping at a rate of 0.1 and its basis selection bias is 0.5, means its probability to choose a basis will be same for all choices and it will not be biased. She intercepts the qubits, randomly measures them in one of the two mentioned bases either rectilinear or diagonal and thus destroys the originals because a photon will be lost once it is measured, and then sends a new batch of qubits corresponding to her measurements and basis choices to Bob. Since Eve can choose the right basis only 50% of the time on average, about 1/4 of her bits differ from those of Alice.

Phase 2.1: Sifting

When Bob receives the qubits, he measures them by randomly choosing the basis for the qubits and announces on a public classical channel. Alice and Bob then reveal and exchange the bases they used.

All Rights Reserved © 2017 IJARCET

They authenticate these three message exchanges. Whenever the bases happen to match - about 50% of the time on average - they both add their corresponding bit to their personal key. If there is no channel noise then the two keys should be identical unless there has been an eavesdropper. Further details:

- The sifting phase started with 500 transmitted qubits and the resulting bit string was reduced to 257 bits.
- 0.514 of Alice's and Bob's chosen measurement bases match. 0.486 of their chosen bases do not match.
- 0.716 of the two parties measured qubits match before sifting and 0.284 of them do not.
- 0.9144 of the two parties measured qubits match after sifting and 0.0856 of them do not.

Phase 2.2: Sifting Authentication - Linear Feedback Shift Register (LFSR) Universal Hashing

Alice and Bob authenticate their basis exchange messages using the LFSR [11] universal hashing scheme and a mutually preshared secret key for authentication. 3 messages are authenticated in the sifting phase. Further details:

- Bob informs Alice of the qubits he managed to successfully measure and he appends an authentication tag to his message. Authentication cost in terms of key material: 64
- Bob informs Alice of the bases he has chosen for measuring the qubits and he appends an authentication tag to his message. Authentication cost in terms of key material: 64
- Alice informs Bob of the bases she has chosen for preparing the qubits and she appends an authentication tag to her message. Authentication cost in terms of key material: 64

Phase 3.1: Reconciliation - Error estimation

Alice and Bob estimate the error rate in their sifted keys to determine whether they should proceed to error correction or whether they should abort the protocol based on a predefined error tolerance threshold, usually around 11%. Further details:

- Alice and Bob permute their sifted keys in order to flatten the errors across the entire bit string. They then perform the error estimation by comparing a subset of their error-flattened sifted keys.
- An error rate of 0.0784 was estimated using a sample size of 51 given a sampling ratio of 0.2

Phase 3.2: Reconciliation - Error Correction, Cascade

Alice and Bob perform an interactive error correction scheme called Cascade [11] on the public channel in order to locate and correct the erroneous bits in their sifted bit strings. Further details:

- Cascade was run 6 rounds in order to correct the errors.
- 18 erroneous bits were detected and corrected.
- 114 bits were leaked in order to correct the errors.
- With an error probability of 0.0874, the Shannon bound for the number of leaked bits is 89.0, compared to the actual number of leaked bits: 114.

Phase 4: Error Correction Confirmation and Authentication

Alice and Bob confirm and authenticate the error correction phase by computing the hash of their error corrected keys using their mutually pre-shared secret key and by comparing their respective digests. Further details:

- 64 bits of key material (pre-shared secret key) were used to authenticate.
- The Linear Feedback Shift Register (LFSR) universal hashing scheme was used for authentication.

Phase 5: Privacy Amplification

Alice and Bob compute the overall information leakage and run a privacy amplification protocol in order to reduce/minimize Eve's knowledge gained on the key by having eavesdropped on the channel. They do so by locally applying a universal hashing scheme based on Toeplitz matrices [12]. The hashing function will be indexed using yet another chunk of their pre-shared secret keys. They can also define a security parameter to minimize Eve's knowledge to an arbitrary amount. Further details:

- 146 bits were leaked up to this point.
- The key length before running privacy amplification: 206 bits.
- The final key length is 40 bits.
- The chosen security parameter is 20.

All Rights Reserved © 2017 IJARCET

All these steps are repeated for different no of qubits.

Table 1: Simulation results with attack

Initial number of qubits	Final key length	Estimated error
500	40	0.0784
510	30	0.0588
520	73	0.06
530	63	0.0962
540	64	0.0545
550	59	0.0877
Average		0.0726

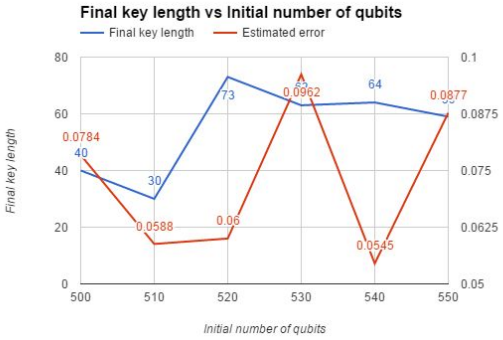

Fig 1: Graph between Final key length vs Initial number of qubits and Estimated error for simulation with attack

Table 2: Simulation results without attack

Initial number of qubits	Final key length	Estimated error
500	68	0. 0408
510	67	0.08
520	68	0.0638
530	82	0.0769
540	102	0
550	89	0.0741
	Average	0.05593

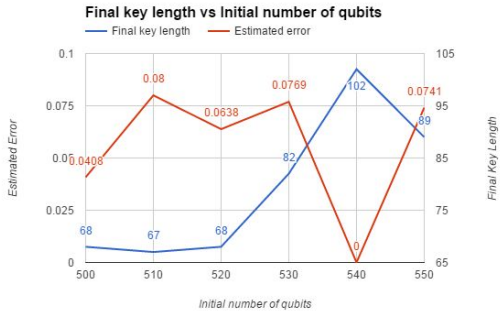

Fig2: Graph between Final key length vs. Initial number of qubits and estimated error for simulation without attack

III. CONCLUSION

QKD is a technique to generate the secret key for an encryption algorithm that takes the data in the form of a light photon. It makes use of Quantum physics and hence theoretically impossible to crack.

In QKD, the attack is identified based on the error. If the error rate is up to a threshold value then participating parties are good to go with the communication but if the error is above a threshold value then they conclude that there is a third party that wants to sniff the communication so based on this error based strategy they take measure to stop these attacks by stopping the communication and protecting the data.

As we have seen that the attack is measured in the form of error in the communication so we can see from the data that we have gathered that the average error in the communication when there is no attack is small compared to the communication while eve is attacking.

From the simulation we can see that due to the different errors the length of the final key is small compared to the initial no of quantum bits but they are unique and secret.
Also, it is hard to know the length of the final key because of the different errors that may occur during the key generation.

The presence of attacker is caught as the increase in the error. If the attacker is present then the error is increased.

All Rights Reserved © 2017 IJARCET

The keys obtained using the quantum technique can be used together with one-time pad algorithm to create the cryptosystem that is perfectly secure.

IV. REFERENCE

[1]. *QKD Simulator - Analysis and Simulation of Quantum Key Distribution*, www.qkdsimulator.com. Accessed 19 Feb. 2017.

[2]. Bennett, Charles H., et al. "Quantum Cryptography, or Unforgeable Subway Tokens." *Advances in Cryptology*, 1983, pp. 267-275.

[3]. C.A.Fuchs, N.Gisin, R.B.Griffiths, C.S.Niu, and A.Peres, Optimal eavesdropping in quantum cryptography. I. Information bound and optimal strategy, Physical Review A 56, 1163 (1997).

[4]. Johnson, R. Colin. "MagiQ employs quantum technology for secure encryption." EE Times. 6 Nov. 2002. URL: http://www.eetimes.com/article/showArticle.jhtml?articleId=16506194 (19 February 2017).

[5]. "Quantum Key Distribution QKD." www.cse.wustl.edu/~jain/cse571-07/ftp/quantum/. Accessed 19 Feb. 2017.

[6]. MagiQ Technologies, Inc. – "Any Sufficiently Advanced Technology is Indistinguishable from Magic.", www.magiqtech.com/Products_files/QBox%20Datasheet-2011.pdf.

[7]. Rieffel, Eleanor, and Wolfgang Polak. "An introduction to quantum computing for non-physicists." *ACM Computing Surveys*, vol. 32, no. 3, 2000, pp. 300-335.

[8]. Lomonaco, *Samuel* J. "A QUICK GLANCE AT QUANTUM CRYPTOGRAPHY." *Cryptologia*, vol. 23, no. 1, 1999, pp. 1-41.

[9]. Hjelme, Dag R., et al. "Chapter 5 - Quantum cryptography." *A Multidisciplinary Introduction to Information Security*, CRC P, 2012.

[10]. "Linear Feedback Shift Registers." *Department of Mathematical and Statistical Sciences | Mathematical & Statistical Sciences | University of Colorado Denver*, www-math.ucdenver.edu/~wcherowi/courses/m5410/m5410fsr.html.

[11]. Sugimoto, T., and K. Yamazaki. "Study on secret key reconciliation protocol 'Cascade'IEICE Transactions on Fundamentals of Electronics, Communications and Computer Sciences." (1987).

[12]. "Toeplitz Matrices, Algorithms and Applications." *ERCIM - the European Research Consortium for Informatics and Mathematics*, www.ercim.eu/publication/Ercim_News/enw22/toeplitz.html.

Suhail Akhtar has received his B.Tech. degree in Computer Science from Uttar Pradesh Technical University, Lucknow, now known as Dr. A.P.J. Abdul Kalam Technical University. Currently, he is pursuing M.Tech. in Maulana Azad National Urdu University in Hyderabad.

Dr. Pradeep Kumar is Associate Professor in the Department of Computer Science & Information technology at Maulana Azad National Urdu University, Hyderabad (Telangana State). He received his Master's degree in Computer Technology and Applications from Delhi Technological University, formerly Delhi College of Engineering, Delhi University. He completed his Ph.D. at the University School of Information & Communication Technology (USICT), Guru Gobind Singh Indraprastha University (GGSIPU), Delhi. His research interests include software reliability engineering, models for software metrics, machine learning, neural network modeling and soft computing. He has more than 25 publications in journals of international repute including national journals, conferences, and proceedings of the international conferences. He is a Member of Association for Computing Machines (ACM), India.

Prof. Abdul Wahid is Dean of School of Computer Science & Information Technology and Head, department of CS&IT at Maulana Azad National Urdu University, Hyderabad (Telangana State), Pin- 500032, India. He is a Member of Association for Computing Machines (ACM), India, Member of Computer Science Teachers Association (CSTA), USA, Senior Member of International Association of Engineers (IAENG), Member of International Association of Computer Science and Information Technology (IACSIT), Singapore and Senior member of Universal Association of Computer and Electronics Engineers. He is a member of editorial board for various national and international journals in the field of Web software engineering.

All Rights Reserved © 2017 IJARCET

ARTICLE IN PRESS

Superlattices and Microstructures xxx (2017) 1–7

Contents lists available at ScienceDirect

Superlattices and Microstructures

journal homepage: www.elsevier.com/locate/superlattices

Realization of all optical logic gates using universal NAND gates on photonic crystal platform

Preeti Rani [a], Shiba Fatima [a], Yogita Kalra [a, *], R.K. Sinha [a, b]

[a] TIFAC-Centre of Relevance and Excellence in Fiber Optics and Optical Communication, Department of Applied Physics, Delhi Technological University (Formerly Delhi College of Engineering), Bawana Road, Delhi, 110042, India
[b] CSIR-Central Scientific Instruments Organization (CSIO), Sector-30C, Chandigarh, 160 030, India

ARTICLE INFO

Article history:
Received 24 February 2017
Available online xxx

Keywords:
Photonic crystal
All-optical logic gates
Response period
Bit rate

ABSTRACT

In this paper, the design of all-optical logic gates using the combination of universal NAND gates has been proposed. The photonic crystal structure consists of triangular lattice arrangement of air holes in silicon. Initially, the all optical NAND gate has been designed and optimized. Further, the optimized NAND gates have been used and arranged in a combination such that the combined structure behaves as an all-optical logic gate specifically, NOT, AND, OR, XOR and XNOR. The truth table for the designed all-optical logic gates has been verified at an operating wavelength of 1.55 μm. The proposed all optical gates exhibit a response period of 2.168 ps with a bit rate of 0.461 Tb/sec. Further, the contrast ratio for the designed gates has also been obtained.

© 2017 Elsevier Ltd. All rights reserved.

1. Introduction

The increase in the speed of the telecommunication systems crossing over the limit of the electronic devices requires the development of the several basic designs such as add-drop multiplexer, header recognition switch, packet synchronization and signal regeneration on the same platform. Logic gates are one of the essential elements to realize all-optical functions for optical signal processing and networking. Recently, various schemes for all-optical logic operations based on linear and nonlinear effects have been reported such as using semiconductor optical amplifier (SOA) [1], ultrafast nonlinear interferometer [2,3], terahertz optical asymmetric de-multiplexer [4], electro-absorption modulators [5], four wave mixing [6] and cross polarization modulation in SOA [7], nonlinear micro ring resonators [8–13], and photonic crystal waveguides [14–16]. All the proposed designs include designing of basic logic gates. In this paper, we propose the design of all optical logic gates using the combination of universal NAND gates. The proposed optical logic gates are based on the phenomenon of optical interference effect and are designed in two dimensional photonic crystal wave-guides composed of air holes in silicon. Initially, the NAND logic gate has been designed and optimized. Further, the combination of three NAND gates has been used to design all optical logic gates. The contrast ratio defined as $CR = 10\log(P_1/P_0)$ dB, where P_1 represents power for logic '1' and P_0 represents power for logic '0', response time and bit rate [17] for the proposed optical logic gates have been calculated. The optimized structures have been analyzed using finite difference time domain (FDTD) method with perfectly matched layer using RSoft Fullwave software.

* Corresponding author.
E-mail address: dryogitakalra@gmail.com (Y. Kalra).

http://dx.doi.org/10.1016/j.spmi.2017.05.046
0749-6036/© 2017 Elsevier Ltd. All rights reserved.

Please cite this article in press as: P. Rani et al., Realization of all optical logic gates using universal NAND gates on photonic crystal platform, Superlattices and Microstructures (2017), http://dx.doi.org/10.1016/j.spmi.2017.05.046

2. Design of all-optical logic gates using NAND gate

In this paper, the combination of three NAND gates has been used to design all optical logic gates. Initially, the universal NAND gate has been designed and optimized similar to [16] as shown in Fig. 1. To design all optical logic NAND gate two dimensional (2D) photonic crystal (PhC) structure consisting of triangular lattice of air holes in silicon with refractive index n = 3.5 has been considered. The band diagram of the bulk PhC as shown in Fig. 1 shows that the light within the wavelength range of 1.2848−1.7017 μm for TE modes cannot pass through the uniform PhC structure. In the optimized design the radius 'r' of air holes is 0.3a, where, 'a' is the lattice constant equal to 0.352 μm. The radius of the center hole has been taken as $r_c = 0.24a$. The radius of six air holes have been taken as $r_b = 0.15a$ and radius of the inner edge air hole of the input waveguide and air holes near to central edge of the output waveguide has been reduced to $r_s = 0.17a$, for an optimized design.

2.1. Realization of all-optical logic gates

A combination of NAND gates has been used to realize all optical logic gates.

2.1.1. NOT gate

A single NAND gate can behave as optical logic NOT gate as shown in Fig. 1. When none of the inputs have been applied at the input ports A and B and only the reference port R have been excited with light having phase angle $\phi = 0^{\circ}$ then logic "1" is obtained at the output port Y. Similarly, when both the inputs have been applied at the input ports A and B with phase angle $\phi = 0^{\circ}$ along with the reference signal R having phase angle $\phi = \pi$ then logic '0' is obtained at the output port Y. The contrast ratio has been calculated to be 3.74 dB. The realized truth table for NOT gate has been summarized in Table 1.

2.1.2. AND gate

To design an optical logic AND gate a combination of optimized NAND gates has been used. Each NAND gate is composed of two input signals, one reference signal and one output signal. Reference signal R and input signals A and B have been introduced into the NAND gate1 and NAND gate 2 respectively. The output Y_1 of NAND gate 1 and Y_2 of NAND gate 2 along with the reference signal R' serve as the input signals for the NAND gate 3 and the final output is Y as shown in Fig. 2. The operation of the AND logic gate for different input combinations of input signal A and B and reference signals R and R' is as follows:

(i) For A = 0, B = 0, R = 1 with phase angle $\phi = 0^{\circ}$ leads to logic '1' for output Y_1 and Y_2. The outputs Y_1 and Y_2 with $R' = 1$ with phase angle $\phi = \pi$ for NAND gate 3 leads to logic '0' at the output port Y.
(ii) When either of the inputs is high i.e. A = 1, B = 0 or A = 0, B = 1 with phase angle $\phi = 0^{\circ}$ with R = 1 with phase angle $\phi = 0^{\circ}$ leads to logic '1' for output Y_1 and Y_2. The outputs Y_1 and Y_2 with $R' = 1$ with phase angle $\phi = \pi$ for NAND gate 3 leads to logic '0' at the output port Y.
(iii) When A = 1, B = 1, with phase angle $\phi = 0^{\circ}$ and R = 1 with phase angle $\phi = \pi$ leads to logic "0" for output Y_1 and Y_2. The outputs Y_1 and Y_2 along with the $R' = 1$ with phase angle $\phi = 0^{\circ}$ for NAND gate 3 leads to logic '1' at the output port Y. The realized truth table for the optical logic AND gate has been summarized in Table 2 and the contrast ratio has been calculated to be 11.47 dB.

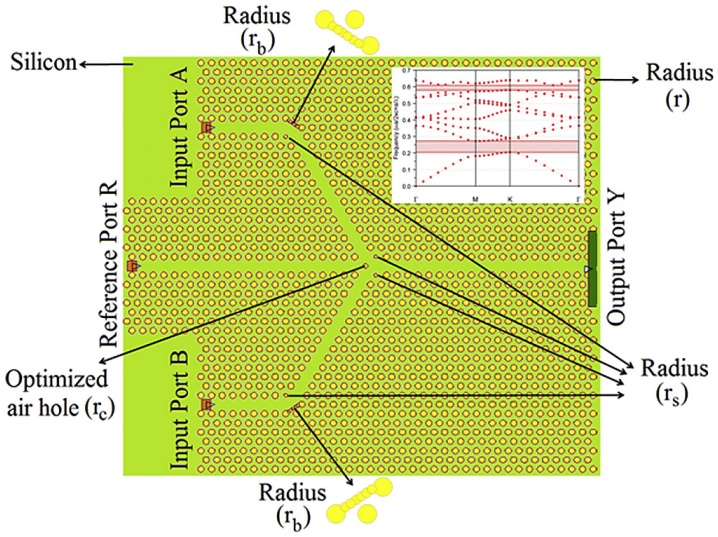

Fig. 1. Layout of optimized logic NAND gate.

Please cite this article in press as: P. Rani et al., Realization of all optical logic gates using universal NAND gates on photonic crystal platform, Superlattices and Microstructures (2017), http://dx.doi.org/10.1016/j.spmi.2017.05.046

Table 1
Truth table for NOT logic gate where output Y is in terms of input power P.

Input A ($\phi = 0^{\circ}$)	Input B ($\phi = 0^{\circ}$)	Reference signal (R)	Logic output	Normalized Output Y
0	0	1($\phi = 0^{\circ}$)	1	0.772 P
1	1	1($\phi = \pi$)	0	1.326 P

2.1.3. OR gate

To design an optical logic OR gate, both the inputs of the NAND gate 1 have been considered as input A and for NAND gate 2 as input B as shown in Fig. 3. The function of optical logic OR gate using the combination of three NAND gates has been demonstrated as follows:

(i) When A = 0, B = 0 and only the reference signal R = 1 with phase angle $\phi = 0^{\circ}$ leads to logic "1" for both the outputs Y_1 and Y_2 of NAND gate 1 and NAND gate 2, respectively. The outputs Y_1 and Y_2 along with the reference signal $R' = 1$ with phase angle $\phi = \pi$ for NAND gate 3 results into logic '0' at the output port Y.
(ii) When A = 0, B = 1 with phase angle $\phi = 0^{\circ}$ along with the reference signal R = 1 with phase angle $\phi = 0^{\circ}$, then outputs Y_1 and Y_2 obtained are logically '1' for NAND gate 1 and NAND gate 2. The outputs Y_1 and Y_2 along with the reference signal $R' = 1$ with phase angle $\phi = 0^{\circ}$ for NAND gate 3 results into logic '1' at the output port Y.
(iii) Similarly, when A = 1, B = 0 with phase angle $\phi = 0^{\circ}$ along with the reference signal R = 1 with phase angle $\phi = 0^{\circ}$ then output Y_1 and output Y_2 obtained is logically '1' for NAND gate 1 and NAND gate 2 and the output Y_1 and Y_2 along with the reference signal $R' = 1$ with phase angle $\phi = 0^{\circ}$ for NAND gate 3 results into logic '1' at the output port Y.
(iv) When A = 1, B = 1 with phase angle $\phi = 0^{\circ}$ along with the reference signal R = 1 with phase angle $\phi = \pi$ then the output Y_1 and Y_2 for NAND gate 1 and NAND gate 2 is logically "0". The output Y_1 and Y_2 along with the reference signal $R' = 1$ having phase $\phi = 0^{\circ}$ for NAND gate 3 resulting into logic "1" at the output port Y. The realized truth table for the OR gate are summarized in Table 3 and the contrast ratio has been obtained to be 12.48 dB.

2.1.4. XOR gate

XOR logic gate can be designed by using combination of three NAND gates when the input A and input B along with their complements has been applied as shown in Fig. 4. The complement of input A has been taken as $C = \overline{A}$ and the complement of input B has been taken as $D = \overline{B}$. The reference signal for NAND gate 1 has been taken as R_1 and for NAND gate 2 as R_2. The NAND gate 3 has input signals Y_1 and Y_2 with reference signal R'. The working principle of XOR logic gate using the proposed combined structure is explained as follows:

(i) When A = 0, B = 0: For the NAND gate 1, A = 0 and C = 1 with phase angle $\phi = 0^{\circ}$ and reference signal $R_1 = 1$ with phase angle $\phi = 0^{\circ}$ then logic "1" is obtained at the output Y_1. Similarly, for the NAND gate 2, B = 0 and D = 1 with phase angle $\phi = 0^{\circ}$ and reference signal $R_2 = 1$ with phase angle $\phi = 0^{\circ}$ then logic '1' is obtained at the output Y_2. The outputs Y_1 and Y_2 along with the reference signal $R' = 1$ having phase angle $\phi = \pi$ for the NAND gate 3 leads to logic '0' at the output port Y.
(ii) When A = 0, B = 1: For the NAND gate 1, B = 1 and C = 1 with phase angle $\phi = 0^{\circ}$ and reference signal $R_1 = 1$ with phase angle $\phi = \pi$ then logic '0' is obtained at the output Y_1. Similarly, for the NAND gate 2, A = 0 and D = 0 with phase angle $\phi = 0^{\circ}$ and the reference signal $R_2 = 1$ with phase angle $\phi = 0^{\circ}$ then logic '1' is obtained at the output Y_2. The outputs Y_1 and Y_2 along with the reference signal $R' = 1$ having the phase angle $\phi = 0^{\circ}$ for the NAND gate 3 leads to logic '1' at the output port Y.
(iii) When A = 1, B = 0: For the NAND gate1, C = 0 and B = 0 with phase angle $\phi = 0^{\circ}$ and the reference signal $R_1 = 1$ with light having phase angle $\phi = 0^{\circ}$, then logic '1' is obtained at the output Y_1. For the NAND gate 2, A = 1 and D = 1 with phase angle $\phi = 0^{\circ}$ and the reference signal $R_2 = 1$ with phase angle $\phi = \pi$ then logic '0' is obtained at the output Y_2. The outputs Y_1 and Y_2 along with the reference signal $R' = 1$ having the phase angle $\phi = 0^{\circ}$ for the NAND gate 3 leads to logic '1' at the output port Y.
(iv) When A = 1, B = 1: For the NAND gate 1, C = 0 and B = 1 with phase angle $\phi = 0^{\circ}$ and the reference signal $R_1 = 1$ with phase angle $\phi = 0^{\circ}$ then logic '1' is obtained at the output Y_1. Similarly, for the NAND gate 2, A = 1 and D = 0 with phase angle $\phi = 0^{\circ}$ and the reference signal $R_2 = 1$ with phase angle $\phi = 0^{\circ}$ then logic '1' is obtained at the output Y_2. The outputs Y_1 and Y_2 along with the reference signal $R' = 1$ with the phase angle $\phi = \pi$ for the NAND gate 3 leads to logic '0' at the output port Y. The realized truth table for XOR logic gate have been summarized in Table 4 and the contrast ratio has been found to be 6.50 dB.

2.1.5. XNOR gate

XNOR logic gate can be designed using the combination of three NAND gates when input A and input B along with their complementary inputs i.e. $C = \overline{A}$ and $D = \overline{B}$ have been applied as shown in Fig. 5.

Please cite this article in press as: P. Rani et al., Realization of all optical logic gates using universal NAND gates on photonic crystal platform, Superlattices and Microstructures (2017), http://dx.doi.org/10.1016/j.spmi.2017.05.046

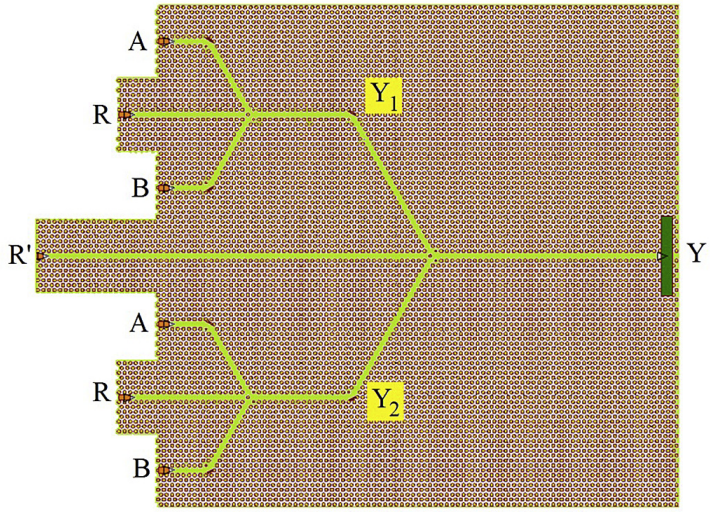

Fig. 2. Optical logic AND gate layout using three NAND gates.

Table 2
Truth table for AND logic gate where output Y is in terms of input power P.

Input A ($\phi = 0^{\circ}$)	Input B ($\phi = 0^{\circ}$)	Reference signal (R)	Reference signal (R')	Logic output	Normalized Output Y
0	0	$1(\phi = 0^{\circ})$	$1(\phi = \pi)$	0	0.051 P
0	1	$1(\phi = 0^{\circ})$	$1(\phi = \pi)$	0	0.132 P
1	0	$1(\phi = 0^{\circ})$	$1(\phi = \pi)$	0	0.131 P
1	1	$1(\phi = \pi)$	$1(\phi = 0^{\circ})$	1	1.717 P

The working principle of XNOR logic gate using the proposed combined structure is explained as follows:

(i) When A = 0, B = 0: For the NAND gate 1, A = 0 and B = 0 and the reference signal $R_1 = 1$ with phase angle $\phi = 0^{\circ}$ then logic '1' is obtained at the output Y_1. Similarly, for the NAND gate 2, C = 1 and D = 1 with phase angle $\phi = 0^{\circ}$ and reference signal $R_2 = 1$ with phase angle $\phi = \pi$ then logic '0' is obtained at the output Y_2. The outputs Y_1 and Y_2 as the inputs signals for the NAND gate 3 along with the reference signal $R' = 1$ with the light having the phase angle $\phi = 0^{\circ}$ leads to logic '1' at the output port Y.

(ii) When A = 0, B = 1: For the NAND gate 1, A = 0 and B = 1 and reference signal $R_1 = 1$ with phase angle $\phi = 0^{\circ}$ then logic '1' is obtained at the output Y_1. Similarly, for the NAND gate 2, C = 1 and D = 0 and the reference signal $R_2 = 1$ with phase angle $\phi = 0^{\circ}$ then logic '1' is obtained at the output Y_2. The outputs Y_1 and Y_2 as the inputs signals for the NAND gate 3 along with the reference signal $R' = 1$ with the light having the phase angle $\phi = \pi$ leads to logic '0' at the output port Y.

(iii) When A = 1, B = 0: For the NAND gate1, A = 1 and B = 0 and reference signal $R_1 = 1$ with light having phase angle $\phi = 0^{\circ}$ then logic '1' is obtained at the output Y_1. For the NAND gate 2, C = 0, D = 1, and reference signal $R_2 = 1$ with phase angle $\phi = 0^{\circ}$ then logic '1' is obtained at the output Y_2. The outputs Y_1 and Y_2 as the inputs signals for the NAND gate 3 along with the reference signal $R' = 1$ with the light having the phase angle $\phi = \pi$ leads to logic '0' at the output port Y.

(iv) When A = 1, B = 1: For the NAND gate 1, A = 1 and B = 1 with phase angle $\phi = 0^{\circ}$ and reference signal $R_1 = 1$ with light having phase angle $\phi = \pi$ then logic '0' is obtained at the output Y_1. Similarly, for the NAND gate 2, C = 0 and D = 0 and the reference signal $R_2 = 1$ with light having phase angle $\phi = 0^{\circ}$ then logic '1' is obtained at the output Y_2. The outputs Y_1 and Y_2 as the inputs signals for the NAND gate 3 along with the reference signal $R' = 1$ with light having the phase angle $\phi = 0^{\circ}$ leads to logic '1' at the output port Y. The realized truth table has been summarized in Table 5 and the contrast ratio for XNOR logic gate has been found out to be 6.50 dB.

2.2. Response time of all-optical logic gate structure using three NAND gates

The response time for the all optical logic gates have been determined using time evolving curve of the output power as shown in Fig. 6. At steady-state, the time taken to reach output power from 0 to 90% of the average output power (P_{av}) is ct = 197 μm or t = 2.298 ps. This time consists of two parts one of which is time due to transmission delay i.e. $t_1 = 1.756$ ps and another is time taken by output power to climb from 0.1% to 90% of P_{av} i.e. $t_2 = 0.542$ ps. It has been expected that the falling time from P_{av} to 10% of P_{av} is approximately equal to t_2. Thus, a narrow pulse width of $2t_2 = 1.084$ ps can be produced and

Please cite this article in press as: P. Rani et al., Realization of all optical logic gates using universal NAND gates on photonic crystal platform, Superlattices and Microstructures (2017), http://dx.doi.org/10.1016/j.spmi.2017.05.046

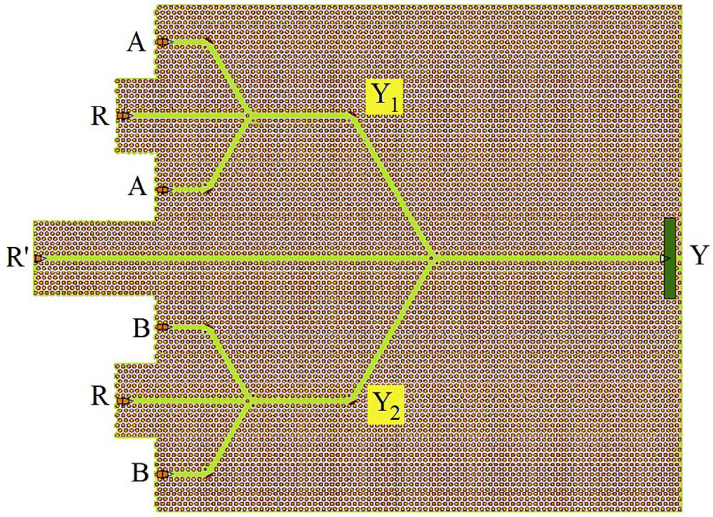

Fig. 3. Optical logic OR gate layout using three NAND gates.

Table 3
Truth table for OR logic gate where output Y is in terms of input power P.

Input A ($\phi = 0^{\circ}$)	Input B ($\phi = 0^{\circ}$)	Reference signal (R)	Reference signal (R')	Logic output	Normalized Output Y
0	0	$1(\phi = 0^{\circ})$	$1(\phi = \pi)$	0	0.051 P
0	1	$1(\phi = 0^{\circ})$	$1(\phi = 0^{\circ})$	1	0.904 P
1	0	$1(\phi = 0^{\circ})$	$1(\phi = 0^{\circ})$	1	0.891 P
1	1	$1(\phi = \pi)$	$1(\phi = 0^{\circ})$	1	0.717 P

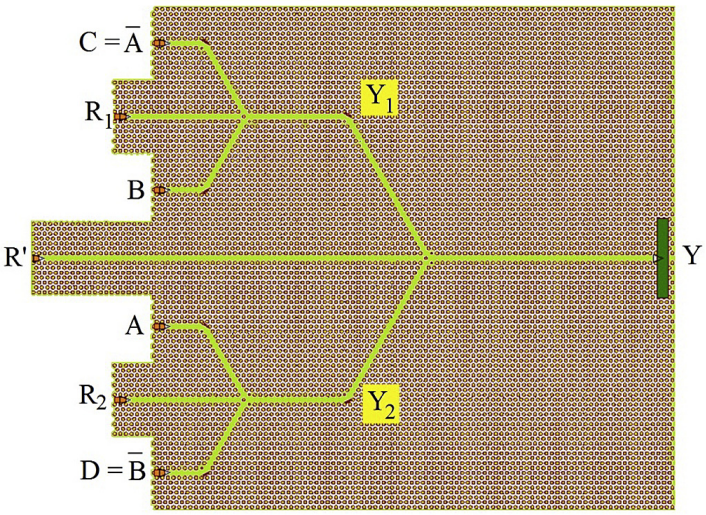

Fig. 4. Optical logic XOR gate layout using three NAND gates.

Table 4
Truth table for XOR logic gate where output Y is in terms of input power P.

Input A ($\phi = 0^{\circ}$)	Input B ($\phi = 0^{\circ}$)	Input C (complement of A) ($\phi = 0^{\circ}$)	Input D (complement of B) ($\phi = 0^{\circ}$)	Reference signal(R_1)	Reference signal(R_2)	Reference signal (R')	Logic Output	Normalized Output Y
0	0	1	1	$1(\phi = 0^{\circ})$	$1(\phi = 0^{\circ})$	$1(\phi = \pi)$	0	0.130 P
0	1	1	0	$1(\phi = \pi)$	$1(\phi = 0^{\circ})$	$1(\phi = 0^{\circ})$	1	0.574 P
1	0	0	1	$1(\phi = 0^{\circ})$	$1(\phi = \pi)$	$1(\phi = 0^{\circ})$	1	0.581 P
1	1	0	0	$1(\phi = 0^{\circ})$	$1(\phi = 0^{\circ})$	$1(\phi = \pi)$	0	0.133 P

Please cite this article in press as: P. Rani et al., Realization of all optical logic gates using universal NAND gates on photonic crystal platform, Superlattices and Microstructures (2017), http://dx.doi.org/10.1016/j.spmi.2017.05.046

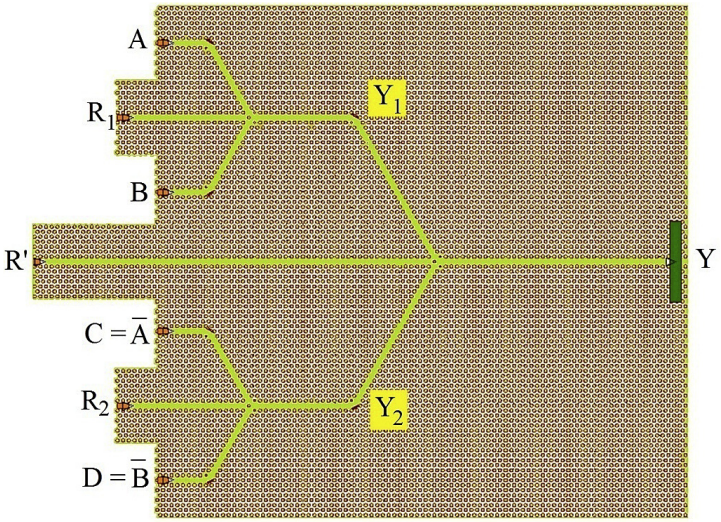

Fig. 5. Optical logic XNOR gate layout using three NAND gates.

Table 5
Truth table for XNOR logic gate where output Y is in terms of input power P.

Input A ($\phi = 0^{\circ}$)	Input B ($\phi = 0^{\circ}$)	Input C (complement of A) ($\phi = 0^{\circ}$)	Input D (complement of B) ($\phi = 0^{\circ}$)	Reference signal(R_1)	Reference signal(R_2)	Reference signal (R')	Logic Output	Normalized Output Y
0	0	1	1	$1(\phi = 0^{\circ})$	$1(\phi = \pi)$	$1(\phi = 0^{\circ})$	1	0.581 P
0	1	1	0	$1(\phi = 0^{\circ})$	$1(\phi = 0^{\circ})$	$1(\phi = \pi)$	0	0.133 P
1	0	0	1	$1(\phi = 0^{\circ})$	$1(\phi = 0^{\circ})$	$1(\phi = \pi)$	0	0.130 P
1	1	0	0	$1(\phi = \pi)$	$1(\phi = 0^{\circ})$	$1(\phi = 0^{\circ})$	1	0.574 P

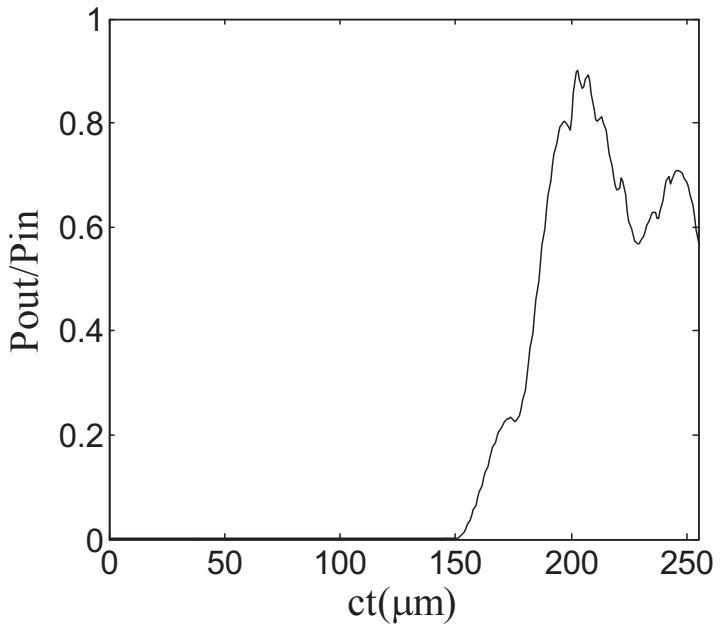

Fig. 6. Time evolution curve for all-optical logic gate structure.

hence the response time of 2.168 ps has been achieved if the ON and OFF time of the signal is same which leads to a bit rate of 0.461 Tbit/s.

3. Conclusion

In this paper, we have proposed the design of all-optical logic gates namely, AND, OR, NOT, XOR and XNOR using the combination of universal optical logic NAND gates in two-dimensional PhC waveguides. The performance of the proposed PhC structure has been analyzed by using PWE method and the optimization characteristics have been simulated using FDTD

Please cite this article in press as: P. Rani et al., Realization of all optical logic gates using universal NAND gates on photonic crystal platform, Superlattices and Microstructures (2017), http://dx.doi.org/10.1016/j.spmi.2017.05.046

method. The optimized NAND gates have been arranged in a combination such that the combined structures behave as all-optical logic gates.

Acknowledgment

Authors gratefully acknowledge (i) the initiatives and support provided by establishment of the TIFAC-Centre of Relevance and Excellence in Fiber Optics and Optical Communication at Delhi College of Engineering, now DTU, Delhi through "Mission REACH" program of Technology Vision-2020″, Government of India, (ii) support through DRDO CARS project on "Modelling and simulation of single mode CW high power fiber lasers".

References

[1] J.Y. Kim, J.M. Kang, T.Y. Kim, S.K. Han, 10Gbit/s all-optical composite logic gates with XOR, NOR, OR and NAND functions using SOA-MZI structures, Electron. Lett. 42 (2006) 303–304.
[2] N.S. Patel, K.L. Hall, K.A. Rauschenbach, 40-Gbit/s cascadable all-optical logic with an ultrafast nonlinear interferometer, Opt. Lett. 21 (1996) 1466–1468.
[3] Y.-D. Wu, T.-T. Shih, M.-H. Chen, New all-optical logic gates based on the local nonlinear Mach–Zehnder interferometer, Opt. Express. 16 (2008) 248–257.
[4] A.J. Poustie, K.J. Blow, A.E. Kelly, R.J. Manning, All-optical binary half-adder, Opt. Commun. 156 (1998) 22–26.
[5] Ehab S. Awad, P. Cho, Julius Goldhar, High-speed all-optical AND gate using nonlinear transmission of electro absorption modulator, IEEE Phot. Technol. Lett. 13 (2001) 472–474.
[6] D. Nesset, M.C. Tathlam, D. Cotter, All-optical AND gate operating on 10 Gbit/s signals at the same wavelength using four-wave mixing in a semiconductor laser amplifier, Electron Lett. 31 (1995) 896–897.
[7] H. Soto, C.A. Díaz, J. Topomondzo, D. Erasme, L. Schares, G. Guekos, All-optical AND gate implementation using cross-polarization modulation in a semiconductor optical amplifier, IEEE Phot. Technol. Lett. 14 (2002) 498–500.
[8] L. Zhang, Electro-optic directed logic circuit based on micro ring resonators for XOR/XNOR operations, Opt. Express 20 (2012) 11605–11614.
[9] Y. Tian, Proof of concept of directed OR/NOR and AND/NAND logic circuits consisting of two parallel micro ring resonators, Opt. Lett. 36 (2011) 1650–1652.
[10] Q. Xu, R. Soref, Reconfigurable optical directed-logic circuits using micro resonators-based optical switches, Opt. Express. 19 (2011) 5244–5259.
[11] S. Pereira, P. Chak, J.E. Sipe, All-optical AND gate by use of a Kerr nonlinear micro-resonator structure, Opt. Lett. 28 (2003) 444–446.
[12] Y. Dumeige, L. Ghisa, P. Féron, Y. Dumeige, Integrated all-optical pulse restoration with coupled nonlinear microring resonators, Opt. Lett. 31 (2006) 2187–2189.
[13] T.A. Ibrahim, K. Amarnath, L.C. Kuo, R. Grover, V. Van, P.-T. Ho, Photonic logic NOR gate based on two symmetric microring resonators, Opt. Lett. 29 (2004) 2779–2781.
[14] P. Rani, Y. Kalra, R.K. Sinha, Realization of AND gate in Y shaped photonic crystal waveguide, Opt. Commun. 298 (2013) 227–231.
[15] S.K. Tripathy, S. Sahu, C. Mohapatro, S.P. Dash, Implementation of optical logic gates using closed 2D photonic crystal structure, Opt. Commun. 285 (13–14) (2012) 3234–3237.
[16] P. Rani, Y. Kalra, R.K. Sinha, Design of all optical logic gates in photonic crystal waveguides, Optik 126 (2015) 950–955.
[17] C.J. Wu, C.P. Liu, Z. Ouyang, Compact and low-power optical logic NOT gate based on photonic crystal waveguides without optical amplifiers and nonlinear materials, Appl. Opt. 51 (5) (2012) 680–685.

Please cite this article in press as: P. Rani et al., Realization of all optical logic gates using universal NAND gates on photonic crystal platform, Superlattices and Microstructures (2017), http://dx.doi.org/10.1016/j.spmi.2017.05.046

Multimed Tools Appl
DOI 10.1007/s11042-017-4767-x

Review based emotion profiles for cross domain recommendation

Shampa Chakraverty[1] · **Mala Saraswat**[1]

Received: 30 June 2016 / Revised: 26 March 2017 / Accepted: 27 April 2017
© Springer Science+Business Media New York 2017

Abstract Several e-commerce sites are reaping the benefits of Cross-Domain Recommendation (CDR) systems to cross-sell products, guide new users and increase revenues. Current research works augment user-item ratings with a variety of auxiliary information such as location, personality, geo-tags and multimedia content that link multiple domains to provide effective CDR. In this paper, we propose a fresh perspective for generating recommendations across different domains by tapping the emotions that are encapsulated within user generated textual content such as reviews, blogs and comments. Such emotions serve as strong socio-psychological links between various entertainments domains and have the potential to obviate the cold start problems. Our CDR scheme uses an enriched emotion lexicon to analyze the emotions in online content expressed by users in the source and target domains and generates emotion-profiles of items and users in both domains. Subsequently, it applies collaborative filtering to match these profiles in order to recommend items in the target domain. We illustrate the working of our emotion-based CDR scheme using the movie and book domains as a case study. Experimental results on Movielens and Bookcrossing datasets yield 28.9% F1-measure which is a marked improvement of 71.1% as compared with a recently reported topic modeling approach to CDR for entertainment domains.

Keywords Recommender system · Cross domain · Emotion · Lexicons · Online content · Collaborative filtering

1 Introduction

As the World Wide Web (www) continues to host an ever-exploding amount of information, it has become rather difficult to retrieve the relevant information among this morass when we search for something specific. Online recommender systems alleviate the information overload

✉ Mala Saraswat
malasaraswat@gmail.com

[1] Department of Computer Engineering, Netaji Subhas Institute of Technology, Delhi, India

Published online: 11 May 2017

problem by drawing upon the cumulative experience of past users to guide current users [1]. Many popular e-commerce websites have boosted their sales and revenues manifold by employing online recommender systems [38]. The success of popular mobile applications like carpooling for taxicab services [47] and travel recommendation [8, 27] prove the leveraging impact of online recommender systems and motivate researchers to enhance their functionality and performance.

Most online recommender systems follow one or a combination of the following classical approaches: Collaborative Filtering (CF) and Content Based Recommender systems (CBR). CF systems utilize the wisdom of crowds to recommend items according to the preferences of users with similar tastes [39]. CBR systems extract content on items and match it with a user's own preferences and profile attributes to recommend new items that are likely to appeal to the user [31]. However, both CF and CBR approaches suffer some limitations. CF based recommender systems cannot deal with sparse rating matrices when newly introduced items are added. They encounter the cold start problem when a new user registers into the website and has no ratings as yet. Pure CBR systems also fail to deal with new users because they have to rate a sufficient number of items before a content-based recommender system can really understand their preferences and present reliable recommendations [1]. In addition, they suffer from content specialization since they tend to recommend items with high similarity to users' preferences only.

Of recent, Cross Domain Recommendation (CDR) systems have carved out a significant space in the domain of online recommender systems. CDR systems mine knowledge on users and items in a *source* domain for improving the quality of the recommendations in a *target* domain. They have the potential to tackle the problems of cold start and sparse ratings by tapping the knowledge gained from one domain and transferring it to another. They can also provide joint recommendations for items belonging to different domains by linking information from both domains [10]. CDR systems have been shown to improve the accuracy, diversity, novelty and serendipity of recommendations [6]. Out of the various existing CDR approaches, some aggregate knowledge from two or more domains by using explicitly specified common information [9, 13, 32, 41] or by transferring latent features [18, 25, 29, 30].

Emotions are integral to all entertainment domains. No wonder that after listening to music, playing a video game or watching a popular television show, many people enthusiastically post reviews to share their feelings and rate them. These reviews convey an array of emotions that reflect users' engagement. However, the potential of emotions as a basis for recommending items across different domains has not been adequately harnessed. In this paper, we bring in a fresh perspective for implementing CDR systems by employing emotion analysis on user generated content in the form of reviews.

- We develop an innovative scheme to build the emotional profiles of items and users in the source and target domains by using reviews and ratings and correlate them across domains to provide recommendations for items to a new user in the target domain.
- We illustrate our approach using movies and books as representative domains, using the Movielens dataset in imdb.com to represent the Movie domain and the Bookcrossing dataset in amazon.com to represent the Book domain. Nevertheless, the approach is essentially applicable to any other pair of source and target domains where human choices are driven by emotions such as music, television shows and video games.
- We adopt a systematic testing approach to verify that users' ratings reflect their degree of acceptance or rejection of the emotional content of items. Based on this

assumption, we evaluate the performance of the proposed emotion-driven CDR system. Experimental results show a marked improvement of 71.1% in the F1 measure over a recently reported CDR approach that employs topic modeling on user reviews in movie and book domains [24].

The rest of the paper is organized as follows. We first explain the motivating factors that led to the current work in section 2. We discuss the most relevant prior works in the domain of CDR in section 3. Section 4 presents the overall framework for our proposed Emotion Driven Cross Domain Recommender (ECDR) system. Section 5 validates the premise of our approach and evaluates the algorithm for prediction accuracy on real world data. We conclude our findings in section 6.

2 Motivation

The driving factor for using emotions as a vehicle for CDR in the current work is the observation that all entertainment domains such as movies, books and television shows, primarily appeal to our emotional sensibilities. These offerings are designed to arouse innate emotions as well as hues of variegated emotions. It is widely recognized that the most powerful way of reaching out to audiences is through emotions of the characters [2].

Reviews bear emotions When people read a book, watch a movie or a television show or listen to music, a whole gamut of emotions comes into play. Whatever the underlying theme, people derive satisfaction when they undergo the desired emotional states while engaging with the offering. On the other hand, if an offering fails to satiate users' emotional urges appropriately, they feel rather disappointed. This is most evident from the reviews written by users. Even a cursory glance through these reviews shows that users rave about movies, books or songs they had liked and decry in no uncertain terms items that disappointed them. Even very short reviews are like bursts of emotional phrases. This observation drives us to tap the opportunity for garnering the abundant emotional content from user reviews and utilize them for performing CDR.

User ratings Not many users write reviews, but most rate the items. We assume that users' rating for an item indicate their overall assessment of the emotion profile of that item. For example, if their ratings for a movie are high, it indicates that they associate deeply with the emotion profile of the movie. If on the other hand, their ratings are low, it shows that they attach little value to its emotion profile. In order to validate this assumption, we conducted an experiment to determine whether one can use emotions to predict a user's item preferences in a given domain. The results reported in section 5 indicate that user ratings do indicate a user's acceptance or rejection of different emotion profiles. We therefore find it judicious to derive a user's emotion profile by weighing the emotion profile of each item by its rating.

Genres and emotions A common feature of most entertainment domains is their categorization into major genres. Film genres and literary genres are both based on the concept of genres as prototypical narratives that invoke emotions [11, 16]. We watch and read comedies because we want to be amused, thrillers because we want to experience cliffhangers and musicals because they touch our hearts. Likewise, television shows are categorized into genres

such as reality shows, fantasy and family drama, each genre having its own emotional appeal. Video games belong to various sub-genres such as platform games, shooting games and survival games which excite different kinds sporting instincts. We therefore contend that one can refine the emotional profiles of items by taking into cognizance the specific role of different emotions in different genres.

The above observations reaffirm the power of emotions, user ratings and genre information as relevant features for linking different entertainment domains. As discussed in the next section, previous research has demonstrated that topics extracted from reviews and artifacts such as emotion tags can be used to link different domains. However, current CDR systems do not utilize the rich presence emotions in reviews. This paper establishes emotions as an important factor for linking items in disparate entertainment domains. Moreover, the relationship between user ratings and the emotional content of items has not been properly examined in the literature. User ratings are integral to any recommendation system. This work further establishes the correlation between users' ratings and their degree of acceptance or rejection for the emotional profiles of the rated items. This provides us a firm ground to build a CDR system by using emotions gathered from user reviews, user ratings and genre information of items in the source and target domains.

3 Prior work

The area of CDR is topical and rife with challenges. To tackle the data sparsity and cold start problems that plagued early CF based recommender systems, existing approaches for CDR systems exploit a variety of artifacts that link different domains. Shi et al. [42] surveyed different sources of rich side information such as tags, geotags, multimedia content, reviews and comments that provide subsidiary information to improve the quality of recommendations. Fernandez et al. [13] use a content based approach by exploiting the DBpedia ontology to build a knowledge-based semantic framework that connects the domains of architecture and music. Social tags [32, 41] have been used as inter-domain links in [32, 41]. In [9], the authors tap the overlap between user and item attributes to connect domains. An alternative approach is to transfer knowledge among domains by sharing their latent features [29, 30] or by transferring rating patterns across the two domains [18, 25]. In [15], the authors exploit the Five Factor Model (FFM) of personality traits as a bridge to transfer user preferences between different domains using Latent Semantic Analysis (LSA).

Topics extracted from unstructured and/or unlabeled data such as reviews and comments gathered from different domains provide an important link for CDR [24, 26, 43]. To solve the problem of different vocabularies in distinct domains, the approach in [24], acronymed SCD, employs semantic clustering with Latent Dirichlet Analysis (LDA) to build a common space for the corpora in both domains. The topics in both domains, which are extracted from semantic word clusters obtained from a common latent space, are compared using cosine similarity. Experimenting with Movielens[1] and Bookcrossings[2] datasets, the authors show that the use of semantic clustering brings about a two-fold increase in the precision of CDR as compared with tag weighted LDA without semantic clustering [24]. The work in [37] further

[1] MovieLens Dataset: http://grouplens.org/datasets/movielens/
[2] BookCrossing Dataset: http://www2.informatik.uni-freiburg.de/~cziegler/BX/

extends the topic modeling approach by employing Pointwise Mutual Information (PMI) and Explicit Semantic Analysis (ESA) for assessing topic similarity.

User generated data such as reviews and comments embody a higher level of connotation of words and sentences that reflect their underlying emotional content. Emotions, being an important element of human behavior, acts as an important factor that generates a liking towards a particular item and helps in decision making. In recent years emotions have been used in various ways for recommending items [14, 40, 45]. Winoto et al. detect and model a user's mood and suggest movies of different genres accordingly [45]. Shi et al. propose a contextual mood specific movie similarity, which is exploited in a joint matrix factorization model [40]. This incorporates movie mood tags from the movie dataset as a regularization term for factorizing the user-item rating matrix. Fernández-Tobías et al. extract emotional information from item annotations in social tagging systems and then transform the tags into emotion oriented item profiles [14]. In [17], the authors build a model for classifying books according to emotional tags by performing a lexical analysis of book blurbs for the social network site Zazie.[3]

All the above emotion driven approaches lend themselves to single domain recommendation systems only. Not much work has been reported on the utility of emotions in the arena of CDR. Kaminskas and Ricci use emotions for recommending music compositions for Places of Interest (POI) by utilizing the emotion tags attached by users' to the places of interest that they had visited such as opera and stadium [22]. Here emotional tags attached to music and POIs act as a common set of descriptive features for establishing a match between these two domains. However, tags are compact descriptions and restrain users form choosing terms freely. Therefore, they do not capture emotions as effectively as reviews. While writing reviews, users freely pen down their thoughts and emotions. Therefore reviews provide a richer source of emotions than tags do.

Taking cues from the above works, we explore how one can exploit emotions extracted from reviews written by users for items in entertainment domains to provide CDR. In our combined approach, we propose to use both content in the form of reviews as well as user preferences in the form of ratings.

4 A framework for emotion driven CDR

Fig. 1 illustrates the framework of the proposed Emotion-driven Cross Domain Recommender (ECDR) system. There are two domains of interest to a user u (1) the Source Domain (DS) in which the user u is active, i.e. purchases and rates its items regularly and (2) the Target Domain (DT) which comprises of items that may be of interest to the user but are hitherto unexplored. The aim of ECDR is to recommend items from DT to u based on the rating patterns in DS and similarities between DS and DT.

The first module M1- *Data Preparation,* extracts user-item rating matrices and user reviews from the source and target domains and prepares a consolidated textual corpus for each item included in the respective domains. These raw corpuses are pre-processed in module M2

[3] Zazie: http://www.zazie.it

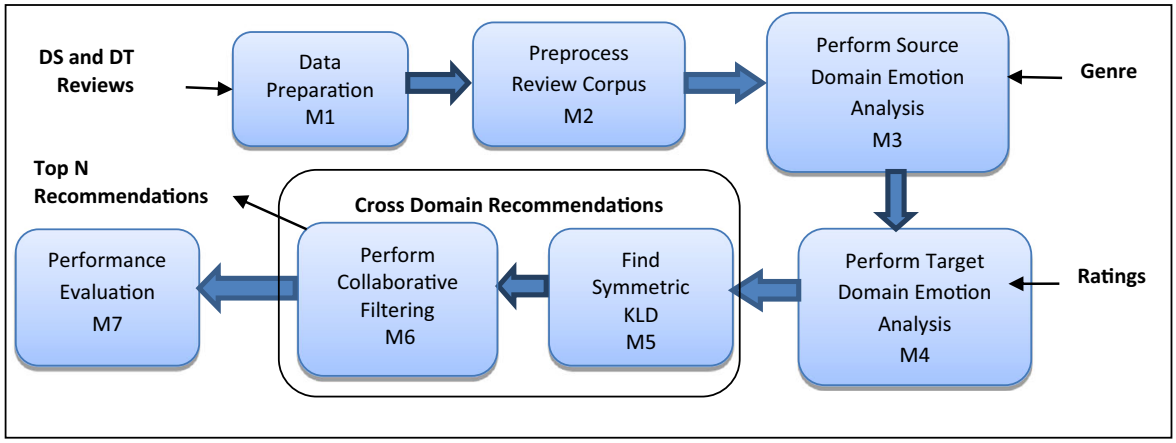

Fig. 1 Block Diagram of the proposed ECDR system

before being processed further for emotion analysis in modules M3 and M4 which generates the following emotion profiles for each domain:

i) The emotion profiles of the items offered in the domain,
ii) The emotion profiles of the users who buy and/or rate those items,
iii) The consolidated emotion profile of the domain itself.

The emotion profiles thus generated serve as links between the two domains to perform CDR. Module M5 first evaluates the distances between users' profiles in source and target domains using symmetric Kullback-Liebler Divergences (KLD) [21]. Module M6 then performs a collaborative filtering to generate Top N recommendations. Module M7 is the Performance Evaluation module that evaluates the performance of the ECDR system.

The generic ECDR framework depicted in Fig. 1 can be applied to any pair of emotion-centric entertainment domains that publish user reviews. To illustrate the proposed ECDR approach, we use movies and books as representative entertainment domains, using the Movielens dataset in *imdb.com* to represent the Movie domain and the Bookcrossing dataset in *amazon.com* to represent the Book domain.

We now focus on each module of the ECDR system shown in Fig. 1.

4.1 Data preparation

The data preparation module M1first extracts the user-item rating matrices for the source and target domains. Users express their experience, sentiment and opinions on their chosen items through reviews on e-commerce websites. Thus, reviews are small capsules of emotional expressions. The data preparation step builds an emotion laden textual corpus for each and every item in a given domain by extracting and concatenating all the reviews related to the item.

– *Source Domain ratings*: We use the publicly available Movielens dataset [20] to obtain user-item ratings in the movie domain. The Movielens dataset contains ratings on 1581 movies given by 943 users. The dataset contains only those movies that have been rated by at least 20 active users who have rated at least 20 items. The user-item rating matrix has a sparsity level of 5.23%.

- *Source Domain item emotion corpus*: Reviews for each of the movies included in the Movielens dataset are extracted from the *imdb.com* website. All the reviews pertaining to a given movie are concatenated to form a document that serves an emotion laden textual Review-corpus for that movie.
- *Target Domain ratings*: We use the Bookcrossing dataset to obtain user-item ratings for the book domain [48]. The complete Bookcrossing dataset comprises of around 1.1 million ratings on 271,379 books provided by 278,858 users on a rating scale of 1 to 10. All ratings are normalized to fit into a range between 1 and 5. From this dataset, we carefully selected 3156 active users who gave at least 20 ratings on 7472 books. Further, each book is rated by at least 20 users. This filtered dataset has a sparsity level of 0.86%. Let **B** be the set of books in the book domain and $\mathbf{U_B}$ be the set of users active in this domain.
- *Target Domain item emotion corpus*: This step obtains all the reviews for each of the books that are included in the user-item matrix filtered from Bookcrossing dataset, from the *amazon.com* website. The separate reviews for a given book are combined together to form an emotion laden textual-corpus.

4.2 Preprocessing

Users typically use an informal style of writing on social media, resulting in spelling errors and mixed casing. The preprocessing Module M2 cleanses the emotion corpuses of such errors and extracts the relevant content. Preprocessing involves the following steps:

i) *Stop word removal*: In the first step, very common words like '*the', 'is', 'at', 'which'* etc. are removed from the corpus because they don't add any value to emotion analysis.
ii) *Tokenization*: Each textual emotion corpus is broken into its constituent words or tokens, $\{\tau_1, \tau_2, \tau_3 \ldots\}$.
iii) *Conversion to lower case*: The entire text is converted to lowercase in order to maintain consistency.
iv) *Word compression*: Users sometimes elongate expressive words like writing 'coooool' instead of 'cool' or "happy' to 'happppy". The preprocessing unit identifies such elongated words containing more than two subsequent occurrences of same character and compresses identical letters to two.
v) *Stemming*: This step reduces the tokens to their root word. For example, the words 'happier', 'happily', 'happiness' all maps to root word 'happy'.

4.3 Emotion analysis

We first explain the generic technique for performing emotion analysis here, before proceeding to explain the emotion profiling of source and target domains separately in subsections 4.4 and 4.5 respectively.

The purpose of emotion analysis is to measure the preponderance of various emotions that users convey through their reviews. The emotion profiles of users are an indication of the various emotions that determine their choice, ratings or liking for various items. The Emotion Analysis process builds emotion profiles for items and users. We represent the complete

emotion profile of an item or a user in the form of an array $E = [e_1\ e_2\ e_3\ e_4\ e_5\ e_6]$. The indices 1 to 6 represent the six basic emotions *love, joy, surprise, anger, sadness* and *fear* respectively. The variable $e(k,l)$ represents the strength of the emotion k for any item or user l as described below.

4.3.1 The emotion lexicon

Literature contains a wide variety of emotion classification models which have been used for different applications. They can be broadly classified as dimensional models [36, 44] and discrete models [12, 19]. Dimensional models, which allow us to map ambiguous and overlapping emotions on a continuous space of few dimensions such as *valence* and *arousal*, are quite suitable for representing emotions in multimedia-based forms of expression such as video and music [14, 46]. Discrete models on the other hand, recognize certain innate, universally identifiable and distinct emotional categories such as those described in [12] and have been widely used for detecting emotions in text [3].

W. Parrott's list of emotions is a mixed, hierarchical model for emotion classification [19]. At the primary level are six distinct, innate emotions: *love, joy, surprise, anger, sadness* and *fear*. Secondary emotions emanate from primary emotions. For example, *cheerfulness* may follow *joy*. Secondary emotions in turn trigger a combination of tertiary emotions such as *jubilation* and *euphoria* which are more overlapping in nature. In our scheme, we extract emotions from movie and book reviews. These are unstructured text typically conveying a mix of distinct as well as spontaneous emotions of various hues. We chose the Parrot's model as it allows us to identify innate emotions as well as an amalgamation of secondary and tertiary emotions that arise from them. It may be noted that Parrot's list of emotions has been utilized in other unstructured text based applications such as emotion detection in emails [23] and in tweets [7].

However, Parrot's list contains a rather limited set of emotion bearing words at each level. As a result, if a particular review did not contain any one of these words, it may falsely convey lack of any emotion. Therefore, we utilize an enhanced emotion lexicon developed in [7], which augments the skeletal list in Parrott's original lexicon by adding synonyms from WordNet [28].

The set of all primary, secondary and tertiary level keywords for a given basic emotion category k forms its lexicon, denoted as Lex(k). The complete augmented emotion lexicon in [7] contains a total of 1166 keywords. Table 1 shows the total number of keywords in each of the six lexicons. Similar to [7], we quantify the intensity of emotions at different levels by assigning a weight of 3 to all Primary Level (PL) keywords, a weight of 2 to all Secondary Level (SL) keywords and a weight of 1 to all Tertiary Level (TL) keywords. Thus,

$$\mathrm{w}(\omega, \mathrm{k}) = \begin{cases} 3, & \omega \in PL \\ 2, & \omega \in SL \\ 1, & \omega \in TL \end{cases} \tag{1}$$

4.3.2 Generating emotion profiles

The process ***EvalEmotionProfile*(.)** in Fig. 2 enumerates the steps involved in obtaining the emotion profile of a given Review-corpus, which may be from the source domain or the target domain.

Table 1 Number of keywords in each emotion in enriched Parrott's Lexicon [7]

S. No	Emotion	No. of keywords in Lexicon	S. No	Emotion	No. of keywords in Lexicon
1.	Love	82	4.	Sadness	200
2.	Joy	357	5.	Surprise	17
3.	Anger	329	6.	Fear	181

Let l be an item, i.e. a movie or a book and let $R(l)$ be the Review-corpus of that item. After initializing all emotions in array E to 0, $R(l)$ is checked one token at a time. If token τ is found in $Lex(k)$, the strength of emotion $e(k,l)$ is incremented by its weight $w(\tau,k)$. The process returns the final emotion profile E.

In order to distinguish the emotion profiles of items and users in the source and target domains, we use the following labels: MI denotes movie items, MU denotes users in the movie domain, BI denotes book items and BU denotes users in the book domain.

4.4 Profiling the movie domain

In order to analyze the Movie domain, the source domain emotion analysis module M3 first builds the emotion profiles of all movies included in the Movielens dataset. Next, it uses these item profiles and combines them with users' ratings to build the emotion profiles of users. Finally, it constructs a consolidated profile of the Movie domain itself.

4.4.1 Emotion distribution of movie items

For profiling the emotions related to a movie l, the emotion corpus $R^{MI}(l)$ is input to the pseudo-code *EvalEmotionProfile*(.) as shown in Fig. 2. This module outputs the movie's emotional profile $E^{MI}(l)$:

$$E^{MI}(l) = \left\{e^{MI}(1,l), e^{MI}(2,l), e^{MI}(3,l), e^{MI}(4,l), e^{MI}(5,l), e^{MI}(6,l)\right\}$$

Where $e^{MI}(k,l)$ is the k^{th} emotion of movie item l.

***EvalEmotionProfile*(.)**

Input: Review-corpus $R(l)$ for item l
Output: Emotion profile E
Initialize:
1. **for** $k = 1, \cdots, 6$ Set $e(k,l) = 0$
Update emotion profile for each token:
2. **while** $R(l)$ **do**
3. Read next token τ
4. **for** $k = 1, \cdots, 6$ **do**
5. **if** $(\tau \in Lex(k))$ **then** $E(k,l) \mathrel{+}= w(\tau,k)$
6. **end for**
7. **end while**
8. **Return** E

Fig. 2 Extracting emotion profile of a review corpus

Using genres to enhance movie emotion profiles There is a strong connection between a movie's genre and the emotions it evokes in a viewer. In [34], the author argues that the main film genres are based on innate features of mind and body, which result from certain mental states. Genres are constructed in such a way as to evoke a characteristic emotion for each genre. Table 2 gives the characteristic emotions that arise from major film genres [34].

In our ECDR scheme we refine the emotion profiles of movies with genre information that is available in the Movielens dataset. The movies in the Movielens dataset are classified according to the following genres: *action, adventure, animation, children, comedy, crime, documentary, drama, fantasy, filmnoir, horror, musical, mystery, romance, Scifi, thriller* and *war*. A movie may belong to one or more genres.

Taking advantage of the clear correlation between genres and the emotions they trigger, we assign a relative weight to each emotion in a movie's emotion profile as governed by its relatedness to the movie's genre. In order to find the relatedness between genre and emotions, we use adapted Lesk score proposed by Banerjee and Pederson in [4], which gives a measure of the semantic co-relatedness between two given terms. We compute the adapted Lesk score ξ of all genres of a movie for each of six basic emotions using WS4J.[4] The adapted Lesk score performs better than the original Lesk algorithm and its variations because it is based on the number of overlaps not only between the glosses of the terms themselves, but also by the number of overlaps between the glosses of their WordNet semantic relations [28]. The adapted Lesk score has been utilized widely by researchers as a reliable measure of semantic relatedness between concepts, such as in the field of medicine in [5] and for Hindi semantic category labeling in [33].

For example, we get ξ(horror, fear) = 133 and ξ(thriller, fear) = 16. This indicates a greater degree of semantic co-relatedness between *horror* and *fear* than between *thriller* and *fear*. Indeed, it is widely recognized that horror genre invokes the primal feeling of fear as listed in Table 2, while thrillers arouse excitement, suspense, anxiety, and tension [11].

The relative weight $w_{q,k}$ of genre q towards emotion k is given by:

$$w_{q,k} = \frac{\xi(q,k)}{\sum_{k=1}^{6} \xi(q,k)} \tag{2}$$

Since a movie l may belong to more than one genre, each emotion strength in $E^{MI}(l)$ is weighted by the summation of the relative weights of the various genres it belongs to. The genre adapted emotion strength for each value of k is thus given by:

$$ew^{MI}(k,l) = \left(\sum_{q} w_{q,k} \right) \times e^{MI}(k,l) \tag{3}$$

Where q is different genres for movie l.

The probability $p(.)$ of emotion k in the emotion distribution of movie l is given by the normalized emotion strength:

$$p\left(ew^{MI}(k,l)\right) = \frac{ew^{MI}(k,l)}{\sum_{k=1}^{6} ew^{MI}(k,l)} \tag{4}$$

[4] 4 https://code.google.com/p/ws4j

Table 2 Major movie genres and their characteristic emotions [34]

S.No.	Genre	Characteristic Emotion	S.No.	Genre	Characteristic Emotion
1	Action, Adventure	Aggressive tensity	4	Pornography	Desire
2	Horror	Fear	5	Tragedy	Sorrow
3	Comedy	Laughter	6	Romance	Romantic Love

The source domain item emotion distribution for movie l is denoted as probability mass function:

$$pmf\left(ew^{MI}(l)\right) = \left\{p\left(ew^{MI}(1,l)\right), p\left(ew^{MI}(2,l)\right), p\left(ew^{MI}(3,l)\right), p\left(ew^{MI}(4,l)\right), p\left(ew^{MI}(5,l)\right), p\left(ew^{MI}(6,l)\right)\right\}$$

4.4.2 Emotion distribution of movie users

As discussed in Section 2, we assume that user' ratings for an item indicates their overall assessment of the emotion profile of that item. Two experiments reported in subsection 5.1 for movie domain and in subsection 5.2 for book domain, are designed to predict whether a user would like or dislike an item based on its emotional profile. Results do indicate that user ratings can be used as indicators of a user's acceptance or rejection of the emotions conveyed by a movie or a book. Hence, we compute the emotion profile of an active user by weighting each item with the given rating for that item and aggregating these values for all the items rated by them.

Consider a user j who is active in the movie domain. Let $r(j,l)$ denote the rating given by user j to movie l. The rating-weighted emotion strength $er^{MU}(k,j)$ for emotion k by user j is given by:

$$er^{MU}(k,j) = \frac{\sum_l ew^{MI}(k,l) \times r(j,l)}{\sum_l r(j,l)} \tag{5}$$

The probability $p(.)$ of each emotion k in a user's j emotion distribution is given by the normalized rating-weighted emotion strength:

$$p\left(er^{MU}(k,j)\right) = \frac{er^{MU}(k,j)}{\sum_{k=1}^{6} er^{MU}(k,j)} \tag{6}$$

Thus, emotion distribution for user j in the movie domain is given by:

$$pmf\left(er^{MU}(j)\right) = \left\{p\left(er^{MU}(1,j)\right), p\left(er^{MU}(2,j)\right), p\left(er^{MU}(3,j)\right), p\left(er^{MU}(4,j)\right), p\left(er^{MU}(5,j)\right), p\left(er^{MU}(6,j)\right)\right\}$$

4.4.3 Overall emotion distribution of movie domain

The emotion profile of a domain is the consolidated emotion profile of all the items included in the domain and all the users who are active in it. Let $\mathbf{M}$ be the set of movies in the movie domain and $\mathbf{U_M}$ be the set of users who are active in this domain.

Movie domain item profile The average probability of emotion k considering all movies in the source domain is given by:

$$\widetilde{p}\left(ew^{MI}(k)\right) = \frac{\sum_{l \in M} p(ew^{MI}(k,l))}{|M|} \tag{7}$$

Movie domain user profile The average probability of emotion k considering all users in the movie domain is given by:

$$\widetilde{p}\left(e^{MU}\left(k\right)\right) = \frac{\sum_{j \in U_M} p(er^{MU}(k,j))}{|U_M|} \tag{8}$$

4.5 Profiling the book domain

The target domain emotion analysis module M4 develops emotion profiles for the items and users of the book domain as well as the consolidated emotion profile of the book domain itself in a manner similar to the movie domain.

4.5.1 Emotion distribution of book items

For profiling the emotions related to a book l, the emotion corpus book $R^{BI}(l)$ is input to the process ***EvalEmotionProfile*(.)** shown in Fig. 2. This module outputs the book's emotional profile $E^{BI}(l)$:

$$E^{BI}(l) = \left\{e^{BI}(1,l), e^{BI}(2,l), e^{BI}(3,l), e^{BI}(4,l), e^{BI}(5,l), e^{BI}(6,l)\right\}$$

Unlike the Movielens dataset for movies, the Bookcrossing dataset for books does not contain any information regarding genres of the books. Therefore we have not used genre to weight the emotion profile of books. The normalized emotion strength represents the probability $p(.)$ of each emotion k in the emotion distribution of book l:

$$p\left(e^{BI}(k,l)\right) = \frac{e^{BI}(k,l)}{\sum_{k=1}^{6} e^{BI}(k,l)} \tag{9}$$

Thus, the target domain item emotion distribution for book l is:

$$pmf\left(e^{BI}(l)\right) = \left\{p\left(e^{BI}(1,l)\right), p\left(e^{BI}(2,l)\right), p\left(e^{BI}(3,l)\right), p\left(e^{BI}(4,l)\right), p\left(e^{BI}(5,l)\right), p\left(e^{BI}(6,l)\right)\right\}$$

4.5.2 Emotion distribution of book users

Similar to movie users, the emotion profile of an active user is computed by aggregating the rating-weighted emotion profiles of all the items rated by them. Let $r(j,l)$ denote the rating by user j to book l. The rating-weighted emotion strength $er^{BU}(k,j)$ for emotion k is given by:

$$er^{BU}(k,j) = \frac{\sum_l e^{BI}(k,l) \times r(j,l)}{\sum_l r(j,l)} \tag{10}$$

The probability $p(.)$ of emotion k in a user's j emotion distribution is given by the normalized rating-weighted emotion strength:

$$p\left(er^{BU}(k,j)\right) = \frac{er^{BU}(k,j)}{\sum_{k=1}^{6} er^{BU}(k,j)} \tag{11}$$

The target domain user emotion distribution for user j is given by:

$$pmf\left(er^{BU}(j)\right) = \left\{p\left(er^{BU}(1,j)\right), p\left(er^{BU}(2,j)\right), p\left(er^{BU}(3,j)\right), p\left(er^{BU}(4,j)\right), p\left(er^{BU}(5,j)\right), p\left(er^{BU}(6,j)\right)\right\}$$

4.5.3 Overall emotion distribution of book domain

Similar to movie domain overall emotion distribution of book domain is computed. Let **B** be the set of books in the book domain and $\mathbf{U_B}$ be the set of users who are active in this domain.

Book domain item profile The average probability of emotion k considering all books in the target domain is given by:

$$\widetilde{p}\left(e^{BI}(k)\right) = \frac{\sum_{l \in B} p(e^{BI}(k,l))}{|B|} \tag{12}$$

Book domain user profile The average probability of emotion k considering all users in the book domain is given by:

$$\widetilde{p}\left(e^{BU}(k)\right) = \frac{\sum_{j \in U_B} p(er^{BU}(k,j))}{|U_B|} \tag{13}$$

4.6 Executing ECDR

Let us consider a user u who is active in a source domain DS and seeks recommendations from a target domain DT. At its core, the ECDR system uses the emotion profile of a user in the source domain to find users with similar emotion profiles in the target domain. It then performs collaborative filtering to recommend target items.

4.6.1 Finding similar users across domains

Module M5 calculates the distance between emotional profiles of users who are active in different domains. We adopt the symmetric KLD to measure the distance between the emotion distributions of users who are active in the source and target domains. The standard Kullback-Liebler Divergence (KLD) is not symmetric [21]. Therefore it is not strictly a distance metric. The symmetric-KLD measures the distance between two probability densities $p(.)$ and $q(.)$ of the form:

$$\mathrm{D}(p||q) = \sum_{x} (p(x) - q(x)) \ln \frac{p(x)}{q(x)} \tag{14}$$

Accordingly, the parameter $\Delta_{u,v}$ which is the symmetric KLD between the emotion distributions of user u active in the movie domain and user v active in the book domain is given by:

$$\begin{aligned}\Delta_{u,v} = \quad & KLD \quad \left(pmf\left(er^{MU}(u)\right), pmf\left(er^{BU}(v)\right)\right) \\ & = \sum_{k=1}^{6}\left(p\left(er^{MU}(k,u)\right) - p\left(er^{BU}(k,v)\right)\right) ln\frac{p(er^{MU}(k,u))}{p(er^{BU}(k,v))}\end{aligned} \tag{15}$$

It can be seen that lower is the value of $\Delta_{u,v}$, greater is similarity between the emotion distributions of user u and v.

4.6.2 Generating recommendations

The cross domain recommender module M6 generates recommendations from the target domain to a user in the source domain. The pseudo-code ***CDR_CF*(.)** in Fig. 3 gives the steps involved in obtaining the recommendations. Given a candidate user u in source domain (*DS*), the process returns a set K of items from the target domain *DT*, which is recommended to u.

The process begins by initializing K to *null* (line 1) and evaluating the probability mass function $pmf\left(er^{MU}(u)\right)$ of u from DS (line 2). Next it evaluates the *pmf*(.) of each user v in the target domain and computes its KLD $\Delta_{u,v}$ from the *pmf*(.) of u (lines 3 to 6). It arranges all users in the target domain in ascending order of $\Delta_{u,v}$ (line 7) to yield U_{TN}, the top N users with similar profiles (line 8). Next it performs collaborative filtering to predict ratings for user u for items in target domain by using Resnick's formula [35] (lines 9–14):

$$r'(u,i) = \bar{r}(u) + \frac{\sum_{v \in U_{TN}}\left(r(v,i) - \bar{r}(v)\right)}{\sum_{v \in U_{TN}} \Delta_{u,v}} \times \Delta_{u,v} \tag{16}$$

Here, $\bar{r}(u)$ is average rating of user u for all their rated items in source domain, $\bar{r}(v)$ is the average rating of user $v \in U_{TN}$ for all their rated items in target domain, $r(v,i)$ is the actual rating given by user v to item i.

If the predicted rating $r'(u,i)$ is 4 or 5, the process adds item i to the set of recommended items K (line 12). The process finally returns the set K of recommended items (line 15).

4.7 Performance evaluation of ECDR

Module M7 conducts a performance evaluation of the EDCR system. In the case of Movie and Book domains, their respective datasets Movielens and Bookcrossing have no common users. Therefore it is not possible to directly assess the accuracy of cross domain recommendations. We adopt an approach suggested in [24] to evaluate the system performance. The pseudo-code ***ECDR_Eval*(.)** shown in Fig. 4 outlines this approach.

Consider an active user u. Let I_{DS} be the set of all items in source domain, $J_{DS}(u)$ be the subset of items rated by u, and $L_{DS}(u)$ be the subset of items liked by u, i.e. rated 4 or 5. For each candidate user u, the system first cross recommends items from target (book) domain using ECDR to yield set $K_{DT}(u)$ (lines 2 to 4).

The system now assumes a hypothetical user u who likes these recommended items in the target domain. It constructs the emotion distribution of the hypothetical user by using the emotion profiles of the recommended items and their predicted ratings (lines 5 to 6). The

***CDR_CF*(.)**

Input: User u, Source Domain DS, Target Domain DT
Output: Set of Recommended Items K

Initialize:
1. $K=\emptyset$
2. Evaluate source domain candidate user's emotion distribution $pmf\left(er^{MU}(u)\right)$

Find similarity with target domain users:
3. **for** each user $v \in U_{DT}$ **do**
4. Evaluate rating-weighted emotion distribution $pmf\left(er^{BU}(v)\right)$
5. Find KL Divergence $\Delta_{u,v}$ using Eq. 15
6. **end for**

Find Top N similar users in target domain:
7. Sort users in U_{DT} in ascending order of $\Delta_{u,v}$
8. Set $U_{TN} = Top\ N$ users in sorted U_{DT}

Predict candidate user's ratings and recommend:
9. **for** each user $z \in U_{TN}$ **do**
10. **for** each item I from DT that z has rated **do**
11. Calculate corresponding predicted rating $r'(u,i)$ for u using Eq. 16
12. **If** $(r'(u,i) \geq 4)$ **then** $K = K \cup i$
13. **end for**
14. **end for**
15. **return** K

Fig. 3 Generating cross domain recommendations using emotion distributions of users in source and target domains

system then uses this emotion distribution to cross recommend items from the source (movie) domain to u (line 7). Let this set be denoted as $K_{DS}(u)$.

Next, *ECDR_Eval*(.) assesses the performance of the ECDR system. It calculates the True Positives (TP), True Negatives (TN), False Positives (FP) and False Negatives (FN) by comparing the items originally liked by candidate user u in the source domain with those that were cross recommended to the hypothetical user u (lines 8 to 13). Thus,

– TP is the set of items that are liked by u and are also cross recommended to u:

$$TP = L_{DS}(u) \cap K_{DS}(\hat{u}) \tag{17}$$

– TN is the set of items that are not liked by u and are not recommended to u:

$$TN = \{I_{DS} - L_{DS}(u)\} \cap \{I_{DS} - K_{DS}(\hat{u})\} \tag{18}$$

– FP is the set of items that are not liked by u but are cross recommended to u:

$$FP = K_{DS}(\hat{u}) \cap \{I_{DS} - L_{DS}(u)\} \tag{19}$$

– FN is the set of items that are liked by u but are not cross recommended to u:

$$FN = L_{DS}(u) \cap \{I_{DS} - K_{DS}(\hat{u})\} \tag{20}$$

Next, the system computes the performance metrics for u, giving precision $\alpha(u)$, recall $\beta(u)$ and F-measure $\gamma(u)$ (line 13). The system finally computes the overall performance by macro-averaging α, β and γ across all users (line 15).

***ECDR_Eval*(.)**

***Input**:* User u, Source Domain DS, Target Domain DT
***Output**:* Precision α, Recall β, F1-measure γ

begin

1. **for** each user $u \in U_{DS}$ **do**

***Cross recommend items from DT to user in DS*:**

2. **for** each item in $J_{DS}(u) \subseteq I_{DS}$ rated by u **do**
3. Cross-recommend items from *DT* to u: $K_{DT}(u)$=***CDR_CF*(*u, DS, DT*)**
4. **end for**

***Cross recommend items from DS to hypothetical user in DT*:**

5. Create hypothetical user $\hat{u}$ who gives predicted ratings to recommended items in $K_{DT}(u)$
6. Generate emotion distribution $pmf\left(er^{BU}(\hat{u})\right)$, for user $\hat{u}$
7. Cross-recommend items from *DS* to $\hat{u}$: $K_{DS}(\hat{u})$ = ***CDR_CF*(*û*, *DT, DS*)**

***Compute performance of ECDR*:**

8. Compute per user performance metrics:
9. $|TP| = |L_{DS}(u) \cap K_{DS}(\hat{u})|$
10. $|TN| = |\{I_{DS} - K_{DS}(\hat{u})\} \cap \{I_{DS} - L_{DS}(u)\}|$
11. $|FP| = |K_{DS}(\hat{u}) \cap \{I_{DS} - L_{DS}(u)\}|$
12. $|FN| = |L_{DS}(u) \cap \{I_{DS} - K_{DS}(\hat{u})\}|$
13. $\alpha(u) = \frac{|TP|}{|TP|+|FP|}$ $\beta(u) = \frac{|TP|}{|TP+|FN|}$ $\gamma(u) = \frac{2\times\alpha(u)\times\gamma(u)}{\alpha(u)+\gamma(u)}$
14. **end for**

***Compute system performance*:**

15. $\alpha = \frac{\sum_{u\in U_{DS}}\alpha(u)}{|U_{DS}|}$ $\beta = \frac{\sum_{u\in U_{DS}}\beta(u)}{|U_{DS}|}$ $\gamma = \frac{\sum_{u\in U_{DS}}\gamma(u)}{|U_{DS}|}$

end

Fig. 4 Performing ECDR and evaluating system performance

5 Experimental results

We now present the results of experiments on the proposed ECDR system using the datasets described in section 3. We compare our approach with two recently reported approaches namely, Cosine Based Cross Domain Recommendation (CD) and Semantic Clustering Based Cross Domain Recommendations (SCD) [24].

5.1 Relationship between ratings and emotional profiles of movie items

In the first experiment, we investigate whether users' ratings reflect their acceptance or rejection of the emotional profiles of movies. We considered all active users who rated at least 50 movies. For each user, we grouped their ratings into two classes: *like* and *dislike*. Movies with ratings 4 or 5 were labeled as *like* and those with ratings 1 or 2 ratings were labeled as *dislike*. Movies with rating 3 were not considered as it indicates a neutral opinion. Next, using the emotion distribution of rated movies as features, we trained a Random Forest Classifier using 10 fold cross validation and used it to predict the labels (*like or dislike*) of test cases. Fig. 5a shows the histogram for the prediction accuracy. The mean prediction accuracy is 0.799 and the standard deviation is 0.096. With a confidence level of 0.95 the prediction accuracy of movies has a confidence interval ranging from 0.7987 to 0.80. This validates our contention that statistically speaking, a

typical user's ratings do reflect their liking or disliking for the underlying emotional profiles of movies rated by them.

5.2 Relationship between ratings and emotional profiles of book items

In this experiment, we examine whether users' ratings indicate their acceptance or rejection of the emotional profiles of books rated by them. Proceeding in the same way as for movies, we computed the prediction accuracy for all eligible users in Bookcrossing dataset by using the emotion distributions of books as classification features. Fig 5b shows the histogram for the prediction accuracy of books. We get a mean prediction accuracy of 0.845 and a standard deviation of 0.07. With confidence level of 0.95, the prediction accuracy of books has the confidence interval ranging from 0.8447 to 0.8453. These results give credence to our assumption that users' ratings reflect their overall assessment of the emotional profile of books rated by them.

5.3 Similarity in emotion distributions of source and target domains

The success of any CDR system hinges on the ability to find correspondences between the various domains so as to form a connecting link between them. Since ECDR uses *emotions* as a conduit between the source and target domains, we seek to find out similarities between their emotion distribution patterns.

In this experiment we qualitatively analyze the similarities between the emotion distribution patterns in movie and book domains. For all items and users, we find the average probability of emotion k in both movies and book domain.

Item emotion distribution Fig. 6a shows the emotion distributions of items in the movie and book domains. We observe a striking similarity between these patterns.

i) *Joy* is the predominant emotion in both domains. In the Movie domain, $\tilde{p}(e^{MI}(joy)) = 42.86\%$. It is followed by *love* with $\tilde{p}(e^{MI}(\text{love}))=29.84\%$. In the Book domain $\tilde{p}(e^{BI}(joy)) = 59.9\%$ followed by *love* with $\tilde{p}(e^{BI}(\text{love})) = 28.53\%$

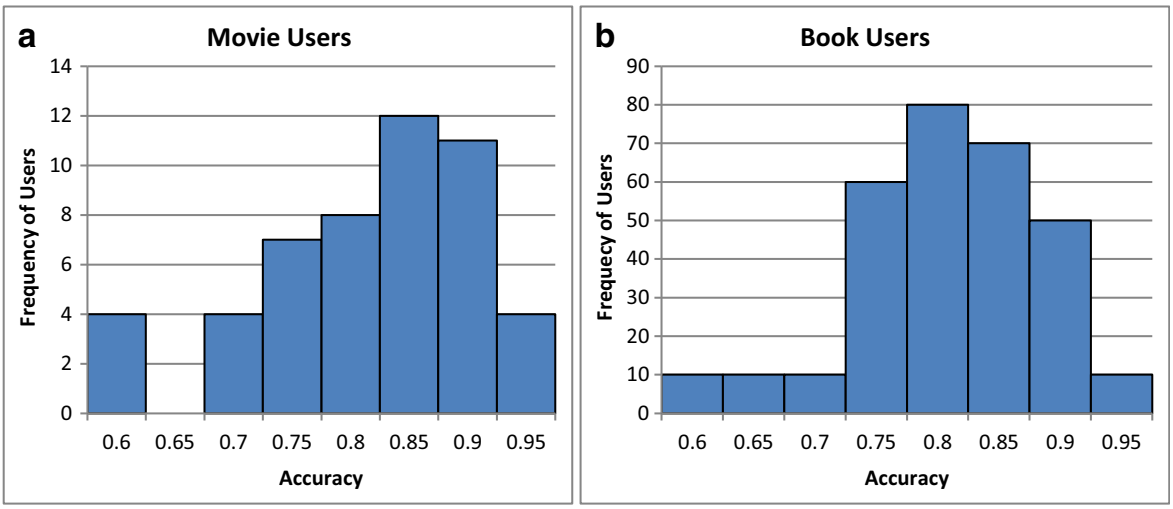

Fig. 5 **a** Histogram of Like/Dislike prediction accuracy in movie domain. **b** Histogram of Like/Dislike prediction accuracy in book domain

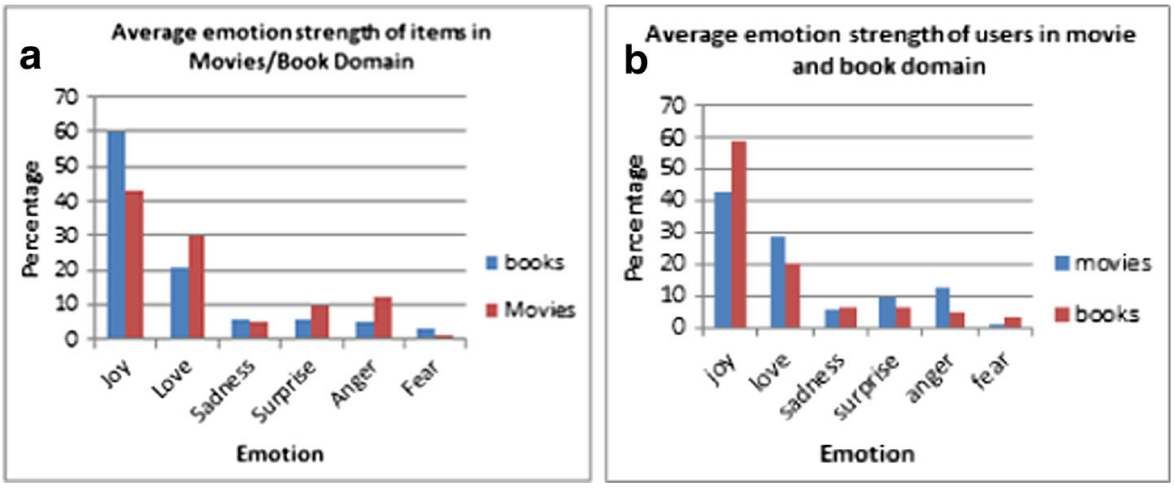

Fig. 6 **a** Average emotion strength of items. **b** Average emotion strength of users

ii) In both domains *fear* has the least presence with $\tilde{p}(e^{MI}(\text{fear})) = 5\%$ the movie domain and $\tilde{p}(e^{BI}(\text{fear})) = 3.2\%$ in the book domain.
iii) In between these extremes lie the emotions *anger*, *surprise* and *sadness*. They have closely matching values in both domains. For example, $\tilde{p}(e^{MI}(\text{sadness})) = 4.8\%$ while $\tilde{p}(e^{BI}(\text{sadness})) = 5\%$.

User emotion distribution Figure 6b shows the emotion distributions of users in the movie and book domains. As in the case of items, here too we notice a striking similarity between them.

i) For movie domain *joy* is the predominant emotion with highest $\tilde{p}(e^{MU}(joy)) = 42.65\%$, followed by *love* with $\tilde{p}(e^{MU}(\text{love})) = 28.53\%$. In book domain *joy* remains the predominant emotion with highest $\tilde{p}(e^{BU}(joy)) = 59.1\%$ followed by *love* with $\tilde{p}(e^{BU}(\text{love})) = 20.5\%$.
ii) *Fear* is the least significant emotion in both domains with $\tilde{p}(e^{MU}(\text{fear})) = 1.2\%$ and $\tilde{p}(e^{BU}(\text{fear})) = 3.3\%$.
iii) The remaining emotions occupy mid-positions in both domains. In the Movie domain. $\tilde{p}(e^{MU}(\text{sadness})) = 5.3\%$, $\tilde{p}(e^{MU}(\text{surprise})) = 9.5\%$ and, $\tilde{p}(e^{MU}(\text{anger})) = 12\%$. In the Book domain, the corresponding contributions are as follows: $\tilde{p}(e^{BU}(\text{sadness})) = 6\%$, $\tilde{p}(e^{BU}(\text{surprise})) = 6.1\%$ and $\tilde{p}(e^{BU}(\text{anger})) = 5\%$.

The emotion distribution of items from the source domain and that of items from the target domain have a cosine similarity of 0.949. Similarly the emotion distribution of users from the source domain and that of users from the target domain have a cosine similarity of 0.953.

Earlier, we discussed the qualitative impact of *emotion* in entertainment domains and hypothesized its role as connecting glue between them. This experiment brings to light the statistical similarity between the emotion distributions of the two domains. This gives further credence to our belief that emotions have the potential to bridge the two apparently heterogeneous domains.

5.4 Evaluating the performance of ECDR

Table 3 shows the effect of top N recommendations on precision, recall and F1-measure. Fig. 7 depicts the trend graphically. With an increase in the number N for top-N recommendations, recall increases steadily while precision decreases. As the number of recommendations increase from 5 to 20, recall increases by as much as 95% while precision drops by 23%. This shows that, as more recommendations are provided to the user, there is a tradeoff between the precision and recall. Due to the participation of more users in the recommendation process, a user gets more relevant choices of their liking although the percentage of relevant ones among all choices decreases.

5.5 Comparison with recent works

The CD and SCD approaches reported in [24] both apply topic modeling on reviews of movies and books for performing CDR. While the CD based approach defines topics as single words, the SCD based approach defines topics as distributions over word-clusters in order to capture the inherent similarities between the vocabularies of multiple domains.

Table 4 compares the precision, recall and F1-measure gathered from an analysis of our experimental results with the corresponding values reported for the CD and SCD approaches for top 10 recommendations.

On comparing ECDR with CD, we find that ECDR yields a precision of 0.232 which is 76.02% higher precision than the precision of CD at 0.1318. The recall of ECDR at 0.3834 is as much as 269.72% higher recall than that of CD at 0.1037 – a more than three-fold gain. Thus, ECDR emerges the clear winner with an F1 measure of 0.289, which is 149.13% higher than the F1-measure of CD at 0.116.

In comparison with the SCD approach, the recall value of ECDR is higher by 228.81%. However, this comes at the cost of a lower precision. The precision of ECDR is lower than that of SCD by 24.28%. Nevertheless, the overall performance of ECDR is still better as its F1 measure at 0.289 is higher than that of SCD at 0.1689 by 71.1%.

From the above observations, we infer that the proposed emotion driven ECDR approach is significantly better than the CD and SCD based approaches that use topic modeling [24].

5.6 Discussion

We now summarize the main findings from our experiments. Firstly, the experiments in subsections 5.1 and 5.2 demonstrated that the emotion profiles of items can be used as features to predict ratings with high accuracy. Therefore, users' ratings can be perceived as their acceptance of the emotional content of the rated items or rejection thereof. This observation

Table 3 Prediction performance of ECDR for different Top N recommendations

ECDR Top N	PRECISION	RECALL	F1-MEASURE
ECDR Top 5	0.25431	0.27787	0.2655
ECDR Top 10	0.232	0.3834	0.289
ECDR Top 15	0.2066	0.4472	0.2826
ECDR Top 20	0.1956	0.5407	0.2873

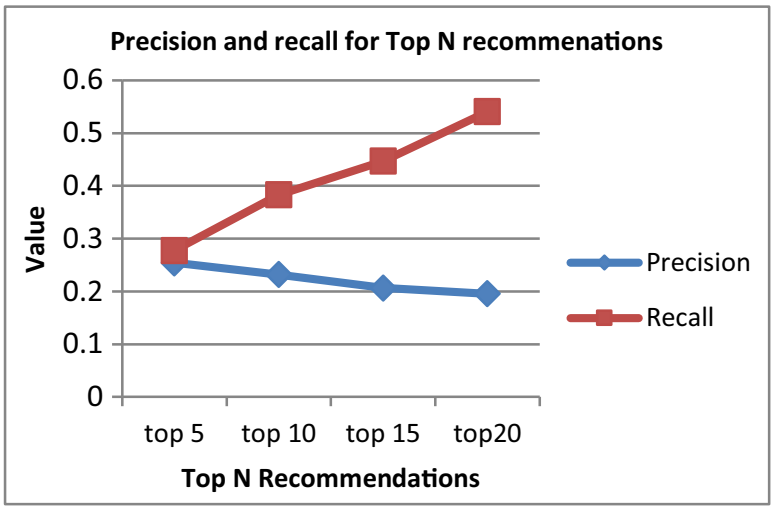

Fig. 7 Variation of precision and recall with N for Top-N recommendations

allows us to include many users to participate in the CDR process, since many more users rate items in comparison with few who post reviews on them.

The next experiment in subsection 5.3 revealed that the collective emotion distributions of items and users in movie and book domains exhibit marked similarities. Users' comments imbue similar spread of various emotions and user ratings are similarly distributed across the emotion profiles of different items. This observation strengthens our premise that emotions can serve to bind the two domains.

Finally, the results of performance evaluation of the ECDR system and comparison with previous approaches reported in subsections 5.4 and 5.5 are encouraging. Overall, the F1 measure of the ECDR system surpasses that of a recent topic modeling approach in [24] by as much as 71.1%. This clearly indicates the potential of using emotions as a vehicle for performing CDR and serves as proof-of-concept for the idea that emotions extracted from user generated reviews, coupled with their ratings and genre information of items, act together to connect entertainment domains. One can transfer the learning gained from an emotion analysis of one domain to generate recommendations in the other domain. Where available, genre information can be utilized to further refine the emotion profiles of items. We utilized the genre information available in *movielens* to give relative weights to different emotional categories while generating music items' emotion distributions.

Though we used movie and book domains to illustrate our approach, it can be extended for performing CDR in other domains where human choices have an emotional basis. There are certain limitations of this approach. Firstly, we have used reviews to capture the emotional content of items. An analysis of the actual content of the items, such as audio features and lyrics for songs and textual content for books may generate more accurate emotion profiles. But this may entail much higher computational cost and preclude real time analysis. Secondly, we find that each entertainment domain may have its characteristic emotion classification. For

Table 4 Prediction Performance of different CDR systems for Top10 recommendation

METRIC	CD	SCD	ECDR
PRECISION	0.1318	0.3064	0.232
RECALL	0.1037	0.1166	0.3834
F1-MEASURE	0.116	0.1689	0.289

example, in the music domain, a continuous spectrum of emotions is more relevant than a discrete emotion categorization that is more useful for books. This may make it difficult to match the emotion distributions of items from different domains. Lastly, we observe a skew in the emotion distributions with a predominance of position emotions such as joy and love in comparison with negative emotions such as anger and fear. This may have resulted from users generally being more enthusiastic in expressing positive emotions and suppressing negative ones. Thus, emotions captured from user-generated content may not truly reflect the emotion profiles of items. We can further strengthen the quality of the CDR system by combining emotions with other features.

6 Conclusion

We proposed a new method for cross domain recommender system that establishes linkages between the source and target domains by using the emotional profiles of users and items. We used an enriched emotion lexicon to extract the intensity of emotions in the user reviews of items. We combined them with user ratings to build the distribution of each user's emotional inclinations across the six basic emotion categories namely, *love, joy, anger, surprise sadness* and *fear.* These user emotion profiles serve as vehicles to perform CDR where there is no user/item overlap across the source and target domains.

We experimentally verified our premise that emotions extracted from reviews and comments act as important links between the two domains. Our approach provided 77.1% better F1-measure than existing semantic clustering based approach [24]. As an extension to the proposed emotion driven CDR, we are investigating how to enrich the emotional profiles further by tapping multiple media such as tags, images, video and other attributes associated with items. We are working towards extending our approach for performing multi-domain CDR.

References

1. Adomavicius G, Tuzhilin A (2005) Toward the next generation of recommender systems: a survey of the state of-the-art and possible extensions. IEEE Trans Knowl Data Eng 17:734–749. doi:10.1109/TKDE.2005.99
2. Alderson M (2016) Connecting with audiences through character emotions. https://www.writersstore.com/connecting-with-audiences-through-character-emotions. Accessed 21 Oct 2016
3. Aman S, Szpakowicz S (2007) Identifying expressions of emotion in text. In: International Conference on Text, Speech and Dialogue. Springer, Berlin, pp 196–205
4. Banerjee S, Pedersen T (2002) An adapted Lesk algorithm for word sense disambiguation using WordNet. Proc Springer Berlin Heidelberg. International Conference on Intelligent Text Processing and Computational Linguistics: pp. 136–145
5. Bill RW, Liu Y, McInnes BT, Melton GB, Pedersen T, Pakhomov S. (2012) Evaluating semantic relatedness and similarity measures with standardized meddra queries. AMIA Annual Symposium Proc, volume 2012, page 43 American Medical Informatics Association
6. Cantador I, Fernández-Tobías I, Berkovsky S et al (2015) Cross-domain recommender systems. In: Recommender systems handbook. Springer US, p 919–959
7. Chakraverty S, Sharma S, Bhalla I (2015) Emotion–location mapping and analysis using twitter. Journal of Information & Knowledge Management 14(03):1550022
8. Chiang HS, Huang TC (2015) User-adapted travel planning system for personalized schedule recommendation. Information Fusion 21:3–17
9. Chung R, Sundaram D, Srinivasan A (2007) Integrated personal recommender systems. Proc ACM ninth international conference on Electronic commerce, p 65–74

10. Cremonesi P, Tripodi A, Turrin R (2011) Cross-domain recommender systems. Proc 2011 I.E. 11th International Conference on Data Mining Workshops 496–503
11. Derks T (n.d.). Filmsite Horror Films. http://www.filmsite.org/horrorfilms.html. Accessed 21 Oct 2016
12. Ekman P (1992) An argument for basic emotions. Cognit Emot 6(3–4):169–200. doi:10.1080/02699939208411068
13. Fernández-Tobías I, Cantador I, Kaminskas M, Ricci F (2011) A generic semantic-based framework for cross-domain recommendation. Proc of the ACM 2nd International Workshop on Information Heterogeneity and Fusion in Recommender Systems: 25–32
14. Fernández-Tobías I, Cantador I, Plaza L (2013) An emotion dimensional model based on social tags: Crossing folksonomies and enhancing recommendations. Proc Springer Berlin Heidelberg. International Conference on Electronic Commerce and Web Technologies, p 88–100
15. Fernández-Tobías I, Braunhofer M, Elahi M et al (2015) Alleviating the new user problem in collaborative filtering by exploiting personality information. User Model User-Adap Inter 1–35
16. Find me an Author (n.d.). http://www.findmeanauthor.com. Accessed 21 Oct 2016
17. Franzoni V, Poggioni V, Zollo F (2013) Automated classification of book blurbs according to the emotional tags of the social network Zazie. In: ESSEM@ AI* IA, p 83–94
18. Gao S, Luo H, Chen D et al (2013) Cross-domain recommendation via cluster-level latent factor model. Proc Joint European Conference on Machine Learning and Knowledge Discovery in Databases: 161–176
19. Handel S (2011) Classification of emotions. http://www.theemotionmachine.com/classification-of-Emotions. Accessed Oct 2016
20. Harper FM, Konstan JA (2016) The movielens datasets: history and context. ACM Transactions on Interactive Intelligent Systems (TiiS) 5(4):19. doi:10.1145/2827872
21. Johnson DH, Sinanovic S (2001) Symmetrizing the Kullback–Leibler ´ distance, Technical Report, Rice University
22. Kaminskas M, Ricci F (2011) Location-adapted music recommendation using tags. Proc Springer Berlin Heidelberg. International Conference on User Modeling, Adaptation, and Personalization, p 183–194
23. Karthik K, Ponnusamy R (2011) Adaptive machine learning approach for emotional email classification In: International Conference on Human-Computer Interaction. Springer, Berlin, pp 552–558
24. Kumar A, Kumar N, Hussain M, et al (2014) Semantic clustering-based cross-Domain recommendation. Proc Computational Intelligence and Data Mining (CIDM):137–141
25. Li B, Yang Q, Xue X (2009) Transfer learning for collaborative filtering via a rating-matrix generative Model. Proc of the 26th Annual International Conference on Machine Learning: 617–624
26. Low Y, Agarwal D, Smola AJ (2011) Multiple domain user personalization. Proc of the 17th ACM SIGKDD international conference on Knowledge discovery and data mining, p 123–131
27. Majid A, Chen L, Chen G et al (2013) A context-aware personalized travel recommendation system based on geotagged social media data mining. Int J Geogr Inf Sci 27(4):662–684
28. Miller GA (1995) WordNet: a lexical database for English. Commun ACM 38(11):39–41
29. Pan W, Liu NN, Xiang, EW et al (2011) Transfer learning to predict missing ratings via heterogeneous user feedbacks. Proc International Joint Conference on Artificial Intelligence 22(3): 2318
30. Pan W, Xiang EW, Yang Q (2012) Transfer learning in collaborative filtering with uncertain ratings. In AAAI
31. Pazzani MJ, Billsus D (2007) Content-based recommendation systems. In: The adaptive web. Springer, Berlin, p 25–341
32. Rawashdeh M, Alhamid MF, Alja'am JM et al (2016) Tag-based personalized recommendation in social media services. Multimedia Tools and Applications 75:13299. doi:10.1007/s11042-015-2813-0
33. Reddy S, Inumella A, Singh N, Sangal R (2010) Hindi semantic category labeling using semantic relatedness measures. In: Proceedings of Global WordNet Conference, p 448–453
34. Redfern N (1995) Emotion, Genre and the Hollywood Paranoid Film. https://nickredfern.wordpress.com/2009/05/07/emotion-genre-and-the-hollywood-paranoid-film/. Accessed 21 Oct 2016
35. Resnick P, Iacovou N, Suchak M et al (1994) GroupLens: an open architecture for collaborative filtering of net news. In: Proceedings of the 1994 ACM conference on Computer supported cooperative work, p 175–186. ACM
36. Russel JA (1980) A circumplex model of affect. J Pers Soc Psychol 39:1161–1178. doi:10.1037/h0077714

37. Saraswat M, Chakraverty S, Mahajan N, Tokas N (2016) On using reviews and comments for cross domain recommendations and decision making. In: Computing for Sustainable Global Development (INDIACom), 2016 3rd International Conference on IEEE, p 3656–3659
38. Schafer JB, Konstan J, Riedl J (1999) Recommender systems in e-commerce. Proc1st ACM conference on Electronic commerce p 158–166
39. Schafer JB, Frankowski D, Herlocker J et al (2007) Collaborative filtering recommender systems. The adaptive web Springer, Berlin Heidelberg, pp 91–324
40. Shi Y, Larson M, Hanjalic A (2010) Mining mood-specific movie similarity with matrix factorization for context-aware recommendation. Proc of the workshop on context-aware movie recommendation, p 34–40
41. Shi Y, Larson M, Hanjalic A (2013) Generalized tag-induced cross-domain collaborative filtering. CoRR, abs/1302:.4888. doi: 10.1145/0000000.0000000
42. Shi Y, Larson M, Hanjalic A (2014) Collaborative filtering beyond the user-item matrix: a survey of the state of the art and future challenges. ACM Comput Surv, 47(1)
43. Tang J, Wu S, Sun J, Su H (2012) Cross-domain collaboration recommendation. Proc of the 18th ACM SIGKDD international conference on Knowledge discovery and data mining, p 1285–1293
44. Thayer RE (1990) The biopsychology of mood and arousal. Oxford University Press
45. Winoto P, Tang TY (2010) The role of user mood in movie recommendations. Expert Syst Appl 37(8): 6086–6092
46. Yang YH, Lin YC, Su YF, Chen HH (2007) Music emotion classification: a regression approach. In: 2007 I.E. International Conference on Multimedia and Expo, p 208–211
47. Zhang D, He T, Liu Y et al (2014) A carpooling recommendation system for taxicab services. IEEE Transactions on Emerging Topics in Computing 2(3):254–266
48. Ziegler CN, McNee SM, Konstan JA et al (2005) Improving recommendation lists through Topic diversification. Proc in ACM 14th international conference on World Wide Web, p 22–32

Dr. Shampa Chakraverty is Professor and Head in Department of Computer Engineering in Netaji Subhash Institute of Technology, New Delhi. She received her BTech degree in Electronics and Communication from Delhi College of Engineering, M. Tech from I.I.T.-Delhi and Ph.D. from Delhi University. She has over 27 years academic experience besides 5 years of industry experience. Her area of research includes analysis of big social data and recommender system, e-learning and e-governance, machine learning, digital database watermarking.

Mala Saraswat is working as an Teaching cum Research Fellow in Department of Computer Engineering in Netaji Subhash Institute of Technology, New Delhi. Her research interest is focused on studying behavior of cross domain recommender systems.

Volume 5, Issue 1 (2017) 24-29 ISSN 2347 - 3258
International Journal of Advance Research and Innovation

Structural Design &Optimization Of An Unmanned Aerial Vehicle Wing For SAE Aero Design Challenge

Harsh Raj Chauhan*, Harsh Panwar*, Vikas Rastogi
Department of Mechanical Engineering, Delhi Technological University (Formerly DCE), New Delhi-110042, India

Article Info
Article history:
Received 16 February 2017
Received in revised form
16 February 2017
Accepted February 2017
Available online March 2017

Keywords
UAV, Structural Design, Optimization, MATLAB

Abstract
Aircraft design is a multi-disciplinary iterative design process which follows a Systems Engineering approach and Unmanned Aerial Vehicle design follows one such design methodology. This paper is an attempt to formulate the structural design process for a UAVwing and subsequent optimizationfor SAE India Aero Design Challenge 2017.The design starts with the identification of structural design parameters and challenge requirements in the Pre-design/Conceptual Design phase. Based on the engineering values, a mathematical interface is coded in MATLAB to calculate the mechanical equivalents for the wing at individual sections and to prepare an internal structural layout adhering to the selected material properties. The structural design of the wing is then modelled in Solidworks and final mass is calculated in the Preliminary Design phase. For initial estimates, the static structural analysis of the layout is performed theoretically.The final design of the wing is then fed in ANSYS Finite Element Solver for Static Structural analysis. Now, successive iterations are performed for the optimization of a critical structural parameter with bound constraints directly affecting the mass of the structure using MATLAB in the Detailed Design phase. The optimized version is then finally validated.

1. Introduction

SAE Aero Design Challenge 2017 is a UAV design challenge to be held in March 2017 in India. The competition aims at maximizing the payload carrying capacity of the UAV while completing a full circuit of the airfield. The constraint of maximizing the payload of the UAV directly influences the engineering design of the wing of the UAV since wings prove to be an important subsystem which provide both aerodynamic worth and structural integrity to the UAV. It therefore calls for the design and analysis of wings carefully engineered so as to cater to the requirements of the challenge.An attempt has been made through this research, to comply by the requirements as close as possible while reaching towards an optimized version of the wing. Any research work is never complete since there is always a scope for better solutions as we progress and touch newer domains.The focus of this research is limited to the structural design and optimization of the wing of the unmanned aerial vehicle only, although, other subsystems of the UAV were designed and developed too. Following is the design methodology developed for this research work.

2.Conceptual Design Phase

The design process of the wing starts with the identification of critical structural design inputs that are derived from the set of competition requirements which are fed into MATLAB for further mathematical modelling.

2.1 Structural Design Inputs

The structural design inputs were derived by identifying the most influential parameter from the set of design parameters for the competition. The payload capacity proved to be the most influential parameter and was taken as the basis for further design of the wing.
The corresponding starting value for the influential parameter was taken as 5g ie. the designed wings should be able to sustain 5 times its own weight without structural failure. The other structural parameters like exposed wing area, root chord and tip chord were calculated during the aircraft design and have not been included in this research. The design factor of 1.5 has been taken for maximum reliability of around 99%. The wing airfoil for the aircraft was taken as Selig 1210.

***Corresponding Author,**
E-mail address:harshchauhan1995@gmail.com; Phone No-+91-9818886652; harshpanwar788@gmail.com; Phone No-+91-9891197447
All rights reserved: http://www.ijari.org

3.Preliminary Design Phase

The preliminary design phase starts with mathematical modelling of the structural design in MATLAB. The design method adopted has been displayed in a flowchart in figure 2.

3.2Structural Sizing

The developed mathematical model is now run in MATLABas a live script. The code initiates with a prompt command where it asks the user to enter 13 values and the code then calculates the rest of the variables as described in the flowchart.
After dividing the wing into number of divisions, the location of center of pressure is taken as well as the position of the front spar and the rear spar.
Center of Pressure= 45% of chord length from the leading edge
Front spar position= 25% of chord length
Rear spar position = 62% of chord length
Further sizing of the wing components were done keeping into consideration the maximum values of shear force and bending moment distribution on the spars.
Maximum Bending moment=78384 N-mm
Maximum shear force = 85.1575 N

Material for front spar= AA 6061 T-6
Material for rear spar= Birchwood
Volume of front spar = 45555 mm^3
Volume of rear spar= 67767 mm^3
Total volume= 113322 mm^3
Total mass of the spars= 316.1701 gms

3.3 Performance Charts

After the mathematical model displayed and stored the mechanical values for the wing, performance charts were plotted on MATLAB for variables as a function of the chord length at each section from tip to root for both the front and rear spars. The following plot shows the variation of shear force due to torsion and the total shear force as a function of chord length.

3.4 Initial Blueprint

The obtained wing design from the mathematical model is then modelled in Solidworks for further analysis in the detailed design phase.

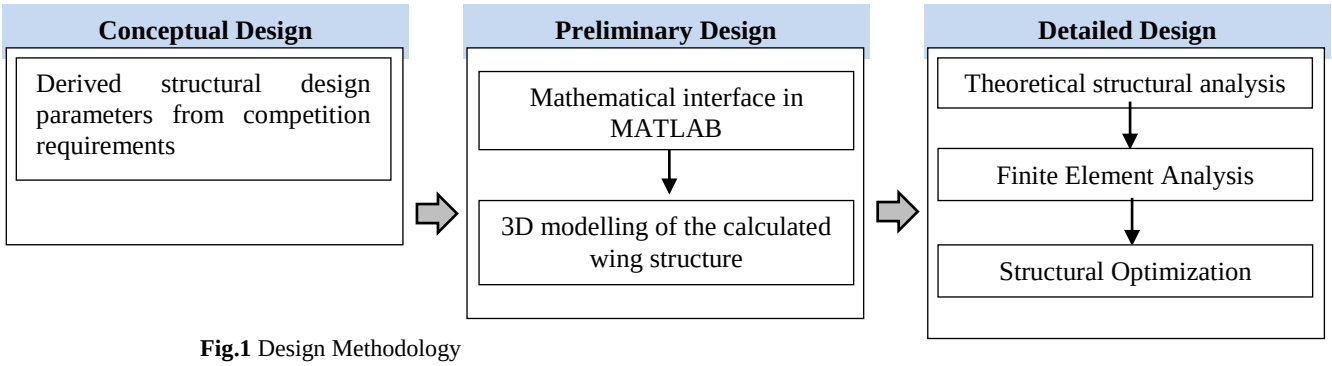

Fig.1 Design Methodology

Table 1 Competition Requirements

S.No	Design Parameter	Objective
1.	Time Limit	< 180 sec
2.	Take-off distance	< 400 feet
3.	Landing Distance	< 400 feet
4.	GTOW (excluding payload)	< 5 kgs
5.	Payload	**Maximise**

Table 2. Derived structural parameters

S.No	Structural Parameter	Value/Range
1.	Root chord/Tip Chord	380/230 mm
2.	Exposed span	2000 mm
3.	Aircraft weight	<= 50N
4.	Lift Load	5g
5.	Design Factor	1.5
6.	Exposed wing area	726000 mm^2

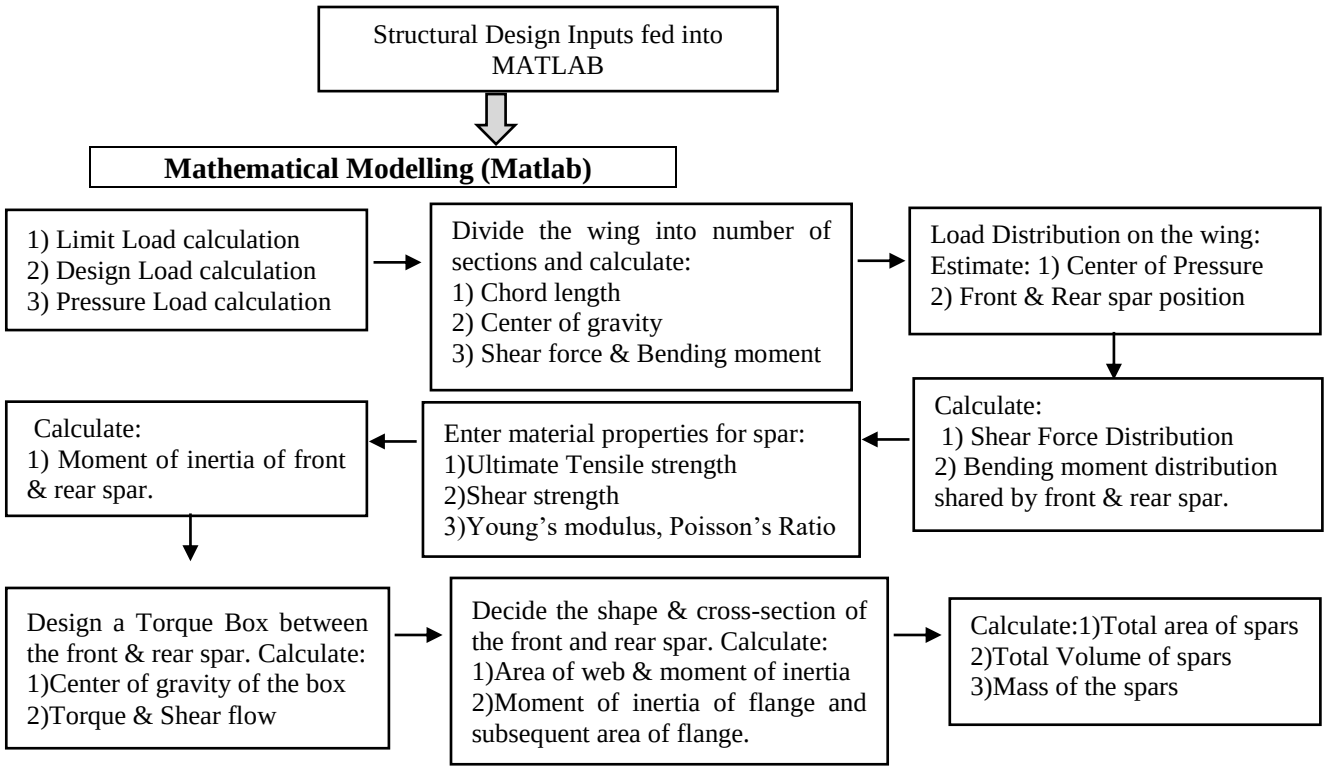

Fig.2 Mathematical Modelling flowchart

```
prompt1= 'What is the root chord of your plane in mm?';
Root_chord=input(prompt1)

prompt2= 'What is the tip chord of your plane in mm?';
Tip_chord=input(prompt2)

prompt3= 'What is the semi-span length of your wing in mm?';
Semispan_length=input(prompt3)
```

```
Root_chord = 380

Tip_chord = 230

Semispan_length = 1127
```

Fig.3 User I/O live script in MATLAB to input design parameters

```
%% Chord Length calculation %%
L(1)=230;
for i=2:11
    L(i)=Root_chord - ((Root_chord-L(1))/Exposed_span)*(Exposed_span-((i-1)*(h)))
end
```

Fig.4 Chord length calculations by dividing the wing into number of sections

```
%% Cumulative Shear Force at each section %%

P_matrix=[P(1) P(2) P(3) P(4) P(5) P(6) P(7) P(8) P(9) P(10)];
csf=cumsum(P_matrix)
```

Fig.5 Cumulative shear force calculation

```
BM_at_tip=0;
BM(1)=P(1)*CG(1);
BM(2)=P(1)*CG(1)+P(2)*CG(2)+P(1)*h;
BM(3)=P(1)*CG(1)+P(2)*CG(2)+P(3)*CG(3)+2*P(1)*h+P(2)*h;
BM(4)=P(1)*CG(1)+P(2)*CG(2)+P(3)*CG(3)+P(4)*CG(4)+3*P(1)*h+2*P(2)*h+P(3)*h;
```

Fig.6 Bending moment calculation

Table 3. Shear Force & Bending moment distribution on the front and rear spar

Sections on the wing (mm)	Chord length at each section (mm)	Shear Force on front spar (N)	Bending Moment on front spar (N-mm)	Shear Force on rear spar (N)	Bending Moment on rear spar (N-mm)
TIP-1127	230	-	-	-	-
S1-1014.3	245	5.6364	569	6.6311	671
S2-901.6	260	11.6289	2300	13.6810	2711
S3-788.9	275	17.9773	5263	21.1498	6204
S4-676.2	290	24.6817	9531	29.0373	11234
S5-563.5	305	31.7421	15174	37.3436	17884
S6-450.8	320	39.1585	22262	46.0688	26240
S7-338.1	335	46.9308	30869	55.2128	36383
S8-225.4	350	55.0592	41063	64.7755	48399
S9					
ROOT-0	380	72.3839	66503	85.1575	78384

Table 4. Moment of inertia of spars; Torque box design, cumulative torque and shear flow on wing

Table 4. Moment of inertia of spars; Torque box design, cumulative torque and shear flow on wing

Sections on the wing (mm)	Moment of inertia of front spar (mm^4)	Moment of inertia of rear spar (mm^4)	CG of torque box from rear spar position (mm)	Cumulative Torque (N-mm)	Shear Flow (N/mm)
TIP-1127	-	-	0	-	-
S1-1014.3	23.3	21.6	47.122	67.1	0.0163
S2-901.6	94.2	87.4	50.007	214.1	0.0490
S3-788.9	215.6	200.1	52.8921	454.4	0.0984
S4-676.2	390.5	362.4	55.7771	802.4	0.1647
S5-563.5	621.6	576.9	58.6621	1273	0.2485
S6-450.8	912	846.4	61.5471	1882.1	0.3501
S7-338.1	1264.6	1173.7	64.4322	2646.4	0.4703
S8-225.4	1682.3	1561.3	67.3172	3583.1	0.6095
S9-112.7	2167.9	2012	70.2022	4710.6	0.7683
ROOT-0	2724.5	2528.5	73.0872	6047.7	0.9474

```
%% Moment of Inertia calculations %%

for i=1:10
    I_fs(i)=BM_fs(i)*(FS_h(i)/2)/Ultimate_Tensile_strength
end
```

Fig.7 Moment of inertia calculation

```
% Area of the torque box %

for j=2:11
    Area_TB(j)=0.5*(FS_h(j-1)+RS_h(j-1))*c_dash(j)
end
```

Fig.8 Torque box area calculation

Table 5. Moment of inertia of web

Sections on the wing (mm)	Moment of inertia of web for front spar (mm^4)	Moment of inertia of web for rear spar (mm^4)
TIP- 11227	0	0
S1-1014.3	1.5715	1.1203
S2-901.6	3.3437	2.3069
S3-788.9	5.3181	3.7226
S4-676.2	7.4971	5.2064
S5-563.5	9.8834	6.8137
S6-450.8	12.4804	8.5461
S7-338.1	15.2916	10.4055
S8-225.4	18.3209	12.3936
S9-112.7	21.5724	14.5125
ROOT-0	25.0502	16.7643

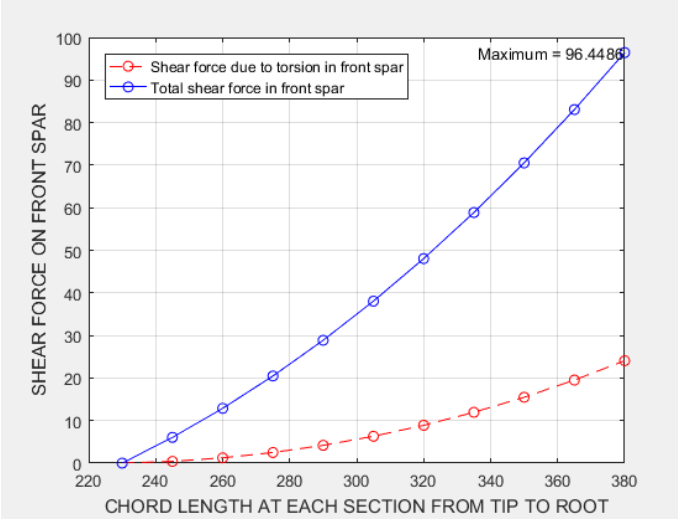

Fig.9 Shear Force due to torsion; Total shear in front spar

Fig.10 Shear Force due to torsion; Total shear in rear spar

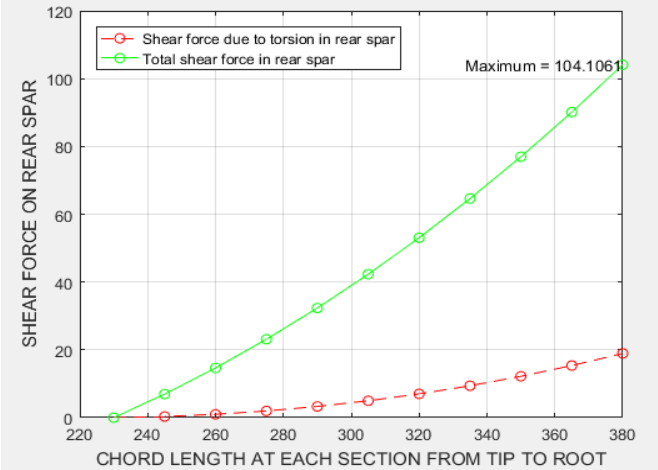

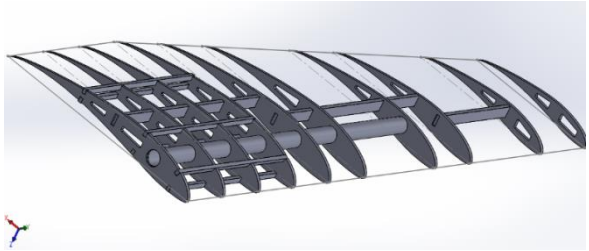

Fig.11 Internal structure of the wing (Isometric View)

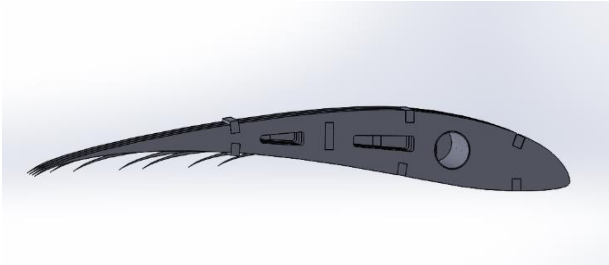

Fig.12 Internal structure of the wing (Top View)

Table 6. Mechanical Parameter values for spar

STRUCTURAL PARAMETERS	VALUE
Max Principal stress	83.2 Mpa
Max Von-Mises stress	56.2 MPa
Max Strain Energy	8.04e9 J
Max equivalent elastic strain	.00079
Total deformation	7 mm
Yield strength of AA 6061 T-6	310 MPa
Safety factor	3.73

4.Detailed Design Phase

The detailed design phase starts with the analysis of the initial blueprint of the wing using some initial hand calculations and Finite Element solver like ANSYS. The results are then optimized for appropriate weight reduction.

The structural optimization flowchart is as follows. The whole process is an iterative one, ie. Iterations keep taking place till we get the optimized result.

4.1 Detailed Design Flowchart

Statistics	
Nodes	63144
Elements	17849
Mesh Metric	None

Fig.15 Mesh statistics

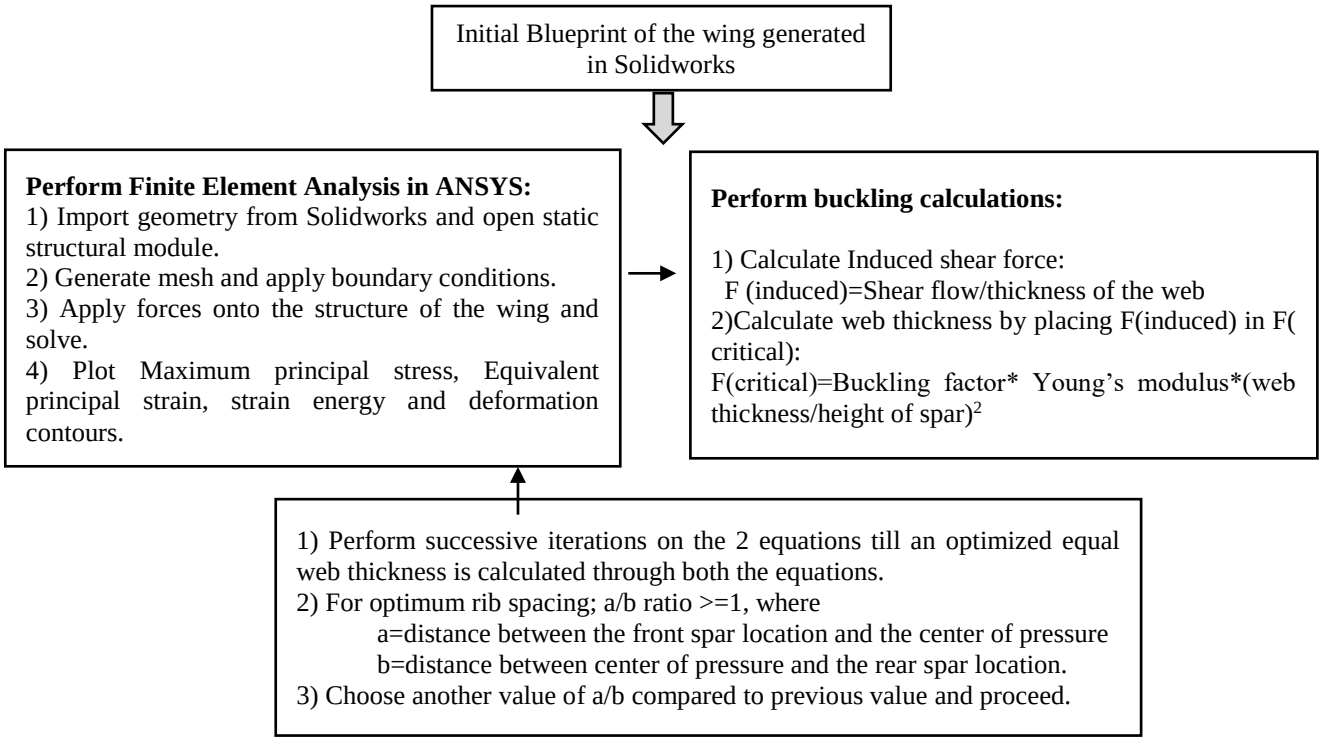

Fig.13 Structural optimization flowchart

The flowchart shown as figure 13, terminates at the point in MATLAB when, for a particular value of a/b and web thickness, the mass reduces and subsequently gets verified through Finite Element solver ie. ANSYS through stress and strain contour plots with a significant reduction in a value.

4.2 Finite Element Analysis

Finite Element Analysis is a computerized method which is used to predict the behavior of a mechanical model in response to an applied force, provided a set of boundary conditions. The modelled wing on Solidworks is now analyzed in ANSYS, a finite element solver when the wing is exposed to various mechanical forces of varying magnitudes. The material properties for the ribs was added in ANSYS for balsawood and birchwood

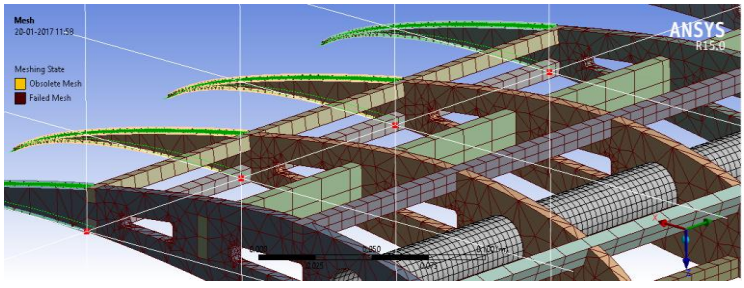

Fig.14 Failed & Obsolete Mesh (1st attempt)

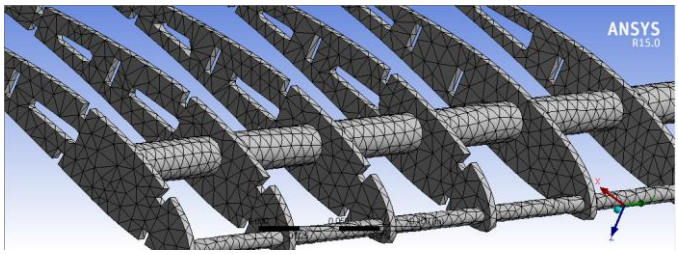

Fig.16 Successfully generated mesh

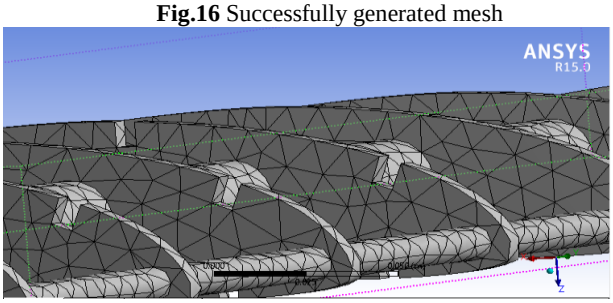

Fig.17 Tetrahedron element close-up

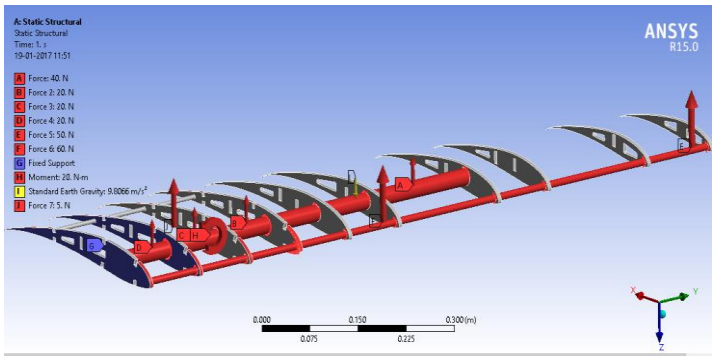

Fig.18 Force application on the wing

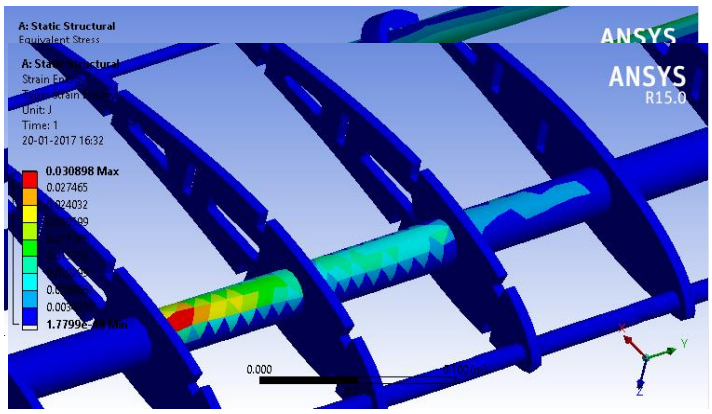

Fig.19 Equivalent Von-Mises stress contours

Fig.20 Strain energy contours

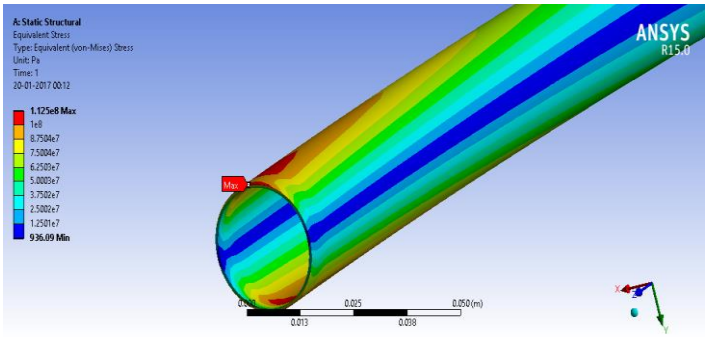

Fig.21 Equivalent Von-mises stress contours in spar

When the CAD model of the wing was first imported in ANSYS and the mesh was generated, the mesh failed at certain contact points of the assembly, shown by red blips in Fig.12. It was observed that the meshing method was not accurate and the element size was large at thin trailing edges which led to failure at such points. The meshing method was then changed to Tetrahedron elements with a Patch Independent algorithm limited by maximum element size. The mesh was then generated successfully.

The meshed wing is now opened in ANYS Mechanical and 4 types of force are applied onto the entire structure

1) Uniformly varying load on the front supporting spar
2) Uniformly varying load on the primary AA 6061 T-6 spar
3) Moment along the transverse axis of the wing
4) Standard earth gravity on all bodies

Table 7. Mechanical Parameter values for the internal structure

STRUCTURAL PARAMETERS	VALUE
Max principal stress	68 MPa
Max Von-Mises stress	70 MPa
Max strain energy	30 mJ
Max equivalent elastic strain	0.139 mJ
Normal stress	17.87 MPa
Total deformation	11.8 cm

Table 8. Weight optimization by changing the position of front spar, keeping rear spar fixed

Iteration	Position of front spar from leading edge	Position of rear spar from leading edge	a/b ratio	Total mass of the spars (gm)
1	25 %	62%	1.17647	316.71
2	22%	62%	1.353	310.55
3	20%	62%	1.4706	302.88
4	18%	62%	1.588	299.25
5	30 %	62 %	0.8823	323.10 s

By shifting the position of the front spar ie. Increasing a/b ratio, a maximum reduction of 17.46 gms was achieved, but the placement of spar was not feasible at 18% chord. Hence, the placement of spar at 22% chord was finally selected with the total mass of spars equaling 310.55 gms.

5. Conclusions

The paper demonstrates the design methodology undertaken in the structural design and optimization of a UAV wing for the SAE India Aero Design Challenge 2017. The final analysis and calculations can be accepted of a structurally fit pair of wings for the UAV. The most influential parameter of the competition ie. Payload capacity seems to be fulfilled through this design, as the wing is designed for a lift load factor of 5. The final simulation on the wing also gave us a safety factor of 3.73 which validates it completely.

References

[1] Bruhn EF. Analysis & design of flight vehicle structures. 1 ed. USA: Tri-state offset company, 1973.
[2] Sadraey M., Aircraft Design: A Systems Engineering Approach, 2012, Wiley Publications
[3] UAVs: An Overview, Peter van Blyenburgh, Air & Space Europe 1(5/6) – 1999
[4] Raymer DP. Aircraft Design: A Conceptual Approach, American Institute of Aeronautics and Astronautics, Washington D.C, 1992
[5] Roskam J. Airplane Design, Roskam Aviation and Engineering Corporation, 1985
[6] Bruno Jorge, Pereira Cadete: Aero-Structural Optimization of Sailplane Wings, Sintra, December 2011

GAVIN PUBLISHERS

Advances in Biotechnology and Biochemistry

SinghVK, et al. Adv Biotechnol Biochem 2017: J119.

Research Article

Structural Insights of Induced pluripotent stem cell regulatory factors Oct4 and its Interaction with Sox2 and Fgf4 Gene

Vimal Kishor Singh[1*], Neeraj Kumar[2], Ramesh Chandra[2]

[1]Department of Biotechnology, Stem Cell Research Laboratory, Delhi Technological University, Delhi, India

[2]Department of Chemistry, University of Delhi, Delhi, India

[*]**Corresponding author 1:** Vimal Kishor Singh, Department of Biotechnology, Stem Cell Research Laboratory, Delhi Technological University, Shahbad Daulatpur, Bawana Road, Delhi-110042 E-mail: vim_kissor@yahoo.co.in; vimalkishorsingh@gmail.com; vimalksingh@dce.ac.in

Corresponding author 2: Ramesh Chandra, Department of Chemistry, University of Delhi, Delhi, India, Email: acbrdu@hotmail.com

Citation: Singh VK, Kumar N, Chandra R (2017) Structural Insights of Induced pluripotent stem cell regulatory factors Oct4 and its Interaction with Sox2 and Fgf4 Gene. Adv Biotechnol Biochem 2017: J119.

Received Date: 9February,2017; **Accepted Date:** 13March,2017; **Published Date:** 20March, 2017

Abstract

Pluripotency of stem cells is governed by various factors, and Octamer-binding transcription factor 4 (Oct4) has been shown to be most essential regulator of Embryonic Stem Cells (ESCs) pluripotency. It is a key molecule for the reprogramming process and vastly used for IPSCs generation in research laboratories. Oct4 interacts directly with another important molecule Sox2 and elicitvarious downstream signals during the reprogramming. Sox2 is sex determining region-Y protein and involved in reprogramming through interaction with Oct4 and other pluripotency factors. Both of these transcription factors are known to bind enhancer element of specific genes regulating pluripotency such as fibroblast growth factor 4 (Fgf4) gene. Fgf4 has been proposed to promote self-renewation in human ESCs and support proliferation of mouse inner cell mass. The molecular mechanism for Oct4 interactions with Sox2 and their target gene(s) remain cryptic. The present study focuses on these aspects, and a comprehensive in silico analysis of Oct4-Sox2 and Fgf4 structure and their interactions are reported here. Briefly, the Three-Dimensional (3D) models of Oct4 and Sox2 were generated and analyzed using de novo structure prediction approach. Further, these molecules were used to define the mechanism of their interactions to each other (Oct4 and Sox2); and their complex interaction with Fgf4 gene by molecular docking. The interaction of proteins and enhancer element of Fgf4 gene and resulting complexes were further evaluated through Dim plot analysis. This work reports that Oct4 binds to Sox2 with significant stability as indicated by their binding energy score (-618.95 kJ/mol) and two hydrogen bonds in between Gly307-Ser228 of 2.97 Å and Glu219-His260 of 3.02 Å bond lengths with hydrophobic interfaces. More importantly, we found that Oct4 in complex formation with Sox2 bind moreefficientlywithscore-615.86kJ/molthenOct4andSox2bindsindividuallywiththescoreof-585.22 and -395.99 kJ/mol respectively.

We suggest Oct4-Sox2 complex play a crucial role by synergistically increasing their binding to enhancer element of Fgf4 gene. Insights into the molecular mechanism of interaction of Oct4 and Sox2 would help to better understand the reprogramming regulatory network.

Keywords: Molecular Docking; Protein-Protein Interactions; Reprogramming; Pluripotency Transcription Factor.

Introduction

Oct4 is a master transcription factor for regulating early mammalian development and pluripotent cell self-renewation. Oct4 expression starts from the oocyte stage, becomes confined to Inner Cell Mass (ICM) of the blastocyst and ultimately remains only in primordial germ cells and maintains the pluripotency. Oct4 known as POU5F1, a homeodomain transcription factor of the

Pit1-Oct1/4-Unc-86 (POU) family consists a bipartite DNA binding domain [1]. Oct4 in combination with othertranscription factors mainly Sox2, Klf4, and C-Myc are responsible for the generation of Induced Pluripotent Stem Cells (iPSCs) from somatic cells [2].

iPSCs are pluripotent stem cells and possess the important property of self-renewability, and they can give rise to all three germ layers endoderm, mesoderm, and ectoderm. This reversion of adult cells to a reprogrammed state which resembles ESCs offers a non-diminishing potential source for the pluripotent cells with enormous applications such as generation of patient-specific tissues to facilitate disease modeling. Further, it is highly applicable in screening methods of drugs to develop new therapies [3].

In 2006, Yamanaka first time reported the generation of iPSCs. Initially, they have used 24 transcription factors for reprogramming, and in the consequent studies, they reported the four transcription factors for the generation of iPSCs which are Oct4, Sox2, Klf4, C-myc. Further, in the subsequent studies on iPSCs generation, many reports suggest the Oct4 as a master regulator of source cells for reprogramming. Oct4 in cooperation to a Sox2 transcription factor is involved in somatic cell reprogramming. Sox2 is Sex determining region-Y box-2 related proteins which are activated in response to Leukemia Inhibitory Factor (LIF), which regulates the JAK-STAT signaling pathway. Downstream expression of signaling pathway results in Sox2 activation [4]. Both Oct4-Sox2 alone have been reported to generate iPSCs. Sox2 is a key factor required for iPSCs also thought to regulate Oct4 expression [5]. During early embryonic development, Members of POU family and Sox family exemplify functional cooperation and Sox proteins interact specifically with each other and bind to DNA [6]. Transcription regulation by Oct4 and Sox2 transcription factors reflects many of regulations showing the combinatorial control. Previous studies have demonstrated that specific promoters are selectively responsive to members of Oct family. Oct4 bind to the promoter element of Fgf4 gene adjacent of a Sox2 transcription factor. FGF4 gene promotes the auto self-renewable of the human ESCs and both Oct4 and Sox2 transcription factors are known to regulate the Fgf4 gene [7,8]. Fgf4 enhancer element was the first of the DNA elements found to contain composite DNA binding element of Oct4 and Sox2 [9].

Transcription factors regulations involve the protein-protein interaction for formation of regulatory complex and further their interaction with DNA binding element of a gene that can interact with and modulate the downstream genes responsible for maintaining the pluripotency. Their functional partnership has been characterized by regulatory elements in various species, including human, mouse, and the fruit fly. During development, POU and Sox proteins are expressed differentially, and their interactions may lead to a differential expression of the genes which are important for the determination of cell-fate [10]. The genes encoding the transcription factors Oct4 and Sox2 are critically regulated during embryonic development and somatic cell reprogramming. Their combinatorial role is critical, asit functions to specify the three germ layers of the mammalianembryo [11]. Although Sox2 and Oct4are considered to have a combinatorial role in vivo, the binding of POU factors by Sox2 isindiscriminate in vitro [12]. Biological data indicates that DNA binding region of two proteins synergizes the interaction with target genes, however not elucidate the combinatorial control at the molecular level and also the mechanism of interactions. Therefore, we have chosen the Oct4-Sox2-Fgf4 element ternary complex tostudy.

These transcription factors play a pivotal role in the development of embryonic stem cells and iPSCs generation, however; mechanism of their interactions for iPSCs generation is not well understood. Hence, detailed study is required to demonstrate the interaction of Oct4 and Sox2 proteins. It is also unclear how these four transcriptions factors Oct4, Sox2, Klf4 and Nanog lead to changes in the cellstate and systematic analysis of these transcription factors are lacking. Unearthing the interactions of Oct4, would provide insight to how this transcription factor interaction acts importantly to the decision of cell fate and maintenance of stem cellpluripotency.

Present study elucidates the molecular mechanistic interactions involved among Oct4/Sox2 and target gene Fgf4 to demonstrate important regulatory element in the overall process of pluripotency. Interactions of Oct4 protein and Sox2 protein have been done by using Molecular docking methods. Subsequently, Oct4 and Sox2 protein complex were evaluated to define its ability to interact with their direct target Fgf4 gene. These studies revealed the structural information of Oct4 and Sox2 transcriptionfactors and may exemplify their downstream interactions during the reprogramming. Moreover, this studies would help in better understand the mechanistic interaction between Oct4 and Sox2 proteinswith their regulatory Fgf4gene.

Methodology

Primary Structural Analysis of Oct4 and Sox2

The amino acid sequences of Oct4 and Sox2 proteins were retrieved from the NCBI protein sequence database (http://www.ncbi.nlm.nih.gov/protein) in Fasta format. Sequence analyses of Oct4 and Sox2 were done by local alignment and multiple sequence alignment using Basic Local Alignment Search Tool (BLAST)(http://blast.ncbi.nlm.nih.gov/Blast.cgi[13]andT-Coffee (http://www.ebi.ac.uk/Tools/msa/tcoffee/) [14] respectively.

Physicochemical properties of proteins were studied using the Expasy's Protparam server (http://web.expasy.org/protparam/).

Physicochemical properties including molecular weight, theoretical Isoelectric Point (pI), molecular formula, the number of negative and positive residues, extinction coefficient, instability index, aliphatic index and grand average hydropathy (GRAVY) were determined [15]. The models quality was checked by energetic and geometricmeans (figure 1).

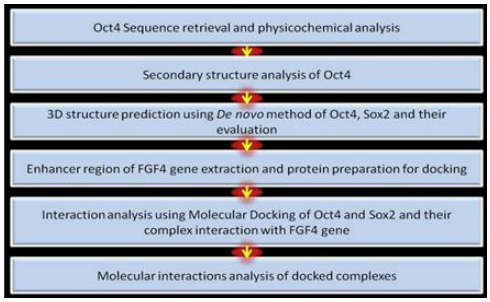

Figure 1: Flow chart diagram of the methodology used: Oct4 and Sox2 transcription factors sequence analysis and 3D structure prediction. Molecular interaction analysis of Oct4 and Sox2 and their heterodimer complex interaction with Fgf4 gene through docking.

3D Structure Prediction

The amino acid sequence of Oct4 and Sox2 were subjected to BLAST to find out the template for structure prediction through homology modeling. Lack of suitable structural template for Oct4 and Sox2 resorted to de novo structure modeling of Oct4 and Sox2 using iterative threading assembly refinement (I-TASSER) (http://zhanglab.ccmb.med.umich.edu/I-TASSER/).It is a web-based protein 3D structure prediction tool. It involves the simulation of protein structures as well as domains of the proteins andTm score and active sites. Tm score in which smaller distance between the structures is weighted high. The tm-score range is a value of more than 0.5 ensures a model of right topology and a value of 0.17 refer to random similarity or structure would be discarded [16]. With these parameters, the complete models wereobtained.

3D Structure Assessment

Predicted structures of Oct4 and Sox2 proteins were evaluated. I-TASSER server resulted in the generation of five structures for the each protein. Predicted structures were evaluated using the Rampage for Ramachandran plot, Verify3D, Errat and Prosa web interface. Ramachandran plot is to visualize dihedral angles phi (Φ) and psi (ψ)of amino acid residues in the proteins structures. It shows the possible allowed conformation of Oct4 and Sox2 polypeptides. Rampage server (http://mordred.bioc.cam.ac.uk/~rapper/rampage.php) was used to analyzes the stereochemical properties to assess the quality of the structures, the planarity of the peptide bond, the main chain hydrogen bond energy; Cαchiralities, non-bonded interactions. The Errat (http://services.mbi.ucla.edu/ERRAT/) algorithm based on the statistical parameters of non-bonded interactions between different types of atoms and subsequently provides the accuracy of the protein models [17]. Verify3D (http://services.mbi.ucla.edu/Verify_3D/) analyze the compatibility of the predicted 3D structure with its primary amino acid sequence structural properties. A high Verify3D profile score indicates a better quality of model [18]. Prosa web interface (https://prosa.services.came.sbg.ac.at/prosa.php)calculatestheoverallquality ofthestructures;scoreshould be in the range of native experimentally determined protein structures. Prosa score (Z-score) determines the overall model quality and fold reliability of the predicted structure [19].

Oct4 and Sox2 Interaction Analysis through Molecular Docking and their Interaction Sites Identification

Interaction study of Oct4 and Sox2 was done by molecular docking. There are various tools available for protein-protein interactions docking. In the present study, we have used Hex 8.0 cuda program forthe molecular docking simulations. Hex determines the steric shape, electrostatic potential and the charge density of each protein. Molecular docking analysis was accomplished to obtain the best native conformation of protein-protein docked complex [20]. In the case of Hex, the input parameters were the Oct4 transcription factor PDB coordinate files for receptor protein and Sox2/Fgf4 as ligand files with set parameters. The total energy of interactions was calculated based on shape and electrostatics, and the final search was set to 25 (N= 25), and the angular search range of interaction was confined by selecting interface residues for Oct4 with angle 45° range. Other parameters were set to default values. The best model of docking complex, which showed the largest binding affinity were subjected to further molecular interactionstudies.

Predicated protein structure Oct4 and Sox2 were prepared before molecular docking since, these PDBs may contain some unwanted ligands or repetition of chains. Proteins were prepared using build/check/repair application of WhatIF server (http://swift.cmbi.ru.nl/servers/html/index.html) [21]. We studied the interactions of Oct4 and Sox2 proteins with Fgf4 gene enhancer element. First, we have studied the interaction of Oct4 and Sox2 proteins, and then Oct4 protein interaction with the enhancer element of Fgf4 gene and similarly Sox2 protein was docked with the target Fgf4 gene through molecular docking. Furthermore, we studied the interaction of Oct4-Sox2 heterodimer complex with the enhancer element of Fgf4 gene by molecular docking. Fgf4 enhancer element was extracted from the crystal structure of POU/HMG/DNA ternary complex available at protein data bank (PDB ID 1GT0), using Swiss PDBviewer.

Molecular Interactions Analysis

The molecular interaction plots between proteins were gen-

erated using Dimplot application of Ligplot software (v. 4.5.3). The Dimplot program gives a plot of the interactions across a protein-protein domain interface. Interactions plot includes hydrogen bonds, hydrophobic interactions and non-bonded contacts [22]. Molecular interactions (hydrogen bonds and hydrophobic interactions) of docked complex of Oct4-Sox2 and Oct4/Sox2-Fgf4 gene were determined using the Ligplot.

Results

Protein Sequence and Physicochemical Analysis of Oct4 and Sox2

The amino acid sequence of the Oct4 transcription factor of *Homosapiens* was obtained from NCBI protein database with accession number GenBank: AAI17436.1. On analyzing Oct4 sequence, we found 371 variants for *Homosapiens* and 109 variants for *Mus musculus* of different length present on NCBI, among which most sequences were of 360 amino acids. BLAST analysis of Oct4 (100 hits) showedmore than 90% sequence identity for *Homosapiens* variants and more than 86% identity with variantsin other organisms. Multiple sequence alignment of Oct4 in different organisms was done by T-Coffee, which showed that major regions where amino acids differ in organisms are 101 and 244 amino acids (Figure2(a)). The position101of Oct4 has Valto Alaaminoacid change in *Callithrixjacchus,Chlorocebussabaeus, Colobus angolensispalliatus, Saimiriboliviensis, Papioanubis, Mandrillusleucophaeus, Macacafascicularis, Macacamulatta, Rhinopithecusroxellana* and at 224 position Asn to Ser amino acid change in *Chlorocebussabaeus, Colobus angolensispalliatus, Macacafascicularis, Macacamulatta, Papioanubis, Mandrillusleucophaeusand Rhinopithecusroxellana. Capra hircus* has been found to have different amino acids at 7 different positions (247, 248, 293, 306, 327, 332, 347,352),*Saimiriboliviensis* differedat5 positions(27,101,108,110,351),*Callithrixjacchus* at 5 positions (27,55,108,133,351), *Mandrillusleucophaeus* at 4 positions (101, 244, 352, 354),*Papioanubis* at 3 positions (39,101, 244) and Gorilla at only position 51. These results showed Oct4 is conserved protein, present in various organisms and putative conserved domains are POU domain and DNA-binding homeodomain.

Similarly, the amino acid sequences of the Sox2 transcription factor of *Homosapiens* was obtained from NCBI protein database with sequence accession number: NP_003097.1. Through Sox2 sequence analysis, we found Sox2 has 108 variants of different amino acid length for *Homosapiens* but mostly of size 317 amino acids. Sox2 has 90% and more identity with other variants of *Homosapiens* and other organisms. Multiple sequence alignment showed that between 20-21 amino acid position of Oct4, Gly residues are added in various other organisms (Figure 2(b)). *Leptonychotesweddellii* of size 322 amino acids consisted of four added Gly at the same position. Moreover, Salmo salar with 100% coverage of Sox2 and 87% identity found to have different amino acids at 90,143, 146, 152, 156, 172, 175, 177, 181,195, 196, 207, 217, 236, and 253 positions and *Buceros rhinoceros silvestris* with 96% coverage and90% identity at 143, 146, 293, 172, 175, 177, 181, 195, 251 and 253 positions. *Mus musculus* found to be different at only 301 position (Ser to Ala) and *Papioanubis* at 246 amino acid position (Gly to Ser). This suggests Sox2 is a conserved protein and its putative conserved domains are DNA-binding HMG- box region and Sox transcription factor domain of size ~80 aminoacids.

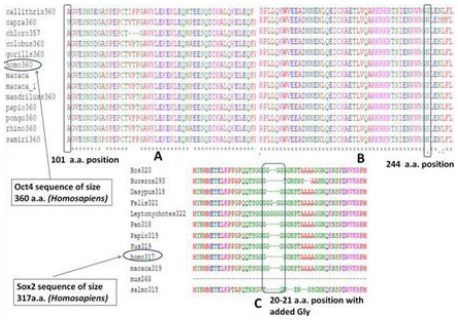

Figure 2: Multiple sequence alignment results of Oct4 and Sox2 in different organisms

(A) Oct4 protein sequence (Homosapiens) at 101 amino acid position shows changes from Val to Ala

(B) 244 amino acid position of Oct4 of Homosapiens shows changes from Asn to Ser

(C) Sox2 sequence at 20-21 amino acid position shows the different number of added Gly in the protein sequences of other organisms.

The primary structural features of Oct4 and Sox2 were studied using Protparam Tool and are described in (Table 1). As indicated, Oct4 protein (Human) consists 360 amino acids and molecular weight of 38570.6 daltons and molecular formula C1718H2657N469O517S13. The calculated Isoelectric Point (pI) for Oct4 was 5.69, suggesting more negatively charged residues. Oct4 possess the higher extinction coefficient value which was 36940 M-1cm-1and indicating the presence of Cys, Trp, and Tyr in abundance. A Higher number of these residues aid to the quantitative study of protein-protein interactions. The aliphatic index value of Oct4 found to be 66.61 indicating its stability at a wide range of temperature. However, instability index value 53.24 (more then 40) indicates it may be thermally unstable. The Grand average hydropathy (GRAVY) value of Oct4 was -0.435, suggesting a hydrophilic pattern with high interaction with watermolecules.

Properties	Oct4 Protein	Sox2 Protein
Accession number	NCBI-GenBank: AAI17436.1	NCBI Reference Sequence: NP_003097.1
Molecular formula	C1718H2657 N469O517S13	C1467H2321 N443O457S26
Molecular weight	38570.6	34309.8
Amino acids	360	317
pI (Isoelectric Point)	5.69	9.74
Negative Residues	38	21
Positive Residues	33	34
Extinction Coefficient	36940	37360
Instability Index	53.24	58.73
Aliphatic Index	66.61	48.71
GRAVY	-0.435	-0.742

Table 1:Physico-chemical properties of Oct4 and Sox2 protein.

Whereas, Sox2 consists of 317 amino acids and molecular weight 34309.8 daltons, molecular formula C1467H2321N443O457S26 and pI 9.74 representing the basic nature of the protein. Extinction coefficient value was 37360 M-1-cm-1suggesting the presence of aromatic amino acids. Sox2 has aliphatic indexand instability index value 48.71 and 58.73 respectively, indicating the stability of Sox2. GRAVY value of Sox2 was -0.742, shows the hydrophilic pattern of the protein with more interaction with water.

3D Structure Prediction and Evaluation

Due to unavailability of suitable templates with appropriate sequence identity with proteins which is essential for protein homology modeling, we have designed the 3D structure for both the Oct4 and Sox2 (Human) proteins using de novo method through I-TASSER. I-TASSER is the hierarchical approach for protein 3D structure prediction, in this approach templates are identified by multiple threading approach and models are designed by adjoining the multiple fragment assembly simulations. I-TASSER generatedthe five models of acceptable high physicochemical properties, and out of them, high score model with best properties was selected as measured by TM-score. The Oct4 protein model-1 has TM-score forOct4 0.33 ± 0.11, which represents the absolute high quality of predicted structures. The Sox2 protein model-1 has TM-score0.45 ± 0.14, signifying the overall good quality of predicted structure (figure3).

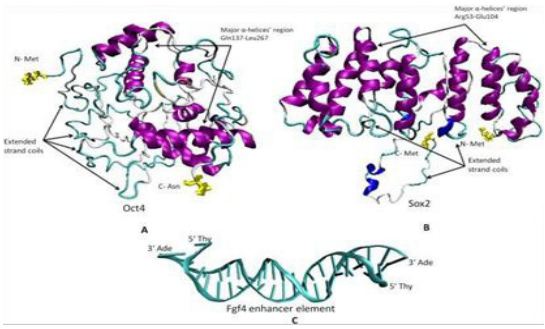

Figure 3: Diagram depicting 3D de novomodels

(A) Predicted structure of Oct4 protein, showing major region of alpha helices Gln137-Leu267 (purple) and extended strand coiled region (sky blue)

(B) Predicted structure of Sox2 protein showing the major region of alpha helices Arg53-Glu104 (purple) and extended strand coiled region (sky blue)

(C) Enhancer element (24 nucleotides) of Fgf4 gene extracted from the crystal structure of POU/HMG/DNA ternary complex

3D Structures Quality Assessment

The physicochemical quality of predicted structures of Oct4 and Sox2 were further assessed by Ramachandran plot, Prosa –web server, Verify-3D, and Errat. The stereochemical quality and accuracy of predicted models were evaluated by Ramachandran plot using Rampage server. For Oct4, the number of residues falling in the most favored regions of Ramachandran plot obtained by Rampage amounted to 72.1% and 17.9% in the allowed region and 10.1% in the outlier region. For Sox2, the number of residues which fall in the most favored region is 73.3% and 18.7% in the allowed region and 7.9% in the outlier region (figure 4).

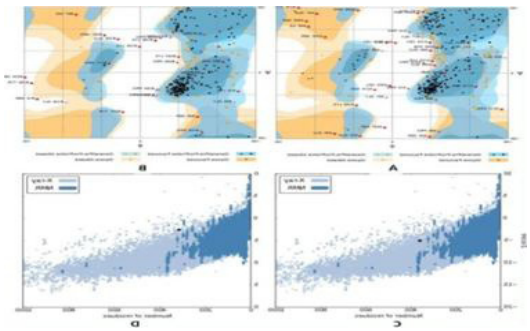

Figure 4: Diagram depicting the

(A) Ramachandran plot of predicted Oct4 structure, shows the 72.1% and 17.9% in the most favored and allowed regions

(B) Ramachandran plot of predicted Sox2 protein structure, shows 73.3% and 18.7% regions in most favored and allowed region respectively. Ramachandran plot shows the phi (φ)-psi (ψ) torsion angles for all amino acid residues and mostfavored and additional allowed regions of the structures.

(C) NMR/X-ray plot of the Oct4 structure through Prosa-web interface

(D) NMR/X-ray plot of Sox2 protein structure using Prosa-web

The Z-score represents the overall physio-chemical quality of the predicted protein 3D structure. The Z- score plot for Oct4 using Prosa-web showed the Z score -5.1, which was within the range of template proteins used for structure prediction (figure 4). Most identical template proteins PDBs were 3I1P,1GT0 and 2XSD and they have Z-score values of -3.88, -4.87 and -5.18 respectively. Similarly, Z-score for the Sox2 structure was obtained which was -2.62, shows the overall quality of thepredicted structure. Z-score of Sox2 also found to be within range with the templates used for structure prediction using de novo methods. Identical templates were 4N16, 1J46 and their Z-scores were -1.78 and-3.34.

For analyzing the statistics of non-bonded interactions and crystallographic model building Errat server was used. The overall quality score for Oct4 found to be 76.657 (as evaluated by Errat), representing the crystallographic model building and its refinement. Whereas, Sox2 predicted structure overall quality score was 93.793 suggest better crystallographic properties and non-bonded interactions. Both predicted structures were further evaluated through Verify 3D tool, which assesses the three-dimensional profile and entails at least 80% of amino acids residues should show absolute quality interactions (alpha, beta, loop, polar, non-polar, etc) and location in the predicted structure. Verify 3D resulted-in81.39% residues of Oct4 shows the absolute the 3D crystallographic properties. On the hand, only 56.47% residues of Sox2 protein possess the 3D absolute qualities and indicates the moderate 3D structure qualities.

Oct4 and Sox2 Interaction Analysis

The protein interactions of Oct4 and Sox2 with Fgf4 gene was analyzed in two different manners.Firstly, the Oct4 protein and Sox2 were interacted to each other to form their heterodimer protein complex as depicted in (Table-2) (Figure 5). In the second approach, the Oct4 protein was used to interact with enhancer element of Fgf4 gene, and then Sox2 protein interacted with the Fgf4 gene. Then Oct4/Sox2 heterodimer complex was docked with enhancer element of Fgf4 gene. For the molecular docking PDB files of proteins were prepared and docked though Hex cuda 8.0. Hex docking module withsettingtheparameterswasrun.Hexshowedsignificantbindingenergytotalscore(E-totalscore)-618.95 kJ/mol for Oct4 and Sox2 protein. Fgf4 enhancer element PDB file was extracted from the1GT0 PDB and prepared for the molecular docking. Extracted Fgf4 enhancer element consists of two chains A and B of length 24 nucleotides each. Hex was run with receptor protein Oct4 and DNA PDB file with protein-DNA docking module selection. For Oct4 and enhancer element of Fgf4 gene, Hex resulted in binding energy total score -615.86 kJ/mol. Next, Sox2 was docked with the enhancer element ofFgf4gene,whichshowsenergytotalscore-395.99kJ/mol(Table-2).Oct4-Sox2proteincomplexalso docked with the enhancer element of Fgf4 gene, which resulted in higher energy total score of -615.86 kJ/mol, their interacting complex shown in figure 6. Higher energy total score of heterodimer complex of Oct4 and Sox2 then the individually interact with Fgf4 gene, indicates their synergistic enhancement in binding to the target gene.

Receptor	Ligand	E-total (kJ/mol)	Bonds	Hydrophobic interfaces
4-Oct	Sox2	-618.95	Two hydrogen bonds: Gly307-Ser228 of 2.97Å and Glu219-His260 of 3.02 Å bond lenghts	Oct4 residues: Pro346, Pro347, Phe345, Val348, Pro340, Pro338, Pro309, Leu226, Phe305, Ser306, Gly308, Ser335, Ser336, Gly342, Cys221, Phe312, Thr225, Gln224, Lys222 and Ala223. Sox2 residues: Lys122, Lys121, Met120, Thr118, Lys117, Gly190, Ala191, Tyr277, Tyr227, Gln229, Met194, His189, Thr85, Ser259, Ser261, Ser258, Gln282 and Arg262.
4-Oct	Fgf4(Enhancer element)	-585.22	One external bond between : Pro119- guanine15 of Fgf4	Oct4 residues: Lys206, Pro95, Glu96, Ala121, Val122, Lys123, Glu98 and Gly100.
Sox2	Fgf4(Enhancer element)	-395.99	No bond	Sox2 residues: Asn33, Gln34, Met1, Tyr2, Met276, Pro279 and Met4.
Oct4-Sox2 Comple x	Fgf4(Enhancer element)	-615.8	Three hydrogenbonds: 1. Gly120-guanine 7 of 3.2 Å, 2. Val117-thymine 5 of 2.59 Å, 3. Glu210-adenine13 of 2.54 Å bond lengths	Oct4 residues: Glu209, Lys206, Gln205, Thr116, Val117, Thr118, Ala121, Val122, and Gly83.

Table 2: Table is enlisting the energy total scores, hydrogen bonds and hydrophobic interfaces residues of docked complexes of Oct4/Sox2/Fgf4, through molecular docking interaction analysis using Hex cuda8.0.

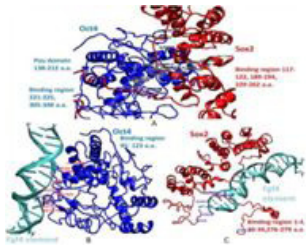

Figure 5: Diagram depicting the

(A) Oct4-Sox2 protein complex resulting from molecular docking, where blue color ribbon coiled structure is Oct4 protein, and red color ribbon coiled structure is Sox2 protein.

(B) Oct4-enhancer element Fgf4 gene (DNA strands in blue color) complex and shows the binding domain of Oct4 protein to DNA element

(C) Sox2 protein docking complex with the enhancer element of Fgf4 gene through molecular docking

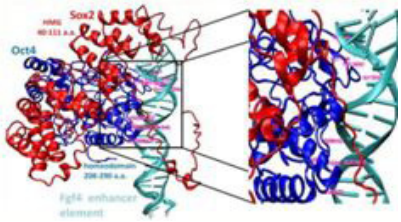

Figure 6: Diagram depicting the molecular interactions of docked complex of an Oct4-Sox2 heterodimer with enhancer element of Fgf4 gene and enlarged view of binding domains of Oct4 and Sox2 transcription factors to the enhancer element DNA strands of Fgf4 gene.

Molecular InteractionAnalysis

The molecular interactions (hydrogen bonds and hydrophobic interactions) of Oct4/Sox2 docked complex were identified by using Dimplot. We found, two intermolecular hydrogen bonds in the Oct4- Sox2 protein complex. Hydrogen bonds were in between amino acid Gly307-Ser228 of2.97 Åand Glu219-His260 of 3.02 Å bond lengths with various hydrophobic interactions. Hydrophobic residues of the Oct4 protein responsible for interactions were Pro346, Pro347, Phe345, Val348, Pro340, Pro338, Pro309, Leu226, Phe305, Ser306, Gly308, Ser335, Ser336, Gly342, Cys221, Phe312, Thr225, Gln224, Lys222, and Ala223. Hydrophobic residues of Sox2 were Lys122, Lys121, Met120, Thr118, Lys117, Gly190, Ala191, Tyr277, Tyr227, Gln229, Met194, His189, Thr85, Ser259, Ser261, Ser258, Gln282 andArg262. Hydrophobic interactions and hydrogen bonds between Oct4 and Sox2 indicate, the strong interactions between them.

Furthermore, the molecular interactions of Oct4 and Sox2 with enhancer element of Fgf4 gene were studied. Oct4-Fgf4 gene complex showed one external bond between Pro119-Guanine15 of Fgf4 gene and amino acids Lys206, Pro95, Glu96, Ala21, Val122, Lys123, Glu98, and Gly100 were involved in the hydrophobic interactions. Whereas, Sox2-Fgf4 gene complex showed the hydrophobic interactions only with amino acids Asn33, Gln34, Met1, Tyr2, Met276, Pro279, and Met4. Moreover, molecular interactions of Oct4-Sox2 heterodimer complex with Fgf4 gene were analyzed. Docked complex of Oct4-Sox2 with enhancer element Fgf4 gene showed the three hydrogen bonds between amino acids and various hydrophobic interactions (figure 7). Hydrogen bonds were in between Gly120- Guanine7, Val117-Thymine 5 and Glu210-Adenine13 of 3.2 Å, 2.59 Å and 2.54 Å bond lengths respectively and Glu209, Lys206, Gln205, Thr116, Val117, Thr118, Ala121, Val122 and Gly83 residues of Oct4 were involved in the hydrophobic interactions with the Fgf4gene. This molecular interaction analysis showed the cooperative enhancement in interaction of Oct4-Sox2 complex with Fgf4 gene with more number of hydrogen bonds and hydrophobic interactions.

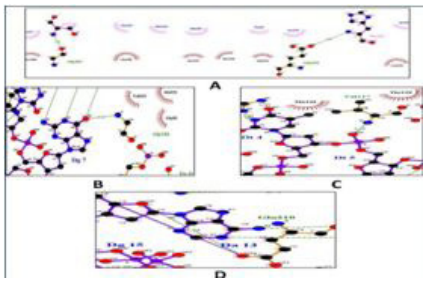

Figure 7: Diagram showing the hydrogen bonds and hydrophobic interactions of docked PDB complexes between (a) Oct4-Sox2 complex with enhancer element of Fgf4 gene, showing the first H-bond. (B) Second H-bond of Oct4/Sox2/Fgf4 ternary complex (C) Third H- bond of Oct4/Sox2/Fgf4 ternary complex. Hydrogen bonds are shown by dashed lines (green), and hydrophobic interactions are shown by spoked arcs (red) between residues.

Discussion

Oct4 is an important transcription factor, employed in the reprogramming of somatic cells in combination with other transcription factors Sox2, Klf4, and c-Myc. Oct4 interacts with Sox2 in pluripotency regulation networks and is useful for iPSCs generation.The Oct4-Sox2 complex has been known to regulate Fgf4 gene which helps in maintaining pluripotency of embryonic stem cells. However mechanism of interaction of pluripotency transcription factors and with downstream target Fgf4 gene is not known hence molecular interactions analyses have been performed.

Firstly, we have studied the physicochemical properties of Oct4 and Sox2 proteins. Oct4 has isoelectric point 5.69 which indicates it has more negatively charged residues and Sox2 has 9.74 shows the basic nature of more positive charged residues. The ali-

phatic index value of Oct4 and Sox2 were found tobeand 48.71 respectively, show the hydrophilic patterns of proteins and indicates Oct4 and Sox2 being stable at a wide range oftemperature.

We have generated the 3D structures of Oct4 and Sox2 transcription factors through de novo method using I-TASSER. The qualities of generated structures were ensured by TM-score. TM-score signifies the absolute quality of both the structures with scores of 0.33 ± 0.11 and 0.45 ± 0.14 for Oct4 and Sox2 respectively. Furthermore, modeled structures were evaluated by the Psi/Phi angle based backbone conformation, bond lengths using Ramachandran plot and found most of the residues of Oct4 andSox2-are in the favored region and allowed region. Both models were analyzed using Prosa and Errat. Z- Scores using the Prosa-web for Oct4 and Sox2 shows over all residues energies value within the rangeof templates used for structure prediction and Errat scores of Oct4 and Sox2 were found to be 76.657 and 93.793 respectively. These results represent a quality indicator for non-bonded atomic interactions, and its high score implies the better quality of structures. The above mentioned validating parameters assured the quality and reliability of models. To get insight into mechanistic interactions and their binding to the target gene, molecular docking method has beenemployed.

Oct4 protein is known to interact with Sox2 directly and regulates the various genes including the Fgf4 gene by binding to its transcription domain or enhancer element. Our results showed that Oct4 binds potently with Sox2 with a significant binding energy total score -618.95 kJ/mol with two hydrogen bonds and various hydrophobic interactions, shown in the table-2. For analyzing the binding specificity of Oct4 and Sox2 with Fgf4 gene, both proteins were docked individually with enhancer element ofFgf4 gene, and then their heterodimer complex was docked with Fgf4 gene element. Oct4-Fgf4 complex resulting in binding energy score -585.22 kJ/mol with eight hydrophobic interfaces and Sox2-Fgf4 complex had a score of -395.55 kJ/mol with seven hydrophobic residues only which shows Oct4 binds more potently than Sox2 with Fgf4 gene to regulate its expression. Next, molecular docking of Oct4-Sox2 protein heterodimer complex with enhancer element of Fgf4 gene showed a higher binding energy total score of -615.86 kJ/mol than Oct4 and Sox2 individual binding scores with Fgf4 gene. Oct4-Sox2 heterodimer complex through docking with Fgf4 gene showed three hydrogen bonds and strong hydrophobic interactions of Oct4 protein with promoter element, which suggest Oct4 is major protein responsible for binding and subsequent regulation of Fgf4 gene and binding of Sox2 to Oct4 introduces some conformational changes that resulted in the synergistic enhancement in binding of Oct4-Sox2 heterodimer complex with Fgf4 gene and possible reason for higher reprogramming efficiency when Oct4-Sox2 together induced in source cells for iPSCs derivation than lone Oct4 or Sox2 induced to the sourcecells.

Conclusion

We have generated the 3D structures of Oct4 and Sox2 transcription factors and found to be stable. We found Oct4 protein has DNA binding motif in homeodomain region. We found Oct4 binds strongly to a Sox2 protein with the formation of 2 hydrogen bonds and hydrophobic interactions. We also depict Oct4 binds more efficiently with Fgf4 gene in association with Sox2, forming 3 hydrogen bonds and strong hydrophobic interactions and suggest the possible cause of enhancement of binding of Oct4 with Fgf4 gene in the presence of Sox2 may be attributed to the possibility that Sox2 creates some conformational change in Oct4 and/or Fgf4 gene. Oct4-Sox2 complex results in better binding to Fgf4 gene than which is attained in individual binding and resulting in higher reprogramming efficiency of iPSCs generation with both Oct4 and Sox2 transcription factors together.

Acknowledgment

We thank the honorable vice chancellor Delhi Technological University for providing essential support. Dr. Vimal Kishor Singh particularly thanks, Department of Science & Technology/Indian National Science Academy (DST/INSA) for providing the funds for ongoing research. Neeraj Kumar particularly thanks, Department of Biotechnology (DBT-JRF) for providing the fellowship for ongoing research.

References

1. Guang JP, Chang ZY, Scholer HR, Duanqing PEI (2002) Stem cell pluripotency and transcription factor Oct4. Cell Research 12: 321-329.
2. Takahashi K, Yamanaka S (2006). Induction of pluripotent stem cells from mouse embryonic and adult fibroblast cultures by defined factors. Cell 126: 663-676.
3. Singh VK, Kalsan M, Kumar N, Saini A, Chandra R (2015) Induced Pluripotent Stem Cells: Applications in regenerative medicine, disease modelling and drug discovery. Front. Cell Dev Bio l3: 2.
4. Singh VK, Kumar N, Kalsan M, Saini A, Chandra R (2015) Mechanism of induction: Induced PluripotentStem Cells (iPSCs). Journal of Stem Cells 10: 43-62.
5. Zhao R, Daley GQ (2008) From fibroblasts to iPS cells: induced pluripotency by defined factors. J Cell Biochem 10: 949-955.
6. Herr W, Cleary MA (1995) The POU domain: Versatility in transcriptional regulation by a flexible two-in-one DNAbinding domain. Genes & Dev 9: 1679-1693.
7. Dailey L, Yuan H, Basilico C (1994) Interaction between a novel F9-specific factor and octamer-binding proteins is required for cell-type-restricted activity of the fibroblast growth factor 4 enhancer. Mol Cell Biol 14: 7758-7769.
8. Ambrosetti DC, Basilico C, Dailey L (1997) Synergistic activation of the fibroblast growth factor 4 enhancer by Sox2 and Oct-3 depends on protein protein interactions facilitated by a specific spatial arrangement of factor binding sites. Mol Cell Biol 17: 6321-6329.

Citation: Singh VK, Kumar N, Chandra R (2017) Structural Insights of Induced pluripotent stem cell regulatory factors Oct4 and its Interaction with Sox2 and Fgf4 Gene. Adv Biotechnol Biochem 2017: J119.

9. Yuan H, Corbi N, Basilico C (1995) Developmental-specific activity of the FGF-4 enhancer requires the synergistic action of Sox2 and Oct-3. Genes Dev 9: 2635-2645.

10. Dailey L, Basilico C (2001) Coevolution of HMG domains and homeodomains and the generation of transcriptional regulation by Sox/POU complexes. J Cell Physiol1 86: 315-328.

11. Niwa H, Miyazaki J, Smith AG (2000) Quantitative expression of Oct-3/4 defines differentiation, dedifferentiation or self-renewal of ES cells. Nat Genet 24: 372-376.

12. Avilion AA, Nicolis SK, Pevny LH, Perez L, Vivian N,et al. (2003) Multipotent cell lineages in early mouse developmentdepend on SOX2 function. Genes & Dev 17: 126-140.

13. Camacho C, Coulouris G, Avagyan V, Ma N, Papadopoulos J, et al. (2008) "BLAST+: architecture and applications." BMC Bioinformatics 10: 421.

14. Notredame C, Higgins DG, Heringa J (2000) T-Coffee: A novel method for fast and accurate multiple sequence alignment. Journal of molecular biology 302: 205-217.

15. Gasteiger E, Hoogland C, Gattiker A, Duvaud S, Wilkins MR, et al. (2005) Protein Identification and Analysis Tools on the ExPASy Server; (In) John M. Walker (ed): The Proteomics Protocols Handbook, Humana Press, 571-607.

16. Yang J, Yan R, Roy A, Xu D, Poisson J, et al. (2015) The I-TASSER Suite: Protein structure and function prediction. Nature Methods 12: 7-8.

17. Colovos C, Yeates TO (1993) Verification of protein structures: patterns of nonbonded atomic interactions. Protein Sci 2: 1511-1519.

18. Lüthy R, Bowie JU, Eisenberg D (1992) Assessment of protein models with three-dimensional profiles. Nature 356:83-85.

19. Wiederstein M, Sippl M. J (2007) ProSA-web: interactive web service for the recognition of errors in three-dimensional structures of proteins. Nucleic Acids Res35: 407-410.

20. Ghoorah AW, Smail-Tabbone M, Devignes MD, Ritchie DW (2013) Protein Docking Using Case- Based Reasoning. Proteins: Structure, Function, Bioinformatics 81: 2150-2158.

Volume 5, Issue 1 (2017) 83-85 ISSN 2347 - 3258
International Journal of Advance Research and Innovation

Study of Concentrated Solar Power and Their Application in Metro Stations

Hukam Singh*, [1], Shailesh Kumar Singh[1], Ashutosh Kumar Rai[2], Rangnath MS[2].
[1] Department Of Mechanical Engineering, Krishna Engineering College, Ghaziabad India-201007
[2]Department of Mechanical Engineering Delhi Technological University, Delhi India 110042

Article Info
Article history:
Received 25 January 2017
Received in revised form
20 February 2017
Accepted 28 February 2017
Available online 15 March 2017

Keywords
Concentrated solar power;
Case study; Metro station

Abstract
The inadequate supply and the shortage of water has been taken centre stage in recent times. High expansion of population coupled with rapid industrial development in Indian subcontinent resulted in shortage of clean drinking water for people living in rural areas and remote villages especially in desert. Main components of concentrated solar power can be used in the form transparent cover, Absorber Plate, Heat transport system including fluid and Insulating Material. Besides these, tilt angle and direction with respect to Sun is also very important. Different materials available for all these components must be compared for their properties and configurations in various designs. Present study is review of various component material options improvement techniques. Current study deals with the concentrated solar power application with a case study in a metro station.

1. Introduction

Energy is an essential ingredient for human life. Energy can best be described as one of the major component for building a modern society. Energy is needed to produce goods from natural resources. Energy prevails in all sectors of society and is one of the most critical resources for human beings. Energy might best be described, in terms of what it can do. We cannot see energy, only its effects, we can not make it, only use it; and we can not destroy it, only waste it through inefficient use. Unlike food and housing, energy is not valued itself, but for what can be done with it. Energy is not end itself. Energy is a basic concept in all the science and engineering disciplines. Energy is not created or destroyed, but it is just converted or redistributed from one form to another. Understanding energy means, understanding energy resources and their limitations, as well as the environmental consequences of its use. The industrial revolution came with new energy resources: fossil fuels- like coal, then oil and natural gas. Although they are the remnants of the biomass of a remote past, these fuels are extracted from the earth's crust much more quickly than they naturally evolved. Consequently they are not renewable. Further more, these resources are undoubtedly limited, and will be exhausted in foreseeable future.So far, since the industrial revolution, energy consumption and population have been increasing by orders of magnitudes and very large inequalities between different countries are observed. Such a situation cannot last for long. It would force the countries to formulate intelligent energy policies to find ways towards the so-called sustainable development.

2. Litrature Review

As per John Dascomb Concentrating solar power is a method of increasing solar power density. He demonstrated the basic principle of CSP using a magnifying glass to set a piece of paper on fire. The first documented use of concentrated power comes from the great Greek scientist Archimedes (287-212 B.C.). Stories of Archimedes repelling the invading Roman fleet of Marcellus in 212 B.C. by burning their ships with concentrated solar rays were told by Galen (A.D. 130-220). Canan Kandilli dealt with the exergetic analysis and the performance assessment of the system based on the idea of transmission concentrated solar energy via optical fibres (TCSEvOF). **Wang et. al.** designed three-dimensional model of parabolic dish-receiver system with argon gas as the working fluid to simulate the thermal performance of a dish-type concentrated solar energy system. The temperature distributions of the receiver wall and the working gas are presented. As per Jonathan C. Tempies studies undertaken by Eskom in 2001 identified three sites near the Northern Cape Town of Upington which are suitable for a 100 MW Concentrating Solar Power (CSP) generating plant**. Atmaja et. al** conducted a review of how to optimize the concentrated solar power plant by increasing the stored energy capacity or by stabilizing the absorptance and emittance in the solar absorber [1-6].

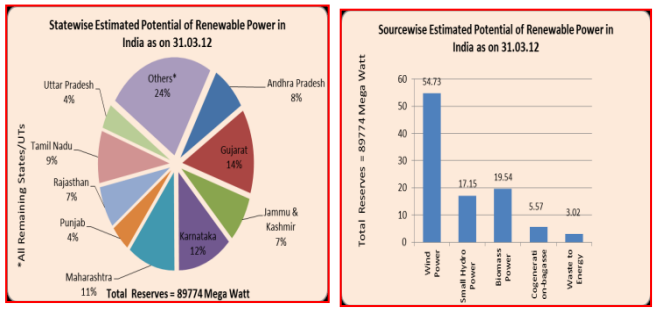

Fig.1 Energy Senario

3.0 Experimental Set-up

3.1 Concentrated Solar Power

Concentrated Solar Power (CSP) systems operate on the principle of concentrating the incident solar irradiation into small enclosures via parabolic reflectors. Comparing to the parabolic trough system with the concentration ratio of 100 Suns and the central tower system with the concentration ratio of 1000 Suns, the parabolic dish system can achieve concentration ratio of 10,000 Suns. Therefore, high collection efficiencies can be achieved in a parabolic dish system due to its high concentration ratio. In addition, the quality of the thermal energy in this system is high because the receiver has very small opening and could be assumed as a blackbody. Thus, the temperatures inside the receiver are considerably higher than other types of CSP systems. Receiver fluid temperature of over 2000 K has been suggested in previous studies [7].

3.2 Types of CSP

3.2.1Parabolic Trough Reflectors (PFR)

Parabolic trough systems consist of parallel rows of mirrors (reflectors) curved in one dimension to focus the sun's rays. The mirror arrays can be more than 100 m long with the curved surface 5 m to 6 m across.With approximately 985 MW of installed capacity globally (REN21, 2011), parabolic trough systems embody the most mature CSP electricity generation technology. They generally consist of large arrays of solar collector assemblies (tracking groups of parabolic collectors with metal support structure, receiver tubes and tracking systems), a HTF or direct steam generation (DSG) system, a Rankine steam cycle turbine and optional thermal storage and/or fossil fuelled accompaniment [8].

Corresponding Author,
E-mail address: hukambij@yahoo.com
All rights reserved: http://www.ijari.org

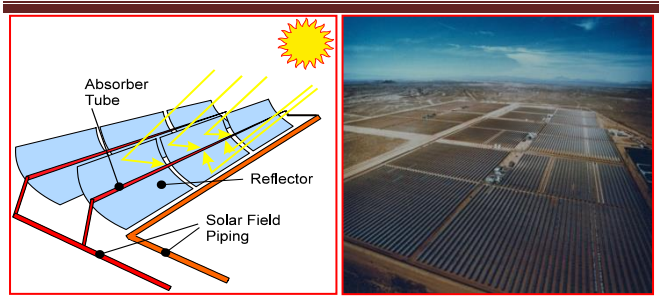

Fig.2 Solar Collector

3.2.2Solar Cooker

Solar energy used coocker is a device operating by the energy of sun for heat and cooking purpose at very low cost. Many solar cookers are relatively inexpensive although some of them are as expensive and advanced, large-scale solar cookers can cook for many people. Concerned to green revolution it is also very useful because it does not use any fuel and can be use for out-door cooking and the health and environmental consequences of alternatives are severe.[6-9]

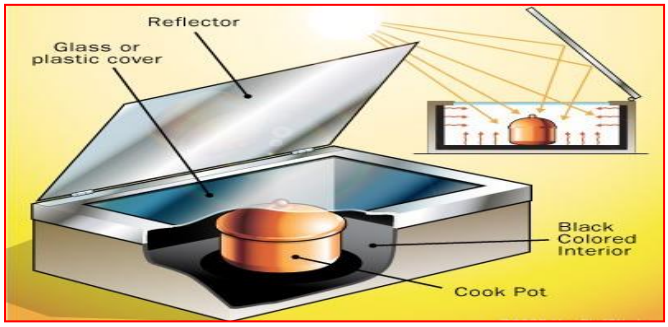

Fig. 3 Solar Cooker

Simple solar cookers use the following basic principles: It works at the Concentrating phenomenon of sunlight by reflective mirror of polished glass, metal or metalized film from sun to required area and absorption system of light converts the sun's visible light into heat, substantially improving the effectiveness of the cooker.

3.2.3 Solar pumping

Operation of solar powered pumps is economical due to lower operation and maintenance costs and has less environmental impact compare to other engines. Solar pumps are useful where grid electricity is unavailable and alternative sources (in particular wind) do not provide sufficient energy. Solar powered water pumps can deliver drinking water as well as water for livestock or irrigation purposes. Solar water pumps may be especially useful in small scale or community based irrigation, as large scale irrigation requires large volumes of water that in turn require a large solar PV array As the water may only be required during some parts of the year, a large PV array would provide excess energy that is not necessarily required, thus making the system inefficient.[6-10]

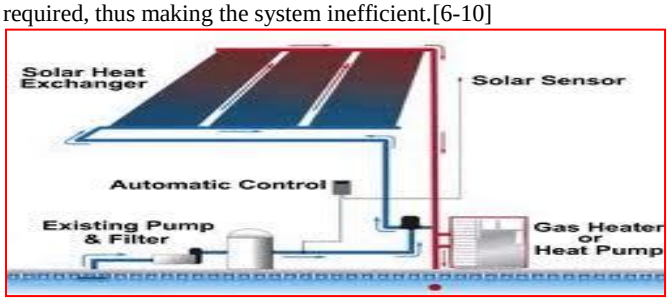

Fig. 4 Schematic Solar Pumping Diagram

4. Case Study

A comparative analysis of Solar Energy support mechanisms for Lighting System for a Delhi Metro Station. Electricity is used on a metro station in many forms like for running the computer system for controlling and ticketing, lighting the station, cleaning apparatus, signals etc. Lighting system does require un interrupted supply. Hence, for our study lighting system of Shivaji Stadium of Delhi Airport Metro corridor is taken. This station is underground station consist of three levels.

- Ground level
- Concourse level
- Platform level

At Ground level entrance form outside is made to the station. At Concourse level ticketing and security area is made. At platform level the metro train arrives.

Reference: Study is made on the basis of respective drawings of each level

- EPMC-DTD-SHJ-E –PLAN-101/4 (Ground level Plan Lighting and Power Layout)
- EPMC-DTD-SHJ-E –PLAN-101/2 (Concourse level Plan Lighting and Power Layout)
- EPMC-DTD-SHJ-E –PLAN-001/2 (Platform level Plan Lighting and Power Layout)

4.1Result and Discussion

One of most sustainable energy source is sunlight that too is totally inexhaustible and available free of cost, as far as we know for thousands of years. Often one can use as an excellent supplement to other renewable sources. The solar energy produced is very clean with no pollutants. The burning of oil releases carbon dioxide and other greenhouse gases and carcinogens into the air. Whereas solar crematorium needs no fuel and produces no waste and no pollution. There is no any problem of global warming with solar power which is common problem with any other conventional fuels. All of us are aware of the rising cost of fuels. Although solar reflectors or combustion chamber, etc. may be expensive to buy at the onset, you can save money in the long run. After all, you do not have to pay the money for the energy from the sun. Solar reflectors are totally silent. They can extract energy from the sun without making a peep. Now imagine the noise that the giant machines used to do. Solar powered lights and other solar powered products are also very easy to install. You do not even need to worry about wires. In sunny countries, solar power can be used where there is no easy way to get electricity to a remote place. Handy for low-power uses such as solar powered garden lights and battery chargers.

In 2011, According to IEA “the development of affordable, inexhaustible and clean solar energy technologies will have huge longer-term benefits. that will increase self-reliability of countries in energy matter, reduce pollution, mitigate climate change, and keep fossil fuel prices lower than otherwise. These advantages are global. Hence the additional costs of the incentives for early deployment should be considered; they must be wisely spent and need to be widely shared.As per Energy Statics of Govt. of India, the total energy requirement by the year of 2030 for our country would increase to 400000 MWs from the existing 210000 MWs. Ideally India has to plan for 215000 MWs of power to be realized from renewable energy resources like hydel, wind, solar, nuclear and conversion of municipal waste into energy by 2030. India can generate additional solar energy to the extent of 60000 MWs by having large scale solar power plants. Gujarat State has already generated 680 MWs of solar electric power through public-private partnership program and the power is being fed to the grid. Here we have to consider the reduction in load factor in solar, wind and hydel which will necessitate generation of 20 to 30.

5. Conclusions

Solar power can play a significant role in a secure and diversified energy future for India as the country becomes a hub for solar projects. More specifically, concentrated solar power (CSP) could have a unique role in India’s energy mix. Its potential to use hybrid technologies and easily add storage could unlock dispatch-able and base-load power, setting the stage for larger renewable energy penetration. In middle east and North Africa the solar energy offers

a unique opportunity for competitive, secure and sustainable energy for electricity and seawater desalination.CSP is present state of the art, the resources are almost unlimited, and the necessary investments are affordable. The resources exceed by far the present Middle East oil exports and are still untapped. While projects are already in operation or being built for electricity generation in the US and Spain, the basic engineering of a first plant for the combined generation of electricity and heat for power, cooling and seawater desalination started in Aqaba, Jordan in 2007. It will be the first economically competitive solar power station without any financial public support. CSP is of vital importance for the MENA region, as it is the only available resource that is large and affordable enough to cope with the challenge of growing electricity consumption and increasing shortage of potable water. It will, however, take at least a decade to introduce noticeable CSP shares into the energy portfolio. Some conclusions have been drawn by the above case study-

- Concentrated solar power technologies are very efficient in compare to conventional energy collectors**.**
- Case study is also showing the application of concentrated solar energy system is eco-friendly compare to conventional system.
- Concentrated solar power by using hybrid technologies and easily add storage could unlock dispatch-able and base-load power, setting the stage for larger renewable energy penetration Large amount of reduction in carbon dioxide is confirming by the application of solar system in metro station.

References

[1] Johan Dascomb, Low cost Concentrating solar collector for Steam generation, Floria State University 2009

[2] Canan Kandilli, Eregetic Assesment of transmission Model of Parabolic Dish Receiver, 2010.

[3] Mo Wang and Kamran Siddiqui, Design Three Diamensional model of Pabolic Dish Receiver, 2010.

[4] Jonathan C. Tempies, ATechnical Evaluation of Concentrating Solar Thermal Power Generation Technologies for the Upington area of South Africa, 2012.

[5] Tinton Dwi Atmaja, Ghalya Pikra. Absorber layer addition and thermal storage media, comparison for concentrated solar power plant optimization, Energy Procedia 32, 2013, 74 – 83

[6] Prabhakar Sharma, Sanjeev Kumar. A review of solar desalination methods for remote areas International Journal of Advance Research and Innovation, 4(3), 2016, 503-507

[7] Aravind Kumar Chaturvedi a review of solar flat plate liquid collector‟s components, International Journal Of Advance Research and Innovation, 3(1), 2015, 138-141

[8] AC Kashyap , JP Kesari, AK Rai, Hukam Singh. Study of Designing a Solar Concentrator for Crematorium using Solar Energy, International Journal of Advance Research and Innovation, 2(3), 2014, 564-567

[9] Kesari JP, Krishen, PB Sharma. Solar Power is a Panacea for Changing Rural India; The role of CSP under Indo-Japan Collaboration, Proceedings of 2nd International Symposium – collaborative research project of CSP for India and Japan , 25 April 12, Tokyo Institute of Technology, Tokyo, Japan, 2012.

[10] Kesari JP, Jaspreet Singh, Sushant Kumar Singh, Rohit Gupta, PB Sharma. Development of Solar Electric Hybrid Vehicle, paper accepted for publication in SAE International, 2012 for SIIMC

STUDY OF SHEAR BEHAVIOUR OF YAMUNA SAND BLENDED WITH SOFT SOIL

Deepak Rana[1], Ankit Soni[2], Farukh Ali[3]

[1]*M. Tech (Geotechnical Engineering), Department of Civil Engineering, Delhi Technological University, Delhi, India*
[2]*M. Tech (Geotechnical Engineering), Department of Civil Engineering, Delhi Technological University, Delhi, India*
[3]*Assistant Professor, Department of Civil Engineering, Sanskar College of Engineering & Technology, Ghaziabad, India*

Abstract

The structure resulting from compacting the soil at different water contents and energy levels can have a substantial effect on its shear strength. While the shear strength can be estimated based on the saturated shear strength parameters and the unsaturated angle of shearing resistance, limited studies have explored the variation of shear strength properties with different compaction states. In the present study, shear behavior of virgin Yamuna sand and Yamuna sand blended with two clays of different mineralogy i.e. bentonite and kaolinite was investigated by Direct Shear test and Unconsolidated Undrained Tri-axial test. Index properties and compaction characteristics of soil are also studied in this project. It was aimed to observe the shear behavior of sand-bentonite and sand-kaolinite mixtures. Various tests conducted on virgin soil were performed for the determination of following parameters: field moisture content, Atterberg Limits, Grain Size Analysis, Standard Proctor Compaction test, Direct Shear and Triaxial Unconsolidated Undrained test. Compaction tests were conducted on mixtures of 5%,10%,15%,20% by weight bentonite and kaolinite. Direct Shear test and UU Triaxial tests were performed on mixes with 5%,10%,15%,20% by weight of bentonite and kaolinite. It was found that there is increase in MDD and OMC of the soil mixes for both kaolinite and bentonite. Maximum MDD was achieved with kaolinite clay and maximum OMC with bentonite clay. Direct shear test resulted in the increase in cohesion and decrease in friction angle for both bentonite and kaolinite. Similar results are obtained in UU Triaxial tests. However, shear parameters obtained in Direct Shear test is slightly more than obtained in Triaxial tests.

Keywords: *Shear Behavior, Yamuna Sand, Bentonite, Kaolinite.*

----------***----------

1. INTRODUCTION

1.1 General

Yamuna sand is chiefly found alongside the river Yamuna in Delhi .It has low load carrying capacity and also get eroded easily. Delhi lies in the seismic zone 4 which is high damage risk or seismic active zone. Moreover, Yamuna sand in Delhi as well as NCR region contains remarkable quantity of silt and thus it is in peril to liquefaction during earth tremor below ground water table. At several places ground water is at shallow depth and structures built over sand under such conditions are not safe. Therefore, understanding the shear behavior of Yamuna sand and its improvement in shear strength is necessary. One of the best method to improve the strength of sand is to blend it with soft soil. Soft soil is mainly clay that is expansive in nature, highly compressible, low permeability; have high specific surface and large water holding capacity as well as cohesion when come in contact with water. There are two type of clays used in the present study namely: 1) bentonite clay and 2) kaolinite clay.

Bentonite clay is essentially absorbent aluminum phyllosilicate clay that contains primarily of montmorillonite mineral. It is highly plastic clay formed by the weathering of volcanic ash generally in presence of water. There are three types of bentonite based on the dominant element present in them:

1. Sodium bentonite
2. Potassium bentonite
3. Calcium bentonite

Sodium bentonite has property to enlarge several times of its dry mass in presence of water. It is used in several geotechnical explorations such as drilling mud for gas and oil wells,in boreholes ,as a low permeability liner in various landfills etc.

Potassium bentonite has potassium as its main element. It is formed from the alteration of volcanic ash and contains illite clay mineral.

Calcium bentonite is fundamentally used as adsorbent in ionic solution and also in oils. It is important element in the fuller's earth which is used as an rinsing agent. Calcium bentonite can be converted into sodium bentonite by ion exchange process.

Bentonite is also used in several geotechnical works such as drilling mud, as a binder, purification, ground water barrier and also bentonite slurry walls used in modern construction. Sand- bentonite mixtures have been used as a liner in the landfills due to its low permeability. In the present study Yamuna sand has been mixed with varying proportions of

bentonite and its effect on shear behaviour is studied. Bentonite used in the project was procured from a dealer in delhi.

Kaolinite is a clay mineral that has low swelling and shrinkage property. It also exhibits low cation exchange capacity. It has generally white color, soft and earthlike. It occurs in large quantity in soils that are formed by the chemical weathering of rocks in warm climates such as tropical rainforest. Rocks having kaolinite as main clay mineral are called as kaolin or china clay. In the present study an attempt has been made to study shear behavior of sand mixed with varying proportions of kaolinite clay. Kaolinite powder used in the present study was obtained from a dealer in Delhi.

1.2 Objectives of Present Study

- To determine the basic properties of Yamuna sand.
- To study the effect of different proportions of bentonite and kaolinite on the compaction characteristics of Yamuna sand.
- To study the effect of varying proportions of bentonite and kaolinite on shear strength parameters of Yamuna sand by direct shear test.
- To study the effect of different proportions of bentonite and kaolinite on shear strength parameters of Yamuna sand by UU tri-axial test.
- To compare the results obtained on mixing bentonite in varying proportions in Yamuna sand with results obtained on mixing kaolinite in different proportions in Yamuna sand.

2. MATERIALS USED AND METHODOLOGY

2.1 Materials Used in Present Study

2.1.1 Sand

In this project Yamuna sand is taken from the alongside of river Yamuna. It is firstly washed and the wetted soil is passed through 4.75 mm sieve and retained on 75 micron sieve, then soil is oven dried, is taken. This sand was subjected to various laboratory tests as per IS codes to determine particle size distribution, specific gravity, OMC & MDD etc.

Table 2.1: Geotechnical properties of Yamuna sand

Properties	Values
Sand content (4.75-0.075mm),%	92.4
Fine soil fraction (<75μ),%	7.6
Coefficient of uniformity, C_u	1.37
Coefficient of curvature, C_c	2.87
Effective size of particle,D_{10} (mm)	0.0845
Soil classification	SP-SM
Specific Gravity	2.65
Maximum dry density (MDD) kN/m^3	16.94
Optimum moisture content (OMC),%	11.2

2.1.2 Bentonite Clay

It is basically bentonite powder collected from a dealer in Delhi. It was subjected to various laboratory tests as per IS codes to determine particle size distribution, specific gravity, consistency limits etc.

Table 2.2: Geotechnical properties of Bentonite Clay

Properties	Values
Sand content (4.75-0.075mm),%	1.9
Fine soil fraction (< 75μ),%	98.1
Clay content (< 2μ),%	89.4
Liquid limit,%	550
Plastic limit,%	87.46
Soil classification	CH
Specific gravity	2.2

2.1.3 Kaolinite Clay

It was purchased in powdery form from a dealer in Delhi. It was subjected to various laboratory tests as per IS codes to determine particle size distribution, specific gravity, consistency limits etc.

Table 2.3: Geotechnical properties of Kaolinite Clay

Properties	Values
Sand content (4.75-0.075mm),%	3.8
Fine soil fraction (< 75μ),%	96.2
Clay content (< 2μ),%	65.6
Liquid limit,%	71.6
Plastic limit,%	41.67
Soil classification	OH
Specific gravity	2.62

2.2 Sample Mixes Used in the Study

Yamuna sand was mixed with the bentonite and kaolinite separately in different proportions and their effect on compaction behaviour and shear behaviour of the Yamuna sand was investigated. Sample mixes are as follows:

Table 2.4: Sample Mixes

Sample name	Proportioning of materials
SM0	Virgin Yamuna sand
SMB5	95% Yamuna sand + 5% Bentonite
SMB10	90% Yamuna sand + 10% Bentonite
SMB15	85% Yamuna sand + 15% Bentonite
SMB20	80% Yamuna sand + 20% Bentonite
SMK5	95% Yamuna sand + 5% Kaolinite
SMK10	90% Yamuna sand + 10% Kaolinite
SMK15	85% Yamuna sand + 15% Kaolinite
SMK20	80% Yamuna sand + 20% Kaolinite

2.3 Laboratory Experiments Conducted

The particle morphology of Yamuna sand, Bentonite clay and Kaoloinite clay was analyzed using scanning electron

microscope in Nano Science Laboratory of DTU Delhi. Particle size analysis of Yamuna sand, Bentonite clay and Kaoloinite clay was carried out as per IS: 2720 (Part IV)-1985. The specific gravity of Yamuna sand, Bentonite clay and Kaoloinite clay is determined as per IS: 2720 (Part III/Sec I)-1980. The liquid limit and plastic limit of Bentonite clay and Kaoloinite clay were determined as per the procedure lay down in IS: 2720 (Part V)-1985. MDD and OMC of Yamuna sand, Bentonite clay, Kaoloinite clay and sample mixes is determined as per IS: 2720 (Part VII) 1980. Direct shear test was conducted on sample mixes as per IS: 2720 (Part XIII)-1986 and UU Tri-axial test was conducted on various soil mixes as per procedure lay down in IS: 2720 (Part XI)-1993.

2.3.1 Direct Shear Test

This test was carried out on soil to determine the shear parameters of soil. A standard size (60mm x 60mm) Direct Shear box was used for the investigation. The tests were conducted on three different normal stress i.e. 50, 100 & 150 kPa and the angle of internal friction & cohesion values were obtained by plotting a straight line through the plot of shear stress versus the normal stress. Direct Shear tests were performed strictly according to IS: 2720 (Part XIII)-1986 on Yamuna sand and Yamuna sand mixed with different proportions of bentonite and kaolinite. All the tests were performed at MDD and OMC of the soil sample

2.3.2 Unconsolidated Undrained (UU) Tri-axial Test

A series of unconsolidated and undrained triaxial compression tests was performed on virgin Yamuna sand and Yamuna sand blended with varying proportions of bentonite and kaolinite separately(10%, 15 %and 20%). Tests were performed as per IS: 2720 (Part XI)-1993. All test specimens were 38 mm in diameter and 76 mm high. All tests were performed at MDD and OMC. The soil sample and amount of water is weighed and then mixed in the evaporating dish with the help of spatula. The mix is then poured in mould. The soil is compacted with a small tamper into three layers in a mould. After each compaction soil surface is scratched and next layer is filled and compacted. Sample was extracted from mould with the help of sample extractor machine. Sample was then placed in triaxial cell having porous stone with filter paper at bottom and glass stopper at top. Rubber membrane is then placed on the sample with the help of sampler. The cell in then filled with water and then required cell pressure is applied. Displacement is set to zero. Tests were performed at 1, 2, 3 kg/cm^2. Displacement (mm) and load (kg) readings were taken at regular intervals at 0.25mm, 0.50mm, 0.75, 1.0mm, 1.25mm and so on up to failure or 15.2 mm whichever is earlier. Then cell pressure was released and water from triaxial cell was drained. The sample was taken out carefully to observe the failure. In the present study 38 tests were performed of which 27 were successful. All the tests were performed at HEICO Engineering Services Pvt. Ltd., A13, Phase-2, Naraina Industrial Area, New Delhi.

3. RESULTS AND DISCUSSIONS

3.1 Scanning Electron Microscope (SEM) Test

3.1.1 SEM Test on Yamuna sand

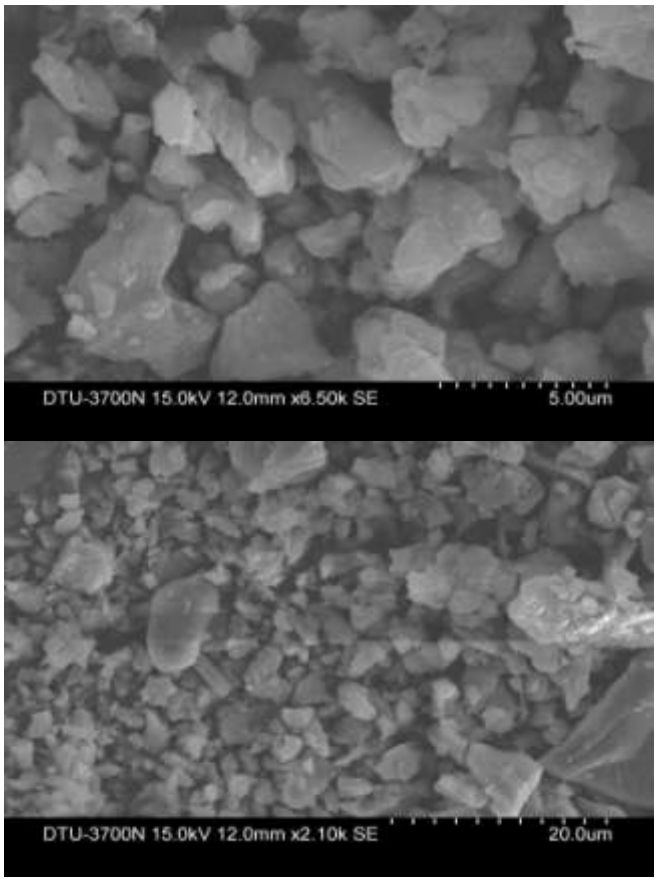

Fig. 3.1: Particle morphology of Yamuna sand

It has been observed from SEM images (Fig. 3.1) that Yamuna sand particles are angular, experienced non uniform weathering and has larger silica dissolution.

3.1.2 SEM Test on Bentonite Clay

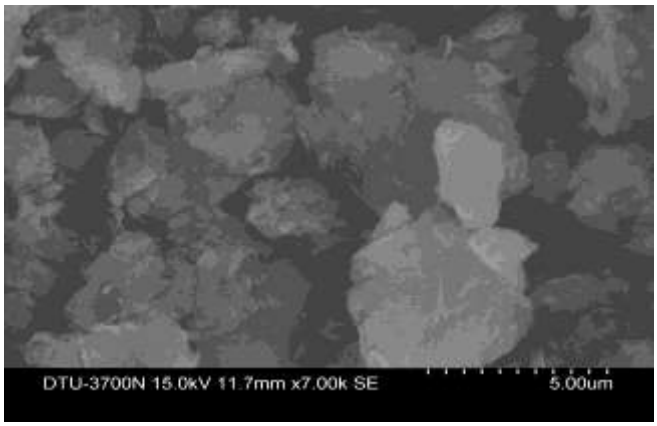

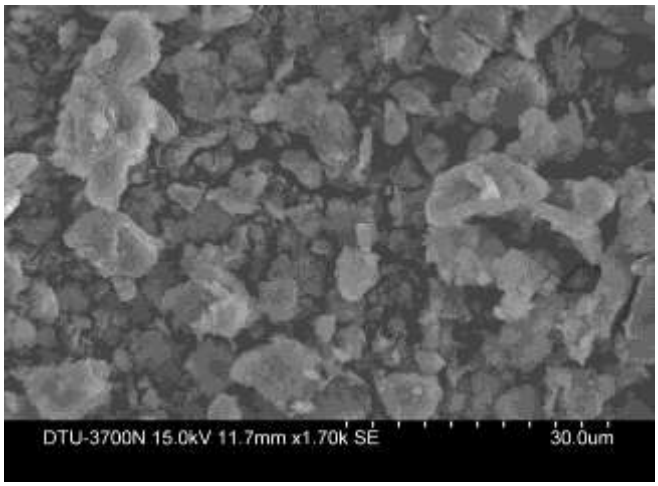

Fig. 3.2: Particle morphology of Bentonite clay

It can be seen in SEM images (Fig. 3.2) that particles present in bentonite sample are of irregular size and shape and having large voids. Moreover, it has agglomerated due to the presence of water in the atmospheric condition. This establishes the hygroscopic nature of bentonite.

3.1.3 SEM Test on Kaolinite Clay

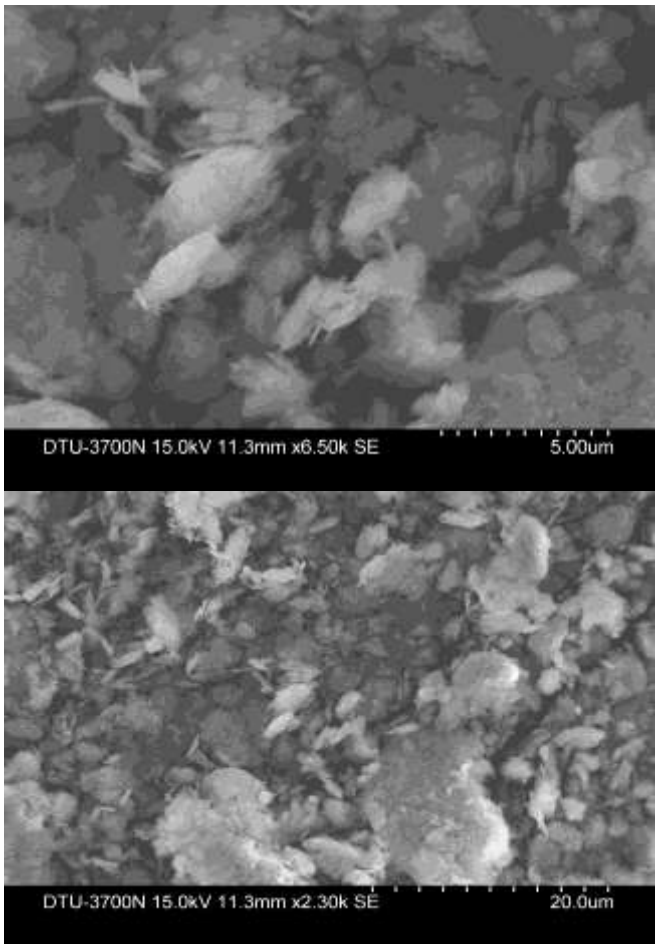

Fig. 3.3: Particle morphology of Kaolinite clay

It can be observed that particles present in bentonite sample are of irregular size and shape and having large voids.

3.2 X-ray Diffraction (XRD) Test

Various sample mixes was subjected to XRD test in Nano Science Laboratory of DTU Delhi and the results obtained are as follows:

3.2.1 XRD Test on Yamuna sand

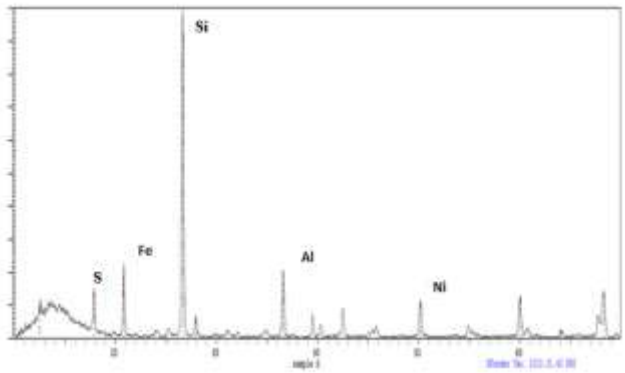

Fig. 3.4: XRD spectrum of Yamuna sand

It has been observed from XRD spectrum (Fig. 3.4) that Yamuna sand contains Sulphur, Nickel, Quartzite, Aluminum, and Silicon.

3.2.2 XRD Test on Bentonite clay

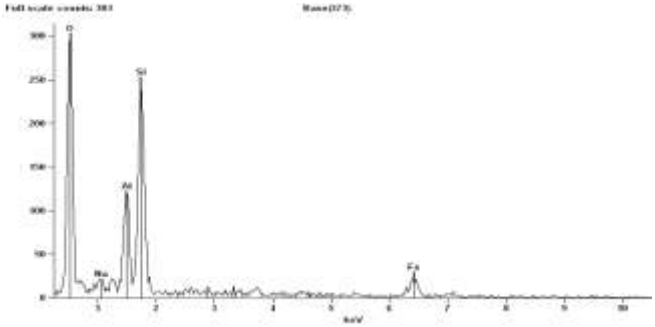

Fig. 3.5: XRD spectrum of bentonite clay

It has been observed from XRD spectrum (Fig. 3.5) that bentonite clay contains Sodium, Aluminum, Iron, Oxygen and Silicon. The spectrum achieved from the XRD shows that there are traces of sodium ions in bentonite samples which goes to show that the bentonite used in work is a type of sodium bentonite.

3.2.3 XRD Test on Kaolinite clay

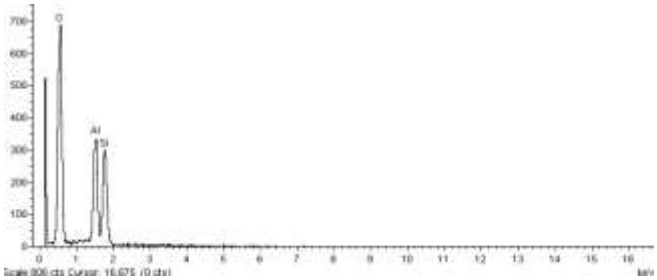

Fig. 3.6: XRD spectrum of kaolinite clay

It has been observed from XRD spectrum (Fig. 3.6) that kaolinite clay contains Oxygen, Calcium, Aluminum, Iron, and Silicon.

3.3 Light Compaction Test

Compaction behavior of different sample mixes is shown in following figures:

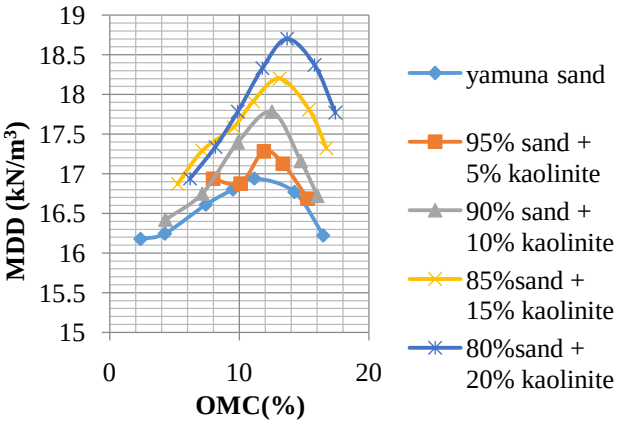

Fig. 3.7: Compaction behavior of Yamuna sand mixed with varying proportion of kaolinite clay

Table 3.1: Variation of OMC and MDD for various Yamuna sand-kaolinite mixes

Sample	OMC (%)	MDD (kN/m^3)
Yamuna sand	11.20	16.94
SMK5	11.87	17.28
SMK10	12.51	17.78
SMK15	13.11	18.20
SMK20	13.67	18.70

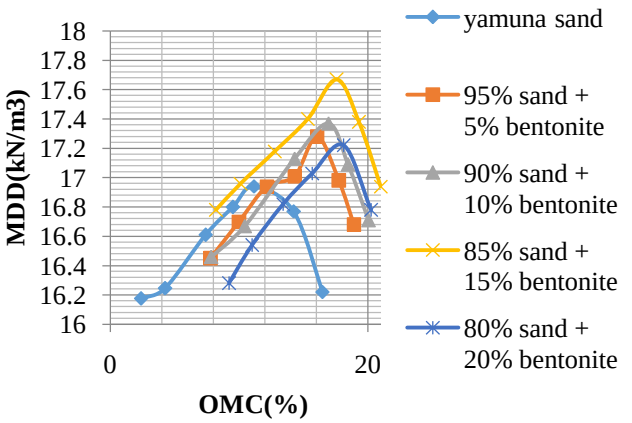

Fig. 3.8: Compaction behavior of Yamuna sand mixed with varying proportion of bentonite clay

Table 3.2: Variation of OMC and MDD for various Yamuna sand-bentonite mixes

Sample	OMC (%)	MDD (kN/m^3)
Yamuna sand	11.20	16.94
SMB5	16.05	17.24
SMB10	16.95	17.38
SMB15	17.56	17.67
SMB20	18.10	17.22

3.4 Direct Shear Test

Shear behavior of different sample mixes is shown in the following figures:

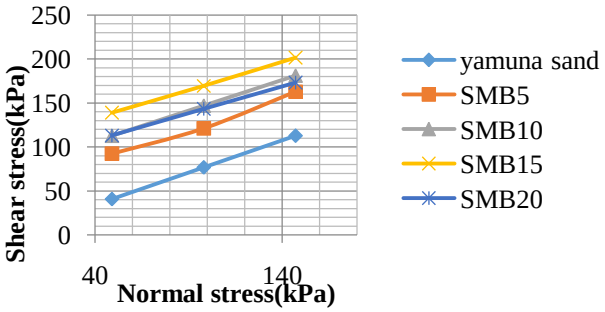

Fig. 3.9: Shear behavior of various Yamuna sand-bentonite mixes

Table 3.3: Variation of shear strength parameter (c-ϕ) for various Yamuna sand-bentonite mixes

Sample	Cohesion, c (kPa)	ϕ (Degree)
Yamuna sand	4.91	36.31
SMB5	54.63	35.62
SMB10	78.43	34.91
SMB15	107.53	32.49
SMB20	83.53	31.38

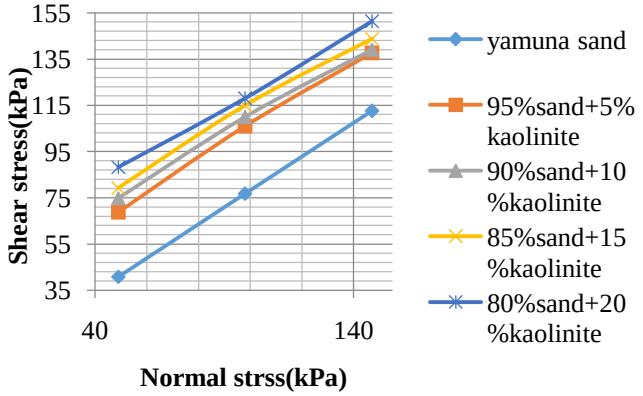

Fig. 3.10: Shear behavior of various Yamuna sand-kaolinite mixes

Table 3.4: Variation of shear strength parameter (c-ϕ) for various Yamuna sand-kaolinite mixes

Sample	Cohesion, c (kPa)	ϕ (Degree)
Yamuna sand	4.91	36.31
SMK5	35.28	35.06
SMK10	43.85	34.71
SMK15	47.07	32.91
SMK20	56.22	32.62

3.5 Unconsolidated Undrained Tri-axial Test

Deviator stress vs. axial strain behavior is shown in the following figures:

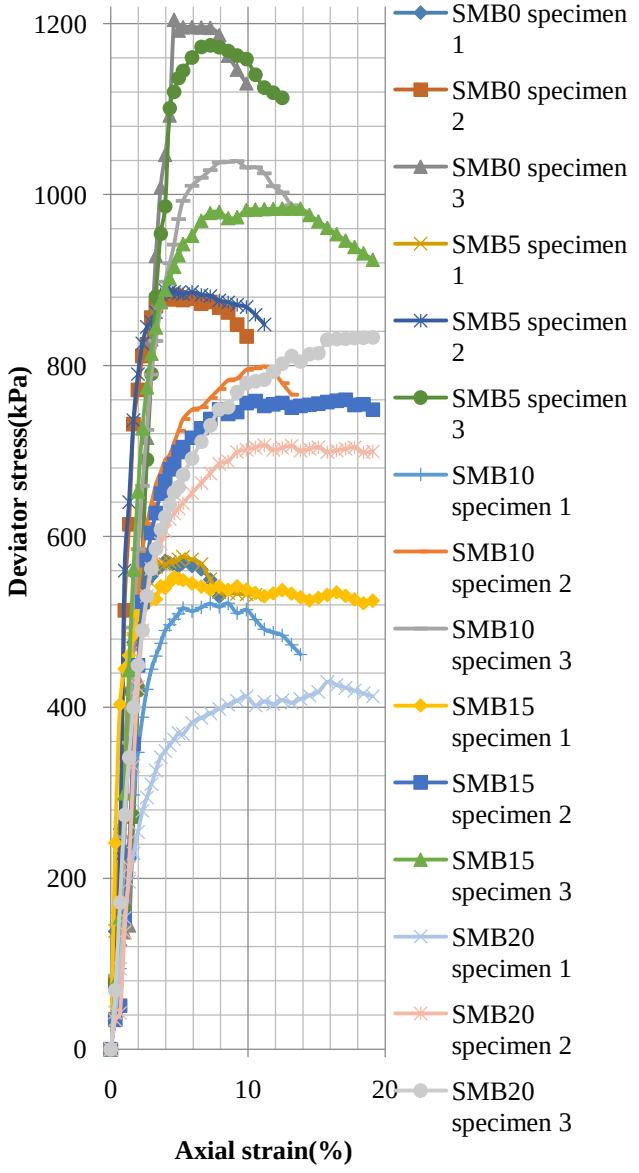

Fig. 3.11: Deviator stress vs. axial strain curve variation for various Yamuna sand-Bentonite mixes

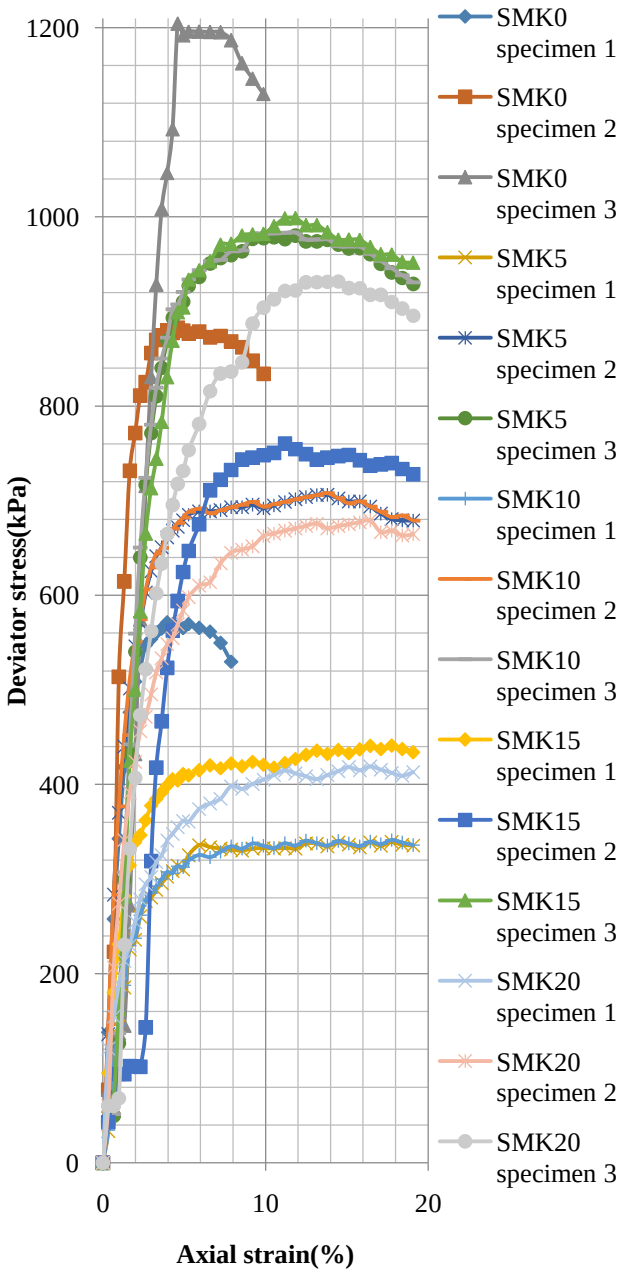

Fig. 3.12: Deviator stress vs. axial strain curve variation for various Yamuna sand-Kaolinite mixes

Table 3.5: Variation of shear strength parameter (c-ϕ) for various Yamuna sand-bentonite mixes

Sample	Cohesion, c (kPa)	ϕ (Degree)
Yamuna sand	3.92	35.90
SMB5	50.01	34.70
SMB10	74.53	34.10
SMB15	93.15	31.60
SMB20	69.62	30.80

Table 3.6: Variation of shear strength parameter (c-ϕ) for various Yamuna sand-kaolinite mixes

Sample	Cohesion, c (kPa)	ϕ (Degree)
Yamuna sand	3.92	35.90
SMK5	23.53	35.40
SMK10	36.28	33.90
SMK15	40.20	32.90
SMK20	50.99	32.10

4. CONCLUSION

This research was carried out to study the effect of bentonite and kaolinite on compaction behavior and shear behavior of Yamuna sand yielded following conclusions:

Light Compaction Test

1. With the increase in bentonite content there is increase in OMC of the soil mix having maximum value at 20%. This may be attributed to the high specific surface and large water holding capacity of bentonite.
2. As the bentonite content increases there is increase in MDD upto 15% and then MDD decreases at 20%. The reason for this might be that bentonite particles fill the voids of the sand thereby increasing maximum dry density upto 15% and afterwards decrease in MDD is due to the fact that clay particles start taking up the space which would have been taken by the sand.
3. With the increase in kaolinite content there is increase in OMC of the soil mix which is due to the high specific surface of kaolinite.
4. As the kaolinite content increases there is increase in MDD of the soil mix. The maximum value of MDD is at 20% mix. This due to the fact that kaolinite particles fill the voids of the sand thereby increasing MDD.

Direct Shear Test

1. There is increase in cohesion with the increase in bentonite and kaolinite content.
2. Angle of internal friction decreases as the bentonite and kaolinite content increased with max decrement at 20% for both type of clays.
3. Increase in cohesion is more pronounced in case of bentonite as compared to kaolinite.
4. Angle of internal friction decreased more in case of bentonite as compared to kaolinite.

UU Tri-axial Test

1. There is increase in cohesion for both bentonite and kaolinite content increment.
2. Angle of internal friction decreased as the bentonite and kaolinite content increased.
3. For bentonite maximum value of cohesion is 93.15 kPa whereas in case of kaolinite, it is 50.99 kPa.
4. Moreover, it has been observed that C-ϕ values obtained from direct shear test are slightly more than the values observed from UU tri-axial test.

REFERENCES

[1]. Dafalla M. A., (2013), "Effects of Clay and Moisture Content on Direct Shear Tests for Clay-Sand Mixtures", *Advances in Materials Science and Engineering*.

[2]. Georgiannou, Burland, and D. W. Hight (1990), "The Undrained Behaviour of Clayey Sands in Triaxial Compression and Extension", *Geotechnique* 40, No.30, 431-449.

[3]. Georgiannou V. N. (1988), "Behavior of Clayey Sands under Monotonic and Cyclic Loading" Ph.D. thesis, Department of Civil Engineering, Imperial College of Science, Technology and Medicine, London, England.

[4]. Ojha S. and Trivedi A., (2013), "Shear Strength Parameters for Silty Sand Using Relative Compaction", *EJGE*, Vol.18.

[5]. Panwar P. and Ameta N. K., (2013), "Stabilization of Dune Sand with Bentonite and Lime",*EJGE* ,Vol.18.

[6]. Pakbaz M. S. and Moqaddam A. S., (2013), "Effect of Sand Gradation on The Behavior of Sand-Clay Mixtures" *International Journal of Geomate*, Vol. 3, No. 1 (Sl. No. 5), pp. 325-331.

[7]. Purvana Y. M., Nikraj H. and Jitsangiam P., (2012), "Experimental Study of Suction-Monitored CBR Test on Sand-Kaolin Mixture", *International Journal of Geomate*, Vol.3, No.2 (SI.No.6), pp. 419-422.

[8]. Rao, C. H. and Ramana, G. V., (2010), "Characterization of Cyclic Strength of Yamuna Sand", *International Journal of Earth Sciences and Engineering* ISSN 0974-5904, Vol. 03, No. 02, pp. 234-242.

[9]. Sourav De, and Basudhar, P.K., (2008) ," Steady State Behaviour of Yamuna Sand" *Geotech Geol Eng.*

[10]. Simpson D. C. and Evans T. M., (2015), " Behavioral Thresholds in Mixtures of Sand and Kaolinite Clay", *J. Geotech. Geoenviron. Eng.,* ASCE, 2016, 142(2): 04015073.

[11]. Tiwari, A., Suman, S., and Sharma, S., (2016), "Study of Compacted Sand-Bentonite Mixture as Material of Low Hydraulic Conductivity Liner of Landfill for Solid Waste Disposal", *Imperial Journal of Interdisciplinary Research*, Vol-2, Issue-4.

[12]. IS 2720 (Part IV): 1985, "Method of test of soils-Grain size analysis", Bureau of Indian Standards.

[13]. IS 2720 (Part III/Sec II): 1980, "Method of test of soils- Determination of specific gravity", Bureau of Indian Standards.

[14]. IS 2720 (Part V): 1985, "Method of test of soils-Determination of liquid limit and plastic Limit", Bureau of Indian Standards.

[15]. IS 2720 (Part VII): 1980, "Determination of Water Content -Dry Density Relation Using Light Compaction", Bureau of Indian Standards.

[16]. IS 2720 (Part XIII): 1986, "Method of test of soils-Direct shear test", Bureau of Indian Standards.

[17]. IS 2720 (Part 11): 1993, "Determination of the Shear Strength Parameters of a Specimen Tested in Unconsolidated Undrained Triaxial Compression Without the Measurement of Pore Water Pressure", Bureau of Indian Standards.

Available online at www.sciencedirect.com

ScienceDirect

Materials Today: Proceedings 4 (2017) 3685–3693

materialstoday: PROCEEDINGS

www.materialstoday.com/proceedings

5th International Conference of Materials Processing and Characterization (ICMPC 2016)

Two start and Three Start Helical Abrasive Flow Machining for Brittle Materials

Ravi Butola[a], Qasim Murtaza[b]*, R.S.Walia[c], Pradeep kumar[d]

[a,c,d]*Department of Mechanical, Production & Industrial and Automobile Engineering, Delhi Technological University, Delhi 11042, INDIA*

[b]*Department of Mechanical Engineering, Aligarh Muslim University, Aligarh, 202002, INDIA*

Abstract

In the experimental investigation on drill bit assisted AFM setup, a developed spline, two start helical profile and three start helical profile have been studied. It has been found that the use of new developed profile led to an improvement in the response parameter of percentage improvement in surface finish and material removal.Drill bit assisted abrasive flow machining is a non-conventional finishing operation. Before the advent of drill bit assisted abrasive flow machining simple abrasive flow machining was used. In simple abrasive flow machining media is simply move up and down through the work piece. In drill bit assisted abrasive flow machining a drill bit is used which passes through the work piece which helps to define the path of media responsible for finishing operation. In the present work three types of drill bits are used spline, two star helical and three star helical.For the design of experiment, the taguchi method approach has been employed. L_9 OA has been used for the plan of experiments.The three process parameters viz drill bit type, number of cycle, extrusion pressure all have significant effect for the response parameter of MR .The result shows that type of rod have 33.4%, extrusion pressure have 23.46% and number of cycle have 19.53 % contribution for response parameter of MR. At selected parameters a maximum improvement of 69.06% has been observed in the Surface finish. With the initial roughness 6.2 microns, an improvement to 1.91 has been observed on the inner cylindrical surface of the cast iron work piece.

©2017 Elsevier Ltd. All rights reserved.

Selection and peer-review under responsibility of Conference Committee Members of 5th International Conference of Materials Processing and Characterization (ICMPC 2016).

Keywords:Abrasive Flow Machining (AFM); Taguchi method;

* Corresponding author. Tel.+91-011-27871043
E-mail address: qasimmurtaza@dce.ac.in

214-7853©2017 Elsevier Ltd. All rights reserved.

Selection and peer-review under responsibility of Conference Committee Members of 5th International Conference of Materials Processing and Characterization (ICMPC 2016).

1. Introduction

The tooling of Helical-AFM setup consists of fixtures in three parts lower, middle, upper fixtures and in addition to it, it has helical-fluted drill bit. Helical fluted drill bit can be of various types like two start or three start. Drill bit passes through the work piece and is then held stationary. In Helical-AFM, three types of flows occur in finishing zone and remixing of medium at exit from the finishing zone (flow along the flute, axial flow, and scooping flow)[1, 2].Media viscosity, extrusion pressure, and passage dimension determine the media flow rate (the speed of the abrasive slug passing through the restrictive passage) which affects the uniformity of the material removal and the formation of edge radius. Rhoades [3] has reported that media flow rate is less influential parameter in respect to material removal. Slower slug flow rates are best for uniform material removal and high slug flow rates produce large edge radii [Rhoades [4].
It has been noted by Williams et.al. [5] that if volume of flow is constant then the media flow rate is insignificant with regard to material removal. On the other hand, it has been claimed by Singh [6] and Jain and Jain [7] that the media flow rate influences both the material removal and surface roughness process.Williams and Rajurkar [8] and Williams et. al. [5] have reported that the viscosity of the media is one of the significant parameters of the AFM process. Keeping all other parameter constant, an increase in viscosity improves both material removal and surface roughness. Przyklenk [9] has observed that the material removal capacity of the least viscous media differs from the most viscous one. This difference could be as much as 300 times.A number of cycles are required to achieve the desired surface finish and material removal It has been reported in a number of studies that abrasion is more pronounced in some initial cycles after which improvement in the surface finish stabilize or reduce in some cases [10, 11, 5] and [9]. Total number of process cycles range from one to several hundred [12]. Within 1 to 8 cycles, a linear dependence between material removal and surface roughness versus number of cycles was indicated. In AFM the forward and backward extrusion to the initial stage completes a cycle.From the experimental results reported by Weller [13], it can be interpreted that an increase in temperature during processing results in faster cutting of the material than the cutting at constant temperature.It has been found that cutting is faster at an increased extrusion pressure, with all other parameters remaining constant. A part of total pressure is lost within the media due to its internal resistance to flow and rest is imparted to abrasion particles contacting the work piece surface [5,9] and [4]. Jain and Jain [10] reported that at higher pressure the improvement in material removal just tends to stabilize probably due to localized rolling of abrasion particles. Jain and Adsul [14] in their study mentioned that material removal is governed by initial surface roughness and work piece hardness. Softer material has higher material removal and more improvement in surface finish as compared to harder material. Material and geometrical dimensions of work piece are reported to greatly influence the abrasion process [11, 5, 7].Walia and Shan [16] have shown by their experiments that if a centrifugal force is provided in machining zone then the parameters can be affected positively. They showed that if centrifugal action is provided by rotating the workpiece then both material removal and surface finish increases.

2. Experimental procedure

The experiments were designed to study the effect of some of the Drill bit assisted AFM parameters on Response characteristics of Drill bit assisted AFM process. The design was accorded to an L9 orthogonal array based on Taguchi method to study the effect of helix rod and other main AFM process parameters. The main parameters Shape of helix rod (H), Number of cycle (N), Extrusion pressure (p) have been selected at three levels considering no-interaction among them. The non-linear behavior existing among the process parameters can be studied if more than two levels of the process parameters are used. The quality characteristics under the consideration are material removal and percentage improvement in surface roughness (ΔRa). The selected number of process parameter and their levels are given in table no 1. In this experiment the work piece was cylindrical so a proper design of fixture (fig.1a) was used which could hold a cylindrical work piece.A two start helical profilea drill bit of length 95mm, diameter 6.5 mm and Flute

length 65 mm is welded.The diameter of the disc attached to the drill bit is 48mm and width 15mm this disc is movable and can move up and down.A three start helical profile was chosen which is made up of steel rod. The length of rod, diameter flute length and lead were 95 mm, 5.8mm, 65mm and 40 mm respectively. Then helical profile was welded to the steel disc. The three star start profile was developed so that whole of the surface had helical grooves so that media was uniformly distributed around the helical rod thus the abrasive laden media makes more surface contact with the inner surface of the work piece.
In the present investigation, a brittle material cast iron was selected as workpiece materials. The cavity to be machined in the test specimen was prepared by drilling operation followed by boring to the required size. The size of cylindrical work piece was of length 15 mm, internal and external diameters were 8 and 12.6 mm as shown in figure 3. This internal cylindrical surface was finished by Drill bit assisted-AFM process. The work-piece was taken out from the setup and cleaned with acetone before the subsequent measurement.

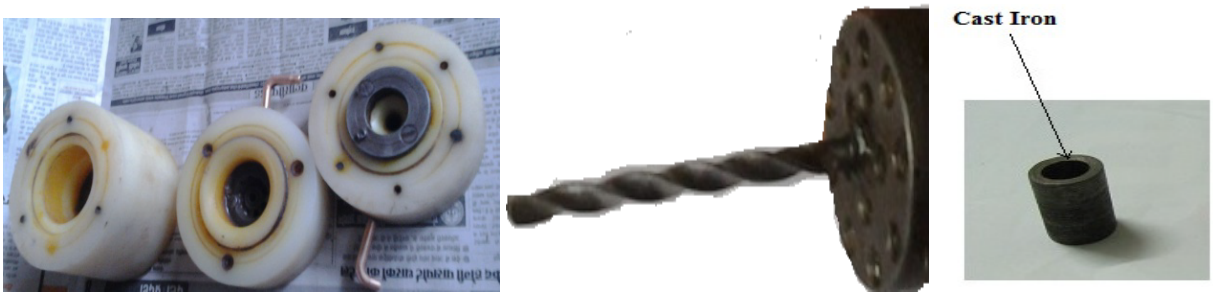

Fig.1.(a)Fixture in three parts, (b) Three start drill bit, (c)Work-piece.

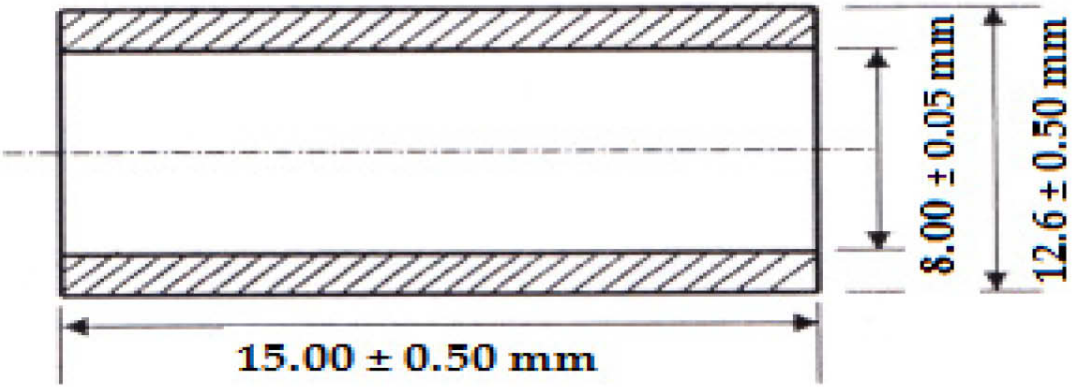

Fig.2. Work piece dimension

Table 1.Process parameters and their values at different levels

SYMBOL	PROCESS PARAMETERS	UNITE	LEVEL1	LEVEL2	LEVEL3
H	TYPE OF DRILL BIT		SPLINE	TWO START	THREE START
P	PRESSURE	N/mm^3	3	5	7
N	NUMBER OF CYCLE	N	2	4	6

Polymer to gel ratio:1:1,Workpiece material:Castiron,Abrasive type:Al_2O_3,Grit size: 200, Media Flow Volume: 290 cm^3, Reduction Ration: 0.95, Temperature: 32 $^{+}$. 2°C, Extrusion Pressure (P): 7N/mm^2, Flow Rate (F): medium and constant Approximate Pressure difference: 15N/mm), MediaViscosity: 810 Pas

3. Results and discussion

Each experiment is repeated three times to avoid experimental error.Each set of experiments were performed at room temperature in a narrow range (32 ± 2°C).The four process parameters viz. type of Drill Bit Status, Extrusion Pressure and Number of Cycles are selected as given in Table 1. Experiments were conducted according to the test conditions specified by the L9OA (Table 2). Each experiment was repeated three times in each of the trial conditions. Thus, 27 work-pieces were selected having initial surface in close range of (6.2-7.4) micron. In each of the trial conditions for every replication, the percentage improvement in surface roughness and material removal were measured.

Table 2. Orthogonal array L9 with experimental results of various Response characteristics Process parameters at different level.

Exp No.	Run Order	%Improvement in Ra			S/N Ratio(d)	Material Removal(mg) MR			S/N Ratio(db)
		R1	R2	R3		R1	R2	R3	
1	2	8.25	5.5	6.09	16.40	1.3	1.3	1.1	1.82
2	1	14.35	23.2	37.79	27.99	2.5	2.6	1.9	7.35
3	3	2.86	9.7	2.1	13.78	3.7	3.6	2.9	10.62

4	4	11.5	32.24	14.2	25.71	2.6	2.8	1.9	7.72
5	7	20.85	3.63	13.1	21.95	3.9	3.2	3.9	11.28
6	5	7.83	5.2	9.2	17.39	3.8	2.7	2.1	9.14
7	8	7.04	8.3	9.2	18.25	3.8	3.9	3.2	11.20
8	6	11.42	20.84	20.9	24.96	3.8	4	2.1	10.37
9	9	23.16	23.65	23.52	27.40	3.9	4.1	4	12.04
Total		107.26	132.26	136.1		29.3	28.2	23.1	
		$T_{\Delta Ra}$ = Overall mean of ΔRa =13.91				T_{MR} = Overall mean of MR =2.98mg			

3.1. Effect on material removal

The average value of material removal (MR) and S/N ratio for each parameter at levels L_1, L_2, L_3 are calculated and given in table 3.

Table 3. Average Values and Main Effect: Material Removal, MR (in mg)

Process parameter	Level	Shape of Drill Bit(H)		Extrusion pressure		Number Of Cycle(N)	
Type of data		Raw Data(mg)	S/N Ratio	Raw Data(mg)	S/N Ratio	Raw Data(mg)	S/N Ratio
Average value	L1	2.32	6.43	2.43	6.73	2.46	6.45
	L2	2.98	8.97	3.1	9.16	2.92	8.82
	L3	3.64	10.78	3.42	10.30	3.56	10.91
Main Effect	L2-L1	0.66	2.53	0.66	2.43	0.45	2.37
	L3-L2	0.65	1.81	0.32	1.13	0.64	2.087
DIFFERENCE $((L_3-L_2)-(L_2-L_1))$		0.01	-0.72	-0.34	-1.29	0.18	-0.28

L_1, $L_2$and L_3 represent levels 1, 2 and 3 respectively of parameters. L_2-L_1 is the average main effect when the corresponding parameter changes from level1 to level 2. L_3-L_2 is the main effect when the corresponding parameter changes from level 2 to level 3.

3.2 Type of Materials

Fig 1. shows that max material removal is at third level(H3)cast iron as workpiece materials. It means that max material removal takes place when three start Helix drill bit is used. Lowest material rate is at first level(H1) i.e. in case of spline. Material removal is more in case of three start helical drill bit because in case of helical Drill bitt the abrasive particles flow in three type of motion. The abrasiv particles near the surface moves in axial direction where the particles moving near the drill bit follow a helical path and particles in between scoop up towards the work surface.

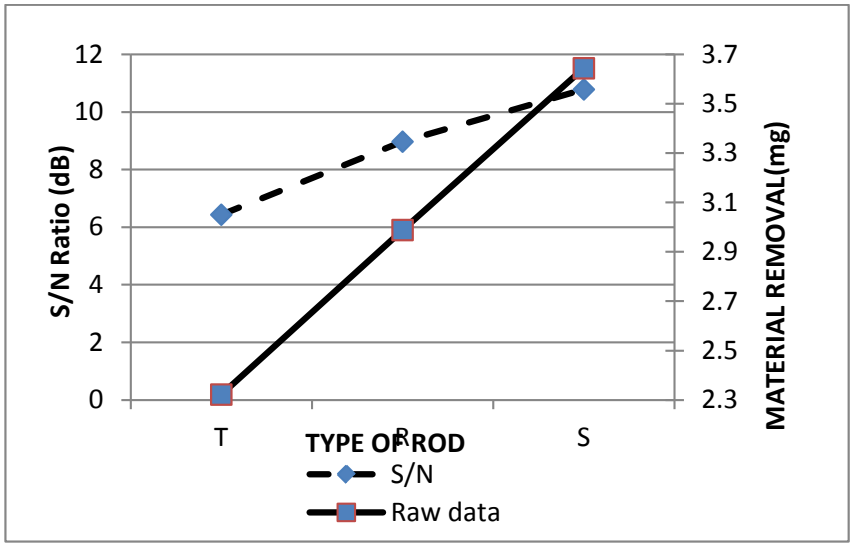

Figure 3. Effect of shape of dill bit on(MR and S/N Ratio)

3.3 Extrusion pressure

Figure 2shows that with the increase of extrusion pressure material removal increases which is maximum at third level i.e. at 7MP and minimum at first level i.e. at 3MP. This is due to the fact that with the increase of pressure the cutting forces involved in cutting action increases .Due to the increase in cutting force material removal increases. The rate of material removal is more with initial increase of pressure from 3MP to 5MP but less in later increase of pressure from 5MP to 7MP. This behaviour may be due to the fact that with increase of pressure from 5MP to 7MP cutting force increases but there is lesser rolling of abrasive particles in the media due to which fresh cutting edges do not come in contact with work piece, figure 4.

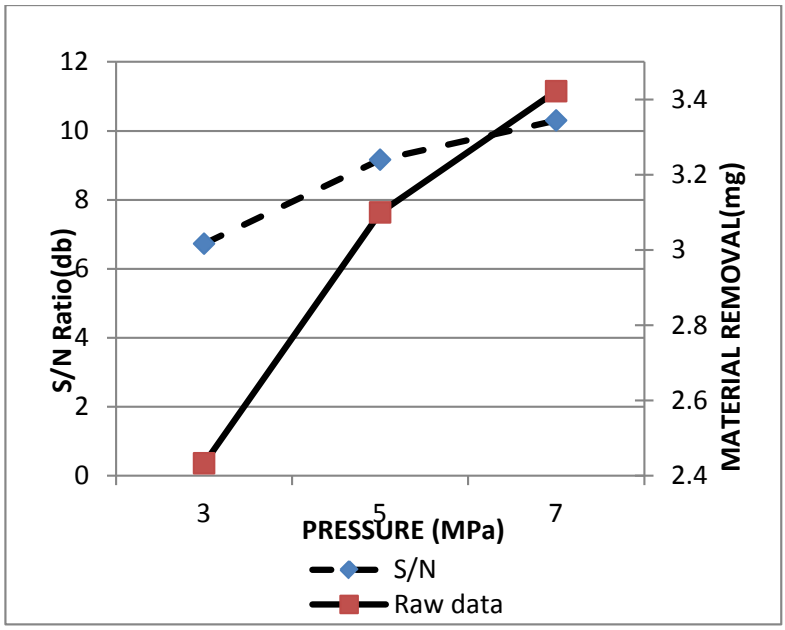

Figure 4. Effect of Extrusion Pressure on (MR and S/N Ratio)

3.4 Number of cycles

It is clearly shown in fig 5 that as the number of cycle increases from 2 to 6, the material removal increases .More number of cycle means more abrasion action hence more material removal .Initially the material removal rate is low but as the number of cycle increases, material removal rate increases. The reason is as the number of cycle increases some of the abrasive particles become dull so in addition to cutting action rubbing action also takes place which result in more material removal rate.

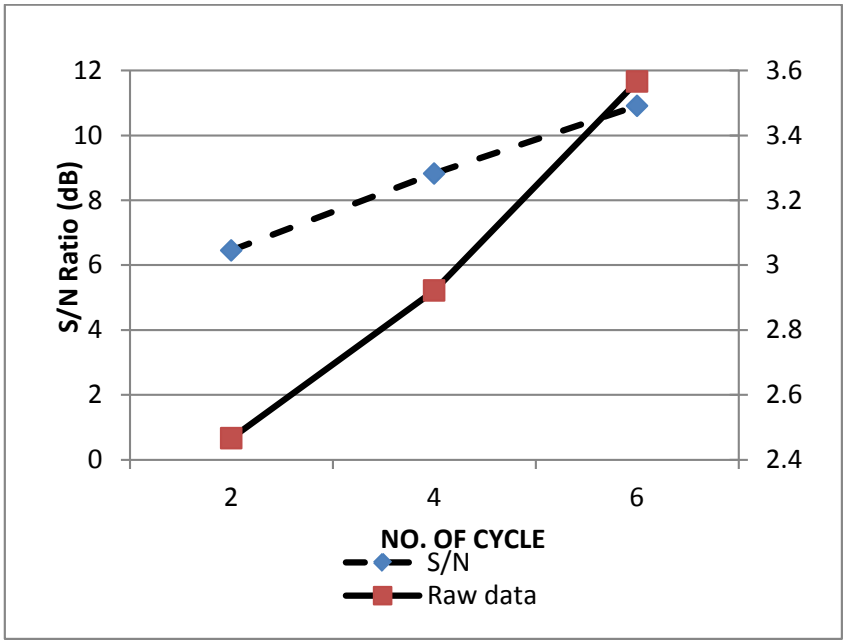

Figure 5. Effect of No of Cycle on S/N Ratio(db) and MR

4. Selection of optimal levels

The Analysis of Variance (ANOVA) was performed to study the significance of process parameter towards the percentage improvement in R_a. The pooled version of ANOVA of raw data and the S/N data for ΔR_a are given in Table 6.5. From the table it is clear that type of rod is significant for variation but insignificant for mean, extrusion pressure significant for mean but insignificant for variation, whereas number of cycle is significant for both mean and variation. The percentage contribution of number of cycle is maximum i.e. 47.22% followed by extrusion pressure which contribute 12.67% and the contribution of helical profile is 4.08% .The percentage improvement in $R_a$is "higher the better" type of quality characteristics. Therefore higher value of ΔR_a are considered to be optimal.

Table 4. Pooled ANOVA (S/N Ratio Data, %age imp in ΔR_a)

SOURCE	SS	DOF	V	F-RATIO	P%
TYPE OF DRILL BIT	59.310	2	29.65	19.78*	20.86
EXTRUSION PRESSURE	25.647	2	12.82	8.555	9.021
NUMBER OF CYCLE	196.34	2	98.17	65.49*	69.06
ERROR	2.99	2	1.499		1.054
TOTAL	284.30	8			100
*Significant at 95% confidence level, $F_{critical}$= 3.85 , SS-Sum of squares, DOF-Degree of freedom, V-variance					

The mean at the optimal MR (optimum values of the response characteristics) is estimated as

$$MR = N_3 + P_3 + H_3 - 2T$$

T = overall mean of the response = 2.98 mg, Average value of MR at the third level of type of rod = 3.64 mg. Average value of MR at the third level of extrusion pressure = 3.42 mg, Average value of MR at the third level of no. of cycle = 3.56 mg, Substituting these values, MR = 4.66 mg The confidence interval of confirmation experiments (CL_{CE}) and of population (CL_{POP}) is calculated by using the following equation.

$$CI_{CE} = \sqrt{F_a(1, f_e)V_e\left[\frac{1}{n_{eff}} + \frac{1}{R}\right]}$$

$$CI_{POP} = \sqrt{\frac{F_a(1, f_e)V_e}{n_{eff}}}$$

where $F_\alpha(1, f_e)$ = The F- ratio at the confidence level of (1-α) against DOF 1 and error degree of freedom f_e= 4.41 (Tabulated F value), f_e = error DOF = 18 (Table 6.2), N = Total no of result =27 (treatment =9, repetition =3), R = Sample size for confirmation experiments = 3, V_e = Error variance =1.189.

$$n_{eff} = \frac{N}{1+[DOFassociatedintheestimateofmeanresponce]} = 3.85$$

So, $CL_{CE} = \pm 1.76$and $CL_{POP} = \pm 1.165$

The 95% confirmation interval of predicted optimal range (for confirmation run of three experiment) is:

Mean MR – CI_{CE}<MR >MR + CI_{CE}45.31< MR >48.83

The 95% confirmation interval of the predicted mean is:

Mean MR – CI_{CE}<MR >MR + CI_{CE}45.90< MR >48.24

5. Conclusion

In the experimental investigation on drill bit assisted AFM setup, a developed spline, two start helical profiles and three start helical profile have been studied. It has been found that theoverall metal removal rate is increased with three start helical abrasive flow machining of cast iron. The three process parameters viz drill bit type, number of cycle, extrusion pressure all have significant effect for the response parameter of MR .The result shows that type of rod have 33.4%, extrusion pressure have 23.46% and number of cycle have 19.53 % contribution for response parameter of MR.

References

[1] Mamilla R.K., Jain, V.K., and kumar, R.J., "Experimental investigations into rotating workpiece abrasive flow finishing (2009)" Department of Mechanical Engineering. Indian Institute Technology, Kanpur, India
[2] Rahul Kumar, R., Murtaza, Q., Walia, R.S., "Three Start Helical Abrasive Flow Machining For Ductile Materials Procedia Materials Science, (2014), Vol.6, pp. 1884–1890
[3] Rhoades L.J. "Abrasive flow machining and its use", Proc. Non-Traditional Machining Conference (1985), Cincinnati, OH, pp. 111-120.
[4] Rhoades L.J. "Abrasive flow machining-progress in productivity", SME Technical paper (1993), pp. 1-16.
[5] William R.E., and Rajurkar K.P. "Stochastic modelling and analysis of abrasive flow machining", Trans. ASME, J Engg. For Ind. (1992), Vol. 114, pp. 74-81
[6] Singh Sehijpal "Studies in metal finishing with magnetically assisted abrasive flow machining (2002)", Ph.D. Thesis. IIT Roorkee, INDIA
[7] Jain R.K. and Jain V.K. "Abrasive fine finishing processes- a review", Int. J. of Manufacturing Science and Production (1999). Vol. 2(1). pp. 55-68.
[8] Williams R.E., and Rajurkar K.P. "Monitoring of abrasive flow machining using acoustic emission", Proc. First S.M. Wu Symposium on Manufacturing Sciences (1994), Vol. 1, pp. 35-41.
[9] Przyklenk K. "Abrasive flow machining- A process for surface finishing and deburring of work ieces with a complicated shape by means of abrasive laden media", Advances in Non-Traditional /lachining, PED, ASME (1986). Vol. 22, pp. 101-110.
[10] Jain R.K., Jain V.J.C., and Dixit P.M. "Modelling of material removal and surface roughness in abrasive flow machining process"(1999). Int. J. of Machine Tool and Manufacture. Vol. 39. pp. 1903-1923
[11] Shan U.S., and Dubey A.K."Micro machining by flow of abrasives". Proceedings 17th MMTDR Conference, Warangal, India (1997). pp. 269-275
[12] Benedict G.F. "Nontraditional Manufacturing Processes (1987)", Marcel Dekker, New York
[13] Weller E.J. "Nontraditional Machining Processes" 2nd edition, *SME* (1984), pp. 52-65.
[14] Jain V.K., and Adsul S.G. "Experimental investigations into abrasive flow machining (AFM)", Int. J. of Machine Tools and Manufacture (2000). vol. 40. pp. 1003-1021.
[15] Davies P.J., and Fletcher A,J., "The assessment of rheological properties of various olyborosiloxane/grit mixture as utilized in AFM". Proc Instt. of Mech. Engrs. (1995), Vol. 209. p. 409-418
[16] Walia R. S., H. S. Shan, and P. Kumar 2006 Abrasive flow machining with additional centrifugal force applied to media. PhD Thesis, Indian Institute of Technology of Rookree, Rookree, INDIA.

Volterra Model of Silicon Controlled Rectifier

Amit Kumar Gautam [1 a)], Sudipta Majumdar[1 b)]

[1](*Electronics & Communication Engineering Department, Delhi Technological University, Shahbad Daulatpur, Delhi, 110042, India)*

[a)] Corresponding author: amitgautam.cicdu@gmail.com,
[b)] korsudipta@rediffmail.com

Abstract. This paper presents Volterra model of silicon controlled rectifier (SCR). As the SCR circuit nonlinearities appear due to transistors, we used the classical mathematical model, namely, Ebers-Moll model together with perturbation theory to obtain closed form Volterra expressions between input and output of SCR. The derived equations can be used as a model in SIMULINK for designing, analysis and development of new integrated circuits in advance before the formation of chips. The closed form expressions can also be used for circuit parameter estimation purpose. The derived equations are useful as a model in SIMULINK software, as this software provides direct access to circuit parameters.

INTRODUCTION

SCRs are very popular devices for the front ends in modern adjustable speed drive system [16]. SCR is a reliable power electronics switch and also used in high ratings [14]. It is used in bridge-type fault current limiter [6]. Power SCRs are useful for high voltage applications such as PLDMOS [3]. Electrostatic discharge (ESD) is an important reliability issue in IC applications. SCR provides good anti electrostatic device (ESD) robustness per unit length [15, 8, 4]. [5] proposed ESD protection design realized by the stacked high holding voltage silicon controlled rectifier (HHVSCR) device. SCR has been also used in high voltage ICs typically, the laterally diffused metal-oxide semiconductor (LDMOS) [8] transistor that has applications in RF and microwave communication power amplifier modules. These LDMOS transistors are used in many systems such as dc-dc converters, power management ICs, power electronic modules, automotive MCU, LED and liquid crystal display drivers. High holding voltage SCR stacking structures are useful for 60 V pins of a battery monitoring IC. SCRs are also used in continuous torus [13] to trigger the circuit. A new electrostatic discharge protection device called quad-silicon controlled rectifier has been introduced in [1]. SCR is also used in line commuted converter (LCC) for speed control of DC motors [2].

An accurate model of SCR is required for simulation of on chip circuits, though models are available based on observed experimental behaviour of the SCR, but nonlinear closed form relation between input and output of SCR is not available. Also, these models have been developed using the existing device models which makes the overall model of SCR complicate, but, the model derived in this paper helps to use single block as a model of SCR in software like SIMULINK, which gives flexibility and provides access to all the SCR circuit parameters [10]. The derived equation are useful for using the SCR model for computer aided design purposes. The SCR model is typically useful for design of electrostatic discharge (ESD) protection applications [11].

Thyristor based tap changing transformers are used in many different applications ranging from very high power aluminum potline to small hydrogen electrolyzer for gas station. In [7], it is used for ESD protection of ICS operated in K/Ka band $(26.5-40GHz)$ developed for short range communication. It is also used for ESD issue of differential low noise amplifier [9], which has applications in RF receiver. An inductor assisted light activated silicon controlled rectifier (LASCR) [7] is useful to protect the Gigahertz ICs in nano scale CMOS technologies from ESD.

Simulation plays an important part in designing of integrated circuits. It reduces the time required for designing the circuit. It also provides the verification, testing and early corrections of circuits before producing the chips. But, accurate simulation requires mathematical expressions of the circuit. Also, the nonlinearity characteristic of the device is an important parameter, so we derived closed form nonlinear expressions of SCR input and output using Ebers-Moll model and perturbation theory.

PERTURBATION THEORY

Perturbation theory is a mathematical method to find an approximate solution of the system that can be modelled as a small deformation. The method is implemented by adding a small term to the solution of exactly solvable problem.

VOLTERRA SERIES

A Volterra series gives input - output relation of a nonlinear, causal and time invariant system with fading memory. The discrete time domain Volterra series is given by

$$y(n) = \sum_{p=1}^{P}\sum_{i_1=1}^{M}\cdots\sum_{i_p=1}^{M} h_p(i_1,\ldots,i_p)\prod_{j=1}^{p} x(n-i_j) \tag{1}$$

where $x(n)$ and $y(n)$ are input and output respectively and $h_p(i_1,i_2,\ldots,i_p)$ is the p^{th} order Volterra kernels.

MATHEMATICAL ANALYSIS OF SCR USING PERTURBATION THEORY

The Figure 1 shows the circuit of SCR having input resistance R_g and output resistance R_{E_1}. We assume that the transistors Q_1 and Q_2 having current amplification factors β_1 and β_2 respectively. Triggering voltage, namely, the gate voltage V_g has been applied to transistor T_2. Sinusoidal input v has been applied through the resistor R_{E_1}. Implementation of Kirchhoff's laws give

$$-v + I_{E_1}\times R_{E_1} + v_{EB_1} + v_{CE_2} = 0 \tag{2}$$

$$-V_g + (I_{B_2} - I_{C_1})\times R_g + v_{BE_2} = 0 \tag{3}$$

$$\left(1+\frac{1}{\beta_1}\right)\times I_{C_1} - I_{E_1} = 0 \tag{4}$$

where, $v_{E_2} = 0$, $v_{B_2} = v_{C_1}$, $v_{C_2} = v_{B_1}$. So, we have three state variables, namely, v_{E_1}, v_{B_1}, v_{C_1}, I_B, I_C and I_E are the base, collector and emitter currents respectively. Eq.(2) and Eq.(3) are obtained by applying Kirchhoff voltage law (KVL). Eq.(4) is obtained by using Kirchhoff current law (KCL).

At the first stage circuit is replaced by the Ebers-Moll model [12]. Using this model, the collector I_C and emitter current I_E can be written as

$$I_C = \alpha_F I_{ES}\left(exp\frac{v_{BE}}{V_T}-1\right) - I_{CS}\left(exp\frac{v_{BC}}{V_T}-1\right) \tag{5}$$

$$I_E = -I_{ES}\left(exp\frac{v_{BE}}{V_T}-1\right) + \alpha_R I_{CS}\left(exp\frac{v_{BC}}{V_T}-1\right) \tag{6}$$

where α_F is current gain in forward mode, α_R is current gain in reverse mode, V_T is thermal voltage, I_{ES} is reverse saturation current at emitter junction and I_{CS} is the reverse saturation current at collector junction.

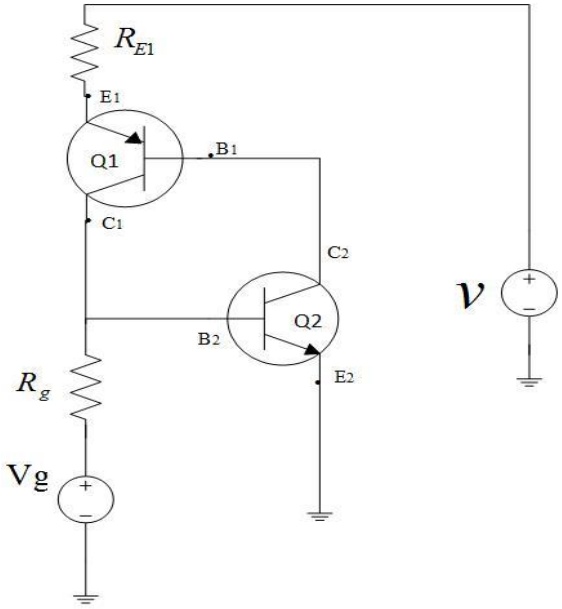

FIGURE 1. Circuit diagram of SCR using NPN and PNP transistors.

Now we separate linear and nonlinear parts of the collector and emitter currents for both transistors as given below:

$$I_{C_1} = a_{11}v_{B_1} + a_{12}v_{C_1} + a_{13}v_{E_1} + \varepsilon f_1(v_{B_1}^{(0)}, v_{C_1}^{(0)}, v_{E_1}^{(0)}, v_{B_2}^{(0)}, v_{C_2}^{(0)}, v_{E_2}^{(0)})$$
$$= a_{11}v_{B_1} + a_{12}v_{C_1} + a_{13}v_{E_1} + \varepsilon(b_{11}v_{B_1}^{2(0)} + b_{12}v_{C_1}^{2(0)} + b_{13}v_{E_1}^{2(0)} + b_{14}v_{B_1}^{(0)}v_{E_1}^{(0)} + b_{15}v_{B_1}^{(0)}v_{C_1}^{(0)}) \quad (7)$$

$$I_{C_2} = a_{21}v_{B_2} + a_{22}v_{C_2} + a_{23}v_{E_2} + \varepsilon f_2(v_{B_1}^{(0)}, v_{C_1}^{(0)}, v_{E_1}^{(0)}, v_{B_2}^{(0)}, v_{C_2}^{(0)}, v_{E_2}^{(0)})$$
$$= a_{21}v_{B_2} + a_{22}v_{C_2} + a_{23}v_{E_2} + \varepsilon(b_{21}v_{B_2}^{2(0)} + b_{22}v_{C_2}^{2(0)} + b_{23}v_{E_2}^{2(0)} + b_{24}v_{B_2}^{(0)}v_{E_2}^{(0)} + b_{25}v_{B_2}^{(0)}v_{C_2}^{(0)}) \quad (8)$$

$$I_{E_1} = c_{11}v_{B_1} + c_{12}v_{C_1} + c_{13}v_{E_1} + \varepsilon g_1(v_{B_1}^{(0)}, v_{C_1}^{(0)}, v_{E_1}^{(0)}, v_{B_2}^{(0)}, v_{C_2}^{(0)}, v_{E_2}^{(0)})$$
$$= c_{11}v_{B_1} + c_{12}v_{C_1} + c_{13}v_{E_1} + \varepsilon(d_{11}v_{B_1}^{2(0)} + d_{12}v_{C_1}^{2(0)} + d_{13}v_{E_1}^{2(0)} + d_{14}v_{B_1}^{(0)}v_{E_1}^{(0)} + d_{15}v_{B_1}^{(0)}v_{C_1}^{(0)}) \quad (9)$$

$$I_{E_2} = c_{21}v_{B_2} + c_{22}v_{C_2} + c_{23}v_{E_2} + \varepsilon g_2(v_{B_1}^{(0)}, v_{C_1}^{(0)}, v_{E_1}^{(0)}, v_{B_2}^{(0)}, v_{C_2}^{(0)}, v_{E_2}^{(0)})$$
$$= c_{21}v_{B_2} + c_{22}v_{C_2} + c_{23}v_{E_2} + \varepsilon(d_{21}v_{B_2}^{2(0)} + d_{22}v_{C_2}^{2(0)} + d_{23}v_{E_2}^{2(0)} + d_{24}v_{B_2}^{(0)}v_{E_2}^{(0)} + d_{25}v_{B_2}^{(0)}v_{C_2}^{(0)}) \quad (10)$$

where f_1, f_2, g_1 and g_2 are nonlinear functions of parameters. ε takes a small value, which takes into account the nonlinearity of the circuit. Comparing the Eq. $(5),(7),(8)$ and Eq. $(6),(9),(10)$, the values of a's and b's are:

$$a_{11} = \frac{\alpha_{F_1} I_{ES_1}}{V_T} - \frac{I_{CS_1}}{V_T}, \quad a_{12} = \frac{I_{CS_1}}{V_T}, \quad a_{13} = -\frac{\alpha_{F_1} I_{ES_1}}{V_T}, \quad a_{21} = \frac{\alpha_{F_2} I_{ES_2}}{V_T} - \frac{I_{CS_2}}{V_T}, \quad a_{22} = \frac{I_{CS_2}}{V_T},$$
$$a_{23} = -\frac{\alpha_{F_2} I_{ES_2}}{V_T}, \quad b_{11} = \frac{\alpha_{F_1} I_{ES_1}}{2V_T^2} - \frac{I_{CS_1}}{2V_T^2}, \quad b_{12} = -\frac{I_{CS_1}}{2V_T^2}, \quad b_{13} = \frac{\alpha_{F_1} I_{ES_1}}{2V_T^2}, \quad b_{21} = \frac{\alpha_{F_2} I_{ES_2}}{2V_T^2} - \frac{I_{CS_2}}{2V_T^2},$$

$$b_{22}=-\frac{I_{CS_2}}{2V_T^2},\qquad b_{23}=\frac{\alpha_{F_2}I_{ES_2}}{2V_T^2},\qquad c_{11}=\frac{\alpha_{R_1}I_{CS_1}}{V_T}-\frac{I_{ES_1}}{V_T},\qquad c_{12}=-\frac{\alpha_{R_1}I_{CS_1}}{V_T},\qquad c_{13}=\frac{I_{ES_1}}{V_T},$$

$$c_{21}=\frac{\alpha_{R_2}I_{CS_2}}{V_T}-\frac{I_{ES_2}}{V_T},\quad b_{24}=-\frac{\alpha_{R_2}I_{ES_2}}{V_T^2},\quad b_{25}=\frac{I_{ES_2}}{V_T^2},\quad d_{11}=\frac{\alpha_{R_1}I_{CS_1}}{2V_T^2}-\frac{I_{ES_1}}{2V_T^2},\quad b_{14}=-\frac{\alpha_{F_1}I_{ES_1}}{V_T^2},$$

$$b_{15}=\frac{I_{CS_1}}{V_T^2},\quad d_{21}=\frac{\alpha_{R_2}I_{CS_2}}{2V_T^2}-\frac{I_{ES_2}}{2V_T^2},\quad c_{22}=-\frac{\alpha_{R_2}I_{CS_2}}{V_T},c_{23}=\frac{I_{ES_2}}{V_T},\quad d_{12}=\frac{\alpha_{R_1}I_{CS_1}}{2V_T^2},\quad d_{13}=-\frac{I_{ES_1}}{2V_T^2},$$

$$d_{14}=\frac{I_{ES_1}}{V_T^2},\quad d_{15}=-\frac{\alpha_{R_1}I_{CS_1}}{V_T^2},\quad d_{22}=\frac{\alpha_{R_2}I_{CS_2}}{2V_T^2},\quad d_{23}=-\frac{I_{ES_2}}{2V_T^2},\quad d_{24}=\frac{I_{ES_2}}{V_T^2},\quad d_{25}=-\frac{\alpha_{R_2}I_{CS_2}}{V_T^2}.$$

where ε is assumed to be unity.

$$v_B=v_B^{(0)}+\varepsilon v_B^{(1)} \tag{11}$$

$$v_E=v_E^{(0)}+\varepsilon v_E^{(1)} \tag{12}$$

$$v_C=v_C^{(0)}+\varepsilon v_C^{(1)} \tag{13}$$

$$\begin{aligned}v={}&R_{E_1}c_{11}(v_{B1}^{(0)}+\varepsilon v_{B1}^{(1)})+R_{E_1}c_{12}(v_{C1}^{(0)}+\varepsilon v_{C1}^{(1)})+R_{E_1}c_{13}(v_{E1}^{(0)}+\varepsilon v_{E1}^{(1)})\\&+R_{E_1}\varepsilon(d_{11}v_{B1}^{2(0)}+d_{12}v_{C1}^{2(0)}+d_{13}v_{E1}^{2(0)}+d_{14}v_{B1}^{(0)}v_{E1}^{(0)}+d_{15}v_{B1}^{(0)}v_{C1}^{(0)})+(v_{E1}^{(0)}+\varepsilon v_{E1}^{(1)})\end{aligned} \tag{14}$$

$$\begin{aligned}V_g={}&\left(\frac{R_g a_{21}}{\beta_2}\right)(v_{B2}^{(0)}+\varepsilon v_{B2}^{(1)})+\left(\frac{R_g a_{22}}{\beta_2}\right)(v_{C2}^{(0)}+\varepsilon v_{C2}^{(1)})+\left(\frac{R_g}{\beta_2}\right)\varepsilon(b_{21}v_{B_2}^{2(0)}+b_{22}v_{C_2}^{2(0)}\\&+b_{23}v_{E_2}^{2(0)}+b_{24}v_{B_2}^{(0)}v_{E_2}^{(0)}+b_{25}v_{B_2}^{(0)}v_{C_2}^{(0)})-R_g a_{11}(v_{B1}^{(0)}+\varepsilon v_{B1}^{(1)})-R_g a_{12}(v_{C1}^{(0)}+\varepsilon v_{C1}^{(1)})\\&-R_g a_{13}(v_{E1}^{(0)}+\varepsilon v_{E1}^{(1)})-R_g\varepsilon(b_{11}v_{B_1}^{2(0)}+b_{12}v_{C_1}^{2(0)}+b_{13}v_{E_1}^{2(0)}+b_{14}v_{B_1}^{(0)}v_{E_1}^{(0)}+b_{15}v_{B_1}^{(0)}v_{C_1}^{(0)})\end{aligned} \tag{15}$$

$$\begin{aligned}&\left(1+\frac{1}{\beta_1}\right)[a_{11}(v_{B1}^{(0)}+\varepsilon v_{B1}^{(1)})+a_{12}(v_{C1}^{(0)}+\varepsilon v_{C1}^{(1)})+a_{13}(v_{E1}^{(0)}+\varepsilon v_{E1}^{(1)})]\\&+\varepsilon(b_{11}v_{B_1}^{2(0)}+b_{12}v_{C_1}^{2(0)}+b_{13}v_{E_1}^{2(0)}+b_{14}v_{B_1}^{(0)}v_{E_1}^{(0)}+b_{15}v_{B_1}^{(0)}v_{C_1}^{(0)})]-c_{11}(V_{B1}^{(0)}+\varepsilon v_{B1}^{(1)})\\&-c_{12}(v_{C1}^{(0)}+\varepsilon v_{C1}^{(1)})-c_{13}(v_{E1}^{(0)}+\varepsilon v_{E1}^{(1)})-\varepsilon(d_{11}v_{B_1}^{2(0)}+d_{12}v_{C_1}^{2(0)}+d_{13}v_{E_1}^{2(0)}+d_{14}v_{B_1}^{(0)}v_{E_1}^{(0)}+d_{15}v_{B_1}^{(0)}v_{C_1}^{(0)})=0\end{aligned} \tag{16}$$

On comparing the coefficient of ε in above equations, we find the linear and nonlinear parts of voltages. The linear expressions are:

$$v=R_{E_1}c_{11}v_{B1}^{(0)}+R_{E_1}c_{12}v_{C1}^{(0)}+(1+R_{E_1}c_{13})v_{E1}^{(0)} \tag{17}$$

$$V_g=R_g\left(\frac{a_{22}}{\beta_2}-a_{11}\right)v_{B1}^{(0)}+\left(1-R_g a_{12}+\frac{R_g a_{21}}{\beta_2}\right)v_{C_1}^{(0)}-R_g a_{13}v_{E_1}^{(0)} \tag{18}$$

$$\left\{(1+\frac{1}{\beta_1})a_{11}-c_{11}\right\}v_{B1}^{(0)}+\left\{(1+\frac{1}{\beta_1})a_{12}-c_{12}\right\}v_{C1}^{(0)}+\left\{(1+\frac{1}{\beta_1})a_{13}-c_{13}\right\}v_{E1}^{(0)}=0 \tag{19}$$

The state vector matrix is:

$$X_0(s) = [v_{B1}, v_{C1}, v_{E1}, v_{B2}, v_{C2}, v_{E2}]^T$$

By using the Laplace transform equation, we have solution as:

$$X_0(s) = A^{-1}(s)B(s)v(s) + A^{-1}(s)D(s)V_{CC}$$

where A is

$$A = \begin{bmatrix} R_{E_1}c_{11} & R_{E_1}c_{12} & 1 + R_{E_1}c_{13} \\ R_g\left(\frac{a_{22}}{\beta_2} - a_{11}\right) & 1 - R_g a_{12} + \frac{R_g a_{21}}{\beta_2} & -R_g a_{13} \\ \left(1 + \frac{1}{\beta_1}\right)a_{11} - c_{11} & \left(1 + \frac{1}{\beta_1}\right)a_{12} - c_{12} & \left(1 + \frac{1}{\beta_1}\right)a_{13} - c_{13} \end{bmatrix}.$$

Defining

$$H_i(s) = A^{-1}(s)B(s)$$

we get

$$v_{B1}^{(0)}(t) = h_1(t) * v + \phi_1(t) \tag{20}$$

$$v_{C1}^{(0)}(t) = h_2(t) * v + \phi_2(t) \tag{21}$$

$$v_{E1}^{(0)}(t) = h_3(t) * v + \phi_3(t) \tag{22}$$

where '*' denotes the convolution operator. Laplace transform of above equation gives

$$H_1(s) = \frac{A_{11}}{|A|}, H_2(s) = \frac{A_{12}}{|A|}, H_3(s) = \frac{A_{13}}{|A|}, \phi_1(s) = \frac{A_{21}}{|A|}V_g, \phi_2(s) = \frac{A_{22}}{|A|}V_g, \phi_3(s) = \frac{A_{23}}{|A|}V_g$$

where $\phi(t) = [\phi(t), i = 1,2,3,4]$ is the inverse Laplace transform of $A^{-1}(s)D(s)V_{CC}$. The impulse responses of the small signal equivalent model are

$$v_{B1}^{(0)}(t) = K_1\delta(t) * v + K_2\delta(t)V_g \tag{23}$$

$$v_{C1}^{(0)}(t) = K_3\delta(t) * v + K_4\delta(t)V_g \tag{24}$$

$$v_{E1}^{(0)}(t) = K_5\delta(t) * v + K_6\delta(t)V_g \tag{25}$$

where $u(t)$ is the unit step function.

$$K_1 = \frac{A_{11}}{|A|}, \quad K_2 = \frac{A_{21}}{|A|}, \quad K_3 = \frac{A_{12}}{|A|}, \quad K_4 = \frac{A_{22}}{|A|}, \quad K_5 = \frac{A_{13}}{|A|}, \quad K_6 = \frac{A_{23}}{|A|}$$

To obtain the nonlinear expressions, we compare the coefficients of ε^1

$$u_1(t) = b_{11}v_{B1}^{2(0)} + b_{12}v_{C1}^{2(0)} + b_{13}v_{E1}^{2(0)} + b_{14}v_{B1}^{(0)}v_{E1}^{(0)} + b_{15}v_{B1}^{(0)}v_{C1}^{(0)} \tag{26}$$

$$u_2(t) = b_{21}v_{B2}^{2(0)} + b_{22}v_{C2}^{2(0)} + b_{23}v_{E2}^{2(0)} + b_{24}v_{B2}^{(0)}v_{E2}^{(0)} + b_{25}v_{B2}^{(0)}v_{C2}^{(0)} \tag{27}$$

$$u_3(t) = d_{11}v_{B1}^{2(0)} + d_{12}v_{C1}^{2(0)} + d_{13}v_{E1}^{2(0)} + d_{14}v_{B1}^{(0)}v_{E1}^{(0)} + d_{15}v_{B1}^{(0)}v_{C1}^{(0)} \tag{28}$$

$$u_4(t) = d_{21}v_{B2}^{2(0)} + d_{22}v_{C2}^{2(0)} + d_{23}v_{E2}^{2(0)} + d_{24}v_{B2}^{(0)}v_{E2}^{(0)} + d_{25}v_{B2}^{(0)}v_{C2}^{(0)} \tag{29}$$

$$v_{B1}^{(1)}(s) = \left[\frac{R_g A_{21} - (1+\frac{1}{\beta_1})A_{31}}{|A|}\right]U_1(s) - \left[\frac{R_g A_{21}}{|A|\beta_2}\right]U_2(s) + \left[\frac{A_{31} - R_{E1}A_{11}}{|A|}\right]U_3(s) \tag{30}$$

$$v_{C1}^{(1)}(s) = \left[\frac{R_g A_{22} - (1+\frac{1}{\beta_1})A_{32}}{|A|}\right]U_1(s) - \left[\frac{R_g A_{22}}{|A|\beta_2}\right]U_2(s) + \left[\frac{A_{32} - R_{E1}A_{12}}{|A|}\right]U_3(s) \tag{31}$$

$$v_{E1}^{(1)}(s) = \left[\frac{R_g A_{23} - (1+\frac{1}{\beta_1})A_{33}}{|A|}\right]U_1(s) - \left[\frac{R_g A_{23}}{|A|\beta_2}\right]U_2(s) + \left[\frac{A_{33} - R_{E1}A_{13}}{|A|}\right]U_3(s) \tag{32}$$

$$v_{B1}^{(1)}(t) = K_7\delta(t) * u_1(t) + K_8\delta(t)u_2(t) + K_9\delta(t) * u_3(t) \tag{33}$$

$$v_{C1}^{(1)}(t) = K_{10}\delta(t) * u_1(t) + K_{11}\delta(t)u_2(t) + K_{12}\delta(t) * u_3(t) \tag{34}$$

$$v_{E1}^{(1)}(t) = K_{13}\delta(t) * u_1(t) + K_{14}\delta(t)u_2(t) + K_{15}\delta(t) * u_3(t) \tag{35}$$

Where

$$K_7 = \left[\frac{R_g A_{21} - (1+\frac{1}{\beta_1})A_{31}}{|A|}\right], \quad K_8 = \left[\frac{R_g A_{21}}{|A|\beta_2}\right], \quad K_9 = \left[\frac{A_{31} - R_{E1}A_{11}}{|A|}\right], \quad K_{10} = \left[\frac{R_g A_{22} - (1+\frac{1}{\beta_1})A_{32}}{|A|}\right],$$

$$K_{11} = \left[\frac{R_g A_{22}}{|A|\beta_2}\right], \quad K_{12} = \left[\frac{A_{31} - R_{E1}A_{11}}{|A|}\right], \quad K_{13} = \left[\frac{R_g A_{23} - (1+\frac{1}{\beta_1})A_{33}}{|A|}\right], \quad K_{14} = \left[\frac{R_g A_{23}}{|A|\beta_2}\right],$$

$$K_{15} = \left[\frac{A_{33} - R_{E1}A_{13}}{|A|}\right]$$

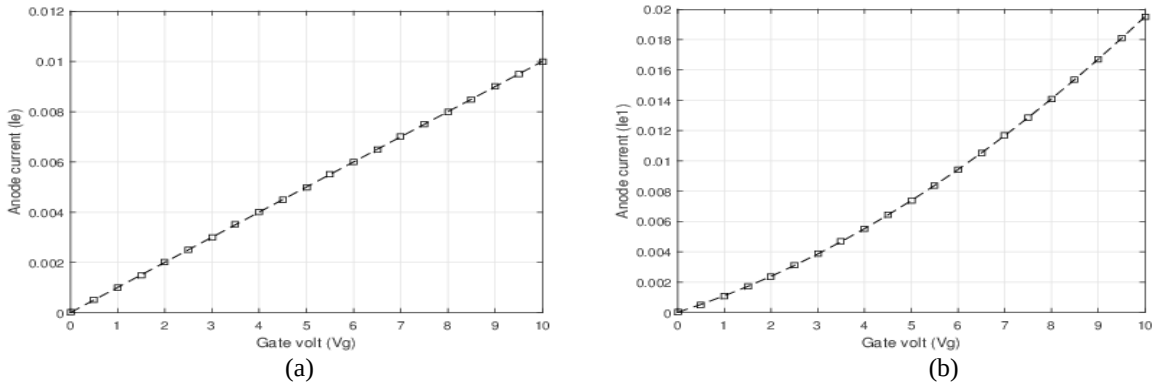

(a) (b)

FIGURE 2. Anode currents of SCR output a) First order nonlinear output; b) Zero and first order output.

SIMULATION RESULTS

The linear (zeroth order) and first order nonlinear output voltages have been plotted for different input voltages and frequencies in MATLAB as shown in Fig. 2. The percentage distortion due to linear term only has been calculated using following expression. The distortion error has been computed by varying input amplitude and frequency as given in Tab.1. Percentage distortion is defined as

$$Distortion = \frac{I_{e1} - I_e}{I_{e1}} \times 100$$

The percentage error shows the importance of nonlinearity consideration. We used the derived equations as a model in SIMULINK software to implement the half wave rectifier circuit as shown in Fig. 3(a). The input output voltages are shown in Fig. 3(b).

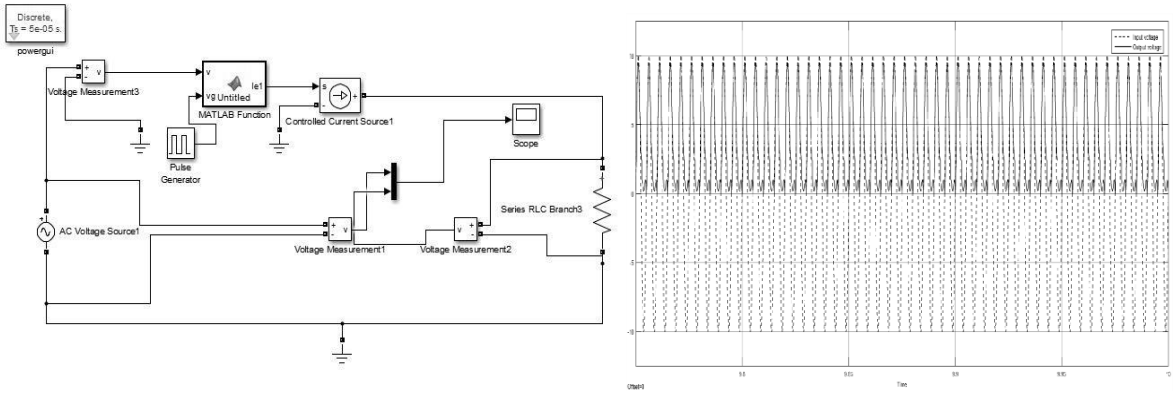

(a) (b)

FIGURE 3. a) Simulation diagram of half wave rectifier using SCR. b) Input and output voltage waveform across series RC component.

TABLE 1. Distortion error percentage for different input values

Peak to peak amplitude (Volts)	Percentage distortion error
0.0010	0.4292
0.01	0.4291
0.1	0.4248
0.5	0.4914
1.00	0.6749

CONCLUSIONS

We derived the closed form nonlinear expressions of SCR. The derived expressions have been used to plot the SCR characteristic in MATLAB. The use of closed form expressions to model SCR in SIMULINK provides direct access to circuit parameters, which is helpful for designing and analysis of new circuits.

ACKNOWLEDGMENTS

First author would like to thank University Grants Commission, Government of India for financial support in terms of research fellowship.

REFERENCES

1. F. A. Altolaguirre and M. D. Ker, *Quad-SCR device for cross-domain* (IEEE Trans. on Electron Devices. 2016), pp. 3177–3184.
2. Z. Ali, K. Saleem, N. Christofides, A. Rashid, H. Zaman, M. Tahir and U. Younas, *"Performance analysis of fuzzy logic control and six-pulse line-commutated converter in dc motor drive application "*in International Conference on IEEE (Emerging Technologies (ICET), 2015) pp. 01–06.
3. S. L. Chen and Y. T. Huang*, Design and layout strategy in the 60-V power PLDMOS with drain-end modulated engineering of reliability considerations* (IEEE Trans. on Power Electronics. 2016), pp. 5113–5121.
4. Q. Cui, J. A. Salcedo, S. Parthasarathy, Y. Zhou, J. J. Liou and J. J. Hajjar*, High-robustness and low-capacitance silicon-controlled rectifier for high-speed i/o ESD protection* (IEEE Electron Device Letters, 2013), pp. 178–180.
5. T. D. Chia, and D. K. Ming. *ESD protection design with stacked high-holding-voltage scr for high-voltage pins in a battery-monitoring Ic* (IEEE Transactions on Electron Devices, 2016), pp. 1996–2002.
6. T. Ghanbari, E. Farjah, and N. Tashakor. *Thyristor based bridge-type fault current limiter for fault current limiting capability enhancement* (IET Generation, Transmission and Distribution, 2016), pp. 2202–2215.
7. C. Y. Lin and R. K. Chang. *Design of ESD protection device for K/Ka-Band applications in nanoscale CMOS process* (IEEE Transactions on Electron Devices, 2015), pp. 2824–2829.
8. H. Liang, G. Xiaofeng, S. Dong and J. J. Liou. *RC-embedded ldmos-scr with high holding current for high-voltage i/o ESD protection* (IEEE Transactions on Device and Materials Reliability, 2015), pp. 495–499.
9. C. Y. Lin, And M. L. Fan. *Design of ESD protection diodes with embedded scr for differential lna in a 65-nm cmos process* (IEEE Transactions on microwave theory and techniques, 2014), pp. 2713–2732.
10. L. Lou, J. J. Liou, S. Dong and Y. Han. *Silicon controlled rectifier (SCR) compact modeling based on VBIC and Gummel Poon models* (Solid-State Electronics, 2009), pp. 195-203.
11. L. Lou, And J. J. Liou. *An Improved Compact Model of Silicon-Controlled Rectifier (SCR) for Electrostatic Discharge(ESD) Applications,* (IEEE Transactions on Electron Devices, 2008), pp. 3517–3524.
12. S. Majumdar and H. Parthasarathy. *Perturbation Approach to Ebers-Moll Equations for Transistor Circuit Analysis* (Circuits, Systems, and Signal Processing, 2010), pp. 431-448.
13. T. Onchi, D. Mccoll, A. Rohollahi, C. Xiao, A. Hirose, M. Dreval and S. Wolfe. *Development toward a repetitive compact torus injector* (IEEE Transactions on Plasma Science, 2016), pp. 195–200.
14. J. Solanki, N. Frohleke, J. Bocker, G. Duppe, A. Averberg and P. Wallmeier. *Voltage sequence control based high-current rectifier system* (IEEE Transactions on Industry Applications, 2015), pp. 3995-4005.
15. R. C. Sun, Z. Wang, M. Klebanov, W. Liang, J. J. Liou and D. G. Liu. *Silicon-controlled rectifier for electrostatic discharge protection solutions with minimal snapback and reduced overshoot voltage* (IEEE Electron Device Letters, 2015), pp. 424–426.
16. Y. Yang, P. Davari, F. Zare And F. Blaabjerg. *A DC-link modulation scheme with phase-shifted current control for harmonic cancellations in multidrive applications* (IEEE Transactions on Power Electronics, 2016), pp. 1837–1840.

Author's Accepted Manuscript

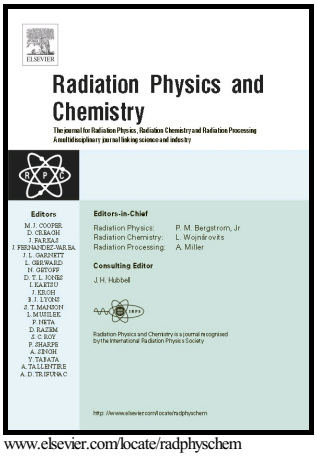

www.elsevier.com/locate/radphyschem

X-ray diffraction patterns and diffracted intensity of Kα spectral lines of He-like ions

Arun Goyal, Indu Khatri, A.K. Singh, Rinku Sharma, Man Mohan

PII: S0969-806X(17)30475-9
DOI: http://dx.doi.org/10.1016/j.radphyschem.2017.04.017
Reference: RPC7527

To appear in: *Radiation Physics and Chemistry*

Received date: 7 August 2016
Accepted date: 26 April 2017

Cite this article as: Arun Goyal, Indu Khatri, A.K. Singh, Rinku Sharma and Ma Mohan, X-ray diffraction patterns and diffracted intensity of Kα spectral lines o He-like ions, *Radiation Physics and Chemistry* http://dx.doi.org/10.1016/j.radphyschem.2017.04.017

This is a PDF file of an unedited manuscript that has been accepted fo publication. As a service to our customers we are providing this early version o the manuscript. The manuscript will undergo copyediting, typesetting, an review of the resulting galley proof before it is published in its final citable form Please note that during the production process errors may be discovered whic could affect the content, and all legal disclaimers that apply to the journal pertain

ACCEPTED MANUSCRIPT

X-ray diffraction patterns and diffracted intensity of Kα spectral lines of He-like ions

Arun Goyal[1], Indu Khatri[1], A. K. Singh[2], Rinku Sharma[3], Man Mohan[1]

[1]Department of Physics and Astrophysics, University of Delhi, Delhi-110007, India.

[2]Department of Physics, Deen Dayal Upadhyaya College, Delhi-110078, India.

[3]Department of Applied Physics, Delhi Technological University, Delhi-110042, India

arun.goyal.du@gmail.com

Accepted manuscript

Abstract

In the present paper, we have calculated fine-structure energy levels related to the configurations 1s2s, 1s2p, 1s3s and 1s3p by employing GRASP2K code. We have also computed radiative data for transitions from 1s2p $^1P_1^o$, 1s2p $^3P_2^o$, 1s2p $^3P_1^o$ and 1s2s $^3S_1$ to the ground state $1s^2$. We have made comparisons of our presented energy levels and transition wavelengths with available results compiled by NIST and good agreement is achieved. We have also provided X-ray diffraction (XRD) patterns of Kα spectral lines, namely w, x, y and z of Cu XXVIII, Kr XXXV and Mo with diffraction angle and maximum diffracted intensity which is not published elsewhere in the literature. We believe that our presented results may be beneficial in determination of the order parameter, X-ray crystallography, solid-state drug analysis, forensic science, geological and medical applications.

Keywords: X-ray diffraction, intensity, Bragg angle, energy levels, radiative data

ACCEPTED MANUSCRIPT

1. Introduction

In recent few years, the investigation and diagnosis of the spectra of high Z ions with fewer numbers of electrons has become the topic of substantial research for the determination of several plasma parameters [1-4]. Most of the radiation emitted from highly ionized high Z ions lie in the region of EUV and X-ray. The Kα transitions connecting to one electron one photon (OEOP) and two electron one photon (TEOP) for helium like and lithium like ions lies in the hard X-ray region. Since the detailed study and analysis of hard x-ray spectra of two electron and three electron systems not only provide the elaborate knowledge of astrophysical and laboratory plasma parameters, but also create a suitable platform for their applications in medical physics and in the study of X-ray crystallography, structural analysis. Therefore, in the present paper, we have studied the X-ray diffraction pattern of Kα transitions of helium like ions.

In the past, a lot of predictions based on experimental observations and theoretical calculations for Kα spectral lines for He-like ions have been published in the literature. On experimental side, early Beier et al. [5] have observed spectra of Mo XLI and Mo XL ions using low inductance vaccum-spark apparatus. Maclaren et al. [6] have studied Kα transitions in the electron beam ion trap (EBIT) X-ray spectrum of helium like Ge with LiF crystal. Briand et al. [7] and Indelicato et al. [8] have also studied the Kα spectrum of He-like Kr by adopting high-resolution crystal spectrometers. Further, the Kα spectrum of heavy ions such as Xe LIII and U XCI have been studied by Briand et al. [9, 10]. Beiersdorfer et al. [11] provided the experimental data for X-ray lines of various helium like ions using crystal spectrometer. Widmann et al. [12, 13] measured Kα transition energies for He-like Kr using EBIT with a von Hamos-type high resolution crystal spectrometer using cylindrically bent 200 LiF crystal. Chantler et al. [14, 15] measured X-ray lines of He-like V and Ti with Gaithersbug electron beam ion trap. Thorn et al. [16] also measured X-ray transitions of He-like Xe at Livermore SuperEBIT. Recently, Szabo et al. [17] studied K-shell spectra from Mo plasmas by a Transmission Crystal Spectrometer (TCS) using quartz crystal. Natrajan et al. [18-21] published theoretical data of Kα and Kβ transitions of for two possible decay modes, namely, OEOP and TEOP in He-like ions. More recently, Beiersdorfer et al. [22] reported the Kα spectrum of He-like Cu carried out at the Livermore electron beam ion trap with LiF crystal.

Although a lot of experimental and theoretical work related to the spectra of He-like ions for Kα transitions has been published in the literature, but no one has studied the X-ray diffraction pattern of He-like Cu, Kr and Mo theoretically. Therefore, in the present work, our aim is to study XRD pattern for He-like ions and to analyze the effect of intensity with the change of Bragg angle. Additionally, we have also reported the energy levels belonging to the configurations 1s2s, 1s2p, 1s3s and 1s3p with respect to the ground state $1s^2$ with increasing

Accepted manuscript

ACCEPTED MANUSCRIPT

active set approach and radiative data for transitions from 1s2p $^1P_1^o$, 1s2p $^3P_2^o$, 1s2p $^3P_1^o$ and 1s2s $^3S_1$ to the ground state $1s^2$ by employing modified version [23] of the GRASP2K code [24] based on the MCDHF method.

2. Method

2.1 Computational procedure

The description of multiconfiguration Dirac-Hartree-Fock (MCDHF) method has been explained recently in an elaborate form by Grant [25]. Therefore, we discuss only brief synopsis here. Dirac-Coulomb Hamiltonian is given by

$$H_{DC} = \sum_{i=1}^{N} (c\alpha_i . p_i + (\beta_i - 1)c^2 + V_i^N) + \sum_{i>j}^{N} \frac{1}{r_{ij}} \quad (1)$$

where α and β are 4x4 Dirac spin matrices, c is the speed of light, V^N represents the monopole part of the electron-nucleus coulomb interaction and last term denotes coulomb potential of the nucleus. An atomic state function (ASF) interpreting fine structure levels for N electron system is constructed by the linear combination of symmetrically fitted and appropriate configuration state functions (CSFs).

$$|\psi_\alpha(\mathrm{PJM})\rangle = \sum_{i=1}^{n} C_i(\delta)|\gamma_i(\mathrm{PJM})\rangle \quad (2)$$

In above equation, $\gamma_i(PJM)$ are CSFs which represent a particular state with a given parity and angular momentum (J, M). δ represents the orbital occupation numbers, population, coupling, etc. The configuration state functions γ_i are fabricated by the multiplication of one-electron Dirac orbitals. In equation (2) C_i (δ) are the expansion mixing co-efficients for each CSFs which are attained by means of diagonalization of the Dirac-Coulomb Hamiltonian, given in equation (1). After this, radial part of the Dirac orbitals and expansion mixing co-efficients are both optimized to self-consistency through relativistic self consistent field (RSCF) method. In the next step, Breit interaction

$$H_{Breit} = -\sum_{i>j}^{N} \left[\alpha_i . \alpha_j \frac{\cos(\omega_{ij} r_{ij}/c)}{r_{ij}} + (\alpha_i . \nabla_i)(\alpha_j . \nabla_j) \frac{\cos(\omega_{ij} r_{ij}/c) - 1}{\omega_{ij}^2 r_{ij}/c^2} \right] \quad (3)$$

due to the exchange of virtual photons between two electrons as well as QED corrections due to vacuum polarization and self energy effects are included by performing relativistic configuration interaction (RCI) calculations.

2.2 Calculation procedure

Accepted manuscript

ACCEPTED MANUSCRIPT

In our MCDHF calculations, we have opted extended optimal level (EOL) scheme. The radial wave functions and mixing coefficients are computed by doing optimization on the weighted average energy of the states. To construct atomic state functions, we have used the active space approach. The basic and fundamental criteria of this method is to excite electrons from filled orbitals to empty orbitals in the active set. Since the orbitals having same principle quantum number acquire similar energies. Therefore, in this work, orbitals are increased in a methodical way in order to control the convergence of our calculations and enhance the active set layer by layer. To reduce processing time as a result of the large number of orbitals, we optimized set of orbitals for even and odd parity states separately. For He-like ions, ground state and first excited state configuration is $1s^2$ and 1s2s respectively. We enlarged active set by taking into account 3s, 3p and 3d as first layer of the set. Thus, we enhanced the size of the active set as shown below until the convergence is not achieved.

AS1 = {n=3, l=0-2}

AS2 = AS1 + {n=4, l=0-3}

AS3 = AS2 + {n=5, l=0-3}

AS4 = AS3 + {n=6, l=0-3}

In our calculations, we considered single and double (SD) excitations from multi-reference set to active set and during each active set only newly added orbitals are optimized by keeping previously optimized orbitals frozen to reduce the computational time. In the next step, we have determined energies and rates from optimized orbitals. To compute transition parameters, we have employed biorthogonal transformation [26] of the ASFs.

3. Results and Discussion

3.1 Energy levels and transition parameters

Since the determination of accurate transition parameters and fine structure energy levels relies on configuration interaction and therefore, to achieve accurate results in our calculations, we have added configurations layer by layer in a simple and systematic way by adopting active set approach. In this approach, we generate jj-coupled CSFs of a particular parity and angular momentum J by doing SD excitations from MR set to the active set. In the present paper, we have presented RCI excitation energies of fine structure levels belonging to the configuration 1s2s, 1s2p, 1s3s and 1s3p relative to the ground state $1s^2$ as functions of the increasing active set for Cu XXVIII, Kr XXXV and Mo XLI. In Table 1, configurations in LSJ coupling are presented under the first column "configuration". From Table 1, one can see that contribution from n=6 is less than 0.009% and also our presented results are in good agreement with the results taken from National Institute of Standards and Technology (NIST) [27, 35-37].

Accepted manuscript

ACCEPTED MANUSCRIPT

The transition parameters such as transition probability (A_{ji}), oscillator strength (f_{ij}) and line strength (S_{ij}) for multipole transitions may be defined in terms of reduced matrix element by the expression given below

$$\left\langle \psi_\alpha(PJM) \middle\| Q_k^{(\lambda)} \middle\| \psi_\alpha(P'J'M') \right\rangle \tag{4}$$

Where $Q_k^{(\lambda)}$ is the corresponding transition operator in length or velocity gauge and $\psi_\alpha(PJM)$ and $\psi_\alpha(P'J'M')$ are initial and final atomic state functions. We are presented transition wavelength along with radiative rate, oscillator strength and line strength in length and velocity form for the transitions from 1s2p $^1P_1^o$, 1s2p $^3P_2^o$, 1s2p $^3P_1^o$ and 1s2s $^3S_1$ to the ground state $1s^2$. We use the notation w, x, y and z in first column "Line Label" in Table 2 for these transitions introduced by Gabriel [28]. In Table 2, we have also provided the values of δT for electric transitions which is an accuracy indicator and it is the deviation of ratio of length and velocity form of line strengths from unity. One can view that the value of δT is not more than 0.54 % and hence confirms the accuracy and reliability of our presented results. We have also made comparison of our computed transition wavelengths with NIST wavelengths in Table 2 and there is no major discrepancy between these two results. Moreover, the transition wavelengths of the w, x, y and z transitions lie within the hard X-ray region and may be useful in X-ray crystallography and diagnosis of X-rays etc.

3.2 Relative intensity

The theoretical expression of relative integrated intensity from X-ray diffraction (XRD) experiment is defined as [29]:

$$I^* = |F|^2 \times P \times A(\theta) \times e^{-2M} \times L.P \tag{5}$$

In the above equation, F and P are structure factor and multiplicity factor for the hkl planes. θ is the Bragg angle of diffraction for the hkl planes and $A(\theta)$ is absorbance factor. e^{-2M} is the temperature factor with M equals to $(\sin\theta/\lambda)^2$. L. P is the Lorentz polarization factor which controls the intensity of diffracted X-rays with respect to diffraction angle and it is given by

$$L.P = \frac{1 + cos^2 2\theta}{2 \times sin2\theta} \times 2\varphi \tag{6}$$

In equation (6), $\frac{1+cos^2 2\theta}{2}$ represents polarization factor due to unpolarized X-ray source and $\frac{2\varphi}{sin2\theta}$ is Lorentz factor where φ is powder ring distribution factor [30] representing geometrical fraction inclined for diffraction and detection. This factor is proportional to 1/sinθ for randomly oriented polycrystalline sample. Lithium Fluoride (LiF) is one of the most probable candidate for dosimeter applications [31] and for optical windows, prisms and lenses in UV to IR region [32]. LiF has another application in X-ray monochromator plates due to its suitable lattice spacing for an analyzer crystal [33]. Therefore, in this work, we consider LiF crystal for our

Accepted manuscript

ACCEPTED MANUSCRIPT

calculations and compute intensities of w, x, y and z transitions for Cu XXVIII, Kr XXXV and Mo XLI by making use of Bragg angle which is estimated by employing Bragg's equation for different values of miller indices for a particular transition. For sufficiently thick specimen, the irradiated area of cross-section and penetration depth balances each other [29] and therefore, effective volume irradiated by incident beam becomes constant and independent of Bragg angle. Hence, the absorption factor in the equation (6) reduces the intensity of all diffracted beams by an equal amount. Therefore, for the specimen of infinite thickness, this factor is almost unity. From the interpretation of "infinite thickness" [29, 34], the thickness of the specimen should be at least 100 to 200μm which is very few thicker than thin films modern magnetic recording media. Therefore, in the present work, we consider the LiF crystal of infinite thickness.

Previously, we have investigated the Extreme Ultraviolet (EUV) and Soft X-ray (SXR) spectral lines for high Z ions [35]. In this paper, we are interested to study X-ray diffraction pattern for high Z ions and to determine the values of miller indices for which we can get the peak of maximum intensity. In Table 2, we have presented the values of diffraction angle ($2\theta_{max}$) at which intensity of diffracted X-rays is maximum. From Table 2, we observe that with increasing nuclear charge, the value of the diffraction angle to determine maximum diffracted intensity decreases for a particular transition. In Fig. 1(a) -1(d), we have plotted X-ray diffraction pattern for w, x, y and z transitions respectively for Cu XXVIII using LiF crystals. Similarly, we have also presented the X-ray diffraction patterns for Kr XXXV and Mo XLI in Fig. 2(a)-2(d) and 3(a)-3(d) respectively. Further, from an experimental point of view, intensities of diffracted X-rays depend on various factors such as specimen, instrument, lattice imperfections and other defects. These factors not only the cause of variation of intensity but also broadens the diffraction lines. Therefore, intensities are presented in arbitrary units (a.u.).

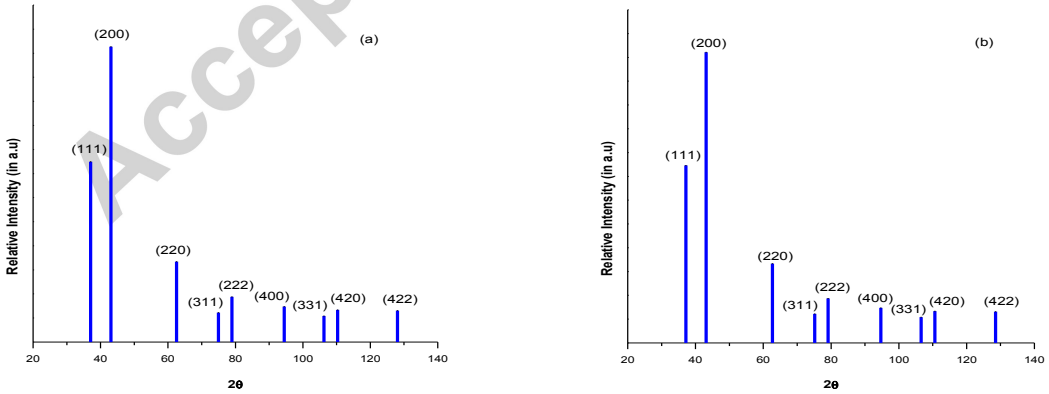

Accepted manuscript

ACCEPTED MANUSCRIPT

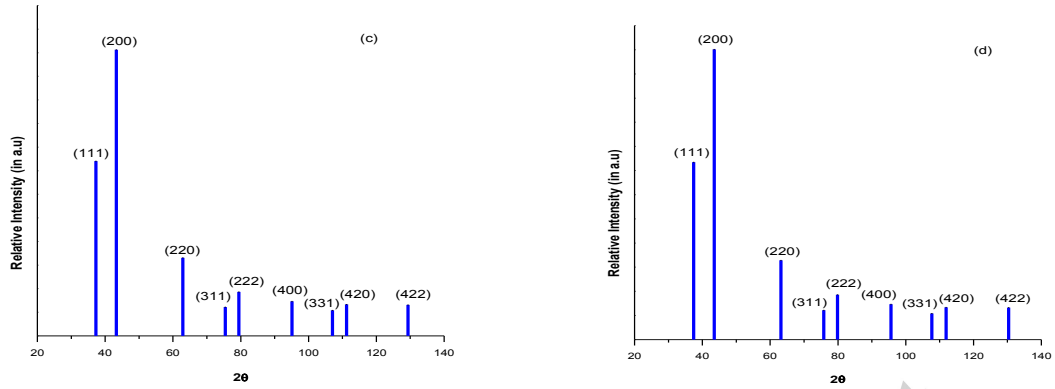

Fig. 1 X- ray diffraction pattern for transitions (a) w, (b) x, (c) y and (d) z for Cu XXVIII

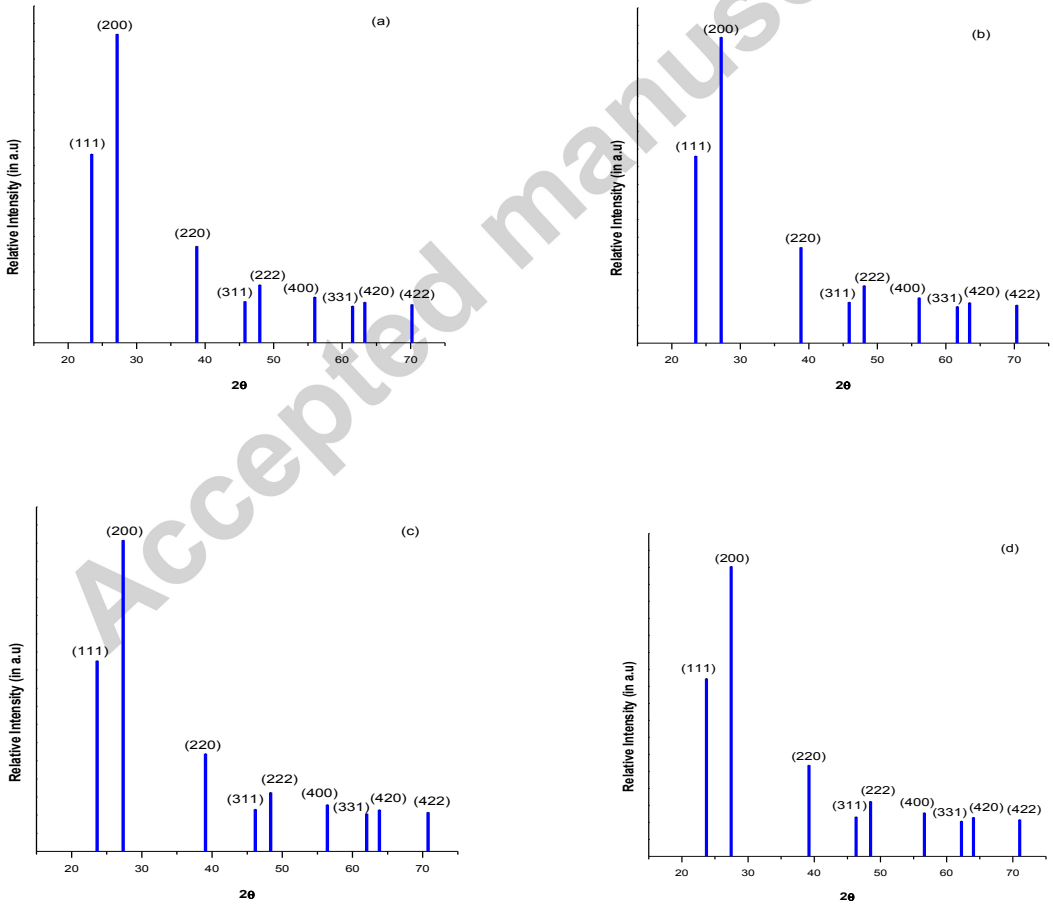

Fig. 2 X- ray diffraction pattern for transitions (a) w, (b) x, (c) y and (d) z for Kr XXXV.

Accepted manuscript

ACCEPTED MANUSCRIPT

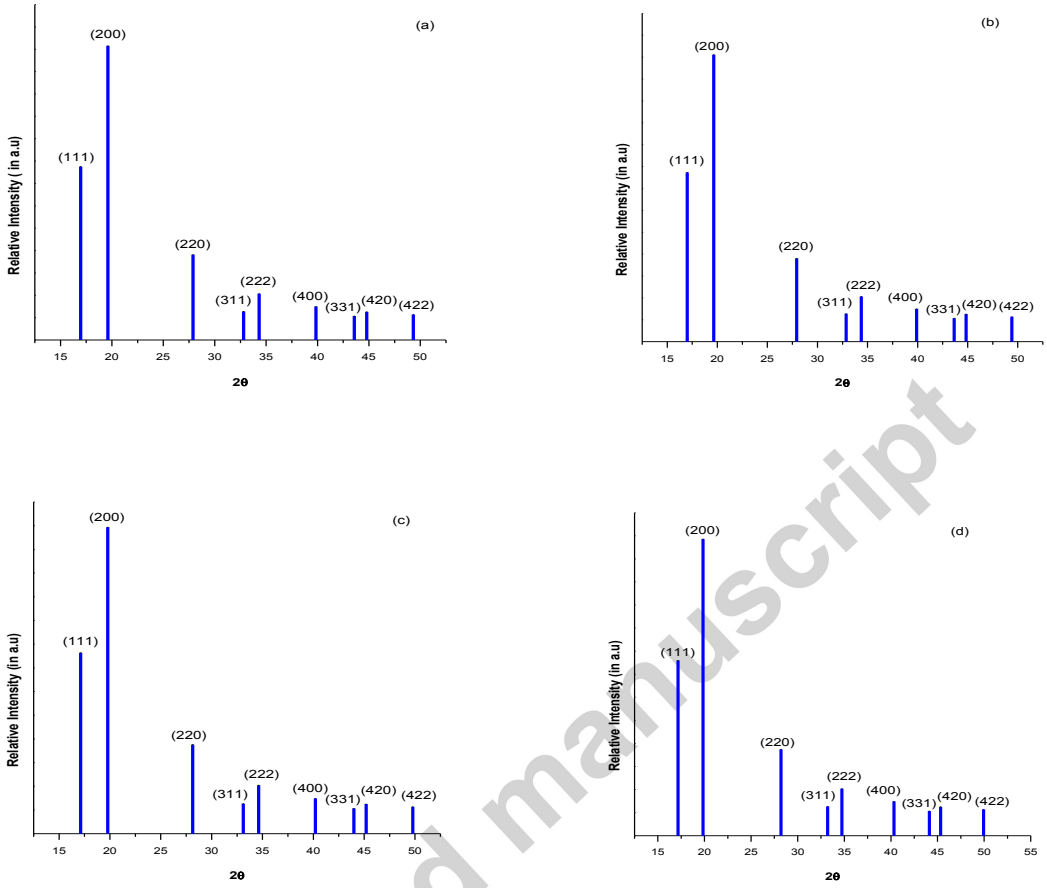

Fig. 3 X- ray diffraction pattern for transitions (a) w, (b) x, (c) y and (d) z for Mo XLI.

Accepted manuscript

From Fig. 1-3, we predict that out of nine peaks corresponding to different hkl planes for a particular transition, the (200) plane diffracts the X-rays with maximum intensity. This reveals that the number of atoms in (200) plane is more as compared to other planes due to which more number of X-rays diffracted from that plane thereby increasing the intensity corresponding to that plane. From Table 2, one can see that for a small deviation in diffraction angle between w, x, y and z transitions for a particular He-like ion, there is a large deviation in maximum intensity. Therefore, role of Bragg angle or diffraction angle is very important in XRD pattern and hence, the contribution of Lorentz-Polarization factor is also significant. Since the value of sinθ increases with θ which in turn decreases the value of temperature factor and therefore, the relative intensity of the diffracted beam decreases with Bragg angle. This is due to the fact that thermal agitation or vibration smears out the lattice planes. To the best of our knowledge, there is no data of Bragg angle and maximum intensity of XRD for LiF crystal using He-like ions in the literature. Therefore, our presented values of Bragg angles and maximum diffracted intensity

ACCEPTED MANUSCRIPT

may be beneficial for experimentalists to get maximum intensity for a particular plane which will save the their time. Further. by matching observed XRD patterns with our theoretically plotted XRD pattern, experimentalists can detect at which (hkl) plane or at which angle they are getting peaks for different He-like ions for LiF crystal. Sometimes it becomes complicated for experimentalists that which crystal they are using then by comparing with our XRD patterns, they can easily find out, the crystal is LiF or not. An XRD- pattern is a direct X-ray image of crystal structures. The parameters associated with crystal structures can be easily accessed. Once an active drug has been used, then the XRD pattern is the most convenient and cheapest method to analyze the crystal structures. For development, testing and production of drug, XRD is a prominent method for the analysis of solid state drugs. Therefore, our XRD patterns may be useful in the pharmaceutical industry. Recently, the evolution and development of XRD have completely changed the geological sciences in such a way that without XRD pattern they are not able to analyze their calculated or any observed data. Nowadays, without knowledge of XRD, geologists involved in mineralogical studies cannot characterize the individual crystal structures. Each mineral type present within a rock or soil sample is defined by the characteristic crystal structure which gives a unique XRD pattern. Therefore, by determining XRD pattern, geologists can analyze the proportion of different minerals of the sample. In this way, our calculated XRD patterns may be beneficial for geologists.

4. Conclusion

In brief, fine structure energy levels belonging to the configuration 1s2s, 1s2p, 1s3s and 1s3p relative to the ground state $1s^2$ for Cu XXVIII, Kr XXXV and Mo XLI computed from MCDHF method including QED and Breit as RCI are presented. We have chosen the active sets judiciously to achieve the convergence in our results. MCDHF results are in excellent agreement with NIST results. Transition wavelengths and radiative data for w, x, y and z transitions with an accuracy indicator dT for electric transitions are also presented. The maximum value 0.54 % of dT indicates the authenticity and accuracy of our results. Inspired by the necessity of the XRD pattern due to a number of applications in various fields, we have studied the XRD pattern of four most important transitions w, x, y and z of He-like ions by using LiF crystal. It is found that (200) plane diffracts the X-ray beam with maximum intensity. Further, the effect of Lorentz-Polarization factor and temperature factor with Bragg angle is also discussed in the present paper.

Ultimately, we believe that the study and analysis of XRD pattern with the effect of various factors on the intensity of diffracted beams in the present work may be useful in various applications such as identification of crystalline phase, Quantification of preferred orientation (texture) in thin films etc.

Accepted manuscript

ACCEPTED MANUSCRIPT

Acknowledgement

We would like to acknowledge University of Delhi, India for giving facilities and Rajan Goyal is also thankful to CSIR for financial support in the form of fellowship under CSIR JRF scheme.

References

[1] K. J. H. Phillips, C. D. Pikes, J. Lang *et al.*,Phys. Rev. A **435,** 888 (1994).
[2] V. Desclaux, P. Beiersdorfer, S. M. Kahn and V. L. Jacobs, Astrophys. J.**482,** 1076 (1997).
[3] J. F. Seely, Phys. Rev. Lett. **42,**1606 (1979).
[4] E. Kallne, J. Kallne, E. S. Marmar andJ. E. Rice, Phys. Scr. **31,** 551 (1985).
[5] R. Beier andH. J. Kunze, Z. Physik**285,** 347-352 (1978).
[6] S. MacLaren, P. Beiersdorfer, D. A. Vogel, *et al.*,Phys. Rev. A **45,** 329-332 (1992).
[7] J. P. Briand, P. Indelicato, M. Tavernier, et al., Z. Phys. A **318,** 1 (1984).
[8] P. Indelicato, J. P. Briand, M. Tavernier and D. Liesen, Z. Phys. D **2,** 249 (1986).
[9] J. P. Briand, P. Indelicato,*et al.*,Europhys. Lett. **9,**225 (1989).
[10] J. P. Briand, P. Chevallier, P. Indelicato,*et al.*,Phys. Rev. Lett. **65,** 2761 (1990).
[11] P. Beiersdorfer, M. Bitter, S. V. Goeler and K. W. Hill, Phys. Rev. A **40,** 150 (1989).
[12] K. Widmann, P. Beiersdorfer,*et al.*,Rev. Sci. Instrum. **66,** 761-763 (1994).
[13] K. Widmann, P. Beiersdorfer, V. Decaux andM. Bitter, Phys. Rev. A **53,** 2200-2205 (1996).
[14] C. T. Chantler, D. Paterson, L. T. Hudson,*et al*., Phys. Rev. A **62,** 042501 (2000).
[15] C. T. Chantler, M. N. Kinnane, J. D. Gillaspy, *et al.*,Phys. Rev. Lett.**109** 153001 (2012).
[16] D. B. Thorn, M. F. Gu, G. V. Brown, *et al.*,Phys. Rev. Lett. **103,** 163001 (2009).
[17] C. I. Szabo, P. Indelicato, L. T. Hudson, J. F. Selly andT. Ma, EPJ Web of Conf. **59** 13007 (2013).
[18] A. Natarajan andL. Natarajan, JQSRT **109,** 2281-2290 (2008).
[19] L. Natarajan andA. Natarajan, Phys. Rev. A **79,** 062513 (2009).
[20] R. Kadrekar andL. Natarajan, Phys. Rev. A **84,** 062506 (2011).
[21] L. Natarajan, Phys. Rev. A **90,** 032509 (2014).
[22] P. Beiersdorfer andG. V. Brown, Phys. Rev. A **91,**032514 (2015).
[23] P. Jö nsson, G. Gaigalas, J. Bieron,*et al.*,Comput. Phys. Commun. **184,**2197 (2013).
[24] P. Jö nsson, X. He, C. F. Fischer, I. P. Grant, Comput. Phys. Commun. **177,** 597-622 (2007).
[25] I. P. Grant, New York: Springer (2007).
[26] J. Olsen, M. R. Godefroid and P. Jö nsson, Comput. Phys. Commun. **52,** 4499-4508 (1995).

Accepted manuscript

ACCEPTED MANUSCRIPT

[27] http://physics.nist.gov/PhysRefData/ASD/levels_form.html
[28] A. H. Gabriel, Mon. Not. R. Astr. Soc. **160,** 99-119 (1972).
[29] B. D. Cullity, Elements of X-ray diffraction. London, U.K.: Addison-Wesley (1978).
[30] J. R. C. Reynolds, Clays Clay Min.**34,** 359-367 (1986).
[31] N. Salah, P. D. Sahare andA. A. Rupasov, Journal of Luminescence**124,**357–364 (2007).
[32] http://crystran.co.uk/lithium-fluoride-lif.htm
[33] http://www.almazoptics.com/LiF.htm
[34] D. C. Berry, Ph.D thesis, Carnegie Mellon Univ., Pittsburgh, PA (2008).
[35] A. Goyal, I. Khatri, S. Aggarwal, A. K. Singh and M. Mohan, JQSRT **161**, 157-170 (2015).
[36] T. Shirai, J. Sugar, A. Musgrove and W. L. Wiese, J. Phys. Chem. Ref. Data **632**(2000).
[37] E. B. Salmon, J. Phys. Chem. Ref. Data **36,** 215-386 (2007).
[38] J. Sugar andA. Musgrove, J. Phys. Chem. Ref. Data **17,** 155-239 (1988).

Accepted manuscript

ACCEPTED MANUSCRIPT

Table 1. Energies (in cm^{-1}.) of fine-structure relativistic levels of 1s2s, 1s2p, 1s3s, 1s3p relative to ground state of He-like Cu, Kr and Mo.

Configuration	Cu XXVIII			
	n=4	n=5	n=6	NIST[36]
$1s^2\ ^1S_0$	0.00	0.00	0.00	0.00
1s2s $^3S_1$	67023729	67027713	67029069	67035380
1s2p $^3P_0^o$	67290387	67295247	67297078	67303150
1s2p $^3P_1^o$	67308885	67313971	67316027	67322950
1s2s $^1S_0$	67326628	67318454	67319154	67324970
1s2p $^3P_2^o$	67505565	67510246	67512307	67519170
1s2p $^1P_1^o$	67666431	67668918	67670982	67678080
1s3s $^3S_1$	79440774	79444410	79446045	79453200
1s3p $^3P_1^o$	79519450	79520604	79522817	79532500
1s3p $^3P_0^o$	79524339	79522438	79523000	79527000
1s3s $^1S_0$	79524791	79523560	79525632	79530300
1s3p $^3P_2^o$	79576785	79582221	79584296	79591200
1s3p $^1P_1^o$	79620047	79625278	79627341	79634300
Configuration		Kr XXXV		
	n=4	n=5	n=6	NIST[37]
$1s^2\ ^1S_0$	0.00	0.00	0.00	0.00
1s2s $^3S_1$	104670758	104675268	104676675	104685170
1s2p $^3P_0^o$	105026112	105031530	105033419	105042090
1s2p $^3P_1^o$	105046893	105051641	105053756	105063130
1s2s $^1S_0$	105066477	105057932	105058642	105066500
1s2p $^3P_2^o$	105569046	105574272	105576391	105585410
1s2p $^1P_1^o$	105761270	105763742	105765863	105775630
1s3s $^3S_1$	124160882	124165040	124166727	124175700
1s3p $^3P_1^o$	124263762	124265524	124267790	124279600
1s3p $^3P_0^o$	124269129	124267677	124268248	124273800
1s3s $^1S_0$	124269636	124268995	124271125	124278000
1s3p $^3P_2^o$	124418921	124424917	124427050	124435300
1s3p $^1P_1^o$	124471034	124476831	124478954	124487500
Configuration		Mo XLI		
	n=4	n=5	n=6	NIST[36,38]
$1s^2\ ^1S_0$	0.00	0.00	0.00	0.00
1s2s $^3S_1$	143954220	143959257	143960738	143972040
1s2p $^3P_0^o$	144397981	144403972	144405949	144418220
1s2p $^3P_1^o$	144409557	144414475	144416674	144429730
1s2s $^1S_0$	144439961	144430989	144431721	144441300
1s2p $^3P_2^o$	145446671	145452448	145454653	145466040
1s2p $^1P_1^o$	145667479	145670563	145672767	145685800
1s3s $^3S_1$	170882985	170887662	170889425	170903110
1s3p $^3P_1^o$	171007210	171011692	171014037	171028620
1s3p $^3P_0^o$	171015586	171013192	171015158	171025510
1s3s $^1S_0$	171015806	171014546	171015407	171027460

Accepted manuscript

ACCEPTED MANUSCRIPT

1s3p $^3P_2^o$	171315817	171322376	171324594	171337280
1s3p $^1P_1^o$	171376468	171382767	171384974	171398130

Accepted manuscript

ACCEPTED MANUSCRIPT

Table 2. Transition data for w, x, y and z transitions for Cu XXVIII, Kr XXXV, Mo XLI from $1s^2$: wavelength λ (in Å), line strength S , oscillator strength f, transition rate A, accuracy indicator dT, diffraction angle $2\theta_{max}$, maximum diffracted intensity $I_{max.}$

Cu XXVIII											
Line Label	λ (in Å)	λ_{NIST} [36] (in Å)	A_l	A_v	f_l	f_v	S_l	S_v	dT	$2\theta_{max}$(in degree)	I_{max} (in 10^4)
w	1.478	1.477	6.85E+14	6.86E+14	6.72E-01	6.74E-01	3.27E-03	3.28E-03	0.00219	43.064	5.634
x	1.481	1.481	1.59E+10	--------	2.61E-05	----------	3.80E-02	-------	---------	43.156	5.608
y	1.486	1.485	9.90E+13	9.94E+13	9.83E-02	9.86E-02	4.80E-04	4.82E-04	0.00368	43.309	5.563
z	1.492	1.491	6.42E+08	----------	6.42E-07	----------	2.37E-04	----------	----------	43.493	5.511
Kr XXXV											
Line Label	λ (in Å)	λ_{NIST} [13] (in Å)	A_l	A_v	f_l	f_v	S_l	S_v	dT	$2\theta_{max}$(in degree)	I_{max} (in 10^4)
w	0.945	0.945	1.50E+15	1.51E+15	6.05E-01	6.07E-01	1.88E-03	1.89E-03	0.00291	27.144	15.410
x	0.947	0.947	9.33E+10	----------	6.27E-05	----------	2.38E-02	----------	----------	27.202	15.340
y	0.952	0.951	3.91E+14	3.93E+14	1.59E-01	1.60E-01	5.00E-04	5.02E-04	0.00446	27.349	15.166
z	0.955	0.955	5.88E+09	----------	2.41E-06	----------	5.70E-04	----------	----------	27.437	15.063
Mo XLI											
Line Label	λ (in Å)	λ_{NIST} [36] (in Å)	A_l	A_v	f_l	f_v	S_l	S_v	dT	$2\theta_{max}$(in degree)	I_{max} (in 10^4)
w	0.686	0.686	2.64E+15	2.65E+15	5.60E-01	5.62E-01	1.26E-03	1.27E-03	0.00338	19.616	30.384
x	0.687	0.687	3.28E+11	----------	1.16E-04	---------	1.69E-02	----------	---------	19.645	30.292
y	0.692	0.692	9.04E+14	9.09E+14	1.95E-01	1.96E-01	4.44E-04	4.46E-04	0.00541	19.789	29.837
z	0.694	0.694	2.86E+10	----------	6.22E-06	---------	1.06E-03	----------	----------	19.847	29.657

Accepted manuscript

Highlights

- X-ray diffraction (XRD) patterns of Kα spectral lines, namely w, x, y and z of He-like Cu, Kr and Mo ions are presented.
- Variation of intensity of the diffracted beam due to slight variation in diffraction angle is studied.
- The importance of Lorentz-Polarization factor and temperature factor are investigated.
- Fine-structure energy levels related to the configurations 1s2s, 1s2p, 1s3s and 1s3p are provided using MCDHF method.
- Radiative data for transitions w, x, y and z are reported.